Materials Horizons: From Nature to Nanomaterials

Sarmila Sahoo *Editor*

Recent Advances in Layered Materials and Structures

Springer

Materials Horizons: From Nature to Nanomaterials

Series Editor

Vijay Kumar Thakur, School of Aerospace, Transport and Manufacturing, Cranfield University, Cranfield, UK

Materials are an indispensable part of human civilization since the inception of life on earth. With the passage of time, innumerable new materials have been explored as well as developed and the search for new innovative materials continues briskly. Keeping in mind the immense perspectives of various classes of materials, this series aims at providing a comprehensive collection of works across the breadth of materials research at cutting-edge interface of materials science with physics, chemistry, biology and engineering.

This series covers a galaxy of materials ranging from natural materials to nanomaterials. Some of the topics include but not limited to: biological materials, biomimetic materials, ceramics, composites, coatings, functional materials, glasses, inorganic materials, inorganic-organic hybrids, metals, membranes, magnetic materials, manufacturing of materials, nanomaterials, organic materials and pigments to name a few. The series provides most timely and comprehensive information on advanced synthesis, processing, characterization, manufacturing and applications in a broad range of interdisciplinary fields in science, engineering and technology.

This series accepts both authored and edited works, including textbooks, monographs, reference works, and professional books. The books in this series will provide a deep insight into the state-of-art of Materials Horizons and serve students, academic, government and industrial scientists involved in all aspects of materials research.

More information about this series at http://www.springer.com/series/16122

Sarmila Sahoo
Editor

Recent Advances in Layered Materials and Structures

Springer

Editor
Sarmila Sahoo
Department of Civil Engineering
Heritage Institute of Technology Kolkata
Kolkata, West Bengal, India

ISSN 2524-5384 ISSN 2524-5392 (electronic)
Materials Horizons: From Nature to Nanomaterials
ISBN 978-981-33-4549-2 ISBN 978-981-33-4550-8 (eBook)
https://doi.org/10.1007/978-981-33-4550-8

This Springer imprint is published by the registered company Springer Nature Singapore Pte Ltd.
The registered company address is: 152 Beach Road, #21-01/04 Gateway East, Singapore 189721, Singapore

Preface

This book *Recent Advances in Layered Materials and Structures* provides a domain for professionals, academicians, researchers, and practitioners working in the fields of materials engineering, layered structures, reliability engineering, materials development and characterization to present their research findings, propose new methodologies, disseminate the latest findings, and learn from each other's research directions. It focuses on applied research in the areas of layered materials and structures with a bearing on inter- and intra-disciplinary research. This book contains full-length research manuscripts, insightful research, and practice notes, as well as case studies.

This book provides a forum for structural engineering educators, materials researchers, and practitioners to advance the practice and understanding of applied and theoretical aspects of structural engineering, materials engineering, and related areas. This book contains empirical and theoretical research on the development, improvement, implementation, and evaluation of layered engineering structures and materials. In addition, this book includes those research studies that show a significant contribution to the area by way of intra- and inter-disciplinary approaches in layered structural engineering as well as layered materials engineering.

This book provides a forum for a broad blend of scientific and technical papers to reflect the evolving needs of the structural engineering and materials communities dealing with layered materials and structures. Contributions deal with applications of structural engineering and mechanics principles in all areas of technology and aspire to a broad and integrated coverage of the effects of dynamic loadings and of the modeling techniques whereby the structural response to these loadings may be evaluated.

This book provides topical information on innovative, structural, and functional materials and composites with applications in various engineering fields covering the structure, properties, manufacturing process, and applications of these materials. This multidisciplinary approach is intended to professionals, students, and all those interested in the latest developments in the materials engineering field.

Chapter 1 titled "**Natural and Synthetic Layered Fillers as Advanced Matter for Improvement of Composites Performance**" discusses the main lamellar fillers applied in preparing nanocomposites; their surface modification and the implication on the properties of the nanocomposites are reported.

Chapter 2 titled "**High-Temperature Tribology of Surface Coatings**" discusses several coating deposition techniques particularly in reference to their high-temperature applicability and the different wear mechanisms observed. An effort has been made in this chapter to review the different surface coating techniques along with their research progress.

Chapter 3 titled "**Aramid Polycarbonate Resin Film Engineered Composite for Ballistic Protection: Engineered Layered Materials**" considers resin-fiber-infusion technique (RFI)-assisted fiber-reinforced-layered polycarbonate composite, which has been further assessed for its perforation and penetration attributes against mild steel core projectile. Polycarbonate composite has been examined for its thermal stability by thermo-mechanical techniques including dynamic mechanical analysis, modulated differential scanning calorimetry, thermo-gravimetric, three-point bend test, and Izod notch impact testing.

Chapter 4 titled "**Fiber-Reinforced Composites for Restituting Automobile Leaf Spring Suspension System**" reviews state of the art of composite and sandwiched-type leaf springs, natural fiber composites, additionally the life cycle assessment and finally concludes with the future scope of leaf springs for automotive applications. Synthetic fiber composites such as glass fiber-reinforced composites and carbon fiber-reinforced composites have been extensively explored for the leaf spring systems.

Chapter 5 titled "**Fabrication of Aluminium Metal Matrix Nanocomposites: An Overview**" discusses aluminum alloy-based composites for obtaining novel, tailor-made property combinations required in high-performance applications. Several solid-state and liquid-state routes are developed for manufacturing these composites which are overviewed highlighting associated prominent features and challenges. Powder metallurgy and liquid metallurgy are mostly used methods for developing aluminum nanocomposites, while their modified versions and hybrid combinations have been used in recent times. Ultrasonic stir casting is found to solve the issue of aluminum–ceramic non-wettability and particle agglomeration to great success.

Chapter 6 titled "**Aluminium Hybrid Composites Reinforced with SiC and Fly Ash Particles—Recent Developments**" provides an overview focusing on silicon carbide (ceramic)- and fly ash (industrial waste)-reinforced AMCs and HAMCs (hybrid). SiC as reinforcement imparts superior mechanical and tribological behavior in aluminum alloy. Fly ash addition into Al-matrix also has potential in lowering the production cost and density while improving strength. The influence of processing parameters, mixing percentage of reinforcements, operating conditions, and responsible tribological factors are thoroughly discussed. Finally, conclusion has been drawn to recognize the expandable area of research on AMCs or HAMCs reinforced with SiC and fly ash.

Chapter 7 titled "**Tribological and Corrosion Behavior of Al-TiB_2 Metal Matrix Composites—An Overview**" deals with Al-TiB_2 metal matrix composites (MMCs). From solid to liquid processing, there are several methods through which reinforcing phases have been incorporated into the metallic phase. A discussion regarding tribological and corrosion behavior of Al-TiB2 composites based on the existing literature has been introduced in this chapter.

Chapter 8 titled "**Mg-WC Nanocomposites—Recent Advances and Perspectives**" summarizes various aspects like fabrication route, microstructural characteristics, mechanical properties, and tribological properties of Mg nanocomposites. The effect of WC particles on microhardness, Rockwell hardness, ultimate tensile strength, and yield strength is also discussed in detail. Finally, wear mechanisms related to different experimental conditions are also mentioned.

Chapter 9 titled "**Understanding Fabrication and Properties of Magnesium Matrix Nanocomposites**" presents a state-of-the-art review of available literatures to discuss the role of various factors on mechanical properties, tribological properties, and corrosion behavior of magnesium-based nanocomposites. In this chapter, liquid metallurgy-based primary processing methods and secondary methods are discussed in detail. Strengthening mechanisms between particle and matrix metal are also presented. The effect of particles on mechanical, tribological, and corrosion behavior is discussed.

Chapter 10 titled "**Dynamics of Axially Functionally Graded Timoshenko Beams on Linear Elastic Foundation**" studies dynamic behavior of axially functionally graded (AFG) non-uniform Timoshenko beam on linear elastic foundation. Geometric nonlinearity is induced in the system through Von Karman's nonlinear strain–displacement relations. The material model is chosen in such a way that exhibits continuous gradation of material properties along the length of the beam. The free vibration study is carried out on statically deflected configuration to determine the backbone curves of the system. Forced vibration problem is solved by assuming dynamic equilibrium under maximum amplitude of excitation. Frequency and amplitude of the harmonic excitation are the parameters that control system response.

Chapter 11 titled "**Dynamic Sensitivity Analysis of Random Impact Behaviour of Hybrid Cylindrical Shells**" investigates the moment-independent sensitivity analysis for hybrid sandwich structures (having cylindrical shell geometry) subjected to low-velocity impact. The probabilistic study is performed for the transient impact response of the structure which in turn is utilized to assess the sensitiveness of the parameters. In order to achieve the computational efficiency, polynomial chaos expansion meta-model is used in conjunction with Monte Carlo simulation approach. The results illustrate the parameters which significantly affect the transient impact response of the structure.

Chapter 12 titled "**Statistical Energy Analysis Parameters Investigation of Composite Specimens Employing Theoretical and Experimental Approach**" considers the loss in transmission of sound and vibration through the complex structural-acoustic systems. Statistical energy analysis (SEA) method was proved to be an effective tool for predicting the response of such complex systems at the early

design stage of the product. In the case of composite plates, the effects of different fiber orientations on the SEA parameters have been studied.

In Chap. 13 titled "**Surrogate Model Validation and Verification for Random Failure Analyses of Composites**," multivariate adaptive regression splines (MARS) is explored as a surrogate model in conjunction with Monte Carlo simulation (MCS) to analyze the random first-ply failure loads of graphite–epoxy-laminated composite plates. The five failure criteria, namely maximum strain theory, maximum stress theory, Tsai–Hill theory, Tsai–Wu theory, and Hoffman theory, are considered. A concise investigation is carried out to examine the capability of MARS model for efficiently predicting the first-ply failure loads. Comparative results are presented using scatter plots and probability density function plots to access the prediction capability with respect to direct MCS.

Chapter 14 titled "**Iosipescu Shear Test of Glass Fibre/epoxy Composite with Different Delamination Geometries: A Shear Behaviour Study**" investigates shear behavior of delaminated as well as non-delaminated GFRP specimen both experimentally and numerically. Iosipescu shear test has been performed on GFRP specimen for understanding the role of delaminations and its geometry on the shear behavior of the specimen.

Chapter 15 titled "**Parametric Study of Dispersed Laminated Composite Plates**" simulates laminated composite plates with one core layer and two surface layers in a comprehensive para**m**etric study. The main objective is to investigate the variation of the buckling load with respect to changes in the stacking sequence. The stacking sequences are ranked according to their corresponding buckling loads, and the best-performing ones are subjected to a closer analysis. The visualization of the results showed that for any given stack of fiber orientation angles, the stacking sequence of the ply thicknesses can have a significant impact on the structural performance.

Chapter 16 titled "**Modeling Fracture in Straight Fiber and Tow-Steered Fiber Laminated Composites—A Phase Field Approach**" deals with the fracture characteristics of laminated composites using the framework of the phase-field method. The influence of the fiber orientation, tow angle, inter-fiber spacing on the peak load carrying capacity, and the crack morphology are systematically studied.

Chapter 17 titled "**An Iso-Geometric Analysis of Tow-Steered Composite Laminates: Free Vibration, Mechanical Buckling and Linear Flutter Analysis**" employs an iso-geometric analysis framework to study vibration, buckling, and linear flutter analysis of tow-steered composite laminates. It systematically considers the effect of plate thickness, spatial variation of the fiber, and the boundary conditions.

The editor would like to thank all the authors for contributing their valuable research work as chapters for this book. The authors submitted the chapters and responded for the revisions on time which could make it possible to publish this book on time. The editor is thankful to all the reviewers who painstakingly reviewed all the submissions and the revisions, wherever needed. Finally, the editor

is thankful to Springer, for allowing publication of this book, and also to the publishing editor and other team members at Springer for their motivation, encouragement, advice, and support provided during organization of this edited volume that led to the publication of this book.

Kolkata, India Sarmila Sahoo
August 2020

Contents

About the Editor

Dr. Sarmila Sahoo is currently an Associate Professor at the Department of Civil Engineering, Heritage Institute of Technology, Kolkata, India. Dr. Sahoo received Bachelor of Engineeing (Civil Engineering) from Bengal Engineering College (D.U.), Shibpur (presently, Indian Institute of Engineering Science and Technology, Shibpur), Master of Civil Engineering (Structural Engineering) from Jadavpur University and Doctor of Philosophy (Engineering) from Jadavpur University. A national scholarship holder throughout career, she was the recipient of GATE fellowship from MHRD and Senior Research Fellowship from Council of Scientific and Industrial Research, Govt. of India. She has worked in Design and Development Unit at Conveyor and Ropeway Services Pvt. Ltd. She has earlier taught Civil Engineering at Meghnad Saha Institute of Technology, Kolkata. Her research interests are finite elements method, vibration of plates and shells, functionally graded materials, composite materials, corrosion protection of construction steel. She is actively engaged in research and currently supervising a number of research students for their doctoral thesis. She has published over 80 research articles in international journals and conference proceedings. She has authored a book with Springer and a number of book chapters so far. She is associated with the editorial and review board of a number of international journals. She is a member of International Association of Engineers.

Chapter 1
Natural and Synthetic Layered Fillers as Advanced Matter for Improvement of Composites Performance

Daniela de França da Silva Freitas and Luis Claudio Mendes

1 Introduction

Reinforcing polymers using inorganic or organic fillers is an usual practice obtain polymeric materials called composites. For decades, the investigations on polymeric composites have been limited to microscale with respect to the filler dimension. From the second half of the 1980s, the polymeric nanocomposites emerged as a material in which one of the filler dimensions is at the nanometer scale. Nanoparticles reveal great interest due to larger superficial area/volume unit ratio allowing an increase of the interactions in molecular level between polymer and filler particle. Because of this, a material with higher properties than pristine polymers and any conventional microcomposites can be achieved [35].

Polymeric nanocomposites are an important category of materials that has been showing outstanding properties that is not expected when fillers are used in macro. Intensive research in this area have been done and attracted the researches and industry interest regarding to their promising potential for many applications and to solve nowadays problems. Polymer nanocomposites comprises of a polymer matrix with nanoparticles well dispersed in a way to enhance adhesion between phases. The decrease in size from microscale to nanoscale can promote to a higher surface area to volume that makes big changes in chemistry and physics of the materials making the properties tunable.

Lamellar fillers are materials of great study to obtain nanocomposites, and for a long time, clays and organoclays were the best choice. However, the great difficulty of incorporation in nonpolar polymers generates an incompatibility of the charge with the polymeric matrix and thus making it difficult to obtain nanocomposites. This leads to the use of compatibilizers as a way to overcome this problem. Also,

D. de F. da S. Freitas · L. C. Mendes (✉)
Instituto de Macromoléculas Professora Eloisa Mano (IMA-UFRJ), Rio de Janeiro, Brazil
e-mail: lcmendes@ima.ufrj.br

S. Sahoo (ed.), *Recent Advances in Layered Materials and Structures*,
Materials Horizons: From Nature to Nanomaterials,
https://doi.org/10.1007/978-981-33-4550-8_1

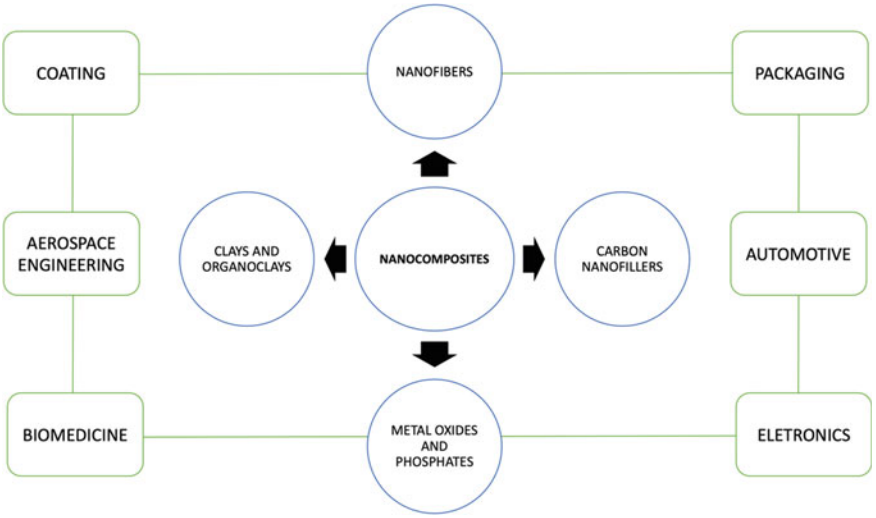

Fig. 1 Trends in nanofillers and application areas for nanocomposites

with time, it achieved nanofillers that was able to improve polymer properties better than the traditional clays.

Usually, with inorganic nature, lamellar fillers are recognized due to their anisotropic properties and hydrophilicity. For improvement of their compatibility with polymer matrix, they require prior chemical modification into the lamellae, technique known as intercalation. It is very common the intercalation of organic molecules into lamellar galleries. Several reaction pathways lead to modified fillers with new chemical and physicochemical characteristics. Thus, inorganic–organic hybrid structures improve their dispersibility and compatibility with the polymeric matrix enhancing the nanocomposite properties and performance [10, 18, 28].

Demand for improvements is always emerging from different areas, as shown in Fig. 1. According to MarketsandMarkets study, the projection is to double the actual nanocomposites market worldwide up to 2024. This is due to the high demand in specific areas like packaging, aerospace, automotive, and electronics industry [51].

This chapter addresses the importance of some natural and synthetic layered fillers—graphene, double lamellar hydroxides, phyllosilicates and tetravalent metal phosphates—with or without chemical modification and their influence on the improvement of composite performance.

2 Nanofillers

An overview concerns the application of graphene, double-layered hydroxides, phyllosilicates, and tetravalent metal phosphates, and as nanofillers for polymeric composites is presented.

2.1 Graphene

Graphite is a lamellar anisotropic material. Each lamella has a carbon atom bonded to three other atoms by covalent bond forming a continuous series of hexagons, as shown in Fig. 2. The unpaired electron interacts to another one located at the adjacent plane through van der Waals interactions, thus allowing its electrical conductivity. Although it has micrometer dimension, its lamel1.la spacing is around 0.335 nm. It can be used as natural, intercalated, or expanded material. Chemical modification may be accomplished in order to increase the interlamellar space. After releasing the intercalating compounds, the exfoliated graphite presents itself as randomly separated sheets called graphene [57].

For intercalating graphite structure, pre-expansion of the filler galleries with molecules and/or ions allows the increase of interlamellar spacing without exchange reactions between host graphite and guest intercalating agent. The intercalation induces high degree of ordering along the direction perpendicular to the planes, forming a superstructure consisting of single graphite lamellae superimposed with intercalated ones [39, 42]. Thermal expansion of the intercalated graphite was

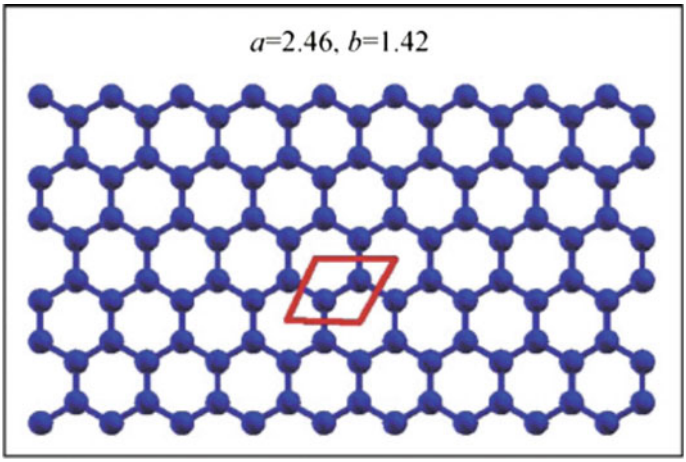

Fig. 2 Graphene structure in top view, where the red square mark the structure unit cell. The numbers are the lattice constant (**a**) and the bond length (**b**) in Angstron [31] (https://creativecommons.org/licenses/by/4.0)

performed changing its micrometer size to nanometer one. Expansion from 0.34 to 0.54 nm was reached after graphite intercalation with potassium molecules [69, 75].

A widely used carbon derivative is graphene oxide (GO), used in oxidized form as a precursor for carbon-based materials due to its powerful dispersibility and processability. The Hummers method is the most used method of synthesis based on mineral graphite flakes that suffer thermal oxidation to accomplish lamellae exfoliation. The resulting material possess high density of groupments like epoxy and hydroxyl groups situated in carbon sheet and carboxyl groups disposed around the edges. This groups are heterogeneous distributed in nanoscale, and after chemical reduction to graphene, they are completely dissipated [30].

Graphite can be used as a nanometer material for nanocomposite use, with similar clays properties characteristics but with electron conduction quality. A graphite is not capable of ion exchange, but when oxidized is able to add parts of organic atoms in interlamellar space. Due to its electron conduction property, it can be utilized as a nanofiller to obtain a conductive nanocomposite [67].

The most common way to modify the graphite structure is through the mixing solution of nitric acid and sulfuric acid. It is believed that the first acid act as oxidizing agent while sulfuric acid as intercalating one. The acid solution leads to a mixing of non-oxidized (aromatic) graphite randomly distributed and six aliphatic rings attached with hydroxyl—located at above and below of each lamella—and carboxyl groups—as edges. After that, calcination at high temperature and different times conducted to an expanded structure. The original XRD diffraction peak disappears, and a new one emerges with higher interlamellar spacing. A work performed by Chen et al. and Pan et al. investigated the transformation of natural graphite into expanded graphite by acid treatment. The authors used the traditional acid treatment, and the mixture was heated in muffle at different times Chen and colleagues obtained a basal spacing of oxidized graphite of the order of 0.34 nm [13, 56]. The Research Groups of Burakowski [9], Uhl [67], Schniepp [63], and McAllister [47] reported having been successful in the process of graphite expansion by the total disappearance of the diffraction peaks (XRD) after fast heat of the material. Full oxidation was detected observing the extinction of the peak equivalent to 0.34 nm graphite interlamellar spacement and the emergence of a peak at 0.65–0.75 nm equivalent that varied with the water content of the material.

Several authors have reported blending expanded graphite with polymers to obtain nanocomposites. Satisfactory results are mentioned using a small fraction of expanded graphite for polymers such as PMMA, Nylon 6, PS, and PS-PMMA, but the presence of aggregates usually occurs due to improper monomers or polymers intercalation within galleries formed by graphite sheets [13].

The use of biosensors with high sensitiveness and selectivity in a low range of detection (picomolar or nanomolar biomolecules concentrations) are significant to the healthcare industry and medicine to evaluate physiological and metabolic parameters. The discovery of graphene accelerated the researches on producing carbon electrodes because it is cheaper and brings unique properties, like high mobility, specific superficial area, enhanced electrical conductivity, optical transparency, and flexibility. Chemical functionalization is favored by oxygenated groupments present

in the filler that turns GO sheets highly hydrophilic, and various types of inorganic nanoparticles can be combined, like semiconducting nanoparticles, metal oxides, biomolecules, polymers, and others [34].

Similar to many others fillers, the use of graphene to increase properties of polymer is accomplished with the equal spread of filler in the matrix. Poorly dispersed graphene can act as stress propagator, which decline properties, e.g. mechanical properties. Functionalization is usually performed because of strong van der Waals dispersion force that promotes attraction between graphene sheets, inducing reaggregation [70].

Yasmin and colleagues studied obtaining epoxy resin nanocomposites and expanded graphite. X-ray showed the characteristic graphite peak at 26.38°. The authors observed a higher elastic modulus and a lower tensile strength comparing to pure epoxy resin [75]. In a study by Kim and co-authors, natural and oxidized graphite were mixed with polyurethane in the molten state. For the pure graphite nanocomposite, it was observed the presence of a tactoid-like structure, indicating agglomeration of the lamellae, besides the presence of the characteristic peak in the graphite X-ray diffractogram. For the oxidized graphite composite, the scanning electron microscopy showed an adequate nanofiller dispersion in the polymer matrix, and XRD showed the absence of diffraction peaks above 3.5°, indicating an exfoliated structure. Regarding the properties, both the electrical conductivity and the elastic modulus increased, using 1.6% by volume of oxidized graphite [33].

Graphene nanosheets are extraordinarily effective when functionalized in order to promote enhancement in properties like fracture toughness, stiffness, strength, and fatigue resistance using considerably low filler quantities compared to the usual nanotubes and clays fillers. This behavior is due to their better geometry, superficial area, and ability to form enhanced adhesion between filler and polymer chain. Rafiee et al. disclose about a good decrease in crack growth rate for epoxy nanocomposite compared to the pure polymer in many stress intensity factor amplitudes. The authors used partially oxygenated graphene sheets obtained by rapid thermal expansion, and they verified that at 0.125 %wt of filler, the Young's modulus of the nanocomposite is up to 50% greater than pure epoxy [59].

For many years, carbon nanotubes were put in the front line of polymeric nanocomposite studies. The emerging interest in graphene was inspired by the chance to improve some properties in comparison with the nanotubes, like the use in membrane technology. Polymer/graphene nanocomposite performance are dependent on the nanofiller and overall nanocomposite structure and the interactions present in the polymer/graphene system. Filler and polymer interaction using graphene imply in electrostatic forces, hydrophilic interaction, hydrogen or covalent bonding, etc. The π-π interaction between the delocalized electrons of aromatic polymers and graphene also is fundamental to evaluate the properties of the obtained nanocomposites [32].

Chang studied poly(vinyl alcohol) (PVA) nanocomposites using graphene sheets organomodified with hexadecylamine (HDA-GSs) as shown in Fig. 3. The authors obtained films using PVA solutions and the filler added was in the range of 0–10 wt%. A well-dispersed filler was obtained for the hybrid containing 5 wt% of nanofiller;

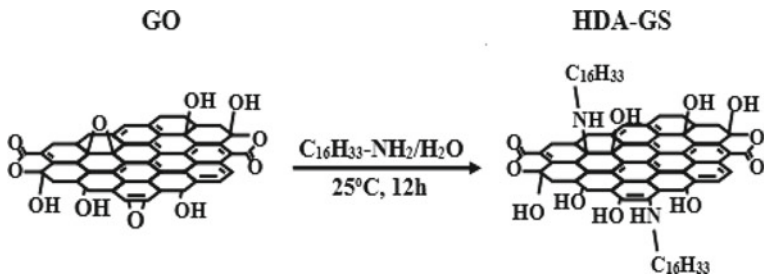

Fig. 3 GO and HDA-GS chemical structures [12]. https://creativecommons.org/licenses/by/4.0/

however, it was observed the presence of aggregates using content of 10 wt% of nanofiller [12].

Yang et al. obtained poly(vinyl alcohol) nanocomposites films using graphene with reducted graphite oxide. They used two methods, the first one using hydrazine after the mixture of GO and PVA solution and a second one oxidizing first the GO prior to add in the PVA solution. It was observed that the first film was smooth, uniform, and flexible, but the second one showed black graphene aggregations, suggesting that the graphene was not well dispersed in the matrix; however, it was discussed the obtaining of graphene aligned and dispersed in poly(vinyl alcohol) (PVA) with notable molecular level interlinkages. This behavior was attributed to a higher glass transition temperature and lower crystallization degree. The graphene range was of 0.5% up to 3.5 wt%. It was observed that the PVA films containing graphene were more ductile and stronger with a significantly lower the crystallinity with nanofiller addition. It was also observed an increase in mechanical properties compared with pure PVA [73].

2.2 Layered Double Hydroxides

Layered double hydroxides (LDH) or anionic clays refer to natural or synthetic mineral containing anionic species into interlamellar region. The layered double hydroxides are constituted by octahedral units having cations coordinated to the hydroxyl groups and linked together through the edges. The lamellae are connected to each other by van der Waals forces and hydrogen bonds. At hydroxide layer, isomorphic trivalent cations replace divalent ones leading to residual charge compensated by the intercalation of hydrated anions. The lamellae are held attached by electrostatic forces from positive charges in the lamellae and the interlamellar anions. Additionally, water molecules are on the edge of the hydroxide layers, and/or hydrogen bond interlamellar anions may occur aiding the structural cohesion [5, 17, 37, 72].

Mineral anionic clays are relatively rare and are associated with metamorphic formations. Their synthesis can be performed at low-cost routes from metal salts dilute solutions with easy isolation and high purity. The major synthesis route

involves nucleation and growth of metallic hydroxide layers by the mix of saline solution with two metal ions in the proximity of aimed anions. Essentially, the properties depend on the mixing procedure and reaction time. Effectively, once the anions cannot withdraw metal ions from the layer, the nature of these anions is free to choice [5, 16, 17].

Replacement of interlamellar inorganic anions by organophilic anions—salts of anionic fatty acids or surfactants—in non-aqueous solvents has been studied by several research groups in view of the delamination of HDL with a decrease in intermolecular interactions and modification of anionic clay surface properties [38]. Figure 4 displays the most usual pathway to obtain a polymer intercalated in inorganic lamellae, suggested by Leroux [37].

Anionic clays are not easily intercalated to neutral species. The difficulty is due to a stronger interaction between the layers and the interlamellar ion in the anionic clays. Insertion is possible as long as an initial exchange is made with a bulky anion or with molecules containing clusters that allow anionic exchange or association. This action increases lamellar spacing, and the entry of neutral species is facilitated [68, 16].

The intercalation of zinc dodecyl sulfate on LDH was accomplished by Adachi-Pagano and collaborators using zinc dodecyl sulfate in butanol under reflux. With chemical formula $[Zn_2\ Al\ (OH)_6]\ [C_{12}H_{25}SO_4 \cdot nH_2O]$ after intercalation, the layers were dispersed and oriented after solvent evaporation or lyophilization [1].

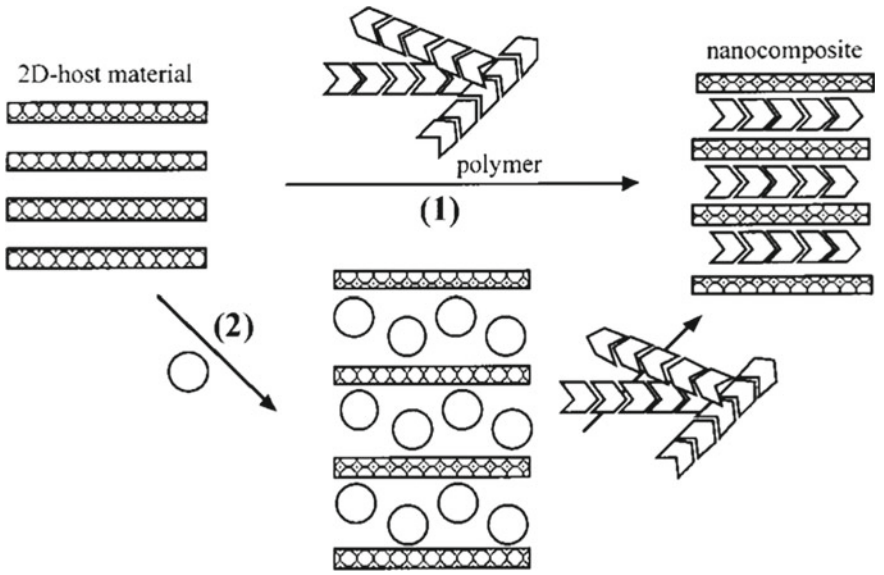

Fig. 4 Pathway for nanocomposite preparation by (1) direct polymer–polymer exchange or (2) prior intercalation of the lamellae before polymer insertion. Reprinted (adapted) with permission from [37]. Copyright © 2001 American Chemical Society

LDH with a mixture of hydrated magnesium and aluminum salts plus acid glycine was synthesized by Hibino and Jones. LDH possesses intercalated glycinate anion being exfoliated by using of formamide at room temperature [29].

Adding double lamellar hydroxides to polymers such as PVC, polypropylene, and ABS can bring benefits—increased flame resistance, thermal stability, and ultraviolet radiation [16]. Polymer/HDL composites can be used in areas, as electrocatalysis, used as protonic conductors, electrodes, batteries, photosensitive materials, catalysts, and others [37].

Chen et al. developed nanocomposites of LLDPE and ZnAl layered double hydroxides by refluxing xylene solution, as shown in Fig. 5. It was observed a slower degradation rate before 400 °C with the nanofiller use. Also, it was observed an improvement in thermal properties of exfoliated nanocomposites, attributed by the authors to a nanofiller dispersion in molecular scale in the LLDPE matrix [14].

Qiu and colleagues investigated polystyrene and HDL nanocomposites synthesized with zinc and aluminum salts. They observed that lamellae with 1 nm were scattered unevenly in the polymer matrix. Increased basal spacing was detected—2.54 to 3.7 nm, indicating an interspersed structure. Improvement in thermal stability was also observed [58].

Polystyrene (PS) and modified Co-Al layered double hydroxide (LDH) nanocomposites by solvent blending technique was investigated by Suresh et al. The authors observed an indicative of an exfoliated composite by XRD technique, while micrography images suggested that some intercalated structures are present in the PS

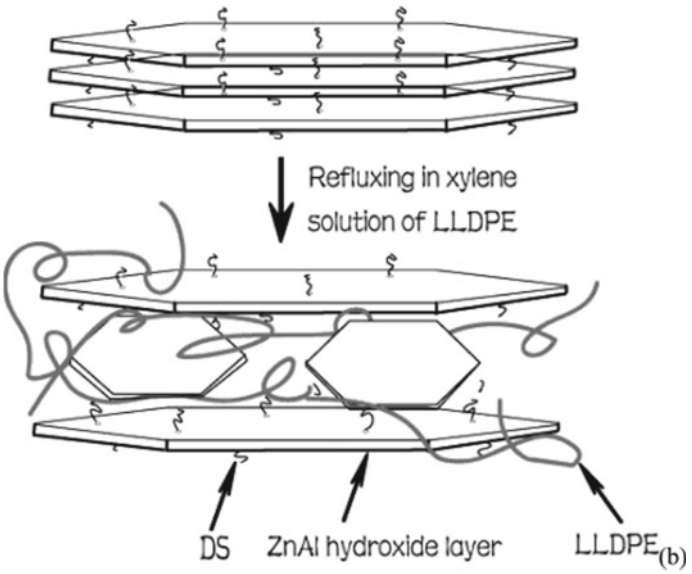

Fig. 5 Sandwiched structure formed by intercalation of LLDPE and ZnAl hydroxide layer from LDH. Reprinted (adapted) with permission from [14]. Copyright© (2004) American Chemical Society

nanocomposites using a higher filler content. The thermal stability of the composites was increased in comparison with pure PS, and it was observed a higher thermal degradation (T_d) temperature in the nanocomposites using with 7 wt% of layered hydroxide, with an increase up to 28.5 °C [65].

A work from Gao and co-authors studied the effect of layered double hydroxides modified with terephthalate (TA-LDHs) to enhance barrier properties of poly(ethylene terephthalate) for packaging industry, particularly liquid foods. The authors affirmed that the composites using 1 or 2 wt% nanofiller presented a behavior of a partially exfoliated nanocomposites, while with higher content of TA-LDHs (5%wt), it was observed an intercalated structure. Regarding the mechanical properties, it was observed that the composites with 2 wt% of nanofiller promoted an improve up to 29.4% in the tensile strength, and the Young's modulus was improved up by 38.9% compared with pristine PET. The oxygen permeation of the composites obtained using 2 wt% of nanofiller by the way was reduced by 46.2% [22].

Layered double hydroxides modified with stearic acid was studied by Mhlabeni and co-authors using matrix of poly(lactic acid) (PLA)/poly[(butylene succinate)-co-adipate] (PBSA) to obtain nanocomposites in the molten state. The authors observed an enhancement of properties like mechanical, thermal, and O2 permeability using low content of nanofiller (0.5 wt%), regarding a better interaction of PLA/PBSA matrix and nanoparticles [50].

Samitha et al. studied the nanofabrics of poly(vinylidene fluoride) (PVDF) and Ca–Al layered double hydroxide (LDH) by electrospinning. It was observed by the authors that the interaction between polymer and LDH promoted by electrospinning technique helps the β phase nucleation up to 82.79%, which seems to be a adequate for application piezoelectric generators. The material showed high dielectric constant and low dielectric loss, and it was attributed to a interfacial polarization at low-frequency using LDH as nanofiller [61].

2.3 Phyllosilicates

Phyllosilicates are hydrated aluminum, iron, and magnesium silicate microparticles characterized by a layered structure separated by compensating cations. Extremely stable compounds, they are formed by TO_4-type tetrahedral structural units, where *T* is a tetravalent or trivalent cation (usually silicon, aluminum, or iron), and also have water molecules adsorbed on the structure. The layer consists of hexagons containing six connected tetrahedra, and at the vertices, there are free valence oxygen atoms orientated in the same direction. It is classified as phyllosilicate when the tetrahedral arrangement is in lamellar form [20, 43].

Belonging to the class of smectites, montmorillonite (MMT) is the most studied phyllosilicates for nanocomposite. Its spatial arrangement consists of two tetrahedral silicates (SiO) lamellae and one central octahedral alumina lamella. Among the lamellar space, adsorbed water molecules and exchangeable cations such as Ca^{++}, Mg^{++}, and/or Na^{+} coexist. When Na^{+} is the predominant cation, the smectites is

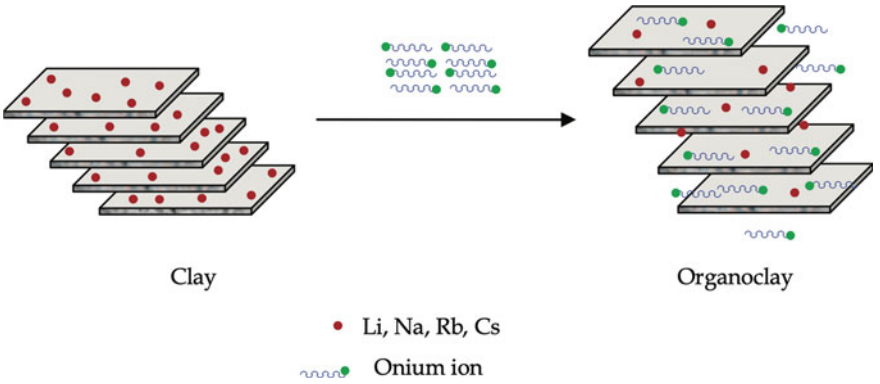

Fig. 6 Modification scheme of clays using organic onium ions [52]

called bentonite or sodium montmorillonite. Since the spaces among lamellae are not electrically neutral, the excess of charge is neutralized by individual cations, hydrated cations, and hydroxide group keeping the silicate layers apart. If the basal spacing is electrically neutral, the interlamellar region is empty, and the adjacent lamellae are maintained through weak van der Waals interactions. Covalent or ionic bonds characterize the intralamellar structure, whereas van der Waals bonds or hydrogen bonds occur between interlamellar surfaces [4, 20].

The interlamellar spacing can be functionalized through the exchange of compensation cations, allowing the intercalation of different cations or chemical groups. The chemical modification creates a hybrid material with different characteristics of the pristine one. The intercalation process consists of the entry of guest molecules leading lamellae separation and accommodation as shown in Fig. 6. Several chemical or physics routes such as adsorption, cations binding, ion exchange, graphitization, acid reaction, and pillarization can be followed in order to modify phyllosilicates [6, 7, 54].

Mostly, the chemical modification and expansion of the phyllosilicates seek to exchange clay compensation cations for organic cations, transforming the surface of hydrophilic (organophobic) into organophilic (hydrophobic), improving the chemical contact of phyllosilicate and polymer backbone. In addition, the basal spacing can be increased according to the length of intercalant molecules and the spatial disposal in the interlamellar region [41, 55]. Figure 7 shows some possible configurations to insertion of organomodifiers in clay layers suggested by Olad [52].

The phyllosilicate interlamellar spacing enlarges as the amount of intercalating until the saturation limit reaches the maximum cation exchange capacity (CEC). The intercalating species can assume variable molecular arrangements inside the lamellar spacing according to their chemical nature and chain length [25, 54].

If amine is the intercalating molecule, it was proposed that the adsorption of amine on the external filler area happen at the beginning. Following, the hydroxyl groups inside the interlamellar region are disturbed leading to the elastic deformation of

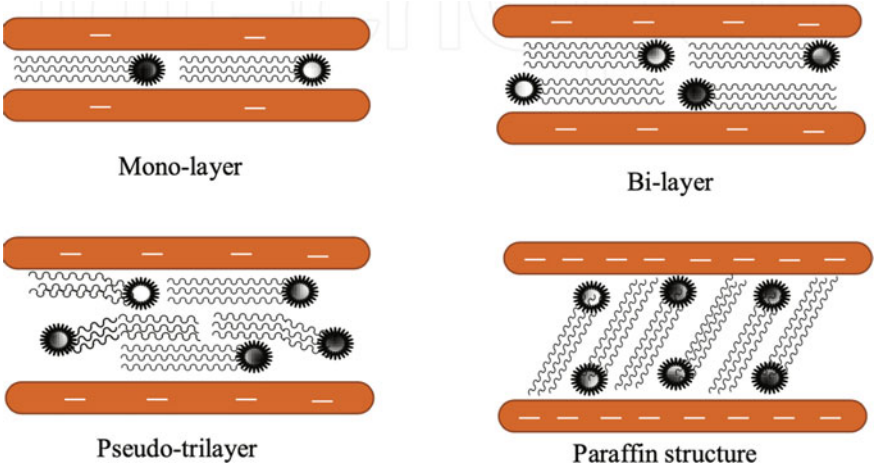

Fig. 7 Some configurations for clay intercalation of organic modifiers [52]

the lamellae. The migration of guest molecules into filler galleries is allowed. They acquired different conformations due to surface geometry and chain wrapping. It was also reported that according to the guest chain length, the intercalation angle of the molecules tends to increase owing to the enhancement of the van der Waals interactions between filler and intercalating [36].

Considered an environmentally correct process and quite feasible for industry, the intercalation process of phyllosilicates through solid-state reactions is based on the ion–dipole interaction. Interlamellar cations attached to the organic molecules displace adsorbed water molecules linked to the filler galleries provided ion exchange and increase of basal spacing [54].

Long-chain amine intercalating montmorillonite at variable reactant ratios, temperature, and reaction time was studied by Bujdák and Slosiariková. Experiments were developed varying the amine (mmol) / clay (g) ratio from 1 to 4, 24 h of reaction and temperature up to 150 °C. They observed that the intercalation occurred by water desorption and partial protonation of amine groups from octadecylamine and as higher the temperature higher was the interlamellar spacing obtained, reaching 3.85 nm of interlamellar spacing with the highest temperature and amine/clay ratio [8].

Intercalation of montmorillonite with decylamine, hexadecylamine, and octadecylamine was accomplished by Ganguly et al., where the interlamellar spacing duplicated its value. The amines were previously protonated using hydrochloric acid, and it was dripped in the clay dispersion. It was proposed that monolayer, lateral bilayer, and pseudo trilayer amine molecules arrangements are reached when montmorillonite was intercalated with octadecylammonium bromide, at different amine:clay ratios. The results showed that interlamellar spacing changed from 1.25 to 2.3 nm using hexadecylamine or octadecylamine as intercalants [21].

Vermiculite, mica-like mineral, essentially formed by hydrated aluminum and magnesium silicates, was intercalated with long-chain amine by melting process by Weiss et al. The authors used different clay/amine molar ratios (2: 1, 1: 1, 1: 2 and 1: 6) under different reaction times (1–30 h) at 80 °C. It was pointed out that the interlamellar spacing increased until four times and long reaction times was required (1.44 nm to up to 5.84 nm). By monitoring the effects of synthesis parameters—solvent medium, amine:filler ratio and acid: amine ratio—it was pointed out that 1 and 3 mmol/g amine: filler ratio showed the best results. Around 40% of organic matter was inserted, and the lamellar spacing increased twice. It was proposed that the cation exchange reaction would have been initiated by amine molecules adsorption on the external filler surface, inducing to a rearrangement of the intralamellar hydroxyls and causing a bending elastic deformation of the lamellae, followed by their opening to the entrance of the guest molecules. During intercalation—migration into the interlamellar space—intercalating molecules may adopt different conformations due to surface geometry and chain wrapping. Some results showed that in addition with the increasing of chain length, the intercalation angle of the molecules tends to increase due to a higher van der Waals-type interactions between filler and intercalant species [36, 71].

The applied process techniques possess a special behavior in properties as they are fundamental to control clay dispersion in polymer matrix. However, it is important to choose processes that are industry viable, environmentally friendly, and that possess low costs [2].

The nanoclays inclusion in polymer matrix improve physicochemical properties with benefits for many uses, as gas absorber materials, energy, tribological properties, and automotive industries. Silane as coupling agent was used with bentonite clays by Ge et al. to enhance tribological properties of nitrile butadiene rubber (NBR). The adhesion and the hysteresis force were enhanced, and the friction coefficient was significantly reduced [24].

Membrane composite was developed by Fang et al. with montmorillonite and poly(vinylidene fluoride)(PVDF) to develop Li-ion batteries. This nanomaterial improved battery capacity and showed a better cycle performance than the used nowadays [19].

Liu et al. obtained ammonia adsorbers from nanocomposites of poly(acrylic acid) (PAA) with bentonite and palygorskite. As these nanofillers possess unique structures, then the ammonia adsorption behavior was different. The adsorption of NH_3 could be observed with differences in coloration, which allows to predict the residual ability to adsorb. The materials showed to be efficient and a low-cost technique to treat polluted atmosphere [26].

PAA/halloysite nanoclay composites was developed by Smith et al. in a way to obtain a material eco-friendly, fire-retardant coating. The clay acted as a barrier in the composites to avoid any possible transfer during flammability tests. Also, it was observed that the material became self-extinguishing and with ability to decrease the heat release rate and the total smoke release, which is promising for foams with higher fire-preventing behavior [26].

Raji et al. prepared nanocomposites of polypropylene and montmorillonite, halloysite, and sepiolite by melt intercalation, where the nanoclays were modified by grafting with silanes. The nanoclays were effectivelly intercalated as the modification was observed by an increase of their d-spacing. The modification process was helpful to promote a better compatibility between polymer chains and clay platelets, and it observed the mechanical properties of the composites' pre- and post-modification. The chemical modification promoted covalent interaction of nanoclay hydroxyls and PP chains. For non-modified clays, it was observed an increase in Young's modulus for PP nanocomposites from 1034 MPa to 2657.9, 2716.8, and 2956.5 MPa at 5 wt% for montmorillonite, halloysite, and sepiolite. On the other hand, for modified nanoclays, these values were even higher in comparison with the non-treated clays nanocomposites, using the same conditions and contents [60].

Ollier et al. studied the effect of clays on poly(3-hydroxybutyrate) (PHB). The authors promoted chemical modification of bentonite with silanes and ion exchange reactions. It was observed that the modified clays led to a increase in thermal degradation with a indicative of deterioration of the polymer chains of PHB, a fact that is not observed for pristine and simple modified clays [53].

An intercalating substance with neutral nature can penetrate the interlamellar spacing of the clay if the energy from adsorption step is enough to overwhelm the interaction among the sheets. The hydrogen interaction of oxygen atoms of the silicate and the amine (NH) or hydroxyl (OH) functional group from organomolecule is significant when associated with the tetrahedral structure. The presence of interlamellar water molecules considerably reduces the cohesive force between the lamellae and consequently facilitates the penetration of the intercalant molecule. Thus, the organic molecule competes with the water molecule for occupying the coordinating site with the exchangeable cation [5].

Xing et al. studied the modification of montmorillonite (MMT) with 1,3-dihexadecyl-3H-benzimidazolium bromide (Bz) to obtain polyphenylene sulfide (PPS)/MMT nanocomposites in the melt state. The authors observed that the materials obtained are characterized by a mix of intercalated and exfoliated behavior with the presence of some tactoids still present. The composites were submitted to acid environment and heat to measure the oxidation resistance of the polymers in the presence of nanofillers. The mechanical properties of the nanocomposites were enhanced, a fact attributed to a better distribution of the nanosheets Fig. 8 [74].

Santos evaluated the use diverse organomodified clays on the properties of poly(butylene adipate-co-terephthalate) (PBAT) composites. With contents varying from 2.5 to 7.5% and three commercial organoclays, the nanocomposites were prepared by melted blending and injection molded. It was observed by the authors a higher basal spacement by XRD, which is suggestive for intercalation in all the composites investigated and confirmed by TEM analysis. Also, it was observed a little improvement in thermal properties and increase in stiffness, but it was not observed modification in material T_g [62].

Organomontmorillonites (OMt and HOMt) with di-(hydrogenated tallow) dimethyl ammonium chloride (HTA), di(alkyl ester) dimethyl ammonium chloride (EA), trihexyl tetradecyl phosphonium chloride (TDP), and ethoxylated tallow amine

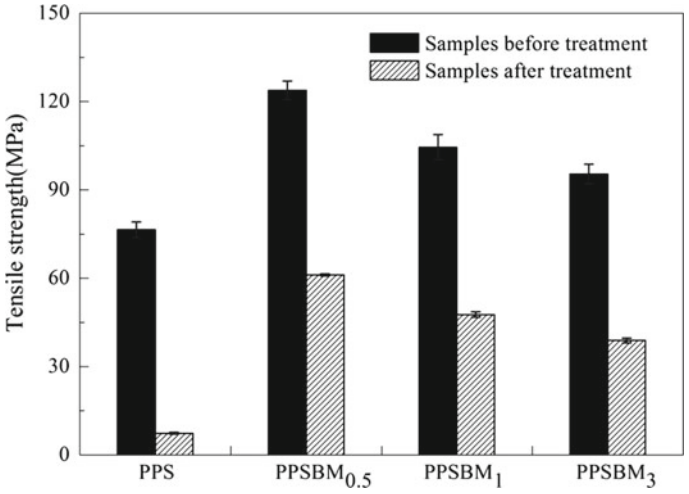

Fig. 8 Tensile strength of PPS and composites after oxidation treatment [74]

(ETA) as modifiers were studied by Alves et al. in poly(lactic acid) (PLA) nanocomposites. The authors confirmed dependence of the modification in the chemical structure and in the properties of the composites, where HOMt nanoparticles with EA and ETA showed a higher affinity with polymer chains and possess a better nanoclay distribution in the matrix. It was also noted that the presence of modified MMT promoted a reduction in T_g of the polymer and increased its crystallinity [3].

Zidan studied the use of organoclay in poly(methyl methacrylate) (PMMA) with 2-methacryloyloxyethyloctadecyldimethylammonium bromide (MEODAB) being used as organomodifier of the clay. It was observed from WAXD and TEM a possible mix of structures from intercalation and exfoliation of clays in the nanocomposites. The improvement in the thermal stability of PMMA/organoclay nanocomposites was not significant by the authors because of the intercalated structure formed [76].

2.4 Tetravalent Metal Phosphates

Transition metal phosphates have been known for over 100 years. In contrast to phyllosilicates, lamellar inorganic phosphates are synthesized and possess the general formula $M(RPO_3)_2$, where M is a tetravalent metal and R is a hydrogen atom (H), a hydroxyl group (OH), or an organic radical [15] [66].

$Zr(HPO_4)$ 2 · H2O (α-ZrP) and $Zr(HPO_4)$ 2 · $2H_2O$ (γ-ZrP) with the interlamellar spacing of 0.76 and 1.2 nm, respectively, are quite studied. Scanning electron microscopy (SEM) reveals structure like hexagonal disks with a diameter around 600 nm. The pioneer and the most studied is α-bis-monohydrogen zirconium phosphate, α-$Zr(HPO_4)0.2 \cdot H_2O$, also called of α-ZrP. It has received a lot of attention due

to the useful features like ionic exchanger, catalysis, intercalation, high aspect ratio, and so on. It is synthesized by the reaction between zirconium oxychloride ($ZrOCl_2 \cdot 8H_2O$) and phosphoric acid. Its properties change according to the P:Zr ratio, reaction temperature, and reflux time. Gamma-type lamellar zirconium phosphate has higher acidity than its corresponding alpha one. It is because of two hydroxyl groupments linked to the same phosphorus atom. As consequence, it possesses interlamellar spacing to accommodate two water molecules per mol of the compound favoring ion exchange process [5, 27].

Alpha-ZrP has high cation exchange capacity (6.64 mmol/g) allowing direct intercalation mostly with base substances such as alcohols and alkylamines. It does not possess a planar structure. The P–OH group is a kind of Brønsted acid, and it is not symmetrically distributed along with the filler lower and upper lamellae. This geometry induces the intercalation of tilted molecules at an appropriate angle settled as zigzag into the filler galleries. The intercalating molecules change the packing angle continuously and also the chain arrangement. This could explain the gradual increase of interlamellar spacing as the amount of intercalating is enhanced [64].

Some results obtained by Marti and Colon on ZrP intercalation are shown. Tris (2,2′-bipyridine) ruthenium (II) intercalating ZrP increased the interlamellar spacing from 0.76 to 1.52 nm. Through solution or microwave tool, 4-methylmercapto aniline promoted intercalation of cationic species. The authors commented on the unfinished intercalation process since several peaks on X-ray diffractograms were noticed. Ethylamine and propylamine (twice) and octadecylamine (seven times higher) increased ZrP interlamellar spacing, but only 60% of cation exchange capacity was reached [46].

Composites of LLDPE and -ZrP (neat and organically modified) were prepared by Mendes et al. The characterization by TG and DSC analyses showed an increasing of extrapolated initial degradation temperature T_{onset}, decreasing of crystallinity degree (X_c), and the melting temperature (T_m), which evidenced that the polyolefin and octadecylamine interacted into the filler galleries in the LLDPE/ZrPOct composite. The appearance in the LLDPE/ZrPOct material of new XRD peaks at low angles strongly indicated formation of nanocomposite. The intercalation process of long-chain amine and the entry of the polymer chains into the filler spacement of the LLDPE/ZrPOct composite were detected by wide-angle X-ray diffraction (WAXD) and hydrogen low field nuclear magnetic resonance (^{1}HLFNMR) making suppose that a nanoscale material was reached. These convergent findings evidenced that nanocomposite with a mix of intercalated and/or exfoliated structure has been achieved for LLDPE/ZrPOct [48].

In further publication, Mendes et al. obtained zirconium phosphate modified with octadecylamine using three amine:ZrP molar ratios (0.5:1,1:1, and 2:1). It was observed that the lamellae/intercalant interactions and the disposal inside basal spacement were evaluated. The intercalation ratio was responsible for the octadecylamine insertion in the ZrP platelets, more evidenced in higher ratios, and observed by XRD. FTIR showed modification of PO_3^- bands and thermocalorimetry indicated fusion and release of amine in different steps, which was an evidence that the Brønsted acid–base reaction between P–OH and amine groups occurred [49].

Alpha-ZrP with octadecylamine was obtained by Lino et al. to achieve composites of polyethylene. The findings from thermal, crystallographic, and mechanical evaluations led to conclude that a microcomposite was achieved. The long-chain amine acted as organic modifier of the phosphate which promoted the increase of basal interlamellar space to allow HDPE chain to enter inside nanofiller galleries, to enhance HDPE properties. The intercalation promoted a decrease of the (001) diffraction peak value, elastic modulus, crystallinity degree, and an increase of thermal stability. The authors proposed that the system obtained present a structure partially intercalated and/or exfoliated [40].

Mariano et al. studied how the screw rotation affects the organomodified nanozirconium phosphate dispersion in polypropylene matrix. The authors observed a synergistic behavior of the screw speed with the nanofiller on components dispersion and thermal characteristics. The increase of the rotation led to a higher filler distribution in the PP, as observed by scanning electron micrography (SEM) and WAXD analyses. Also, the reduction of the nanocomposite crystallinity degree and increase of thermal stability were detected through calorimetry and thermogravimetry. Due to the overlapping of PP and nano-ZrPOct filler absorption bands, it was not observed relevant displacements in the infrared spectra. The convergent evidences led the authors to infer that possible a mix of intercalated and exfoliated structure was obtained in PP/ZrPOct composite [44].

The insertion of intercalant for drug delivery is also a possibility for the use of zirconium phosphate materials. The insertion of zinc gluconate (ZnG) molecule as an intercalant into (α-ZrP) as a shelter was performed by Carvalho and co-authors. The authors evaluated the interrelationship and the intercalation ability of the ZnG into the phosphate basal spacing, where it was observed some indications that the drug molecule was able to be inserted into phosphate lamellar spacing. By thermogravimetry, it was deduced that among the phosphate lamellae some gluconate molecules are free, and some are linked. WAXD patterns, as shown in Fig. 9, infrared

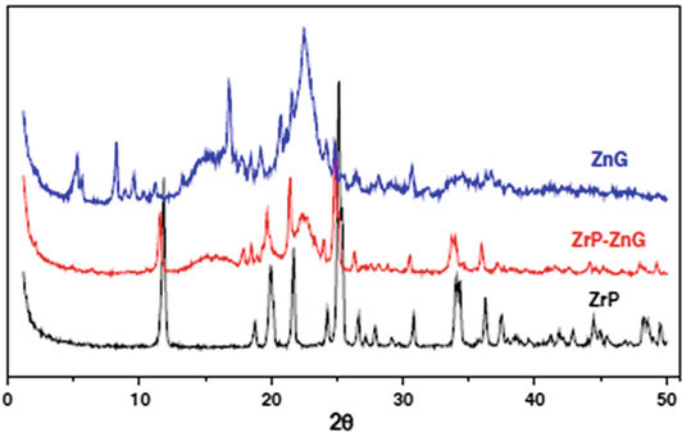

Fig. 9 WAXD patterns of zirconium phosphate (ZrP), zinc gluconate (ZnG), and ZrP-ZnG [11]

spectroscopy, and relaxometry by nuclear magnetic resonance displayed that ZnG intercalation occurred and that there is interaction between phosphate and gluconate. Even with hydroxyl groupments anchored in phosphate, it possesses extremally weak basic force, which reduces the chance of reaction with phosphate acid groups in the phosphate interlamellar space. The results supported that in the intercalation of ZnG into ZrP filler predominated physical interaction [11].

From in situ caprolactam (CL) polymerization, Garcia et al. investigated the pure and organomodified zirconium phosphate in PA-6 hygroscopicity. Powerful interaction between polyamide and organophosphate was evidenced by infrared and rheological analysis. The polymer crystallinity was decreased in the nanocomposites, and a lower hygroscopicity (almost 40% smaller than pristine PA-6) was assigned to poor affinity of ZrP/water and water-repellent octadecylamine intercalated molecules in the composite, as shown in Fig. 10 [23].

Mariano and co-authors investigated the insertion of ether-amine oligomer in zirconium phosphate basal space. FTIR indicated a powerful interaction between phosphate and amine groupments. Thermogravimetry (TGA) displayed that amine was incorporated by ZrP, where the expand of basal space was quadruplicated indicating success in the modification. SEM/EDX analysis Fig. 11 showed that the ether-amine was intercalated in phosphate lamellae, and it is an indicative that acid P–OH

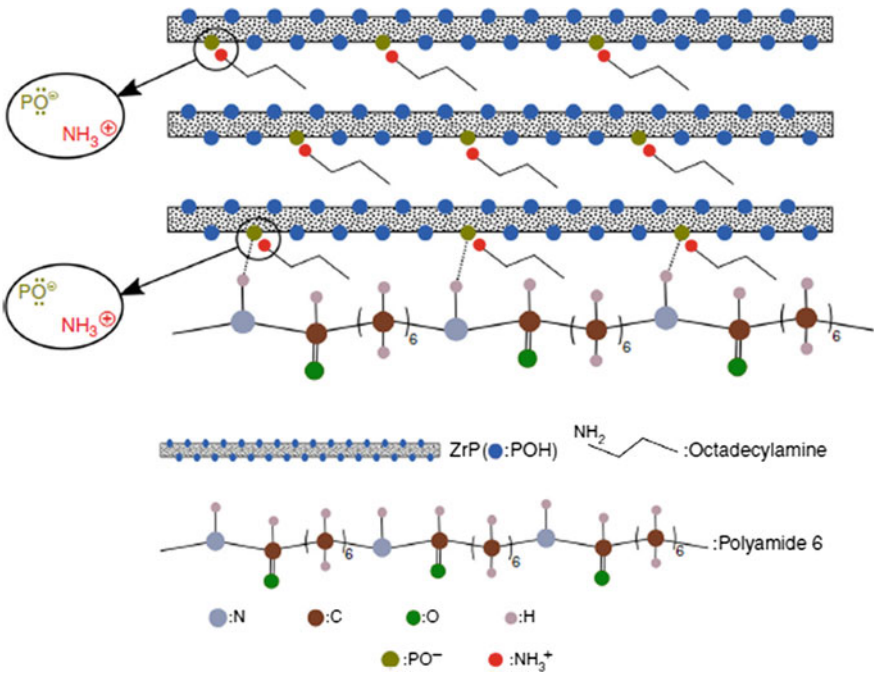

Fig. 10 Representation of the supposed exchange between PA-6 and $[PO_3^{-}\,{}^{+}NH_3\,–(CH_2)_{17}\,–CH_3]$ in PA-6/ZrPOct nanocomposite [23]

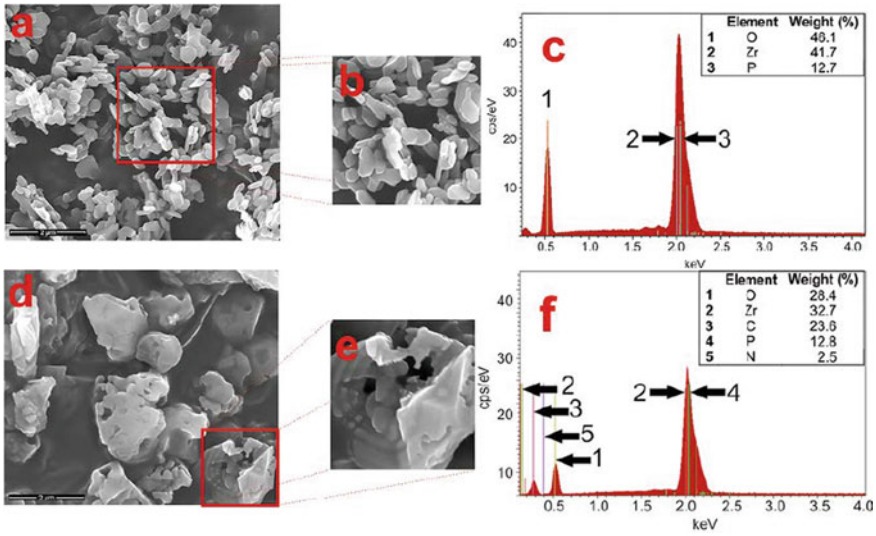

Fig. 11 SEM/EDX analyses of ZrP (**a**, **b** and **c**) and E-A/ZrP (**d**, **e** and **f**) [45]

groupment reacted with basic amine groupment, and formed an ionic bond $PO^{-+}{}_3HN$–[–(CH_2–CH_2–O) m–(CH_2–C–H(CH_3)–O)$_n$–]. The authors concluded that a partially intercalated nanofiller were achieved [45].

3 Final Considerations

The search sources to accomplish this chapter revealed the interest of the scientific and technological sectors on modification of lamellar fillers. There is similarity in the intercalation treatments of clay minerals and tetravalent metal phosphates once they are cation exchange materials.

The versatility of graphene/polyolefin nanocomposites suggests a great potential for application in the automotive, aerospace, electronics, and packaging industry. In relation to graphite, a non-polar polycarbon, there is a need for the lamellar functionalization through acid etching and subsequent heat treatment to expand the load galleries. Some barriers still avoid the full use of this nanofiller like the difficult dispersion and handling of the sheets.

In the case of double lamellar hydroxides, the treatment is similar to that applied to clay minerals and phosphates, but it should be noted that these are anion exchange materials.

The lamellar filler modification steps have proved to be extremely important for obtaining polymeric materials with different properties and thus with different applications, increasing the possibility of use in the market. Regarding the properties of polymers, most studies emphasize the importance of full exfoliation of the nanofiller

in order to obtain better properties compared to original polymer. Both clay minerals and zirconium phosphate show an enhance in the thermal characteristics of nanocomposites, while graphite considerably increases the elastic modulus, thermal, and electrical conductivity of the material. Few studies highlight the property improvements using double lamellar hydroxides, possibly due to their difficult polymer intercalation and exfoliation.

References

1. Adachi-Pagano M, Forano C, Besse J (2000) Delamination of layered double hydroxides by use of surfactants. Chem Commun 1:91–92. https://doi.org/10.1039/a908251d
2. Adak B, Joshi M, Butola B (2018) Polyurethane/clay nanocomposites with improved helium gas barrier and mechanical properties: direct versus master-batch melt mixing route. J Appl Polym Sci 135(27):46422. https://doi.org/10.1002/app.46422
3. Alves J, Rosa P, Realinho V, Antunes M, Velasco J, Morales A (2019) Influence of chemical composition of Brazilian organoclays on the morphological, structural and thermal properties of PLA-organoclay nanocomposites. Appl Clay Sci 180:105186. https://doi.org/10.1016/j.clay.2019.105186
4. Amorim L, Gomes C, Silva F, Ferreira H (2002) Comportamento reológico de dispersões de argilas bentoníticas: efeitos do tipo de ferramenta, velocidade e tempo de agitação. Cerâmica 48(308):234–238. https://doi.org/10.1590/s0366-69132002000400012
5. Auerbach S, Carrado K, Dutta P (2004) Handbook of layered materials. M. Dekker, New York
6. Barbosa R, Araújo E, Oliveira A, Melo T (2006) Efeito de sais quaternários de amônio na organofilização de uma argila bentonita nacional. Cerâmica 52(324):264–268. https://doi.org/10.1590/s0366-69132006000400009
7. Belver C, Aranda P, Martín-Luengo M, Ruiz-Hitzky E (2012) New silica/alumina–clay heterostructures: Properties as acid catalysts. Microporous Mesoporous Mater 147(1):157–166. https://doi.org/10.1016/j.micromeso.2011.05.037
8. Bujdák J, Slosiariková H (1992) The reaction of montmorillonite with octadecylamine in solid and melted state. Appl Clay Sci 7(4):263–269. https://doi.org/10.1016/0169-1317(92)90014-e
9. Burakowski L, Rezende M (2001) Modificação da rugosidade de fibras de carbono por método químico para aplicação em compósitos poliméricos. Polímeros 11(2):51–57. https://doi.org/10.1590/s0104-14282001000200006
10. Cardoso W, Gushikem Y (2005) Preparação de compostos lamelares: síntese do hidrogenofosfato de zircônio cristalino e sua intercalação com aminas. Um experimento para estudantes de graduação. Química Nova 28(4):723–726. https://doi.org/10.1590/s0100-40422005000400029
11. Carvalho A, Freitas D, Mariano D, Mattos G, Mendes L (2018) The influence of zinc gluconate as an intercalating agent on the structural, thermal, morphologic, and molecular mobility of lamellar nanofiller. Colloid Polym Sci 296(6):1079–1086. https://doi.org/10.1007/s00396-018-4319-6
12. Chang J (2019) Comparative analysis of properties of PVA composites with various nanofillers: pristine clay, organoclay, and functionalized graphene. Nanomaterials 9(3):323. https://doi.org/10.3390/nano9030323
13. Chen G, Weng W, Wu D, Wu C (2003) PMMA/graphite nanosheets composite and its conducting properties. Eur Polymer J 39(12):2329–2335. https://doi.org/10.1016/j.eurpolymj.2003.08.005
14. Chen W, Feng L, Qu B (2004) Preparation of nanocomposites by exfoliation of ZnAl layered double hydroxides in nonpolar LLDPE solution. Chem Mater 16(3):368–370. https://doi.org/10.1021/cm0303484

15. Clearfield A, Stynes J (1964) The preparation of crystalline zirconium phosphate and some observations on its ion exchange behaviour. J Inorg Nucl Chem 26(1):117–129. https://doi.org/10.1016/0022-1902(64)80238-4
16. Crepaldi E, Valim J (1998) Hidróxidos duplos lamelares: síntese, estrutura, propriedades e aplicações. Química Nova 21(3):300–311. https://doi.org/10.1590/s0100-40421998000300011
17. Cunha V, Ferreira A, Constantino V, Tronto J, Valim J (2010) Hidróxidos duplos lamelares: nanopartículas inorgânicas para armazenamento e liberação de espécies de interesse biológico e terapêutico. Química Nova 33(1):159–171. https://doi.org/10.1590/s0100-40422010000100029
18. Esteves A, Barros-Timmons A, Trindade T (2004) Nanocompósitos de matriz polimérica: estratégias de síntese de materiais híbridos. Química Nova 27(5):798–806. https://doi.org/10.1590/s0100-40422004000500020
19. Fang C, Yang S, Zhao X, Du P, Xiong J (2016) Electrospun montmorillonite modified poly(vinylidene fluoride) nanocomposite separators for lithium-ion batteries. Mater Res Bull 79:1–7. https://doi.org/10.1016/j.materresbull.2016.02.015
20. Fonseca M, Airoldi C (2003) Híbridos inorgânico-orgânicos derivados da reação de filossicatos com organossilanos. Química Nova 26(5):699–707. https://doi.org/10.1590/s0100-40422003000500014
21. Ganguly S, Dana K, Ghatak S (2009) Thermogravimetric study of n-alkylammonium-intercalated montmorillonites of different cation exchange capacity. J Therm Anal Calorim 100(1):71–78. https://doi.org/10.1007/s10973-009-0588-0
22. Gao M, Jiao Q, Cui W, Feng C, Zhao Y, Xiang A et al (2019) Preparation of PET/LDH composite materials and their mechanical properties and permeability for O2. Polym Eng Sci 59(s2):E366–E371. https://doi.org/10.1002/pen.25067
23. Garcia E, Freitas D, Cestari S, Coval D, Mendes L, Albitres G (2019) Zirconium phosphate changing hygroscopicity of polyamide-6 in nanocomposites PA-6/ZrP. J Therm Anal Calorim. https://doi.org/10.1007/s10973-019-08396-1
24. Ge X, Zhang Y, Deng F, Cho U (2015) Effects of silane coupling agents on tribological properties of bentonite/nitrile butadiene rubber composites. Polym Compos 38(11):2347–2357. https://doi.org/10.1002/pc.23817
25. Guégan R (2010) Intercalation of a nonionic surfactant (C10E3) bilayer into a Na-Montmorillonite clay. Langmuir 26(24):19175–19180. https://doi.org/10.1021/la1039267
26. Guo F, Aryana S, Han Y, Jiao Y (2018) A Review of the synthesis and applications of polymer-nanoclay composites. Appl Sci 8(9):1696. https://doi.org/10.3390/app8091696
27. Ha B, Char K, Jeon H (2005) Intercalation mechanism and interlayer structure of hexadecylamines in the confined space of layered α-zirconium phosphates. J Phys Chem B 109(51):24434–24440. https://doi.org/10.1021/jp055563h
28. Herrera-Alonso M, Abdala A, McAllister M, Aksay I, Prud'homme R (2007) Intercalation and stitching of graphite oxide with diaminoalkanes. Langmuir 23(21):10644–10649. https://doi.org/10.1021/la0633839
29. Hibino T, Kobayashi M (2005) Delamination of layered double hydroxides in water. J Mater Chem 15(6):653. https://doi.org/10.1039/b416913a
30. Hu K, Kulkarni D, Choi I, Tsukruk V (2014) Graphene-polymer nanocomposites for structural and functional applications. Prog Polym Sci 39(11):1934–1972. https://doi.org/10.1016/j.progpolymsci.2014.03.001
31. Jiang J (2015) Graphene versus MoS2: a short review. Front Phys 10(3):287–302. https://doi.org/10.1007/s11467-015-0459-z
32. Kausar A (2018) Applications of polymer/graphene nanocomposite membranes: a review. Mater Res Innov 23(5):276–287. https://doi.org/10.1080/14328917.2018.1456636
33. Kim H, Miura Y, Macosko C (2010) Graphene/Polyurethane nanocomposites for improved gas barrier and electrical conductivity. Chem Mater 22(11):3441–3450. https://doi.org/10.1021/cm100477v

34. Krishnan S, Singh E, Singh P, Meyyappan M, Nalwa H (2019) A review on graphene-based nanocomposites for electrochemical and fluorescent biosensors. RSC Adv 9(16):8778–8881. https://doi.org/10.1039/c8ra09577a
35. Koo J (2019) Polymer nanocomposites. Mcgraw-Hill Education, [S.L.]
36. Lagaly G (1986) Interaction of alkylamines with different types of layered compounds. Solid State Ionics 22(1):43–51. https://doi.org/10.1016/0167-2738(86)90057-3
37. Leroux F, Besse J (2001) Polymer interleaved layered double hydroxide: a new emerging class of nanocomposites. Chem Mater 13(10):3507–3515. https://doi.org/10.1021/cm0110268
38. Li L, Ma R, Ebina Y, Iyi N, Sasaki T (2005) Positively charged nanosheets derived via total delamination of layered double hydroxides. Chem Mater 17(17):4386–4391. https://doi.org/10.1021/cm0510460
39. Li J, Vaisman L, Marom G, Kim J (2007) Br treated graphite nanoplatelets for improved electrical conductivity of polymer composites. Carbon 45(4):744–750. https://doi.org/10.1016/j.carbon.2006.11.031
40. Lino A, Mendes L, Silva D, Malm O (2015) High density polyethylene and zirconium phosphate nanocomposites. Polímeros 25(5):477–482. https://doi.org/10.1590/0104-1428.2030
41. Lopes C, Penha F, Braga R, Melo D, Pergher S, Petkowicz D (2011) Síntese e caracterização de argilas organofílicas contendo diferentes teores do surfactante catiônico brometo de hexadeciltrimetilamônio. Química Nova 34(7):1152–1156. https://doi.org/10.1590/s0100-40422011000700009
42. Lueking A, Gutierrez H, Fonseca D, Dickey E (2007) Structural characterization of exfoliated graphite nanofibers. Carbon 45(4):751–759. https://doi.org/10.1016/j.carbon.2006.11.023
43. Luna F, Schuchardt U (1999) Argilas pilarizadas - uma introdução. Química Nova 22(1):104–109. https://doi.org/10.1590/s0100-40421999000100017
44. Mariano D, Freitas D, Mendes L (2017) Nanocomposite of polypropylene/octadecylamine lamellar-zirconium phosphate: influence of nanofiller and screw speed. J Compos Mater 52(5):701–711. https://doi.org/10.1177/0021998317713832
45. Mariano D, Freitas D, Mendes L, Carvalho A, Ramos F (2019) Investigation on structural, morphological and relaxometric properties of lamellar Zrp modified with long chain amine. Mater Res 22(2). https://doi.org/10.1590/1980-5373-mr-2018-0493
46. Martí A, Colón J (2003) Direct Ion exchange of Tris(2,2‘-bipyridine)ruthenium(II) into an α-Zirconium phosphate framework. Inorg Chem 42(9):2830–2832. https://doi.org/10.1021/ic025548g
47. McAllister M, Li J, Adamson D, Schniepp H, Abdala A, Liu J et al (2007) Single sheet functionalized graphene by oxidation and thermal expansion of graphite. Chem Mater 19(18):4396–4404. https://doi.org/10.1021/cm0630800
48. Mendes L, Silva D, Lino A (2012) Linear Low-density polyethylene and zirconium phosphate nanocomposites: evidence from thermal, thermo-mechanical, morphological and low-field nuclear magnetic resonance techniques. J Nanosci Nanotechnol 12(12):8867–8873. https://doi.org/10.1166/jnn.2012.6718
49. Mendes L, Silva D, Araujo L, Lino A (2014) Zirconium phosphate organically intercalated/exfoliated with long chain amine. J Therm Anal Calorim 118(3):1461–1469. https://doi.org/10.1007/s10973-014-4056-0
50. Mhlabeni T, Kesavan Pillai S, Ray S (2019) Effect of organically modified layered double hydroxides on the properties of poly(lactic acid)/poly[(butylene succinate)-co-adipate] immiscible blends. J Appl Polym Sci 48654. https://doi.org/10.1002/app.48654
51. Nanocomposites Market Global Forecast to 2024 | MarketsandMarkets (2020) Retrieved 9 Jan 2020, from https://www.marketsandmarkets.com/Market-Reports/nanocomposites-market-141476334.html
52. Olad A (2011) Polymer/clay nanocomposites, advances in diverse industrial applications of nanocomposites, Boreddy Reddy, IntechOpen. https://doi.org/10.5772/14464. Available from: https://www.intechopen.com/books/advances-in-diverse-industrial-applications-of-nanocomposites/polymer-clay-nanocomposites

53. Ollier R, D'Amico D, Schroeder W, Cyras V, Alvarez V (2018) Effect of clay treatment on the thermal degradation of PHB based nanocomposites. Appl Clay Sci 163:146–152. https://doi.org/10.1016/j.clay.2018.07.025
54. Paiva L, Morales A, Díaz F (2008) Argilas organofílicas: características, metodologias de preparação, compostos de intercalação e técnicas de caracterização. Cerâmica 54(330):213–226. https://doi.org/10.1590/s0366-69132008000200012
55. Pérez-Santano A, Trujillano R, Belver C, Gil A, Vicente M (2005) Effect of the intercalation conditions of a montmorillonite with octadecylamine. J Colloid Interface Sci 284(1):239–244. https://doi.org/10.1016/j.jcis.2004.09.066
56. Pan Y, Yu Z, Ou Y, Hu G (2000) A new process of fabricating electrically conducting nylon 6/graphite nanocomposites via intercalation polymerization. J Polym Sci, Part B: Polym Phys 38(12):1626–1633. https://doi.org/10.1002/(sici)1099-0488(20000615)38:12%3c1626::aid-polb80%3e3.0.co;2-r
57. Pierson H (2001) Handbook of carbon, graphite, diamond, and fullerenes. Noyes Publications, Park Ridge, N.J
58. Qiu L, Chen W, Qu B (2005) Structural characterisation and thermal properties of exfoliated polystyrene/ZnAl layered double hydroxide nanocomposites prepared via solution intercalation. Polym Degrad Stab 87(3):433–440. https://doi.org/10.1016/j.polymdegradstab.2004.09.009
59. Rafiee M, Rafiee J, Srivastava I, Wang Z, Song H, Yu Z, Koratkar N (2010) Fracture and fatigue in graphene nanocomposites. Small 6(2):179–183. https://doi.org/10.1002/smll.200901480
60. Raji M, Mekhzoum M, Rodrigue D, Qaiss A, Bouhfid R (2018) Effect of silane functionalization on properties of polypropylene/clay nanocomposites. Compos B Eng 146:106–115. https://doi.org/10.1016/j.compositesb.2018.04.013
61. Shamitha C, Mahendran A, Anandhan S (2019) Effect of polarization switching on piezoelectric and dielectric performance of electrospun nanofabrics of poly(vinylidene fluoride)/Ca–Al LDH nanocomposite. J Appl Polym Sci 48697. https://doi.org/10.1002/app.48697
62. Santos T, Almeida T, Morais D, Magalhães F, Guedes R, Canedo E, Carvalho L (2019) Effect of filler type on properties of PBAT/organoclay nanocomposites. Polym Bull. https://doi.org/10.1007/s00289-019-02778-z
63. Schniepp H, Li J, McAllister M, Sai H, Herrera-Alonso M, Adamson D et al (2006) Functionalized single graphene sheets derived from splitting graphite oxide. J Phys Chem B 110(17):8535–8539. https://doi.org/10.1021/jp060936f
64. Sun L, O'Reilly J, Kong D, Su J, Boo W, Sue H, Clearfield A (2009) The effect of guest molecular architecture and host crystallinity upon the mechanism of the intercalation reaction. J Colloid Interface Sci 333(2):503–509. https://doi.org/10.1016/j.jcis.2009.02.028
65. Suresh K, Kumar R, Pugazhenthi G (2016) Processing and characterization of polystyrene nanocomposites based on CoAl layered double hydroxide. J Sci Adv Mater Dev 1(3):351–361. https://doi.org/10.1016/j.jsamd.2016.07.007
66. Szirtes L, Riess L, Megyeri J, Kuzmann E (2007) Comparative study of layered tetravalent metal phosphates containing various first-row divalent metals. Synthesis, crystalline structure. Open Chem 5(2). https://doi.org/10.2478/s11532-007-0003-2
67. Uhl F, Wilkie C (2004) Preparation of nanocomposites from styrene and modified graphite oxides. Polym Degrad Stab 84(2):215–226. https://doi.org/10.1016/j.polymdegradstab.2003.10.014
68. Ulibarri M, Labajos F, Rives V, Trujillano R, Kagunya W, Jones W (1994) Comparative study of the synthesis and properties of vanadate-exchanged layered double hydroxides. Inorg Chem 33(12):2592–2599. https://doi.org/10.1021/ic00090a019
69. Viculis L, Mack J, Mayer O, Hahn H, Kaner R (2005) Intercalation and exfoliation routes to graphite nanoplatelets. J Mater Chem 15(9):974. https://doi.org/10.1039/b413029d
70. Wei J, Saharudin M, Vo T, Inam F (2018) Effects of surfactants on the properties of epoxy/graphene nanocomposites. J Reinf Plast Compos 37(14):960–967. https://doi.org/10.1177/0731684418765369

71. Weiss Z, Valášková M, Křistková M, Čapková P, Pospíšil M (2003) Intercalation and grafting of vermiculite with octadecylamine using low-temperature melting. Clays Clay Min 51(5):555–565. https://doi.org/10.1346/ccmn.2003.0510509
72. Wypych F, Arízaga G (2005) Intercalação e funcionalização da brucita com ácidos carboxílicos. Química Nova 28(1):24–29. https://doi.org/10.1590/s0100-40422005000100005
73. Yang X, Li L, Shang S, Tao X (2010) Synthesis and characterization of layer-aligned poly(vinyl alcohol)/graphene nanocomposites. Polymer 51(15):3431–3435. https://doi.org/10.1016/j.polymer.2010.05.034
74. Xing J, Xu Z, Deng B (2018) Enhanced oxidation resistance of polyphenylene sulfide composites based on montmorillonite modified by benzimidazolium salt. Polymers 10(1):83. https://doi.org/10.3390/polym10010083
75. Yasmin A, Luo J, Daniel I (2006) Processing of expanded graphite reinforced polymer nanocomposites. Compos Sci Technol 66(9):1182–1189. https://doi.org/10.1016/j.compscitech.2005.10.014
76. Zidan T (2019) Synthesis and characterization of modified properties of poly(methyl methacrylate)/organoclay nanocomposites. Polym Compos 1–9. https://doi.org/10.1002/pc.25388

Chapter 2
High Temperature Tribology of Surface Coatings

Arkadeb Mukhopadhyay, Tapan Kumar Barman, and Prasanta Sahoo

1 Introduction

Coating is deposited onto a substrate to modify it surface properties. The coating deposited is generally protective in nature and improves surface finish, wear resistance, scratch resistance, corrosion resistance, hardness, etc. Thus, a thin layer of a coating effectively improves surface properties without the need to alter the bulk properties of a material. Surface coatings may be soft or hard with anti-friction and anti-wear characteristics, respectively [50]. Nevertheless, the coatings may also be typically classified according to their deposition techniques [47]. The classification of coatings based according to their deposition techniques is presented in Fig. 1.

Hard surface coatings are used for improving wear resistance of the substrates and enhancing tribological behavior of mating parts in cylinder liners, piston rings, etc. Hard ceramic coatings are used in bearings and seals operating in extreme conditions, slurry pump seals, valves, knife sharpeners, gas turbine blades, etc. [50]. In various industries, several mating components are exposed to high temperature sliding conditions and environments. Generally, the interfaces of various moving assemblies in automotive, power generation, aerospace as well as metal working process involve high temperature mating components. High temperature exposure leads to morphological as well as microstructural changes due to enhancement of reactions and various other interactions of parameters. The mechanical properties of the materials are also affected due to oxidation and diffusion phenomenon. Thus, the synergistic effect of these entire phenomena affects the friction and wear behavior of materials

A. Mukhopadhyay (✉)
Department of Mechanical Engineering, Birla Institute of Technology, Mesra, Ranchi 835215, India
e-mail: arkadeb.mukhopadhyay@bitmesra.ac.in

T. K. Barman · P. Sahoo
Department of Mechanical Engineering, Jadavpur University, Kolkata 700032, India

S. Sahoo (ed.), *Recent Advances in Layered Materials and Structures*,
Materials Horizons: From Nature to Nanomaterials,
https://doi.org/10.1007/978-981-33-4550-8_2

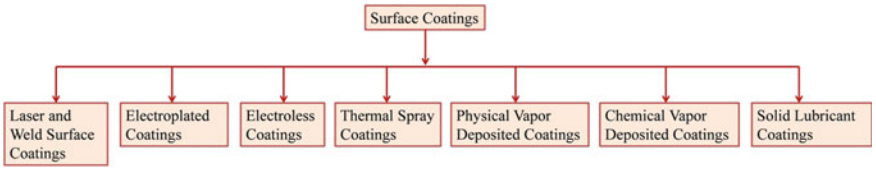

Fig. 1 General classification of coatings [47]. Reprinted from Encyclopedia of Tribology, In: Wang Q.J., Chung YW. (eds), Caroline Richard, Tribological coatings for high temperature applications, 2013, with permission from Springer

at high temperature. Recent developments have seen mono- or multi-layered coatings with several functionalities that prevent components from degradation due to friction, wear, or corrosion. Tribo-corrosion, i.e., the synergy of tribology as well as corrosion phenomenon also magnifies degradation of mating components. In such cases, modern coatings have been successfully utilized. For high temperature applications, where conventional lubricants fail, suitable surface modification and surface coatings find usage [47]. It is desirable that these coatings should have high thermal stability and capability of providing self-lubrication. Super hard materials and nano-composites referred to as diamond or diamond-like-carbon coatings are finding increasing usage [47]. The thermal stability as well as tribological characteristics may be improved by deposition of multi-layered coatings thus combining individual properties of various coatings. Deposition of poly-alloyed coatings also serves the purpose of achieving a wide range of enhanced characteristics and mechanical properties for use in the high temperature domain. Electrodeposition and electroless nickel coatings also provide superior wear resistance at elevated temperatures [38].

Surface coatings are gaining significant importance in the high temperature domain. Some typical examples of the high temperature industrial applications include metal processing, automotive, and aerospace industries. Hot drawing is extensively used in the automotive industry for manufacturing parts like bumpers, door beams, hood reinforcements, etc. Friction and wear of tool occur during dry contact of the tools with sheet. The hot drawing process may be optimized by the use of high temperature coatings which will in turn reduce manufacturing costs [47]. Further, thermal barrier coatings are effective in reducing losses arising due to oxidation and wear of vanes of gas turbine or aero-engines and highly loaded turbine blades [47]. Researchers have also shown that thermal sprayed coatings may be successfully used in aerospace, mining, and automotive industries [41, 55]. Plasma-sprayed PS series coatings developed at National Aeronautics and Space Administration (NASA) were also seen to be efficient over a broad operating temperature range and it was concluded that PS400 series coatings were suitable for aerospace applications [48]. Recent studies have also shown that electroless deposited alloy coatings have enhanced tribological characteristics at high temperatures of 500 °C [36].

Therefore, with rising industrial demands and harsh environments, there is a need to study different coating methods which have been explored by researchers for the high temperature domain. The present chapter aims to provide a concise discussion

on high temperature-based coating design and deposition techniques. Recent developments and future trends are also discussed with an aim to enhance the surface engineering techniques for high temperature-based tribological applications.

2 Surface Coating Deposition Techniques

Surface engineering has gained immense importance since components are subjected to various surface attacks in the form of friction, wear, and corrosion. Automotive, aviation, power, chemical, etc., industries depend heavily on surface engineering and coatings. To meet demanding needs and cater into leading-edge technology, it is necessary to optimize both volumes of components as well as surface properties. There are several methods of coating deposition. The properties of the coatings depend on the process chosen. Further, the parameters of coating deposition in a certain process also control the friction, wear, and corrosion resistance of the coatings [7]. A coating process is also selected based on environmental condition, loading, operating temperature, cost effectiveness, etc. Right choice of coating material and process parameters would allow components working in severe environments to excel in high temperature conditions. Some techniques which are used for deposition of coatings related to high temperature applications are discussed subsequently.

2.1 Vapor Deposition Techniques

Vapor deposition technique refers to the deposition of a material which is in vapor state and condensed onto a substrate. In this method, ions, atoms, or molecules in gaseous phase are utilized to deposit coatings having excellent tribological characteristics. The process is versatile and produces coatings with high purity and adhesion to the substrate. They also replicate the surface of the substrate and there is no requirement of post finishing operations. Since vapor deposition takes place in a vacuum chamber, the cost of the system is comparatively higher. Vapor deposition may be broadly classified as:

- Physical vapor deposition (PVD)
- Chemical vapor deposition (CVD).

2.1.1 Physical Vapor Deposition (PVD)

In PVD, the starting material is in the form of a solid. As energy is introduced, the solid is transformed to gaseous or plasma phase [30]. High vacuum is used to condense the vapor (10^{-8} to 10^{-1} torr) on the substrate [50]. The steps involved in PVD include (a) generation of gaseous phase, (b) transport of particles, and (c) condensation and growth of layer [30]. The different ways by which coatings are

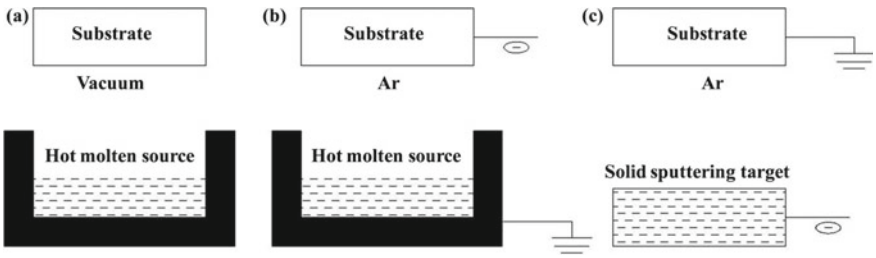

Fig. 2 Schematic diagram of PVD processes: **a** evaporation, **b** ion-plating and **c** sputtering

deposited by PVD for high temperature applications are mainly through arc PVD, sputtering, and ion-plating. The PVD process is shown schematically in Fig. 2. The different PVD processes are discussed in brief as follows:

Arc PVD: By this process, the solid metallic coating material is evaporated by running an arc having diameter of a few microns. Due to the high current, high energy plasma is formed and the material that is evaporated is almost totally ionized. A reactive gas is passed through the chamber wherein the metal ions combine with it and get deposited on the substrate or component. Thus, a thin and highly adherent coating is formed.

Sputtering: Sputtering is a widely used vapor deposition technique. The solid coating material is dislodged into the vapor phase due to bombardment of energetic particles and positive ions of heavy inert gas (argon ions). A negative voltage is applied to the target. Due to the applied negative voltage, the positive Ar ions are accelerated towards the target. The atoms or ions required for deposition are ejected by momentum transfer. The particles that are evaporated are finally introduced into a chamber with a gas containing the non-metallic component of the hard coating. Sputtering being a high energy process, any material may be deposited since the coating material is passed into the vapor phase by mechanical process.

Ion-plating: When the starting material is ionized in plasma, high energy ionized particles are yielded for coating deposition. This is known as ion-plating. To increase the adhesion of coating to the substrate, partial ionization of the vapor is carried out. Either the material to be deposited is passed through a gaseous glow discharge (plasma) or an external ionization gun is utilized as the bombardment source. Adhesion of ion beam-type coatings is found to be excellent even at low substrate temperature.

2.1.2 Chemical Vapor Deposition (CVD)

In CVD technique, the components in gaseous phase react close to or on the substrate to be coated [30]. A volatile component of the coating is reacted with gases or vapor or decomposed thermally on to the hot substrate [50].Chemical reaction is initiated at 150–2200 °C. The pressure is kept at 0.5–760 torr. The substrate is heated by

laser or a heater. Coatings with excellent quality and adhesion are produced by low pressure CVD with high deposition rate [50]. Since deposition at high temperature is involved in CVD, it limits the deposition on substrates with low melting point.

2.2 *Electrodeposition*

This is an electrochemical deposition process wherein a current is passed externally. This allows influence over direction in which the reaction proceeds and metal deposition [30]. current is passed through a solution called the electrolyte. Generally, DC current source is applied and at times, pulsed technique is employed. The pulsed process enables deposition of graded and multi-layer coatings. The dissolution of metal ion to be deposited takes place either by dissolution of anode or the electrolyte [30]. The material to be coated is cathode. Thus, reduction of metal ions takes place at the cathode. One of the pre-requisites is that the substrate must be electrically conductive. A variety of metals can be deposited by electrodeposition. The electrodeposition setup is presented schematically in Fig. 3.

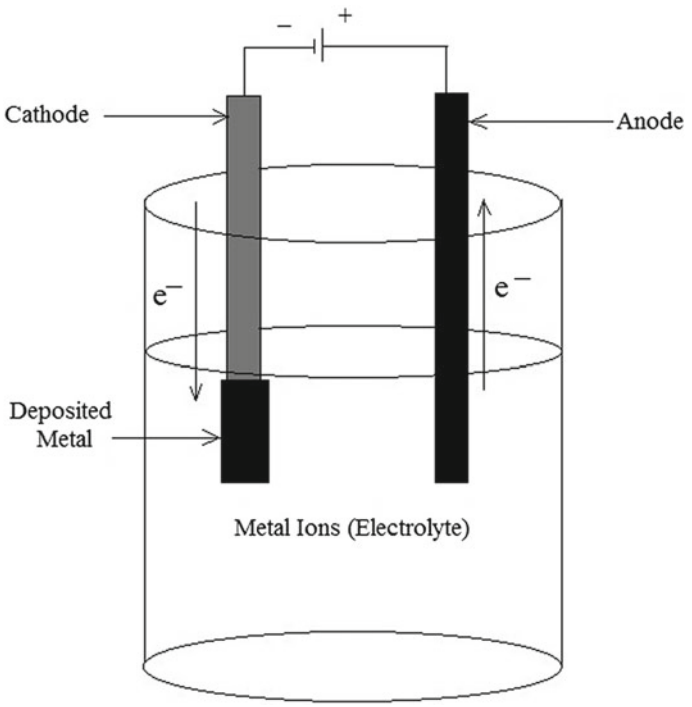

Fig. 3 Electrodeposition setup

2.3 Electroless Deposition

Electroless process is a chemical process and is also known as autocatalytic process. It takes place by autocatalytic chemical reduction. There is no aid of electricity to trigger reactions. The coating bath consists of a reducing agent. This reducing agent provides electrons to reduce metallic ions on to the substrate which must be catalytically active. Since it is not necessary that the substrate be electrically conducting, this process is flexible and a broad type of substrates can be plated easily. Even though electroless deposition is receiving widespread attention now, the reduction of nickel from its aqueous solution from a hypophosphite based bath was made by Wurtz [51]. Wurtz idea was not developed for a whole century until Brenner and Riddell [3] conducted the first laboratory experiment and were given the credit for introducing electroless nickel coating to the world. Basically, electroless nickel coatings may be classified as Ni–P- or Ni–B-based alloy and composite coatings. After receiving significant attention, it has grown into a wide family of functional coatings serving several industrial needs. The main application of electroless nickel is based on its corrosion resistance and anti-wear characteristics. The main disadvantage of this process is its finite bath life. The electroless nickel deposition process has been schematically depicted in Fig. 4.

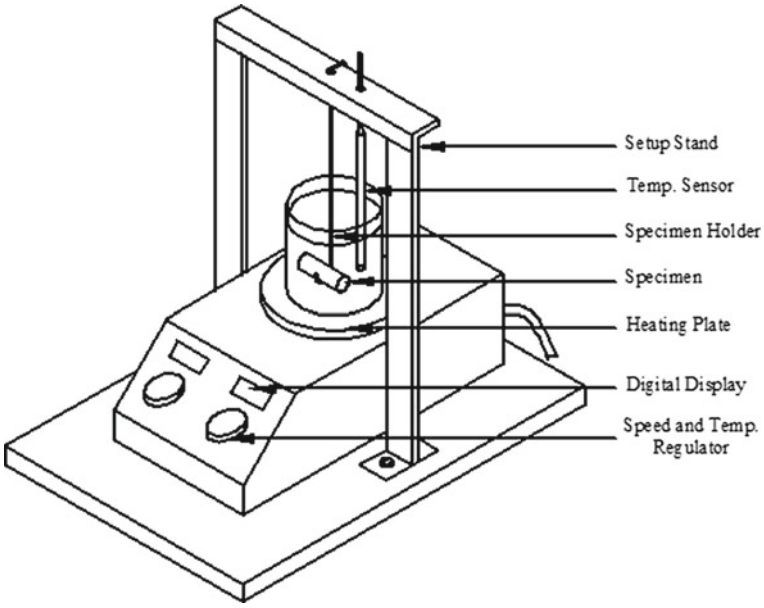

Fig. 4 Electroless nickel deposition setup

2.4 Hard Facing

Hard facing may be done by thermal spraying, welding, or cladding [50]. Thick and hard coatings are produced by hard facing. The coating is melted in a heating zone and sprayed on to a cooled substrate material. Thermal energy for melting the material is obtained by a flame, electric plasma, detonation of gases by a spark plug, etc. [50]. When coating material is supplied in the form of a powder, wire or rod and heat are produced by a gas, flame, or electric arc, and the process is known as welding deposition. In cladding, a metallic foil or sheet is metallurgically bonded to a metallic substrate. There are several methods by which a metal or alloy may be clad such as deformation cladding, braze cladding, diffusion bonding, weld cladding, and laser cladding. Plastic deformation applied through pressure/impact along with heat results in a true metallurgical bond and the process is known as deformation cladding. Diffusion bonding relies on the principle of coalescence of contacting surfaces by the application of pressure and heat for short time. When surfaces are sandwiched by a brazing material in the form of a paste, foil or powder, it is known as braze cladding. The stack is heated by a heat source to form metallurgical bond [50]. In weld and laser cladding, the metal is clad by melting it and fusing it to the substrate.

3 High Temperature Tribology of Coatings Deposited by Different Techniques

3.1 PVD/ Arc-PVD Coatings

Tribologically protective coatings were deposited onto tools and components by deposition of ions, atoms, or molecules in gaseous phase by PVD process [30]. Several research works regarding PVD for high temperature applications have been carried out. Nohava et al. [40] demonstrated the tribological behavior of Al–Cr-based wear-resistant coatings that are suitable for the high temperature domain (oxynitride and oxide coatings). An industrial rotating arc-cathode PVD process was used for coating deposition. High wear resistance was observed for AlCrN coatings up to 600 °C. But the coatings failed at 800 °C. Severe wear was exhibited by all nitride and oxynitride coatings at 800 °C. But α-$(Al,Cr)_2O_3$ coating exhibited outstanding wear resistance at 800 °C. This was attributed to its stable alpha-alumina structure. This hindered oxidation of the coating at high temperature and consequently a severe wear. It was concluded that not only the ability of the coating to prevent oxidation of the substrate but also its excellent abrasion resistance led to high wear resistance at 800 °C. $(Ti_{0.7}Al_{0.3})$ N coatings deposited by PVD process were also considered to be wear resistant at high temperatures [49]. Hence, these coatings were deposited on AISI H13 steel which is generally used as dies in hot extrusion. The wear resistance of the coatings was investigated at room temperature as well as at 600 °C. As-received and gas-nitrided coatings were considered. Different substrates, coatings,

Table 1 Nomenclatures of heat-treated AISI H13 steel substrates and coatings considered by Rodríguez-Baracaldo et al. [49]

Nomenclature	Cooling	Other treatments	Coating
HA	Air	–	–
HAN		Nitriding	–
HAB		–	TiAlN
HANB		Nitriding	TiAlN
HO	Oil quenched	–	–
HON		Nitriding	–
HOB		–	TiAlN
HONB		Nitriding	TiAlN

Reprinted from Wear, 262, Rodríguez-Baracaldo et al., High temperature wear resistance of (TiAl)N PVD coating on untreated and gas nitrided AISI H13 steel with different heat treatments, 380–389, 2007, with permission from Elsevier

and their nomenclature are shown in Table 1 while their COF and wear volume are presented in Table 2. The gas nitride coatings exhibited satisfactory wear resistance compared to bare steel or the as-deposited coatings. High load carrying capacity and H/E ratio were the reason behind excellent wear resistance which allowed the presence of higher elastic strain. Further oxidation of the coating was prevented by dense oxide formation in the wear track. Though it was reported by Nohava et al. [40] that $(Al,Cr)_2O_3$ coatings were more wear resistant than TiAlN coating variants.

The high temperature tribological behavior of Ti6Al4V was improved by nitriding and subsequent application of TiAlN coatings prepared by cathode arc-evaporation technique [39]. The test temperature was changed from 25 to 600 °C. Wear rate was observed to be lowest at 500 °C. The higher wear resistance was attributed to the tribo-chemical films of Al_2O_3 and TiO_2. Similar results were also observed for $Ti_{55}Al_{45}N$ and $Ti_{35}Al_{65}N$ nitride coatings prepared by cathode arc-evaporation technique [16].

Table 2 COF and wear volumes of AISI H13 steel (coated and non-coated) at room and high temperatures investigated by Rodríguez-Baracaldo et al. [49]

Temperature (°C)	Sample	COF	Wear volume (mm^3)
600	HA	0.55	0.083
600	HAN	0.6	0.015
600	HAB	0.65	0.054
600	HANB	0.95	–
600	HO	0.52	0.143
600	HON	0.60	0.017
600	HOB	0.67	0.030
600	HONB	0.93	–

Reprinted from Wear, 262, Rodríguez-Baracaldo et al., High temperature wear resistance of (TiAl)N PVD coating on untreated and gas-nitrided AISI H13 steel with different heat treatments, 380–389, 2007, with permission from Elsevier

The wear resistance was significantly improved at 600 °C with an increase in Al. Zr–Si–N coatings was deposited by cathodic arc technique on WC–Co substrates [60]. The Si content was varied from 0.2 to 6.3 at.%. Consequently, there was a change in microstructure from columnar to nanocomposite. It was suggested that columnar-structured coatings and higher Si yields superior macro-scale wear resistance at room and elevated temperature (500 °C). Hot forging tools were seen to be efficiently protected by nitriding and PVD coating [13]. Hybrid layers of Cr/CrN/AlTiCrN coating, Cr/CrN coating, and CrN/AlCrN/AlCrTiSiN coating were applied on hot forging tool steel. Cr/CrN coatings were effective in protecting the tool steel from wear. This was attributed to its high adhesion and resistance to abrasion. Further, Cr/CrN/AlTiCrN coating was also effective in improving the lifetime of tool steel due to its high resistance to abrasion. It also formed a thermal barrier. This resulted in a limited heat transfer. The PVD process also includes sputtering and ion-plating and has been discussed subsequently.

3.1.1 Sputtered Coatings

TiN and CrN coatings were deposited by low voltage arc deposition technique. Further, TiCN was also deposited by magnetron sputtering. Their high temperature tribo-performance was examined [44]. Significant oxidation of the coatings was observed at temperatures above 300 °C when sliding against Si_3N_4 balls. Austenitic steel substrate coated with TiCN by unbalanced magnetron sputtering was also tested at different temperatures while sliding against 100Cr6 balls [45]. Plastic deformation was dominant for TiCN coatings below 200 °C while within 300–500 °C, the major wear mechanisms observed were fracture, delamination and oxidative. TiN coatings deposited by high impulse magnetron sputtering were seen to exhibit high wear resistance at 300 °C [24]. But above 450 °C, oxidation of the coating was unavoidable. Further at 600 °C, the coatings were oxidized and cracked easily. The COF decreased as test temperature increased as shown in Fig. 5. WS_x co-deposited along with TiN

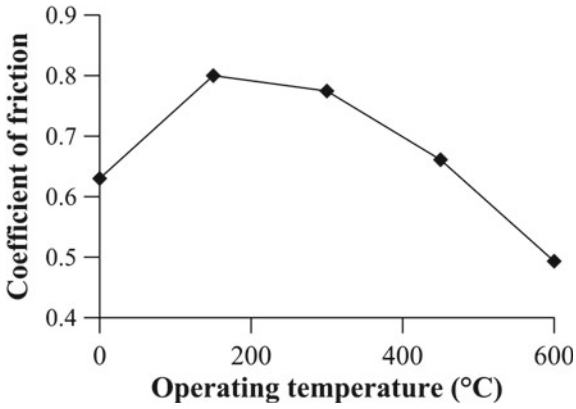

Fig. 5 COF of high impulse magnetron sputtered TiN coatings at room and high temperature [24]. Reprinted from Coatings, 9, Kuo et al., High temperature wear behavior of titanium nitride coating deposited using high power impulse magnetron sputtering, 555, 2019

coatings by reactive magnetron sputtering was investigated by Serra et al. [52]. Coated specimens containing 4 at. % WS_x were not effective at 343 K and its properties deteriorated. But on increasing the WS_x content to 19 at. %, a low COF and optimum wear rate of 0.86×10^{-17} m^2/N was observed without any cracking.

Adaptive and friction reducing coatings were produced by unbalanced magnetron sputtering that consisted of niobium nitride with silver nano-inclusions [57]. Tribological tests at 25–1000 °C was carried out while sliding against Si_3N_4 counterface. Above 700 °C, the coefficient of friction (COF) was within 0.15–0.30. At lower temperatures, COF was low due to the migration of silver to the surface. On the other hand, at high temperature, lubricious glazes were formed and responsible for the reduction of COF. The coatings were further doped with MoS_2. A low temperature lubricant like MoS_2 was added to investigate its effect on tribological behavior at high temperature. There was no appreciable change in COF at room temperature on addition of MoS_2. The COF at high temperatures was appreciably lower due to synergy of lubricating effects of molybdates and silver niobates. Silver tantalate coatings produced by unbalanced magnetron sputtering were investigated at ~750 °C [56]. They exhibited COF in the range 0.06–0.15. Reconstruction of self-lubricating $AgTaO_3$ into a mechanically mixed layer (MML) comprising Ta_2O_5, $AgTaO_3$ and Ag nano-particles were attributed to this low COF. Furthermore, magnetron-sputtered VN/Ag coatings were found to be adaptive and self-lubricating at high temperatures [2]. The COF of the coatings was found to be in the range of 0.15–0.20 at 700–1000 °C. Analysis of wear tracks using EDX and XRD revealed silver vanadate, silver, and vanadium oxide formation. Due to the layered atomic structure of Ag_3VO_4 such low COF was observed.

For high temperature friction and wear resistance, magnetron-sputtered multilayered CrAlN/VN coatings were deposited and investigated by Wang et al. [59]. Preferable anti-wear characteristics were observed at 700 °C. This was attributed to interfacial strengthening and the formation of lubricated vanadium oxide layers on the worn surface. The anti-wear property of the multi-layered coatings at high temperature was due to contribution of the respective elements and structural strengthening. Sputtered CrV_xN coatings with varying V content were studied by Rapoport et al. [46]. Their friction behavior at high temperature was also investigated. The stick–slip phenomenon was also observed. Experiments were performed from 25 to 700 °C under low sliding velocities. Experimental results revealed that with an increase in V up to 27–35 at.% resulted in an increase in hardness, fracture toughness, and a decrease in grain size. Consequently, the tribological behavior improved. Strong stick–slip was observed at room temperature due to mechanical interlocking as a result of adhesion. Lower wear and stick slip at high temperature was associated with formation of low shearing tribofilm of V_2O_5. DC magnetron-sputtered MoS_2 and $MoSe_2$ coatings were prepared [20]. Their tribological characteristics were measured at high temperature and in air with varying humidity levels. The high temperature tests were carried out on a ball-on-disc high tribometer. Results revealed that air humidity did not influence the COF of $MoSe_2$ [20].

3.1.2 Ion-Plated Coatings

High temperature tribological behavior and adhesion strength of ion-plated TiN coating with Ni–W interlayer was deposited [14]. The substrate considered was a hot work die steel. Crsytallization was observed during TiN deposition. The precipitation hardening of Ni–W interlayer was also reported. Considering the thermal aspects of the deposition, an interface diffusion layer was also formed. Precipitation hardening of the Ni–W interlayer resulted in an effective support of the TiN coating due to an increased toughness as well. The adhesion of TiN coating with Ni–W interlayer improved consequently. In comparison with single TiN coating, the duplex coating had a significantly higher wear resistance at 500–700 °C. The predominant wear mechanism at elevated temperature was abrasive and adhesive. The tribo-perfromance of AlTiN coating deposited by cathodic arc ion-plating was investigated at 700–900 °C [8]. Oxides of Al_2O_3 and TiO_2 were formed which provided a lubricating effect at high temperature. The average COF of the AlTiN coating was 0.77, 0.65, and 0.57 at 700 °C, 800 °C, and 900 °C, respectively. Oxidative, abrasive, fatigue, and adhesive wear were the predominant mechanism. Cathodic arc ion-plating was used to deposit VN and VCN coatings [32]. Lower COF and wear was exhibited by VCN coating compared to VN coating at different operating temperatures. Formation of a self-lubricating oxide of V_2O_5 and carbon phase indicated that the coating may be used for potential applications and tribo-components working under high temperature. Cathodic arc ion-plating was used to deposit CrN coatings on YT14 cemented carbide cutting tools [15]. At 3 N load, the high temperature friction and wear characteristics were excellent but at 7 N, the coatings failed. Abrasive, oxidative, adhesive, and plastic deformation was the dominant wear mechanisms. At 300, 400, and 500 °C, the COF of CrN coatings was 0.50, 0.62, and 0.43, respectively [53]. Abrasive wear was dominant at 300 and 400 °C. At 500 °C, slight oxidation along with abrasive wear was dominant.

3.2 CVD Coatings

CVD coatings have been investigated as potential candidates for high temperature extrusion process. H11 tool steel was surface engineered for aluminum extrusion dies. The tribological configuration involved sliding of 6082Al disc against die block at high temperatures [43]. Comparison of base steel and nitrided steel was carried out. Furthermore, deposition of commercially available duplex CVD and PVD coatings were considered. The ability of surface finish in influencing the tribo-performance was also investigated and no significant effect was concluded. Heavy damage was observed for the steel and nitride samples. Surface examination post wear tests revealed delamination pits and large craters in the sub-surface region. In the compound layer of coating, the hard duplex PVD coating was seen to be delaminated only in the outermost region. Compared with PVD, the bi-layered TiC-TiN CVD coating with lower load bearing capacity showed lesser damage. The influence

of temperature on the wear performance of CVD coating deposited on CoCrFeMnNi high entropy alloy (HEA) bonded Ti(C,N)-based cermets was studied by Chai et al. [4]. Five layers of CVD coating in the sequence TiN, MT-TiCN, transition layer (TiCO), α-Al_2O_3, and TiN were deposited. The substrate was HEA-bonded cermet. Wear test was carried out at 700 °C. Excellent wear resistance was observed compared to Ni-bonded cermet and this was attributed to small grain size, good adhesion, and hardness. Adhesive, abrasive, and oxidative wear was seen to be predominant.

3.3 Electrodeposited Coatings

Hot dip aluminized Zn–Ni coatings were electrodeposited on manganese boron flat steel. The hot forming application was simulated [19]. The tribo-performance of the coatings was investigated in the form of hot strip drawing and hot forming. Al-Si coatings were also considered. Higher COF was observed for Al-Si coatings compared to Zn-Ni coatings. This was attributed to the formation of a zinc oxide layer. The ZnO was also responsible for the enhancement of wear of work piece. Tribological characteristics of pure Ni coating and with micro/nanoSiC were observed at room as well as high temperature (300 °C) by Lekka et al. [26] under high load conditions. At room temperature, the wear resistance of pure Ni as well as with micro-SiC was almost similar. Inclusion of nanoSiC led to a 70% decrease in wear rate. All the coatings presented a higher wear rate at 300 °C due to lowering of mechanical strength and an increase in ductility of the matrix. But compared to pure Ni, the wear rate decreased by 63 and 88% on inclusion of micro-SiC and nano-SiC, respectively. The increased wear resistance of Ni-nano-SiC coatings was attributed to the uniform distribution of SiC throughout the deposit which inhibited plastic deformation. The wear mechanism at high temperature was observed to be tribo-oxidative and presence of micro-particles favored the mechanical adhesion of nickel oxide. Compared to DC current, pulsed current (PC) has the capability to produce lamellar structure and increase deposition of micro-SiC [25]. A clear grain refinement was observed when Ni-nano-SiC coatings were electrodeposited using PC. Compared to DC, the hardness of composite coatings improved when PC was applied. The wear mechanism at 300 °C was predominantly tribo-oxidation along with abrasion for the composite coatings.

Ni–SiC, Ni–SiC–MoS_2, and Ni–SiC–Gr composite coatings were fabricated by electrodeposition. This was done by a suspension of reinforcement particles well dispersed in a Ni sulfamate plating bath [9]. The COF of Ni–SiC coating was stable at room temperature. An increase in operating temperature resulted in a decrease in COF. At 100, 200, and 300 °C, the increase in COF was 17%, 80%, and 67%, respectively, compared to room temperature (25 °C). Wear surface examinations revealed spalling as the prevalent wear mechanism at various temperatures. At low temperature, the COF was smoother due to lower delamination. But the ductility of Ni matrix increased with an increase in temperature resulting in more plastic deformation. Addition of solid lubricating particles such as graphite or MoS_2 increased

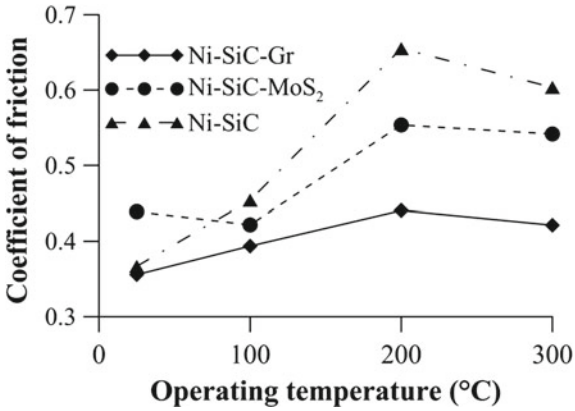

Fig. 6 COF of electrodeposited Ni with inclusion of SiC, MoS_2, and Gr at different temperatures [9]. Reprinted from Surface and Coatings Technology, 254, Fazel et al., Effect of solid lubricant particles on room and elevated temperature tribological properties of Ni–SiC composite coating, 252–259, 2014, with permission from Elsevier

the stability of COF at high temperature. A consequent reduction of 10–15% in COF was seen. Strong adhesive wear was reduced on addition of graphite providing effective lubrication at high temperature. The reduction in COF was more than 30% for graphite containing coating at high temperatures as indicated in Fig. 6.

3.4 Electroless Deposited Coatings

Electroless deposited coatings have high hardness and enhanced tribological characteristics. They have proven self-lubricating nature and anti-wear behavior at room temperature [33, 37]. Recently, their ability to provide effective wear resistance at room and high temperatures has been explored. At 550 °C, electroless Ni–P coating with 10 wt.% P in as-deposited condition was observed to exhibit the best wear resistance [31]. The wear rate and COF dropped due the oxide glaze formation. As-plated Ni–P coatings show better wear resistance at operating temperatures near the phase transformation temperature [21]. Heat treatment was received by the coatings during the sliding wear at elevated temperatures. As a result, microstructural changes were induced and optimum grain size was achieved which prevented propagation of dislocation [21, 31]. The tough Ni matrix provides support to the oxide glazes and the tribological characteristics are enhanced. On the other hand, an aging effect takes place for the already heat-treated coating leading to deterioration in wear resistance and COF.

The high temperature tribology of Ni–P coatings with varying phosphorus content was investigated by Ghaderi et al. [12]. Wear behavior at high temperature for electroless nickel coating with 3.5, 5, 9, and 12 wt% phosphorous was studied. The range of changes in phosphorous content for Ni–P coating in between 3.5 and 12 wt% led to a change in hardness in the range of 555 and 710 HV. Wear resistance at high temperature for electroless coating was the highest and the lowest for Ni-3 wt% P and Ni-12 wt% P, respectively. Results show that in case of low phosphorous

electroless coating, an oxide film was formed, and this film led to the lubrication and a decrease in friction between the two surfaces subjected to wear while the worn surface of electroless high phosphorous nickel coating lacked an oxide film. The wear mechanism for these coatings was of adhesive type. When wear test ran over 750 m, electroless Ni–12 wt% P coating experienced adhesive and abrasive wear, hence they created more severe mass loss. Coating hardness after wear test at 250 °C for electroless Ni-9 wt% P increased by 10 Vickers. This happened because of grain growth and crystallization of nickel remaining from the amorphous phase. In case of low phosphorous coating, there was no hardness change.

High temperature tribology of electroless Ni–P–W coatings was investigated by Kundu et al. [22]. The influence of load, speed, and temperature on the tribo-performance as-plated and heat treated coatings was studied. Ni–P–W coatings exhibited a stable friction and wear behavior at 100–500 °C. The wear resistance of as-deposited coatings was particularly enhanced at 300–500 °C due to exposure at high temperature. An increase in microhardness of the as-deposited coatings post wear test substantiated the fact that the toughness of the coatings improved due to the heat treatment it received during sliding wear at elevated temperature. The predominant wear mechanism was adhesive as well as abrasive. The tribological performance of Ni–P-B coatings was governed by formation of MML, oxidative layer, and phase transformations [23]. Recent studies have revealed excellent tribology of electroless Ni–B deposits sliding against hardened steel at elevated temperature [42]. This is because of the high melting point of the hard boride phases. At high temperature of 500 °C, the worn surface of Ni–B coating was characterized by glazed oxide layer, depletion of boron, and oxidation [36]. At 300 °C (temperature near phase transformation), the wear rate observed for Ni–B coatings was lower than that at 500 °C (Fig. 7). Also as the temperature was increased to 500 °C, the COF decreased (Fig. 8) due to formation of low shear strength oxide layers. But the wear rate increased at 500 °C due to oxidation and depletion of B. It was further observed that high temperature stability of Ni–B coatings could be improved by deposition of ternary Ni–B–W and Ni–B–Mo coatings [34]. XRD of worn specimens at 500 °C revealed crystallization of the as-plated binary and ternary alloys. Inclusion of W improved the wear resistance whereas Mo improved the COF [34]. The tribological behavior of Ni–P–BN (h) coating deposited by electroless method was studied at 25–400 °C [27]. The COF and wear resistance both deteriorated with an increase in temperature. At 100 °C, failure of coatings took place by adhesive and fatigue mode. While at high temperatures, there was pronounced increase in adhesion due to softening of the coating and gross plastic deformation.

Franco et al. [11] observed an improvement in high temperature performance of Ni–P coatings at 200 °C on reinforcing SiC particles and heat treatment. XRD of worn track revealed phase evolution and slight crystallization at 200 °C. The worn surface of coatings without reinforcement indicated adhesive wear with micro-cracks. Sub-surface cracks were formed at high temperature due to the cyclic nature of loading during sliding wear. In Ni–P–SiC coatings, fine abrasive grooves and polishing were noticed. The reinforcement hindered micro-crack formation and a

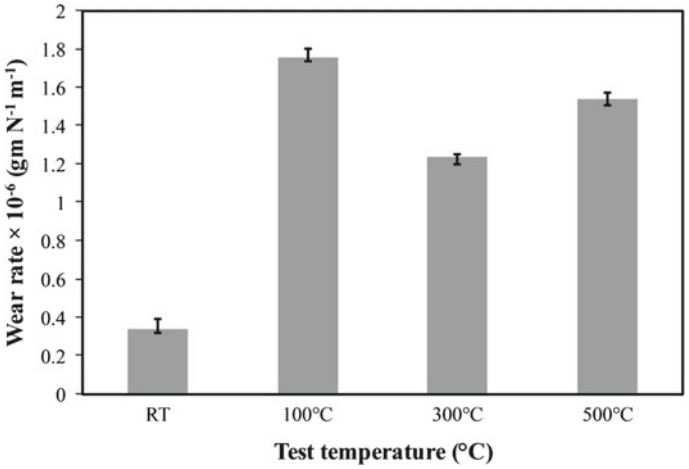

Fig. 7 Wear rate of electroless deposited Ni–B coatings [36]. Reprinted from Tribology Transactions, 61, Mukhopadhyay et al., Effect of operating temperature on tribological behavior of as-plated Ni–B coating deposited by electroless method, 41–52, 2018, with permission from Taylor and Francis

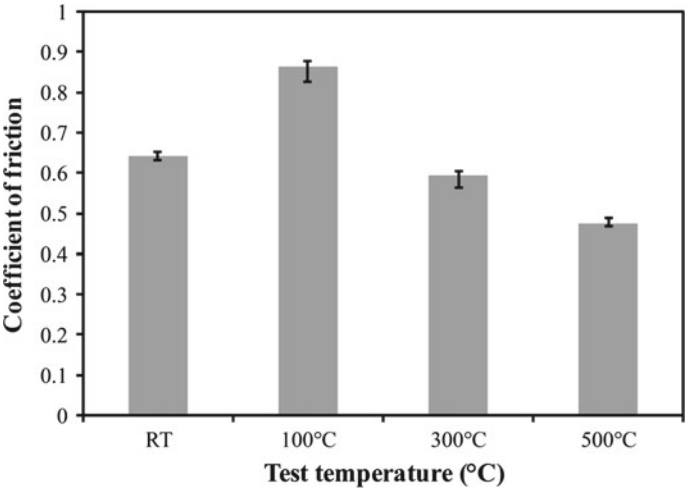

Fig. 8 Friction coefficient of electroless deposited Ni–B coatings [36]. Reprinted from Tribology Transactions, 61, Mukhopadhyay et al., Effect of operating temperature on tribological behavior of as-plated Ni–B coating deposited by electroless method, 41–52, 2018, with permission from Taylor and Francis

consequent reduction in wear rate took place. On inclusion of MoS_2 to form Ni–P–MoS_2 coating, the tribological behavior at high temperature improved due to formation of NiO and MoO_3 which have lubricating effects [28]. The COF decreased as the test temperature increased from 400 to 500 °C. But at 600 °C, the tribological characteristics deteriorated due to coating softening. Self-lubricating behavior at high temperature was also observed for Ni–P coatings with Ag and Ag + Al_2O_3 [1]. Silver particles decreased the fluctuations of friction coefficient and the coatings demonstrated a 'chameleon' behavior at elevated temperature.

3.5 Plasma-Sprayed and Plasma-Transferred Arc Coatings

A self-lubricating composite coating designated as PS304 was deposited on steam turbine governor valve lift rods. The high temperature wear and galling performance at 540 °C were investigated [58]. The chrome-oxide coating designated as PS304 was plasma sprayed. Silver and BaF_2/CaF_2 particles were co-deposited to function as solid lubricants. After 8500 h of operation, the surface of the rod was inspected. It was seen that the surface was well protected. The effective protection from wear and galling was due to formation of lubricious glaze. This protective layer consisted of barium/calcium fluorides, silver, and chrome-oxide.

Plasma spray technique was used to deposit nano-structured and ultra-fine WC–Co coatings [5]. The high temperature tribological behavior and failure mechanism were investigated. At high temperature, the nano-structured coatings had better wear resistance than ultra-fine coatings. In ultra-fine coatings, brittle fracture and adhesive wear were seen to dominate followed by abrasive wear. In nano-structured coatings, toughness fracture and abrasive wear were seen to dominate followed by adhesive wear.The wear rate and COF of TiC/Ti_3AlC_2–Co cermet coatings (deposited by atmospheric plasma spraying) at 600 °C were studied by [6]. Coated specimens with 30 wt. % Ti_3AlC_2 exhibited smallest COF and wear rate. Compared to TiC-Co cermet, the wear rate was 1.26 times lower. Whereas compared to TiC–Ni cermet, the wear rate of the coating was 10 times lower.

Plasma-transferred arc welding was used to deposit Colmonoy 5 powder on 316L stainless steel substrate [18]. The hardness of the coatings was 2.5 times higher than the substrate. As test temperature increased, wear loss and COF decreased. The wear track was characterized by severe abrasion and ploughing at room temperature during the initial sliding distance. The wear mechanism was shifted to delamination and mild abrasion as the sliding distance increased. For a shorter sliding distance at 573 K, the wear mechanism was mild ploughing. An increase in sliding distance shifted it to tribo-oxidation. Adhesive wear was observed at 823 K during initial sliding distance. Tribo-oxidation occurred at greater sliding distance. Plasma-transferred arc method was used to deposit hardfaced nickel based coatings [10]. The substrate material was gray cast iron. Even though hardness of gray cast iron was lower than the Ni coatings, both showed a similar wear rate due to formation of tribo-layer of C. Material softening occurred as a result of oxidation at 550 °C. Hence wear rate

increased abruptly for both the coatings and gray cast iron. The Ni based coatings were effectively protected by Ni–O. At 700 °C, the wear resistance of coatings improved. But the wear of gray cast iron was intensified. High amounts of oxide wear debris agglomerated to form an oxide layer which improved the wear resistance of the coatings.

3.6 Laser Clad Coatings

Laser cladding technique was used to deposit Ni60 and Ni60-hBN composite coatings on Ti6Al4V [29]. The coatings with 10% hBN exhibited excellent wear resistance at 300 and 600 °C. Wear performance of laser clad FeNiCoAlCu HEA coating was investigated at room temperature, 200, 400, 600, and 800 °C [17]. Oxide film formation resulted in excellent wear resistance of the coatings at high temperature. Abrasive and oxidative wear were dominant for the coatings at high temperature. CoCrNiSiBFe HEA powder was laser clad on low carbon steel and the wear behavior at high temperature was investigated [54]. At 500 °C, abrasive wear was observed for amorphous layer while whereas adhesive for the crystallized layer. This led to a decrease of 10% in mass loss of the amorphous layer.

4 Tribo-mechanisms Observed at Elevated Temperatures

4.1 Abrasive Wear

Abrasive wear may be characterized by the formation of parallel grooves along the direction of sliding. When the counterface material mates with the coated surface, due high hardness of the counterface, the asperities of the coatings may be sheared leading to the formation of wear debris. This may be useful or harmful to the elevated temperature tribological performance depending on the shape and size of the debris. The wear debris if small and spherical may cause a rolling effect thereby reducing friction and wear or it may cut through the coating creating grooves along the sliding direction and displacing material to the side of the wear track. A typical abrasive worn surface at 300 °C is illustrated in Fig. 9.

4.2 Adhesive Wear

Adhesive wear mechanism is observed when formation of bond between the two mating surfaces takes place due to high normal loads or high temperature. Bonding takes place due to adhesion and the contacts get sheared during sliding leading to the

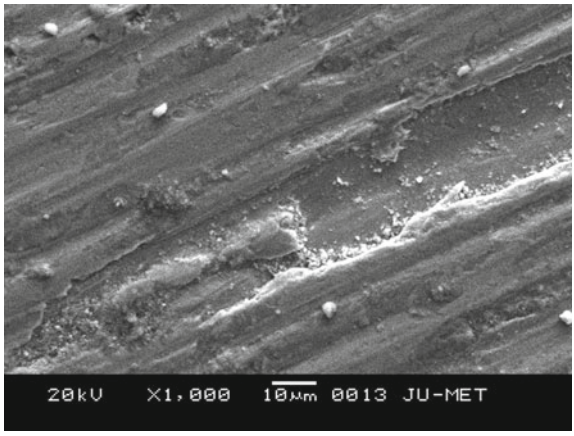

Fig. 9 Abrasive wear mechanism at elevated temperature observed for Ni–B coatings [35]. Reprinted from Surface Review and Letters, 24, Mukhopadhyay et al., Effects of heat treatment on tribological behavior of electroless Ni–B coating at elevated temperatures, 1850014, 2017, with permission from World Scientific Publishing Company

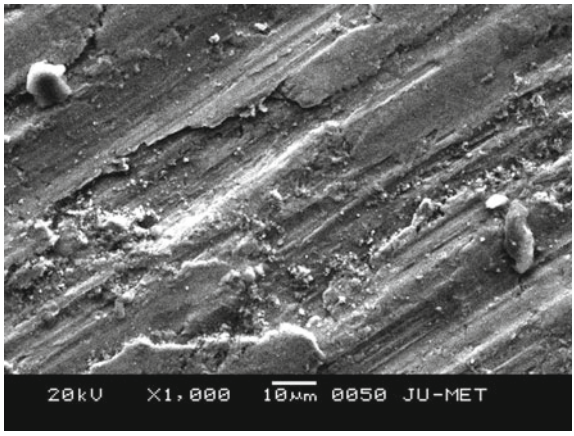

Fig. 10 Adhesive wear mechanism at elevated temperature for Ni–B coating [35]. Reprinted from Surface Review and Letters, 24, Mukhopadhyay et al., Effects of heat treatment on tribological behavior of electroless Ni–B coating at elevated temperatures, 1850014, 2017, with permission from World Scientific Publishing Company

detachment of material fragments. Such surfaces are generally characterized by the formation of 'pits' and 'prows' instead of parallel grooves or plastic deformation. A surface with the formation of pit due to adhesion at high temperature (100 °C) is shown in Fig. 10.

4.3 Fatigue Wear

At elevated temperatures, formation of cracks may take place during sliding wear tests due to the repeated loading and unloading conditions prevailing. This leads to the formation of crack. As due to the harsh conditions, accumulation of strain becomes enough causing opening of the crack and its propagation. Due to repeated cycles, surface or subsurface cracks are induced after a critical number of cycles,

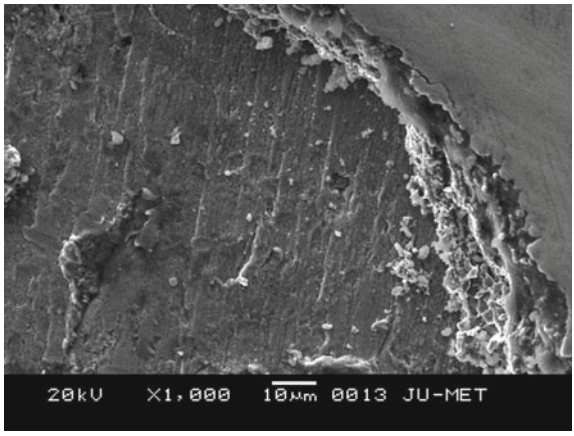

Fig. 11 Fatigue-fractured surface of Ni–B coating at elevated temperature [35]. Reprinted from Surface Review and Letters, 24, Mukhopadhyay et al., Effects of heat treatment on tribological behavior of electroless Ni–B coating at elevated temperatures, 1850014, 2017, with permission from World Scientific Publishing Company

resulting in formation of large pits and detachment of materials. Wear caused due to fatigue wear is less crucial, but what is more important is the useful life in terms of number of cycles of operations before fatigue occurs. Material removal caused by fatigue wear and formation and propagation of cracks causing detachment of surface coatings at 500 °C is illustrated in Fig. 11. Micro-cracks are clearly visible in the SEM micrograph of wear track of electroless nickel coating (Fig. 11) during sliding wear tests at 500 °C.

4.4 Mechanically Mixed Layers (MML) Formation

MML formation is another important observation during wear tests at demanding condition. The tribology of a surface coating or a metallic material at demanding conditions is largely affected by this phenomenon. Wear debris is formed during the wear process due to adhesion, abrasion, fatigue, and a synergy of all these processes. This entrapped wear debris is flattened at different portions of the material as wear progresses. Moreover, some amount of the counterface material is also seen as transfer layers. This along with oxygen may form protective MML. These flattened areas act as load bearing sites and also leads to a smoothening effect causing a decrease in the specific wear rate or COF. MML formation and flattened areas as patches are depicted in Fig. 12.

4.5 Tribo-oxide Scales Formation

Formation of oxide layers which are protective in nature has been reported in several studies. This phenomenon is observed both under ambient as well as high temperature

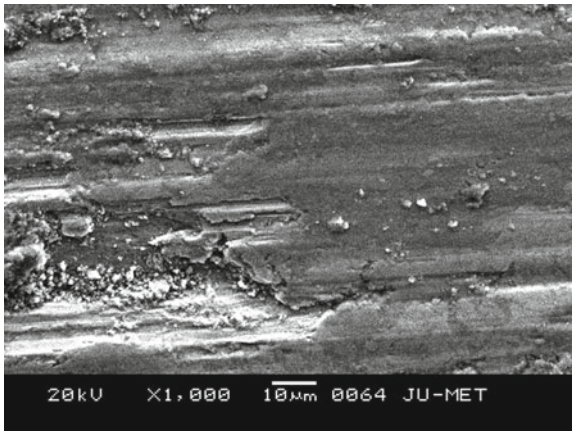

Fig. 12 Formation of mechanically mixed layers for Ni–B coating at elevated temperature [35]. Reprinted from Surface Review and Letters, 24, Mukhopadhyay et al., Effects of heat treatment on tribological behavior of electroless Ni–B coating at elevated temperatures, 1850014, 2017, with permission from World Scientific Publishing Company

condition. A stable thick oxide layer formation results in improved tribo-performance of the metallic materials or coatings under demanding conditions as it tends to protect the layer below it. Though, periodic formation and removal of oxide layers may lead to unstable COF during the wear process and with high fluctuations in the same. When tribo-oxide patches are formed, reduction in specific wear rate is observed. The shear stresses caused during the sliding wear creates resistance to motion and act either within the tribo-patches or at the boundary between the patches and sub-surface material. Formation of blackish oxide layer at 500ºC sliding wear test for electroless nickel coating is illustrated in Fig. 13.

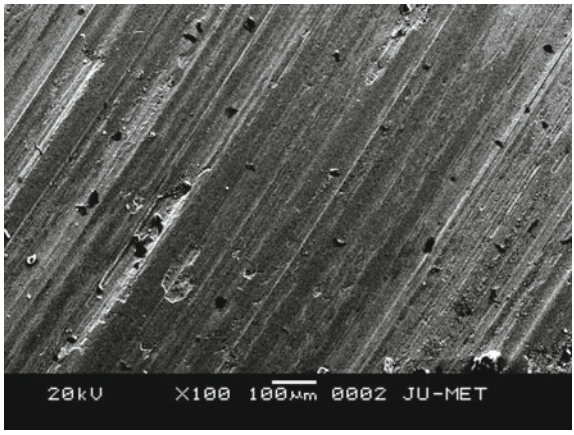

Fig. 13 Formation of tribo-oxide scales for Ni–B coatings at 500 °C [35]. Reprinted from Surface Review and Letters, 24, Mukhopadhyay et al., Effects of heat treatment on tribological behavior of electroless Ni–B coating at elevated temperatures, 1850014, 2017, with permission from World Scientific Publishing Company

5 Conclusions and Future Research Directions

From the foregoing discussion, it can be seen that the investigation of tribological behavior of several materials as well as protective surface coating at high temperatures is gaining significant importance. With the rising demands of industries and aerospace applications, it is, therefore, necessary to obtain tailor made surface properties for components subjected to high temperatures. Among several methods discussed in this study, PVD-CVD coatings were seen to be largely explored for applications at high temperature. Even nickel coatings deposited by electroless method can be used as potential high temperature materials. This is because nickel has a high melting point. Furthermore, it is oxidation resistant up to 500 °C. The Ni–B variants also have high thermal stability. The use of reinforcements in metallic materials helps in dispersion strengthening of the matrix. A consequent improvement in wear and friction performance could be achieved. Various tribo-mechanisms are observed at elevated temperatures. These include adhesion, abrasion, fretting, fatigue, galling, MML, and oxide scales. A combination of the aforesaid wear mechanisms may be also observed. The synergistic effects of temperature as well as the wear mechanisms that occur determine the tribological behavior at demanding conditions. Therefore, the study of high temperature tribological behavior is necessary. Tailor-made coatings with nano-particles need to be explored further for providing effective protection at high temperatures. Nano-particle inclusion with self-lubricating ability and adaptability is the future of surface engineering for high temperature applications.

References

1. Alirezaei S, Monirvaghefi SM, Saatchi A, Ürgen M, Motallebzadeh A (2013) High temperature friction and wear behaviour of Ni–P–Ag–Al_2O_3 hybrid nanocomposite coating. Trans IMF 91(4):207–213
2. Aouadi SM, Singh DP, Stone DS, Polychronopoulou K, Nahif F, Rebholz C et al (2010) Adaptive VN/Ag nanocomposite coatings with lubricious behavior from 25 to 1000 °C. Acta Materialia 58(16):5326–5331
3. Brenner A, Riddell GE (1946) Nickel plating on steel by chemical reduction. J Res Natl Bur Stand 37(1):54–56
4. Chai B, Xiong J, Guo Z, Liu J, Ni L, Xiao Y, Chen C (2019) Structure and high temperature wear characteristics of CVD coating on HEA-bonded cermet. Ceram Int 45(15):19077–19085
5. Chen H, Gou G, Tu M, Liu Y (2010) Research on the friction and wear behavior at elevated temperature of plasma-sprayed nanostructured WC-Co coatings. J Mater Eng Perform 19(1):1–6
6. Chen H, Du Y, Wang D, Zhang C, Yang G, Liu B et al (2018) TiC/Ti_3AlC_2–Co plasma-sprayed coatings with excellent high-temperature tribological properties. Ceram Int 44(18):22520–22528
7. Das SK, Sahoo P (2011) Tribological characteristics of electroless Ni–B coating and optimization of coating parameters using Taguchi based grey relational analysis. Mater Des 32(4):2228–2238
8. Dejun K, Haoyuan G (2015) Friction-wear behaviors of cathodic arc ion plating AlTiN coatings at high temperatures. Tribol Int 88:31–39

9. Fazel M, Jazi MG, Bahramzadeh S, Bakhshi SR, Ramazani M (2014) Effect of solid lubricant particles on room and elevated temperature tribological properties of Ni–SiC composite coating. Surf Coat Technol 254:252–259
10. Fernandes F, Polcar T, Loureiro A, Cavaleiro A (2015) Effect of the substrate dilution on the room and high temperature tribological behaviour of Ni-based coatings deposited by PTA on grey cast iron. Surf Coat Technol 281:11–19
11. Franco M, Sha W, Aldic G, Malinov S, Çimenoğlu H (2016) Effect of reinforcement and heat treatment on elevated temperature sliding of electroless Ni–P/SiC composite coatings. Tribol Int 97:265–271
12. Ghaderi M, Rezagholizadeh M, Vaghefi SM, Heidary A (2016) Investigation of high temperature wear resistance of electroless nickel coating with different contents of phosphorous. Protect Metals Phys Chem Surf 52(3):538–542
13. Gronostajski Z, Kaszuba M, Widomski P, Smolik J, Ziemba J, Hawryluk M (2019) Analysis of wear mechanisms of hot forging tools protected with hybrid layers performed by nitriding and PVD coatings deposition. Wear 420:269–280
14. Hu SB, Tu JP, Mei Z, Li ZZ, Zhang XB (2001) Adhesion strength and high temperature wear behaviour of ion plating TiN composite coating with electric brush plating Ni-W interlayer. Surf Coat Technol 141(2–3):174–181
15. Hui S, Wen Z, Shouyu Z, Dejun K (2019) Friction-wear performances of cathodic arc ion plated CrN coating at elevated temperatures. Powder Metall Met Ceram 58:73–80
16. Jianxin D, Aihua L (2013) Dry sliding wear behavior of PVD TiN, $Ti_{55}Al_{45}N$, and $Ti_{35}Al_{65}N$ coatings at temperatures up to 600°C. Int J Refract Metal Hard Mater 41:241–249
17. Jin G, Cai Z, Guan Y, Cui X, Liu Z, Li Y, Dong M (2018) High temperature wear performance of laser-cladded FeNiCoAlCu high-entropy alloy coating. Appl Surf Sci 445:113–122
18. Kesavan D, Kamaraj M (2010) The microstructure and high temperature wear performance of a nickel base hardfaced coating. Surf Coat Technol 204(24):4034–4043
19. Kondratiuk J, Kuhn P (2011) Tribological investigation on friction and wear behaviour of coatings for hot sheet metal forming. Wear 270(11–12):839–849
20. Kubart T, Polcar T, Kopecký L, Novak R, Novakova D (2005) Temperature dependence of tribological properties of MoS_2 and $MoSe_2$ coatings. Surf Coat Technol 193(1–3):230–233
21. Kundu S, Das SK, Sahoo P (2018) Tribological behaviour of electroless Ni-P deposits under elevated temperature. Silicon 10(2):329–342
22. Kundu S, Das SK, Sahoo P (2019a) Friction and wear behavior of electroless Ni-PW coating exposed to elevated temperature. Surf Interf 14:192–207
23. Kundu S, Das SK, Sahoo P (2019b) Tribological behavior of autocatalytic Ni–P–B coatings at elevated temperatures. Appl Phys A 125(8):520
24. Kuo CC, Lin YT, Chan A, Chang JT (2019) High temperature wear behavior of titanium nitride coating deposited using high power impulse magnetron sputtering. Coatings 9(9):555
25. Lanzutti A, Lekka M, de Leitenburg C, Fedrizzi L (2019) Effect of pulse current on wear behavior of Ni matrix micro-and nano-SiC composite coatings at room and elevated temperature. Tribol Int 132:50–61
26. Lekka M, Lanzutti A, Casagrande A, deLeitenburg C, Bonora PL, Fedrizzi L (2012) Room and high temperature wear behaviour of Ni matrix micro-and nano-SiC composite electrodeposits. Surf Coat Technol 206(17):3658–3665
27. Leon OA, Staia MH, Hintermann HE (2003) High temperature wear of an electroless Ni–P–BN (h) composite coating. Surf Coat Technol 163:578–584
28. Li Z, Wang J, Lu J, Meng J (2013) Tribological characteristics of electroless Ni–P–MoS_2 composite coatings at elevated temperatures. Appl Surf Sci 264:516–521
29. Lu XL, Liu XB, Yu PC, Qiao SJ, Zhai YJ, Wang MD et al (2016) Synthesis and characterization of Ni60-hBN high temperature self-lubricating anti-wear composite coatings on Ti6Al4V alloy by laser cladding. Opt Laser Technol 78:87–94
30. Mang T, Bobzin K, Bartels T (2011) Industrial tribology: tribosystems, friction, wear and surface engineering, lubrication. Wiley

31. Masoumi F, Ghasemi HR, Ziaei AA, Shahriari D (2012) Tribological characterization of electroless Ni–10% P coatings at elevated test temperature under dry conditions. Int J Adv Manuf Technol 62(9–12):1063–1070
32. Mu Y, Liu M, Zhao Y (2016) Carbon doping to improve the high temperature tribological properties of VN coating. Tribol Int 97:327–336
33. Mukhopadhyay A, Barman TK, Sahoo P (2017a) Tribological behavior and corrosion resistance of electroless Ni-B-W coatings. J Mol Eng Mater 5(03):1750010
34. Mukhopadhyay A, Barman TK, Sahoo P (2017b) Tribological behavior of sodium borohydride reduced electroless nickel alloy coatings at room and elevated temperatures. Surf Coat Technol 321:464–476
35. Mukhopadhyay A, Barman TK, Sahoo P (2017c) Effects of heat treatment on tribological behavior of electroless Ni–B coating at elevated temperatures. Surf Rev Lett 24(Supp01):1850014
36. Mukhopadhyay A, Barman TK, Sahoo P (2018a) Effect of operating temperature on tribological behavior of as-plated Ni-B coating deposited by electroless method. Tribol Trans 61(1):41–52
37. Mukhopadhyay A, Barman TK, Sahoo P (2018b) Tribological behavior of electroless Ni-B-Mo coatings under dry and lubricated conditions and corrosion resistance in 3.5% NaCl solution. J Tribologi 18:108–124
38. Mukhopadhyay A, Barman TK, Sahoo P (2019) Friction and wear performance of electroless Ni-B coatings at different operating temperatures. Silicon 11(2):721–731
39. Niu R, Li J, Wang Y, Chen J, Xue Q (2017) Structure and high temperature tribological behavior of TiAlN/nitride duplex treated coatings on Ti6Al4V. Surf Coat Technol 309:232–241
40. Nohava J, Dessarzin P, Karvankova P, Morstein M (2015) Characterization of tribological behavior and wear mechanisms of novel oxynitride PVD coatings designed for applications at high temperatures. Tribol Int 81:231–239
41. Ouyang JH, Sasaki S (2005) Tribological characteristics of low-pressure plasma-sprayed $A1_2O_3$ coating from room temperature to 800 °C. Tribol Int 38(1):49–57
42. Pal S, Sarkar R, Jayaram V (2018) Characterization of thermal stability and high-temperature tribological behavior of electroless Ni-B coating. Metal Mater Trans A 49(8):3217–3236
43. Pellizzari M (2011) High temperature wear and friction behaviour of nitrided, PVD-duplex and CVD coated tool steel against 6082 Al alloy. Wear 271(9–10):2089–2099
44. Polcar T, Kubart T, Novák R, Kopecký L, Široký P (2005) Comparison of tribological behaviour of TiN, TiCN and CrN at elevated temperatures. Surf Coat Technol 193(1–3):192–199
45. Polcar T, Novák R, Široký P (2006) The tribological characteristics of TiCN coating at elevated temperatures. Wear 260(1–2):40–49
46. Rapoport L, Moshkovich A, Perfilyev V, Lapsker I, Kugler M, Kailer A et al (2014) High temperature friction behavior of CrV_xN coatings. Surf Coat Technol 238:207–215
47. Richard C (2013) Tribological coatings for high-temperature applications. In: Wang QJ, Chung YW (eds) Encyclopedia of tribology. Springer, Boston, MA
48. Radil K, DellaCorte C (2017) The performance of PS400 subjected to sliding contact at temperatures from 260 to 927 °C. Tribol Trans 60(6):957–964
49. Rodriguez-Baracaldo R, Benito JA, Puchi-Cabrera ES, Staia MH (2007) High temperature wear resistance of (TiAl) N PVD coating on untreated and gas nitrided AISI H13 steel with different heat treatments. Wear 262(3–4):380–389
50. Sahoo P (2014) Engineering tribology. PHI Learning Pvt. Ltd. Delhi 110092, India
51. Sahoo P, Das SK (2011) Tribology of electroless nickel coatings–a review. Mater Des 32(4):1760–1775
52. Serra EC, Soares VFD, Fernandez DAR, Hübler R, Juste KRC, Lima CL, Tentardini EK (2019) Influence of WS_2 content on high temperature wear performance of magnetron sputtered TiN-WSx thin films. Ceram Int 45(16):19918–19924
53. Shouyu Z, Dejun K (2018) Microstructures and friction–wear behaviors of cathodic arc ion plated chromium nitride coatings at high temperatures. J Tribol 140(3):031602
54. Shu FY, Wu L, Zhao HY, Sui SH, Zhou L, Zhang J et al (2018) Microstructure and high-temperature wear mechanism of laser cladded CoCrBFeNiSi high-entropy alloy amorphous coating. Mater Lett 211:235–238

55. Sivakumar R, Mordike BL (1989) High temperature coatings for gas turbine blades: a review. Surf Coat Technol 37(2):139–160
56. Stone DS, Harbin S, Mohseni H, Mogonye JE, Scharf TW, Muratore C et al (2013) Lubricious silver tantalate films for extreme temperature applications. Surf Coat Technol 217:140–146
57. Stone DS, Migas J, Martini A, Smith T, Muratore C, Voevodin AA, Aouadi SM (2012) Adaptive NbN/Ag coatings for high temperature tribological applications. Surf Coat Technol 206(19–20):4316–4321
58. Wang W (2004) Application of a high temperature self-lubricating composite coating on steam turbine components. Surf Coat Technol 177:12–17
59. Wang Y, Lee JW, Duh JG (2016) Mechanical strengthening in self-lubricating CrAlN/VN multilayer coatings for improved high-temperature tribological characteristics. Surf Coat Technol 303:12–17
60. Yalamanchili K, Jiménez-Piqué E, Pelcastre L, Bakoglidis KD, Roa JJ, Jöesaar MJ et al (2016) Influence of microstructure and mechanical properties on the tribological behavior of reactive arc deposited Zr-Si-N coatings at room and high temperature. Surf Coat Technol 304:393–400

Chapter 3
Aramid Polycarbonate Resin Film Engineered Composite for Ballistic Protection: Engineered Layered Materials

Ramdayal Yadav, Minoo Naebe, Xungai Wang, and Balasubramanian Kandasubramanian

1 Introduction

The modern battlefield involves threats not only from the enemy combatants but also includes continuous friction and low-velocity impact hazards from the civilian populace, and it is intensified as conflict matures [14]. Carr et al. have reported that such a dynamic state of circumstances in the battlefield renders major causalities due to the generation of lethal fragments compare to those caused by a bullet [14]. The importance of protection was realized through the outnumbered causalities during World War I and various other conflicts around the world [77]. In the recent years, the new avenue of materials has been extensively exploited based on natural armor design strategies imitating the interdigitating hierarchal structures of natural species like mollusk shells, lotus leaves, spider silk, etc. These structures are exploited due to their multifunctional ability and high mechanical properties compared to their constituent material composition, lightweight, and multi-hit capabilities. [4, 23]. Though, a number of such natural structures have been studied extensively but imitating those hierarchies in synthetic materials at a various length scale are yet to achieve. However, among various reported studies on natural architecture, layer by layer assembly of nacreous structure has been widely explored due to their high mechanical properties like high strength as well as high toughness in addition to their multi-hit capabilities. Mollusk shells are regarded as layered structure with calcite (rhombohedral) or aragonite (orthorhombic) (95–99%) and organic materials (0.1–5%) like proteins and polysaccharides [34].

R. Yadav · M. Naebe · X. Wang
Institute for Frontier Materials (IFM), Deakin University, Melbourne, Australia

B. Kandasubramanian (✉)
Defence Institute of Advanced Technology, Deemed University (DU), Ministry of Defence, Pune, India
e-mail: meetkbs@gmail.com

S. Sahoo (ed.), *Recent Advances in Layered Materials and Structures*,
Materials Horizons: From Nature to Nanomaterials,
https://doi.org/10.1007/978-981-33-4550-8_3

Though various materials and combination of the process were exploited to biologically mimicking the hierarchical architecture of nacre and its emulation in commercially available systems have been least reported. In recent years, fiber-reinforced composites have been extensively exploited for the development of efficient ballistic material due to their high strength, stiffness, and specific strength [3]. The ballistic response of fiber-reinforced composite utilizes thermoset and thermoplastic as a polymer matrix. Though thermoset has demonstrated superior tensile, shear, and compressive strength but low-temperature storage, hot/wet stability, and long curing process curtails its exploitation as fiber-reinforced polymer matrix [9, 15–17]. In the recent years, thermoplastic are preferred widely as matrix over thermoset due to their ability to recycle, relatively easy processing into different shapes and sizes as well as long shelf life [45, 69]. Apart from thermoplastic, a number of fibers have been employed for the development of ballistic composite including E-Glass, S-Glass, aramid (Kevlar®-29,49, 129), Nylon 66, poly (p-phenylene benzobisoxazole) (Zylon®), etc. [19, 36, 76]. Among all the class of lightweight fibrous materials, aramid fiber has been gleaned as a prominent example of laboratory experimentation to commercialization. Aramid fiber is a long polymer chain of poly-paraphenylene teraphthalamide that exhibits extraordinary mechanical properties like high strength to weight ratio, high modulus, and toughness with excellent dimensional stability [31, 47, 67].

In the current study, we have demonstrated the utilization of resin transfer molding technique (resin-fiber-infused technique) for fabricating high-performance reinforced polycarbonate composite to mimic the natural nacreous design strategies. Though, various combinations of thermoplastic and high-performance fiber have been exploited [3, 8, 25, 26, 28, 68], but the elucidation of polycarbonate for ordinance velocity range has been least reported in the context of layered natural armor exoskeleton. In addition to ballistic efficacy, we have also discerned the thermal attribute of developed composite and demonstrated that fiber reinforcement had eclipsed the thermal characteristics of polycarbonate in addition to its mechanical property (impact characteristic). The thermal stability of the composite was also evaluated on the basis of the linear approximation of Arrhenius equation at the onset temperature of degradation and in the region of degradation.

2 Materials and Experimental Details

Polycarbonate (PC) (MFI = 10.5 g/10 min, viscosity 22 cp, LEXAN grade 143R) was purchased from SABIC Innovative Plastics India Pvt Ltd, India. Aramid fiber was obtained from the Naval Materials Research Laboratory (NMRL), DRDO, Ambernath, India. The composite was fabricated via a resin-fiber-infusion technique, as illustrated in Fig. 1 [59]. The fabrication method includes transferring the desired dimension of polycarbonate at aramid fabric (placed over metallic mold plate), ensuring proper interaction between fabric and polycarbonate film. This process was further repeated until the required dimension and thickness is not achieved. The

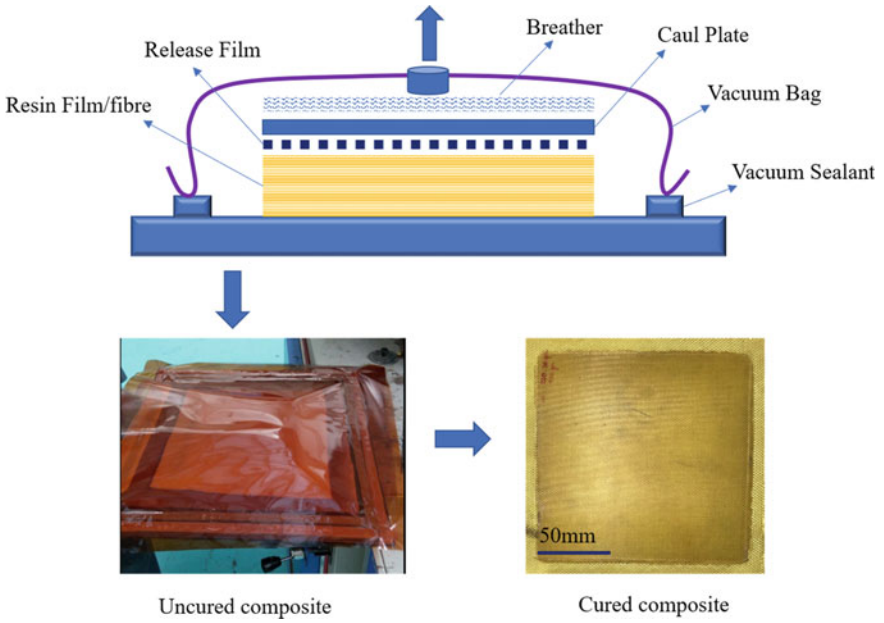

Fig. 1 Processing technique for fiber-reinforced layered polycarbonate composite (FRL PC composite)

layered stacks were placed inside the vacuum bag, as illustrated in Fig. 1, followed by the increasing temperature at 2°C/min till 285°C (melting temperature of polycarbonate). The layered stacks of polycarbonate and aramid have been allowed to be held until the complete infusion is not achieved (the time was optimized for 20 min). The curing process was performed in the oven followed cooling to room temperature before demolding [7]. The standard operating procedure utilized in the current study has been provided in Table 1. The impact property of developed composites was conducted as per ASTM standard D256, while thermomechanical properties were evaluated by dynamic mechanical analysis (TA Q800-USA) under the condition 2

Table 1 Standard operating procedure for developing polycarbonate layered composite

Conditions	Operations
Reinforcement	Aramid fiber (223GSM)
Matrix	Polycarbonate (250GSM)
Required dimension	150 mm × 150mm
Targeted fiber volume fraction	57%
Weight of uncured composite	218.72 g
Curing condition	Ramp from ambient to 285 °C at the rate of 5 °C/min
Dwell time	20 min at 285 °C

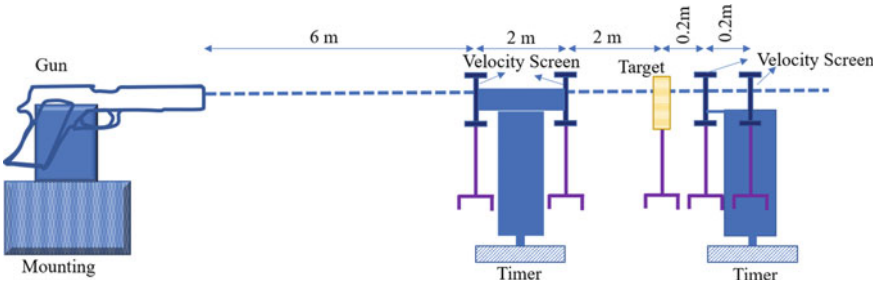

Fig. 2 Ballistic test setup

°C/min heating rate from room temperature to 200 °C. Thermal properties of developed layered composites have been evaluated by differential scanning calorimetry in addition to temperature modulated conditions (TA Q200-USA). Thermal gravimetric analysis was also conducted to understand the degradation phenomenon (TA Q50-USA. Field emission scanning electron (FESEM) microscope was utilized to conduct the fracture surface analysis for the samples (FESEM, Carl-Zeiss, Germany).

2.1 Ballistic Experiment

Ballistic efficacy of layered polycarbonate/aramid composite was assessed by inhouse small arm ballistic facility of Defence Metallurgical Research Laboratory, DRDO, Kanchanbagh Hyderabad, India as elucidated in Fig. 2. 7.62 × 39 mm mild steel core projectile was fired at the distance of 10 m from the muzzle end of the gun [60].

3 Results and Discussion

The development of nacreous structure in nature is a slow process and involves the absorption of minerals and organic matter for intermittent deposition in brick and mortar architecture [18, 49]. The imitation of such slow growth process with analogous environmental stimulus in laboratory is not apparent, but the extensive effort has been employed to mimic natural exoskeleton in artificial materials [65, 66, 71–74, 81]. Self-assembly and sequential deposition are widely exploited methodology for developing a natural armor system in artificial materials in terms of nano and micro-dimensionality. Yao et al. have reported the vacuum filtration or water evaporation technique to mimic the nacreous structure in chitosan and montmorillonite bionanocomposite film [79]. They have demonstrated that the incorporation of nacreous architecture in hybrid building block has rendered augmented

Young's modulus and ultimate tensile strength in addition to enhanced fire retardancy. In another study, Cheng et al. have demonstrated the cross-linking of two-dimensional graphene oxide sheets with π-conjugated long-chain polymers made of 10,12-pentacosadiyn-1-ol (PCDO) monomers via a conjugated cross-linking method. Graphene oxide sheets in this study have been considered as a brick, while PCDO is gleaned from being a mortar phase in artificial nacre [20]. The developed composite avails comparable organic content to the natural nacre in the composite in addition to the distinct organic and inorganic phase with excellent tensile and toughness.

It has been observed that most of the work mainly focuses on an emulation of analogous mollusk architecture at nano or micro-dimension, but we have demonstrated that even macroscopic mimicking of such structure possesses the ability to demonstrate enhanced mechanical property [75]. In this abstraction, we have demonstrated the hypothesis of mollusk layered assembly architecture where polycarbonate has been considered as a soft organic phase, while aramid fiber is contemplated as a hard rick structure. The macroscopic exoskeleton of developed composite layered fiber-reinforced composite has been elucidated in Fig. 3 a–d. Figure 3b delineates the intact layered architecture analogous to the nacreous structure reported by Yao et al. and Cheng et al. in the previously elaborated study, while Fig. 3c renders intermittent alternative assembly of polycarbonate and aramid fiber. The thermal and mechanical

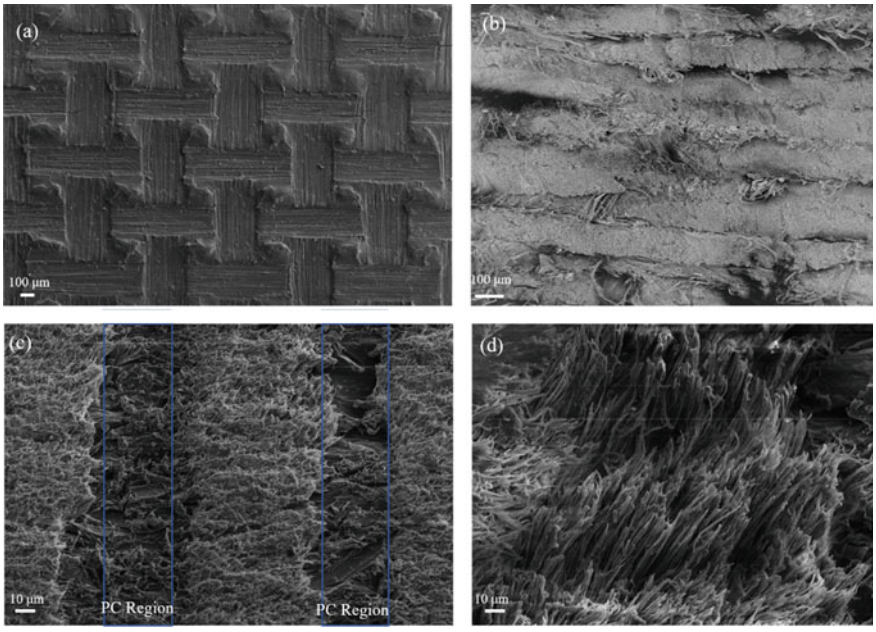

Fig. 3 Layered assembly of polycarbonate and aramid fiber **a** top view of the composite, **b** cross-sectional view, **c** cross-sectional view at higher magnification, and **d** cross-section view of reinforced fiber

property of the developed composite has been elaborated in a later section in addition to the ballistic efficacy against high-speed muzzle velocity.

Polycarbonate has been considered as a prominent commercially available amorphous polymer due to its high toughness and impact resistance [28, 39] and exhibits nearly all mechanical attributes of the glassy polymer at the different combination of time and temperature [80]. The characteristics of polycarbonate have been explored by number of methodology including dynamic mechanical analysis [74, 80], positron lifetime spectroscopy [44], dielectric [53] and nuclear magnetic spectroscopy [54]. Among various reported techniques, dynamic mechanical analysis has been observed to be the prominent technique which possesses the ability to resolve elastic and viscous component of polymer [64]. Dynamic mechanical analysis of polycarbonate was studied by Illers et al. at 1 Hz frequency from torsional pendulum reported three relaxation peaks at +155, +80 and −97 °C, subsequently corroborated as α, β, and γ, respectively [40, 80].

Among these three relaxations, α transition is enumerated to the glass transition temperature, while β transition is related to the small localized chain motion or processing condition [29, 37]. γ transition in polycarbonate is a debatable point and extensively deliberated by Yee et al. [80]. In the current study, we are mainly concentrated on structural and impact application of the developed composite; therefore, the relaxation related to the glass transition is primarily focused. Figure 4a–c and d–f elucidated the dynamic mechanical analysis of pristine polycarbonate and FRL PC composite, evaluated by tensile and 3-point bend test, respectively. As delineated in Fig. 4b–c and e–f, the storage (elastic component) and loss modulus (viscous component) were observed to be augmented in FRL PC composite. In our previous study, we have demonstrated that the peak of Tan δ (ratio of loss modulus to storage modulus) can be associated with the α transition or glass transition temperature [77]. The corresponding peak can be rationalized to the segmental chain mobility and increased degree of freedom due to the conformational arrangement of the polymer chain. It is essential to mention here that the enhanced glass transition temperature for fiber-reinforced composite (Table 2) in both the testing mode cannot be substantiated to just polycarbonate of the composite. Although the shift in glass to rubbery transition temperature for composite emerged, due to the restricted segmental motion polycarbonate in aramid fiber as per the concept of glass transition temperature as isoviscous state [51]. We postulated that the diminishing peak height of Tan δ can be contemplated to the improved working temperature since high Tan δ values demonstrate non-reversible structural deformation in the polymeric system [64].

The dynamic mechanical response from polymeric materials involves physical change as a function of temperature, while the thermal or heat effect can be exemplified via differential scanning calorimetry (DSC) and temperature modulated DSC [63]. DSC is one of the most accepted methodologies to measure the heat flow in the polymer system as the function of temperature and subsequently identifies its glass transition temperature. Höhne et al. have elucidated that during the glass transition temperature, the intrinsic attributes of polymer and measurement variables turned into a time-dependent phenomenon, and system passes through the non-equilibrium

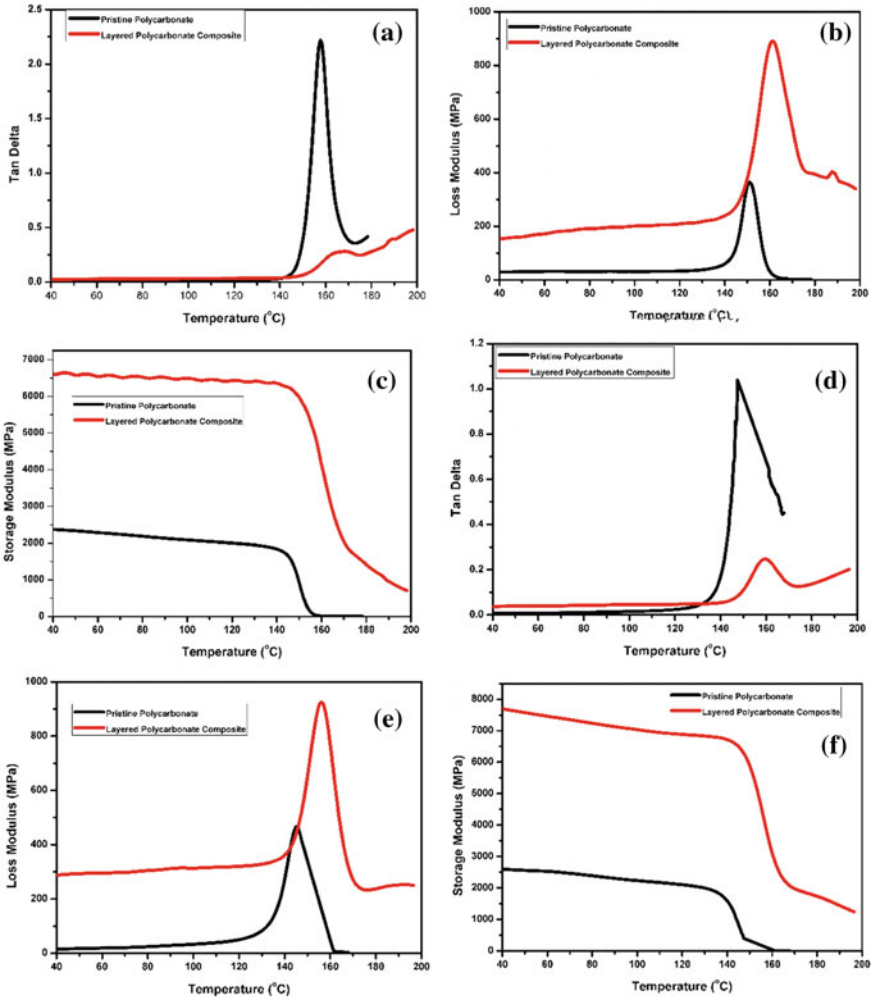

Fig. 4 Dynamic mechanical analysis for pristine polycarbonate and fiber-reinforced composite **a–c** tensile mode of DMA, **d–f** 3-point bend mode

state where classical thermodynamics is not applicable [33]. Therefore, the second-order transition (glass transition) requires heat to pass through that non-equilibrium relaxation stage and subsequently renders step in DSC spectra (circled region in Fig. 5a). Although the evaluation of Tg from the step transition is subjective [63], but in the current study, the onset temperature of the relaxation has been considered as glass transition temperature (Table 3). Since DSC evaluates the combined effect of heat capacity and enthalpic relaxation, therefore, its inadequacy to resolve step transition in some systems curtails its effective utilization, as illustrated in Fig. 5a (for fiber-reinforced PC composite). In this context, temperature modulated DSC

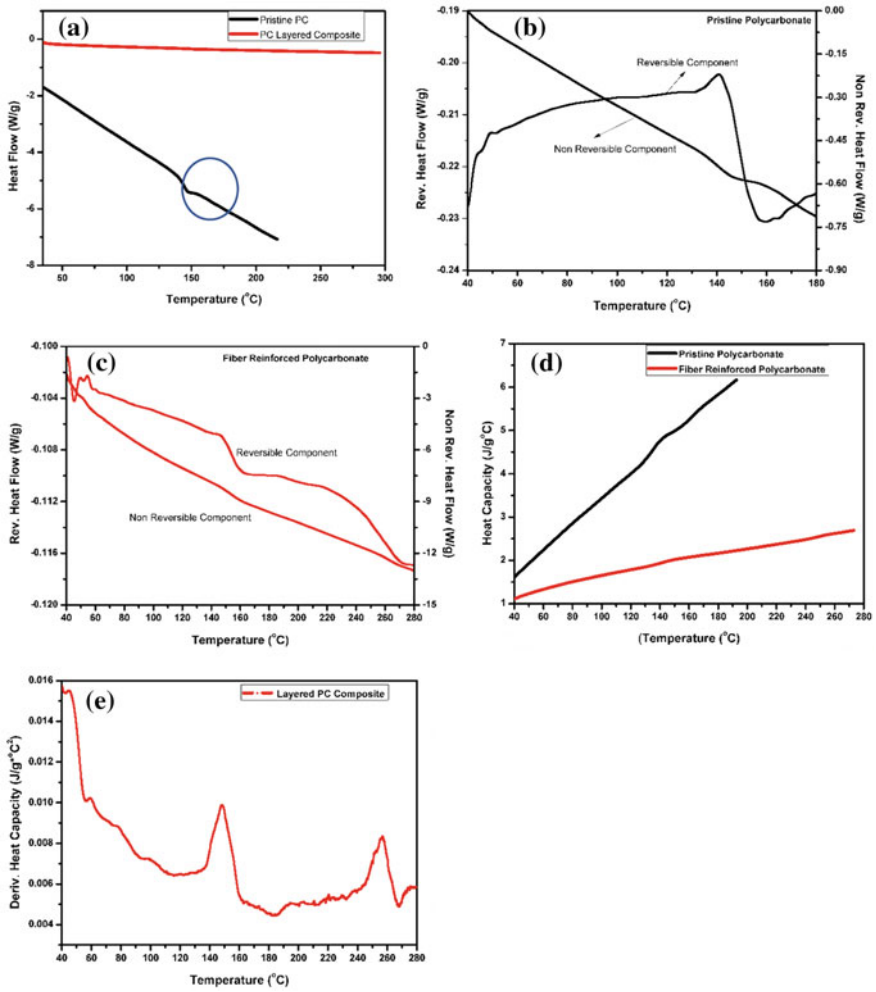

Fig. 5 **a** Differential scanning calorimetry for PC and FRL PC composite, **b** temperature modulated DSC of polycarbonate, **c** temperature modulated DSC of FRL PC composite, **d** heat capacity for PC and FRL PC composite, and **e** derivative heat capacity for FRL PC composite

can provide significant insight by the virtue of its efficacy to measure reversible (heat flow-change of heat capacity with temperature) [58] and non-reversible heat flow (non-reversible heat flow-change of heat capacity with time) [58] separately as discerned in Fig. 5b, c. In addition to rev and non-rev heat flow component, Fig. 5d exhibits the heat capacity difference between the pristine polycarbonate and fiber-reinforced PC composite which can be effectively explained on the basis of fundamental hypothesis related to the heat capacity. The heat capacity of a polymeric system mainly deliberated in two components, i.e., lattice vibration (skeleton vibration: low frequency acoustic vibration) and vibration from internal motion (high

frequency vibration compare to lattice vibration) [30]. The contribution of internal motion to the heat capacity is considerably higher compared to the lattice vibration at the working temperature of the polymer (>100 K) [30]. Such atomic motion in macromolecules involves bond stretching, bond bending, torsional oscillation, flipping of structural unit from one equilibrium to another equilibrium, and cooperative motion [10]. Therefore, any hinderance to the motion of atom or group of atoms largely influences the characteristics of heat capacity. In this context, it can be enumerated that the significant reduction in heat capacity of fiber-reinforced PC composite emerged due to the restricted intermolecular and intramolecular motion of PC in the entire temperature range. Hourston et al. have demonstrated that the temperature derivative of heat capacity can be effectively utilized to illustrate various transitions observed in the temperature modulated DSC [38]. Figure 5e delineates the derivative heat capacity of the fiber-reinforced PC composite, where the first peak of the spectra can be corroborated to the α relaxation of the polymer while the secondary peak corresponds to the melting of the PC matrix.

Thermogravimetric analysis has been considered as another efficient technique other than DSC and temperature modulated DSC to evaluate the thermal stability of the polymeric system and its composite. Thermogravimetric analysis of the pristine polycarbonate and fiber-reinforced PC composite has been delineated in Fig. 6a, b, where Fig. 6a elucidated the loss weight fraction with the function of temperature and Fig. 6b demonstrates the rate of loss of weight fraction (a derivative of mass loss). The degradation mechanism of polycarbonate and aramid fibers has been extensively reported elsewhere [1, 12, 13, 24, 43, 46, 50, 55–57], and therefore the current study

Table 2 Structural stability in terms of temperature (obtained from DMA)

	Pristine polycarbonate (tensile mode)	FRL PC composite (Tensile Mode)	Pristine polycarbonate (3-point mode)	FRL PC composite (3-point mode)
Storage modulus (°C) onset	145.66	153.35	139.51	149.13
Loss modulus (°C) peak position	151.69	161.21	145.76	156.07
Tanδ (°C)peak position	157.74	169.32	147.41	159.22

Table 3 Thermal attributes of polycarbonate and its FRL composites

	Onset temperature of degradation (°C)	Ea (kJ/mol.)	T_{50}	Ea (kJ/mol.)
Pristine polycarbonate	475.56	123.79	515.46	121.38
Aramid fiber	504.51	25.60	533.29	147.40
FRL PC composite	429.27	63.42	551.68	41.57

mainly focused on the evaluation of thermal stability expressed in terms of temperature where 50% (T_{50})of the mass has been lost compared to its final value in inert environment [32]. Fiber-reinforced PC composite has demonstrated the augmentation in thermal stability (T_{50} = 551.68) as elucidated in Table 3. It is evident from Fig. 6b, FRL PC composite exhibits the characteristics of thermal spectra of neither polycarbonate nor aramid fiber. Such stimulating attributes can be predominantly explained by more detailed elemental analysis for detailed contemplation on degradation mechanism, but the activation energy can provide insight into the thermal stability in addition to T_{50}. Apparent activation energy from thermogravimetry data can be obtained from linear extrapolation of Arrhenius equation (Eq. 1) assuming degradation process as first-order kinetic with its applicability to the small extent of degradation [22, 78]. The slop of the linear approximation plot of Arrhenius equation discern the apparent activation energy, as demonstrated in Fig. 6c–d and further tabulated in Table 3. It is evident from the table that the available activation energy for FRL PC composite is between the activation energy of pristine polycarbonate and aramid fiber before the onset of the degradation process. Essentially, the decomposition process, by definition, refers to the breaking of materials by physical or chemical means and providing initial alteration in structural characteristics for total degradation to be ensued [42]. The initiation or completion of the decomposition process requires some form of energy, and therefore, if available energy at an instance is comparatively smaller, then the system is gleaned from being thermally stable. In this context, we envisioned that the developed FRL PC composite thermally more stable beyond the onset of degradation phenomenon (475–550 °C) (Fig. 6d) compare to both aramid and pristine PC, but its thermal stability is not comparable to aramid during the onset of decomposition (Fig. 6c).

$$\ln\left[\frac{\ln\frac{w_o}{w}}{t}\right] = \left(-\frac{E_a}{R}\right)\frac{1}{T} + \ln k_o \tag{1}$$

where w_o = initial weight w = weight at the time t (min) E_a = apparent activation energy R = ideal gas constant (8.314 J/K. mol.) T = absolute temperature k_o = Arrhenius constant.

In order to further evaluate the mechanical characteristics of polycarbonate, we have exploited the utilization of the notch impact testing technique followed by high-velocity muzzle impact. It is widely acknowledged that polycarbonate is notch sensitive, and sharpening the notch dimension can transform its ductile fracture attribute to the brittle fracture characteristic [21]. It is obvious from Fig. 7 that polycarbonate in the current study exhibits sufficiently high impact energy, but the fiber reinforcement in PC augmented the impact energy by many folds, and complete fracture along the width was not observed even with the application of 22 J load pendulum. The fracture surface of FRL PC composite has been demonstrated in Fig. 3c, d, which clearly elucidate that fracture phenomenon is significantly eclipsed by fiber splitting and fibril fracture without discerning the failure phenomenon of PC particulate.

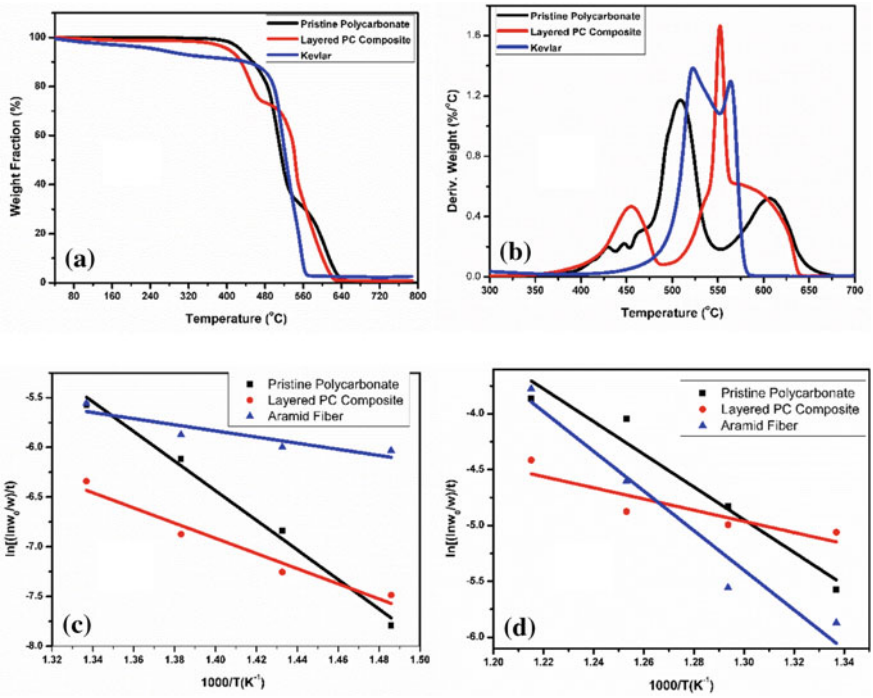

Fig. 6 **a** Thermogravimetric analysis for PC, aramid, and FRL PC composite, **b** derivative weight fraction of PC, aramid, and FRL PC composite, **c** Arrhenius approximation before the onset of degradation, and **d** Arrhenius approximation beyond the onset of degradation

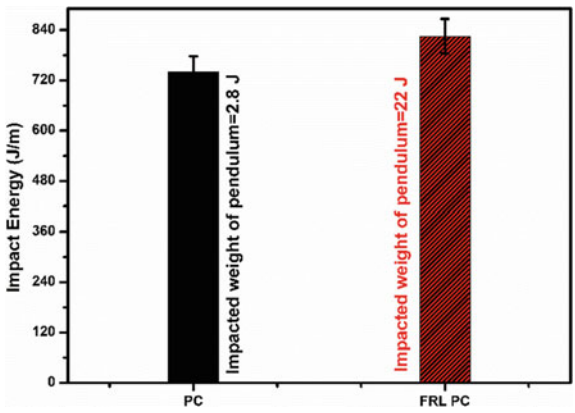

Fig. 7 Elucidation of impact energy for PC and FRL PC composite

Polycarbonate was first instituted for the development of lightweight and transparent protection equipment like safety goggles, industrial machine guards, aircraft windscreen, and police riot shields [52]. Wright et al. have evaluated the perforation and penetration phenomenon in polycarbonate and demonstrated that five main attributes can be realized against the subordinance velocity impact depending on thickness of the sheet or plate, i.e., elastic dishing, deep penetration, cone cracking, and plugging [72, 73]. Edward et al. have further reported that though a wide range of ballistic phenomena was exploited by Wright et al., but the ductile to brittle transition was not effectively discussed [27]. They have performed an experiment on polycarbonate by throwing the materials utilized in riots, i.e., brick (11.7 ± 2.5 m/s), golf ball (24.2 ± 5.3 m/s), and ball bearing (23.2–96.2 m/s). The obtained results were concluded as (i) the velocity achieved by the rioter was found to be lower which do not possess the ability to produce any macroscopic damage to polycarbonate, (ii) at the velocity greater than 50 m/s, the damage become the function of mass and shape of the impacting the projectile. Therefore, the terminal ballistic phenomenon in polycarbonate can be corroborated to the number factor that includes shape of the projectile, thickness of the target, and type of the projectile and velocity of the projectile. Polycarbonate is mainly exploited as ballistic materials in the combination of glass (connected with polyvinyl butyral), which shattered when fired the bullet and retard the projectile enough so that PC prevents the penetration of the projectile [6, 35, 41, 70].

The stimulating characteristics of impact result enticed further to evaluate the developed composite against the high-velocity muzzle impact. As elucidated earlier that high impact velocity on developed composite was performed by 7.62×39 mm steel core projectile with the velocity of 747 ± 15 m/s at the distance of 10 m. Before performing the ballistic impact on the FRL PC composite, an x-ray tomographic scan was carried out to contemplate available defects, as exemplified in Fig. 8a and scanning video provided in supporting information (video V-1) [59]. As ascertained in the figure and video imaging of the composite sample, common laminated composite defects like voids, interlayer, or intralayer delamination and cracks are not visually available [2]. In this context, we have postulated that the developed FRL PC composite is dimensionally and structurally integrated and intact, which was also observed in dynamic mechanical analysis in tension and 3-point bend mode. Later, the analogous tomographic scan was performed after the ballistic impact (Fig. 8b and supporting information video V-2) and the ballistic efficacy was evaluated, based on absorbed energy (calculated as per Eq. 2) [48, 60]. The absorbed energy by the FRL PC composite was observed to be 240.22 J (calculated from Eq. 2) for the velocity range provided in Fig. 8b. The failure phenomenon of polycarbonate [5, 62, 72, 73], and aramid fibers have been extensively reported separately [11, 76] failure phenomenon in the current study requires further deliberation because we did not observe any characteristic fracture features like delamination, interfacial debonding, intra and interlaminar fiber shear or high-temperature localized melting under computed tomographs.

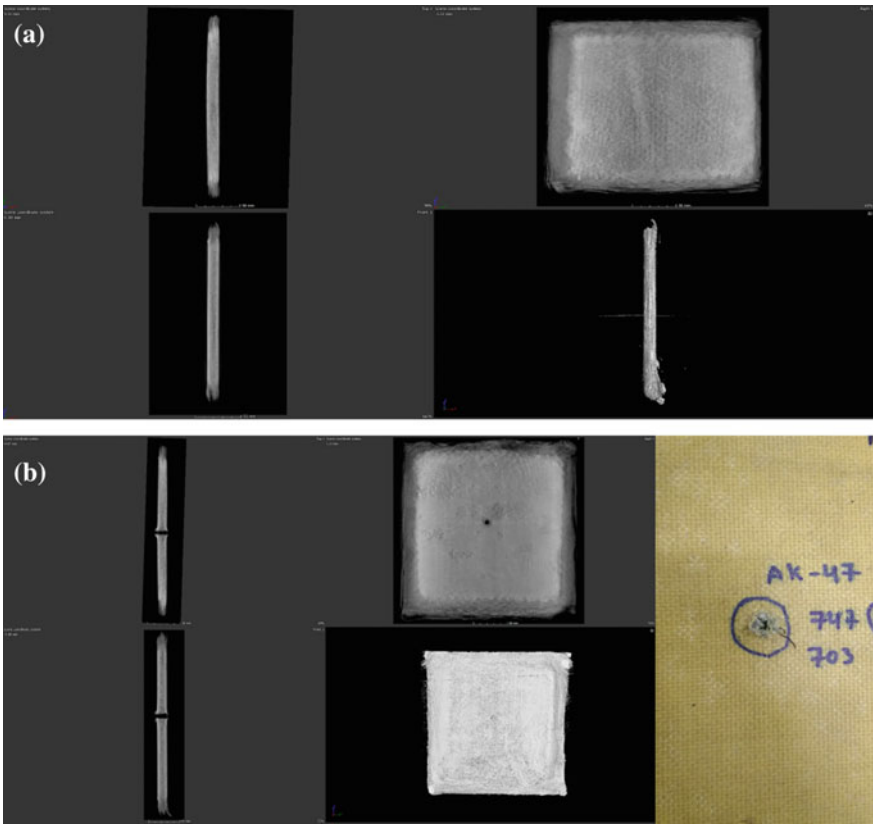

Fig. 8 **a** Computed tomographic image of FRL PC composite before ballistic impact and **b** computed tomographic image after ballistic impact

$$E_{abs} = \frac{1}{2} m_p (V_i^2 - V_r^2) \tag{2}$$

where E_{abs} = energy absorbed by the composite (J);m_p = mass of the projectile (kg);V_i = impacted velocity (m/s); V_r = residual velocity (m/s).

The response of the ballistic materials under low-velocity impact is primarily limited to the elastic range of the materials without any practical damage. Whereas the ordnance velocity (500 to 2000 m/s) impart gross deformation, localized melting and even complete disintegration of impacted materials as observed in the current study [62]. The comprehensive account for temperature variation becomes essential in dynamic conditions (strain rate more than 10^{-2} s) for the distinctive property evaluation of the impacted materials. In the current study, it is believed that the failure phenomenon in developed composite was induced when the structure approached the critical state, and its load capacity diminished. In this view, the dynamic strength of materials is subjugated by the strength at high temperature and pressure in the shocked

state [61]. In the current study, the developed composite demonstrated augmented structural and thermal stability at high temperature, observed from dynamic mechanical analysis and DSC studies. It is envisioned that such high-temperature stability of layered composite essentially contributed to its ballistic performance. Primarily, the ballistic performance of polyaramid fibers depends on the effective distribution of impact energy via a number of factors including yarn pull out, inter and intra-yarn friction, etc. Such phenomenological attributes of polyaramid fiber were not observed under the ballistic impact, therefore, it is believed that thermal characteristics of the composite turned into compelling aspects of the developed composite.

4 Conclusions

The current study explicates the method and its validation in terms of biomimicking the mollusk structure in engineering thermoplastic and high-performance aramid fiber to elucidate the effect of layered architecture on its thermomechanical property. The initial section of the study mainly focused on the thermal property of polycarbonate and its composite under various techniques including DSC, temperature modulated DSC, DMA, and thermogravimetric analysis. The dynamic mechanical analysis and DSC spectra have illustrated significant improvement in thermomechanical property of the FRL PC composite due to the restricted motion of localized atom or group of atoms in addition to the impeded cooperative segmental motion. The insight into the thermal stability was further evaluated by Arrhenius approximation for thermogravimetric analysis, which rendered that the available energy before the onset point is significantly low to trigger the decomposition phenomenon as observed in polycarbonate. The second section of the study involves the mechanical validation of developed composite, which consists of low energy impact (Izod notch test) and high-speed projectile impact. The fracture surface of the developed composite demonstrated the predominance of fiber splitting and fibril fracture as a failure mechanism instead of visible failure characteristics of polycarbonate. It is essential to note that though the current study does not elucidate the detailed ballistic failure phenomenon, we envisioned that the utilized process for mimicking nacreous architecture and stimulated thermomechanical property of the composite to possess the ability to be exploited as high impact material with some further structural deliberation.

Acknowledgements The authors acknowledge Vice-Chancellor, Deakin University, Australia, for their continuous encouragement and support. Authors also acknowledge the assistance provided by Deakin technical staff in performing thermal characterization of the sample. Authors also acknowledge the support from Alex Daniel, ASL DRDO, Government of India and PR Subba Reddy, DRDL DRDO, Government of India for their extensive support in carrying the ballistic as well industrial computed tomographic test.

References

1. Abbås KB (1980) Thermal degradation of bisphenol A polycarbonate. Polymer 21(8):936–940
2. Adams R, Cawley P (1988) A review of defect types and nondestructive testing techniques for composites and bonded joints. NDT International 21(4):208–222
3. Agarwal BD, Broutman LJ, Chandrashekhara K (2017) Analysis and performance of fiber composites, Wiley
4. Aizenberg J, Fratzl P (2009) Biological and biomimetic materials. Adv Mater 21(4):387–388
5. Al-Lafi W, Jin J, Song M (2016) Mechanical response of polycarbonate nanocomposites to high velocity impact. Eur Polymer J 85:354–362
6. Allen G, Morley D, Williams T (1973) The impact strength of polycarbonate. J Mater Sci 8(10):1449–1452
7. Anand A, Harshe R, Joshi M (2013) Resin film infusion: toward structural composites with nanofillers. J Appl Polym Sci 129(3):1618–1624
8. Bandaru AK, Ahmad S, Bhatnagar N (2017) Ballistic performance of hybrid thermoplastic composite armors reinforced with Kevlar and basalt fabrics. Compos a Appl Sci Manuf 97:151–165
9. Bandaru AK, Chavan VV, Ahmad S, Alagirusamy R, Bhatnagar N (2016) Ballistic impact response of Kevlar® reinforced thermoplastic composite armors. Int J Impact Eng 89:1–13
10. Bicerano J (2002) Prediction of polymer properties: cRc Press
11. Briscoe BJ, Motamedi F (1992) The ballistic impact characteristics of aramid fabrics: The influence of interface friction. Wear 158(1):229–247. https://doi.org/10.1016/0043-1648(92)90041-6
12. Brown J, Ennis B (1977) Thermal analysis of Nomex® and Kevlar® fibers. Text Res J 47(1):62–66
13. Cai GM, Yu WD (2011) Study on the thermal degradation of high performance fibers by TG/FTIR and Py-GC/MS. J Therm Anal Calorim 104(2):757–763
14. Carr DJ, Lewis EA, Breeze J (2017) Ballistic threats and body armour design. Military Injury Biomech (pp 5–18), CRC Press
15. Chang I, Lees J (1988) Recent development in thermoplastic composites: a review of matrix systems and processing methods. J Thermoplast Compos Mater 1(3):277–296
16. Cheeseman BA, Bogetti TA (2003a) Ballistic impact into fabric and compliant composite laminates. Compos Struct 61(1):161–173. https://doi.org/10.1016/S0263-8223(03)00029-1
17. Cheeseman BA, Bogetti TA (2003b) Ballistic impact into fabric and compliant composite laminates. Compos Struct 61(1–2):161–173
18. Chen R, Wang C-A, Huang Y, Le H (2008) An efficient biomimetic process for fabrication of artificial nacre with ordered-nanostructure. Mater Sci Eng, C 28(2):218–222
19. Chen X (2016) Advanced fibrous composite materials for ballistic protection, Woodhead Publishing
20. Cheng Q, Wu M, Li M, Jiang L, Tang Z (2013) Ultratough artificial nacre based on conjugated cross-linked graphene oxide. Angew Chem 125(13):3838–3843
21. Cho K, Yang J, Il B, Chan K, Park E (2003) Notch sensitivity of polycarbonate and toughened polycarbonate. J Appl Polym Sci 89(11):3115–3121
22. Corrêa RA, Nunes RC, Lourenco VL (1996) Investigation of the degradation of thermoplastic polyurethane reinforced with short fibres. Polym Degrad Stab 52(3):245–251
23. Council NR, Committee SSS (2008) Inspired by biology: from molecules to materials to machines: National Academies Press
24. Davis A., Golden J (1968) Thermal degradation of polycarbonate. J Chem Soc B: Phys Organic, pp 45–47
25. Dogan A, Arikan V (2017) Low-velocity impact response of E-glass reinforced thermoset and thermoplastic based sandwich composites. Compos B Eng 127:63–69
26. Eagles DB, Blumentritt BF, Cooper SL (1976) Interfacial properties of kevlar-49 fiber-reinforced thermoplastics. J Appl Polym Sci 20(2):435–448

27. Edwards M, Waterfall H (2008) Mechanical and ballistic properties of polycarbonate apposite to riot shield applications. Plast, Rubber Compos 37(1):1–6
28. El-Shekeil Y, Sapuan S, Abdan K, Zainudin E (2012) Influence of fiber content on the mechanical and thermal properties of Kenaf fiber reinforced thermoplastic polyurethane composites. Mater Des 40:299–303
29. Gilbert M (2016) Brydson's Plastics Materials, William Andrew
30. Godovsky YK (2012) Thermophysical properties of polymers, Springer Science and Business Media
31. Gore PM, Kandasubramanian B (2018) Functionalized Aramid Fibers and Composites for Protective Applications: A Review. Ind Eng Chem Res 57(49):16537–16563
32. Groenewoud WM (2001) Thermogravimetrical analysis characterisation of polymers by thermal analysis, pp 60–75, Elsevier
33. Günther H, Wolfgang FH, Flammersheim H-J (2003) Differential Scanning Calorimetry. Springer-Verlag, Berlin Heidelberg, Germany
34. Hare P (1965) Amino acid composition of some calcified proteins. Carnegie Inst Washington Yearbk. 64:223–232
35. Hazell P, Edwards M, Longstaff H, Erskine J (2009) Penetration of a glass-faced transparent elastomeric resin by a lead–antimony-cored bullet. Int J Impact Eng 36(1):147–153
36. Hearle JW (2001) High-performance fibres, Elsevier
37. Heijboer J (1965) Physics of non-crystalline solids. JA Prins 231
38. Hourston DJ, Song M, Pollock HM, Hammiche A (1997) Modulated differential scanning calorimetry. J Therm Anal 49(1):209–218. https://doi.org/10.1007/bf01987441
39. Hudgin D, Bendler T (2000) Handbook of polycarbonate science and technology: Marcel Dekker, New York
40. Illers K, Breuer H, Kolloid Z, (1961) CrossRefl Web of Science® Times Cited, 125, 176, 110
41. Illinger JL, Lewis RW, Barr DB (1975) Effects of adhesive structure on impact resistance and optical properties of acrylic/polycarbonate laminates. Adhesion Sci Technol pp 217–232, Springer
42. Iyer R, Vijayan K (1999) Decomposition behaviour of Kevlar 49 fibres: Part I. AtT≈ T d. Bull Mater Sci 22(7):1013–1023
43. Jang BN, Wilkie CA (2004) A TGA/FTIR and mass spectral study on the thermal degradation of bisphenol A polycarbonate. Polym Degrad Stab 86(3):419–430
44. Kluin J, Yu Z, Vleeshouwers S, McGervey J, Jamieson A, Simha R (1992) Temperature and time dependence of free volume in bisphenol A polycarbonate studied by positron lifetime spectroscopy. Macromolecules 25(19):5089–5093
45. Kulkarni S, Gao X-L, Horner S, Zheng J, David N (2013) Ballistic helmets–their design, materials, and performance against traumatic brain injury. Compos Struct 101:313–331
46. Lee LH (1964) Mechanisms of thermal degradation of phenolic condensation polymers. I. Studies on the thermal stability of polycarbonate. J Polym Sci Part A General Papers 2(6):2859–2873
47. Lee SM (1989) International encyclopedia of composites, VCH
48. Lee YS, Wetzel ED, Wagner NJ (2003) The ballistic impact characteristics of Kevlar® woven fabrics impregnated with a colloidal shear thickening fluid. J Mater Sci 38(13):2825–2833
49. Li H, Ding F, Wang G, Zhang J, Bian X (2001) Evolution of small nickel cluster during solidification. Solid State Commun 120(1):41–46
50. Li XG, Huang MR (1999) Thermal degradation of Kevlar fiber by high-resolution thermogravimetry. J Appl Polym Sci 71(4):565–571
51. Lipatov Y (1978) The iso-free-volume state and glass transitions in amorphous polymers. Polymer Chem, pp 63–104, Springer
52. Malcolm CH (2012) Transparent Armour. In: Laible R (ed) Ballistic materials and penetration mechanics, vol 5. Elsevier, New York, pp 116–134
53. Mantia FL, Spadaro G, Acierno D (1981) Moisture effect on dynamic-mechanical and dielectric properties of some polycarbonates. Acta Polym 32(4):209–211

54. Matsuoka, S, Ishida Y (1966) Multiple transitions in polycarbonate. J Polym Sci Part C: Polymer Symposia 247–259
55. McNeill I, Rincon A (1991) Degradation studies of some polyesters and polycarbonates—8. Bisphenol A polycarbonate. Polymer Degradation and Stability, 31(2):163–180
56. McNeill I, Rincon A (1993) Thermal degradation of polycarbonates: reaction conditions and reaction mechanisms. Polym Degrad Stab 39(1):13–19
57. Mosquera ME, Jamond M, Martinez-Alonso A, Tascon JM (1994) Thermal transformations of Kevlar aramid fibers during pyrolysis: infrared and thermal analysis studies. Chem Mater 6(11):1918–1924
58. Reading M, Hourston DJ (2006) Modulated temperature differential scanning calorimetry: theoretical and practical applications in polymer characterisation (vol 6), Springer Science and Business Media.
59. Reddy M, Lukose S, Subramanian M, Rao G, Muralidhar C, Balasubramaniam K (2011) Industrial computed tomography system for aerospace applications: development and characterisation. Insight-Non-Destructive Testing and Condition Monitoring 53(6):307–311
60. Reddy PRS, Reddy TS, Madhu V, Gogia A, Rao KV (2015) Behavior of E-glass composite laminates under ballistic impact. Mater Des 84:79–86
61. Rosenberg Z, Dekel E (2012) Terminal ballistics, Springer
62. Rosenberg Z, Kositski R (2017) Deep indentation and terminal ballistics of polycarbonate. Int J Impact Eng 103:225–230
63. Saldivar-Guerra E, Vivaldo-Lima E (2013) Handbook of polymer synthesis, characterization, and processing. Wiley
64. Sepe M (1998) Dynamic mechanical analysis for plastics engineering: William Andrew.
65. Sun J, Bhushan B (2012) Hierarchical structure and mechanical properties of nacre: a review. RSC Adv 2(20):7617–7632
66. Tang Z, Kotov NA, Magonov S, Ozturk B (2003) Nanostructured artificial nacre. Nat Mater 2(6):413
67. Tanner D, Fitzgerald JA, Phillips BR (1989) The kevlar story—an advanced materials case study. Angew Chem, Int Ed Engl 28(5):649–654
68. Thomason J, Vlug M (1997) Influence of fibre length and concentration on the properties of glass fibre-reinforced polypropylene: 4. Impact properties. Composites Part A: Appl Sci Manuf 28(3):277–288.
69. Vieille B, Casado VM, Bouvet C (2013) About the impact behavior of woven-ply carbon fiber-reinforced thermoplastic-and thermosetting-composites: a comparative study. Compos Struct 101:9–21
70. Walley S, Field J, Blair P, Milford A (2004) The effect of temperature on the impact behaviour of glass/polycarbonate laminates. Int J Impact Eng 30(1):31–53
71. Wang J, Cheng Q, Tang Z (2012) Layered nanocomposites inspired by the structure and mechanical properties of nacre. Chem Soc Rev 41(3):1111–1129
72. Wright S, Fleck N, Stronge W (1993a) Ballistic impact of polycarbonate-an experimental investigation. Int J Impact Eng 13(1):1–20
73. Wright SC, Fleck NA, Stronge WJ (1993b) Ballistic impact of polycarbonate—an experimental investigation. Int J Impact Eng 13(1):1–20. https://doi.org/10.1016/0734-743X(93)90105-G
74. Wyzgoski MG, Yeh GS-Y (1973) Relation between free volume and the low-temperature "Beta" Transition in Glassy Polycarbonate. Polym J 4(1):29
75. Yadav R, Goud R, Dutta A, Wang X, Naebe M, Kandasubramanian B (2018) Biomimicking of Hierarchal Molluscan Shell Structure Via Layer by Layer 3D Printing. Ind Eng Chem Res 57(32):10832–10840. https://doi.org/10.1021/acs.iecr.8b01738
76. Yadav R, Naebe M, Wang X, Kandasubramanian B (2016) Body armour materials: from steel to contemporary biomimetic systems. RSC Advances 6(116):115145–115174
77. Yadav R, Naebe M, Wang X, Kandasubramanian B (2017) Structural and Thermal Stability of Polycarbonate Decorated Fumed Silica Nanocomposite via Thermomechanical Analysis and In-situ Temperature Assisted SAXS. Scientific Reports 7(1):7706

78. Yang W, Macosko C, Wellinghoff S (1986) Thermal degradation of urethanes based on 4, 4′-diphenylmethane diisocyanate and 1, 4-butanediol (MDI/BDO). Polymer 27(8):1235–1240
79. Yao HB, Tan ZH, Fang HY, Yu SH (2010) Artificial Nacre-like Bionanocomposite Films from the Self-Assembly of Chitosan-Montmorillonite Hybrid Building Blocks. Angew Chem Int Ed 49(52):10127–10131
80. Yee A, Smith S (1981) Molecular structure effects on the dynamic mechanical spectra of polycarbonates. Macromolecules 14(1):54–64
81. Zhang Y, Gong S, Zhang Q, Ming P, Wan S, Peng J, Cheng Q (2016) Graphene-based artificial nacre nanocomposites. Chem Soc Rev 45(9):2378–2395

Chapter 4
Fiber-Reinforced Composites for Restituting Automobile Leaf Spring Suspension System

M. V. Sarath, Swaroop S. Gharde, Odelu Ojjela, and Balasubramanian Kandasubramanian

1 Introduction

Vibrations can be seen in our day-to-day life in various forms including those we listen to, the highly erratic tremors causing natural calamities, the reciprocation of energy in the atomic levels [160] and also the kind we experience while traveling in a vehicle but which are controlled to the extent of not causing inconvenience [22]. The shock absorbers are seen even in bicycles [166] to alleviate the uneasiness caused due to the bumps confronted while riding it. The physiological and hazardous effects on human beings caused by vibrations in the low-frequency range include mechanical damage to the heart and lungs, brain injuries, tearing of abdominal and chest cavity membranes [21]. These are based on the tests conducted on animal and human subjects [109] as per ISO 2631, where an experimental investigation was done using simulated laboratory environments, which satisfies the conditions similar to that of while traveling in a vehicle. The sources for the vehicle vibrations can be listed as road roughness, engine unbalances, sudden brakes [30], speed fluctuations and the kind referred to as road excited body noise. The sounds which are produced by the passage of wheels over the road surface due to the mechanical transmission of waves through structural components could also lead to noise pollution. Therefore, it is of great priority to damp these vibrations by providing a smooth suspension [136], along with proofing the noises to harness the perturbations caused to the environment. The necessity of providing ride comfort is also paramount when it

M. V. Sarath · O. Ojjela
Department of Applied Mathematics, Defence Institute of Advanced Technology, Deemed University (DU), Pune, India

S. S. Gharde · B. Kandasubramanian (✉)
Department of Metallurgical and Materials Engineering, Defence Institute of Advanced Technology, Pune, India
e-mail: meetkbs@gmail.com

S. Sahoo (ed.), *Recent Advances in Layered Materials and Structures*,
Materials Horizons: From Nature to Nanomaterials,
https://doi.org/10.1007/978-981-33-4550-8_4

comes to the case of farm animals being transported in heavy trucks [134], as they are kept immobilized and are more susceptible to injuries and health hazards. Hence, an efficient suspension system is ineluctable for any automobile for the sleek and comfortable ride concomitantly protecting the vehicle from high impact forces.

Leaf spring is purported to absorb the shocks and judder of the automobile, playing a puissant role in the suspension system by undergoing deflections in order to achieve road flexibility for the automobile and ride comfort to the occupants. Leaves, generally made of spring steel 56SiCr7 [43], are stacked vertically and tightened by means of central bolts with suitable geometry to form the leaf spring suspension system whose early stages of usage were contemplated as laminated springs in carriages in the eighteenth century; hence, the name carriage spring was in wide usage formerly ("Carriage Springs," [25]). Since the embarkment of commutation in animal-driven vehicles [117], the suspension system has been employed, which could be related to the primitive form of a leaf spring. In the first decades of the twentieth century, the four-wheeled motor vehicles could be apprised of being equipped with elliptic leaf springs ("With the Automotive Inventors," [181]) for the purpose of passenger comfort and the vehicle safety. The location of spring is fixed to have a configuration that segregates the body, avoiding direct contact with the wheel axle, which permits the motion of the axle independent of the body [114]. This, in turn, prevents high impact loads being transferred from axle to chassis and causing disturbance to the passengers. Suspension system balances the center of gravity of automobile combined with occupants as it raises when the vehicle passes over a speed breaker or irregular track. Figure 2 illustrates the location of suspension springs in a light motor vehicle so as to perform its functions and support the unsprung weight. The secondary objective of leaf spring is to maintain stability [151] of the vehicle by undergoing deflections to a certain limit and also, to bear the shock and dynamic loads it is subjected to, while the ride goes through uneven terrains. Presently, leaf springs are manufactured solely for heavy transport vehicles and railway carriages due to the fact that they distribute the load uniformly in contrast to the coil springs, which are widely used in light motor vehicles (Fig. 1).

Coil springs transfer the load to a single point, which is not desirable in case of heavy vehicles that carry large loads (~1–10 tons). The automotive industry's mission is to design components with advanced materials as metal leaf springs are not preferred nowadays in light commercial vehicles as they add more weight to the automobile and are sentient to corrosion [175], considerably reducing the service life. Spring steels are popularly employed for manufacturing of leaf springs, due to their high tensile strength [164] imparting those products, the ability to regain original shape when subjected to deformation together with providing good fatigue [88] properties [155]. Spring steels are characterized by a high elastic limit and the capacity to withstand high stresses under repeated loadings; however, they are limited by their inability to resist corrosion. Therefore, the usage of steels in the manufacturing of leaf springs is not being encouraged by the automotive industry as they clearly indicate a proclivity to achieve the weight minimization and efficiency maximization criteria together with preventing corrosion [94]. Figure 3 depicts the

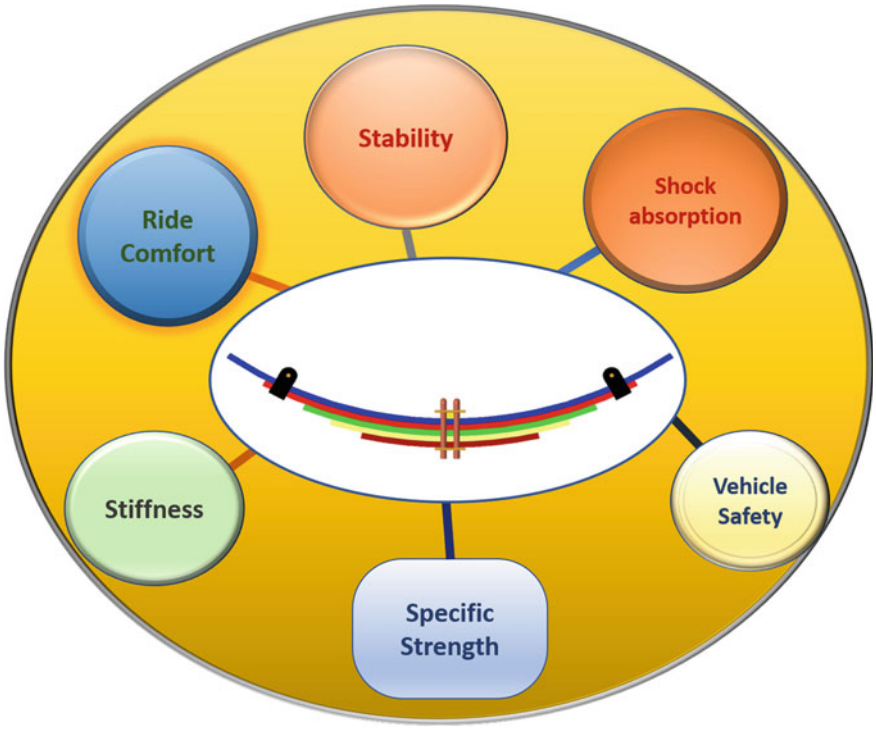

Fig. 1 Characteristics of a leaf spring suspension system

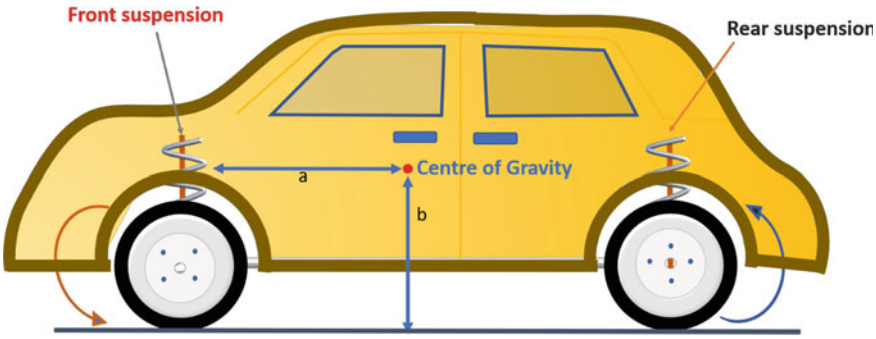

Fig. 2 Position of the suspension system

coil spring attached to the rear axle of an automobile suspension system.spring steels as they are subjected to repetitive

Springs in the shock absorption system act as a medium which stores elastic strain energy as it is subjected to dynamic loads and instantly damps out the energy gradually, which renders the comfort to the occupants [99]. Figure 4 outlines the

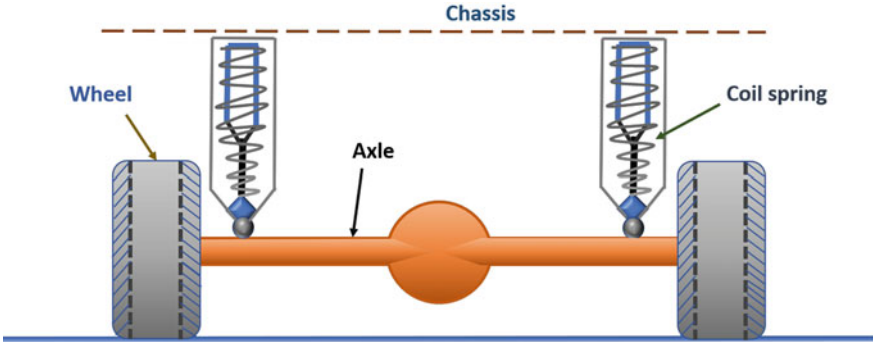

Fig. 3 Rear-axle view of a coil spring suspension system

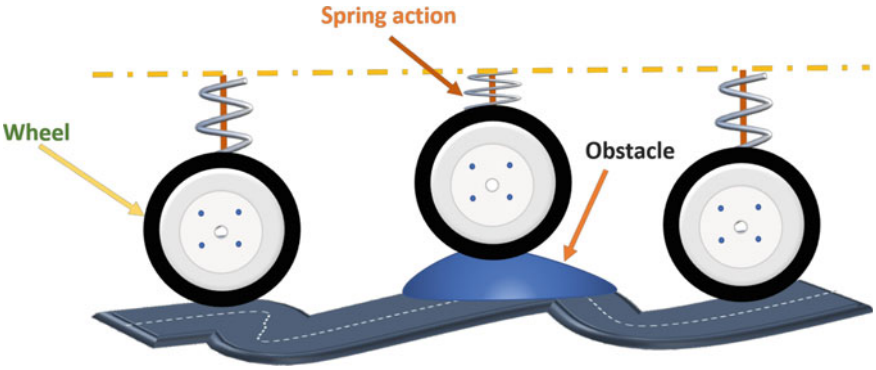

Fig. 4 Shock absorption of suspension due to uneven terrain

functioning of the suspension system when the vehicle encounters a sudden bump in the road where the spring absorbs the shock load. The road irregularities play a major role in exciting the wheel motion to generate vibrations, and they are being transferred from tyres to the suspension system where damping occurs due to stiffness of both tyres and leaf springs [66]. Stiffness or spring rate is another property of a leaf spring which is of prime importance with regard to the material and functioning, rendering the ability to handle the judder and sudden shock loads. Moreover, elasticity is the material property by which the spring material undergoes deformation by the dynamic loads and returns to the initial state by releasing the stored energy. The conversion of the kinetic energy of the wheel motion to potential energy which is stowed in the spring is an inevitable energy transformation which is responsible for the smooth functioning of an effective suspension system. With this respect, the composite materials [157] have high elastic strain energy storage ability together with resistance to corrosion and also minimum weight comparing with pure metallic springs. Being the backbone of a suspension system, leaf springs have to tackle vibration, and they are subjected to repeated stress, which causes fatigue failure ("Fatigue

Phenomena in Metals," [41]). Material selection of any component is primarily based on its performance and failure characteristics, as of here, a spring element fails due to repeated loading and without revealing any clear indication of the weakness. From the mid-nineteenth century, the use of carriage springs and its gradual improvement (Patent No. 139,325, [167]) could be seen, which clearly indicates the history of leaf springs in the vehicle suspension system. By taking a glimpse at the present scenario, it is learned that composites [50–53, 56, 58, 67, 70, 77, 87, 169, 183, 184] have marked signature in the field of automotive component production [44], with the sole impression of enhancing the material properties, conjointly to reduce the weight of the system and accomplish longer service life. Glass fiber-reinforced composites [85] are colossally exercised in automotive [14] and structural applications [189] with regard to their supercilious strength to weight ratio [71], untainted corrosion resistance and lower stress values compared to steels. Carbon fiber composites and boron fiber composites also proffer predominant strength characteristics juxtaposed to that of glass fiber composites, along with same method of fabrication and processing; hence, they suffice to be vital candidates as modern material [18]. Composites constituting carbon fibers and boron fibers have superior mechanical properties essentially Young's modulus which is greater than that for glass fiber composites primarily with S-glass and E-glass fibers [15]. Researches highlighted the specific strength for metal matrix composites employing boron fibers and are electable to design structural members such as trusses and columns. [148]. Metal matrix composites articulated with aluminum and boron carbide [187] have also been employed as a substitute for spring steels like EN45A, as the composite leaves are having evenly matched strength (ultimate tensile strength ~600–700 MPa) and low density ~2.6–2.8 g/cc [104]. Recent advancements in field of polymer matrix composites (PMC) [90] in structural, automotive, [141] space [33] applications [143] elicit the striking aspects of the desired properties achieved by their versatile nature and flexibility in fabrication [24, 44]. Composites [98] have made a benchmark in all research fields due to their elite properties and ability to impart advanced characteristics to the products implementing them [120]. Even from the most facile components to the superlative [128] kind adapted in applications [113] which demand top priority [149] to quality and unrivaled performance [122] in the system availing their functions [119], composite materials have duly undergone extravagant changes finally acquiring a diverse range of versatility. The automotive industrial [23] research [54] is the penchant to optimize the use of resources and to implement advanced materials [36] as to overcome the drawbacks of conventional metallic parts. The increasing demand of low weight components and effective utilization of resources have led to the exploration of natural fiber engineered composites [19] for automotive applications [5, 76, 93]. The widely used natural fibers [45] include flax [20], hemp [13], sisal [179], kenaf and jute [103], most of them being commercially accessible for more than a century [108] and are having the dexterity [17] and potential to gradually supersede the glass fiber-reinforced composites in the industry due to the features such as ease of processing, reduced cost of production, recyclability, stability, eco-friendliness [129, 173]. In order to effectively reduce the energy consumption [37], tooling and machining cost [16] by moving away from the traditional way of manufacturing and

materials, industry paves the way for novel incipience in the production sector. This review encompasses state of the art on leaf springs, from the outlook of materials which have been instrumented throughout the history of its life, commencing from the conventional steel leaf springs, metal matrix composite, synthetic composite, and the least explored natural fiber-reinforced composite leaf springs. As there is no elaborate literature available on leaf springs, notably disserting on multifarious kinds of materials that have been explored to date, this paper is an endeavor to explore the materials tailored with the peculiar features that would enhance the functioning of the leaf spring suspension system.

2 Materials

2.1 Spring Steel

Steel and alloy of carbon and Iron [27] have been an essential element in the manufacturing industry due to its multifarious properties and qualities, which are exploited since the beginning of its implementation in commercial applications [38, 65]. Particularly, spring steels [112] are extensively employed in the production of valve springs, coil springs and leaf springs due to their high tensile strength (~1200–1800 MPa), fatigue life, good hardenability, ductility and toughness exhibited in their operating temperatures with regard to the application. In automotive applications, the parts which employ spring steels are generally operated in a temperature range of ~−40 to 50 °C in particularly suspension system where they are being exposed to ambient conditions [138]. Ductility is the remarkable property by which steels are able to deform under tensile loads without sudden fracture, enabling to mend them into desired shapes and dimensions [186]. After the elastic limit, steel starts yielding and undergoes plastic deformation, whereas brittle material is subjected to sudden fracture. However, for steels, failure [147] is initiated by necking, which is the phenomenon that occurs at the onset of fracture, which could be promulgated as the reduction in diameter at the cross section along with the elongation, thus maintaining the volume to be constant. Even though aluminum has almost equal stiffness and better corrosion resistance, low values for modulus of elasticity and rigidity modulus compared to steel, high cost and low strength are its limiting factors. Unlike brittle materials which fail without any warning, steel does not yield to sudden fractures and in the applications where it is labored at normal atmospheric temperatures. Structural steel has also been employed for the production of leaf springs due to the strength characteristics and having wide industrial popularity in the manufacturing sector.

2.2 Stiffness

Stiffness is a significant property ascribable to the efficient performance of the automotive suspension system employing them, which by definition, could simply mean the resistance offered against deformation by the spring. Mathematically, spring rate or spring constant K is the force per unit deflection measured in Newtons per length unit (mm). From a simple perspective, all the objects possess some stiffness up to a limit restricted by their material properties, and substances which are pliant are observed to be less stiff.

$$\text{Spring rate, } K = \frac{F}{x} \tag{1}$$

where F is the applied load, x denotes the extension. Spring constant is a dominant attribute of the spring, which is coalesced to the proficient action of the suspension system rendering ride comfort to the occupants. Controlling the spring rate is, therefore, of topmost priority when it comes to the design of the suspension system. While selecting material for the leaf spring, ductile spring steels are employed as they are well characterized by the ability to deform under the dynamic loads and to withstand the load, which also includes the unsprung load of the vehicle.

2.3 Strain Energy Storage

The ability to absorb energy is highly sought-after property when it comes to applications involving springs, which are meant to undergo elastic deformations to store this potential energy and to release it appropriately. It is inevitable for an elastic material to store the energy, which is then utilized for regaining its original state on the removal of load. Mathematically, it is formulated as an expression involving the material property, which is the elastic modulus and stress [156].

$$\text{Strain energy, } U = {\sigma^2}/{2E} \tag{2}$$

When a load is applied on elastic material, it undergoes deformation and stores the work done on the element by the load as potential energy or strain energy of deformation. For specific strain energy, the material with low density and low elastic modulus has a higher capacity to store; however, steels are having medium density and high elastic modulus [137]. With this respects, materials characterizing low weight density, low elastic modulus and high specific strength will supersede the spring steel in the performance as well as a quality criterion. Material subjected to applied load undergoes linear variation up to elastic limit till where the stored energy is elastic. The element can recover the original state for any deformation within this elastic limit, after which it sustains as plastic.

Where S is the stress at proportional limit and E, the modulus of elasticity. Stress is generated in the material as it is subjected to loading the molecules are forced to shift from their equilibrium state, and when the applied load is removed, the body utilizes stored energy during deformation to retain its equilibrium position. Thus, materials which are elastic in nature could be employed for applications involving shock absorption which utilizes the energy storage ability as in suspension system, kinetic energy is transformed to potential energy when the vehicle encounters with a judder.

2.4 *Fatigue Life*

Fatigue is referred to repeated cycles of loading in applications where the material employed could fail due to the factors like areas where stress get concentrated, corrosion of material, microstructural properties [73], residual stresses [191] and temperature. Figure 5 states different factors mustering fatigue failure. The machine elements, such as a leaf spring, could suddenly breakdown with providing some significant symptoms of weakness, like an initiation of cracks due to metallurgical factors [26], or other visible marks on the body. Therefore, it is of cardinal magnitude to scrutinize the fatigue properties of material exercised in these kinds of applications, and suitable material has to be chosen as the failure is under the fluctuating stress

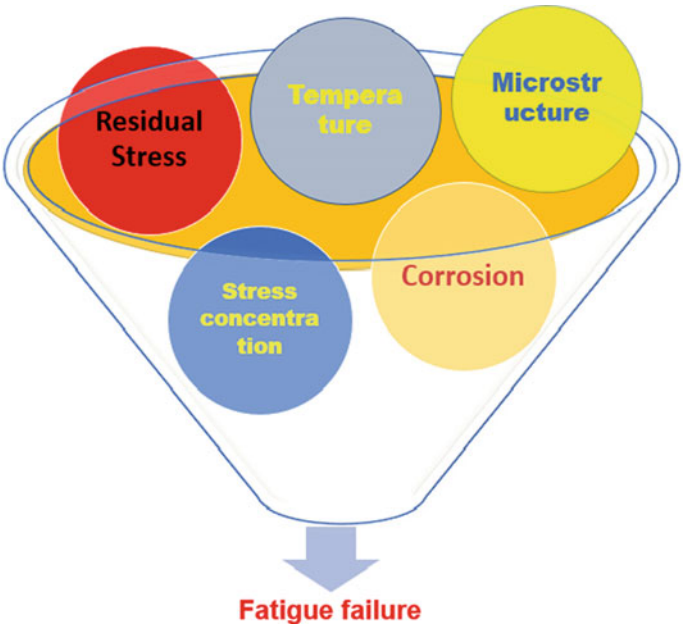

Fig. 5 Schematic of parameters affecting fatigue failure

amplitudes. Methods of enhancing the fatigue life [62] include shot peening, which is generally employed for spring steels as they are subjected to repetitive shock loads [47]. When a spherical object called the shot strikes on the specimen surface and compressive stresses are rendered on the surface, which prevents the procreation of cracks and thereby improves the material life. The time period in a number of cycles for which the object persists to perform its function under the repeated loads before failure is called as the fatigue life and the machine part is said to have infinite life as long as it is subjected to loading under its endurance limit. It is expressed in the mathematical form given by the *S–N* diagram or Wohler curve which is plotted between the logarithm of stress amplitude (S_a) and the logarithm of the number of cycles (N) and this curve is implemented to determine the fatigue limit of a material [180]. Based on number of cycles, the fatigue life is categorized into regimes of finite life and infinite life ($N > 10^{6-7}$) where they are further classified into low cycle fatigue [57] ($1 < N < 10^3$) and high cycle fatigue [100] ($N \geq 10^3$) regions; also, the endurance limit of the material is defined at 10^8 cycles. The governing equations for fatigue life cycle are Manson–Coffin equation [4] and Basquin relation [3] which are expressed as given below

$$N\sigma_a^p = \mathrm{C} \tag{3}$$

where N corresponds to number of cycles, σ_a denotes stress amplitude p and C are empirical constants [91].

$$(\Delta\varepsilon p)/2 = \varepsilon_f'(2N)c \tag{4}$$

where $(\Delta\varepsilon p)/2$ denotes the plastic strain amplitude, ε_f' designates the fatigue ductility coefficient, $2N$ gives number of strain reversals and c indicates fatigue ductility exponent [11]. The surface roughness [115] can significantly affect the fatigue property [6] of a specimen as more polished the surface using several treatments like shot peening crack growth or initiation can be prevented; on the other hand, machining can induce tensile residual stresses [131]; therefore, relieving these stresses is vital. Figure 6 elucidates the shot surface of a specimen where compressive stresses are induced, causing the suppression of crack growths and thereby improving the fatigue life of the element. This is an additional cost and labor for enhancing fatigue property of spring steel and is avoided when a material having good fatigue strength is utilized for the manufacture of leaf spring. Composites [34] like glass/epoxy have better fatigue resistance [10] compared to steels and are fabricated in a much simpler way eliminating all surface treatments for improving properties [69]. For the betterment of fatigue life, compressive stresses are to be generated on the surface of the machine part, and from the design point of view, stress concentrations are avoided, and if present, strain hardening operations like cold working are employed during manufacturing stage as it can aid to hinder the crack initiation. Internal defects such as shrinkages, blowholes and cavities formed due to the inefficient processes undertaken in the production period also result in the component being subjected to fatigue failure [150].

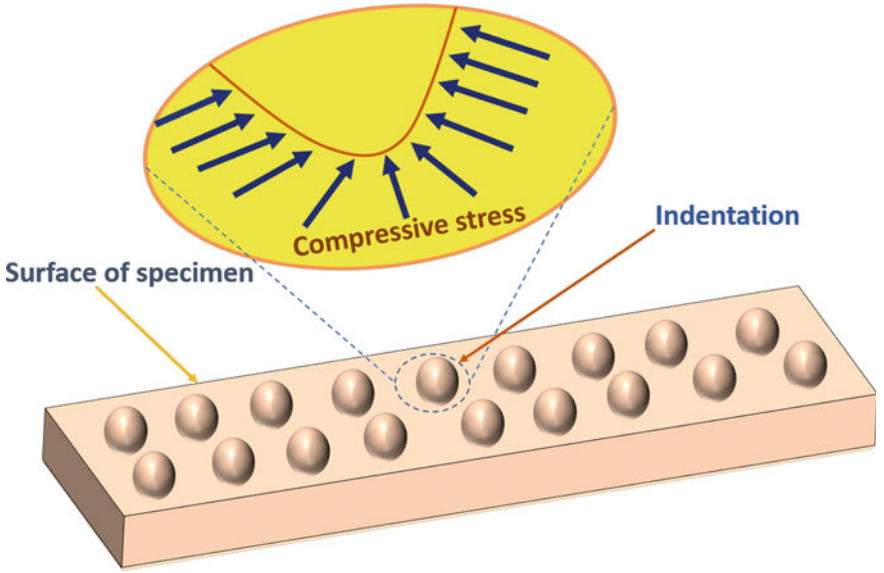

Fig. 6 The shot peened surface of a specimen

2.5 Case Studies

Rahman and Kowser [130] designed and demonstrated the working of a stainless steel leaf spring, performed the nonlinear analysis by implementing cantilever beam model and conducted a numerical simulation in C using Runge–Kutta technique. The results obtained in the experimental analysis were compared with the numerical method. Fatigue failure is one of the most prominent issues in steel leaf springs, which are due to the repetitive loadings and crack initiation due to corroded points [171] (Table 1). Aggarwal [2] experimentally studied the fatigue strength of EN45A leaf springs, compared the results with that predicted by the mathematical model based on stress approach, with emphasis given on fatigue life estimation coined a term called full-scale correlation factor(FSCF) for prediction of fatigue life which varied linearly with the stress. The bending stress (σ_b) of leaf spring was evaluated using the mathematical expression,

$$\sigma_b = \frac{6PL}{nbt^2} \tag{5}$$

where p is the load acting, L is half of the spring span, n indicates the number of leaves, b denotes the width of each spring and t corresponds to the thickness of an individual leaf. Kumar and Aggarwal [88, 89] demonstrated the refinement attained in properties by changing the design from flat-leaf springs to parabolic, where they achieved a deduction in von Mises stress from 1096 to 1083.2 MPa, weight reduced

Table 1 Studies on steel leaf spring

Authors	Materials	Property	Results	References
Aggarval et al.	EN45A Spring steel	Fretting fatigue	3,64,000 fatigue cycles	Aggarwal [2]
Kumar et al.	EN45A	Von Mises stress, weight, fatigue life	Weight reduced from 9.507 to 8.62 kg, fatigue life increased from 77410 to 81150 cycles	Kumar and Aggarwal [89]
Fragoudakis et al.	56SiCr7	Fatigue life	Shot peening enhanced the fatigue life from 4 $\times$ 10^4 to 1.5 $\times$ 10^5 cycles	Fragoudakis et al. [43]
Vukelic et al.	61SiCr7	Hardness, tensile strength	Vickers test gave 590 HV Tensile strength obtained was 1888 MPa	Vukelic and Brcic [171]
Clarke et al.	Spring steel	Failure analysis	Corrosion due to chemical contamination	Clarke and Borowski [29]
Aher et al.	SAE 5160H	Von Mises stress, fundamental frequency, fatigue life	592.43 MPa 10.68 Hz 1.47 $\times$ 10^7 fatigue life cycles	Aher and Sonawane [3]
Akiniwa et al.	EN 10270	Fatigue strength for torsional and axial loading	Fatigue strength between 468 MPa and 520 MPa for torsional loading and 650 MPa for axial loading in the giga cycle regime	Akiniwa et al. [4]
Kong et al.	Parabolic leaf spring	Effect of roll, brake, roll stiffness	Vertical stiffness of 295 N/mm, the stress of 1450 MPa	Kong et al. [81]
Sert et al.		Fishhook test, tilt table test	Static stability factor 1.058, rollover probability of 40.32%, front leaf stiffness of 23 kg/mm	Sert and Boyraz [151]

(continued)

Table 1 (continued)

Authors	Materials	Property	Results	References
Badkar et al.	60Cr4V2	Improving payload capacity, suspension design	Stiffness – 3646 N/mm at a load of 95.65 kN	Prahalad and Badkar [124]

from 9.507 to 8.62 kg along with an increase in fatigue life from 77410 to 81150 cycles. Fragoudakis et al. [43] delved into the microstructure of 56SiCr7 steel leaf springs at the different stages of manufacturing and also tested the fatigue life of specimen, which gave results as an average of ~$(1 \times 10^5 - 2 \times 10^5)$ cycles with shot peening and a maximum value of 4×10^4 cycles for the specimen which was not shot peened. In shot peening, the specimen is subjected to bombardment with a spherical object called shot, which on impact causes an indention on the surface [1]. Figure 7 portrays a pictorial representation of shot peening consisting of a nozzle from which spherical shots are pumped and allowed to strike on the surface of the machine element, which leaves the indentations, inducing compressive stress on the surface. Cases involved the breakdown of the spring element with corrosion delineated as the main factor which bossed the failure due to the inept painting coated over it. Vukelic and Brcic [171] exercised visual inspection of coil spring of material 61SiCr7 and checked the damage occurred to the protective layer of paint due to direct contact between the adjacent layers, and by availing the scanning electron microscope (SEM) probed the surface to determine the crack initiation point, obtained the value of the ultimate tensile strength (UTS) of the specimen to be 1888 MPa found using hardness measurement method. According to Boyer and Gall, the relation between tensile strength (UTS) and hardness value is given by Eq. [6]

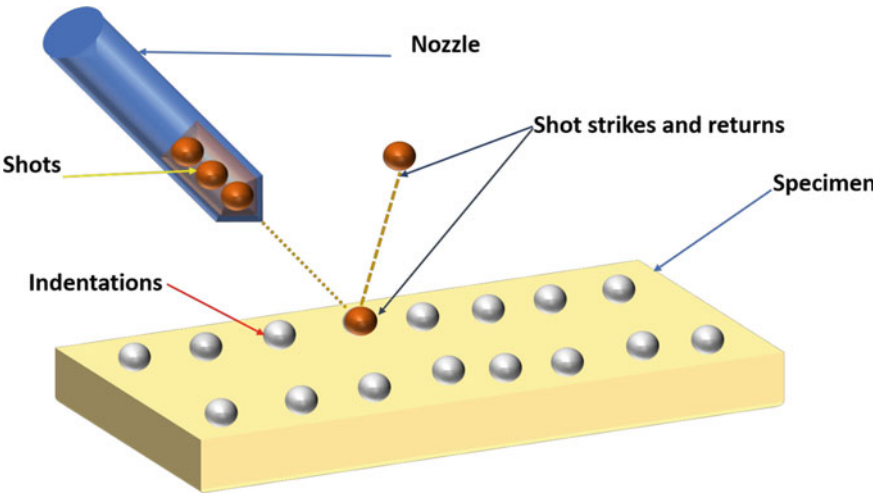

Fig. 7 Schematic of shot peening of a machine element

$$\text{UTS} = 3.2 * \text{HV} \tag{6}$$

where HV is the Vickers hardness number of the specimen.

Clarke and Borowski [29] examined the rear leaf spring of a sports utility vehicle on account of its failure, analyzed stress, and observed rust and chemical contamination in the specimen, which could be pointed out as the cause of the fracture. Evidently, this indicates the susceptibility of steel leaf springs to corrosion even though the element having coated with a protective layer of paint, a tiny space or opening could become the active site, so the atmospheric oxygen starts to attack and initiates degrading the material. Aher and Sonawane [3] applied finite element model and arrived at the fatigue life measurement of a leaf spring (material SAE 5160H which is a low carbon steel) employed in light commercial vehicles, conducted static analysis and obtained von Mises stress values 592.43 MPa at a load of 6 KN, found the fundamental frequency of leaf spring to be 10.68 Hz along with a fatigue life of 1.47×10^7 cycles. In an isolated case suspension system components in particularly leaf springs, failed within a brief time period of its implementation as in public vehicle transports, which exercise them widely. An investigation conducted by Herrera et al. [63] on the failure of leaf springs in Venezuelan buses, included fatigue tests (SAE J1528), Rockwell and Brinell hardness measurements of failed specimens (ASTM E18 and ASTM 110) accentuated on the mechanical fatigue which was fecundated due to the deficiencies in the design and manufacturing processes adapted, also emphasized that tensile stress was highest at the central hole region. The metallurgical studies revealed the role played by improper design and inefficiently employed manufacturing processes, which gradually engendered the precocious failure of springs. Das et al. [32] studied the failure analysis of a passenger vehicle spring (SAE 9260 steel) and pointed the prime cause to be of ineffectual shot peening after the microstructure analysis and residual stress measurement was performed, as deducted due to the short lifespan and premature failure of the component. Atig et al. [7] administered an analytical model on asymmetric leaf spring with parabolic cross section to determine the bending stress distribution by surmising it to be a simply supported beam, also generated fatigue life diagram. Akiniwa et al. [4] experimented on fatigue properties of spring steel (EN 10270) employing ultrasonic machine setup for testing fatigue under axial and torsional loadings under giga cycle regime, thereby obtained comparable fatigue strengths of 468 and 520 MPa, respectively, in both the above conditions. Wang et al. [174, 175] applied automatic geometric data acquisition (AGDA) on a parabolic leaf spring and conducted stress analysis utilizing absolute nodal coordinate formulation (ANCF) to learn the interleaf contact stress also pointed out that parabolic design is better than uniform thickness due to diminished weight and less interleaf friction. Kong et al. [81] analyzed parabolic leaf spring purported in buses, studied the effect of the roll, brake, and related the roll stiffness of spring to the vehicle roll stability, found the vertical stiffness to have a value of 295 N/mm for roll stress of 1450 MPa. Changes in spring design were attributed to refurbishment in the load-carrying ability of the vehicle, also by enhancing the vertical stiffness directly improves the roll and the wind-up stiffnesses of the suspension system. Furuya et al. [46] demonstrated fatigue tests on billets of

spring steel (class of 1800 MPa) in both rolling and transverse directions and had the fatigue strength controlled by inclusions which were found to be twice in the rolling direction; they also identified fish-eyed fracture in the specimen which had occurred due to the improper inclusions. Sert and Boyraz [151] conducted parametric sensitivity analysis on minibus suspension system along with fish hook test and virtual tilt table test in a simulated platform, studied the vehicle roll behavior and calculated the value of static stability factor (SSF) as 1.058 together with rollover probability of 40.32% for spring stiffness of 23 kg/mm in the front leaf. Static stability factor gives the quantum of the vehicle's ability to contravene the possibility of getting capsized, which should have higher values implying low risk to the occupants. The parameter SSF is defined as the ratio of track width of the vehicle to twice the distance of the center of gravity from the ground [68]. Krason and Wysocki [84] investigated the contact friction between layers of multi-leaf spring of steel (Grade 60S2A) and a mathematical model was developed for the friction; also, the numerical analysis was conducted along with the characteristics of thermal stresses, and the temperature distribution was explicated. Malikoutsakis et al. [97] construed on the optimization of composite parabolic leaf springs employed in front axle suspension of a truck (payload of 8 tons), gauged the durability of the spring using finite element analysis and also scrutinized the performance of the spring element in terms of ride comfort; steering action of the vehicle has been improved by altering the design aspects of eyes of the master leaf. Roy and Saha [137] employed variational method and exercised nonlinear analysis of a parabolic leaf spring where it was modeled as a cantilever beam, adapted Galerkin's method to find a solution of displacement model. Karditsas et al. [74] worked on analyzing the front axle mono-leaf suspension spring (51CrV4) of a heavy truck illustrated the influence of eye lever in the steering performance and also studied that the spring rate plays a significant role in the magnitude of stress developed. Prahalad and Badkar [124] embroidered the payload capacity of a 4 × 4 heavy-duty truck (BEML TATRA tonnage 40) by comprehending alterations in the suspension design, advocated with a 60Cr4V2 leaf spring system also reported a spring rate of 3646 N/mm at a rated load of 95.65 kN. Figure 8 images the driving force of industrial research in the field of fiber-reinforced composites by the limiting factors of traditional materials.

2.6 Limiting Factors of Steel

From the above case studies on conventional steel leaf springs, evidently, researchers have focused on weight reduction, which has been emerged as a prominent issue and eventually led to the evolution of fiber-reinforced composite leaf spring. Automotive industries strive to optimize the design for achieving minimum weight for the automobile and increasing energy efficiency. Low fatigue life, low strain energy storage, large weight of steel leaf springs and additional cost of manufacturing incurred, including tooling and other heat treatments, urge the manufactures to pioneer novel composite materials.

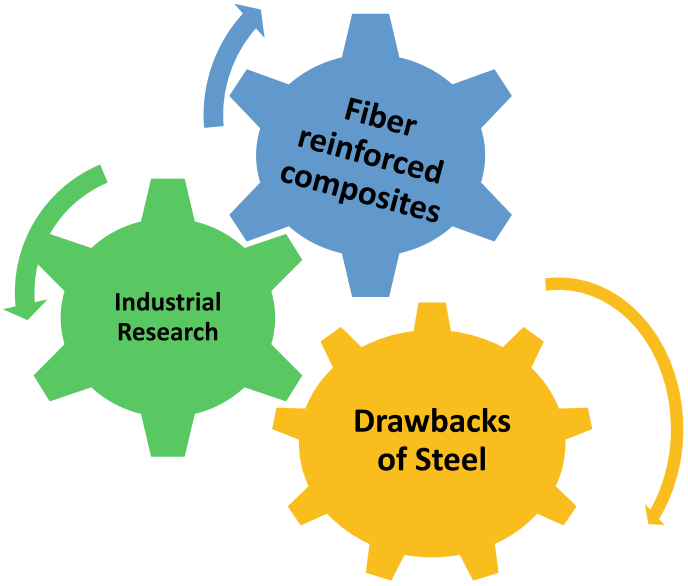

Fig. 8 From steel to synthetic composite leaf springs

Most of the studies have been concentrated on the fatigue properties of steel springs, which was revamped by exercising methods like shot peening, where the synthetic fiber-reinforced composites do not require such operations. Some studies circumscribed on the susceptibility of steel leaf springs to corrosive failure and the degradation of the protective coating of paint due to the interleaf contact friction and wear, which could be eliminated by using composite instituted leaf springs. Therefore, overcoming the drawbacks of multi-leaf steel springs is plausible by implementing suspension systems with single leaves of carbon or glass fiber-reinforced composites (Table 2).

3 Synthetic Composite Leaf Springs

Composite fibers have revolutionized the automobile, aerospace [78, 105], manufacturing [44] and construction industries [153] by accruing the enhancement of material properties [60] along with achieving desired functions for which they are being employed [177]. As the industrial research is looking forward to realizing sustainability in the modern materials and production, composites since their entry [178] manifested elite nature and flexibility with this regard [42]. Composites [116] are cogitated as the best alternative in lieu of conventional materials when it comes to rigorous design factors like boosted specific strength, rigidity, anti-corrosion property and also to harvest versatile functions for advanced automotive applications

Table 2 Microstructural and theoretical studies on steel springs

Authors	Material	Experiments	Results	References
Fuentes et al.	SAE J1528	ASTM E18 and ASTM	Mechanical fatigue initiated by tensile stress at the central hole	Herrera et al. [63]
Das et al.	SAE 9260	Microstructure analysis, fatigue strength	Ineffectual shot peening reduced fatigue life	Das et al. [32]
Krason et al.	60S2A	Contact friction, thermal stresses, numerical analysis	Temperature distribution	Krason and Wysocki [84]
Karditsas et al.	51CrV4	Steering performance, eye design, stiffness, stress	Spring rate influenced the magnitude of stresses	Karditsas et al. [74]

[101, 133]. The behavioral features of composites when being subjected to various environments directed by manifold parameters including high temperature, humidity and pressure, etc. are exceptionally competent [9, 59] in comparison with their traditional counterparts [185]. Carbon fibers are attributed to having superior strength qualities, remarkable impact behavior [55] and strikingly low weight compared to steels which are being reinstated on account of the fact that the aforementioned composites are being highly coveted by the [168] fabrication industries [72]. After the embarkment of its journey in commercial applications since the early 1960s, composites have phenomenally influenced all possible fields together with paved the way for upgradations in the manufacturing technology [24, 79]. Specific modulus is the most highlighted property [92] of composites, which has been most sought after regarding research interests. Figure 9 drafts the multiple peripherals of composites which renders them superior preference over conventional materials. Most importantly, these elite composites such as carbon fibers have ventured onto a major production role in the industries through prepreg machines [95] which are available as fully automated making it swift, employing automated tape laying (ATL) and automatic fiber placement (AFP) [152] suited for large-scale manufacturing including structural applications, thus allaying the cost [82, 158]. Figure 10 illustrates the stepwise procedure employed for the fabrication of a fiber-reinforced composite leaf spring. The various steps in manufacturing a fiber engineered product adapting prepreg include preforming, pressing and final processing. Glass fiber-reinforced composites are popular when it comes to automotive applications [102] as the former also belong to the same class of carbon fiber instituted composites due to the fact that they have properties and processing methods [170] equivalent to carbon fiber composites provided the only disparity lies in the material cost; however, the mechanical properties are surprisingly comparable. [48] emphasized on augmenting the mechanical strength of carbon fibers by adapting methods of influencing interfacial properties such as chemical implantations making use of polyamido amine (PAMAM) using

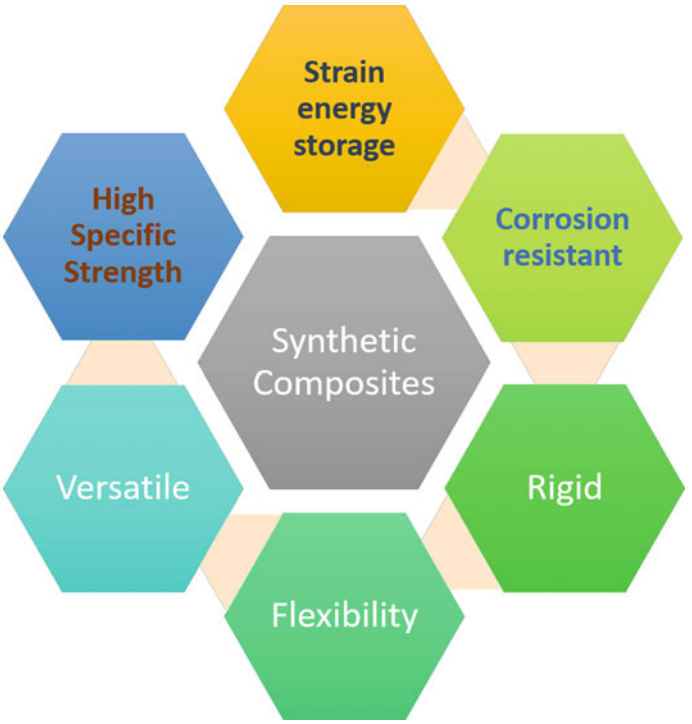

Fig. 9 Characteristics of composites

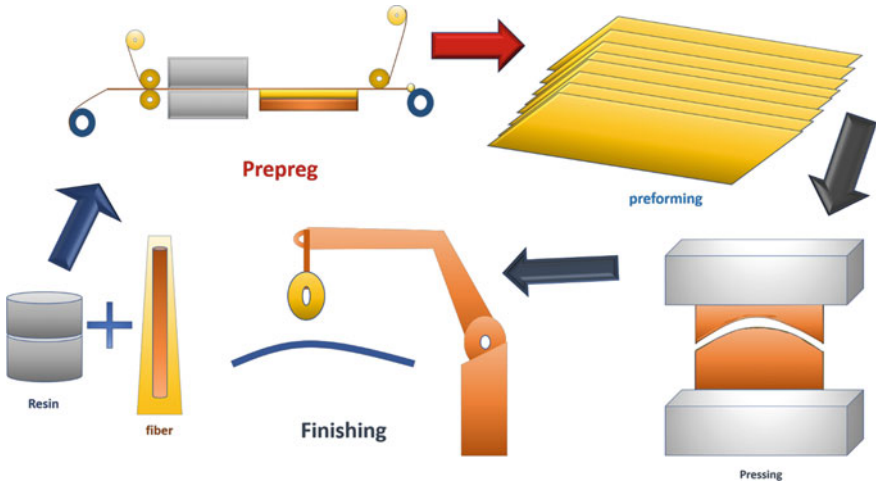

Fig. 10 Fabrication of fiber engineered composite spring using prepreg process

epoxy resin to wrap the surface of carbon fiber. These composites are suited for advanced high-end applications as desirable performance is promised by their versatile nature to adapt changes in their constituent elements, fabricated by the austere hand lay-up method [39]. Heightening of surface energy of the carbon fibers is influenced by altering the interfacial bonding by embedding dendrimers into the interface, together with reaching desired variations in the interlaminar shear strength which was raised from 62.46 to 86.23 MPa and fiber tensile strength enabling the element to withstand external loads [190].

3.1 Mechanical Behavior of Fiber Composites

A composite in the constituent level will consist of a fiber and matrix material, so failure can occur either for the matrix or for the fibers. Figure 11 depicts the propagation of a crack in a fiber-reinforced composite structure. Debonding can occur in a composite structure over the course of time due to manifold parameters governing the interfacial strength betwixt the matrix along with the constituent fibers as it greatly influences the failure of an element [188]. Figure 12 shows the inside view of a composite involving fiber and matrix. For a composite structure, the deformation happens in different stages where at the onset, both the matrix and fibers undergo linear elastic deformation. Gradually as the load increases, matrix initiates plastic deformation; however, fibers have more strength; hence, they continue to deform elastically. When the load transcends the tensile strength of fibers in the final stages, the fiber will also plastically deform with the matrix, and then the fiber undergoes breakage leading to composite failure. The failure of a matrix can occur when the applied load generates stress crossing its ultimate value, and Figure 13 sketches the crack causing matrix failure. The loosening of the bond between matrix and fiber is another major mode causing the component to fail under operation [126]. The fibers show more strength compared to the matrix when loading is increased, as

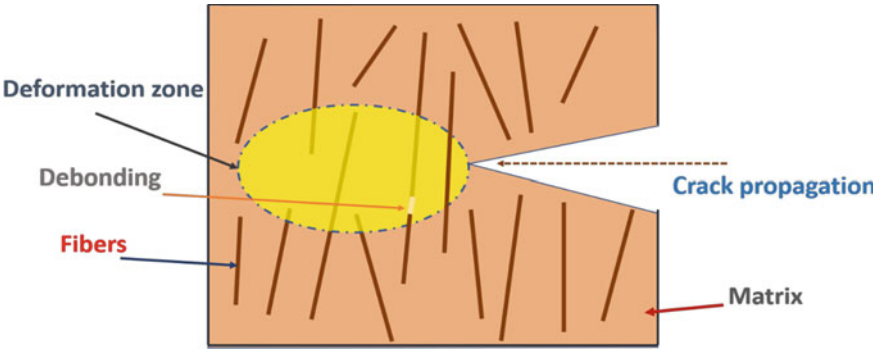

Fig. 11 Crack propagation leading to debonding

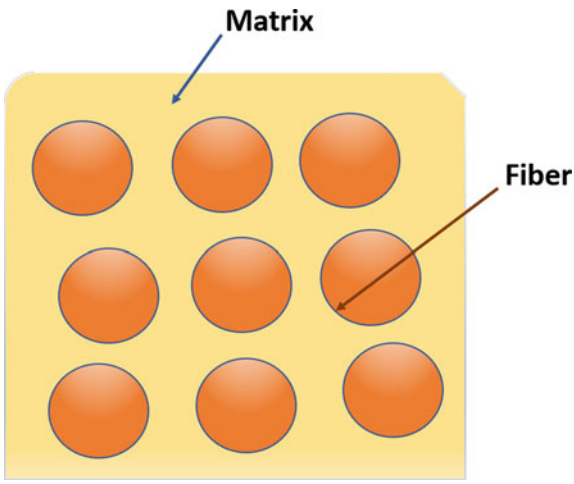

Fig. 12 A view of a composite at the inner level

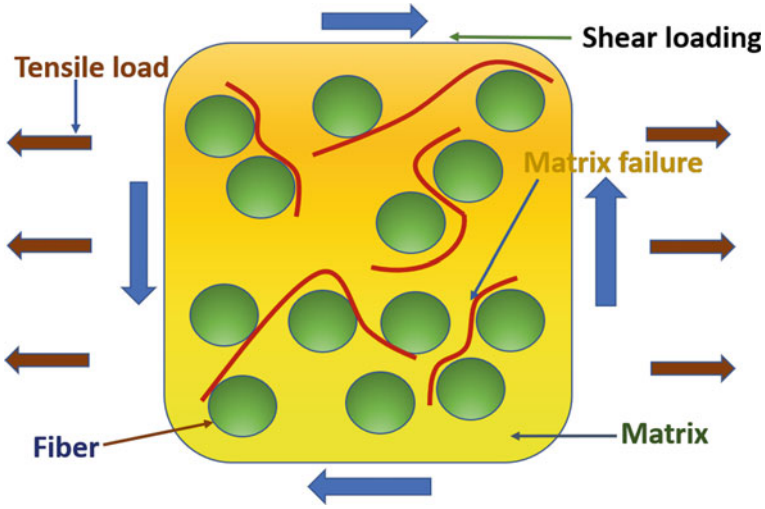

Fig. 13 Cross-sectional view showing crack propagation causing matrix failure

stated in Fig. 14 and they sustain the load even after the matrix fails for a duration, which depends on the tensile strength of fiber. When the fibers are exhibiting brittle characteristics, then the failure of the component will be expedited under tensile loading, as illustrated in Fig. 15 the failure of the composite structure may also be initiated by the crack growth through the matrix (Table 3).

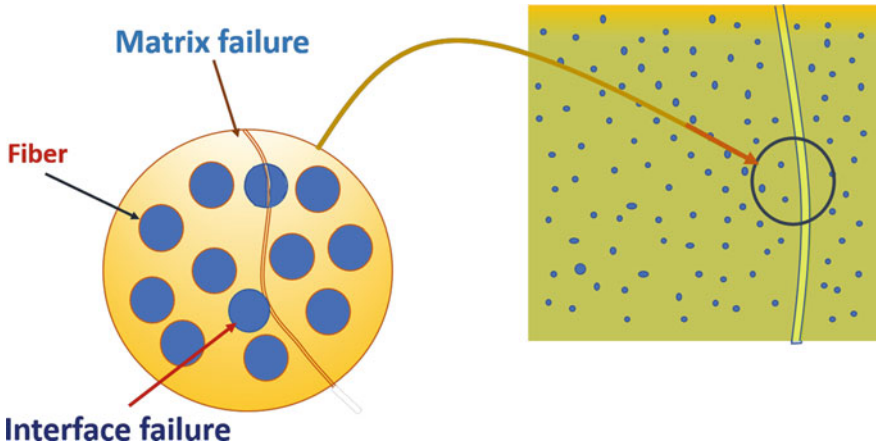

Fig. 14 Failure of composites initiated by matrix rupture and interface failure

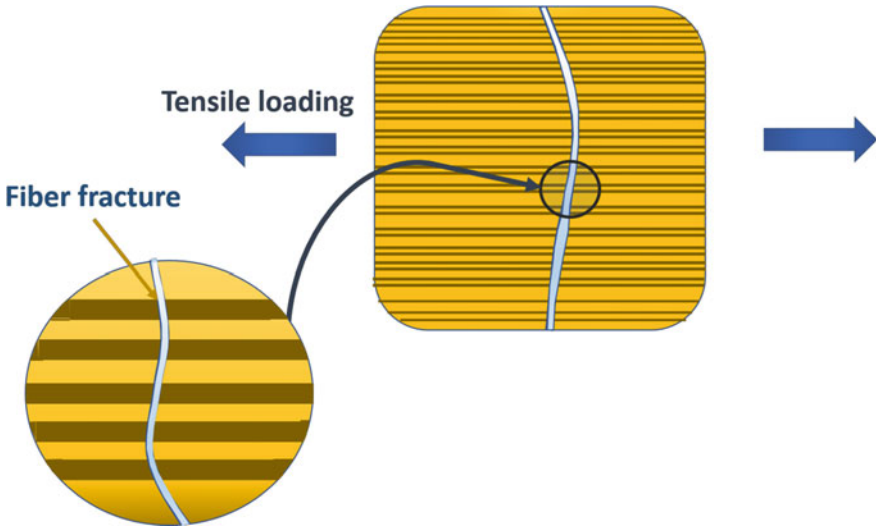

Fig. 15 Failure of brittle fiber in a composite material

3.2 Case Studies on Fiber-Reinforced Composite Leaf Springs

Sancaktar [140] designed a composite leaf spring of material E-glass roving with property values tensile modulus 8.14×10^4 MPa, fiber strength 3.45×10^3 MPa and implemented it on a light vehicle run on solar power with the design parameters such as spring rate (70 N/mm), mass of spring system (1.361 kg), with the prime

Table 3 Studies on fiber-reinforced composite leaf springs

Authors	Materials	Property	Results	References
Sancaktar et al.	E-glass/epoxy	Fiber strength, tensile modulus, spring rate	3.45×10^3 MPa, 8.14×10^4 MPa, spring rate 70 N/mm	Sancaktar [140]
Mahdi et al.	Elliptic spring	Design parameters	Ellipticity ratio 2 gave the highest spring rate	Mahdi [96]
Shokrieh et al.	Fiberglass/epoxy replaced steel leaf spring	Stress, natural frequency, weight	80% weight reduction	Shokrieh and Rezaei [156]
Shi et al.	Parabolic leaf spring	Stiffness sensitivity, layer thickness	Spring rate—118 N/mm	Shi et al. [154]
Jancirani et al.	Fiber-reinforced leaf springs of E-glass/epoxy Carbon/epoxy Graphite/epoxy EN45	Weight, stress, deflection, natural frequency	Von Mises 1083.2 MPa for EN45, EN45 spring deflection—107.5 mm at 503.3 MPa FRP spring deflection—105 mm at 473 MPa and natural frequency of FRP spring—102.14 and 93.56 Hz for steel spring	Jancirani and Assarudeen [71]
Mithari et al.	E-glass/epoxy mono-composite leaf spring	Weight	84.4% weight reduction	Mithari et al. [106]
Subramanian et al.	Glass fiber-reinforced polypropylene	Stiffness, fiber length, strength	Joint strength increased with the fiber length	Subramanian and Senthilvelan [163]
Muhammed et al.	Hybrid-reinforced composite leaf spring	Stress analysis, bending stiffness, elastic modulus	Longitudinal modulus of elasticity varied inversely with bending stiffness	Muhammed and Ismaeel [111]
Qian et al.	Fabrication of composite leaf spring	Stacking sequence, spring rate	Stiffness—120.34 N/mm falls to 117.50 N/mm after failure	Qian et al. [127]
Hou et al.	Glass fiber-reinforced polyester	Maximum load, fatigue strength	Static load of 150 kN, 1,000,000 fatigue life cycles	Hou et al. [64]
Krall et al.	CFRP leaf spring	Fundamental frequency	First mode frequency of 24.3 Hz for steel and 61.2 Hz for CFRP	Krall and Zemann [83]

(continued)

Table 3 (continued)

Authors	Materials	Property	Results	References
Karlus et al.	E-glass epoxy leaf spring and steel (55Si2Mn90)	Deflection, stress, weight	Reduced weight from 4.613 to 0.905 kg, stress lowered from 450.73 to 316.71 MPa and deflection decreased from 65.118 to 14.262 mm	Karlus et al. [75]
Devarakonda et al.	E-glass/epoxy leaf spring compared with steel	Ant colony optimization for leaf spring design and genetic algorithm	Reducing weight from 8.54 to 1.7543 kg and stress values lowered from 718.87 to 543.02 MPa	Sameer Kumar et al. [31]
Venkatesan et al.	E-glass/epoxy composite Leaf spring compared with steel	Weight reduction, stiffness, load-carrying capacity, natural frequency	76.4% lowered weight, stress decreased by 67.35% and stiffness raised by 64.95%	Kueh and Faris [86]
Pozhilarasu et al.	Glass fiber-reinforced composite	Weight, deflection, bending stress	71.4% weight reduction, for a static load of 4 kN, deflection of steel spring was 198 mm and E-glass/epoxy spring deformed by 180 mm and bending stress was 949.63 and 911.79 MPa, respectively	Pozhilarasu and Pillai [123]
Saini et al.	E-glass/epoxy Graphite/epoxy Carbon/epoxy	Weight, stress, deflection	Weight diminution of 81.72% for E-glass/epoxy, 90.51% for graphite epoxy and 91.91% for carbon/epoxy and stress results gave von Mises stresses as 453.92 MPa for steel, 163.22 MPa E-glass/epoxy, 653.68 MPa—graphite epoxy, 300.3 MPa—carbon epoxy	Saini et al. [139]
Thippesh et al.	Glass fiber-reinforced leaf spring	Weight, bending stress	80% weight reduction, for a static load of 7.7 kN the bending stress of steel leaf—512 MPa, and bending stress of composite spring—417 MPa	Thippesh [165]

(continued)

Table 3 (continued)

Authors	Materials	Property	Results	References
Wadile et al.	E-glass/epoxy composite	Experimental analysis, stress, deflection	For a static load of 4 kN, the deflection was found to be 43 mm and stress of 480.7 MPa	Wadile and Mahajan [172]

objective of overall weight reduction was achieved. Most of the emerging design variations have highlighted the sole purpose of reaching the criterion of minimum weight, high specific strength and load-carrying ability along with sustainability [146]. Researchers have also focused on the geometric factors in the composition of a composite leaf spring that directly affected the stiffness, failure load and thus the performance of the suspension system. Apart from constant thickness leaf springs, novel designs have intercalated varying thicknesses such as parabolic and elliptic leaf springs. Mahdi [96] emphasized on the ascendancy of ellipticity ratio on the working of elliptical leaf spring, scrutinized the effect of ellipticity ratio (a/b), i.e., the ratio of major diameter of the ellipse to its minor diameter on spring rate and maximum failure load and the highest stiffness value was achieved at ellipticity ratio of 2. Shi et al. [154] explicated a theoretical model for stiffness ascertainment of a composite leaf spring on the basis of mechanics of composite materials and illustrated the prime factors which are the thickness of leaf spring, number of long layers, angle of layer or ply orientation and layer width where the sensitivity of spring stiffness was highly instigated by the layer thickness. They compared the value of spring rate obtained by numerical simulation (119.0374 N/mm) and finite element analysis (119.8 N/mm) with the value obtained on experimental testing (118 N/mm) and also claimed to have an error between the results ~0.8–1.6%. Thippesh [165] exercised the swapping of standard steel leaf spring with glass fiber-reinforced leaf spring and zoomed in the comparison of properties where deflection, weight and strength were focused. The deflection for any load was lower for composite leaf spring when differentiated with steel leaf spring and they also highlighted a remarkable weight decrement of 80% along with the maximum bending stress of 512 MPa for steel and 417 MPa for composite leaf springs at a static load of 7700 N were reported. Jancirani and Assarudeen [71] reviewed and investigated the performance of fiber-reinforced leaf spring juxtaposed with that of typical leaf spring (EN45), remarked on the chipping of the material from the spring when subjected to poor road conditions which palpably does not depend on the spring design aspects. They conducted finite element analysis and found the von Mises stress on EN45 leaf spring to be 1083.2 MPa in contrast to composite leaf spring which had 503.3 MPa, also reported weight reduction of 84.4% for E-glass mono-leaf spring, 85% for E-glass/epoxy leaf spring, 91% for graphite/epoxy leaf spring and 90% for carbon/epoxy leaf spring over steel leaf spring. Mithari et al. [106] reported the comparison of mono-composite leaf spring with steel leaf spring where they achieved 84.40% weight reduction and presented natural frequency test results in which composite leaf spring had higher values. The

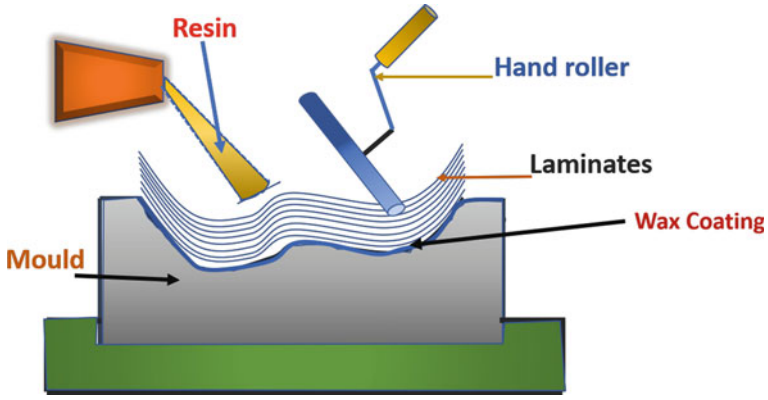

Fig. 16 Schematic of hand lay-up method of processing composites

influential effect of fiber length on the working of a composite leaf spring (glass fiber-reinforced polypropylene) was construed by Subramanian and Senthilvelan [163] and found that the joint strength varied directly proportional to the fiber length, also pointed out that large fiber length is suited for high fatigue loading than short fiber layered leaf spring. One of the most general methods of fabrication and processing for continuous fiber composite parts is the hand lay-up which is illustrated in Fig. 16. Muhammed et al. [111] fabricated a hybrid fiber-reinforced composite leaf spring using hand lay-up method [40] and also expounded on the fiberglass spray lay-up method, made mathematical model of the spring and performed stress analysis based on mechanics of composites, also explored the inversely varying relationship between longitudinal modulus of elasticity and bending stiffness of the element. Rajesh et al. [132] demonstrated on substituting conventional steel leaf spring with laminates of bidirectional glass fiber engineered composites together with carbon fiber sandwiched composites and also illustrated the weight reduction obtained along with the lowest flexural deformation of 2.84 mm at a load of 100 N when the laminates were reconciled such that top stratum was of glass fiber and the bottom layer made of carbon fiber. Qian et al. [127] examined the fatigue reliability of parabolic leaf spring of stiffness 120.34 N/mm, which was fabricated using ply scheme where the order of stacking was optimized by employing genetic algorithm, exercised fatigue bench tests to identify the weak location and onset of fracture, also studied the delamination failure of leaves. Krall and Zemann [83] performed impact tests and shaker tests on carbon fiber-reinforced leaf springs using spring steel (51CrV4) as a reference, studied the natural frequencies of the composite spring. Karlus et al. [75] reported on the comparison of composite leaf spring (E-glass/epoxy) with steel leaf spring (55Si2Mn90/EN45) conducted static stress analysis elucidated on the drastic changes achieved as in reducing weight from 4.613 to 0.905 kg, decrement in stress from 450.73 to 316.71 MPa and a considerable reduction in maximum deflection from 65.118 to 14.262 mm. Shokrieh and Rezaei [156] exercised finite element method to study the stress on rear suspension leaf springs also reported the fiberglass/epoxy

leaf spring to have lower stress, elevated natural frequency along with a depletion in weight of 80% collated to the former steel leaf spring. Sameer Kumar et al. [31] implemented ant colony optimization (ACO) theory in optimizing the design of the suspension system where the steel leaves were replaced by mono-composite leaf reduced the unsprung weight of the automobile by considering minimization function to be the leaf spring weight. The parameters influencing the spring weight were identified as material density, thickness, width and length of the spring, and mathematically, the product of these gave the weight which was optimized using ACO and made a comparison of the results with that obtained by genetic algorithm. Venkatesan et al. [86] employed the measurements of traditional steel spring purported in a light automobile to assemble and reinstitute it with a glass fiber sandwiched leaf spring and analogized the deflection, performed finite element analysis, and weight reduction of 85%, stress to be truncated 67.35%, stiffness to be 64.95% raised, and elevated natural frequency was reported. Pozhilarasu and Pillai [123] manifested hand lay-up method to construct glass fiber-reinforced composite leaf spring where a weight shrinkage of 71.4% was reported and conducted deformation tests evaluated with comparison to that of a steel leaf spring where for a static load of 250 N, epoxy glass-reinforced spring underwent a deflection of 173 mm and steel spring deformed by 185.50 mm; also, the bending stress recorded was 593.75 and 620 MPa for glass fiber and steel leaves, respectively. Hou et al. [64] improvised on designing the eye of a glass fiber-reinforced polyester leaf spring, studied the interlaminar shear stress concentrations, delamination failure in the leaves, and improved fatigue strength with the application of open-eye design. Saini et al. [139] performed stress analysis on various composite springs collated with steel spring, obtained von Mises stresses as 453.92 MPa for steel, 163.22 MPa for E-glass/epoxy, 653.68 MPa for Graphite/epoxy, 300.3 MPa for carbon/epoxy leaf spring and also reported weight abatement of 81.22% for E-glass/epoxy, 91.95% for graphite/epoxy and 90.51% for carbon/epoxy leaf springs. Wadile and Mahajan [172] conducted experimental stress analysis on E-glass/epoxy sandwiched leaf spring and reported the maximum stress to be 480.7 MPa. They also exercised a strain gauge measurement method to enumerate the deformation of leaf spring, which was found to be 43 mm at a load of 4 kN.

3.3 Limiting Factors of Synthetic Fibers

The above studies clearly indicate the diminution of leaf spring suspension system achieved and the low value of stresses, superior corrosion resistance, and higher stiffness values in comparison to spring steel by incorporating synthetic fiber composites as the material of the spring. Fatigue properties of composites have also shown to be dominating over the fatigue life of steel. Fiber-reinforced composites are having the characteristics, superseding the properties of spring steel, which are being employed for leaf spring suspensions in heavy vehicles. Even though the low weight and corrosion resistance of the synthetic composites exhibits enormous potential for replacing the steel leaf spring, their biodegradability and recycling is an issue. With this regard,

novel advancements instituting natural fibers are relevant for structural applications owing to their characteristics and eco-friendliness.

Synthetic fiber composites are expensive due to their processing methods and not being available in abundant volumes in contrast to natural fibers, and their raw form is also costly to procure along with high fabrication costs. Conventional materials have gone far from being the subject of study for present-day researches, which led to the boosting of new incipience in the composite mechanics, and components were made from carbon fibers and glass fibers with competent features conjointly with a high cost of processing and material cost. Therefore, the industrial motive of accomplishing low-cost criterion, eco-friendly material characteristics and paramount performance is to be perfectly balanced for the successful exertion of fiber engineered composites.

4 Natural Fiber Substituted Composites

Natural fibers are found in nature in plenitude and are capable of being employed in multifarious applications such as in automotive Sanoj and Kandasubramanian [142, 144] and aerospace industries as they have remarkable properties and eco-friendliness [76]. They are widely used and have a long history of being commercially available in textile markets. They can be articulated into woven or non-woven composite structures. Even the luxury brand automakers have exhibited a keen interest in exploring the various natural fiber composites for structural applications. Figure 17 sketches the woven fiber composite structures and Figure 18 elucidates the non-woven type of fiber composite structure, respectively [121]. The most popular natural fibers include sisal, hemp, kenaf, jute, etc. which also have the characteristics to match the strength of conventional metals and are favorable to employ in usage as their biodegradability and recyclability are highly appreciated. The mechanical properties are tailored using various surface treatments to change the fiber matrix orientations, properties of both

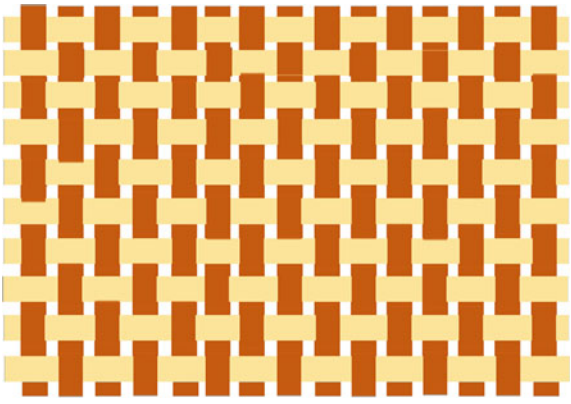

Fig. 17 Schematic of woven fibers

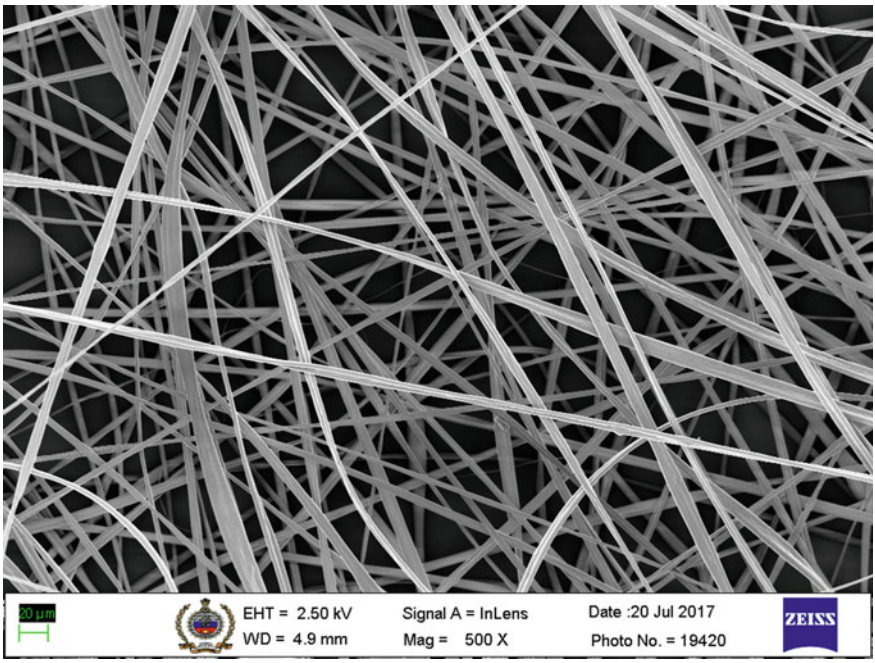

Fig. 18 FE-SEM micrograph of non-woven fibers

fiber and the matrix and interaction of the constituents. The bonding at the interfacial level should be very effective in transferring the stress so as to have high strength composites. Methods which improve the surface area of fiber by changing long bundles into groups of small bundles can efficiently aggrandize the mechanical characteristics and rendition of the natural fiber instituted composite. Sustainability is of great significance when the research of advanced materials is heading forward, along with unleveled performance in high-end applications. Natural fiber composites are potent candidates in substituting glass fiber composites due to lightweight [145], eco-friendliness, even mechanical properties, lower density and recyclability.

4.1 Case Studies

The fibers transfer stress adequately only when the surface area available is high, and on the increase of applied load for a high volume fraction, the effective area is will be reduced which in turn induce brittleness in the fibers and decreasing the tensile strength [162]. Factors affecting the tensile strength of natural fiber sandwiched composites include the orientation of fibers, the coupling betwixt matrix and fiber, fabrication process, fiber volume fraction, porosity and loading characteristics. During the manufacturing, stage priority should be given to impregnate all the

regions efficaciously in order to avoid the generation of porosity in the long fibers and which could lead to the rise of stress concentrations.

4.2 Jute-Reinforced Composite Leaf Spring

Jute has been commercially available for centuries for its textile properties and has become a potential candidate for being employed as a substitute for synthetic fibers. Recent demand for fibers found in nature is due to the fact that usage of synthetic fibers is substantiated only for high-end applications like aerospace structures where the quality supersedes cost criterion [107]. Babu and Kumar [8] amalgamated jute fibers along with synthetic fiber composite leaf having glass fiber layers fabricated a mono-leaf fiber-reinforced composite spring. The effectiveness of the spring was then differentiated with that of the steel spring (55Si7), and the stress analysis results reported lower stress values for the hybrid composite leave springs. They claimed to have found the elastic strain energy storage ability of jute-reinforced composite leaf is patronizing to that of the steel spring.

4.3 Banana Fiber-Reinforced Composite Leaf Spring

Banana fibers are often left as domestic waste or categorized for feeding cattle until recent studies on the strength properties of its fibers were focused by the researchers. Natural fibers such as banana fibers are so environment-friendly and eliminate the degradability issues and abundantly available as mostly they are thrown away and left to decay. Exploiting similar fibers for implementing novel material designs for the advancements of design and manufacturing for engineering applications is still on the verge of the onset of the long run. Assarudeen [61] employed the hand lay-up technique for fabricating the hybrid leaves for the spring with E-glass and banana fiber and compared the properties with steel leaf spring (65Si7) [49, 61, 125, 135, 159].

Table 4 contemplates that the mechanical strength of composite incorporated with natural fibers being comparable to both steel and E-glass/epoxy leaf spring with even lower density. The strain energy storage ability based on equation no. [2] is higher

Table 4 Properties of the hybrid composite leaf spring in comparison with steel leaf spring

Material	Elastic modulus (MPa)	Density (Kg/m^3)
Steel (65Si7)	2.1×10^5	7860
Banana/E-glass/epoxy	1.7×10^5	1420
E-glass/epoxy	1.9×10^5	2600
Jute/E-glass/epoxy	1.7×10^5	1460
Flax fiber	0.7×10^5	1400

as both the jute and banana fiber-reinforced composites have low density and low elastic modulus. Sanoj and Balasubramanian [141] conducted structural analysis on the jute fibril-reinforced composite spring and glass fiber engineered leaf spring, also administered tensile tests (ASTM D638) and flexural strength tests (ASTM D790), reported 28% rise in tensile modulus, 23% enhancement in flexural modulus and Charpy impact test (D6110) results in 48% melioration in the impact strength of hybrid leaf spring. George and Sarathdas [49] fabricated a hybrid composite leaf spring by embedding flax fibers with E-glass/epoxy, also endeavored to make a hybrid spring specimen of E-glass/banana/epoxy material and compared the properties with (65Si7) steel spring. They employed hand lay-up method to make specimens of E-glass and banana fibers and flax fiber with epoxy resin, performed the tensile testing (ASTM D638) and flexural bending tests (ASTM D790) and also found the ultimate tensile strength (UTS) of E-glass/banana/epoxy as 162.97 MPa with extension of 3.93 mm at an extreme load of 9.7 kN and the UTS of E-glass/flax/epoxy to be 182.89 MPa with an elongation of 3.76 mm at maximum load of 10.96 kN. The above studies lucidly propound the potential features of natural fibers eliciting interest for exercising in advanced composites to reinstate both the conventional materials and gradually the synthetic fibers soon. However, the properties of natural fibers are least explored for the leaf spring applications and are still at the initial stage of being the subject of discussion by the industrial research. The lean literature survey of natural fiber-reinforced springs is attributed to the absence of a focused research on the properties of natural fibers pertained to the applications of the vehicle suspension system.

5 Life Cycle Assessment (LCA)

The processes involved in the manufacture of leaf springs have ecological impacts on nature, and it can also be analyzed based on aftereffects of the products formed, the used-up substances during the production which remains unsuited for recycling. In particular, if we are talking of steel leaf springs, the initial setup starts at manufacturing together with other multifarious operations and treatments done to steel. Therefore, when it comes to the analysis of the life cycle of a product made from steel, the influential effects during its fabrication on the environment could be observed in several steps. Iron and steel industries [110, 182] are one of the cardinal partakers to contribute in the notable increase in atmospheric carbon dioxide (CO_2) levels, a potent greenhouse gas which directly aids in global warming which tends to raise the ambient temperature [176]. The fact that spring steels are widely employed for leaf springs for heavy transport vehicles could elucidate the depth to which leaf spring industries act as benefactor of raising the undesirable emissions of CO_2 [80], oxides of sulfur, oxides of nitrogen, etc. due to their steel consumption. If the role of steel in present infrastructure industry is considered the other products manufacturers requiring steel as the basic raw material which demands for the production of steel, cyclopean volumes of gases and by-products are released into atmosphere

in which harmful oxides, acid rain causing compounds and other pollutants are present in the particulate matter form [28] together with aiding air pollution [35]. The measures taken by ruling bodies are checking the compliance of any organization which employs the manufacturing processes releasing undesirable products, with the ISO 14000, which clauses the industrial standards helping in reducing the environmental impacts. Primarily controlling the content of these pollutants is inevitable as they greatly affect the ambient air quality which in turn has the prospective to sway the health of human beings [161] and the animal life as well as plant life [118] in the vicinity of these industries. Natural resources when are badly affected; evidently, it urges a proper monitoring of the quality of waste management and whole lot of cooperation from the industries to accomplish the rigorous actions of recyclable processing of by-products, reducing the huge amount of scrap which are being expelled in a way destroying the fertile nature of soil, affecting water resources and the ecosystems to which they end up with. Proper cutting of workpiece by strictly following the specific dimensions could help in eliminating the wastage of raw material. Steel industries extensively make use of pit furnaces for heating and melting purpose that requires a voluminous amount of coal to fire it up, which adds to the consumption of a valuable non-renewable resource. Transportation of this fuel is another major issue that requires the consumption of diesel fuel, and also the exhaust emissions from heavy vehicles do have environmental impacts. Nevertheless, the efficient use of coal or implementing other methods for melting and heat treatments is quintessential for reducing the hazardous effects on nature induced by the particulates, volatile inorganic compounds (VOC), etc. released by the chimney emissions [12]. Reusability of the leaf springs is to be considered as having major consequences in reducing scrap, wastage of resources and could agitate the prolonged service life of the product in the market in contrast to dumping the used springs into the soil or sea or public places and letting it undergo corrosion. On the grounds of the life cycle study of a leaf spring, manufacturing stages are thoroughly analyzed and does have highlighted effects on the ecological balance along with the welfare of human beings and animal life. The oil, one of the major substances which are utilized in the production process of steel leaf springs during the heat treatment stages like the quenching process, is disposed of in an unsafe manner after it becomes used. Recycling of used oil is a hurdle for the steel industries, and its safe disposal is highly crucial to maintain the ecological balance of resources which otherwise are left harmed.

6 Conclusion

The automobile industry will perpetually keep on evolving day by day with advancements in materials, novel design concepts and methods of improving efficiency with resource optimization. When the industrial motive does not remain constricted to launch models to attract customers with their catchy styles, advertising skills, and marketing strategies, boosting productive research in advanced materials scope of instituting natural fiber-reinforced composites in component design is on board.

Leaf springs are currently being manufactured in full-fledged mode exclusively for heavy transport vehicles, namely buses, trucks and railway locomotives and are given only scant amount of research interest with respect to light motor vehicles. Recent advancements in the field of composites have incorporated the use of new materials like glass fiber, and carbon fiber instituted composites for the spring material to replace the spring steel due to weight and susceptibility to corrosion. The extensive usage of conventional steel spring is continued to be seen in heavy vehicles where the research is not being much encouraged in improving the design parameters involving advanced materials. Gaining higher energy efficiency is not appreciated as the top priority by the heavy vehicle manufacturers as their motive is limited to provide the means for transporting cargo. The small and medium vehicle industries are zealously exhibiting great interest in the advancements and research in modern materials to be advocated in the manufacture of automotive modules. With the advent of materials incorporating natural fiber-reinforced composites, the dependence on synthetic fibers can be considerably reduced, thereby exploiting the natural fibers by virtue of their properties for the automotive germaneness. Recycling of synthetic fibers is a major hurdle regarding its cost, wherein the biodegradability of natural fibers supersedes the carbon fibers and glass fibers together with competent structural properties. The automotive industry constantly strives to optimize the available resources and look forward to achieving higher energy efficiency, therefore, encourages the endeavor of improving the scientific research of modern materials. With this respect, the implementation of lightweight and strong structures made of fiber-reinforced composites for industrial applications enhances the mission of achieving higher efficiency. In automotive components like the suspension system, the use of natural fibers is to be encouraged, and the research is still at the stage of its inception, and a more elaborate study is required in the future for employing jute, hemp, kenaf for advanced structural applications. Experimental concepts of incorporating glass fibers and carbon fibers sandwiched with potentially strong natural fibers are still to be explored on a large scale for structural and automotive components.

References

1. Aggarwal M, Agrawal V, Khan R (2006) A stress approach model for predictions of fatigue life by shot peening of EN45A spring steel. Int J Fatigue 28(12):1845–1853
2. Aggarwal ML (2006) A stress approach model for predictions of fatigue life by shot peening of EN45A spring steel. Int J Fatigue 28:1845–1853
3. Aher VK, Sonawane PM (2012) Static and fatigue analysis of multi leaf spring used in the suspension system of LCV. Int J Eng Res Appl 2(4):1786–1791
4. Akiniwa Y, Stanzl-Tschegg S, Mayer H, Wakita M, Tanaka K (2008) Fatigue strength of spring steel under axial and torsional loading in the very high cycle regime. Int J Fatigue 30(12):2057–2063
5. Al-Qureshi HA (2001) Automobile leaf springs from composite materials. J Mater Process Technol 118(1–3):58–61
6. Ås SK, Skallerud B, Tveiten BW (2008) Surface roughness characterization for fatigue life predictions using finite element analysis. Int J Fatigue 30(12):2200–2209

7. Atig A, Ben Sghaier R, Seddik R, Fathallah R (2018) A simple analytical bending stress model of parabolic leaf spring. Proc Instit Mechan Eng Part C: J Mechan Eng Sci 232(10):1838–1850
8. Babu KN, Kumar PS (2016) Design and analysis of jute/e-glass/epoxy/composite mono leaf spring of varying cross-section using Catia V5 and ANSYS 14.5. Int J Innov Eng Technol 7(1):244–254
9. Badhe Y (2014) Novel hybrid ablative composites of resorcinol formaldehyde as thermal protection systems for re-entry vehicles. RSC Adv 4(55):28956
10. Bae JM, Kim KN, Hattori M, Hasegawa K, Yoshinari M, Kawada E, Oda Y (2004) Fatigue strengths of particulate filler composites reinforced with fibers. Dent Mater J 23(2):166–174
11. Bai Y, Guan S, Flórez-López J (2017) Development of a damage model for assessing fracture failure of steel beam-to-column connections subjected to extremely low-cycle fatigue. Eng Fail Anal 82:823–834
12. Ball DJ, Caswell R (1983) Smoke from diesel-engined road vehicles: An investigation into the basis of british and european emission standards. Atmos Environ 17(1):169–181
13. Barnat-Hunek D, Smarzewski P, Brzyski P (2017) Properties of hemp-flax composites for use in the building industry. J Nat Fib 14(3):410–425
14. Beardmore P, Johnson CF (1986) Potential Composit Struct Automot Appl 26:251–281
15. Beaumont PWR (1974) A fracture mechanics approach to failure in fibrous composites. J Adhesion 6(1–2):107–137
16. Ben-Arieh D (2000) Cost estimation system for machined parts. Int J Prod Res 38(17):4481–4494
17. Bhowmick M, Mukhopadhyay S, Alagirusamy R (2012) Mechanical properties of natural fibre-reinforced composites. Text Progr 44(2):85–140
18. Biron M (2004) Composites. Thermosets Compos 343–463
19. Bledzki A (1999) Composites reinforced with cellulose based fibres. Prog Polym Sci 24(2):221–274
20. Bos H, Van Den Oever M, Peters O (2002) Tensile and compressive properties of flax fibres for natural fibre reinforced composites. J Mater Sci 37:1683–1692
21. Brammer AJ, Von Gierke HE (2002). Effects of shock and vibration on humans
22. Burdzik R (2017) Novel method for research on exposure to nonlinear vibration transferred by suspension of vehicle. Int J Non-Linear Mech 91:170–180
23. Businaro UL (1983) The automotive industry needs research. Interdisc Sci Rev 8(2):146–157
24. Carlsson LA, Adams DF, Pipes RB (2013) Basic experimental characterization of polymer matrix composite materials. Polym Rev 53(2):277–302
25. Carriage Springs (1857) Sci Am 12(18):144–144
26. Chan KS (2010) Roles of microstructure in fatigue crack initiation. Int J Fatigue 32(9):1428–1447
27. Chapman AC (1925) ©1925 Nature Publishing Group. © 1925 Nature Publishing Group
28. Chen Y-C, Chiang H-C, Hsu C-Y, Yang T-T, Lin T-Y, Chen M-J et al (2016) Ambient PM 2.5-bound polycyclic aromatic hydrocarbons (PAHs) in Changhua County, central Taiwan: Seasonal variation, source apportionment and cancer risk assessment. Environ Pollut 218:372–382
29. Clarke CK, Borowski GE (2005) Evaluation of a leaf spring failure. J Fail Anal Prev 5(6):54–63
30. Crolla DA, Lang AM (1991) Paper VII (i) Brake Noise and Vibration—The State of the Art. In: Tribology Series vol 18, pp 165–174
31. Sameer Kumar D, Sajja R, Suman KNS (2011) Improved design optimization of a composite leaf spring using swarm intelligence. Int J Appl Eng Res 6(2):193–200
32. Das SK, Mukhopadhyay NK, Kumar BR, Bhattacharya DK (2007) Failure analysis of a passenger car coil spring. Eng Fail Anal 14(1):158–163
33. Delicano JA (2018) A review on abaca fiber reinforced composites. Compos Interfaces 25(12):1039–1066
34. Demers CE (1998) Fatigue strength degradation of E-glass FRP composites and carbon FRP composites. Constr Build Mater 12(5):311–318

35. Derwent RG, Stewart HNM (1973) Air pollution from the oxides of nitrogen in the United Kingdom. Atmosph Environ (1967) 7(4):385–401
36. Drissi-Habti M, Suzuki K, Nakano K, Kanno Y (1999) Cost-Effectiveness Concept applied to the development of advanced materials. Adv Compos Mater 8(1):87–96
37. Eberspächer P, Lechler A, Verl A (2016) Control-integrated consumption graph-based optimisation method for energy reduction of machine tools with automated parameter optimisation. Int J Comput Integr Manuf 29(12):1307–1316
38. Ehlers BWA (1917) I-Ieat treatment of metals. The art of treating low and high carbon steel with gaseous fuel (2179)
39. Elkington M, Bloom D, Ward C, Chatzimichali A, Potter K (2015) Hand layup: understanding the manual process. Adv Manuf Polym Composit Sci 1(3):138–151
40. Elkington M, Ward C, Chatzimichali A, Potter K (2015) Studying effects of preshearing on hand layup. Adv Manuf Polym Composit Sci 1(2):80–93
41. Fatigue Phenomena in Metals (1920) Sci Am 1(3):221–228
42. Feest EA, Group T, Laboratoo H, Ora OXII (1986) Metal matrix composites for industrial application 7:58–64
43. Fragoudakis R, Savaidis G, Michailidis N (2017) Optimizing the development and manufacturing of 56SiCr7 leaf springs. Int J Fatigue 103:168–175
44. Friedrich K, Almajid AA (2013) Manufacturing aspects of advanced polymer composites for automotive applications. Appl Compos Mater 20(2):107–128
45. Fuqua MA, Huo S, Ulven CA (2012) Natural fiber reinforced composites. Polym Rev 52(3):259–320
46. Furuya Y, Matsuoka S, Abe T (2004) Inclusion-controlled fatigue properties of 1800 MPA-class spring steels. Metall Mater Trans Phys Metall Mater Sci 35(12):3737–3744
47. Ganesh P, Sundar R, Kumar H, Kaul R, Ranganathan K, Hedaoo P et al (2014) Studies on fatigue life enhancement of pre-fatigued spring steel specimens using laser shock peening. Mater Des 54:734–741
48. Gao B, Zhang R, Wang C (2016). Enhanced mechanical properties of carbon fiber composites by grafting different structural poly (amido amine) onto fiber surface. Polym Test
49. George AM, Sarathdas S (2017) Design and analysis of leaf spring by using hybrid composite material. Int Res J Eng Technol (IRJET) 2235–2241
50. George SM, Kandasubramanian B (2019) Advancements in MXene-Polymer composites for various biomedical applications. Ceram Int
51. Gharde S, Goud R, Nimje S, Kandasubramanian B (2019) Aggrandized flexural properties of assorted natural biological materials. In Kumar K, Davim JP (eds) Biodegradable composites, pp 111–140
52. Gharde S, Kandasubramanian B (2019) Mechanothermal and chemical recycling methodologies for the fibre reinforced plastic (FRP). Environ Technol Innov 14:100311
53. Gharde S, Surendren A, Korde JM, Saini S, Deoray N, Goud R et al (2019) Recent advances in additive manufacturing of bio-inspired materials. Biomanufacturing, pp 35–68
54. Gobble MM (2010) Industry-defined fundamental research: creating an agenda for basic research. Res Technol Manage 53(5):55–62
55. Golovoy A, Cheung MF, Oene H Van (1984) The impact behavior of glass and carbon fiber composites. Polym-Plast Technol Eng 23(2):217–227
56. Gore PM, Kandasubramanian B (2018) Functionalized aramid fibers and composites for protective applications: a review. Ind Eng Chem Res 57(49):16537–16563
57. Goswami T (1997) Low cycle fatigue life prediction—a new model. Int J Fatigue 19(2):109–115
58. Goud R, Yadav R, Wang X, Naebe M, Kandasubramanian B (2020) Mollusk-inspired 3D printing of polycarbonate via fused deposition modelling. In: Handbook of polymer and ceramic nanotechnology, pp 1–12
59. Gupta R, Kandasubramanian B (2015) Hybrid caged nanostructure ablative composites of octaphenyl-POSS/RF as heat shields. RSC Adv 5(12):8757–8769

60. Gustafson C, Echtermeyer A (2006) Long-term properties of carbon fibre composite tethers. Int J Fatigue 28(10):1353–1362
61. Assarudeen H (2015) Structural analysis of Banana/E-Glass woven fiber reinforced epoxy based hybrid composite on mono leaf spring using FEA. J Chem Pharm Sci 7:253–257
62. Harada Y, Tanaka S, Itoh M, Nakatani M (2014) Effect of microshot peening on fatigue life of spring steel SUP9. Procedia Eng 81:1493–1498
63. Herrera EJ, Fuentes JJ, Aguilar HJ (2009) Premature fracture in automobile leaf springs 16:648–655
64. Hou JP, Cherruault JY, Nairne I, Jeronimidis G, Mayer RM (2007) Evolution of the eye-end design of a composite leaf spring for heavy axle loads. Compos Struct 78(3):351–358
65. Howe AA, Farrugia DCJ (1999) Alloy design: from composition to through process models. Mater Sci Technol 15(1):15–21
66. Howell LL, Midha A, Norton TW (2016) L. L Howell 118(March 1996):126–131
67. Hufenbach W, Böhm R, Thieme M, Winkler A, Mäder E, Rausch J, Schade M (2011) Polypropylene/glass fibre 3D-textile reinforced composites for automotive applications. Mater Des 32(3):1468–1476
68. Huston RL, Kelly FA (2014) Another look at the static stability factor (SSF) in predicting vehicle rollover. Int J Crashworthiness 19(6):567–575
69. Hwang W, Han KS (1986) Fatigue of composites—fatigue modulus concept and life prediction. J Compos Mater 20(2):154–165
70. Inamdar A, Cherukattu J, Anand A, Kandasubramanian B (2018) Thermoplastic-toughened high-temperature cyanate esters and their application in advanced composites. Ind Eng Chem Res 57(13):4479–4504
71. Jancirani J, Assarudeen H (2015) A review on structural analysis and experimental investigation of fiber reinforced composite leaf spring
72. Jeffries R (1971) Prospects for carbon fibres. Nature 232(5309):304–307
73. Jiang R, Karpasitis N, Gao N, Reed PAS (2015) Effects of microstructures on fatigue crack initiation and short crack propagation at room temperature in an advanced disc superalloy. Mater Sci Eng 641:148–159
74. Karditsas S, Savaidis G, Malikoutsakis M (2015) Advanced leaf spring design and analysis with respect to vehicle kinematics and durability. Int J Struct Integr 6(2):243–258
75. Karlus EN, Himte RL, Rathore RK (2014) Optimization of mono parabolic leaf spring. Int J Adv Eng Technol 7(1):283–291
76. Karus M, Kaup M (2002) Natural fibres in the european automotive industry. J Indus Hemp 7(1):119–131
77. Kashyap S, Kabra S, Kandasubramanian B (2020). Graphene aerogel-based phase changing composites for thermal energy storage systems. J Mater Sci
78. Khatavkar N, Kandasubramanian B (2016) Composite materials for supersonic aircraft radomes with ameliorated radio frequency transmission-a review. RSC Adv 6(8):6709–6718
79. King RL (1982) A production engineers view of advanced composite materials. Part 2 The manufacture of advanced composites, components and structures. Mater Des 3(5):580–588
80. Kirschen M, Risonarta V, Pfeifer H (2009) Energy efficiency and the influence of gas burners to the energy related carbon dioxide emissions of electric arc furnaces in steel industry. Energy 34(9):1065–1072
81. Kong YS, Omar MZ, Chua LB, Abdullah S (2013) Explicit nonlinear finite element geometric analysis of parabolic leaf springs under various loads
82. Kosugi K, Maekawa S, Hirose Y, Sana T, Hatakeyama T, Tamura H (2001) Low cost manufacturing approach for composite outer wing of SST. Adv Compos Mater 10(2–3):229–236
83. Krall S, Zemann R (2015) Investigation of the dynamic behaviour of CFRP leaf springs. Procedia Eng 100:646–655
84. Krason W, Wysocki J (2017) Investigation of friction in dual leaf spring. J Frict Wear 38(3):214–220
85. Kretschmer J (1988) Composites in automotive applications–state of the art and prospects. Mater Sci Technol 4(9):757–767

86. Kueh JJ, Faris T (2012) Finite element analysis on the static and fatigue characteristics of composite multi-leaf spring. J Zhejiang Univ Sci A 13(3):159–164
87. Kumar CV, Kandasubramanian B (2019) Advances in ablative composites of carbon based materials: a review. Ind Eng Chem Res 58(51):22663–22701
88. Kumar K, Aggarwal ML (2017) Science direct optimization of various design parameters for EN45A flat leaf spring. Mater Today: Proc 4(2):1829–1836
89. Kumar K, Aggarwal ML (2015) Simulation for optimized modelling of En45A leaf spring. Int J Recent Adv Mechan Eng 4(3):129–142
90. Kurihara Y (1995) Polymer matrix composite materials in automobile industries. Adv Compos Mater 4(3):209–219
91. Kwofie S, Chandler HD (2007) Fatigue life prediction under conditions where cyclic creep-fatigue interaction occurs. Int J Fatigue 29(12):2117–2124
92. Lee DG, Lee CS, Lee HG, Hwang HY, Kim JW (2004) Novel applications of composite structures to robots, machine tools and automobiles. Compos Struct 66(1–4):17–39
93. Ling S, Kaplan DL, Buehler MJ (2018) Nanofibrils in nature and materials engineering. Nat Rev Mater 3(4):18016
94. Liu M, Guo Y, Wang J, Yergin M (2018) Corrosion avoidance in lightweight materials for automotive applications. NPJ Mater Degrad 2(1):24
95. Lukaszewicz DHJA, Ward C, Potter KD (2012) The engineering aspects of automated prepreg layup: history, present and future. Compos B Eng 43(3):997–1009
96. Mahdi E (2006) Light composite elliptic springs for vehicle suspension 75:24–28
97. Malikoutsakis M, Savaidis G, Savaidis A, Schwaiger F (2016) Design, analysis and multi-disciplinary optimization of high-performance front leaf springs design, analysis and multi-disciplinary optimization of high. Theor Appl Fract Mechan
98. Mallick PK (2007) Fiber-reinforced
99. Mansfield NJ (2012) Human response to vehicle vibration. In: Automotove ergonomics: driver-vehicle interaction, pp 77–94
100. Marines I (2003) An understanding of very high cycle fatigue of metals. Int J Fatigue 25(9–11):1101–1107
101. Marsh G (2002) Composites strengthen aerospace hold. Reinf Plast 46(7–8):40–43
102. Mathijsen D (2016) Thermoplastic composites keep gaining momentum in the automotive industry. Reinf Plast 60(6):408–412
103. Matsuzaki R, Ueda M, Namiki M, Jeong T-K, Asahara H, Horiguchi K et al (2016) Three-dimensional printing of continuous-fiber composites by in-nozzle impregnation. Sci Rep 6(1):23058
104. Mazaheri Y, Meratian M, Emadi R, Najarian AR (2013) Materials Science & Engineering: a comparison of microstructural and mechanical properties of Al–TiC, Al–B4C and Al–TiC–B4C composites prepared by casting techniques. Mater Sci Eng A 560(4):278–287
105. Mills A (2001) Automation of carbon fibre preform manufacture for affordable aerospace applications. Compos A Appl Sci Manuf 32(7):955–962
106. Mithari R, Patil A, Aitavade EN (2012) Analysis of composite leaf spring by using analytical & FEA. Int J Eng Sci Technol (IJEST) 4(12):4809–4814
107. Mohanty AK, Misra M (1995) Studies on jute composites—a literature review. Polym-Plast Technol Eng 34(5):729–792
108. Morris D (1895) Commercial fibers. Sci Am 40(1042):16659–16661
109. Mountcastle VB, LaMotte RH, Carli G (1972) Detection thresholds for stimuli in humans and monkeys: comparison with threshold events in mechanoreceptive afferent nerve fibers innervating the monkey hand. J Neurophysiol 35(1):122–136
110. Mousa E, Wang C, Riesbeck J, Larsson M (2016) Biomass applications in iron and steel industry: an overview of challenges and opportunities. Renew Sustain Energy Rev 65:1247–1266
111. Muhammed L, Ismaeel A (2015) Optimization and static stress analysis of hybrid fiber reinforced composite leaf spring
112. Murakami Y (2002) Spring steels. In: Metal fatigue, pp 163–183

113. Narici L, Casolino M, Di Fino L, Larosa M, Picozza P, Rizzo A, Zaconte V (2017) Performances of Kevlar and polyethylene as radiation shielding on-board the international space station in high latitude radiation environment. Sci Rep 7(1):1644
114. Neubrand J (2014) Possibilities of coil springs and fiber-reinforced suspension parts. In: Encyclopedia of automotive engineering, pp 1–11
115. Novovic D, Dewes RC, Aspinwall DK, Voice W, Bowen P (2004) The effect of machined topography and integrity on fatigue life. Int J Mach Tools Manuf 44(2–3):125–134
116. O'rourke BP (2000) Formula 1 applications of composite materials. In: Comprehensive composite materials, pp 381–393
117. Omar MA, Shabana AA, Mikkola A, Loh WYI, Basch R (2004) Multibody system modeling of leaf springs. JVC/J Vibr Control 10(11):1601–1638
118. Pandey J, Agrawal M (1994) Growth responses of tomato plants to low concentrations of sulphur dioxide and nitrogen dioxide. Sci Hortic 58(1–2):67–76
119. Park H (2016) A study on structural design and analysis of small wind turbine blade with natural fibre (flax) composite. Adv Compos Mater 25(2):125–142
120. Patel SR, Patel RG (1992) Physicomechanical properties of carbon fiber reinforced epoxy composites. Polym-Plast Technol Eng 31(7–8):705–712
121. Pervaiz M, Panthapulakkal S, Birat KC, Sain M, Tjong J (2016) Emerging trends in automotive lightweighting through novel composite materials. Mater Sci Appl 7(1):26–38
122. Peterson CW (1990) High-performance parachutes. Sci Am 262(5):108–116
123. Pozhilarasu V, Pillai TP (2013) Performance analysis of steel leaf spring with composite leaf spring and fabrication of composite leaf spring. Int J Eng Res Sci Technol 2(August):10
124. Prahalad P, Badkar S (2013) Design improvements of leaf spring of BEML Tatra 815 VVNC 8 X 8 Truck 3(1):318–324
125. Punchaipetch P, D'Souza NA, Brostow W, Smith JT (2002) Mechanical properties of glass fiber composites with an epoxy resin modified by a liquid crystalline epoxy. Polym Compos 23(4):564–573
126. Pupurs A (2016) Fiber failure and debonding in composite materials. In: Modeling damage, fatigue and failure of composite materials, pp 173–196
127. Qian C, Shi W, Chen Z, Yang S, Song Q (2017) Fatigue reliability design of composite leaf springs based on ply scheme optimization. Compos Struct
128. Qin Y, Wang X, Wang ZL (2008) Microfibre–nanowire hybrid structure for energy scavenging. Nature 451(7180):809–813
129. Rahimi A, García JM (2017) Chemical recycling of waste plastics for new materials production. Nat Rev Chem 1(6):46
130. Rahman MA, Kowser MA (2010) Inelastic deformations of stainless steel leaf springs-experiment and nonlinear analysis. Meccanica 45(4):503–518
131. Rajaguru J, Arunachalam N (2018) Investigation on machining induced surface and subsurface modifications on the stress corrosion crack growth behaviour of super duplex stainless steel. Corros Sci 141:230–242
132. Rajesh S, Bhaskar GB, Venkatachalam J, Pazhanivel K, Sagadevan S (2016) Performance of leaf springs made of composite material subjected to low frequency impact loading. J Mech Sci Technol 30(9):4291–4298
133. Rajesh V, Rao PMV, Sateesh N (2017) Investigation of carbon composites subjected to different environmental conditions. Mater Today: Proc 4(2):3416–3421
134. Randall JM (1992) Human subjective response to lorry vibration: implications for farm animal transport. J Agric Eng Res 52:295–307
135. Reis JML (2006) Fracture and flexural characterization of natural fiber-reinforced polymer concrete. Constr Build Mater 20(9):673–678
136. Robson JD, Dodds CJ (1976) Stochastic road inputs and vehicle response. Veh Syst Dyn 5(1–2):1–13
137. Roy DK, Saha KN (2013) Nonlinear analysis of leaf springs of functionally graded materials. Proc Eng 51(NUiCONE 2012):538–543

138. Sharp RS, Crolla DA (1987) Vehicle suspension system design—a review. Veh Syst Dyn Int J Veh Mechan Mobility 16(June 2013):167–192
139. Saini Pankaj, Goel Ashish, Kumar D (2013) Design and analysis of composite leaf spring for light vehicles. Int J Innov Res Sci Eng Technol 2(5):1–10
140. Sancaktar E (2017) Design, analysis, and optimization of composite leaf springs for light vehicle applications, p 8223
141. Sanoj P, Balasubramanian K (2014) High performance structural nano cellulose composites for motor vehicle spring suspension system. Int J Plast Technol 18(3):383–389
142. Sanoj P, Kandasubramanian B (2013) Hybrid Sandwich composite or leaf spring components in automobiles. In: 4th international conference on recent advances in composite materials, ICRACM-13, International Centre Goa, 18–21 Feb 2013
143. Sanoj P, Kandasubramanian B (2014) Hybrid carbon-carbon ablative composites for thermal protection in aerospace. J Composit 2014:1–15
144. Sanoj P, Kandasubramanian B (2014b) Hybrid Sandwich composites for leaf spring component in automobile suspension system. Adv Manuf Technol
145. Sanoj P, Kandasubramanian B (2014c) Light weight green composite leafspring with enhanced dynamic response for automotives. In: International APM conference, Bhubhaneshwar
146. Sapuan SM (2017) Design for sustainability in composite product development. In: Composite materials, pp 273–294
147. Sarrak VI, Mishin VM (1992) Delayed failure of steels 5:419–420
148. Schuerch H (1966) Prediction of compressive strength in uniaxial boron fiber-metal matrix composite materials. AIAA J 4(1):102–106
149. Scott B (1997) Stopping bullets. Sci Am 276(3):132
150. Serrano-Munoz I, Buffiere J-Y, Mokso R, Verdu C, Nadot Y (2017) Location, location & size: defects close to surfaces dominate fatigue crack initiation. Sci Rep 7(1):45239
151. Sert E, Boyraz P (2017) Engineering Science and Technology, an International Journal Optimization of suspension system and sensitivity analysis for improvement of stability in a midsize heavy vehicle. Eng Sci Technol Int J
152. Shadmehri F, Hoa SV, Fortin-Simpson J, Ghayoor H (2018) Effect of in situ treatment on the quality of flat thermoplastic composite plates made by automated fiber placement (AFP). Adv Manuf Polym Compos Sci 4(2):41–47
153. Shaw SJ (1987) High-temperature polymers for adhesive and composite applications. Mater Sci Technol 3(8):589–599
154. Shi W, Qian C, Chen Z, Song Q (2017) Establishment of theoretical model of composite leaf springs by using the mechanics of composite materials, p 5988
155. Shin J, Lee S, Ryu JH (1999) Correlation of microstructure and fatigue properties of two high-strength spring steels. Int J Fatigue 21:571–579
156. Shokrieh MM, Rezaei D (2003) Analysis and optimization of a composite leaf spring. Compos Struct 60(3):317–325
157. Singh H, Brar GS (2018) Characterization and investigation of mechanical properties of composite materials used for leaf spring. Mater Today: Proc 5(2):5857–5863
158. Soares BAR, Henriques E, Ribeiro I, Freitas M (2018) Cost analysis of alternative automated technologies for composite parts production. Int J Prod Res 1–14
159. Sobczak L, Lang RW, Haider A (2012) Polypropylene composites with natural fibers and wood—general mechanical property profiles. Compos Sci Technol 72(5):550–557
160. Sproull RL (1962) The conduction of heat in solids. Sci Am 207(6):92–106
161. Stone V, Donaldson K (2006) Environmental pollutants | overview. In: Encyclopedia of respiratory medicine, pp 90–96
162. Subbiah R, Tjong J, Nayak SK, Sain M (2017) Effect of natural fiber network on permeability and tensile strength of composites through vacuum infusion process. J Nat Fib 14(2):278–286
163. Subramanian C, Senthilvelan S (2010) Effect of reinforced fiber length on the joint performance of thermoplastic leaf spring. Mater Des 31(8):3733–3741
164. Taylor G, Orowan E (1963) The strength of steel

165. Thippesh L (2018) Science direct fabrication of hybrid composite mono-leaf spring with unidirectional glass fibers. Mater Today: Proc 5(1):2980–2984
166. Thite AN, Gerguri S, Coleman F, Doody M, Fisher N (2013) Development of an experimental methodology to evaluate the influence of a bamboo frame on the bicycle ride comfort. Veh Syst Dyn 51(9):1287–1304
167. Murgatroyd T (1922) Patent No. 139,325. United States Patent Office, US
168. Tirumali M, Kandasubramanian B, Kumaraswamy A, Subramani NK, Suresha B (2018) Fabrication, physicochemical characterizations and electrical conductivity studies of modified carbon nanofiber-reinforced epoxy composites: effect of 1-butyl-3-methylimidazolium tetrafluoroborate ionic liquid. Polym Plast Technol Eng 57(3):218–228
169. Trailer T (1987) Leaf spring for tank trailer suspensions. J Reinf Plast Compos 6:100–112
170. Vaidya UK, Chawla KK (2008) Processing of fibre reinforced thermoplastic composites. Int Mater Rev 53(4):185–218
171. Vukelic G, Brcic M (2016) Failure analysis of a motor vehicle coil spring. Proc Struct Integr 2:2944–2950
172. Wadile PD, Mahajan KA (2017) Experimental investigations of composite leaf spring. IOSR J Mech Civil Eng 17(1):18–23
173. Wambua P, Ivens J, Verpoest I (2003) Natural fibres: can they replace glass in fibre reinforced plastics? Compos Sci Technol 63(9):1259–1264
174. Wang T, Tinsley B, Patel MD, Shabana AA (2018) Nonlinear dynamic analysis of parabolic leaf springs using ANCF geometry and data acquisition. Nonlinear Dyn 93(4):2487–2515
175. Wang X, Chen Y, Niu G (2018) The study on corrosion resistance of high-strength spring steel. Corros Eng Sci Technol 53(1):54–64
176. Wang X, Jiang D, Lang X (2017) Future extreme climate changes linked to global warming intensity. Sci Bull 62(24):1673–1680
177. Wang Z, Subramanian N, Gunasekaran A, Abdulrahman MD, Liu C (2015) Composite sustainable manufacturing practice and performance framework: Chinese auto-parts suppliers' perspective. Int J Prod Econ 170:219–233
178. Waterman N (1984) Materials for the 80's and 90's. Mater Des 5(3):121–125
179. Wei C, Zeng M, Xiong XM, Zhang FA (2010) Thermal and frictional properties of modified sisal fibre/phenolic resin composites. Plast, Rubber Compos 39(2):61–66
180. Weiss MP, Lavi E (2016) Fatigue of metals—what the designer needs? Int J Fatigue 84(November):80–90
181. With the automotive inventors (1927) Sci Am 137(1):62–62
182. Xu B, Lin B (2016) Assessing CO_2 emissions in China's iron and steel industry: a dynamic vector autoregression model. Appl Energy 161:375–386
183. Yadav R, Goud R, Dutta A, Wang X, Naebe M, Kandasubramanian B (2018) Biomimicking of hierarchal molluscan shell structure via layer by layer 3D printing. Indus Eng Chem Res acs.iecr.8b01738
184. Yadav R, Naebe M, Wang X, Kandasubramanian B (2017) Review on 3D prototyping of damage tolerant interdigitating brick arrays of nacre. Ind Eng Chem Res 56(38):10516–10525
185. Younes A, Seidel A, Engler T, Cherif C, Ehlig D (2013) Mechanical behaviour of carbon and glass filament yarns under high temperatures for composite applications. J Text Inst 104(3):251–259
186. Zacby VF (1968). Strong and ductile steels, pp 36–45
187. Zhang H, Chen MW, Ramesh KT, Ye J, Schoenung JM, Chin ESC (2006) Tensile behavior and dynamic failure of aluminum 6092/B4C composites. Mater Sci Eng, A 433(1–2):70–82
188. Zhang H, Ericson ML, Varna J, Berglund LA (1997) Transverse single-fibre test for interfacial debonding in composites: 1. experimental observations. Compos Part A: Appl Sci Manuf 28(4):309–315
189. Zhang J, Chaisombat K, He S, Wang CH (2012) Glass/carbon fibre hybrid composite laminates for structural applications in automotive vehicles. In: Sustainable automotive technologies 2012, pp 69–74

190. Zhang RL, Gao B, Zhang J, Cui HZ, Li DW (2015) Propagation of PAMAM dendrimers on the carbon fiber surface by in situ polymerization: a novel methodology for fiber/matrix composites. Appl Surf Sci 359:812–818
191. Zhang W, Fang K, Hu Y, Wang S, Wang X (2016) Effect of machining-induced surface residual stress on initiation of stress corrosion cracking in 316 austenitic stainless steel. Corros Sci 108:173–184

Chapter 5
Fabrication of Aluminium Metal Matrix Nanocomposites: An Overview

Deepak M. Shinde and Prasanta Sahoo

1 Introduction

Improved fuel economy, reduced vehicle emission, increased safety, attractive styling options and better features of comfort and luxury to passengers at competitive cost are the challenges being faced by automotive and aerospace industries these days. This has prompted continuous research on developing light-weight materials with desired and tailored properties. Aluminium and its alloys have become obvious choice due to low cost availability, low density, better strength, corrosion resistance, near-infinite recyclability and casting ease. Aluminium composites in particular have attracted researchers due to properties like high strength and stiffness, increased resistance to wear and corrosion and improved high-temperature performance [6, 74]. Successful automotive applications of Al include transmission components, brake elements, structural parts like chassis, suspension, body parts including bumpers, doors and interiors [36, 79]. Improvement in properties of aluminium is affected by reinforcing with ceramic phase to produce so-called aluminium metal matrix composites (AMMCs). It is because aluminium and ceramics have vastly different properties making it possible to obtain desired property combinations. Large number of MMCs are now commercially being produced and used with major contribution of particulate-reinforced Al composites on mass basis [111]. Different micro/nano-scale particles such as TiB_2, SiC, TaC, TiC, SiO_2, TiO_2, Si_3N_4, TiN, Al_2O_3 and B_4C are used to produce metal matrix composites via different solid- and liquid-state fabrication routes.

Aluminium-based microcomposites have been successfully utilized in different sectors like ground transportation, aerospace, electronics, recreational goods industries for structural and wear resistance applications. It is also clearly demonstrated

D. M. Shinde (✉) · P. Sahoo
Jadavpur University, Kolkata, India
e-mail: dmshinde1975@gmail.com

S. Sahoo (ed.), *Recent Advances in Layered Materials and Structures*,
Materials Horizons: From Nature to Nanomaterials,
https://doi.org/10.1007/978-981-33-4550-8_5

in several studies in recent past that nanoparticle reinforced composites outperform microcomposites in many respects. For instance, the compressive strength performance of A356 alloy composites reinforced with 20 μm and 50 nm size Al_2O_3 particles was compared [82] and reported 610 MPa strength for 3 wt% alumina nanocomposite as compared to 453 MPa measured for 10 wt% alumina microcomposite. But the critical issue in producing MMNCs is the uniform dispersion of nanoparticles in metal matrix because due to large surface area they tend to form clusters under the influence of Van der Waals force of attraction. During conventional liquid processing, limited wettability of ceramic particles and particle getting pushed by the solidification front leads to their agglomeration near grain boundaries and also formation of pores/voids which seriously affect properties diminishing the beneficial effects of nanoparticles.

Fabrication of nanocomposite is relatively complex on account of very fine size particles which are difficult to handle and introduce uniformly into the matrix. Researchers are continuously trying to promote suitable methods for low-cost defect-free production of nanocomposites with possible industrial scalability. But still most of these efforts are of laboratory scale. It is essential to promote commercial ultilization of MMNCs which in turn may help in their developmental efforts. Most of the existing methods of fabricating MMNCs are similar to MMCs but being modified to tackle added challenges posed by nanoparticles. This paper takes an overview of the fabrication methods proposed and published in the literature regarding aluminium nanocomposites while highlighting their prominent features and challenges which may stand useful for students and researchers working in the area of nanocomposite fabrication.

2 Fabrication Methods

Different methods employed for fabricating aluminium metal matrix nanocomposites can be divided into three major groups, viz. solid-state processing, semisolid-state processing and liquid-state processing. Some attempts have been made to combine above principal methods for availing their benefits in the improvement of properties and so can be termed as hybrid methods. Some novel routes for nanocomposite fabrication have also been reported in recent times. Solid- and liquid-state processes are either ex situ or in situ type depending upon whether the reinforcement particles are generated during the fabrication process or are available for incorporation beforehand. Ex situ is when the hard/soft reinforcement particles in solid form are added externally to the solid or liquid metal matrix. In situ involves production of reinforcement particles inside the metal matrix during ongoing fabrication process as a result of reaction between the phase elements involved.

2.1 Solid-State Processing

Solid-state processing techniques of nanoparticle reinforced composites are typically based on the conventional powder metallurgy route and its modified versions in terms of powder size modification, compaction techniques, sintering methodologies and secondary process utilized for microstructure refinement. Material processing takes place below solidus temperature, and hence, it reduces undesirable reactions between the matrix and reinforcements which remain in solid state throughout the process.

2.1.1 Powder Metallurgy (PM)

In conventional powder metallurgy method, fine metallic powder and reinforcement particles in required relative amount along with additive lubricants are mixed in mechanical mixture. The mixed powder is then compacted using uniaxial/isostatic cold or hot compaction. Compaction pressure is typically maintained between 400 and 900 MPa considering reinforcement size and area of compact while holding period is varied from few to several minutes. For hot compaction, processing temperature in the range of 500–600 °C and pressure of 250–300 MPa is employed. Green compacts are then sintered usually in inert atmosphere for obtaining dense microstructure. Compact is heated to temperature near to the melting point of matrix material, for instance 550–650 °C for aluminium-based composites. Dense compacted specimens may be further subjected to secondary processes such as extrusion, rolling, heat treatment for microstructure refinement and uniform distribution of reinforcement particles. Powder metallurgy has benefits which include capability of producing near net shaped parts, possibility of incorporation of large volume reinforcement content and ability to manufacture parts in large batches, especially for the automotive sector. PM may also be applied to the matrix/reinforcement system which cannot be realized by liquid processing route. However, it suffers from the limitation on the size of part, industrial scalability, flexibility in tailoring properties, complexity as well as relative cost of manufacturing and high porosity which necessitates secondary processing such as extrusion, rolling and forging. Basic structural arrangement of the process is shown in Fig. 1.

Classical powder metallurgy route was employed [89] to produce Al-MWCNT nanocomposites. Authors used varying CNT contents (0.25–2 wt%) for mixing with pure Al powder of APS 22 μm after giving ultrasonic bath to reinforcements in ethanol for 15–90 min. Mixing of Al and CNT was done in Turbula for 60–600 min followed by uniaxial pressing up to 300 MPa. Green compacts were subjected to sintering at 500–640 °C for 30–90 min. Nanocomposites on examination displayed well dispersed and embedded CNTs for incorporation up to 0.75 wt% but with further addition of CNTs (1 and 2 wt%), large clusters developed. However, for 0.75 wt% CNT, measured values of tensile strength 196 MPa and hardness 50 Hv were 200 and 50% higher than those for unreinforced aluminium.

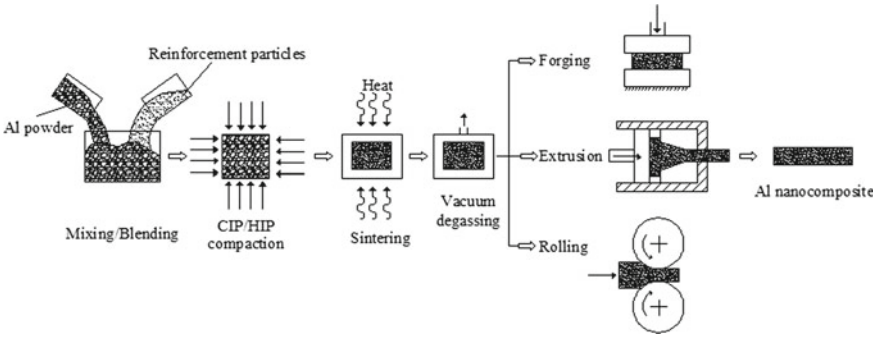

Fig. 1 Powder metallurgy (PM) process

Al-Si_3N_4 nanocomposite was synthesized [64] by powder metallurgy (PM) technique. They mixed 15 nm size Si_3N_4 particles with atomized aluminium powder of 20 μm size, hot pressed the mixture in vacuum at 600 °C and then extruded the compact at 420 °C with 20:1 extrusion ratio. They observed UTS, YS and % elongation values of 1 vol.% Si_3N_4 nanocomposite to be 180 MPa, 143.7 MPa and 17.4 in comparison to 176.1, 94.3 and 14.5 of Al-15vol.%SiC (3.5 μm) microcomposite, respectively, and the strength values to be much higher than respective values of pure aluminium (102.6, 67.8). They associated this significant rise in strength of nanocomposite to the reduced size of reinforcement and Orowan bowing mechanism of interaction between particles and dislocations.

On the similar line, Al/10 vol.% SiC (13 μm) microcomposite and Al-alumina (1–7 wt%, 50 nm) nanocomposites were fabricated [45]. After powder mixing, cold isostatic pressing (CIP) and extrusion produced 15 mm diameter bars. Finally, annealing heat treatment was done for all bars at 350 °C for 2 h. It was found that 31.8 HRF hardness of pure Al increased to 68.4 HRF for 7 vol.% alumina nanocomposite and was 48.6 HRF for 10 vol.% SiC microcomposite. Effect of grain refinement due to nanoparticles was witnessed as Al grain size of 4.6 μm was reduced with increasing content of nanoparticles and reached 1.2 μm for 4 vol.%. But with further addition of nanoparticles, the benefit of grain refinement diminished due to agglomeration of particles. Improvement in TS and UTS is also observed with respect to microcomposite and pure aluminium but at the cost of reduction in % elongation.

Aluminium nanocomposites containing SiC and Al_2O_3 particles of 200 nm and 60 nm size and up to 5 vol.% each were produced [59]. Particles were mechanically mixed with aluminium powder (99.7% pure, 10–100 μm) along with 0.5–1.5 wt% paraffin wax in blender, and the homogeneous mixture was then cold compacted by 500 MPa pressure followed by sintering the compact under argon atmosphere at 600 °C for 100 min. Composite billets were later extruded at 500 °C temperature with extrusion ratio of 2:1. Microhardness values of MMNCs were much higher than aluminium and increased with increasing reinforcement vol.% content and particle size. Al/SiC MMNC exhibited higher hardness and corrosion resistance than Al/Al_2O_3 MMNC and pure aluminium. Effective production of bulk MMNCs

by PM process however displayed particle agglomerations near grain boundaries with size varying between 1 and 5 μm for Al/Al_2O_3 and 0.5 and 10 μm for Al/SiC MMNCs, respectively.

2.1.2 Mechanical Alloying (MA)

The issue of formation of particle clusters in traditional powder metallurgy can be effectively diminished by employing mechanical alloying technique for enhancing particle dispersion. MA involves high energy ball milling employed for repetitive cold welding, plastic deformation induced fracture and rewelding of powder particles (Fig. 2). Mechanical attrition in presence of nanoparticles accelerates fracture and welding process and on reaching equilibrium, produces equiaxed fine particles [43, 46] with random orientation which are then compacted and sintered to produce bulk parts. Mechanical alloying is unique in terms of forming nanometre size mixtures of immiscible elements, generation of uniformly dispersed intermetallic phases, solid solutions and alloys. Suryanarayana [93] described in detail the results of three mechanically alloyed systems, viz. $Al–Al_2O_3$, $TiAl–Ti_5Si_3$ and $MoSi_2–Si_3N_4$, and demonstrated that MA is ideal for dispersing large volume fraction reinforcements of nanometre range in variety of metallic matrices. This promising technique of nanocomposite fabrication involving mechanochemical milling of various combinations of oxides, metals and especially carbides get influenced by processing parameters like miller type, ball–powder ratio, speed, time, process control agent (PCA) and milling environment.

Mechanical alloying method was used [75] to study the effect of different fraction (20, 30, 50 vol.%) alumina content as well as particle size variation 50 nm, 150 nm and 5 μm on the dispersion of particles in the aluminium (44 μm APS) powder

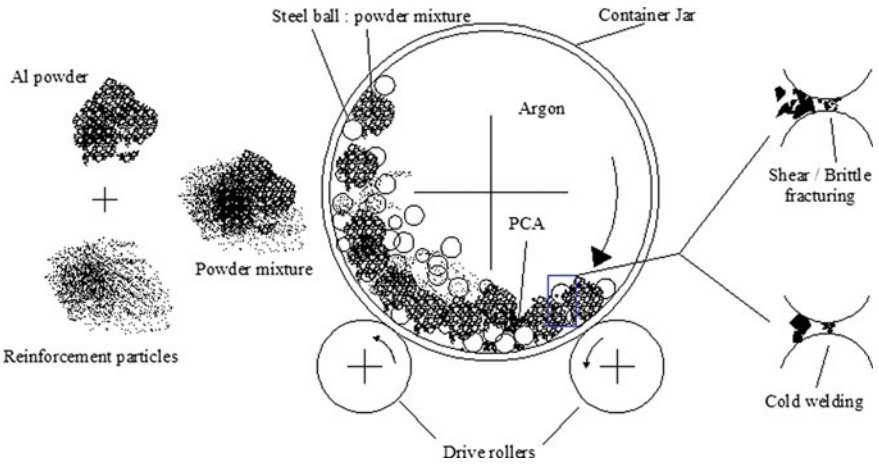

Fig. 2 Schematic diagram of mechanical alloying process

matrix. Al/alumina mixture was milled in SPEX 800 mixer with 0.5–1 wt% stearic acid as PCA under argon atmosphere and 10:1 steel ball–powder ratio. Powder was taken out at 5, 10, 15 and 20 h for characterization study and observed mechanical attrition induced continuous refinement of mixture with milling time. They successfully demonstrated that uniform distribution of particles with content fraction as high as 50 vol.% and size as low as 50 nm can be effectively achieved on milling for 20 h without phase transformation in metastable alumina.

In a research work [19], Al6061 powder with 10 and 20 vol.% ZrO_2 particles of APS 15 nm were mixed and subjected to high energy planetary ball milling at 200 rpm for 40 h in argon-filled container. Mixture was then uniaxially compacted at 600 MPa pressure and 380 °C temperature in 10^{-1} bar vacuum condition. Microstructural characterization revealed the formation of nanocrystalline aluminium solid solution (50 nm grain size) with homogeneously dispersed ZrO_2 particulates. After hot vacuum compaction, grain size became 80 nm due to recrystallization with finer dispersions. Compression strength of 20 vol.% nanocomposite increased to 1000 MPa. Microhardness (applied load, 1 N) of 10 and 20 vol.% nanocomposites obtained at the end of 40 h milling were measured as 280 HV and 369 HV, respectively.

Similar investigations with high energy milling and consolidation methods like cold or hot isostatic compaction, uniaxial pressing or hydraulic pressure to obtain bulk composites with different material systems such as Al-SiC [20, 95, 100], Al-Al_2O_3 [2, 40, 41, 47, 71], Al-TiC [10, 39–41], Al-BN [29] are reported in the literature. Most of these involved sintering of green compacts in the temperature range of 400–600 °C for durations up to 3 h. Some other works have reported extrusion process been employed after compaction or sintering for obtaining finer and homogeneous microstructure of nanocomposite systems, viz. Al-AIN [99], Al-Al_2O_3 [3, 50], Al-SiC [21, 27, 51], Al-Al_3Mg_2 [76] and Al-TiB_2 [1]. They carried out extrusion at temperature around 500 °C with extrusion ratio up to 20:1. All these investigators have similar findings and common consensus as regards improvement in mechanical properties, hardness rise and refinement of structure with increase in reinforcement volume fraction and milling time.

2.1.3 Cryomilling

In conventional milling of powder mixture, frictional temperatures induce severe recovery and recrystallization of microstructures. Low-temperature processing suppresses such effect in cryomilling which is usually carried out in cryogenic medium like liquid nitrogen. So cryomilling is beneficial in obtaining refined nanocrystalline grain structure more rapidly [101] besides avoiding undesirable chemical reactions between reinforcements and matrix material.

Al-B_4C nanocomposite [107] was produced using cryomilling method. Al5083 alloy powder of APS 40 μm and boron carbide powder of 1–7 μm were mixed together with 0.2–1 wt% stearic acid. Milling of mixture was carried out for 8 h in attritor mill at 180 rpm while maintaining 32:1 ratio of ball to powder. Complete

immersion of powder mixture and milling balls was ensured inside the milling tank filled with liquid nitrogen. The tank was maintained at minus 180 °C temperature using K type thermocouple controlled nitrogen flow. On characterization, authors found uniformly dispersed B_4C particles in Al matrix with slight reduction in size and no particle agglomeration. Clean particle–matrix interface with no voids or cracks around is seen and more importantly no detrimental phases such as $Al_3B_{48}C_2$, $AlB_{24}C_4$ and Al_4C_3 were observed in the composite due to cryomilling which otherwise appear in high-temperature processing.

2.1.4 Microwave Sintering (MWS)

Microwave sintering process is advantageous for time and energy saving. It is considered as unique technique which involves instantaneous conversion of electromagnetic energy into thermal energy for efficient volumetric heating of powder compact. It avoids variation of microstructure along thickness of specimen as observed in any differential heating. Microwaves penetrate deep into powder compact, and the generated heat radiates outwards. MWS is found better for fabricating nanocomposites with enhanced properties due to merits like high heating rate, short processing time and homogeneous microstructure [78].

Very recently [63] Al-Al_3N_4 nanocomposite is fabricated by employing microwave sintering route. They took aluminium powder of APS 10 μm and blended with (0, 1, 2, 3 wt% fraction) Al_3N_4 particles of 15–30 nm size in planetary ball mill for 2 h at 200 rpm. The mixed powder was then compacted uniaxially at 50 MPa with 1 min holding time. Compacted specimens were later placed and subjected to heating at 10 °C/min for 30 min in microwave furnace at 550 °C. Authors reported uniformly dispersed silicon nitride particles and increase in UTS, YS, compressive strength and hardness of the microwave sintered specimens.

2.1.5 Spark Plasma Sintering (SPS)

Novel technique called spark plasma sintering is also known as field-assisted sintering (FAS) and plasma-assisted sintering (PAS). It is used for consolidating powders to relatively high density with fine crystalline structure by generating plasma spark between gaps of compacted powders via electric DC pulse discharge. The process is popular for low processing temperature, self-purification of particle surface and short sintering time compared to conventional PM. Moreover, it overcomes the drawbacks of traditional powder metallurgy method such as coarse microstructure, low adhesion, reduced strength and hardness at high temperatures [17]. Effective consolidation of nanostructured Al alloy composites by SPS is done by optimizing process parameters like temperature, applied pressure, heating/cooling rate and cyclic pulse duration.

In a recent research work, [15] Al-SiO_2 nanocomposites were densified containing 0, 3 and 6 wt% SiO_2 (50 nm) powder using spark plasma sintering technique. Under 50 MPa pressure, they raised temperature of the compact to 550 °C with heating rate

of 100 °C/min followed by holding period of 5 min and then cooling rate of 30 °C/min. Authors reported improvement in hardness and 25% rise in the tensile strength of Al-3%SiO_2 composite. But 6 wt% composite exhibited reduction in strength due to agglomeration of particles and intergranular mode of fracture. Several attempts to fabricate nanostructured aluminium composites [12, 52, 69, 80] have been reported in the last decade proving SPS to be effective method of powder compaction.

2.1.6 Friction Stir Processing (FSP)

Friction stir processing, a relatively new process under developmental stage and derived from friction stir welding, is employed, especially for fabricating surface nanocomposites. An exhaustive review paper on FSP has been published by Arora et al. [9]. At first, a groove of desired size is made in the composite and it is then filled by required amount of reinforcement particles. A blunt pin less non-consumable rotating tool is plunged into workpiece to close the groove encapsulating reinforcements inside. Later on, a rotating tool with pin is pushed inside the surface and moved along the groove to spread particles by strong stirring action. The pin can be moved several times along the groove for improving the particle distribution. Successful fabrication of surface composite by FSP depends on processing parameters like tool size, speed and number of passes. Uniform dispersion of particles and surface finish obtained are the main challenges of FSP process. Basic layout of FSP is shown in Fig. 3.

Sharifitabar et al. [87] for instance filled 50 nm size Al_2O_3 particles into groove (1 mm × 2 mm) made in 4 mm thick Al5052-H32 rolled plate and employed FSP to obtain surface nanocomposite. They applied different ratios of tool rotation to tool travel speeds from 8 to 100 rev/mm and tilt angle of pin from 2.5° to 5° to see their effect in producing defect-free stir zones. Hardened steel pin of diameter 5 mm, length 3.7 mm and shoulder size Ø13.6 mm was employed for stirring groove line area after initially closing the groove by pin-less tool. On finding optimum parametric conditions, they investigated the influence of number of passes on mechanical properties and specimen microstructure with or without Al_2O_3 powder. They suggested use of

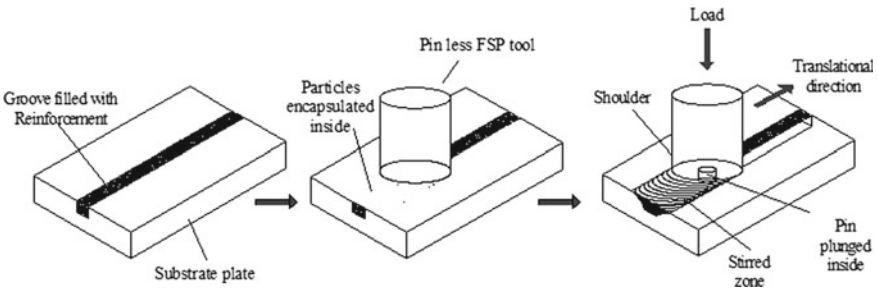

Fig. 3 Friction stir processing method

higher tilt angle of pin and high ratio of tool rotational to travel speed for obtaining defect-free surface composite. Also found that increasing number of passes resulted in improved mechanical properties like tensile and yield strength due to reduced grain size and better dispersed particles. Observations for aluminium nanocomposites like increased hardness, better particle dispersion with number of passes and improved mechanical properties due to refined grains caused by heavy plastic deformation and dynamic recrystallization employing optimized FSP process are reported by several researchers [38, 49, 58, 65, 85].

2.1.7 Accumulative Roll Bonding (ARB)

In this process, metallic sheets after wire brush cleaning to remove oxides and contaminants are stacked over each other with uniformly spread reinforcement particles in between. The stacked sheets are then rolled together to reduce the stacked thickness by up to 50% in single rolling cycle (Fig. 4). The roll bonded sheets are then cut into two pieces and stacked again for rolling in order to reduce the thickness by half. This process is continued several times and examined periodically to obtain uniformly dispersed particles embedded inside the bulk material.

Alizadeh and Paydar [7] fabricated SiC reinforced aluminium nanocomposites by accumulative roll bonding process. They took eight strips of 200 mm × 30 mm × 0.4 mm size made of Al1050 alloy and spread 5 μm size 1 vol.% SiC powder in between each two of them. Before it, all the strips were cleaned with acetone and subjected to wire brush cleaning using 90 mm circumferential diameter brush of 0.35 mm diameter wire at 14 m/s surface speed. Laboratory rolling mill having roll diameter 170 mm and 15 rpm rolling speed was used to reduce the initially

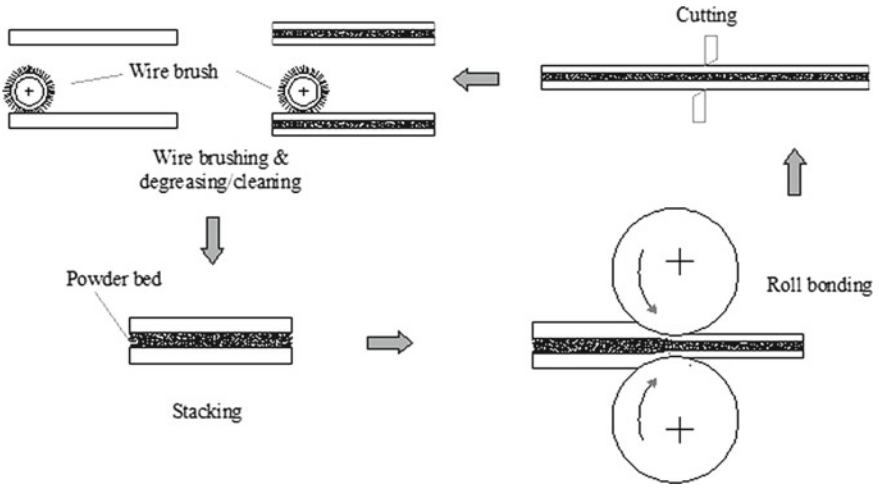

Fig. 4 Accumulative roll bonding (ARB) method

stacked thickness by 66%. Roll bonded strip was cut into two pieces and annealed for an hour at 350 °C. The heat-treated strips after cleaning and wire brushing were stacked again and rolled to reduce thickness by 50%. The process is repeated eight times with no additional reinforcements and heat treatment. The bulk nanostructured composite thus produced after eight accumulative ARB cycles was further examined for microstructure and mechanical properties. Microstructure exhibited uniformly dispersed SiC particles with ultrafine grains of 180 nm size. At the end of 8th ARB cycle, specimen tensile strength increased by 4.1 times to reach 243.3 MPa while elongation increased by 17%.

ARB process was originally developed and introduced in 1998 [81] and later on followed by different researchers for producing aluminium composite materials [90, 98, 106] with remarkably improved material properties on account of grain refinement and dislocation strengthening.

2.1.8 Laser Cladding

This process also termed as laser additive manufacturing is relatively recent method of producing nanocomposites with some reported publications in the last decade. In this effective method, nanocomposite is developed by additively depositing new layer onto substrate by laser melting blown reinforcement powders or already preplaced powder bed. Rapid heating and cooling experienced by deposited powder and substrate develop strong metallurgical bond-forming cladded nanocomposite without changing initial composition and properties of added materials. Different combinations of powder mixtures can be deposited on substrate to develop tailored surface with desired properties like improved strength, hardness, thermal stability, corrosion and wear resistance. Selection of optimized process parameters such as laser power, speed and beam diameter is required to avoid melting of nanoparticles [113]. This process is in the developmental stage, and issues like nanoparticle powder handling and delivery, agglomeration, particle dissolution, health hazards and fabricating 3D parts are being addressed. Better interface bonding between particles and matrix with improved properties of aluminium nanocomposites such Al-Al_2O_3 [32], Al-SiC [16], Al-TiB_2 [104] and Al-TiO_2/B_4C [62] have been demonstrated in research works.

Gu et al. [30] for instance produced TiC reinforced Al10SiMg alloy nanocomposite by laser cladding. YLR-200-SM ytterbium laser with power 200 W and 70 μm spot size was selected to deliver power of 80–140 W with scan rate of 100–150 mm/s. Aluminium substrate was first fixed to levelled platform in sealed chamber filled with argon gas. Mechanically alloyed mixture of TiC (50 nm) and AlSi10Mg (30 μm) powders was deposited onto the substrate by layering mechanism creating powder bed of 30 μm thickness. Specimen CAD data was used to scan powder bed selectively following raster scan pattern. The process was then repeated layer by layer until finally to get the bulk specimen of 20 mm × 10 mm × 6 mm size. Unreinforced specimens were also fabricated by the same process for comparing microstructure and tribo-mechanical properties. It was observed that near full density (98%) composites with hardness of 184.7 HV (20% higher than unreinforced alloy) and increased wear

resistance with friction coefficient as low as 0.28 were successfully developed by laser additive manufacturing process.

2.2 Semisolid-State Processing

Semisolid method consists of processing the metallic systems in between solidus and liquidus temperatures wherein the partial solid slurry contains nearly globular grains with 20–60% solid fractions. Due to semisolid condition, it is possible to produce castings having low shrinkage pores and less thermochemical degradation to reinforcements on account of low processing temperatures. Two types of semisolid processing methods, viz. compocasting and thixoforming, are seen for fabricating metal matrix nanocomposites.

2.2.1 Compocasting

Compocasting also termed as rheocasting involves producing semisolid slurry by lowering the molten metal temperature during casting process itself to reach between liquidus and solidus line. In this condition, the required amount of preheated reinforcements are added into the slurry and stirred vigorously for uniform incorporation. Compocasting is found suitable for producing aluminium nanocomposite with improved mechanical properties due to refinement of grains as demonstrated in the published literature [37, 42, 83].

In one of the reported works [23], A356 alloy was reinforced with (1, 2, 3 wt%) 50 nm Al_2O_3 particles using compocasting technique. They charged 3 kg of base aluminium alloy in graphite crucible at 630 °C. The melt was then degassed using hexachloroethane tablet and brought down to a temperature range of 590–605 °C to have semisolid melt slurry. Alumina nanoparticles wrapped in aluminium foils and preheated at 200 °C were introduced into melt slurry and stirred at 1000 rpm for 1 min. The slurry on pouring into preheated mould, developed nanocomposite cast specimen. Composite sample exhibited rise in strength, hardness and ductility by 34, 31 and 90%, respectively.

2.2.2 Thixoforming

In thixoforming process, a solid feedstock or slug is reheated to semisolid state and formed to shape in partially melted condition with liquid fraction between 30 and 50%. It can form complex near net-shaped components using thixotropic behaviour of materials in the semisolid condition thus saving manufacturing cost. Thixoforming process outperforms traditional casting in terms of reduced porosity because semisolid metal flow is not turbulent but laminar. Although the process is

found implemented for microcomposites, its application for fabricating metal matrix nanocomposites is not given consideration yet.

The only publication to date as per our knowledge is of the fabrication of A356/SiC and A356/TiB_2 nanocomposites [44]. SiC and TiB_2 of 20–30 nm size each were first mixed with A356 powder of APS 60 μm size and compacted to produce green tablets. The composite tablets were introduced into A356 melt to produce 0.8 wt% nanocomposites of SiC and TiB_2 particles each using ultrasonic stir casting process. The cast nanocomposites then were taken for thixoforming process. A356/SiC and A356/TiB_2 billets were placed in thixoforming press and induction heated to 575 °C (approximately 30% liquid fraction) in three steps of 500, 560 and 575 °C. Semisolid slurry was held for 9 min at each step to reduce temperature gradient of billet. The slurry was then forced into preheated (300 °C) tool steel die by applying ram with stroke velocity of 70 mm/s thus producing thixoformed A356/SiC and A356/TiB_2 nanocomposite samples.

2.3 Liquid-State Processing

In the liquid metallurgy route, matrix material of composite is heated well above its melting point and then solid reinforcement particles are added from outside into it or created inside the melt by affecting thermochemical reactions between composite constituents. Nanoparticles are dispersed inside the melt by employing techniques like mechanical stirring, electromagnetic stirring or ultrasonic vibrations. Liquid infiltration and disintegrated melt deposition are other liquid processing methods of composite fabrication.

Although liquid processing is widely studied due to relative simplicity and flexibility, it is identified to have some critical issues, especially in case of fabricating nanocomposites [11, 14, 54, 60] as briefed below. As nanoparticles provide large surface area, Van der Waals force of attraction induce them to agglomerate near the grain boundaries and fail to disperse uniformly in the matrix which effectively reduce their strengthening potential. It has been found that the aggregation rate of 20 nm size particles is four orders of magnitude higher than that of 1 μm size particles. Ceramics are found to have limited wettability with liquid aluminium which can create poor interfacial bonding between particles and matrix. Interface debonding occurs during plastic deformation affecting strength and stiffness of the composite. Nanoparticles on account of their large surface area increase the interfacial reactions manyfold producing reaction products which at times may be undesirable and spoil composite properties. There is a critical size of nanoparticles below which if they added to the matrix will deteriorate material properties due to negative Hall–Petch effect. Also there is limit for addition of nanoparticles in the liquid melt above which if added form clusters reducing the effectiveness of dislocation hindrance and thereby lower the mechanical strength. However, it is to be noted that nanoparticles on adding homogeneously into the matrix in stable form can dramatically improve the mechanical properties as compared to microcomposites and unreinforced alloys.

Several studies reported so far have shown improvement in hardness, yield strength, compressive strength, wear and corrosion resistance of aluminium alloy because of uniform distribution of nanoparticles and refined microstructure. Nanoparticles are observed to restrict grain growth by acting as obstacles called Zener pinning effect.

2.3.1 Stir Casting

It is a widely used liquid-state processing method for fabricating composites for simplicity and low cost. A typical experimental layout of the method is shown in Fig. 5. In the process, metal alloy ingots are heated for complete liquification inside furnace crucible of the stir casting setup. The reinforcement particles are then dropped manually over the surface of melt which is then stirred for spreading the particles inside. Mechanical stirring rod carries impeller blades attached at the bottom and is dipped inside the melt to stir it before and after particle addition. Stirring action creates vortex inside the melt which helps to suck in particles due to differential pressure gradient. However, as aforementioned, it is usually difficult to distribute particles uniformly inside the melt because of their low wettability and tendency to cluster [34, 91] while the situation aggravates further for nanoparticles due to the increased surface area. Large density difference between particles and alloy can make the situation even more challenging as the particle can start moving to float or sink the moment stirring is stopped. To tackle with these issues, different ways and means have been tried like preheating the particles [92], coating or pretreating them to enhance wettability [13], modified stirring [31, 110], introducing particles with the help of master alloy powder [97] and addition of Mg [86] and K_2TiF_6 salt flux

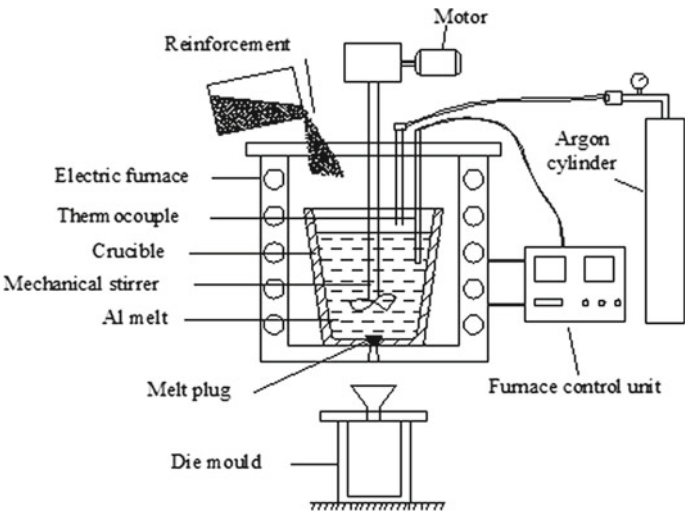

Fig. 5 Stir casting experimental setup

with some reported success. Air entrapment due to stirring can increase porosity in the cast composite. Hence, for better densification efforts like use of melt degassing tablet, particle addition using argon gas-assisted injection, continuous supply of inert gas inside the furnace, bottom pouring and vacuum-assisted casting are employed.

Mazahery and Ostadshabani [66] for instance followed stir casting route to develop A356/alumina nanocomposite reinforced with 0.75–5 vol.% alumina particles. They initially produced master alloy powder by mixing Al (16 μm) and alumina (50 nm) with Al/alumina ratio of 1.67 using ball milling process. A356 ingots weighing 450 g were charged into the furnace for melting at two temperatures, 800 °C and 900 °C. 1 wt% Mg was added for improving wettability. When vortex was created in the melt at 600 rpm stirring speed, the master alloy powder (1 g) packed in aluminium foil packets were dropped into melt one at every 20 s till the required volume fraction addition is achieved. Stirring was continued for 15 min while continuously passing argon gas in the crucible. Slurry was then poured into CI mould to cast composite specimen. Authors observed reasonable distribution of particles inside the matrix with few agglomeration sites. Tensile strength and compressive strength improved initially, and highest values were measured for 1.5 and 2.5 vol.% nanocomposites, respectively, but declined further. Porosity increased slightly with increase in nanoparticle addition. Moreover, % elongation decreased and reached to almost half for 5 vol.% composite.

2.3.2 Electromagnetic Stir Casting

Electromagnetic stirring a novel method also known as induction heating is useful for grain refinement and homogeneous addition of nanoparticles into the metallic melts by means of external magnetic field [26, 88]. In this process, electric current is passed through induction coils fixed around the crucible which create alternating magnetic field introducing Lorentz forces in the melt. These forces are found to generate vortex type flow pattern and strong stirring action to disperse nanoparticles by breaking their clusters. The process parameters like stirring time, electromagnetic frequency, temperature and current intensity are controlled for best results.

Yu [108] produced A356/SiC nanocomposite using electromagnetic stirring. He used induction heating unit which could convert 50–60 Hz, 3-phase power into single-phase high-frequency output. He charged 198 g A356 ingots into crucible and raised the temperature of melt to 750–800 °C. After adding 2 wt% SiC nanoparticles (50–60 nm) using aluminium foil capsules, the melt was treated to electromagnetic stirring with 60 Hz output frequency for 60 min. 2 wt% Mg was added for improving wettability. Uniform dispersion of particles with 22% rise in hardness of fabricated nanocomposite was observed. Successful preparation of Al/Al_2O_3 nanocomposite [53] has been reported recently.

2.3.3 Ultrasonic Stir Casting

Ultrasonic stir casting is observed as the most effective method for uniform distribution of very fine particles by breaking their clusters in melt, refined microstructure and improvement in wettability, especially of ceramics in aluminium [55, 61, 103]. It involves treating nanocomposite melt by ultrasonic waves with approximate frequency of 20 kHz using high power density ultrasound (100 W/cm^2). Typical schematic of ultrasonic stir casting setup is shown in Fig. 6. Sonotrode made of titanium or niobium alloy on account of high temperature stability is dipped in the melt to pass in high-frequency ultrasonic waves. It gives rise to two principal effects in the melt called as cavitation and acoustic streaming. During negative part of the ultrasonic wave, air bubbles are created in the melt under tensile stress. Under positive cycle, bubbles shrink under compressive stress of wave. Air entrapped in voids of clusters is believed to provide nucleation sites for bubble growth. On reaching critical size, bubbles burst creating local microsites of very high temperatures (5000 °C) and pressures (1000 atm) called hot spots. This effect of formation and collapse of transient hot spots is called as cavitation effect which can clean the particle surface for improved wettability. Due to high pressure gradient in several small places in the bulk melt, strong macroscopic flow circulation effect is created called acoustic streaming which help in dispersing loose particles. Moreover, as the melt is not agitated, air entrapment is diminished. This promising technique however suffers from the fact that very large volume of melt cannot be treated because of the need of corresponding ultrasonic high power source which limits its industrial scalability. Ultrasonic treatment of continuously flowing liquid can be seen as a possible solution for scaling up. But still the fact of particle movement and settling in the melt on account of density difference after stopping of ultrasonication prevails and can lead to marginal porosity.

Ultrasonic vibration-assisted stir casting process is employed for fabricating several aluminium-based nanocomposites reinforced with SiC, Al_2O_3, B_4C, TiB_2,

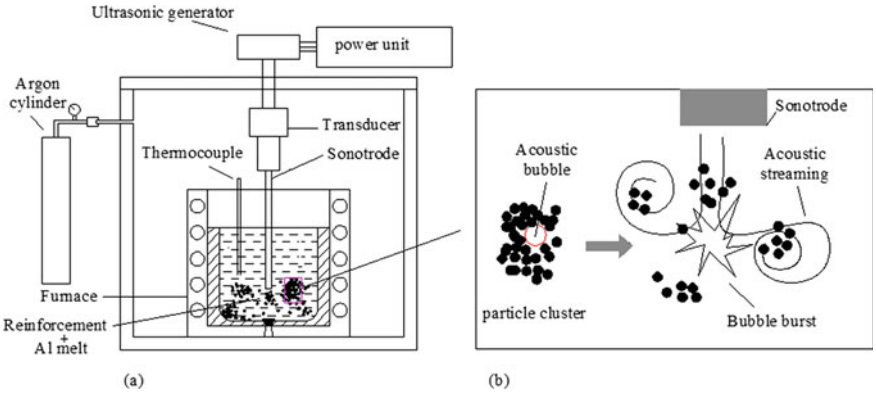

Fig. 6 **a** Schematic of ultrasonic stir casting setup; **b** mechanism of particle deagglomeration

SiO_2, GNPs and h-BN [5, 18, 24, 33, 48, 56, 68, 84]. Researchers have reported superior particle incorporation, wettability, improved densification, grain refinement and mechanical properties, for instance 92% rise in hardness for just 2% Al_2O_3 [68] and 134% enhancement in tensile strength for 5 vol.% GNP [5] incorporation. In a research work by Poovazhagan and Kalaichelvan [72], the effectiveness of ultrasonication treatment was exhibited on characterizing the fabricated AA6061-SiC nanocomposites. AA6061 alloy ingots weighing 800 g were melted in graphite coated SS crucible at 680 °C and chocked for 10 min. Mechanical stirring was performed before and after adding SiC particles in required volume fraction. Then, titanium sonotrode was dipped into the melt for performing ultrasonication for 45 min. Ultrasonic generator with 2 kW power producing 20 kHz frequency was used for melt treatment. After ultrasonic treatment, the melt temperature was again raised to 800 °C for improving its fluidity and poured in preheated steel die for casting to shape. Different nanocomposites containing 0.3–1.5 vol.% SiC were produced the same way. In microstructural investigation, EDS elemental mapping images revealed very good dispersion of particles. Tensile strength of just 1.25 vol.% composite increased by more than 100% while 1.5 vol.% composite displayed 74% rise in BHN value.

2.3.4 Liquid Infiltration

In liquid infiltration method, liquid metal is incorporated into the preformed porous solid of reinforcement under either the influence of applied pressure or allowed to seep in with time without external pressure. The slurry consisting of reinforcements and liquid binder carrier is formed to the required shape under pressure. Thereafter, preform is heat treated and dried for its dimensional stability. During liquid infiltration process, preform is placed into die and liquid metal is poured over it. Melt is then forced to infiltrate the preform by applying ram pressure. Liquid infiltration process is also referred as squeeze casting and may take the form wherein the composite slurry of metal and reinforcements is squeezed into the die under pressure. Contact angle between melt and nanoparticle is required to be less than 90° to ensure wetting. This process is preferred for being inexpensive and allows incorporation of as high as 50% nanoparticle fraction into the metal matrix. However, it takes long time for casting, especially in case of pressureless infiltration [116]. Aluminium nanocomposites reinforced with SiC, CNT and CuO [25, 96, 112] have been produced by squeeze casting method.

Geng et al. [28] produced hybrid nanocomposite of Al2024 alloy reinforced with SiC whiskers (20 vol.%) and SiC nanoparticles (2, 5 7 vol.%, 35 nm) by squeeze casting method. They initially prepared homogeneous slurry of whiskers and fine particles of SiC mixed with alcohol by mechanical blending and dried to get solid hybrid preform. Alloy temperature was raised to 800 °C for melting while preform heated to 500 °C. Thereafter, molten alloy was forced into reinforcement preform at low infiltration pressure of 2 MPa and later solidified under pressure of 50 MPa. Tensile strength and elastic modulus of (20% SiC_w +7 vol.% SiC_{np}) nanocomposite

were reported to be 620 MPa and 127 GPa, respectively, as compared to corresponding values of 206 MPa and 70 GPa for Al2024 alloy. But % elongation of alloy reduced from 17 to very low value of 0.77 due to reinforcement by this method.

2.3.5 Disintegrated Melt Deposition (DMD) and Spray Co-deposition

In disintegrated melt deposition process, superheated and stirred mixture of metal and reinforcement is allowed to fall under gravity from crucible through small nozzle into a chamber filled with inert gas. The falling slurry is disintegrated by two argon gas jets arranged normal to the metal flow which then solidifies on a metallic substrate (Fig. 7). Despite process being suitable for both Al and Mg alloys, it is specifically adopted for fabricating Mg-based composites. It is because Mg is highly oxidizable and DMD process reduces formation of oxides in the casting. The cast specimen obtained by this process is usually extruded in order to reduce porosity.

In a reported research work, Hemanth [35] (102) produced LM13-ZrO_2 (50–80 nm, 3–15 wt%) nanocomposites by DMD process. The preheated reinforcement particles (200 °C) were added to the superheated (720 °C) LM13 alloy melt and stirred

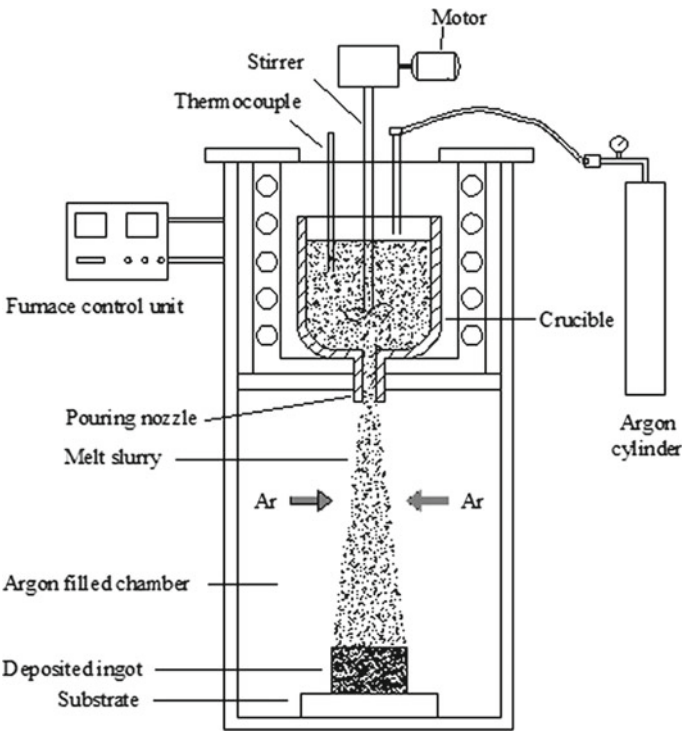

Fig. 7 Typical experimental setup of disintegrated melt deposition process

at 450 rpm speed for better dispersion. Fabricated nanocomposites were extruded by hydraulic press at 200 °C in order to refine microstructure. On characterization, they revealed much refined grain structure, uniformly distributed particles and minimal porosity. Besides, significant rise in hardness (128 Hv) and UTS (258 MPa) was seen for 12 wt% nanocomposite in comparison to 98 Hv and 170 MPa values measured for unreinforced LM13 alloy produced by the same method. Spray co-deposition [115] is a method close to DMD process. In this technique, molten metal stream is allowed to fall into inert chamber and is incorporated with reinforcement particles sprayed onto it through jets of argon gas while simultaneously disintegrating the falling mass. Layers of fallen metal droplets on substrate create composite material after solidification.

2.4 Hybrid/Combination Processing

Different processes available for nanocomposite fabrication are sometimes combined to draw in benefits of individual process. Such approach can improve product quality as no single process is perfect in all respects.

Some researches have combined mechanical alloying technique with liquid metallurgy route to fabricate AMMNCs [4, 67, 94, 114]. For instance, Tahamtan et al. [94] fabricated A206-5vol.% Al_2O_3 nanocomposite by adopting this hybrid route. They mixed powders of aluminium (74 μm), alumina and Mg (100 nm each) and ball milled the mixture up to 9 h to create master powder for reinforcement. Milling was performed in argon atmosphere with 1.7 wt% stearic acid as PCA. In addition, compacted powder tablets of 20 mm × 3 mm size were prepared for incorporation. Besides, they produced master metal matrix composites by melt process using as received alumina powder and also using milled powder. In this manner, four different forms of reinforcement addition, viz. as received alumina, master powder, master tablet and master composite, were created for producing different nanocomposite specimens. Later on, again two ways of fabrication such as semisolid stirring and liquid-state stirring were used. They heated base matrix to temperature of 745 °C for liquid processing and incorporated reinforcements slowly over period of 15–30 min with melt stirring at 400 rpm. Alumina powder and master alloy/composite were preheated at 400 and 200 °C, respectively, before addition to melt. Less melt turbulence was reported for addition of master alloy in place of nanoparticles leading to decreased porosity. Semisolid processing was performed at 640 °C temperature (20% solid fraction). Ball milling improved wettability and uniform distribution of particles, and decreased reaction products, and hence, tensile properties were enhanced.

Stir casting and cross accumulative roll bonding were combined [8] to produce Al-Al_2O_3 nanocomposites. Authors initially produced Al-2vol.% Al_2O_3 (100 nm) nanocomposite by stir casting method by employing argon gas-assisted particle injection into melt at 670 °C while stirring at 500 rpm. Cast specimen was then machined to 120 mm × 100 mm × 4 mm size specimens. All specimens after annealing at

540 °C for 2 h were cold rolled to obtain 100 mm × 100 mm × 1.5 mm strips. Two such strips were taken for roll bonding process after acetone bath, wire brush cleaning and the stack reduced to 50% thickness at the end of the first rolling pass. Bonded strip was cut into two pieces, cleaned them, stacked and subjected to second roll pass by changing the orientation to 90° with respect to previous pass. The process repeated eight times, and after every pass, the strip was characterized for microstructure and tensile properties. Cross orientation at every pass elongated the strip in both linear and transverse directions resulting in 71 nm crystal size. Tensile strength at the end of the eighth pass increased to 344 MPa (213% rise) and elongation % increased to 6.4 (205% rise).

Xiong et al. [102] combined pressureless infiltration and ball milling to produce Al-3%Mg/SiC nanocomposite having reinforced with 40 nm size SiC particles with varying volume (3, 6, 14) percentages. Al and Mg powder each of 70 μm size particles and SiC reinforcement were first ball milled in argon atmosphere for 10 h at 450 rpm and ball–powder ratio of 4:1. Powder was cold compacted at 50 GPa pressure to prepare preforms of size 40 mm × 40 mm × 80 mm. Base matrix material was later melted in furnace at 700 °C with addition of (NaCl + KCl) salt mix for reducing melt oxidation and held for 20 min. Preform was then added to melt, kept in suspension for 2 h for infiltration and allowed the slurry to solidify in the furnace itself. Authors detected MgO at the particle–matrix interface which they claimed to improve wettability. Tensile properties improved with retained ductility.

In another research work [22], rheocasting and squeeze casting were combined to fabricate A356/MWCNTs (0.5–2.5 wt%) nanocomposite. Initially, Al powder and MWCNTs were ball milled for 8 h at 200 rpm in presence of stearic acid. Blocks were then prepared by compacting mix at pressure of 70 MPa for 15 min duration in steel mould. A356 ingots were melted at 660 °C in argon atmosphere, and after degassing the melt using hexachloroethane tablet, the melt temperature was reduced to 601 °C (solid fraction 30%). On adding blocks, the semisolid slurry was stirred for 1 min at 750 rpm. It was next poured in preheated (250 °C) steel die at the same temperature and immediately squeezed to acquire mould shape. For the optimum 1.5 wt% MWCNT composite, tensile strength and elongation % enhanced by 50 and 280%, respectively, which was attributed to uniform particle dispersion and grain refinement.

2.5 In Situ Methods

Formation of inhomogeneous microstructure and detrimental reaction phases are the issues to be tackled for ex situ fabrication of nanocomposites. In situ fabrication involves thermochemical reactive processes between the constituents of composite material resulting in creation of very small, low range particulate reinforcements dispersed well in the entire microstructure. The advantages of the approach include formation of clean particle–matrix interface, thermodynamic stability, combination of variety of matrix materials and reinforcing particles, scalability and absence of

detrimental phases. Initially, the reactive constituents of composite material can be in various physical states such as solid–solid, solid–liquid, liquid–gas, solid–gas and liquid–liquid.

Recently, TiC nanoparticles are created in aluminium matrix by in situ process during mechanical alloying using nanodiamond as precursor [73]. They mixed powders of Al (30–100 μm), titanium (100 μm) and nanodiamond (4–6 nm) and milled the mixture in Retsch PM400 planetary mill at 300 rpm with ball–powder ratio of 10:1. Besides fine TiC particles, intermetallics such as $TiAl_2$ and TiAl were detected in the final mixture. Mechanical attrition activated combustion synthesis has been reported to produce $Al/Al_3Ni + Al_2O_3$ [77] and $Al/TiC + Al_2O_3$ [109] hybrid nanocomposites.

Direct melt reaction in situ technique was employed [105] to produce $Al6061/ZrO_2$ nanocomposites with varying (1–3) volume percentages. K_2ZrF_6 and KBF_4 inorganic salts were mixed in the molar ratio of 1:2:4 and ball milled to get homogeneous mix. Further, it was dehydrated for 2 h in oven at 250 °C. The mixture in required proportion was added slowly to alloy melt at 851 °C and held the composition for 30 min in isothermal condition. Stirring was set for 3 min at 600 rpm and performed with a gap of 2 min in between. Melt was then poured at 750 °C to cast the specimen. Salts were observed to react with aluminium forming ZrB_2 particles in the matrix.

Significant reduction of TiB_2 particle size (800–23 nm) was achieved by ultrasonic stir treatment given to $Al\text{-}4.4Cu/TiB_2$ nanocomposite in situ melt produced [70] by direct melt reaction of aluminium with K_2TiF_6 and KBF_4 halide salts.

Al/AlN nanocomposite is reported [57] to be produced by evaporation of aluminium in the N_2/H_2 mixed atmosphere by plasma arc discharge and consolidating the collection of as-deposited particles by compaction followed by sintering.

3 Summary

This article is an attempt to overview the developments and issues of several different manufacturing techniques employed for obtaining bulk aluminium matrix nanocomposites. Powder metallurgy-based mechanical alloying and stir casting are the two widely used methods for producing AMMNCs. Aluminium nanocomposites are reported to exhibit exceedingly better properties than microcomposites and unreinforced monolithic alloys but their development is limited to lab-scale investigations only. However, considering the performance, nanocomposites have a great future and are likely to replace their micro-counterparts in various applications of automotive, aerospace, electronics, military, sports goods, etc. Agglomeration of nanoparticles is the most prominent issue and needs extreme care for dispersing them in the alloy matrix. Ultrasonic stir casting has so far been observed as the promising route in this regard but suffers from the industrial scalability aspect. Contamination free, careful handling of nanoparticles is essential for better results. Economical synthesis of nanoparticles and developing cost-effective ways of nanocomposite

fabrication should certainly motivate their practical usage. Different solid- and liquid-state processes available are useful and may be modified to produce near net-shaped parts so as to avoid difficulty in further processing imposed by hard reinforcements. Combining production routes have offered better results and can be explored further. Processing with nanoparticles is rather complex than micro-particles as increased surface-to-volume ratio creates challenges of particle clustering and increases the formation of reaction products, especially in liquid processing methods. In situ fabrication is a promising approach for AMMNCs due to formation of clean and strong interfaces as well as very fine dispersoids but not yet tried fully due to limited information.

Conflict of Interest None declared.

References

1. Abu-Warda N, Utrilla MV, Escalera MD (2018) The effect of TiB_2 content on the properties of AA6005/TiB_2 nanocomposites fabricated by mechanical alloying method. Powder Technol 328:235–244
2. Ahamed H, Senthilkumar V (2011) Consolidation behavior of mechanically alloyed aluminum based nanocomposites reinforced with nanoscale Y_2O_3/Al_2O_3 particles. Mater Charact 62:1235–1249
3. Ahamed H, Senthilkumar V (2012) Experimental investigation on newly developed ultrafine-grained aluminium based nano-composites with improved mechanical properties. Mater Des 37:182–192
4. Akbari MK, Baharvandi HR, Mirzaee O (2013) Fabrication of nano-sized Al_2O_3 reinforced casting aluminum composite focusing on preparation process of reinforcement powders and evaluation of its properties. Composites: Part B 55:426–432
5. Alipour M, Eslami-Farsani R (2017) Synthesis and characterization of graphene nanoplatelets reinforced AA7068 matrix nanocomposites produced by liquid metallurgy route. Mater Sci Eng, A 06:71–82
6. Allison JE, Cole GS (1993) Metal matrix composites in the automotive industry: opportunities and challenges. J Mineral Metals Mater Soc 19–24
7. Alizadeh M, Paydar MH (2010) Fabrication of nanostructure Al/SiC_P composite by accumulative roll-bonding (ARB) process. J Alloy Compd 492:231–235
8. Ardakani M, Amirkhanlou S, Khorsand S (2014) Cross accumulative roll bonding—a novel mechanical technique for significant improvement of stir-cast Al/Al_2O_3 nanocomposite properties. Mater Sci Eng A 591:144–149
9. Arora HS, Singh H, Dhindaw BK (2012) Composite fabrication using friction stir processing—a review. Int J Adv Manuf Technol 61:1043–1055
10. Azimi A, Shokuhfar A, Nejadseyfi O (2015) Mechanically alloyed Al7075–TiC nanocomposite: Powder processing, consolidation and mechanical strength. Mater Des 66:137–141
11. Basak AK, Pramanik A, Islam MN (2015) Dong Y, Umer R, Lau AK (eds) Fillers and reinforcements for advanced nanocomposites. Woodhead Publishing, Sawston
12. Bathula S, Anandani RC, Dhar A (2012) Microstructural features and mechanical properties of Al 5083/SiCp metal matrix nanocomposites produced by high energy ball milling and spark plasma sintering. Mater Sci Eng A 545:97–102
13. Beygi H, Sajjadi SA, Zebarjad SM (2014) Microstructural analysis and mechanical characterization of aluminum matrix nanocomposites reinforced with uncoated and cu-coated alumina particles. Mater Sci Eng A 607:81–88

14. Borgonovo C, Apelian D (2011) Manufacture of aluminum nanocomposites: a critical review. Mater Sci Forum 678:1–22
15. Cavalierea P, Jahantigh F, Shabanic A (2018) Influence of SiO_2 nanoparticles on the microstructure and mechanical properties of Al matrix nanocomposites fabricated by spark plasma sintering. Compos B 146:60–68
16. Changjun C, Min Z, Qing-Ming C et al (2008) Laser cladding of ZM5 magnesium base alloy with Al + nano-SiC powder. Lasers Eng 18:85–94
17. Dash K, Chaira D, Ray BC (2013) Synthesis and characterization of aluminium-alumina micro- and nano-composites by spark plasma sintering. Mater Res Bull 48:2535–2542
18. Dehnavi MR, Niroumand B, Ashrafizadeh F (2014) Effects of continuous and discontinuous ultrasonic treatments on mechanical properties and microstructural characteristics of cast $Al_4 1_3$–SiCnp nanocomposite. Mater Sci Eng A 617:73–83
19. Dutkiewicz J, Litynska L, Maziarz W (2009) Structure and properties of nanocomposites prepared from ball milled 6061 aluminium alloy with ZrO_2 nanoparticles. Cryst Res Technol 44(10):1163–1169
20. El-Daly AA, Abdelhammed M, Hashish M (2013) Fabrication of silicon carbide reinforced aluminum matrix nanocomposites and characterization of its mechanical properties using non-destructive technique. Mater Sci Eng, A 559:384–393
21. El-Kady O, Fathy A (2014) Effect of SiC particle size on the physical and mechanical properties of extruded Al matrix nanocomposites. Mater Des 54:348–353
22. Elshalakany AB, Osman TA, Khattab A (2014) Microstructure and mechanical properties of MWCNTs reinforced A356 aluminum alloys cast nanocomposites fabricated by using a combination of rheo casting and squeeze casting techniques. J Nanomater Art 386370:1–14
23. El-Mahallawi I, Abdelkader H, Yousef L (2012) Influence ofAl_2O_3 nano-dispersions on microstructure features and mechanical properties of cast and T6 heat treated AlSi hypoeutectic alloys. Mater Sci Eng, A 556:76–87
24. Estruga M, Chen L, Choi H (2013) Ultrasonic-assisted synthesis of surface-clean TiB_2 nanoparticles and their improved dispersion and capture in Al-matrix nanocomposites. Mater Interf 5:8813–8819
25. Ferguson JB, Aguirre I, Lopez H (2014) Tensile properties of reactive stir-mixed and squeeze cast Al/CuO_{np}-based metal matrix nanocomposites. Mater Sci Eng, A 611:326–332
26. Garrido M, Fautrelle Y, Davoust L (2014) Grain refinement and nanoparticle dispersion using traveling magnetic field. Light Metals 10:1405–1410
27. Gazawi AA, Gabbitas B, Zhang D (2015) Microstructure and mechanical properties of ultrafine structured Al-4 wt%Cu-(2.5–10) vol.%SiC nanocomposites produced by powder consolidation using powder compact extrusion. J Res Nanotechnol 1–15
28. Geng L, Zhang XN, Wang G (2006) Effect of aging treatment on mechanical properties of (SiC_w + SiC_p)/2024A1 hybrid nanocomposites. Trans Nonferr Metals Soc Chin 16:387–391
29. Gostariani R, Asadabad MA, Paydar MH (2017) Morphological and phase evaluation of Al/15 wt.% BN nanocomposite synthesized by planetary ball mill and sintering. Adv Powder Technol 28:2232–2238
30. Gu D, Wang H, Dai D (2016) Laser additive manufacturing of novel aluminum based nanocomposite parts: tailored forming of multiple materials. J Manuf Sci Eng 138(021004):1–11
31. Hamedan A, Shahmiri M (2012) Production of A356–1 wt% SiC nanocomposite by the modified stir casting method. Mater Sci Eng, A 556:921–926
32. Han Q, Geng Y, Setchi R (2017) Macro and nanoscale wear behaviour of Al-Al_2O_3 nanocomposites fabricated by selective laser melting. Compos B 127:26–35
33. Harichandran R, Selvankumar N (2016) Effect of nano/micro B_4C particles on the mechanical properties of aluminium metal matrix composites fabricated by ultrasonic cavitation-assisted solidification process. Archiv Civil Mechan Eng 16:147–158
34. Hashim JL, Looney JL, Hashmi M (1999) Metal matrix composites: production by the stir casting method. Mater Process Technol 92–93:1–7

35. Hemanth J (2009) Development and property evaluation of aluminum alloy reinforced with nano-ZrO_2 metal matrix composites (NMMCs). Mater Sci Eng, A 507:110–113
36. Hirsch J (2014) Recent development in aluminium for automotive applications. Trans Nonferrous Met Soc China 24:1995–2002
37. Hoziefa W, Toschi S, Ahmed M (2016) Influence of friction stir processing on the microstructure and mechanical properties of a compocast AA2024-Al_2O_3 nanocomposite. Mater Des 106:273–284
38. Hsu CJ, Chang CY, Kao PW (2006) Al–Al_3Ti nanocomposites produced in situ by friction stir processing. Acta Mater 54:5241–5249
39. Jeyasimman D, Sivasankaran S, Sivaprasad K (2014) An investigation of the synthesis, consolidation and mechanical behaviour of Al 6061 nanocomposites reinforced by TiC via mechanical alloying. Mater Des 57:394–404
40. Jeyasimman D, Sivaprasad K, Sivasankaran S (2015) Microstructural observation, consolidation and mechanical behaviour of AA 6061 nanocomposites reinforced by γ-Al_2O_3 nanoparticles. Adv Powder Technol 26:139–148
41. Jeyasimman D, Narayanasamy R, Ponalagusamy R (2015) Role of hybrid reinforcement on microstructural observation, characterization and consolidation behavior of AA 6061 nanocomposite. Adv Powder Technol 26:1171–1182
42. Jiang J, Wang Y (2015) Microstructure and mechanical properties of the rheoformed cylindrical part of 7075 aluminum matrix composite reinforced with nano-sized SiC particles. Mater Des 79:32–41
43. Khadem SA, Nategh S, Yoozbashizadeh H (2011) Structural and morphological evaluation of Al-5vol.%SiC nanocomposite powder produced by mechanical milling. J Alloy Compd 509:2221–2226
44. Kandemir S, Atkinson HV, Weston DP (2014) Thixoforming of A356/SiC and A356/TiB_2 Nanocomposites fabricated by a combination of green compact nanoparticle incorporation and ultrasonic treatment of the melted compact. Metall Mater Trans A 45:5782–5798
45. Kang YC, Chan SL (2004) Tensile properties of nanometric Al_2O_3 particulate-reinforced aluminium matrix composites. Mater Chem Phys 85:438–443
46. Kammrani S, Simchi A, Riedel R (2007) Effect of reinforcement volume fraction on mechanical alloying of Al-SiC nanocomposite powders. Powder Metall 50(3):276–282
47. Kallip K, Babu NK, Alogab KA (2017) Microstructure and mechanical properties of near net shaped aluminium/alumina nanocomposites fabricated by powder metallurgy. J Alloy Compd 714:133–143
48. Kannan C, Ramanujam R (2018) Effectiveness evaluation of molten salt processing and ultrasonic cavitation techniques during the production of aluminium based hybrid nanocomposites—an experimental investigation. J Alloy Compd 751:183–193
49. Khodabakhshi F, Gerlich AP, Simchi A (2015) Hot deformation behavior of an aluminum-matrix hybrid nanocomposite fabricated by friction stir processing. Mater Sci Eng, A 626:458–466
50. Khorshid MT, Jahromi SAJ, Moshksa MM (2010) Mechanical properties of tri-modal Al matrix composites reinforced by nano- and submicron-sized Al_2O_3 particulates developed by wet milling and hot extrusion. Mater Des 31:3880–3884
51. Knowles AJ, Jiang X, Galano M (2014) Microstructure and mechanical properties of 6061 Al alloy based composites with SiC nanoparticles. J Alloy Compd 615:S401–S405
52. Kubota M, Kaneko J, Sugamata M (2008) Properties of mechanically milled and spark plasma sintered Al–AlB_2 and Al–MgB_2 nano-composite materials. Mater Sci Eng, A 475:96–100
53. Li G, Wang H, Yuan X (2013) Microstructure of nanometer Al_2O_3 particles reinforced aluminum matrix composites processed by high pulsed electromagnetic field. Mater Lett 99:50–53
54. Li X, Xu J (2018) In: Beaumont PWR, Zweben CH (eds) Comprehensive composite materials II, vol 6, 2nd edn. Elsevier, Amsterdam, pp 97–137
55. Li X, Yang Y, Cheng X (2004) Ultrasonic-assisted fabrication of metal matrix nanocomposites. J Mater Sci 39:3211–3212

56. Liu X, Jia S, Nastac L (2014) Ultrasonic cavitation assisted molten metal processing of cast A356-nanocomposites. Int J Metalcast 8(3):51–58
57. Liu YQ, Cong HT, Wang W, Sun CH, Cheng HM (2009) AlN nanoparticle-reinforced nanocrystalline Al matrix composites: fabrication and mechanical properties. Mater Sci Eng, A 505:151–156
58. Maa SM, Zhang P, Ji G (2014) Microstructure and mechanical properties of friction stir processed Al-Mg-Si alloys dispersion-strengthened by nanosized TiB_2 particles. J Alloy Compd 616:128–136
59. Mahmoud TS, El-Kady EY, Al-Shihri A (2012) Mechanical and corrosion behaviours of Al/SiC and Al/Al_2O_3 metal matrix nanocomposites fabricated using powder metallurgy route. Corros Eng, Sci Technol 47(1):45–53
60. Malaki M, Xu W, Kasar AK (2019) Advanced metal matrix nanocomposites. Metals 9:330
61. Ma L, Chen F, Shu G (1995) Preparation of fine particulate reinforced metal matrix composites by high intensity ultrasonic treatment. J Mater Sci Lett 14:649–650
62. Masanta M, Ganesh P, Kaul R (2009) Development of a hard nano-structured multi-component ceramic coating by laser cladding. Mater Sci Eng A 508:134–140
63. Mattli MR, Matli PR, Shakoor A (2019) Structural and mechanical properties of amorphous Si_3N_4 nanoparticles reinforced Al matrix composites prepared by microwave sintering. Ceramics 2:126–134
64. Ma Z, Li Y, Liang Y (1996) Nanometric Si_3N_4 particulate-reinforced aluminium composite. Mater Sci Eng, A 219:229–231
65. Mazaheri Y, Karimzadeh F, Enayati MH (2011) A novel technique for development of A356/Al_2O_3 surface nanocomposite by friction stirs processing. J Mater Process Technol 211:1614–1619
66. Mazahery A, Ostadshabani M (2011) Investigation on mechanical properties of nano-Al_2O_3-reinforced aluminum matrix composites. J Compos Mater 45(24):2579–2586
67. Mousavian RT, Khosroshahi RA, Yazdani S (2016) Fabrication of aluminum matrix composites reinforced with nano-to micrometer-sized SiC particles. Mater Des 89:58–70
68. Mula S, Pabi SK, Koch CC (2012) Workability and mechanical properties of ultrasonically cast Al-Al_2O_3 nanocomposites. Mater Sci Eng, A 558:485–491
69. Najimi AA, Shahverdi HR (2017) Microstructure and mechanical characterization of Al6061-CNT nanocomposites fabricated by spark plasma sintering. Mater Charact 133:44–53
70. Nampoothiri J, Harini S, Nayak S, Raj B, Ravi K (2016) Post in-situ reaction ultrasonic treatment for generation of Al-4.4Cu/TiB2 nanocomposite: a route to enhance the strength of metal matrix nanocomposites. J Alloy Compd 683:370–378
71. Poirier D, Drewb R, Trudeauc ML (2010) Fabrication and properties of mechanically milled alumina/aluminum nanocomposites. Mater Sci Eng, A 527:7605–7614
72. Poovazhagan P, Kalaichelvan K (2014) Preparation of SiC nano-particulates reinforced aluminum matrix nanocomposites by high intensity ultrasonic cavitation process. Trans Indian Inst Met 67(2):229–237
73. Popov VA, Burghammer M, Rosenthal M, Kotov A (2018) In situ synthesis of TiC nano-reinforcements in aluminum matrix composites during mechanical alloying. Compos B 145:57–61
74. Prasada SV, Asthana R (2004) Aluminum metal–matrix composites for automotive applications: tribological considerations. Tribol Lett 17(3):445–453
75. Prabhu B, Suryanarayana C, Ana L (2006) Synthesis and characterization of high volume fraction Al-Al_2O_3 nanocomposite powders by high-energy milling. Mater Sci Eng, A 425:192–200
76. Ramezanalizadeh H, Emamy M, Shokouhimehr M (2015) A novel aluminum based nanocomposite with high strength and good Ductility. J Alloy Compd 649:461–473
77. Reddy B, Rajasekhar K, Venu M, Dilip J, Das S, Das K (2008) Mechanical activation-assisted solid-state combustion synthesis of in situ aluminum matrix hybrid (Al3Ni/Al_2O_3) nanocomposites. J Alloy Compd 465:97–105

78. Reddy MP, Shakoor RA, Parande G (2017) Enhanced performance of nano-sized SiC reinforced Al metal matrix nanocomposites synthesized through microwave sintering and hot extrusion techniques. Progr Nat Sci Mater Int 27:606–614
79. Rohtgi P (1991) Cast aluminium-matrix composites for automotive applications. JOM 10–15
80. Saheb N, Aliyu IK, Hassan SF (2014) Matrix structure evolution and nanoreinforcement distribution in mechanically milled and spark plasma sintered Al-SiC nanocomposites. Materials 7:6748–6767
81. Saito Y, Tsuji N, Utsunomiya H (1998) Ultra-fine grained bulk aluminum produced by accumulative roll-bonding (ARB) process. Scripta Materiala 39:1221–1227
82. Sajjadi SA, Ezatpour HR, Beygi H (2011) Microstructure and mechanical properties of Al-Al_2O_3 micro and nano composites fabricated by stir casting. Mater Sci Eng, A 528:8765–8771
83. Sajjadi SA, Ezatpour HR, Parizi MT (2012) Comparison of microstructure and mechanical properties of A356 aluminum alloy/Al_2O_3 composites fabricated by stir and compo-casting processes. Mater Des 34:106–111
84. Salehi A, Babakhani A, Zebarjad SM (2015) Microstructural and mechanical properties of Al–SiO_2 nanocomposite foams produced by an ultrasonic technique. Mater Sci Eng, A 638:54–59
85. Salehi M, Farnoush H, Mohandesi JA (2014) Fabrication and characterization of functionally graded Al–SiC nanocomposite by using a novel multistep friction stir processing. Mater Des 63:419–426
86. Schultz BF, Ferguson JB, Rohatgi PK (2011) Microstructure and hardness of Al_2O_3 nanoparticle reinforced Al-Mg composites fabricated by reactive wetting and stir mixing. Mater Sci Eng, A 530:87–97
87. Sharifitabar M, Sarani A, Khorshahian S (2011) Fabrication of 5052Al/Al_2O_3 nanoceramic particle reinforced composite via friction stir processing route. Mater Des 32:4164–4172
88. Sillekens WH, Jarvis DJ, Vorozhtsov A (2014) The ExoMet project: EU/ESA research on high-performance light-metal alloys and nanocomposites. Metall Mater Trans A 45:3349–3361
89. Simoes S, Viana F, Reis MA (2014) Improved dispersion of carbon nanotubes in aluminum nanocomposites. Compos Struct 108:992–1000
90. Soltania MA, Jamaati R, Toroghinejad MR (2012) The influence of TiO_2 nano-particles on bond strength of cold roll bonded aluminum strips. Mater Sci Eng, A 550:367–374
91. Surappa MK (2003) Aluminium matrix composites: challenges and opportunities. Sadhana 28:319–334
92. Suresh SM, Mishra D, Srinivasan A (2011) Production and characterization of micro and nano Al_2O_3 particle-reinforced LM25 aluminium alloy composites. ARPN J Eng Appl Sci 6(6):94–98
93. Suryanarayana C (2011) Synthesis of nanocomposites by mechanical alloying. J Alloy Compd 509S:S229–S234
94. Tahamtan S, Halvaee A, Emamy M (2013) Fabrication of Al/A206-Al_2O_3 nano/micro composite by combining ball milling and stir casting technology. Mater Des 49:347–359
95. Tazari H, Siadati MH (2017) Synthesis and mechanical properties of aluminum alloy 5083/SiCnp nanocomposites. J Alloy Compd 729:960–969
96. Uozumia H, Kobayashia K, Nakanishia K (2008) Fabrication process of carbon nanotube/light metal matrix composites by squeeze casting. Mater Sci Eng, A 495(1–2):282–287
97. Valibeygloo N, Khosroshahi RA, Mousavian RT (2013) Microstructural and mechanical properties of Al-4.5wt% Cu reinforced with alumina nanoparticles by stir casting method. Int J Miner Metall Mater 20(10):978–985
98. Wagih A, Fathy A, Ibrahim D (2018) Experimental investigation on strengthening mechanisms in Al-SiC nanocomposites and 3D FE simulation of vickers indentation. J Alloy Compd 752:137–147
99. Wang J, Yi D, Su X (2009) Properties of submicron AlN particulate reinforced aluminum matrix composite. Mater Des 30:78–81
100. Wan-li GU (2006) Bulk Al/SiC nanocomposite prepared by ball milling and hot pressing method. Trans Nonferrous Met SOC China 16:398–401

101. Witkin DB, Lavernia EJ (2006) Synthesis and mechanical behavior of nanostructured materials via cryomilling. Mater Sci 51:1–60
102. Xiong B, Xu Z, Yan Q (2010) Fabrication of SiC nanoparticulates reinforced Al matrix composites by combining pressureless infiltration with ball-milling and cold-pressing technology. J Alloy Compd 497:L1–L4
103. Xuan Y, Nastac L (2018) The role of ultrasonic cavitation in refining the microstructure of aluminum based nanocomposites during the solidification process. Ultrasonics 83:94–102
104. Xu J, Liu W (2006) Wear characteristic of in situ synthetic TiB_2 particulate-reinforced Al matrix composite formed by laser cladding. Wear 260:486–492
105. Yang R, Zhang Z, Zhao Y, Chen G, Liu M, Jiao L, Chen L (2016) Microstructure-property analysis of ZrB_2/6061Al hierarchical nanocomposites fabricated by direct melt reaction. Mater Charact 112:51–59
106. Yazdani A, Salahinejad E (2011) Evolution of reinforcement distribution in Al-B_4C composites during accumulative roll bonding. Mater Des 32:3137–3142
107. Ye J, He J, Schoenun JM (2006) Cryomilling for the fabrication of a particulate B_4C reinforced Al nanocomposite: part I. effects of process conditions on structure. Metall Mater Trans A 37:3099–3109
108. Yu H (2010) Processing routes for aluminum based nano-composites. Master degree thesis submitted to Wocester polytechnic institute
109. ZarezadehMehrizi M, Beygi R, Mostaan H, Raoufi M, Barati A (2016) Mechanical activation-assisted combustion synthesis of in situ aluminum matrix hybrid (TiC/Al2O3) nanocomposite. Ceram Int 42:17089–17094
110. Zhang L, Qiu F, Wang J (2015) High strength and good ductility at elevated temperature of nano-SiCp/Al2014composites fabricated by semi-solid stir casting combined with hot extrusion. Mater Sci Eng, A 626:338–341
111. Zhang X, Chen Y, Hu J (2018) Recent advances in the development of aerospace materials. Prog Aerosp Sci 97:22–34
112. Zhang X, Geng L, Wang GS (2006) Fabrication of Al-based hybrid composites reinforced with SiC whiskers and SiC nanoparticles by squeeze casting. J Mater Process Technol 176:146–151
113. Zhong, M, Jiang D, Zhang H et al (2014) Fabrication of nanoparticulate reinforced metal matrix composites by laser cladding. J Laser Appl 26(2):1–10
114. Zhou D, Qiu F, Jiang Q (2015) The nano-sized TiC particle reinforced Al-Cu matrix composite with superior tensile ductility. Mater Sci Eng, A 622:189–193
115. Zhuo L, Yang B, Wang H (2011) Spray formed Al-based amorphous matrix nanocomposite plate. J Alloy Compd 509(18):L169–L173
116. Zhou S, Zhang X, Ding Z (2007) Fabrication and tribological properties of carbon nanotubes reinforced Al composites prepared by pressureless infiltration technique. Compos A Appl Sci Manuf 38:301–306

Chapter 6
Aluminium Hybrid Composites Reinforced with SiC and Fly Ash Particles—Recent Developments

Bhabani Ranjan Pal, Shouvik Ghosh, and Prasanta Sahoo

1 Introduction

Material researchers have given much attention on composite materials in the recent past years, because of having desirable properties, unordinarily that could lead to various useful engineering applications in different domains. AMCs which is majorly used in aerospace, defence, nuclear energy, automotive, sports recreational, biotechnology and thermal management must be considered as materials for energy conservation and environmental safeguard [120]. Automotive component application areas of AMCs are fins, gear box housing, disc rotor brakes, rotating blade sleeves, suspension strut, crankshafts, rocker arms, etc. In electronic sector, some of the uses are in the integrated heat sinks, microprocessor lids and microwave manufacturing. Aerospace industries use AMCs as aircraft wings, body structure faming and gears for landing [4]. AMCs have drawn attraction for its economic production and desirable properties. Such desirable properties are higher specific stiffness, specific strength and low coefficient of thermal expansion with better wear and corrosion resistance. Strength along with wear susceptibility is of prime importance for the applicability of AMCs in different service areas [5].

Performance level of MMC depends on:

- Types of reinforcements combined,
- Wt% of reinforcing materials mixed,
- Wettability between matrix and reinforcements,
- Fabrication route selected,
- Metallurgical characteristics of the matrix material [5].

http://orcid.org/0000-0002-1538-0646, http://orcid.org/0000-0003-4207-1176

B. R. Pal (✉) · S. Ghosh · P. Sahoo
Jadavpur University, Kolkata, India
e-mail: bhabaniranjanpal@gmail.com

S. Sahoo (ed.), *Recent Advances in Layered Materials and Structures*,
Materials Horizons: From Nature to Nanomaterials,
https://doi.org/10.1007/978-981-33-4550-8_6

Primary challenging task when processing MMCs is to achieve homogeneous and uniform distribution of reinforcements in the matrix as this puts a great impact on the final properties and the desirable quality of the material. Uniform distribution and prevention of segregation or agglomeration of reinforcements help to get better microstructure that leads to achieve good aggregate characteristic profile of all MMCs. Available processing routes of MMCs can be classified into three types, such as (a) Liquid phase (b) Solid phase and (c) Infiltration technique. Semisolid phase processing such as rheocasting and compocasting is also widely used fabrication process, apart from these three techniques. Liquid phase process mainly includes stir casting, high-energy laser melt injection, plasma spraying and squeeze casting, etc. Ultrasonic cavitation-assisted stircasting process as shown in Fig. 1 has ease in breaking the agglomeration of reinforcing particles. Solid phase incorporates mainly powder metallurgy technique, where microwave sintering (shown in Fig. 2) is gradually taking the place of conventional sintering in MMC production. Infiltration route has application in industry for its large-scale production advantage. Figure 3 shows basic flow diagram of liquid metal infiltration technique. In the route of infiltration problem arises when the reinforcement concentration becomes high. Additional processes are required to dilute the reinforcing agent to the required levels in that

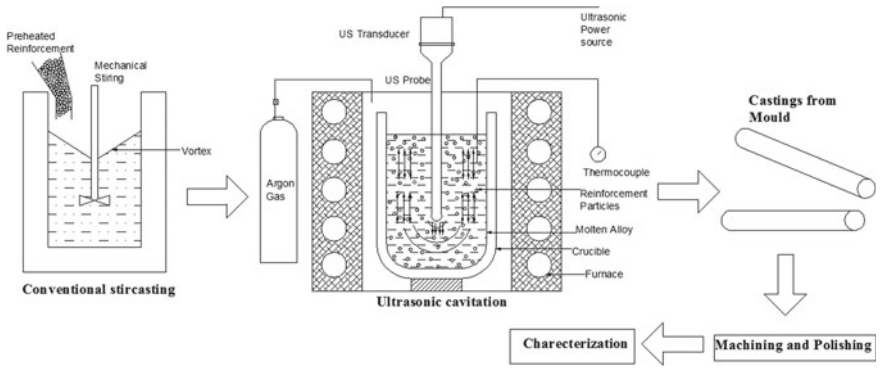

Fig. 1 Schematic diagram of ultrasonic-assisted stircasting

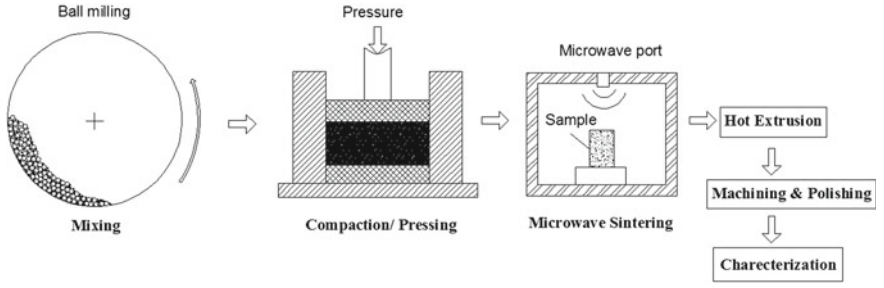

Fig. 2 Schematic diagram of microwave-assisted hot pressing

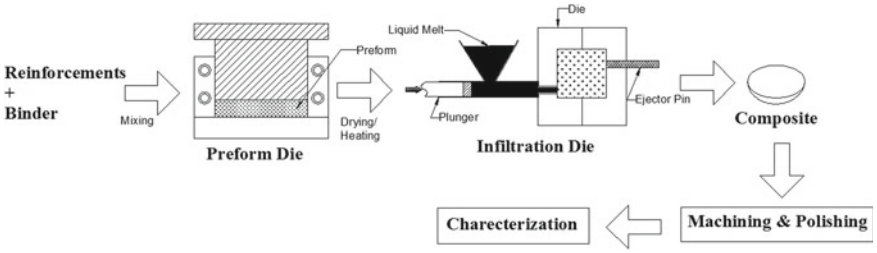

Fig. 3 Schematic diagram of liquid metal infiltration

case. Increased processing times and steps at elevated temperatures often produce a secondary phase as a result of chemical reactions between matrix and particle. This secondary phase usually brittle in nature [100]. Stir casting process has proved to be useful for its simplicity, high productivity and economical [113]. Recently modified stir casting or two-step stir casting are gaining attraction of the researchers for very well dispersion and bonding of reinforcements within the aluminium metal matrix [2]. Particle or fibre reinforced MMC are proofing higher strength and modulus, far better wear resisting behaviour with ease in production and lower cost of preparation [17]. However, too much degradation of ductile behaviour of the MMCs due to higher level of inclusion of ceramic particles is a matter to think about. Interest has been grown by incorporating ceramic particles size of nano-level to produce metal matrix nano-composites (MMNC) that maintain good ductility [78]. Stable and non-reactive performance must be thereby the reinforcements in the range of functioning temperature for better susceptibility to wear [87]. Ceramic powders as reinforcements possess exceptional strength compared to other class of reinforcements; hence, these are majorly useful as primary reinforcements of HAMCs. Ceramics have certain advantages like (a) high hardness, (b) heat resistant, (c) low thermal expansion coefficient, (d) medium conductivity and (e) corrosion resistant. Most commonly used synthetic ceramics reinforcements are SiC, Al_2O_3, SiC, B_4C, ZrO_2 and TiB_2. Secondary reinforcements are used for the purpose of machinability increment, cost reduction and lowering density [112]. The significant input parameters like particle size and types of reinforcement had percentage contribution of 27.30% and 48.72%, respectively, to control the microhardness of AMC [114].

Based on the outcomes of several researches, it has been found that silicon carbide (SiC) can be opted as key ceramic element for aluminium matrix or its alloy base composites [66]. Studies have been done in last two decades for AMC characterization using industrial wastes such as fly ash, red mud, granite dust and agricultural wastes like rice husk ash (RHA), sugar cane bagasse ash (SCBA), coconut shell ash, bamboo leaf ash (BLA), ground nut shell ash, palm oil fuel ash and maze stalk ash. Fly ash is potential discontinuous dispersoids that have got more attention of the researchers among all these waste particulates and results also show to be very promising in tribo-mechanical properties of the fabricated products of AMCs [41].

Strength of aluminium matrix composite not only depends on the reinforcement type, it is also a function of reinforcement size when varied from micro to nano.

Hence, present literature study deals with the different experimental findings achieved by different researchers in the field of Al-MMCs reinforced with micro- or nano-SiC and FA. The microstructural, mechanical, tribological, thermal, machining and some other relevant properties of fabricated AMCs or HAMCs have been progressively reassessed and discussed in detail. Similar experimental conditions have been avoided to focus the objective of this chapter. Major target has been set to illustrate or highlight the influencing parameters and test conditions which greatly affect the properties of ultimate developed AMCs reinforced with this two major synthetic ceramic and agro-industrial waste. Effect of fabrication techniques and reinforcement size (micro/nano) on the distribution of reinforcement in aluminium matrix has been precisely described. This chapter has been organized categorically in five major divisions. First section is introductory part about the reinforcement types and processing methodology of Al-based MMCs. The second, third and fourth sections depict the available research outcomes regarding SiC reinforced AMC, fly ash reinforced AMC and combined SiC, FA reinforced hybrid AMCs. Last section concludes about the prospects in this research area, which helps the researchers from industry or academic to get a motivation about the AMC or HAMC reinforced with micro/nano-SiC and FA.

2 Study on Al-MMC: Reinforced with SiC

In the timeline of AMCs development, different reinforcing materials were used, that are generally grouped into three major types, as (i) synthetic ceramic-based, (ii) industry generated wastes and (iii) agriculture-based wastes. Ceramic particulates reinforced metal matrix composites have favourable properties like high specific strength, better resistance to wear and good capability to retain strength at elevated temperatures [30]. SiC is such a ceramic material which holds high hardness (2800 kg/mm^2), high rigidity (elasticity modulus as 410 GPa), good thermal conductivity (100 W/m K for single crystal and 4–20 W/m K for poly crystal), moderate toughness, low specific gravity (density as 3.2 g/cm^3), low thermal expansion coefficient (4.3×10^{-6}/K) and less responsive against thermal shock (Melting point 2730 °C) [96, 114]. Aluminium or its alloy when reinforced with SiC fulfils the need of lightweight, high strength material in various industries from automotive to aircraft [82]. Many investigations have been executed in last three decades to develop mechanical, tribological and thermal behaviour of SiC reinforced AMCs. Figure 4 presents the future trend and developing areas of AMC synthesis.

It has been reported by the researchers that both the particle size and dispersion have evident effect on mechanical strength of the discontinuously reinforced metal matrix composites (DRMMCs) composites [132]. Outcomes of the use of micro-size and nano-size SiC reinforced Al-MMC are described below.

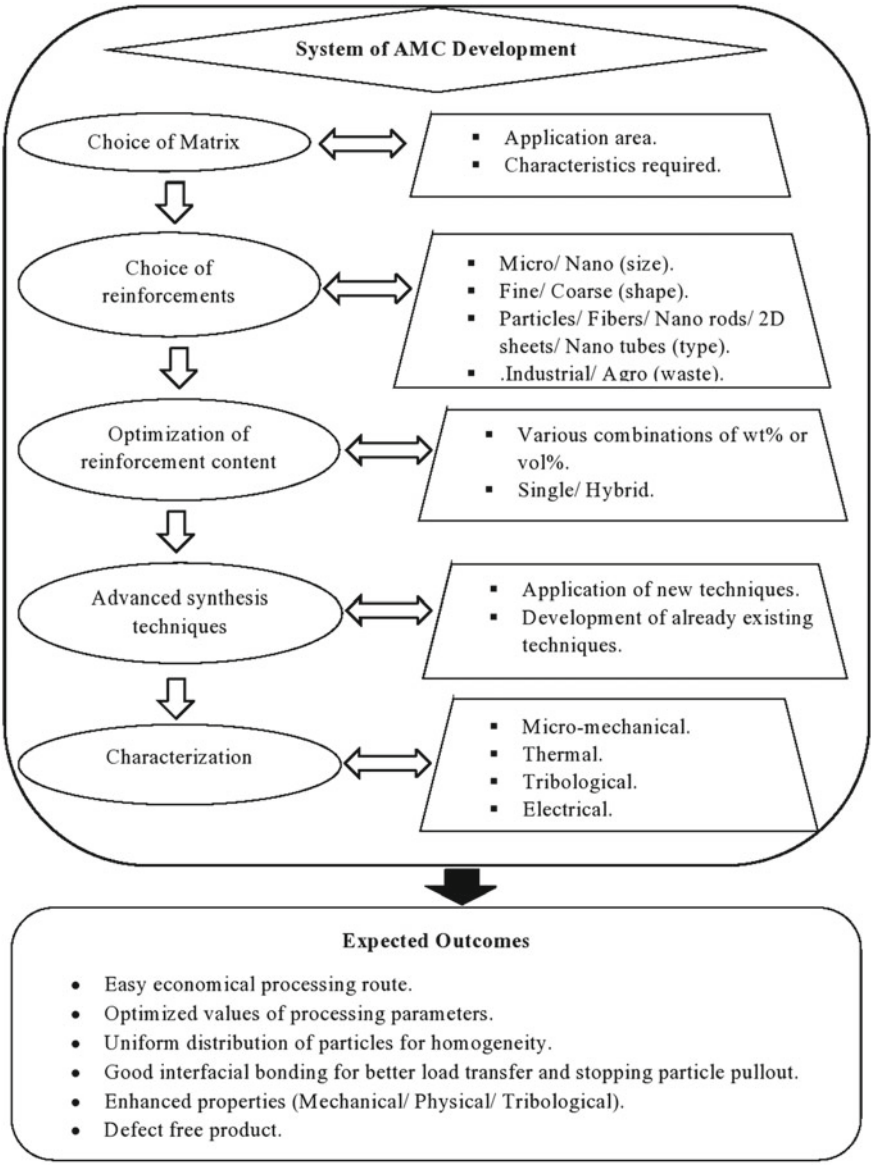

Fig. 4 Trends of aluminium MMC development

2.1 Micro-SiC

2.1.1 Physical and Mechanical Behaviour

Souvignier et al. have shown aluminium matrix composites can be shaped by tool-less manufacturing technique such as extrusion freeform fabrication (EFF). This is one type of rapid prototyping method by multiphase jet solidification technique combined with fused deposition modeling. Silicon carbide particles (5–10 μm) upto 20 vol% were most successful in retaining high density and doubling the strength of the parent metal matrix [117]. The density is prime concern to produce lightweight composite material which needs to be lowered by the inclusion of low density reinforcement addition in to metal matrix. SiC (density = 3.2 g/cc) has slightly greater density than Al-alloy (density = 2.6–2.7 g/cc). The density of AMCs is checked both theoretically (applying rule of mixture) and experimentally (applying Archimedes' principal). 1.30% increment in the density of the Al6061–SiC composite occurred with the rise of SiC wt% from 0 to 6. This is mainly attributed to the more denser solid structure of constituent SiC particles than that of the Al-alloy [128].

Mechanical strength of micro-size silicon carbide particle produced via conventional stir casting or modified stir casting was evaluated on the basis of tensile, impact, compression load sustainability and hardness behaviour, [7, 14, 46, 49, 80, 115, 126, 128]. The UTS, YS, compression strength and resistance to indentation of Al–SiC composites were significantly increased with increase in silicon carbide wt% or vol% in the parent matrix metal and ductility (% of elongation) droped down [14, 49, 116, 128]. This is in line with the other ceramic particulate reinforced composites. Very small amount of magnesium (Mg) (1–1.5 wt%) could be used as wetting agent with SiC where it forms Mg_2Si. This is the compound responsible for achieving more strengthening and better dispersed microstructure of AMC [115]. Comparison between vacuum-assisted high-pressure die casting (HPDC) process and gravity die cast (GDC) process with 10 vol% micro-SiC has cleared that the former process helped to acquire improved particle distribution, reduced porosity and good bonding at matrix/particle interface [46]. Different metal (like Cu and Ni)-coated SiC micro-particles were used to enhance micro-structure and phase composition [35, 47, 48]. Physical and mechanical property results of fabricated 5083 Al-alloy composite using 40 μm SiC show that the ultrasonic assisted stir casting process was beneficial compared to the ordinary stir casting process. This has been attributed to ultrasonic blending process properly distributes the silicon carbide particles into the aluminium matrix by eliminating micro-voids [49]. Micro-hardness of 37 μm SiC reinforced AMC was increased upto 15% because of the strong adhesion between matrix alloy and reinforcement. However, it was found to decrease in hardness at 20% SiC due to the formation of fine cracks at the interface [99]. Uniform particle distribution of SiC reinforcements, reduced porosity level and fine homogeneous microstructural dissipation of the composite through liquid metallurgy process lead to achieve better hardness [7]. Hence, the rotational speed of stirrer and stirring time during addition of particle into the molten aluminium vortex also has influence on the hardness of the

composite. It was evidenced that increased stirring speed and time during semisolid condition results into better distribution of silicon carbide in the aluminium matrix, thus enhanced hardness was achieved [84]. Effects of three different Al-alloy (2124, 5083 and 6063), two different sizes of SiC particles (157 and 511 μm) and two different extrusion ratios (13.63 and 19.63) on impact behaviour were studied at different temperature. The result showed toughness of Al6063 composites increased a bit with increase in the size of SiC particle and extrusion ratio. Though test temperature did not possess any significant effect on the failure of the composites. Four-point bending test was conventionally carried out by hot isostatic pressing (HIP) of 30 μm SiC powder in Al-alloy for checking strength of AMC under bending load [142]. Bending strength was not significantly influenced by the SiC particle size distribution after HIP [125].

2.1.2 Effect of Secondary Treatments

Secondary treatments of composites as casted or infiltrated such as hot extrusion or hot rolling generally helped in reaching the targeted mechanical behaviour of particle reinforced MMCs [81]. Hardness, mechanical and sliding wear resistance properties of AMC can be extended as the consequence of heat treatment and ageing of composites [24]. T6 heat treatment both solutioning and ageing were applied on micro-SiC/Al AMC. Despite suggesting T4 treatment for the composite [123], conventional T6 thermal treatment is widely accepted in SiC/Al composite due to the flexibility of artificial ageing [24, 29, 130]. When SiC_p content in Al-composites is low (8–14 vol%), overageing (OA) plays more important role than peak-ageing (PA). T6 heat treatment of AA2024/40 μm SiC_p composites even exhibited considerably low specific wear rate than grey cast iron as well as H13 tool steel [56]. Main factor to control ageing kinetics of the composites' matrices is the lattice spacing, which reduces as SiC_p vol% increased [57]. More amount of inter metallic dislocation formed as a result of thermal discrepancy in between the aluminium metal matrix and SiC reinforcements was attributed to the better ageing kinetics of Al-alloy. With more SiC particles concentration, this ageing phenomenon (through T6 heat treatment) leads to reduce time required to obtain the maximum hardness [95]. Retrogressed re-ageing (RRA) of the AMC samples at 120 °C for 24 h was used to fully restore the peak aged condition of the T6 treatment. It was concluded from comparative study that T6 treatment improves the mechanical properties of the 7075 Al-alloy system reinforced by 40 μm SiC while RRA made the composite better wear resistant [24]. In due course of enhancing coefficient of thermal expansion (CTE) property of SiC/AMC, T6 tempering is better suggested to minimize the change in dimension at elevated temperatures [29]. Ageing treatment was noticed more beneficial for improving fracture toughness, and its result was found better than that of the Al-borax premixed SiC composites. The improvement attributed to the presence and fine coherent distribution of Mg_2Si precipitates formed in the Al (6063) matrix at the time of ageing process [3]. It was noticed that during powder metallurgy processing small ratio of particle sizes between Al-matrix and reinforcement distributed the SiC

particles homogeneously. It was well understood that much smaller particle size than the matrix powder size can form cluster very easily in the matrix. This will result an inhomogeneous distribution of reinforcements which was already seen by previous researchers [132].

2.1.3 Machining Behaviour

AMC materials become difficult to machine, especially when hard and abrasive reinforcing elements like silicon carbide (SiC) particles are reinforced. Turning operation was conducted on SiC/AMC to figure out the effect of machining criterion, like feed rate, cutting speed, depth of cut on wear rate of tool and surface roughness of specimen [55, 80]. At the condition of turning without coolant, tool wear was increased mainly with increase in the velocity of cutting. Greater content of SiC_p reinforcement increased tool wear; higher cutting speed and lower feed rate were recommended to achieve minimal surface roughness.

2.1.4 Thermal Behaviour

Movement or collision of electron inside any material dominates the heat conduction behaviour of any metal which is denoted by thermal conductivity (W/m K). The presence of ceramic-based SiC particles inside the structure forms resists the motion of aluminium electrons providing conductivity. Thermal conductivity of double phase composite relies on the factors like individual thermal conductivity of the constitutional phases, interaction and spacing between phases and present wt% of phases. Thermal conductivity of the Al-composites drops down with rise in wt% of SiC (referred to Fig. 5), and a reverse phenomenon was detected with increasing size of SiC particle from 70 to 40 μm. This was ascribed to increasing particle size of SiC reduces scattering of electrons and thus mobility of electrons increase [34]. Though SiC reinforced Al-composite had improved heat conductance than the unreinforced matrix alloy [140].

2.1.5 Tribological Behaviour

Al-SiC_p composites processed by liquid metallurgy possess significantly higher wear resistance compared with unreinforced alloy during sliding. Bai et al. reported this increased wear resistance comes from the existing hard silicon carbide particles that can restrict the flow ability tendency of material and avoid the development of iron-rich layers on the composite surface [12]. At the circumstance when the fractural strength of particles is more than applied stress, the SiC particles mainly bear the applied load. The abrasive nature of SiC particles on the mating surface leads to the separation of iron oxide (Fe_2O_3) layers which was placed onto the mating surfaces of composites provides ten times obstruction to the abrasion phenomenon than matrix

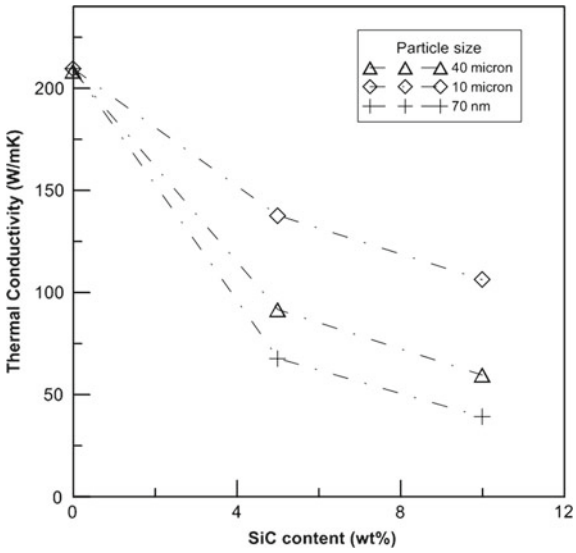

Fig. 5 The effect on thermal conductivity with respect to size and proportion of SiC particle [34]. Reproduced with permission from Elsevier, Copyright (2014)

alloy. SiC particles were fractured under the action of huge localized strain gradients. These strains were then transferred to the aluminium alloy matrix that nucleates subsurface cracks. This cracks were then propagated by decohesion of particle–matrix interfaces. Shifting of wear from mild to severe generally happened in the unreinforced alloy above a critical load. This phenomenon could be suppressed by the addition SiC_p [6]. A mathematical formula was modelled to predict dry sliding wear of MMC and compared experimentally with Al-SiC AMC. In that study adhesion, ploughing and particle fracture are taken as dominating wear mechanism. Hence, sliding friction coefficient is calculated using the following relation (Eq. 1):

$$f = \frac{F_a + F_p + F_f}{P}, \tag{1}$$

where P is applied load, total frictional force, F_t is considered to be caused by adhesive force (F_a), ploughing force (F_p) and fracture force (F_f). The particle fracture force can be calculated using the following Griffith equation (Eq. 2), i.e.

$$F_f = K_2 A_p f_v \frac{K_{1c}}{a^{1/2}} \tag{2}$$

K_{1c} is the fractural toughness of the resulting composite, K_2 being a geometric factor depends on the type of particles reinforced in the composite, a is the particle size, f_v is the particle volume fraction, A_p is the cross-sectional area of scratch [141].

The coefficient of friction of AMC was found 25% higher than the normal casted iron when sliding in similar conditions explored the suitability of SiC/Al-MMC as material for brake rotor applications [79]. The formation of mechanically mixed layer

(MML) due to transfer of iron particle from counterface disc to the pin was observed more with wt% of SiC in Al-composites which is another reason for decreasing nature of wear [45]. Impact of SiC particle content, sliding speed along with applied pressure is the prime concern for manufacturing better wear-resistant AMC, being studied by R. N. Rao and S. Das. Wear rate was observed to decrease at a constant rate with rise in SiC proportion and increases as the sliding speed increased. Though coefficient of friction goes up with SiC particle concentration in Al-alloy, it decreased on attaining higher sliding speed. This rise in coefficient of friction attributed to higher frictional force for sliding as microchips were formed due to micro-cutting of counterface by deep penetration of hard SiC particles. It was also seen that there exists a maximum pressure to be applied on the composite samples beyond which wear rate gets seized after remaining constant before that applied load. The temperature also gradually increases at first when applied pressure was increased, and in the latter stages it increased abruptly, when a critical level of the applied pressure was reached [89]. The composite reinforced with coarse grain of SiC micro-particles (37 μm) showed more wear resisting behaviour than that of the composite being produced with finer particles (13 μm) when rubbed against abrasive Al_2O_3 under dry ambient condition [20]. Wear mechanism map for Al7010-alloys and its composite reinforced with 25 wt% SiC was compared separately depending on wear rate and temperature hike. The plot for composite was divided into four regions—(a) ultra-mild wear, (b) mild wear, (c) oxidative wear and (d) delamination wear, while pure alloy exhibited only two zones—(a) mild wear and (b) severe wear or delamination wear. The plot of wear mechanism for Al7010-25 wt% SiC composites in Fig. 6 depicts the seizure load and transition load (change from mild to severe rate of wear) at different sliding speed. It was found that significantly higher seizure load (~30.7% higher at 0.52 m/s of sliding speed) and transition load (~85.7% higher at 0.52 m/s of sliding speed) required to start transition of mild wear to severe wear in composite in comparison with the base alloy [88]. Similar mechanisms were observed when wear behaviours Al2024/20 vol% SiC composites were investigated by preparing through PM route and artificially ageing at elevated temperature in between 20 and 250 °C. In the prepared composite samples when temperature went above a critical value, a transition of wear mechanism from mild zone to sever zone was found. This critical value of temperature was shifted from 150 to 200 °C by the inclusion of SiC particles than matrix alloy without reinforcements [76].

The tribological testing parameters of micro-SiC reinforced AMCs were optimized by Taguchi's orthogonal array design of experiment. It was noticed that reinforcement volume or weight fraction was the most influencing factor reasonable for the wear properties compared to load and sliding speed whether the composite was either produced by stir casting [38, 39] or PM [101]. Both the main effects and interaction effects of the parameters are studied interaction between load and speed ($L \times S$) which is the significant interaction. Maximum extent of reinforcement content and minimum magnitude of sliding speed, load and sliding time was the optimal combination for minimizing rate of wear [39]. In PM route production, contributions of the grain size and hardness were about 81.57 and 11.09% towards abrasive wear behaviour [101].

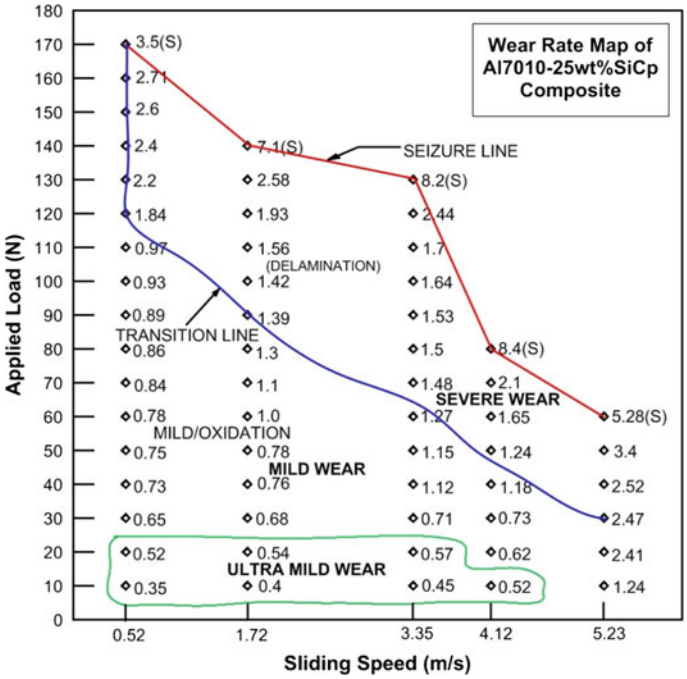

Fig. 6 Wear rate map for Al7010–25% SiC_p [88]. Reproduced with permission from Elsevier, Copyright (2013)

Corrosion study in 3.5% NaCl solution was very commonly done on Al-SiC composite processed by stir casting [58, 111] or squeeze casting [40]. Potentiodynamic polarization test using a potentiostat is generally used for precise corrosion test. The magnitudes of corrosion potential (E_{corr}) and corrosion current density (I_{corr}) at open circuit potential (OCP) condition are noted to evaluate corrosive nature of samples. Corrosion resistance improved with increase in vol% of SiC reinforcements. Addition of 10% SiC_p in the base alloy was appeared to be optimum proportion for the synthesis of a corrosion-resistant Al–Cu alloy-based composite. Reinforcement particles were agglomerated with further increase of SiC_p from 15 to 25 wt%. This agglomeration of SiC_p opened cathodic sites and boosted galvanic effect, hence corrosion rate again started to increase. Rapid pitting corrosion started due to adsorption/diffusion of chloride ions of NaCl [111].

2.2 Nano-SiC

2.2.1 Microstructure and Mechanical Behaviour

Literature available so far reveals that use of nano-size silicon carbide particles or fibre in AMC fabrication has been accepted during start of second decade of twenty-first century. Y. Yasutomi et al. have shown interest to understand the reaction due to diffusion of aluminium into nano-SiC fibre while producing electric cable by bundling 27 SiC fibre/Al composite elemental wires together. Generation of Al_4C_3 and Al_2SiO_5 at the SiC/Al interface can be converted into molten Al through thermal treatment [137]. Use of magnesium enhances the wettability between Al and SiC, also prevents the formation of Al_4C_3 by forming a protective layer of MgO at the interfacial layer between nano-SiC and liquid aluminium. It was also difficult to avoid the formation of Al_4C_3 when lower sizes (like 38 μm) of Al particles are used for AMC produced via powder metallurgy (PM) route. Finer Al particulate was found to be highly active to react and can easily be exposed to surface of SiC_p by embedding into the gap among the big Mg particulate [133]. It is being already reported that strengthening effect of nano-SiC particles is superior over micro-size particles [139]. This was attributed to strong refinement of α-Al dendrites in as-cast Al-composites from dendritic crystal with sizes about 200 μm to equiaxial crystal with sizes about 75 μm [131]. The yield strength, ultimate tensile strength and the modulus of elasticity were significantly improvised when nano-size particles were incorporated, though ductility was found to be decreased with nano-SiC particle (50 nm) addition [72]. As reported by A. Mazahery and M. O. Shabani that highest strength values were reached with the inclusion of 3.5 wt% nano-SiC particles. On the other hand, G. Bajpai et al. have found that resistance against tensile and compressive load including hardness of Al-Nano-SiC composites primarily raised up to 2 wt% content of nano-SiC and then fell down at 3 wt% [13, 122]. Similar result was observed by C. C. Gallardo et al. while in their experiment saturation level of hardness and compressive stress occurred at 2.5 wt% of nano-SiC [21]. Hardness of the nano-SiC reinforced Al6061 alloy increased significantly by 73% compared with the base alloy [70]. It has been noticed after reviewing available literatures that 2–4 wt% of nano-SiC gives better result for increasing mechanical strength. Studies have been done to understand the influencing parameters of stir casting such as stirring rate and stirring temperature on the micro-mechanical behaviour of the Al-composites. There exist an optimum stirring rate and temperature for every mixing at which best properties and dissipation of nanoparticulates might be achieved. Stirring temperature of 750 °C and stirring rate of 700 rpm proved to be fruitful for manufacturing AMC containing 1 wt% of 25–50 nm size SiC particle in A356 aluminium alloy [27]. Non-destructive ultrasonic testing helps to minimize the sample count during any mechanical test. Ultrasonic pulse received from x-cut and y-cut transducer and processed via pulse echo overlap method (PEO) had been successfully employed to evaluate the mechanical behaviour of nano-aluminium-SiC composites [33]. Poisson's ratio indicates that the characteristics of bonding forces whether the material is "stiffer" or "softer"

were found to be decreasing with increasing volume % of nano-SiC. L16 Taguchi orthogonal design of experiments was employed for optimizing different process parameters of friction stir processing route during the production of AA6061/SiC nano-composites. Four factors were considered that were tool penetration depth rotational speed, transverse speed and profile of the pin. ANOVA results confirmed that rotational speed as the most crucial parameter and threaded pin profile is better than square pin in achieving higher ultimate tensile strength (UTS) [10, 11, 103]. FESEM and atomic force microscopy (AFM) images reveal that hardness of AMC generally varies inverse to the inter particle spacing of reinforcements [102].

While going for fine nanoparticles, a chance of agglomeration increases during processing of aluminium metal matrix composite via solidus and liquidus routes. Solid methods like high-energy planetary milling [60, 61, 110] could increase hardness value of the aluminium and 1 vol% nano-SiC composite upto 163 HV. Experimental density closely matched with theoretical density while Al 5083 alloy with 10 wt% SiC_p was prepared via high-energy ball milling along with a process called as spark plasma sintering (SPS) [15]. Various innovative liquid methods such as stir casting with cryorolling [26], cryomilling [124], solvothermal-assisted grapheme encapsulation of SiC nanoparticles [37], ultrasonic cavitation-assisted stir casting [51, 70, 135] were developed to stop this phenomenon. Study on fracture behaviour have shown higher SiC nanoparticle content increases possibility of failure at the weakly bonded particle boundaries causing higher stress concentration during deformation [136]. Finer grain refinement of α-aluminium and eutectic Si phase can be obtained by better dispersion of nano-SiC_p. High-intensity discontinuous ultrasonic treatment (HIDUT) was found to be more effective than high-intensity continuous ultrasonic treatment (HICUT) for improvising mechanical properties. An increase in UTS upto 100 and 126% increase in YS were observed for A413–2% SiC_{np} composite [28]. UV treatment assisted with squeeze casting can efficiently refine α-Al and eutectic Si phase of aluminium matrix nano-composites (AMNC). This refinement along with increased UV time and applied pressure resulted into improvement in tensile properties of the AMNC [138]. The fractographic investigations have also disclosed predominant nano-void coalescence fracture mechanism due to the uniform distribution of nano-SiC particles [37]. Major influencing fracture mechanism was observed as inter-dendritic cracking, and there was no occurrence of debonding at the interface in between parent alloy matrix and the SiC reinforcement particulates [73].

2.2.2 Effect of Secondary Treatment

Strengthening of nano-SiC reinforced (both in wire form and powder form) was done through annealing [134] T4, T6 heat treatment [8, 59]. A considerable improve in the mechanical strength of Al-alloy was observed. Microstructure analysis using SEM disclosed that T6 heat treatment leads to dissociation of dendrite structure of α-Al and pallet like Si particle globule formation in eutectic phase. Using low ageing temperature for the heat treatment process of SiC particles (<500 nm) reinforced

6061 Al-alloy displayed good stress–strain curve (refer to Fig. 7a) and enhanced hardness (refer to Fig. 7b) while maintaining its ductility [59].

2.2.3 Thermal Behaviour

15-nm-sized silicon carbide (0, 0.3, 0.5, 1.0 and 1.5 vol%) was reinforced in 99% pure Al-metal matrix through microwave sintering followed by hot extrusion process. Processed composites were then examined for mechanical strength, fracture behaviour and coefficient of thermal expansion (CTE). Mechanical properties are noticed to be following similar trend as seen by other researchers, best was observed at 1.5 vol% SiC. Thermo-mechanical analyzer with a heating rate of 5 °C/min in between a range of 50–350 °C and argon gas was passed at 0.1 lpm to determine CTE of the prepared samples. Values showed a decreasing trend of CTE with increased addition of hard nano-SiC particles, that indicated better dimensional stability of AMC at higher temperature [94].

2.2.4 Tribological Behaviour

The dominant wear mechanisms in dry sliding wear behaviour of nano-AMC were determined using SEM and EDS microstructural characterization technique on worn surface. The abrasive wear was the controlling wear mechanism for nano-composite sample than sever adhesive wear. The coefficient of friction (cof) values of the SiC reinforced Al-nano-composite was not changed considerably by different applied stresses in between 0.3 and 0.9 MPa. This was attributed to the generation of mechanically mixed layer (MML) by the oxidized debris particle acting as lubricant film at the contact surface of nano-composite [74]. In another study, pin-on-disc dry sliding wear test of Al6061/1.2 wt% nano-SiC (50 nm) was conducted at different load of 10, 20, 30 and 40 N with a fixed sliding velocity of 0.5 m/s for 1000 m sliding distance. Specific wear rate and frictional coefficient decreased with increase of load from 10 to 40 N, whereas normally in case of base alloy Al6061 it has increasing plot. Higher applied load increased temperature at the contact surface causing more oxidization of wear debris from the counterpart (hardened steel disc). The MML layer was formed in case of the nano-composite effectively reduced the wear rate of nano-composite compared to matrix alloy. Surface roughness at the wear zone of the base alloy was reduced from 1.69 to 6.20 μm by the incorporation of nano-size SiC particle via liquid metallurgy. Plastic deformation was reduced to a minimum level as most of the applied pressure was taken by the nano-silicon carbide; hence, the surface roughness of the composite was smoothed. Field effective SEM (FESEM) and SEM of worn surface was checked, and adhesive wear and delamination wear mechanism were found to be presiding. This was being attributed for causing wear in matrix alloy, that changed into abrasion and oxidation in case of nano-composite [70, 75]. A combined dry sliding and corrosive wear tests of nano-SiC composite was performed using high-temperature tribometer (pin-on-disc) with an attached

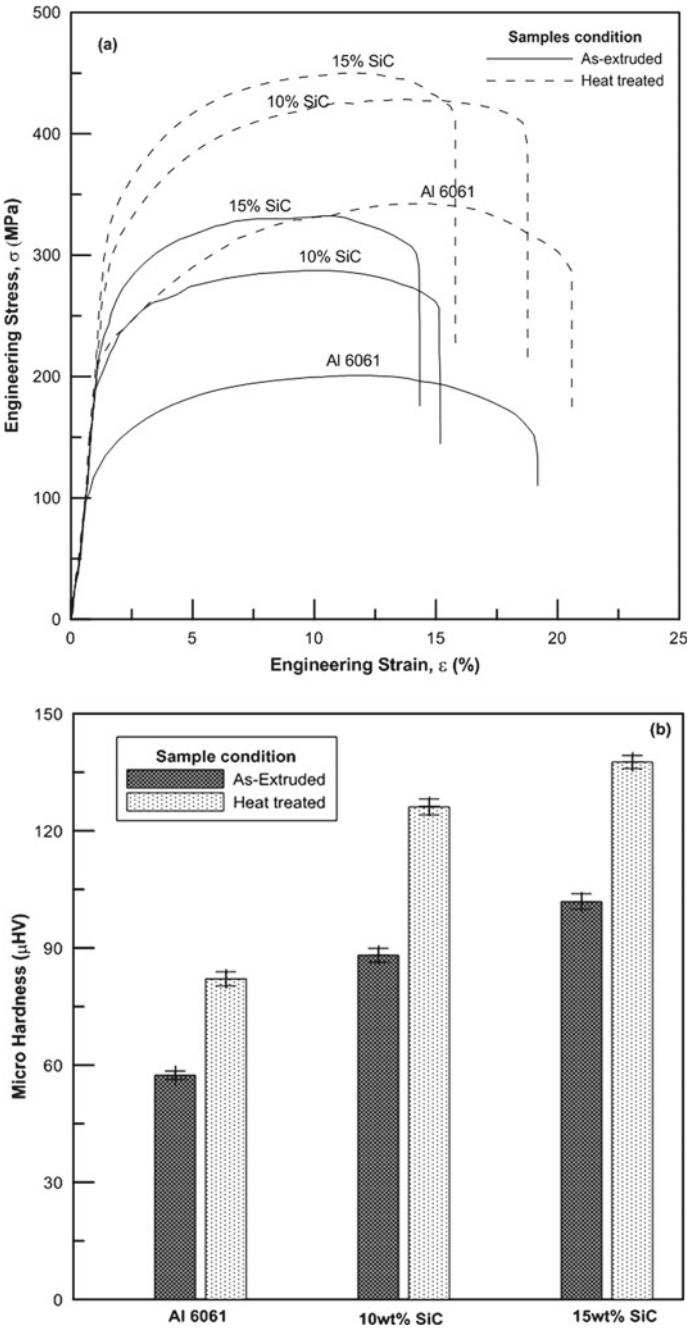

Fig. 7 **a** Stress versus strain curves and **b** Vickers microhardness graph of Al 6061 alloy and 10 wt% SiC and 15 wt% SiC composites [59]. Reproduced with permission from Elsevier, Copyright (2014)

container filled with 3% NaCl solution at 25 °C. 1, 2 and 3% volume fraction of nano-size SiC (25–50 nm) were mixed with Al6061 alloy powder (38–63 μm) using mechanical milling cold pressing and hot extrusion for sample pin preparation. An improved corrosion resisting nature was seen with the increased vol% of nano-SiC due to non-reactivity or inertness of nano-SiC particles with the corrosive solution [75]. Wear test was conducted by placing the sample pin on a flat plate and applying reciprocating motion in between them at a constant rotational speed of 38 rpm for developed Al–SiC nano-composite. Weight loss was reduced by increasing the accumulative roll bonding process (ARB) cycle, and also, the size of SiC particle becomes less than 100 nm which leads to form nano-composite. This refinement of SiC particle reduces weight loss [23].

3 Study on Al-MMC: Reinforced with FA

Fly ash is combustional by-product of pulverized form of coal contain primarily alumina-silicates. Table 1 shows the wt% (approximate) of constituting chemical component of fly ash. Fly ash has lower density in contrast with parent metal (2.6 g/cm^3) and other ceramic particulates commonly reinforced in AMCs, such as SiC (3.2 g/cm^3) and Al_2O_3 (3.9 g/cm^3). Fly ash particles normally mixed with either solid spheres or hollow spheres. Solid one has industrial name of precipitator fly ash (PFA) and hollow lighter one called as cenosphere fly ash (CFA). Density of precipitator fly ash lies in between 2.1 and 2.6 g/cm^3 and often contains pores. The fly ash has particle size ranges of about 1–150 mm during the condition when received from the power plants. Size of cenosphere (CFA) particles usually distributes in between 10 and 250 μm, with approximate density in between 0.4 and 0.6 g/cm^3 [96].

3.1 Micro-FA Particle

3.1.1 Microstructure and Mechanical Charecteristics

Precipitator fly ash has higher modulus of elasticity (143–310 GPa) than base Al-metal (67–79 GPa) [96]. Hence, incorporation of FA can strengthen aluminium metal matrix. Metalographical characteristics of Al–7Si–0.35 Mg alloy composite

Table 1 Chemical composition of fly ash, in weight percent [98].

Al_2O_3	SiO_2	CaO	Fe_2O_3	MgO	K_2O	Na_2O	TiO_2	SO_3	LOI (loss of ignition)
15–30	30–70	1–5	10–20	0–2	1–5	0–2	0–2	0–2	0–10

Reproduced with permission from Elsevier, Copyright (2006)

produced by three different stir casting routes(compocasting, modified compocasting and modified compocasting followed by squeeze casting) were evaluated. Fine fly ash particles with 13 μm average particle size are used as reinforcement. Modified compocasting cum squeeze casting process helps to properly disperse the fly ash micro-particles. Better distribution of FA was then followed by only compocasting process and molten metal stir castinging process with metal moulds [85]. Two types of class C lignite fly ash one with high silicon content (MFA) and one with high calcium content (KFA) were compared in enhancing microstructure of AMC through PM processing. Microstructural morphology and electrochemical behaviour are compared with the help of SEM, EDXS, scanning Kelvin probe force microscopy (SKP-FM), open circuit potential measurements and potentiodynamic polarization. It was noticed that incorporation of the FA particles forms of a strongly heterogeneous microstructure inside AMC [71]. Microstructure and XRD observation revealed that mechanical as well tribological upgrade of AMC was normally attained when finer particulates of high-Ca ash particles were reinforced [25, 50].

Mechanical and wear behaviour of any material potentially help to understand its application area and design of components. Hence, tensile strength, yield strength, ductility, compressive strength, toughness and micro-hardness test have been carried out by most of the researchers during the development of micro-fly ash particle-based AMCs. Several fabrication routes are followed in this regard such as impeller mixing [104], PM [77], stir casting [16], infiltration [62], friction stir processing [90] and compocasting [91]. Overall improved mechanical performance was noted with remarkable increase in tensile strength and hardness. Hardness and tensile strength reduced beyond 10 wt% of FA, attributed to the loss of fly ash due to floatation and removal as dross. Addition of 'Nucleant 2' (containing titanium and boron in the ratio 6:1) as grain refiner showed decreasing trend of percentage of elongation with increase in % of FA cenosphere reinforced with LM6 alloy [121]. Rising wt% of fly ash particles in the AA6063 alloy rapidly lowers the energy absorption capacity during fractural failure. The presence of silica and mullite abundance in fly ash particles enhances the brittle and hard nature of aluminium composites when reinforcing particles content increases [90]. Elastic-plastic fracture toughness (EPFM) of AA2024 fly ash composites was in the range of 6–15 kJ/m^2 where for the base alloy material the value was found to be 25 kJ/m^2 [16]. Machinability (turning) properties were examined minutely when Al-composite was hybridized by FA and graphite. Attempt has been made to optimize the machining parameters using artificial neural network (ANN) technique. Cutting speed and reinforcement percentage were found to be the important parameters which can control the surface finish of the machined composites [64]. Damping capacity of Stircast A356 Al-MMC with 6 and 12 vol% fly ash reinforced composites was 1.2 and 1.5 times the base alloy. Dynamic mechanical thermal analyser (DMTA) was employed to generate the data for damping capacity of the prepared samples, tested under a dynamic load of 10 N and static load of 20 N at 10 Hz [119]. The bending strength of hot extruded aluminium matrix composites reinforced with fly ash (53 μm) was raised from 279 MPa till 302.6 MPa or 8.5% with increasing FA weight percentage from 5 to 12.5 [118].

3.1.2 Thermal and Electrical Behaviour

Thermal properties if compared in between FA and aluminium, it can be seen that precipitator fly ash has thermal conductivity in the range of 0.6–0.16 W/m K and melting point is more than 1200 °C, whereas for Al the values are 237 W/m K and 660 °C, respectively [96]. P. K. Rohatgi and his team have checked pressure infiltrated Al-FA cenosphere composites for some mechanical properties, thermal expansion coefficient (CTE) and chemical reaction between FA and molten aluminium. It was remarked that 20 vol% fly ash showed the significant advantages in aluminium fly ash (ALFA) composites. The density and coefficient of thermal expansion of castings decrease with high applied pressure and infiltration time, their tribological properties improved as the fly ash proportion increases [44, 63, 97]. The thermal elongation of the AA6063-FA decreased with increase in the FA reinforcement content in the matrix. Experimental results showed that the CTE of the FA powder (size 44 μm) increased between 298 and 400 K and remained relatively constant in the range of 400–750 K. The CTE of AA6063 alloy was observed to be in the range of 22.44 × 10^{-6}/K to 24.19 × 10^{-6}/_K at temperature between 298 and 750 K. With 12 wt% FA content, the CTE of composite reduced to 11.5 × 10^{-6}/K. Compared to 24.19 × 10^{-6}/K of pure AA6063 alloy, which is 88% reduction in vlue [91]. Al-FA composites showed initial increase in CTE upto 400 K then remains almost constant. A large difference of CTE between alloy and FA develops internal stress in the composite resulted into reduction of CTE of the composite [63].

Electrical resistance of precipitator fly ash is in the range of 10^{9}–10^{12} Ω cm which is very much higher than aluminium metal (3.15 × 10^{-6} Ω cm) [96]. This gives researchers an option to utilize FA for increasing the electrical shielding effect of Al-alloy. Electrical properties like electical conductivity, electromagnetic interference shielding effectiveness (EMSE) of aluminium alloy fly ash composites were examined by sevaral reserchers [31, 85]. EMSE charecteristics of the base matrix (aluminium alloy) were enhanced under the frequency ranges 30 kHz–600 MHz by using the fly ash cenosphere particles. The results showed satisfactory outcome of using fly ash as reinforcing matrial in Al-composites.

3.1.3 Tribological Behaviour

In the year 1997, P. Rohatgi et al. tested stir casted A356/5 vol% micro-size fly ash cenosphere reinforced composite for abrasive wear nature by rubbing against hard SiC_p abrasive paper [96]. Wear debris analysis along with SEM analysis of the worn out sample surfaces and subsurface revealed that primary wear on the base alloy was caused through micro-cutting, whereas microcutting and delamination caused due to crack propagation were responsible for the composite wear. The cracks propagated through interfaces of FA, abrasive particles and the alloy matrix, those majorly under the rubbing zone. Higher load reduced the specific wear rates and frictional force during abrasive wear. This is because of wear debris those were accumulated in

between the gap of the abrading SiC particles and resulted into lowering the abrasivity of the particles.

Micro-size FA particles mixed with cenosphere and assorted size of 10–100 μm were used to produce AMCs through liquid metallurgy route (squeeze cast and stir cast), and the corrosion behaviour was studied by several researchers [18, 63, 67, 86, 108]. All results show similar result which clears that corrosion resistance of FA reinforced AMC becomes poor with increasing fly ash content. The presence of fly ash particles appeared to initiate pitting corrosion around the particles. Stir caste AMCs containing 5%, 10% and 15 wt% fly ash of size 10 μm were examined under slurry erosive environment, and it was observed that resistance to wear increases with increase in weight percentage of fly ash. This is also seen that erosive wear is extended in the case of basic media than acidic and neutral media [67].

In many literatures, tribological wear performance test using pin-on-disc test rig was conducted under dry sliding condition on Al-fly ash composites reinforced with different wt% [1, 109]. All of them show there is a definite increase in the wear resistance of Al-alloy by the addition of fly ash particles. The wear debris analysis of the specimen concludes that both adhesive and abrasive wear mechanisms dominate wear of composites at light load and denomination is more predominant at heavy load [106]. Taguchi and analysis of variance (ANOVA) techniques confirmed that percentage of FA content and applied load as the primary influencing factors on wear behaviour then sliding speed may be considered secondary factor. Optimized values for minimizing rate of wear were fly ash as 20 wt%, applied load to be 5 N and sliding speed as 1 m/s. Mild wear mechanism was observed when speed becomes higher and applied load was less. On the other hand, severe rate of wear was found at greater applied load and speed [83]. It was also understood that applied load is the main affecting factor that changed the mechanism of wear from mild to severe. Thus, Taguchi and ANOVA combinedly showed a better tool to find out the significance of the influencing parameters in controlling the tribological behaviour of the prepared composites.

3.2 Nano-FA Particle

Nano-size fly ash particles can be produced by high-energy ball milling technique, which will be easy and economical to carry out. This particle size reduction process is applicable to any grade of solid materials and may be scaled up to large-scale production. Improved wettability was observed when nano-aluminium-FA composites were fabricated using ultrasonic cavitation-based mixing route. Melting furnace, ultrasonic probe, ultrasonic generator and transducer and inert gas protection nozzles are used to fabricate the nano-composite. Addition of 3 wt% nano-fly ash particles in AA2024 alloy increases the compressive load taking capacity from 289 to 345 MPa, which is 19.3% improvement [78]. Recently, nano-fly ash (NFA) composite is fabricated through ultrasonic-assisted stir casting process where 76 nm size FA particles are added into Al6063 alloy. Tensile and Vickers hardness increase with increase in

NFA weight percentage beyond 2%. Study revealed that friction stir welding process (FSW) better joins Al6063/NFA composites by achieving grain refinement at the stirred zone [42]. Dry sliding test was carried to understand the impact of exerted pressure, sliding speed, sliding time and wt% of nano-FA particles in the Al-metal matrix composites by Katrenipadu and Gurugubelli [53]. Statistically generated regression model using Minitab R17.1.0 tool was used to forecast the wear rate of the developed samples considering FA %, normal loads and time periods as variables. It was reported that resistance against wear out was improved with higher content of fly ash, upto 10 wt%. Effect of nano-size FA addition was checked again by varying weight percentage in between 5 and 10%. Considerable improvement of composite was noticed in hardness and reciprocating tribological behaviour at 10% FA content in the aluminium matrix [53].

4 Study on Hybrid Al-MMC: Reinforced with FA and SiC (Micro-particles)

Concept of hybrid aluminium metal matrix composites came into force at the end of twentieth century, where individual properties of two discontinuous materials are utilized to get desirable characteristics of Al-alloy. Hybrid AMCs can be formed by the combination of synthetic ceramic, industrial and agro waste derivatives.

Comparison was made using erosive wear response between SiC reinforced AMCs and fly ash reinforced AMCs. This study has claimed that Al-SiC better wear resistant in mining environment than Al-alloy and Al-FA MMC, while poor than matrix alloy in basic environment but better than Al-FA [54]. M. O. Bodunrin et al. have found that the more and more study needed to improve the hybrid AMCs that contains fly ash. Comparison also needs to be made with the single reinforced aluminium metal matrix composites that is being reinforced with synthetic reinforcement [19].

Combinations available so far can be categorized in three types as follows:

1. hybrid AMCs reinforced by double synthetic ceramic phases.
2. hybrid AMCs reinforced by one ash from agro-waste derivative and other with one synthetic ceramic particulate.
3. hybrid AMCs reinforced with waste from industry combined with a synthetic reinforcement [19].

4.1 Microstructure and Mechanical Characteristics

Silicon carbide along with FA particles of 53 μm sizes are well distributed into aluminium 7075 alloy through vortex method in different weight percentage ranging

in between 0 and 10%. Electron backscattered diffraction (EBDS) images in Fig. 8a of hybrid composite samples show that the average grain size inside the aluminium alloy reinforced with FA and SiC particulates is significantly less than the matrix alloy (refer to Fig. 8b). The developed finer grains are attributed to the dynamic re-crystallization owed to well built plastic deformation, and conclusion has been made from the evidence that the FA particles are actually refining grain size [52].

Charles and Arunachalam [22] have fabricated HAMC by mixing different volume fraction (10, 15 and 20%) of SiC particles and fixed 10 vol% of fly ash (both of size 30–100 μm) in to LM10 Al-alloy using both powder metallurgy (PM) and stir casting route. Hardness (refer to Fig. 9a), tensile strength (refer to Fig. 9b) and dry sliding wear test result exhibited better properties of stir casted specimen than produced via PM route. This was attributed to the strong interfacial bonding created inside the casted specimen than PM specimen.

An rising trend of mechanical properties was found with enrichment of SiC particles by keeping fly ash wt% as constant in AA6061 aluminium alloy [105]. Reverse case is also observed by Gikunoo et al. [41] where effect of FA addition into A535 alloy and 10 wt% SiC (size 1–100 μm) AMC through proprietary stir casting technique was investigated. Result shows there was degradation in mechanical characteristics and impact load taking capacity of the MMCs. This was attributed to the depletion of strength between magnesium atoms and the alloy matrix in solid solution and also to the presence of porosity. Also, few findings based on reinforcement particle size are listed in Table 2 and presented with change in percentage of density, tensile strength and hardness.

4.2 Thermal Behaviour

Thermo-mechanical analysis (TMA) was conducted to study thermal expansion coefficient (CTE) of A535 aluminium alloy and its composites when reinforced by FA and SiC. Composite specimens were prepared by combining different proportion of SiC and FA particles in between 5 and 15 wt%. Studies revealed that CTE of A535 alloy reduced with the inclusion of fly ash and silicon carbide as reinforcements. It was also noticed that SiC particulates were more effective in controlling thermal expansion behaviour of the composite than fly ash particles [127]. SiC provides more surface area than FA for good interfacial boding hence provides higher restriction to thermal elongation of matrix alloy. Electromagnetic stir casting (EMS) with stiring speed of 210 rpm setup that was used to fabricate hybrid metal matrix composite (A356/SiC/FA) results into homogeneous spreading of FA and SiC particles in A356 alloy. It was also found that smaller size SiC was deposited at the grain boundaries. HAMC reinforced with different weight fraction combination (0–20%) of SiC and FA (both particle size 25 μm) was heated at 450 °C in electric furnace, and change in dimension of the samples is checked to measure thermal expansion behaviour.

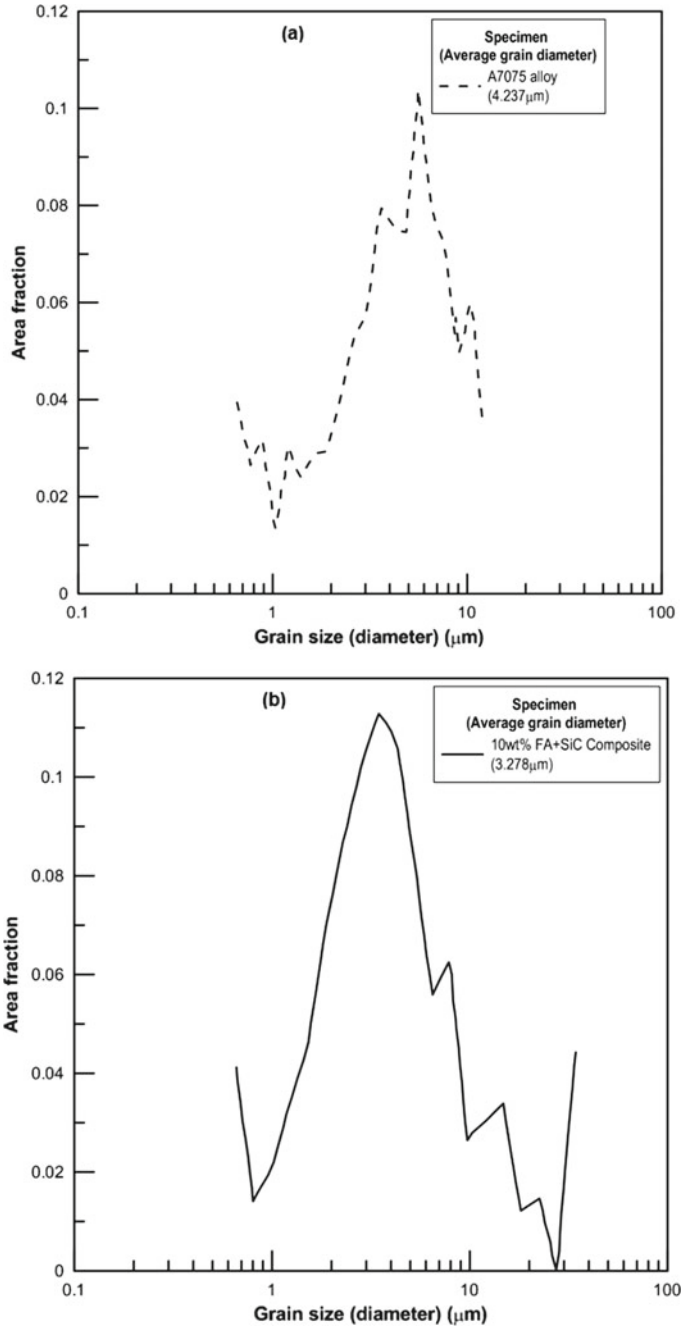

Fig. 8 EBSD analysis for **a** base alloy and **b** 10% (SiC + FA) composite [52]. Reproduced with permission from Elsevier, Copyright (2019)

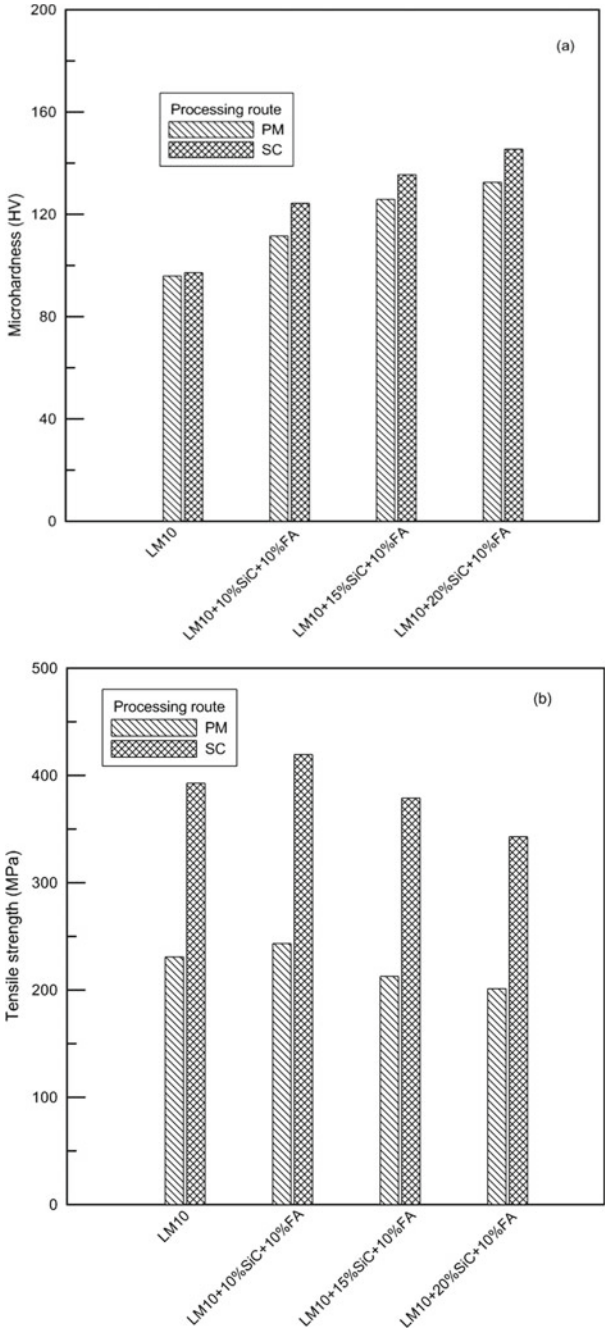

Fig. 9 **a** Microhardness, **b** tensile strength of SiC/FA HAMC [22]

Table 2 Some selected outcome on effect of reinforcement (FA and SiC) content and particle size on density, tensile strength and hardness of HAMC

Source	Aluminium alloy matrix	Fabrication process	Reinforcement			Density	Tensile strength	Hardness
			Material	Size (μm)	wt% combined			
[22]	LM10	SC + PM	SiC + FA	SiC and FA = 30–100	Volume % of SiC = 10, 15 and 20% FA = 15% (Const)	NA	6.82% increase @ 10 vol% SiC and FA	49.81% increase @ 20 vol % SiC and 10 vol% FA
[68]	Al-4.5% Cu alloy	SC subjected to solutionizing and T6 heat treatment	FA + SiC	1–10	FA and SiC combined in 5%, 10, and 15% weight (in equal proportion) + Mg (0.5% by wt) for wettability	~4% decrease @ 7.5 wt% SiC and FA	~15% increase @ 7.5 wt% SiC and FA	~6.5% increase @ 7.5 wt% SiC and FA
[69]	Al2024	Stir casting	SiC + FA + Mg (1.5%)	NA	5–10% alternatively	20.77% decrease @ 10 wt% all	24.15% increase @ 10 wt% SiC and FA	19.77% increase @ 10 wt% SiC and FA
[105]	AA6061	SC	SiC + FA	NA	SiC 7.5–10% + FA 7.5% (fixed) + 1% Mg (for wettability)	NA	23.12% increase @ 10 wt% SiC and 7.5 wt%	15.8% increase @ 10 wt% SiC and 7.5 wt%% FA
[41]	A535	SC subjected to solution heat treatment	SiC + FA	1–100	5% SiC + 5% FA, 10% FA and 15%FA	NA	~ 38% decrease @5wt% SiC and FA	~ 15.7% decrease @5wt% SiC and FA
[32]	A356	EMSC subjected to heat treatment	SiC + FA	25 both	0–20% (SiC:FA = 20:0, 15:5, 10:10, 5:15, 0:20)	12.5% decrease @5wt% SiC and 15wt%FA	58.5% increase @15wt% SiC and 5wt%FA	30.2% increase @15wt% SiC and 5wt%FA

(continued)

Table 2 (continued)

Source	Aluminium alloy matrix	Fabrication process	Reinforcement			Density	Tensile strength	Hardness
			Material	Size (μm)	wt% combined			
[129]	Al6082	SC	SiC, FA, Basalt	NA	10% SiC, 5% SiC + 5% FA and 5% SiC + 5% Basalt	NA	~44.18% increase @ 5 wt% SiC and FA	~22% increase @ 5 wt% SiC and FA
[65]	AA 2024	SC	SiC + FA	FA = 70	2.5, 5 and 7.5% each of SiC and FA equally added	9.43% decrease @ 7.5 wt % SiC and FA	NA	77.42% increase @ 7.5 wt% SiC and FA
[107]	Aluminium powder with 48 μm (250 mesh)	PM	SiC (400 mesh) + FA 53 μm (270 mesh)	SiC = NA FA < 53	SiC = 10% (const), FA = 5,10,15%	~3% decrease @ 10 wt%SiC and 15 wt% FA	NA	~32% increase @ 10 wt% SiC and FA
[92]	Al6082	SC	SiC + FA	SiC = 62 FA = 53	2.5, 5 and 7.5% each of SiC and FA	NA	~13.6% increase @ 7.5 wt % SiC and FA	39.82% increase @ 7.5 wt% SiC and FA
[9]	AA7075	SC	SiC + FA, Al_2O_3 + FA, + 2% Mg	SiC = 53, Al_2O_3 = 53 FA = 53–106	1.5, 3 and 4.5% each in equal proportion	2.5% decrease @ 4.5 wt% SiC and FA	15.02% increase @ 4.5 wt% SiC and FA	82.87% increase @ 4.5% SiC and FA
[52]	A7075	SC	SiC + FA	53	2.5 and 5% each in equal proportion of SiC and FA	13.12% decrease @ 5 wt% SiC and FA	~27.78% increase @ 5 wt% SiC and FA	39.21% increase @ 5 wt% SiC and FA

PM powder metallurgy, *SC* stir casting, *NA* not available, *EMSC* electro magnetic stir casting, *FA* fly ash

A356/15%SiC/5%FA HAMC was observed to be appropriate for various applications for its higher strength characteristics and lower change in dimension during thermal expansion test [32].

4.3 Tribological Behaviour

Pressure infiltration technique was adopted by Escalera-Lozano et al. [36] to prepare hybrid Al/SiC_p/spinel composites from α-SiC_p (size 75 μm), FA (size 90 μm) and recycled aluminium. Two types of specimens are prepared with SiC and FA volumetric ratio of 3:2. Dextrin was added in a weight percentage of eight along with approximate 0.5 ml distilled water. In one type (for type A), FA is used as-received condition, and for another type (type B), FA is calcinated at 900 °C for 30 min. Aluminium composites reinforced with SiC produced by the melt infiltration process under go the following reaction (Eq. 3) which is relevant to the potential attack of Silicon carbide by the melted aluminium and the ensuing degradation.

$$3SiC + 4Al = Al_4C_3 + 3Si \tag{3}$$

Corrosion test was performed with both type A (for 1 month) and B (for 11 months) samples exposed to indoor atmosphere with average relative humidity 54%, ambient temperature (min 15 ± 40 °C to max 26 ± 50 °C). Potential attack of SiC by liquid aluminium was fully avoided by the help of SiO_2 present in the FA, the reaction of present carbon in the FA with aluminium continues to form Al_4C_3. Fourier transform infrared spectroscopy (FTIR), XRD, SEM of powdery corrosion product revealed that calcined fly ash due to the absence of carbon avoids the chemical degradation of the composites rather than as-received condition.

A composite material for bearing bush was suggested using Al-4.5% Cu alloy (fly ash + SiC) after investigation of micro-structure, fluidity, hardness, density, impact load resistance, dry sliding wear along with the slurry erosive wear and fog corrosion test [68]. Samples were prepared after quenching stir casted hybrid composites in hot water by varying combined FA and SiC (both size 1–10 μm) wt% in 5, 10 and 15% (equal proportion). Study shows that mechanical properties (hardness, UTS, compression strength, impact strength) increases while properties like fluidity, density, dry sliding wear, cof, frictional force and corrosion resistance decreases with increasing wt% of SiC and FA. Slurry of silica sand distilled water in ratio 1:2 with different pH values (neutral, basic and acidic) was used for erosive wear test, and the wear in case of basic is more than acidic or neutral media. SEM micrograph of eroded specimen shows pitting at some places.

Thermal treatment like carbothermal reduction of fly ash under reducing environment as shown in Fig. 10 was used to prepare one new in-situ ternary ceramic composite [43, 93]. SEM, XRD and EDX results has confirmed in-situ conversion of SiO_2 to SiC in region of Al_2O_3 available in the FA. Mechanical, physical and tribological performance of novel aluminium fly ash metal matrix composite (ALFMMC) are

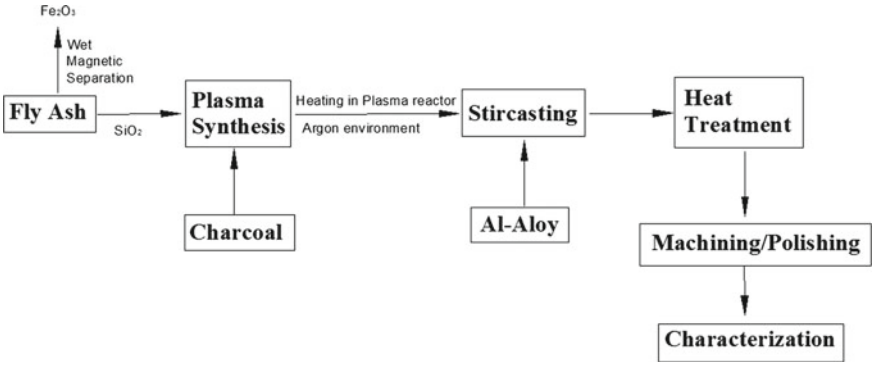

Fig. 10 Schemetic diagram of carbothermal reduction process of ALFMC production

checked for comparison with base alloy. The Accelerated ageing behaviour showed remarkable increase in strength and wear resistance of developed alloy composite. The author concluded that Al6061PSFA composite has great potential for future application considering production cost as well as material characteristics.

Al-hybrid composites reinforced with both silicon carbide and fly ash was developed for conducting wear test under dry sliding condition using Ducom pin-on-disc tribo tester in accordance with the ASTMG-99, [65, 66, 107]. Shaikh et al. study [107] followed solid-state PM route for the fabrication while Kurapati et al. [65] have followed liquid-state stir casting path. Required proportion of aluminium powder of 48 μm (250 mesh), SiC (400 mesh) and FA-53 μm (270 mesh) powder was prepared by planetary ball mill (FRITSCH Pulvrissettle MM-1552) with steel ball of 8 mm diameter, ball-to-powder ratio was 10:1, grinding at 600 rpm for 20 min. Then powders are pressed with uniaxial hydraulic machine run manually with a pressure of 400 MPa in a die lubricated with zinc stearate, compaction dwell 30 s. Then sintered in electrical furnace of tabular shape under argon gas environment at temperature of 450–470 °C. The samples were gradually cooled to normal temperature in controlled environment. AA2024 alloy with 10 wt% SiC and 10 wt% FA showed higher hardness and better wear resisting property; hence, it was suggested to be used for high wear resisting application. Further, increase in FA content sample showed poor wear resistance due to the highest porosity/cluster formation. Statistical analysis of wear done by Kurapati et al. [65] has reported that wear reduces with increasing wt% (5, 10 and 15%) of FA and SiC in equal proportion. Taguchi L27 orthogonal array test design based on Taguchi's signal-to-noise ratio and analysis of variance (ANOVA) were used to find out the influencing factors on the wear behaviour of hybrid composite. Rank of factors got after analysis are: (i) applied load (causes 43.83% of the wear), (ii) sliding time (causing 28.47%), (iii) reinforcement wt% (causing 20.10% of the wear). It was also observed by the author that response surface methodology (RSM) model matched more accurately with the experimental results than multiple linear regression model (MLR).

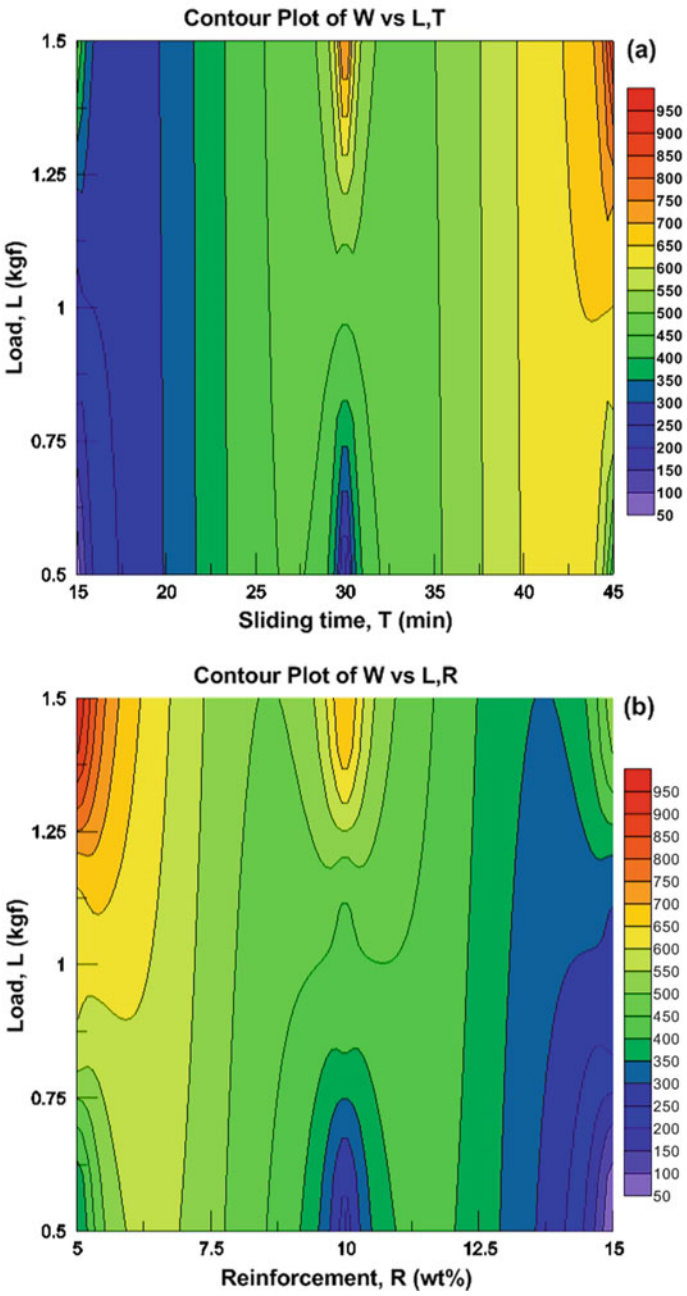

Fig. 11 Two-dimensional (orthographic) coloured map of wear in μm (W). **a** with respect to sliding time (*T*, min), load (*L*, kgf), **b** with respect to reinforcement wt% (*R*), load (*L*, kgf), **c** with respect to sliding time (*T*, min), reinforcement wt% (*R*), [65]

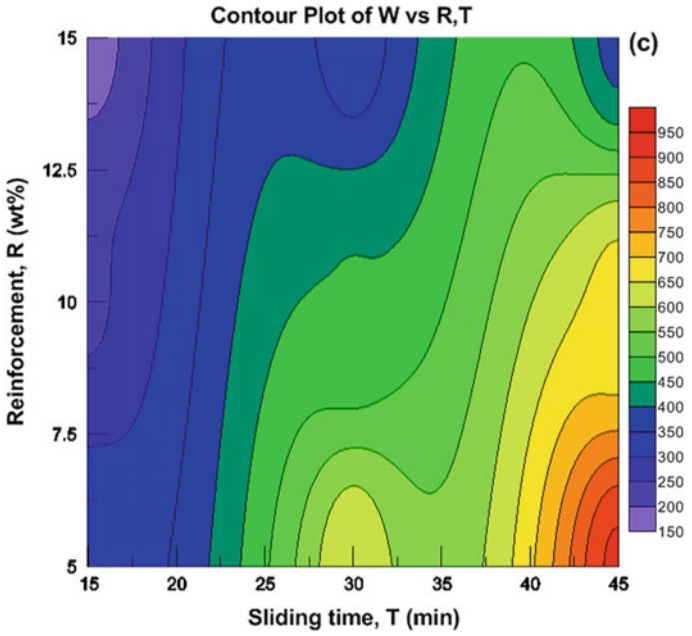

Fig. 11 (continued)

Contour plot of wear in Fig. 11a–c shows different wear loss with reference to any two effecting parameters.

4.4 Machining Behaviour

EDM done on the hybrid composite specimen prepared using copper electrode for 30 min trail run [22] revealed metal removal rate (MRR) and tool wear rate (TWR) decreases on increasing vol% of SiC and pulse duration. Both of these were higher for PM route specimen and increases for increase in current. This was attributed to the higher interfacial bonding achieved by casting than powder metallurgy route. It was also concluded that three-level full factorial technique can be more efficient to develop mathematical model for predicting MRR and TWR in Electric discharge machining of HAMCs.

5 Conclusions

This present review study has focused on effects of SiC and fly ash on Al-alloy for improving physical, chemical, mechanical, tribological and thermal properties. This chapter explained the works done by the investigators towards the development of aluminium metal matrix composites. Various microstructural changes are described to attribute the outcome of strength and wear behaviour. Therefore, it is expected that bunch of opportunities and scopes will be opened with this overview and that will widen the area of product development techniques toward getting reliable material with high quality. Based on the previous studies, conclusions are drawn as below.

1. Hybrid AMCs reinforced with ceramics have improved the mechanical strength more than single reinforcement.
2. Primary reinforcements must be ceramic for better hardness, mechanical strength and wear resistance. Hence, silicon carbide (SiC) can be effective as ceramic with high hardness.
3. Secondary/complementary reinforcement may be agro/industrial waste for low cost, easy availability, improvement in fractural toughness. Fly ash can be effective as it has balanced content of silica (SiO_2) and alumina (Al_2O_3)
4. Reinforcement wt% must be confined within 15% for enhancing the dominating properties.
5. Modified stir casting (two steps) or semisolid stirring along with heat treatment is economical method and quite useful for well dispersion of the reinforcement in the base matrix.
6. Impact strength (fractural toughness), corrosion resistance and ductility (% of elongation) are reducing with increase in wt% (especially FA), which need to be retained or optimized in the timeline of AMC development
7. HAMCs reinforced with SiC and FA have good potential in strengthening mechanical behaviour though literatures on thermal behaviour, machining behaviour and tribological characteristics of AMCs with such hybrid reinforcements for the applicability in different challenging environment are limited.
8. Nano-reinforcement while used in the Al-matrix holds better behavioural characteristics in contrast with micro-size particles though use of nanoscale particles (both SiC and FA) in fabricating HAMC are still at the developing stage.
9. Ultrasonic-assisted stir casting process has more possibilities than the usual stir casting process in case of nanoparticle reinforced Al-composite production. However, still there exist gap of study for opting efficient techniques for homogeneous spreading of nanoscale reinforcements, as agglomeration is a major issue to be dealt with.

References

1. Admile B, Kulkarni K, Sonawane SA (2014) Application of Taguchi method for optimization of process parameters for wear loss of LM25/flyash composite. Int J Innov Eng Technol (IJIET) Appl 4(4):24–29
2. Alaneme KK, Ademilua BO, Bodunrin MO (2013) Mechanical properties and corrosion behaviour of aluminium hybrid composites reinforced with silicon carbide and bamboo leaf ash. Tribol Ind 35(1):25–35
3. Alaneme KK, Aluko AO (2012) Fracture toughness (K 1C) and tensile properties of as-cast and age-hardened aluminium (6063) silicon carbide particulate composites. Scientia Iranica 19(4):992–996. https://doi.org/10.1016/j.scient.2012.06.001
4. Alaneme KK, Ekperusi JO, Oke SR (2018) Corrosion behaviour of thermal cycled aluminium hybrid composites reinforced with rice husk ash and silicon carbide. J King Saud Univ Eng Sci 30(4):391–397. https://doi.org/10.1016/j.jksues.2016.08.001
5. Alaneme KK, Sanusi KO (2015) Microstructural characteristics, mechanical and wear behaviour of aluminium matrix hybrid composites reinforced with alumina, rice husk ash and graphite. Eng Sci Technol Int J 18(3):416–422. https://doi.org/10.1016/j.jestch.2015.02.003
6. Alpas AT, Zhang J (1992) Effect of SiC particulate reinforcement on the dry sliding wear of aluminium-silicon alloys (A356). Wear 155(1):83–104. https://doi.org/10.1016/0043-1648(92)90111-K
7. Amirkhanlou S, Niroumand B (2010) Synthesis and characterization of 356-SiCp composites by stir casting and compocasting methods. Trans Nonferrous Metals Soc China (English Edition) 20(suppl. 3):s788–s793. https://doi.org/10.1016/S1003-6326(10)60582-1
8. Amouri K et al (2016) 'Microstructure and mechanical properties of Al-nano/micro SiC composites produced by stir casting technique. Mater Sci Eng A 674:569–578. https://doi.org/10.1016/j.msea.2016.08.027
9. Anand Babu K, Venkataramaiah P, Dharma Reddy K (2018) Mechanical characterization of aluminium hybrid metal matrix composites synthesized by using stir casting process. Mater Today Proc 5(14):28155–28163. https://doi.org/10.1016/j.matpr.2018.10.058
10. Bahrami M et al (2014) On the role of pin geometry in microstructure and mechanical properties of AA7075/SiC nano-composite fabricated by friction stir welding technique. Mater Design 53:519–527. https://doi.org/10.1016/j.matdes.2013.07.049
11. Bahrami M, Dehghani K, Besharati Givi MK (2014) 'A novel approach to develop aluminum matrix nano-composite employing friction stir welding technique . Mater Design 53:217–225. https://doi.org/10.1016/j.matdes.2013.07.006
12. Bai BNP, Ramasesh BS, Surappa MK (1992) Dry sliding wear of A356-Al-SiCp composites. Wear 157(2):295–304. https://doi.org/10.1016/0043-1648(92)90068-J
13. Bajpai G et al (2017) Investigation and testing of mechanical properties of Al-Nano SiC composites through cold isostatic compaction process. Mater Today Proc 4(2):2723–2732. https://doi.org/10.1016/j.matpr.2017.02.149
14. Balasubramanian I, Maheswaran R (2015) Effect of inclusion of SiC particulates on the mechanical resistance behaviour of stir-cast AA6063/SiC composites. Mater Design 65:511–520. https://doi.org/10.1016/j.matdes.2014.09.067
15. Bathula S, Saravanan M, Dhar A (2012) Nanoindentation and wear characteristics of Al 5083/SiCp nanocomposites synthesized by high energy ball milling and spark plasma sintering. J Mater Sci Technol 28(11):969–975. https://doi.org/10.1016/S1005-0302(12)60160-1
16. Bhandakkar A, Prasad RC, Sastry SML (2014) Fracture toughness of AA2024 aluminum fly ash metal matrix composites. Int J Compos Mater 4(2):108–124. https://doi.org/10.5923/j.cmaterials.20140402.10
17. Bhoi NK, Singh H, Pratap S (2019) Developments in the aluminum metal matrix composites reinforced by micro/nano particles—a review. J Compos Mater 2199831986530. https://doi.org/10.1177/0021998319865307

18. Bieniaś J et al (2003) Microstructure and corrosion behaviour of aluminum fly ash composites. J Optoelectron Adv Mater 5(2):493–502
19. Bodunrin MO, Alaneme KK, Chown LH (2015) Aluminium matrix hybrid composites: a review of reinforcement philosophies; mechanical, corrosion and tribological characteristics. J Mater Res Technol 4(4):434–445. https://doi.org/10.1016/j.jmrt.2015.05.003
20. Candan E, Ahlatci H, Çïmenoğlu H (2001) Abrasive wear behaviour of Al-SiC composites produced by pressure infiltration technique. Wear 247(2):133–138. https://doi.org/10.1016/S0043-1648(00)00499-3
21. Carreño-Gallardo C et al (2014) Dispersion of silicon carbide nanoparticles in a AA2024 aluminum alloy by a high-energy ball mill. J Alloy Compd 586(SUPPL. 1):68–72. https://doi.org/10.1016/j.jallcom.2013.03.232
22. Charles S, Arunachalam VP (2004) Property analysis and mathematical modeling of machining properties of aluminium alloy hybrid (Al-alloy/SiC/flyash) composites produced by liquid metallurgy and powder metallurgy techniques. Indian J Eng Mater Sci 11(6):473–480
23. Darmiani E et al (2013) Reciprocating wear resistance of Al-SiC nano-composite fabricated by accumulative roll bonding process. Mater Des 50:497–502. https://doi.org/10.1016/j.matdes.2013.03.047
24. Dasgupta R, Meenai H (2005) SiC particulate dispersed composites of an Al-Zn-Mg-Cu alloy: Property comparison with parent alloy. Mater Charact 54(4–5):438–445. https://doi.org/10.1016/j.matchar.2005.01.012
25. David Raja Selvam J, Robinson Smart DS, Dinaharan I (2013) Microstructure and some mechanical properties of fly ash particulate reinforced AA6061 aluminum alloy composites prepared by compocasting. Mater Design 49:28–34.https://doi.org/10.1016/j.matdes.2013.01.053
26. Deb S, Panigrahi SK, Weiss M (2018) Development of bulk ultrafine grained Al-SiC nano composite sheets by a SPD based hybrid process: experimental and theoretical studies. Mater Sci Eng A 738:323–334. https://doi.org/10.1016/j.msea.2018.09.101
27. Dehghan Hamedan A, Shahmiri M (2012) 'Production of A356–1wt% SiC nanocomposite by the modified stir casting method. Mater Sci Eng A 556:921–926. https://doi.org/10.1016/j.msea.2012.07.093
28. Dehnavi MR et al (2014) Effects of continuous and discontinuous ultrasonic treatments on mechanical properties and microstructural characteristics of cast Al413-SiCnp nanocomposite. Mater Sci Eng A 617:73–83. https://doi.org/10.1016/j.msea.2014.08.042
29. Dong PY et al (2013) Microstructures and properties of A356–10%SiC particle composite castings at different solidification pressures. Trans Nonferrous Metals Soc China (English Edition) 23(8):2222–2228. https://doi.org/10.1016/S1003-6326(13)62721-1
30. Dong X, Shin YC (2017) Multi-scale modeling of thermal conductivity of SiC-reinforced aluminum metal matrix composite. J Compos Mater 51(28):3941–3953. https://doi.org/10.1177/0021998317695873
31. Dou Z et al (2007) Electromagnetic shielding effectiveness of aluminum alloy-fly ash composites. Compos A Appl Sci Manuf 38(1):186–191. https://doi.org/10.1016/j.compositesa.2006.01.015
32. Dwivedi SP, Sharma S, Mishra RK (2014) Microstructure and mechanical behavior of A356/SiC/Fly-ash hybrid composites produced by electromagnetic stir casting. J Brazilian Soc Mech Sci Eng 37(1):57–67. https://doi.org/10.1007/s40430-014-0138-y
33. El-Daly AA et al (2012) Synthesis of Al/SiC nanocomposite and evaluation of its mechanical properties using pulse echo overlap method. J Alloys Cmpd 542:51–58. https://doi.org/10.1016/j.jallcom.2012.07.102
34. El-Kady O, Fathy A (2014) Effect of SiC particle size on the physical and mechanical properties of extruded Al matrix nanocomposites . Mater Design 54:348–353. https://doi.org/10.1016/j.matdes.2013.08.049
35. Elkady OA et al (2019) Microwave absorbing efficiency of Al matrix composite reinforced with nano-Ni/SiC particles. Results Phys 12:687–700. https://doi.org/10.1016/j.rinp.2018.11.095

36. Escalera-Lozano R et al (2007) Corrosion characteristics of hybrid Al/SiCp/MgAl2O4 composites fabricated with fly ash and recycled aluminum. Mater Charact 58(10):953–960. https://doi.org/10.1016/j.matchar.2006.09.012
37. Fadavi Boostani A et al (2016) Solvothermal-assisted graphene encapsulation of SiC nanoparticles: a new horizon toward toughening aluminium matrix nanocomposites. Mater Sci Eng A 653:99–107. https://doi.org/10.1016/j.msea.2015.12.008
38. Ghosh S, Sahoo P, Sutradhar G (2012) Wear behaviour of Al-SiCp metal matrix composites and optimization using taguchi method and grey relational analysis. J Miner Mater Charact Eng 11(11):1085–1094. https://doi.org/10.4236/jmmce.2012.1111115
39. Ghosh S, Sahoo P, Sutradhar G (2013) Friction performance of Al-10 % SiCp reinforced metal matrix composites using taguchi method. ISRN Tribol 2013:1–9. https://doi.org/10.5402/2013/386861
40. Ghosh S, Sahoo P, Sutradhar G (2014) Tribological properties of Al–SiC metal matrix composites: a comparison between sand cast and squeeze cast techniques. J Inst Eng (India): Series D 95(2):161–171. https://doi.org/10.1007/s40033-014-0044-6
41. Gikunoo E, Omotoso O, Oguocha INA (2005) Effect of fly ash particles on the mechanical properties of aluminium casting alloy A535. Mater Sci Technol 21(2):143–152. https://doi.org/10.1179/174328405X18601
42. Gosangi NR, Dumpala L (2019) Characterization of friction stir welded AL6063/nano fly ash composite. Mater Res Exp 6(7). https://doi.org/10.1088/2053-1591/ab179b
43. Govindarao R et al (2015) Development of a novel aluminium based metal matrix composite using insitu ternary mixture (Al_2O_3-SiC-C) prepared by thermal treatment of fly-ash . Trans Indian Inst Metals 68(5):951–958. https://doi.org/10.1007/s12666-015-0532-x
44. Guo RQ, Rohatgi PK (1998) Chemical reactions between aluminum and fly ash during synthesis and reheating of AI-fly ash composite. Metall Mater Trans B 29(3):519–525. https://doi.org/10.1007/s11663-998-0086-y
45. Hassan AM et al (2009) Wear behavior of Al-Mg-Cu-based composites containing SiC particles. Tribol Int 42(8):1230–1238. https://doi.org/10.1016/j.triboint.2009.04.030
46. Hu Q, Zhao H, Li F (2016) Microstructures and properties of SiC particles reinforced aluminum-matrix composites fabricated by vacuum-assisted high pressure die casting. Mater Sci Eng A 680:270–277. https://doi.org/10.1016/j.msea.2016.10.090
47. Huang C-W, Huang Y-F, Aoh J-N (2019) Strengthening mechanisms of aluminum matrix composite containing Cu-coated SiC particles produced by friction stir processing . J Chin Inst Eng 42(8):653–663. https://doi.org/10.1080/02533839.2019.1660231
48. Huang CW, Aoh JN (2018) Friction stir processing of copper-coated SiC particulate-reinforced aluminum matrix composite. Materials 11(4). https://doi.org/10.3390/ma11040599
49. Idrisi AH, Mourad AHI (2019) Conventional stir casting versus ultrasonic assisted stir casting process: mechanical and physical characteristics of AMCs. J Alloys Cmpd 805:502–508. https://doi.org/10.1016/j.jallcom.2019.07.076
50. Itskos G et al (2012) Synthesis of A356 Al-high-Ca fly ash composites by pressure infiltration technique and their characterization. J Mater Sci 47(9):4042–4052. https://doi.org/10.1007/s10853-012-6258-9
51. Jiang J, Wang Y (2015) Microstructure and mechanical properties of the semisolid slurries and rheoformed component of nano-sized SiC/7075 aluminum matrix composite prepared by ultrasonic-assisted semisolid stirring. Mater Sci Eng A 639:350–358. https://doi.org/10.1016/j.msea.2015.04.064
52. Kanth UR, Rao PS, Krishna MG (2019) Mechanical behaviour of fly ash/SiC particles reinforced Al-Zn alloy-based metal matrix composites fabricated by stir casting method. J Mater Res Technol 8(1):737–744. https://doi.org/10.1016/j.jmrt.2018.06.003
53. Katrenipadu SP, Gurugubelli SN (2019) Regression modeling on wear behaviour of nano fly ash—Aluminium alloy matrix composites. Emerg Mater Res 8(3). https://doi.org/10.1680/jemmr.19.00005

54. Khan MM, Dixit G (2017) Comparative study on erosive wear response of SiC reinforced and fly ash reinforced aluminium based metal matrix composite. Mater Today Proc 4(9):10093–10098. https://doi.org/10.1016/j.matpr.2017.06.327
55. Kiliçkap E et al (2005) Study of tool wear and surface roughness in machining of homogenised SiC-p reinforced aluminium metal matrix composite. J Mater Process Technol 164–165:862–867. https://doi.org/10.1016/j.jmatprotec.2005.02.109
56. Kiourtsidis GE, Skolianos SM (2002) Wear behavior of artificially aged AA2024/40 μm SiCp composites in comparison with conventionally wear resistant ferrous materials. Wear 253(9–10):946–956. https://doi.org/10.1016/S0043-1648(02)00216-8
57. Kiourtsidis GE, Skolianos SM, Litsardakis GA (2004) Aging response of aluminium alloy 2024/silicon carbide particles (SiCp) composites. Mater Sci Eng A 382(1–2):351–361. https://doi.org/10.1016/j.msea.2004.05.021
58. Kiourtsidis G, Skolianos SM (1998) Corrosion behavior of squeeze-cast silicon carbide-2024 composites in aerated 3.5 wt.% sodium chloride. Mater Sci Eng A 248(1–2):165–172. https://doi.org/10.1016/S0921-5093(98)00494-8
59. Knowles AJ et al (2014) Microstructure and mechanical properties of 6061 Al alloy based composites with SiC nanoparticles. J Alloys Cmpd 615(S1):S401–S405. https://doi.org/10.1016/j.jallcom.2014.01.134
60. Kollo L et al (2010) Investigation of planetary milling for nano-silicon carbide reinforced aluminium metal matrix composites. J Alloy Compd 489(2):394–400. https://doi.org/10.1016/j.jallcom.2009.09.128
61. Kollo L et al (2011) Nano-silicon carbide reinforced aluminium produced by high-energy milling and hot consolidation. Mater Sci Eng A 528(21):6606–6615. https://doi.org/10.1016/j.msea.2011.05.037
62. Kountouras DT et al (2013) Fly ash permeability during liquid AA7075 infiltration, as a reutilization method for novel MMCs. J Mater Eng Perform 22(8):2210–2218. https://doi.org/10.1007/s11665-013-0502-6
63. Kountouras DT et al (2015) Properties of high volume fraction fly ash/al alloy composites produced by infiltration process . J Mater Eng Perfor 24(9):3315–3322. https://doi.org/10.1007/s11665-015-1612-0
64. Kumarasamy SP et al (2017) Investigations on mechanical and machinability behavior of aluminum/flyash cenosphere/Gr hybrid composites processed through compocasting. J Appl Res Technol 15(5):430–441. https://doi.org/10.1016/j.jart.2017.05.005
65. Kurapati VB, Kommineni R (2017) Effect of wear parameters on dry sliding behavior of Fly Ash/SiC particles reinforced AA 2024 hybrid composites. Mater Res Exp 4(9). https://doi.org/10.1088/2053-1591/aa8a3e
66. Kurapati VB, Kommineni R, Sundarrajan S (2018) Statistical analysis and mathematical modeling of dry sliding wear parameters of 2024 aluminium hybrid composites reinforced with fly ash and SiC particles. Trans Indian Inst Metals 71(7):1809–1825. https://doi.org/10.1007/s12666-018-1322-z
67. Mahendra KV, Radhakrishna K (2007) Fabrication of Al-4.5% Cu alloy with fly ash metal matrix composites and its characterization. Mater Sci Poland 25(1):57–68
68. Mahendra KV, Radhakrishna K (2010) Characterization of stir cast Al-Cu-(fly ash + SiC) hybrid metal matrix Composites. J Compos Mater 44(8):989–1005. https://doi.org/10.1177/0021998309346386
69. Mahendra Boopathi M, Arulshri KP, Iyandurai N (2013) Evaluation of mechanical properties of aluminium alloy 2024 reinforced with silicon carbide and fly ash hybrid metal matrix composites. Am J Appl Sci 10(3):219–229. https://doi.org/10.3844/ajassp.2013.219.229
70. Manivannan I et al (2017) Tribological and surface behavior of silicon carbide reinforced aluminum matrix nanocomposite. Surf Interfaces 8(February):127–136. https://doi.org/10.1016/j.surfin.2017.05.007
71. Marin E et al (2012) Electrochemical study of aluminum-fly ash composites obtained by powder metallurgy. Mater Charact 69:16–30. https://doi.org/10.1016/j.matchar.2012.04.004

72. Mazahery A, Shabani MO (2012) Characterization of cast A356 alloy reinforced with nano SiC composites. Trans Nonferrous Metals Soc China (English Edition) 22(2):275–280. https://doi.org/10.1016/S1003-6326(11)61171-0
73. Mazahery A, Shabani MO (2013) Plasticity and microstructure of A356 matrix nano composites'. J King Saud Univ Eng Sci 25(1):41–48. https://doi.org/10.1016/j.jksues.2011.11.001
74. Moazami-Goudarzi M, Akhlaghi F (2016) Wear behavior of Al 5252 alloy reinforced with micrometric and nanometric SiC particles . Tribol Int 102:28–37. https://doi.org/10.1016/j.triboint.2016.05.013
75. Mosleh-Shirazi S, Akhlaghi F, Li DY (2016) Effect of SiC content on dry sliding wear, corrosion and corrosive wear of Al/SiC nanocomposites. Trans Nonferrous Metals Soc China (English Edition) 26(7):1801–1808. https://doi.org/10.1016/S1003-6326(16)64294-2
76. Mousavi Abarghouie SMR, Seyed Reihani SM (2010) Investigation of friction and wear behaviors of 2024 Al and 2024 Al/SiCp composite at elevated temperatures. J Alloys Cmpd 501(2):326–332. https://doi.org/10.1016/j.jallcom.2010.04.097
77. Moutsatsou A et al (2010) Microstructural characterization of PM-Al and PM-Al/Si composites reinforced with lignite fly ash. Mater Sci Eng A 527(18–19):4788–4795. https://doi.org/10.1016/j.msea.2010.04.001
78. Narasimha Murthy I, Venkata Rao D, Babu Rao J (2012) Microstructure and mechanical properties of aluminum-fly ash nano composites made by ultrasonic method. Mater Des 35:55–65. https://doi.org/10.1016/j.matdes.2011.10.019
79. Natarajan N, Vijayarangan S, Rajendran I (2006) Wear behaviour of A356/25SiCp aluminium matrix composites sliding against automobile friction material. Wear 261(7–8):812–822. https://doi.org/10.1016/j.wear.2006.01.011
80. Ozben T, Kilickap E, Çakir O (2008) Investigation of mechanical and machinability properties of SiC particle reinforced Al-MMC. J Mater Process Technol 198(1–3):220–225. https://doi.org/10.1016/j.jmatprotec.2007.06.082
81. Ozden S, Ekici R, Nair F (2007) Investigation of impact behaviour of aluminium based SiC particle reinforced metal-matrix composites. Compos A Appl Sci Manuf 38(2):484–494. https://doi.org/10.1016/j.compositesa.2006.02.026
82. Palanikumar K, Karthikeyan R (2007) Assessment of factors influencing surface roughness on the machining of Al/SiC particulate composites. Mater Des 28(5):1584–1591. https://doi.org/10.1016/j.matdes.2006.02.010
83. Palanisamy S, Ramanathan S, Rangaraj R (2013) Analysis of dry sliding wear behaviour of aluminium-fly ash composites: the Taguchi approach. Adv Mech Eng. https://doi.org/10.1155/2013/658085
84. Prabu SB et al (2006) Influence of stirring speed and stirring time on distribution of particles in cast metal matrix composite. J Mater Process Technol 171(2):268–273. https://doi.org/10.1016/j.jmatprotec.2005.06.071
85. Rajan TPD et al (2007) Fabrication and characterisation of Al-7Si-0.35Mg/fly ash metal matrix composites processed by different stir casting routes. Compos Sci Technol 67(15–16):3369–3377. https://doi.org/10.1016/j.compscitech.2007.03.028
86. Ramachandra M, Radhakrishna K (2005) Synthesis-microstructure-mechanical properties-wear and corrosion behavior of an Al-Si (12%)-Flyash metal matrix composite. J Mater Sci 40(22):5989–5997. https://doi.org/10.1007/s10853-005-1303-6
87. Ramnath BV et al (2014) Aluminium metal matrix composites - A review. Rev Adv Mater Sci 38(1):55–60
88. Rao RN et al (2013) Dry sliding wear maps for AA7010 (Al-Zn-Mg-Cu) aluminium matrix composite. Tribol Int 60:77–82. https://doi.org/10.1016/j.triboint.2012.10.007
89. Rao RN, Das S (2011) Effect of applied pressure on the tribological behaviour of SiCp reinforced AA2024 alloy. Tribol Int 44(4):454–462. https://doi.org/10.1016/j.triboint.2010.11.018
90. Razzaq AM et al (2017) Effect of fly ash addition on the physical and mechanical properties of AA6063 alloy reinforcement. Metals 7(11):1–15. https://doi.org/10.3390/met7110477

91. Razzaq AM et al (2019) Influence of fly ash on the microstructure and mechanical properties of AA6063 alloy using compocasting technique. Mater Exp 9(1):1–14. https://doi.org/10.1166/mex.2019.1467
92. Reddy BR, Srinivas C (2018) Fabrication and characterization of silicon carbide and fly ash reinforced aluminium metal matrix hybrid composites. Mater Today Proc 5(2):8374–8381. https://doi.org/10.1016/j.matpr.2017.11.531
93. Reddy G et al (2016) Cast and age hardening behaviour of Al6061 alloy reinforced with an in-situ ceramic composite prepared by carbo thermal reduction of fly ash in plasma reactor. J Compos Mater 50(22):3027–3041. https://doi.org/10.1177/0021998315615203
94. Reddy MP et al (2017) Enhanced performance of nano-sized SiC reinforced Al metal matrix nanocomposites synthesized through microwave sintering and hot extrusion techniques. Prog Nat Sci Mater Int 27(5):606–614. https://doi.org/10.1016/j.pnsc.2017.08.015
95. Reihani SMS (2006) Processing of squeeze cast Al6061-30vol% SiC composites and their characterization. Mater Des 27(3):216–222. https://doi.org/10.1016/j.matdes.2004.10.016
96. Rohatgi PK et al (1997) Friction and abrasion resistance of cast aluminum alloy-fly ash composites. Metall Mater Trans A 28(1):245–250. https://doi.org/10.1007/s11661-997-0102-x
97. Rohatgi PK, Gupta N, Alaraj S (2006) Thermal expansion of aluminum-fly ash cenosphere composites synthesized by pressure infiltration echnique. J Compos Mater 40(13):1163–1174. https://doi.org/10.1177/0021998305057379
98. Rohatgi PK, Kim JK, Gupta N, Alaraj S, Daoud A (2006) Compressive characteristics of A356/fly ash cenosphere composites synthesized by pressure infiltration technique. Compos A Appl Sci Manuf 37(3):430–437. https://doi.org/10.1016/j.compositesa.2005.05.047
99. Saenpong P et al (2018) Microstructures and hardness of A356-SiC composites produced by the mechanical stir casting. Mater Today Proc 5(3):9489–9496. https://doi.org/10.1016/j.matpr.2017.10.129
100. Saheb DA (2011) Aluminum silicon carbide and aluminum graphite particulate composites. J Eng Appl Sci 6(10):41–46
101. Şahin Y (2010) Abrasive wear behaviour of SiC/2014 aluminium composite. Tribol Int 43(5–6):939–943. https://doi.org/10.1016/j.triboint.2009.12.056
102. Salehi M, Farnoush H, Mohandesi JA (2014) Fabrication and characterization of functionally graded Al-SiC nanocomposite by using a novel multistep friction stir processing . Mater Des 63:419–426. https://doi.org/10.1016/j.matdes.2014.06.013
103. Salehi M, Saadatmand M, Aghazadeh Mohandesi J (2012) Optimization of process parameters for producing AA6061/SiC nanocomposites by friction stir processing. Trans Nonferrous Metals Soc China (English Edition) 22(5):1055–1063. https://doi.org/10.1016/S1003-6326(11)61283-1
104. Sarkar S et al (2010) Studies on aluminum-Fly-ash composite produced by impeller mixing. J Reinf Plast Compos 29(1):144–148. https://doi.org/10.1177/0731684408096428
105. Selvam DRJ, Dinaharan DRI (2013) Synthesis and characterization of Al6061-Fly Ashp-SiCp composites by stir casting and compocasting methods. Energy Procedia 34:637–646. https://doi.org/10.1016/j.egypro.2013.06.795
106. Selvam JDR, Smart DSR, Dinaharan I (2016) Influence of fly ash particles on dry sliding wear behaviour of AA6061 aluminium alloy. Kovove Materialy 54(3):175–183. https://doi.org/10.4149/km20163175
107. Shaikh MBN, Arif S, Siddiqui MA (2018) Fabrication and characterization of aluminium hybrid composites reinforced with fly ash and silicon carbide through powder metallurgy. Mater Res Exp 5(4):46506. https://doi.org/10.1088/2053-1591/aab829
108. Shanmughasundaram P, Subramanian R, Prabhu G (2011) Some studies on aluminium-Fly ash composites fabricated by two step stir casting method. Eur J Sci Res 63(2):204–218
109. Sharma VK, Singh RC, Chaudhary R (2017) 'Effect of flyash particles with aluminium melt on the wear of aluminium metal matrix composites. Eng Sci Technol Int J 20(4):1318–1323. https://doi.org/10.1016/j.jestch.2017.08.004

110. Sherif El-Eskandarany M (1998) Mechanical solid state mixing for synthesizing of SiCp/Al nanocomposites. J Alloy Compd 279(2):263–271. https://doi.org/10.1016/S0925-8388(98)00658-6
111. Singh IB et al (2009) Influence of SiC particles addition on the corrosion behavior of 2014 Al-Cu alloy in 3.5% NaCl solution. Corros Sci 51(2):234–241. https://doi.org/10.1016/j.corsci.2008.11.001
112. Singh J, Chauhan A (2016) Overview of wear performance of aluminium matrix composites reinforced with ceramic materials under the influence of controllable variables. Ceram Int 42(1):56–81. https://doi.org/10.1016/j.ceramint.2015.08.150
113. Singh J, Chauhan A (2017) Fabrication characteristics and tensile strength of novel Al2024/SiC/red mud composites processed via stir casting route. Trans Nonferrous Metals Soc China (English Edition) 27(12):2573–2586. https://doi.org/10.1016/S1003-6326(17)60285-1
114. Singh S, Singh R, Gill SS (2019) Investigations for surface hardness of aluminum matrix composites with hybrid reinforcement. Trans Indian Inst Met 72(1):181–190. https://doi.org/10.1007/s12666-018-1472-z
115. Singh VK et al (2015) Enhancement of wettability of aluminum based silicon carbide reinforced particulate metal matrix composite. High Temp Mater Processes (London) 34(2):163–170. https://doi.org/10.1515/htmp-2014-0043
116. Song M (2009) Effects of volume fraction of SiC particles on mechanical properties of SiC/Al composites. Trans Nonferrous Metals Soc China (English Edition) 19(6):1400–1404. https://doi.org/10.1016/S1003-6326(09)60040-6
117. Souvignier CW et al (2001) Freeform fabrication of aluminum metal-matrix composites. J Mater Res 16(9):2613–2618. https://doi.org/10.1557/JMR.2001.0359
118. Subarmono S et al (2010) Mechanical properties of aluminum/fly ash composites produced by hot extrusion. Mater Sci Res India 7(1):95–100. https://doi.org/10.13005/msri/070110
119. Sudarshan, Surappa MK (2008) Synthesis of fly ash particle reinforced A356 Al composites and their characterization. Mater Sci Eng A 480(1–2):117–124. https://doi.org/10.1016/j.msea.2007.06.068
120. Surappa MK (2003) Aluminium matrix composites: challenges and opportunities. Sadhana Acad Proc Eng Sci 28(1–2):319–334. https://doi.org/10.1007/BF02717141
121. Suresh N, Venkateswaran S, Seetharamu S (2011) Studies on eutectic Al-Si alloy-flyash composites. Int J Cast Met Res 24(2):118–123. https://doi.org/10.1179/1743133610Y.0000000013
122. Taherzadeh Mousavian R et al (2016) Fabrication of aluminum matrix composites reinforced with nano- to micrometer-sized SiC particles. Mater Des 89:58–70. https://doi.org/10.1016/j.matdes.2015.09.130
123. Tan M et al (2001) Influence of SiC and Al_2O_3 particulate reinforcements and heat treatments on mechanical properties and damage evolution of Al-2618 metal matrix composites. J Mater Sci 36(8):2045–2053. https://doi.org/10.1023/A:1017591117670
124. Tang F, Hagiwara M, Schoenung JM (2005) Microstructure and tensile properties of bulk nanostructured Al-5083/SiCp composites prepared by cryomilling. Mater Sci Eng A 407(1–2):306–314. https://doi.org/10.1016/j.msea.2005.07.056
125. Thünemann M et al (2007) Aluminum matrix composites based on preceramic-polymer-bonded SiC preforms. Compos Sci Technol 67(11–12):2377–2383. https://doi.org/10.1016/j.compscitech.2007.01.001
126. Tzamtzis S et al (2009) 'Processing of advanced Al/SiC particulate metal matrix composites under intensive shearing - A novel Rheo-process. Compos A Appl Sci Manuf 40(2):144–151. https://doi.org/10.1016/j.compositesa.2008.10.017
127. Uju WA, Oguocha INA (2012) A study of thermal expansion of Al-Mg alloy composites containing fly ash. Mater Des 33(1):503–509. https://doi.org/10.1016/j.matdes.2011.04.056
128. Veeresh Kumar GB, Rao CSP, Selvaraj N (2012) Studies on mechanical and dry sliding wear of Al6061-SiC composites. Compos B Eng 43(3):1185–1191. https://doi.org/10.1016/j.compositesb.2011.08.046

129. Venkatachalam G, Kumaravel A (2017) Mechanical behaviour of aluminium alloy reinforced with SiC/Fly ash/basalt composite for brake rotor. Polym Polym Compos 25(3):203–208. https://doi.org/10.1177/096739111702500304
130. Walczak M, Pieniak D, Zwierzchowski M (2015) 'The tribological characteristics of SiC particle reinforced aluminium composites. Arch Civil Mech Eng. Politechnika Wrocławska 15(1):116–123. https://doi.org/10.1016/j.acme.2014.05.003
131. Wang L et al (2017) Microstructures and tensile properties of nano-sized SiCp/Al-Cu composites fabricated by semisolid stirring assisted with hot extrusion. Mater Charact 131(5988):195–200. https://doi.org/10.1016/j.matchar.2017.07.013
132. Wang Z et al (2011) Effects of particle size and distribution on the mechanical properties of SiC reinforced Al-Cu alloy composites. Mater Sci Eng A 528(3):1131–1137. https://doi.org/10.1016/j.msea.2010.11.028
133. Xiong B et al (2011) Effects of SiC volume fraction and aluminum particulate size on interfacial reactions in SiC nanoparticulate reinforced aluminum matrix composites. J Alloys Cmpd 509(4):1187–1191. https://doi.org/10.1016/j.jallcom.2010.09.171
134. Yang W et al (2015) Strengthening behavior in high content SiC nanowires reinforced Al composite. Mater Sci Eng A 648:41–46. https://doi.org/10.1016/j.msea.2015.09.043
135. Yang Y, Lan J, Li X (2004) Study on bulk aluminum matrix nano-composite fabricated by ultrasonic dispersion of nano-sized SiC particles in molten aluminum alloy. Mater Sci Eng A 380(1):378–383. https://doi.org/10.1016/j.msea.2004.03.073
136. Yao X et al (2017) Effects of SiC nanoparticle content on the microstructure and tensile mechanical properties of ultrafine grained AA6063-SiCnp nanocomposites fabricated by powder metallurgy. J Mater Sci Technol 33(9):1023–1030. https://doi.org/10.1016/j.jmst.2016.09.022
137. Yasutomi Y et al (1999) Effects of the SiC/Al interface reaction on fracture behavior of a composite conductor using SiC fiber reinforced aluminum for next generation power equipment. J Mater Sci 34(7):1583–1593. https://doi.org/10.1023/A:1004524516143
138. Yuan D et al (2018) Development of high strength and toughness nano-SiCp/A356 composites with ultrasonic vibration and squeeze casting. J Mater Process Technol 269:1–9. https://doi.org/10.1016/j.jmatprotec.2019.01.021
139. Zhang LJ et al (2015) High strength and good ductility at elevated temperature of nano-SiCp/Al2014 composites fabricated by semi-solid stir casting combined with hot extrusion . Mater Sci Eng A 626:338–341. https://doi.org/10.1016/j.msea.2014.12.089
140. Zhang Q et al (2004) Microstructure and thermal conduction properties of an Al-12Si matrix composite reinforced with dual sized SiC particles. J Mater Sci 39(1):303–305. https://doi.org/10.1023/B:JMSC.0000007761.85651.d6
141. Zhang Liangchi MY-WZZ (1994) Modelling friction and wear of scratching ceramic particle-reinforced metal composites. Wear 176(94):231–237
142. Zulfia A et al (1999) Effect of hot isostatic pressing on cast A357 aluminium alloy with and without SiC particle reinforcement. J Mater Sci 34(17):4305–4310. https://doi.org/10.1023/A:1004675424845

Chapter 7
Tribological and Corrosion Behavior of Al-TiB_2 Metal Matrix Composites—An Overview

Suswagata Poria

1 Introduction

Impact of a new material on society is immense. A common saying is that we are only as good as our best materials. From stone to silicon, iron to shape memory alloys, materials have experienced a long journey. If growth of civilization is closely observed, it is revealed that development of materials and their applications are the milestones in civilization and economic progress. At the initial stages of mankind, raw materials availed from nature were processed to end products for the purpose of achieving some useful value in daily life. That end product had a definite shape and size based on very primitive knowledge. With time, findings of newer materials added newer dimensions on those end products which primarily resulted in betterment of life. For instance, the introduction of iron as material in mankind made struggle for survival comparatively easy and quality of life improved accordingly. But the quest for easier daily life with more comfort reproduced existing operations in different modified forms. For instance, a man moving on a wooden wheel at a very nominal speed was obsolete with time. Requirements became higher load-bearing capacity of the wheel as well as more speed. To cater to those requirements in end products, materials other than wood were started to be developed industrially.

Before opting for different materials for useful products, initial efforts were made on mechanics and design of products to enhance the load-bearing capacity. At that time, the material was considered homogenous. In accordance with need, strength of material as a subject was developed where the role of external force on material performance was tried to be understood in a simplified form. Shape and size of

S. Poria (✉)
Heritage Institute of Technology, Kolkata, India
e-mail: suswagataporia@gmail.com

S. Sahoo (ed.), *Recent Advances in Layered Materials and Structures*,
Materials Horizons: From Nature to Nanomaterials,
https://doi.org/10.1007/978-981-33-4550-8_7

the product were then modified accordingly. The target was to increase the functioning of the material without yielding. But the industrial revolution in the nineteenth century opened up various fields where structural materials started to be used in sufficient number. Unfortunately, at the same time, several catastrophic failures of boilers and railway equipments took place which resulted in major loss of life. Such incidents coerced better choice of material and increased understanding of material performances at adverse operating conditions. Meanwhile, in the twentieth century, communication became an important parameter and materials of that time were not ready to be adopted. Space research and automobile sectors started to flourish which additionally pushed researchers to find out or develop newer materials capable to perform without failures in extreme conditions.

It is understandable that historically applications played a prominent role in defining and directing the focus of fundamental research on materials. For any product development, materials selection was based on evaluating a series of performance characteristics, process characteristics and sustainability issues. But that approach got changed with time. In recent times, the tremendous advances in understanding of material behavior succeed an increasing trend of using material consisting of various properties together in a balanced way. In automobile industry, some materials are chosen based on better electromagnetic properties in addition to good mechanical properties. In packaging industry, especially for computer hardware and drives, good shock absorption property along with the capacity of electromagnetic interference shielding is desired. In aerospace industry, materials must possess good mechanical strength as well as less overall weight because weight reduction in milligram level even increases sufficient fuel efficiency. Depending on such demands, two important classes of materials have been developed. They are composite materials and electronic materials. From the day of development, those two genres of materials have been considered by industry with great interests. Composites and electronic materials are majorly different from three fundamental classes of materials, e.g., metallic materials, polymeric materials and ceramic materials. A multitude of complex electronic circuits has been transformed into a single 2 cm^2 chip areas or less than that nowadays and it is possible only because of electronic materials. Similarly, improved mechanical properties like transverse strength, stiffness, shear strength, compressive strength along with enhanced wear resistance of composite materials with respect to monolithic metal alloys made these suitable for versatile range of applications. Mass market products of composite materials are increasing progressively and area of applications are spreading accordingly. Besides, day by day, increasing obligation for reduction in fuel consumption and emissions in ground is pressing composite materials into newer challenges. This leads to a journey based on better understanding of composite materials from different approaches. Composite materials also should be evolved accordingly.

2 Composite Materials

The term 'composite' philosophically designates to 'something combining the typical or essential characteristics of individuals making up a group' [11]. Composite materials have been made by combining different type of materials holding different properties and shapes to achieve new properties changed from either of the constituents. Such combination does not hold any atomic level mixture of different constituent materials, rather it is a thermodynamically unstable mixture containing large amount of interface [51]. If any chemical reaction happens at the interface leading toward thermodynamically stable molecular level mixture of elemental materials, then that material cannot be called 'composites.' That is why, constituents of composite materials are chosen accordingly so that stable interface can be achieved. Elements of composite materials are classified by two ranks, matrix and reinforcements. Matrix is the 'softer' phase in which 'harder' phase holding high stiffness and strength is embedded. Matrix portion in composites is relatively higher in amount while reinforcements play pivotal role to change the properties of matrix. Therefore, matrix is the principal phase of composites which possess a constant character and binds the reinforcing phase. The transverse properties, inter-laminar strength and high-temperature strength of the composites are being held by the matrix portion as it is the continuous phase [21]. Additionally, matrix phase is responsible for utilization of the full potential of reinforcement through transferring some portion of external load successfully into it.

Based on different matrix and reinforcements, composite materials are classified into six categories, viz., metal matrix composites (MMC), fiber reinforced plastics (popularly known as FRP), fiber reinforced ceramics ((popularly known as FRC), fiber reinforced glasses (popularly known as FRG), intermetallic compound matrix composites (popularly known as IMC) and carbon fiber reinforced carbon (popularly known as CC) composites [51]. Depending on the size of reinforcements, composites are of three types, viz., particulate reinforced composite, whisker reinforced composite and continuous/discontinuous fiber reinforced composite. With progress in research, various combinations of matrix and reinforcements have been introduced leading to newer classification in composite materials. But, basic approach behind the introduction of composites is fixed which is load-bearing capacity of matrix along with adverse condition stability must increase by incorporation of reinforcements.

To understand the contribution of matrix and reinforcement in composites, fiberglass is taken as an example. Plastic is the matrix in this case while glass is reinforcement. Glass is strong but brittle in nature. Plastic possesses very little strength in comparison with glass but when it binds glass, bending of composites becomes easier and breakage of glass does not happen. Additionally, fiberglass withstands much more load than plastic does independently. Hence, fiberglass as composite material is used vividly nowadays in sports gear, building panels and bodies of automobile [21].

Composites are already established as a better alternative to monolithic metals or alloys. To meet the challenging needs of special design, proper choice of composites

material is an effective method. Major points in composites are that yield strength and tensile strength at room temperature are improved and this performance is also maintained at high temperature, while toughness and ductility are prolonged properly [28]. Creep resistance, wear resistance, fatigue strength and Young's modulus of composites are better than popular alloys or metals at ambient temperature and at elevated temperature also [62].

3 Metal Matrix Composites

The idea of MMCs lies in the principles of dispersion hardening and precipitation hardening where strengthening mechanism depends on restricting the dislocation motion by incorporation of fine oxide particles into metallic matrix. In the year of 1970, 'dual phase steel' has been evolved where martensite particles are distributed over ferrite matrix phase and this phenomenon is very much like the material which is currently referred as discontinuous particulate reinforced MMCs [11]. With time, the definition of MMCs has been modified and it excludes any directionally solidified eutectics or Al-Si alloys or alloys containing any precipitates or segregated inclusions. A material can be called as MMCs only when distinct phases co-exist together throughout its total processing history [15].

Lots of studies reported that MMCs are better than other composite materials. Among other composites, carbon–carbon composites are very popular as material in aerospace applications but they suffer severe high-temperature oxidation which causes rapid degradation and erosion [48]. Oxidation in such composites becomes severe when temperature hits 350 °C. So, an oxidation resistance coating is necessary for the purpose of proper utilization of such composites. MMCs are free from such difficulties. Chawla and Chawla [10] reported that MMCs are more advantageous than polymer-based composites due to several reasons. As per them, metal matrix composites show higher strength, higher stiffness and better service temperature than polymer-based composites. Metal matrix composites also show better electrical and thermal conductivity than polymer composites. Transverse properties of MMCs are also better. MMCs possess better survivability against radiation like laser, UV or nuclear. MMCs also hold little or no contamination.

Evans et al. [15] discussed some more advantages of MMCs over polymer matrix-based composites. Metals as matrix can maintain strength along with toughness at high temperatures. Metals do not soak up moistures. Metals are not degraded by radiation. Melting point of metal is higher than polymers which make them safer as matrix. Heat and electricity can pass through MMCs which helps in many applications to take advantage over polymer-based composites. It is also fact that MMCs are easily joined or can be easily fastened to other metallic components. Over carbon-based, polymer-based, glass-based or ceramic-based composites, MMCs have snatched its position as material in military fighter aircraft, helicopter rotor blades, fuselage struts in the space shuttle orbiter, selected components on the Hubble Space Telescope and enormous applications like this [8]. Basic advantages of MMCs come from the matrix

as metals. But it can be comprehended that MMCs are directed to some specific applications where other composites are not suitable to be used.

4 Particulate Reinforced MMCs

Particulate (or particle) reinforced MMCs (PRMMCs) are combinations of matrix phase (metal or metallic alloy) with second phase that is purposely introduced into the metallic phase for improving properties. Second phase of PRMMCs may be more than one. PRMMCs have been fabricated in universities and R&D laboratories since 1960s for research purpose [45, 85]. Almost two decades later, major productions through several new processes were started.

Among whisker reinforced, particulate reinforced and short/long fiber reinforced composites, particulate reinforced composites are isotropic in nature like metals. Whisker or fiber reinforced composites are anisotropic and properties are dependent on the orientation of the whiskers/fibers. Isotropic materials also can be made from whiskers and fibers through desperate random orientation, but further processing of them like extrusion will again re-orient whiskers resulting in anisotropic properties. In anisotropic materials, mechanical properties, e.g., strength, stiffness, are unidirectional while coefficient of thermal expansion (CTE) is specified in another direction. Additionally, for aligned fiber reinforced composites, strength and stiffness are more in the direction of fiber orientation than perpendicular to them. Being isotropic, PRMMCs are free from such orientation in properties. It is true that PRMMCs show lower strength than the strength of fiber reinforced composites in direction parallel with fiber orientation. But it is also granted that PRMMCs do not show different strength and stiffness in different directions.

Regarding other advantages of PRMMCs over others, it is observed that whiskers cost more than particulate and they are brittle in nature. Whiskers break into shorter lengths at the time of processing and reduce the reinforcement efficiency which makes difficulties in cost justification. In fiber reinforced MMCs, higher difference in coefficient of thermal expansion between constituents yields higher residual stresses at the time of significant temperature change. Those stresses result yielding at the time of cooling. Kainer [28] discussed vividly that PRMMCs are the best in capability to offer targeted applications, and additionally, they are cost effective, show high isotropy of properties and large-scale production is possible for this case. As per literatures, the following advantages of PRMMCs are prominent [15].

- Equiaxed reinforcements are less costly
- Fabrication methods are simple and cost effective
- Material properties are isotropic in nature
- General metal working processes like machining, joining, forming can be applied in this case

5 Fundamental Knowledge on Particulate Reinforced Composites

Composites especially discontinuous particulate reinforced composites are inhomogeneous. That is why basic strength of materials cannot explain the behavior of composites. When load is applied externally on composites, non-uniform distribution of stresses occurs. Such distribution is tried to understand using several models as it determines the behavior alternatively called characteristics of the material. Characteristics of MMCs with nature of stress distribution are very much dependent on microstructures and matrix/reinforcement interfaces. Microstructure and interfaces are results of production processes as well as thermal and mechanical pre-history of matrix and reinforcements. Chemical compositions along with grain size, textures, precipitation behavior and lattice defects are the concerned factors of matrix for determining composite characteristics. While for reinforcing phases, amount, size, distribution and orientation are the related factors. Factors of reinforcements and matrixes along with production processes are approached differently in different models for the sake of the closest prediction of composite behavior. Basic models have been developed by assuming the ideal conditions, e.g., optimal boundary surface formation, uniform distribution with a very small amount of clustering and no influence of the reinforcement phase on matrix phase. In reality, the situation differs from the ideal one because a strong interaction occurs between reinforcement and matrix at the time of mixing. Models are appropriated accordingly with the deviation from reality and several new factors are introduced in the model with increase in understandings. Models based on long fiber reinforcement or short fiber reinforcement, e.g., the slab model, the shear lag model, continuous coaxial cylinder model, finite difference and finite element models are not discussed here though they are vividly presented in several literatures (Clyne and Withers 2014). Focus is kept on understanding the strengthening mechanism of discontinuous particles reinforced MMCs as this study deals with such type of MMCs only. The following discussion is progressed from simple model to very recent observations regarding mechanisms of particulate reinforced MMCs characteristics.

'Rule of mixtures' is the simplest and basic model of predicting composite behavior based on known properties of constituents (matrix and reinforcement). If U_c signifies the property of PRMMCs, V_f as the reinforcement phase volume and U_m as the property of matrix, then following equation is obtained using 'rule of mixtures' [51].

$$U_c = V_f U_f + \left(1 - V_f\right) U_m \tag{1}$$

For more than one reinforcement phase in composites (hybrid composites), Eq. 1 will be modified into general form, which is

$$U_c = \sum_{1}^{n} V_n U_n + \left(1 - \sum_{1}^{n} V_n\right) U_m \tag{2}$$

In Eq. 2, n is the number of reinforcement types. In this model, matrix reinforcement interactions are idealized too much. From this model, CET, thermal conductivity, ultimate tensile strength like properties cannot be predicted accurately as these properties depend on shape, size distribution, interface like several discussed parameters. In further, to predict the behavior of composites with better accuracy, understanding on surface and interface energy was increased. Following equation was developed regarding that purpose [17].

$$\gamma_{ab} = \gamma_a + \gamma_b - 2\emptyset(\gamma_a\gamma_b)^{1/2} \tag{3}$$

In above equation, $\emptyset$ is a constant depends on the characteristics of the system. γ_a and γ_b are the surface energy of constituents (a is matrix and b is reinforcement). Composites contain a large amount of interface. A strong adhesion without chemical reaction at the interface is required for achieving better properties. To achieve that type of interface, idea about the work of adhesion (W_{ab}) is required. Following equation was developed to predict work of adhesion (W_{ab}) for making 'ab' composites.

$$W_{ab} = \gamma_a + \gamma_b - \gamma_{ab} \tag{4}$$

From Eqs. 3 and 4, it is comprehended that interface characteristics majorly depend on the parameter $2\emptyset(\gamma_a\gamma_b)^{1/2}$. The value of $\emptyset$ can be experimentally obtained as well as theoretically following method proposed by Girifalco and Good [17]. Equations 3 and 4 mainly direct interface characteristics for various matrix/particle combinations. Interface characters finally direct in finding out suitable particles compatible with matrixes like Al/Mg.

Llorca and Gonzalez [39] tried something more than simple rule of mixture thing or basic energy exchange thing at the time of fabrication. They predicted tensile behavior of one particulate reinforced composites using the following equation

$$\sigma(\varepsilon) = \sum_i \gamma_i\left[\sigma_i^I(\varepsilon)(1-\rho_i) + \sigma_i^F(\epsilon)\rho_i\right] \tag{5}$$

In this equation, σ is the average compressive stress, ε is plastic strain. Subscript i signifies one small unit which holds same volume fraction of reinforcement. $\sigma_i^I(\varepsilon)$ is the average stress acted on unit where reinforcement is intact, while $\sigma_i^F(\epsilon)$ is the stress of the unit where reinforcement gets fractured. ρ_i is the fraction of total units containing fractured reinforcements. In this model, the material was considered as three-dimensional array of hexagonal prisms whose height and base were equal. The particle was assumed to be positioned at the center of each unit and shape was either spherical or cylindrical. They got partial success in terms of accurate prediction.

At the same time, Young modulus of particle reinforced composites was tried to be estimated by several models. Tsai Halpin model was pioneer in this aspect. Voigt model and Reuss model were also effective to estimate Young's modulus but those models are applicable to those fiber reinforced composite materials whose

stress direction is parallel with the orientation of fiber and also to those layer composite materials when acting load is perpendicular to the layers. As per Tsai halpin model, the composites Young's modulus, E_c can be effectively assumed with the help of geometry factor [22]. This geometry factor takes the shape and size of the reinforcement into consideration. The concerned equation in Tsai Halpin model is

$$E_c = \frac{E_m(1 + 2S \cdot q \cdot f)}{1 - q \cdot f} \tag{6}$$

where

$$q = \frac{\left(\frac{E_P}{E_M}\right) - 1}{\left(\frac{E_P}{E_M}\right) + 2S} \tag{7}$$

In above two equations, E_P signifies particle Young's modulus and E_M signifies matrix Young's modulus; the term 'f' signifies the total volume content of the particles. Though geometry of reinforcement is considered in this model, basic assumptions about production process like no pores, no agglomerations or no non-reinforced areas are still there.

Hence, it is seen that in the initial period of research, separate factors were accommodated one by one in a model. Consideration of one factor with more priority than others results in the development of separate mechanisms like grain refinement, Orowan strengthening, CTE strengthening, Hall–Petch mechanism, etc. To accommodate all factors, nowadays, researchers are inferring such micromechanical model where contributions of all strengthening mechanisms considered together [31]. Conglomerations of several factors in one model to estimate the strengthening mechanism of particles in PRMMCs are quite common findings in literatures [28]. Among those models, following equation is used mostly for combining different strengthening factors.

$$\Delta\sigma = \sqrt{\left(\Delta\sigma^2_{\text{load}}\right) + \left(\Delta\sigma^2_{\text{CTE}}\right) + \left(\Delta\sigma^2_{\text{EM}}\right) + \left(\Delta\sigma^2_{\text{Orowan}}\right) + \left(\Delta\sigma^2_{\text{Hall-petch}}\right)} \tag{8}$$

Several researchers claimed that Eq. 8 provides best validation of experimental results but it is noteworthy that there is no convergence or generalization among researchers regarding this approach [12].

In Eq. 8, $\Delta\sigma$ is the increment in yield strength due to incorporation of particles into base matrix. $\Delta\sigma_{\text{load}}$ is the contribution of load-bearing effect on yield strength of composites [59]. Following equation is used to measure this certain contribution.

$$\Delta\sigma_{\text{load}} = 0.5 V_p \sigma_{ym} \tag{9}$$

In Eq. 9, V_p signifies particles volume fraction while σ_{ym} signifies the matrix yield strength.

$\Delta\sigma_{\text{CTE}}$ is related to strain developed by the disparity in CTE of the matrix and reinforcement of composites [18]. Two equations with different parameters are there for estimating $\Delta\sigma_{\text{CTE}}$ [12].

$$\Delta\sigma_{\text{CTE}} = \sqrt{3}\beta G_m b\sqrt{\rho_{\text{CTE}}} \tag{10}$$

and

$$\Delta\sigma_{\text{CTE}} = \sqrt{3}\beta G_m b\sqrt{\frac{12V_p\Delta\alpha\Delta T}{bd_p}} \tag{11}$$

In Eqs. 10 and 11, β is the strengthening coefficient, $\Delta\alpha$ is the difference of CTE between particle and matrix, ΔT is the difference in processing temperature and temperature at which tensile tests are performed. V_p and d_p signify the amount in volume and diameter of the particles.

$\Delta\sigma_{\text{EM}}$ is originated from modulus mismatch and expressed using following equation [31]

$$\Delta\sigma_{\text{EM}} = \sqrt{3} \propto G_m b\sqrt{\rho_{\text{EM}}} \tag{12}$$

In Eq. 12, $\propto$ is a coefficient depends on material. ρ_{EM} is a function based on bulk strain of the composites.

$\Delta\sigma_{\text{Orowan}}$ and $\Delta\sigma_{\text{Hall-petch}}$ in Eq. 8 are the two contributions based on the famous Orowan equation and Hall–Petch equation, respectively [20]. It is noteworthy that Orowan strengthening mechanism is mainly effective for estimating strength of composites with sub-micron-sized particles [46]. Hall–Petch equation is based on contribution of grain refinement on yield strength of composites.

$$\Delta\sigma_{\text{Orowan}} = \frac{0.13G_m b}{\lambda}\ln\frac{d_p}{2b} \tag{13}$$

G_m represents the shear modulus of matrix, b signifies the Burgers vector, d_p indicates the average diameter of the particles and λ denotes the inter-particle spacing in Eq. 13.

$$\Delta\sigma_{\text{Hall-Petch}} = k_y\left(d^{-\frac{1}{2}} - d_0^{-\frac{1}{2}}\right) \tag{14}$$

In the above equation, k_y is the Hall–Petch slope, the average grain size of matrix before reinforcement is denoted by d_0 and d is the grain size of the composites.

For better understanding of above discussions, a study is chosen as an instance in the following. This study is based on yield strength of PRMMCs (Al–5 wt%TiB_2) and done by Wang et al. [79]. In the study, first yield strength of fabricated composites

is calculated theoretically from three different approaches, e.g., grain refinement strengthening, Orowan strengthening and CTE strengthening. Then ultimate yield strength of composites is calculated as per the proposition of Zhang and Chen [84] using the following equation

$$\Delta\sigma = \Delta\sigma_{\text{grain-refinement}} + \left((\Delta\sigma_{\text{Orowan}})^2 + \left(\Delta\sigma_{\text{CTE}}^2\right)\right)^{1/2} \tag{15}$$

For finding the contribution of grain refinement in final yield strength, Eq. 14 is used. In Eq. 14, the value of d is calculated using the following formulae [16].

$$d = d_0\left(1 + pV_p\right)^{-1/3} \tag{16}$$

In Eq. 16, the refining potency of the reinforcement is p. The value of p is measured empirically by Wang et al. [79] in the study. Regarding contribution of Orowan strengthening, a slight modified version of Eq. 13 is used. Increment in strength by CTE strengthening is estimated by Eq. 10. Value of β is taken as 1.25.

After yielding final value as per Eq. 15, the real experimental values are fitted into estimated values and results show that 35–56% of reinforcing particles take part in strengthening of composites for different base matrix. Most interestingly, those percentages are quite relatable with the microstructures presented in that study. So it can be comprehended that accuracy of prediction of PRMMCs characteristics through model formation becomes enhanced with time which essentially leads to the fact that behavioral understanding of composites has been increased in a sufficient amount.

6 Aluminum-Based PRMMCs and Related Reinforcements

Properties of constituents are mostly retained even after formation of composites. So, composite properties are majorly determined by constituent properties. Accordingly, choice of base matrix and particles is driven by intended applications of the end products. Nowadays, a wide genre of particles, from ceramic to fine red mud, graphene nano-platelets to fly ash are being incorporated into aluminum/magnesium base matrixes [2, 53]. It raises a pertinent question. Can any type of particle be reinforced into any base matrix? The answer is no [51]. Though the aim of composites is tailoring of matrix properties using particles, chemical reactions arise at the interface resulting degradation or disparity of constituents which yields in degraded PRMMCs. So, proper compatibility of matrix and reinforcements is needed before choosing them as the constituent. Appropriate wetting is a major condition for pairing matrix and particle through liquid metallurgy route. Proper wetting helps in stress transfer and stress distribution in solid state of the composites which prevents fracture. Conversely, occurring of any chemical reactions at the interfaces is usually harmful to the properties.

Literatures reveal that light alloys are popular as base matrix based on costing, availability, recycling, etc. Aluminum, magnesium, copper, titanium and iron metals including their alloys are normally used as base matrixes. Among these, selection of specific base matrix depends on industrial applications of composites. Other alloys can be used but only for specific functional purposes.

Al alloys are chosen as base matrix mainly for two factors. First, aluminum (Al) or aluminum alloys (Al alloys) are majorly popular where energy efficiency is the prime concern. Being lightweight material with noteworthy strength, aluminum or aluminum alloys are easy to process and help to reduce energy consumption. Pure Al due to its lack in strength and other compatibility issues is not first hand choice for major structural applications. But when pure Al is embedded by other phases, it becomes competent with strength of steel and develops versatile properties [79]. In automotive components like pistons, engine blocks, etc., aluminum-based particulate reinforced composites as materials are already in use [57]. Even right now, disks, brakes, rotors, connecting rods are also being made of aluminum-based particulate reinforced composites. Among all commercially produced MMCs, composites based on aluminum (Al) alloys are the highest in volume [61]. Industries of ground transportation, aerospace, recreational, thermal management and automotive actually demand materials which hold high structural efficiency along with excellent tribological behavior. Al-based PRMMCs are that type of materials to fulfill such requirements [47].

Secondly, there is a need to maintain high specific strength with increase in operating temperature. Engine heads, pistons and similar components of automotive and transport field are commonly made of Al alloys in peak-aged condition. Definitely, there are some advantages regarding Al alloys as material from material science point of view. But before introduction of Al based PRMMCs, Al alloys were losing its position because when operational temperature was high, softening of alloys occurred which yielded overaged condition of Al. Ceschini et al. [9] discussed that synergistic combination of tough ceramic particles with Al matrix aided in maintaining strength and stiffness at high-temperature operations. Accordingly, use of Al/Al alloys-based composites has progressed. Study of other characteristics, viz., wear, friction, thermal conductivity, formability of Al-based PRMMCs gets required attention to suitably replace Al alloy.

When a composite material is selected for any specific usage, i.e., tribo-material or corrosion resistant material, than in laboratorial scale, it has to go through some steps. Those steps are mentioned in Fig. 1. So depending on the final behavior, reinforcing phase, base alloy and also fabrication routes are selected. Reinforcing phase in PRMMCs actually resists and transfers the load applied externally on the composites [23]. Surappa [70] comprehensively stated that reinforcement in the aluminum matrix is usually non-metallic and commonly ceramic. Till now, lot of reports are available on PRMMCs among which major reinforcing phases are carbide (SiC, TiC, B_4C, WC), nitride (AlN, TiN, Si_3N_4), oxide (Al_2O_3, TiO_2, SiO_2, MgO) or boride (ZrB_2, TiB_2) [32, 65]. Recently, carbon nano-tubes [82] and certain hard intermetallics ($MoSi_2$ [13], Ni_3Al) are being reinforced in a more focused way, though carbon nano-tubes are not generally categorized as particles. There are some

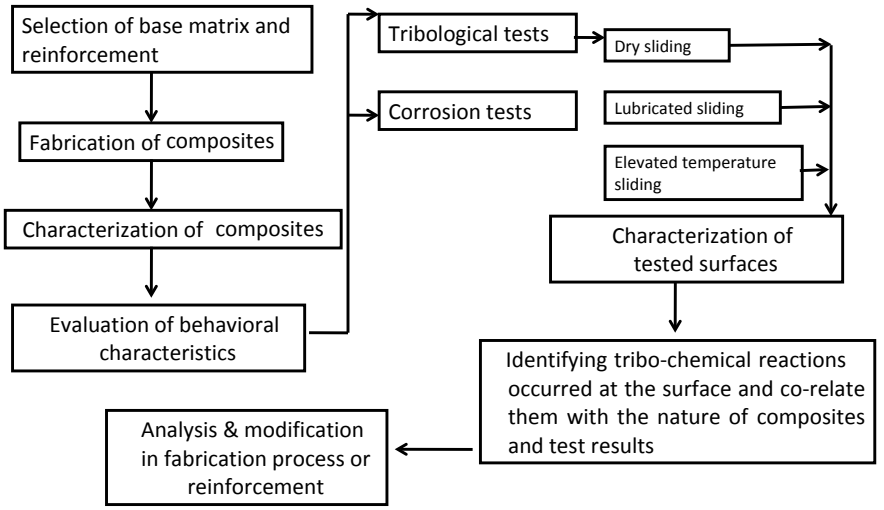

Fig. 1 Block diagram to show how a composite material has been selected for fabrication

common properties among popular ceramic reinforcements. All of them possess density more than 2200 kg m^{-3}, melting point higher than 2000 K, Vicker's hardness more than 600 HV and Youngs' Modulus at least 400 GPa [51]. Such high hardness or mechanical strength of particles is being transmitted into Al through reinforcement. Accordingly, composites show intermediate properties between Al and used ceramic particle. Aluminum-based particulate reinforced metal matrix composites are commonly called as aluminum metal matrix composites (AMCs) or PRAMCs, and in rest of the study, it will be referred as AMCs. The term 'composite' will also essentially signify AMCs in the following discussions.

7 Fabrication of MMMCs

Fabrication of metal matrix composites is the most challenging part. Major cost associated with AMCs/MMCs is involved in fabrication systems. Thorough literature survey on AMCs reveals that composites with same particle along with same shape, size and amounts but fabricated through different routes show different mechanical and tribological behavior under same operating conditions [1]. It happens because orientation and distribution of reinforcements in matrix are affected by the manufacturing processes. Suitable fabrication method depends on two major factors. First, the method needs to be cost effective one to distribute the secondary (reinforcing) phase in the preferred configuration. Second, a strong bond between matrix and the reinforcement is to be achieved at the time of fabrication so that an effective load transfer can occur between phases prior to fracture. Depending on these factors,

Table 1 Processing routes for major three AMCs

Types of AMCs	Fabrication methods	References
Al–SiC	Squeeze casting (liquid state), powder metallurgy (solid state), ultrasonic dispersion (liquid metallurgy)	[35, 36, 83]
Al–Al_2O_3	Cold isotropic pressing (CIP) and sintering (solid state), powder metallurgy (solid sate), milling and hot pressing (semi-solid state), vortex method (liquid state)	[19, 26, 27, 29]

fabrication of composites is performed through solid state and liquid state fabrication methods. Some researchers suggested that gaseous state methods like chemical vapor deposition or physical vapor deposition may be used to make composites by depositing a layer of material on the surface of another material (substrate) [51]. In situ and ex situ techniques are two separate fabrication styles commonly used by the researchers and are distinguished by the process of incorporating ceramic particles into matrix. In situ process involves reaction of at least two (or more) elements inside molten metal for producing required ceramic reinforcement inside the matrix. In ex situ process, ceramic reinforcement is incorporated into matrix in particle form and it involves no reaction for purpose of production of reinforcement. Table 1 provides primary processes which are commonly used by researchers for fabrication of two major AMCs.

Solid sate fabrication technique includes processes like powder metallurgy, mechanical alloying, diffusion bonding and surface oxidation. Major advantage of solid state fabrication method is less chemical interaction between particles and matrix yielding almost no chemical products at the interface. Among all solid process, most popular one is powder metallurgy techniques. These methods actually deal with discontinuous reinforcements, because this process holds the advantage in easiness of mixing and blending. Additionally, this process holds the effectiveness of densification. Targeted ceramic and metal powders are first mixed which is followed by isostatic cold compaction and hot pressing. Novel low-cost approaches, such as sinter-forging, are also part of solid state processing [10].

Processes like pressure infiltration, squeeze casting, compo casting, stir casting, spray deposit method, centrifugal casting deal with liquid metal. Advantages of liquid state method over solid state techniques lie in capability of rapid production. Complex shape parts can be easily fabricated by this method. But capillary forces hinder the combination of molten metal with particles. Ceramic reinforcements are generally 'metal repellent' and metal does not easily bond with something which is 'non-metal.' External forces/energies are required to overcome this energy barrier. In infiltration technique, molten metal is pushed into reinforcement. Some modifications are being practiced to overcome the issue of wettability and ease of mixing. Processing at elevated temperature is one of the modifications which help to increase wettability. In liquid state method, matrix phase solidifies with size constraints as they are placed between reinforcement particles which do not move at the time of solidification. If particles move, matrix metal pushes them into the area solidified in the last. But this results in undesirable shrinkage cavity.

For fabrication of aluminum-based nano-composites in recent times, friction stir processing (FSP) and accumulative roll bonding (ARB) are attempted. During FSP, a tool consisting of a shoulder and a pin rotates and dives into the base matrix surface. Simultaneously, by the pin, grooves are filled with the desired volume fraction of nano-particles. Al [38] and Mg-based nano-composites have been produced by FSP by incorporating ceramic or carbon-based nano-reinforcement. Accumulative roll bonding is a solid state method. Severe plastic deformation processes majorly occur in this process. ARB process develops roll bonding stacked sheets (about 50% of thickness reduction) first, then cuts the roll-bonded material and rolls it again after stacking the pieces over each other [4].

8 Tribological Properties of AMCS

One of the important reasons behind popularity of AMCs is better tribological behavior over base Al matrix at dry condition as well as other operating conditions. Antoniou and Subramanian [5], Balasubramaniam and Maheswaran [6], Lim and Ashby [37], Rao et al. [60], Wilson and Alpas [80], Wilson and Alpas [81] and other researchers reported wear and friction behavior of AMCs and suggested varying mechanisms (adhesive, abrasive, delamination, plowing, etc.) being active on the composite surface at the time of sliding. Some researchers studied effect of mechanical parameters on tribological behavior while some studied influence of material parameters on wear and friction of AMCs.

Like mechanical properties, common observation in wear behavior of AMCs is that wear resistance of composites increases linearly with increase in the amount of particles. Some study reveals that such increase in wear resistance occurs only up to a certain amount of reinforcements after which particles play detrimental role in wear behavior of composites. Wear of composites depends on the reinforcement particle size and increases with increase in size. Wear rate generally increases with increase in the applied load. Wear of composites is also a function of sliding distance and it is observed that volume/weight loss increases with increasing sliding distance. However, wear rate may also increase with increase in sliding velocity. Several studies are also available which show wear rate decreases with increase in sliding velocity of composites. For in situ composites, in situ reaction holding time is an important parameter for influencing the wear rate. It is generally observed that longer reaction time results in reduction in grain size of matrix. Such reduction in grain size directly influences the wear resistance of composite.

Identifying suitable wear mechanism through wear debris and worn surface analysis is a common practice in study of tribological behavior of AMCs. Active wear mechanisms majorly depend on the hardness of reinforced particles and applied contact load. Several tribo-chemical reactions occur on the contact surfaces. Wear mechanisms are modified accordingly. Those reactions are influenced by the presence of lubricant or corrosive solution. Operational environment also influences tribo-chemical reactions. Not only hard particles, soft particles are also incorporated

into Al matrix which enhance wear behavior in a different way. Soft particles either absorb moisture or provide protective layer against hard asperities. So to understand wear behavior of an AMC, it should be studied under varying operating conditions.

Generally, friction of AMCs depends on applied normal load, amount of particles, temperature, sliding distance, sliding velocity, in situ reaction holding time (for in situ composites), processing temperature and existence of protective layer on the surface, etc. In case of in situ Al-TiB_2 composites, it is seen that for a given temperature, friction decreases with increasing wt% of TiB_2 and increases with increase in temperature [49]. Reaction holding time also affects COF and it has been observed that COF increases with increasing reaction holding time [43]. Study shows friction of composites increase with sliding distance and sliding velocity for a fixed amount of reinforcement [58].

9 Al–TiB_2 Metal Matrix Composites

Improvement of properties in AMCs mostly depends on the selection of materials, reinforcement phase and process of synthesis. TiB_2 as reinforcement over Al alloy matrix is a specific area of attention among AMCs for last few years due to some specific advantages of TiB_2 in aluminum alloy matrix as well as varying scopes for fabrication (liquid phase, solid phase, two phase), apart from excellent combination of the properties of final composite [34].

Advantages of titanium diboride (TiB_2) as reinforcement are its high Young's modulus (345–409 GPa), high hardness (3400 HV), low density, high wear resistance [71, 72]. TiB_2 has tendency to not react with molten aluminum/aluminum alloy which results in less reaction product at particle matrix boundary and TiB_2 is also known as the hardest material that can be reinforced in aluminum matrix alloy [74]. It is well documented that mechanical properties, viz., elongation, fracture behavior, tensile strength and tribological properties, viz., wear resistance in dry sliding condition at ambient temperature as well as at high temperature, abrasive wear resistance, friction behavior of aluminum matrix composites enhance qualitatively when TiB_2 particles have been reinforced [3, 41, 49, 75]. According to the literature and several industrial report, major volume of the commercially produced AMCs is held by SiC incorporated AMCs. For incorporation of SiC, casting or powder metallurgy techniques are major choice for fabrication. Still, major drawback of Al–SiC composites exists in formation of aluminum carbide (Al_4C_3) which reduces physical, mechanical and chemical properties of the composites [30]. Literatures reveal that, instead of SiC if reinforcement like TiC, TiB_2 are used, then composites will be free from such drawback of Al–SiC [44]. Moreover, TiB_2 particles act as nucleating agent for aluminum and α-Al matrix grains are refined due to TiB_2 which provide various ways of fabrication compared to any other ceramic particulate reinforced AMCs [63].

10 Fabrication of Al–TiB_2 MMC

Regarding fabrication of Al–TiB_2 metal matrix composites, it can be said that most of the fabrications have been done through in situ methods. In in situ method, TiB_2 has been formed inside molten aluminum ingots through different chemical reactions. Total reactions during in situ fabrication can be divided into three parts [34]. The first one is decomposition of K_2TiF_6 and KBF_4 to KF liquid, TiF_4 and BF_3 gases. Second one is reaction between TiF_4 and BF_3 gases inside the molten ingots to form TiB_2 and AlF_3. The third one is the formation of $3KFAlF_3$ and KF mixture. The overall reaction regarding the formation of TiB_2 can be written as:

$$K_2TiF_6(l) + KBF_4(l) \rightarrow Al(l)TiB_{2(\text{in alloy})} + KFAlF_3(l) + KF(l) + AlF_3(l) \quad (17)$$

The maximum amount of TiB_2 formed in situ is determined by the viscosity of the subsequent melt. Values of up to 12% have been reported till now [41]. During in situ fabrication, there are a lot of factors which can influence the distribution of particle over the base alloy along with the final properties of the fabricated composite. Several studies are also there regarding influence of the overall reaction time on the properties of Al–TiB_2 composites. Lu et al. [41] have reported that grain size of the TiB_2 is a clear function of the reaction duration. Grain size decreases with increase in reaction time at the starting of reaction. Grain refinement decreases at a later stage.

Other than in situ technique, there are also a lot of methods through which researchers have been tried to fabricate Al–TiB_2 metal matrix composites. From several reports, different fabrication techniques for fabrication of Al–TiB_2 composites have been noted in Table 2.

Among ex situ methods, simple stir casting and modified stir casting methods are becoming popular. Simple stir casting is a liquid state method. Schematic diagram of simple stir casting method is presented in Fig. 2. This method is different from infiltration because particles are introduced into molten metal by mechanical forces. Molten metal is agitated by mechanical energy and particles are forcefully distributed in the matrix phase. Stirring is kept on until random but uniform distribution of reinforcements is ensured. Stir casting process is patented by Skibo and Schuster [66] for fabrication of Al–SiC composites. There are several researchers who specifically fabricated Al–TiB_2 composites through these ex situ methods and tested tribological properties of it under different conditions [24, 54, 71, 72]. Some modifications like two-stage stirring, ultrasonic vibration assisted stirring are being used nowadays

Table 2 Processing routes for Al–TiB_2 metal matrix composites

Fabrication methods	References
Exothermic dispersion (solid–liquid state), reactive hot pressing (solid–liquid state), stir casting (liquid state), flux assisted synthesis (liquid state), mechanical alloying (solid state), hot isostatic pressing (solid state)	[7, 14, 42, 52, 73, 74, 76]

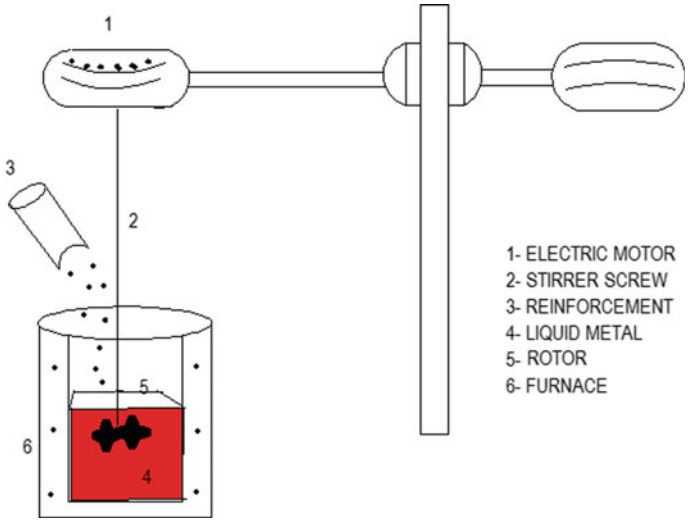

Fig. 2 Schematic diagram of stir casting process

by several researchers. Figure 3 presents schematic diagram of ultrasonic vibration assisted stir casting process. It clearly shows what modifications have been incorporated in the furnace to achieve cluster free cast metal matrix composites.

11 Tribological Properties of Al–TiB_2 MMCs

Al–TiB_2 metal matrix composites show better tribological properties than base aluminum alloy. Accordingly, Al–TiB_2 composites have been used as tribological parts in various applications. Before studying tribological properties of Al–TiB_2 composites, mechanical properties have been thoroughly studied by researchers.

In general, tribological properties of any materials/components denote the wear and friction behavior of it under different operating conditions, i.e., dry sliding, lubricated sliding, elevated temperature sliding. Maximum report on tribological properties of Al–TiB_2 composites has been performed on dry sliding condition. Tribological behavior of T6 treated A356–TiB_2 in situ composites under dry sliding conditions has been reported by Mandal et al. [44]. Tests have been carried out in a pin on disk set up. The wear resistance of Al–TiB_2 composites is significantly improved with increase in the TiB_2 amount in the composites. Regarding friction, no clear trend with respect to the weight percentage of the reinforcement has been observed. Increase in the wear resistance of the composites with respect to the amount of TiB_2 is the contribution of mechanical mixed layer formed on the surface of the pin. This layer is a mixture of the O_2, Fe from counter surface and Al from the base matrix. Niranjan and Lakshminarayanan [50] have studied wear rate of Al–TiB_2

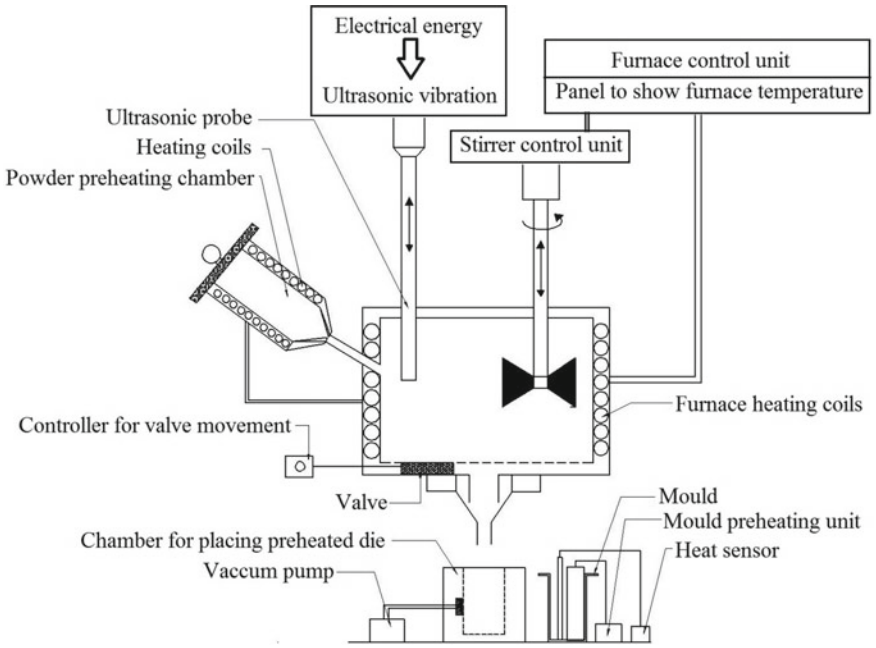

Fig. 3 Schematic diagram of ultrasonic vibration assisted stir casting process

composites with respect to load and weight percentages of TiB_2. They have prepared composites at different melt temperatures with different reaction time. Decrease in wear rate with increase in weight percentage of TiB_2 has been also observed in their study at low load. Al–TiB_2 composites with 6 wt% reinforcement processed at melt temperature 900 °C and reaction time 30 min have shown best wear resistance compared to the other composites processed through different conditions. Natarajan et al. [49] have studied wear resistance of Al–TiB_2 composites at ambient as well as elevated temperature with different operating load. Effect of grain refinement, surface roughness and in situ reaction parameters on wear behavior of Al–TiB_2 composites is also studied by Mallikarjuna et al. (2014). Niranjan and Lakshminarayanan [50] have shown that 6% Al–TiB_2 composite yields maximum wear resistance. Lorusso et al. [40] have reported that 10% micro-TiB_2 reinforced AMC shows worst results when compared with base Al–Si 10 Mg alloy and higher wt% of TiB_2 leads to agglomeration resulting in detrimental effect on properties. Vivekananda and Prabu [78] have studied wear behavior of Al-5 wt% TiB_2 composite by varying the wear test parameters such as operating temperature (in the range of 25–200 °C), applied load (in the range of 10–40 N), sliding velocity (in the range of 0.4–1.3 m/s). They have concluded that at room temperature, the maximum reduction of wear rate of composite is 75% less than Al alloy. Poria et al. [54] have reported the variation of wear depth as a function of applied load for various weight percentages of TiB_2 present in stir cast Al-TiB_2 metal matrix composites. Figure 4 presents that variation

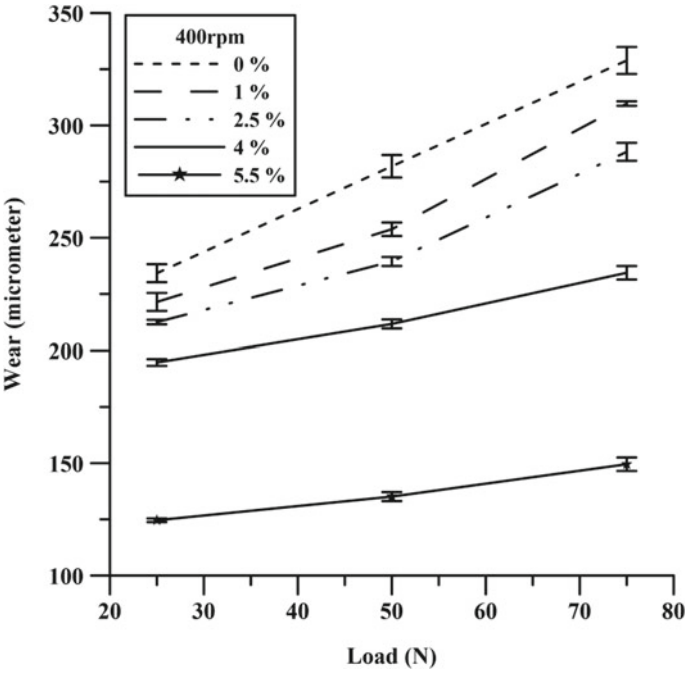

Fig. 4 Wear as function of applied load for different wt% of reinforcement

and it is clearly observed that wear resistance of Al-TiB_2 composites increases with increase of TiB_2 weight percentage.

Reason behind such trend has been mentioned as higher amount of hard TiB_2 particles yields higher hardness of the composite. It is also observed that wear depth increases with increase in applied load for all percentages of reinforcements in the composites. Poria et al. [54] have also reported the friction behavior of Al–TiB_2 composites against weight percentage of reinforcement at different sliding speed for different applied load. Figure 5 is presented here from that report. It is clearly seen that friction is highest for un-reinforced Al alloy and friction has been decreased with increase in weight percentage of reinforcement.

To summarize in nut shell, it can be said that whatever be the fabrication route of the Al–TiB_2 composites, wear resistance improves with addition of the reinforcement. But such improvement persists only up to a certain weight percentage of TiB_2 in base matrix. Further addition of reinforcement generates detrimental effect due to agglomeration of particles inside base matrix. Along with reinforcement, operating load significantly influences the wear and friction behavior of composites. At low load, composites show better tribological behavior which is quite relatable with Archard's wear theory.

Trioblogical properties of Al-TiB_2 composites under elevated temperature sliding condition also have been reported in several work. Actually in many applications of

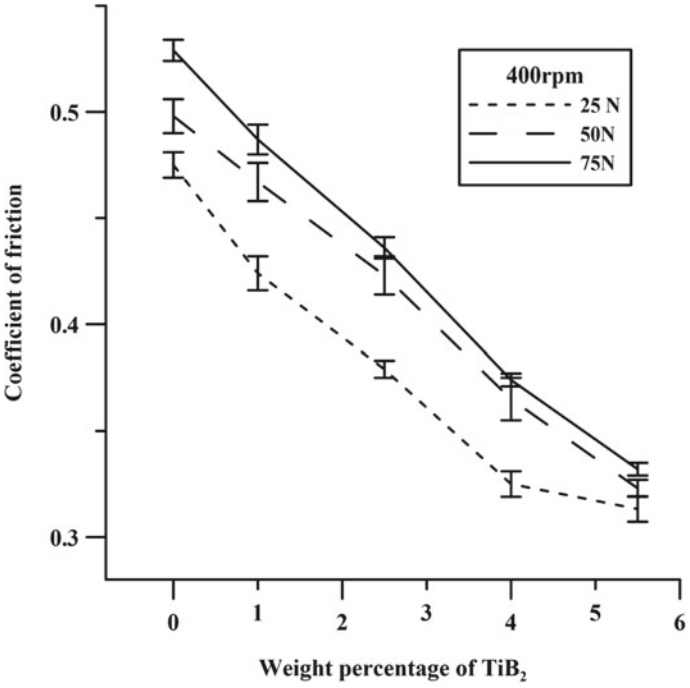

Fig. 5 Friction behavior as function of weight percentages of TiB_2

composite materials, components have to undergo the operating temperature which is nearly 40–50% of the melting point of aluminum alloys/AMCs. That is why tribological performance of composites should be clearly adopted before applying those composites in making industrial components. Kumar et al. [33] have studied Al–TiB_2 composites effect of sliding temperature and load on the wear behavior of Al–4Cu alloy and in situ Al–TiB_2 composites. They have observed that irrespective of the increase in operating temperature, wear resistance increase with weight percentage of TiB_2 composites. When operating temperature has been increased, mild wear has been transformed into severe wear. Temperature at which such transition occurs actually depends on the amount of TiB_2 present inside the composite. General observation of them is that normalized wear rate decreases with increase in temperature for the given amount of TiB_2. Poria et al. [55] have also reported high-temperature tribological performance of Al–TiB_2 composites under five different operating temperatures (50, 100, 150, 200 and 250 °C). From that report, Fig. 6 has been taken to show how wear rate varies at a fixed load with respect to operating temperature and weight percentage of reinforcement. It is seen that wear rate of composites does not change much with increase in operating temperature in the range from 50 to 150 °C, after which it increases sharply in the range from 150 to 200 °C.

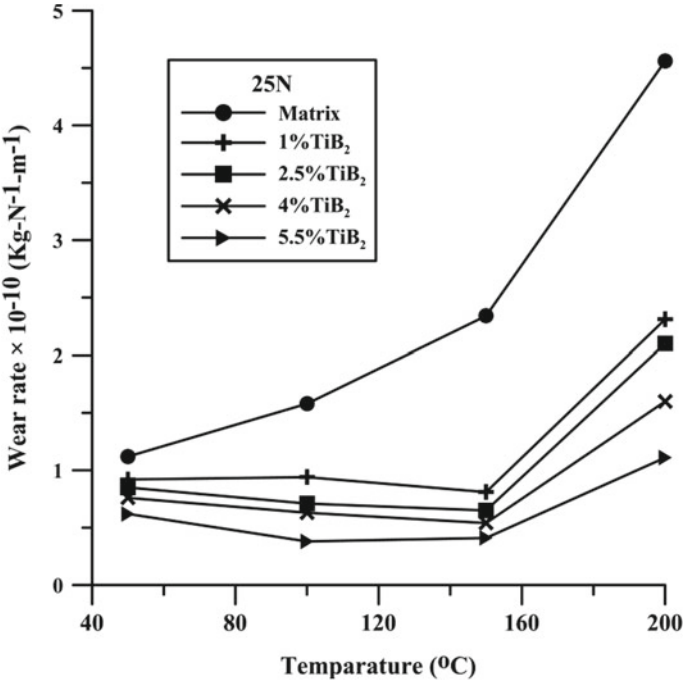

Fig. 6 Wear rate for different temperatures at 25 N load [55]

Some work is also available in lubricated condition tribological behavior of Al–TiB_2 composites. Because the outcome is obvious which is role lubricant is more influential than reinforcement effect on properties.

12 Corrosion Behavior of Al–TiB_2 MMCs

Corrosion of Al–TiB_2 composites also has been reported as the composite has already shown positive outcomes in terms of dry, lubricated and high-temperature tribological behavior. Previously, in steel-TiB_2 composites, it is observed that corrosion resistance of composites increases up to 4 wt% of the reinforcing phase after which corrosion resistance starts to decrease [68]. This phenomenon may happen due to the fact that with increase in the reinforcement phase in composites, fraction of the interface also increases and areas with significant difference in the electrochemical potential also enlarge. Thorough literature survey reveals that if reinforcement phase of AMCs/MMCs is not pure, then galvanic corrosion may increase through dropping in resistivities [25]. Major reinforcements actually do not possess resistivities enough to avoid galvanic corrosion. Sun et al. [69] have established that presence of TiB_2 as reinforcement develops higher corrosion sensitivity of the composites due to the

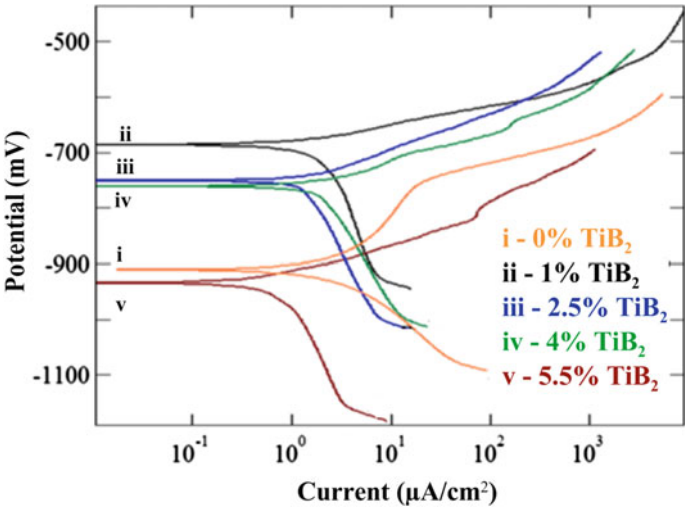

Fig. 7 Tafel plot for base alloy and different wt% of Al–TiB_2 composites

galvanic coupling effect between noble reinforcements (TiB_2) and much more active matrix (Al or Al alloy). Still, Poria et al. [56] have reported corrosion sensitivity of Al–TiB_2 composites through potentiodynamic corrosion test and electrochemical impedance spectroscopy. From their report, Tafel plot and Nyquist plot of base alloy and four different wt% composites have been presented in Figs. 7 and 8. From these two figures, it is clear that corrosion resistance of base alloy sufficiently increases with addition of 1 wt% TiB_2. Further increase in amount of reinforcement leads to decrease in corrosion resistance in terms of corrosion potential though they are better than base alloy until wt% becomes 5.5%. Highest wt% composites exhibit lowest corrosion resistance even lower than base alloy.

13 Conclusion and Future Scope

Starting from laboratory-scale research activities, right now MMCs have established its position in industry level and product level. For example, in applications like exit guide vanes of aircrafts, materials should possess high stiffness along with suitable strength, resistance to erosive wear and aluminum-based MMCs are obvious choice there. Al–TiB_2 composites reported in this chapter have been discussed in terms of their tribological properties and corrosion behavior. Importance of MMCs, why particulate reinforced MMCs are better than other type of composite materials, existing models and theories regarding mechanical properties of particulate reinforced metal matrix composites have been discussed in detail in this chapter. Discussion is also on how MMCs are fabricated and why ex situ techniques for

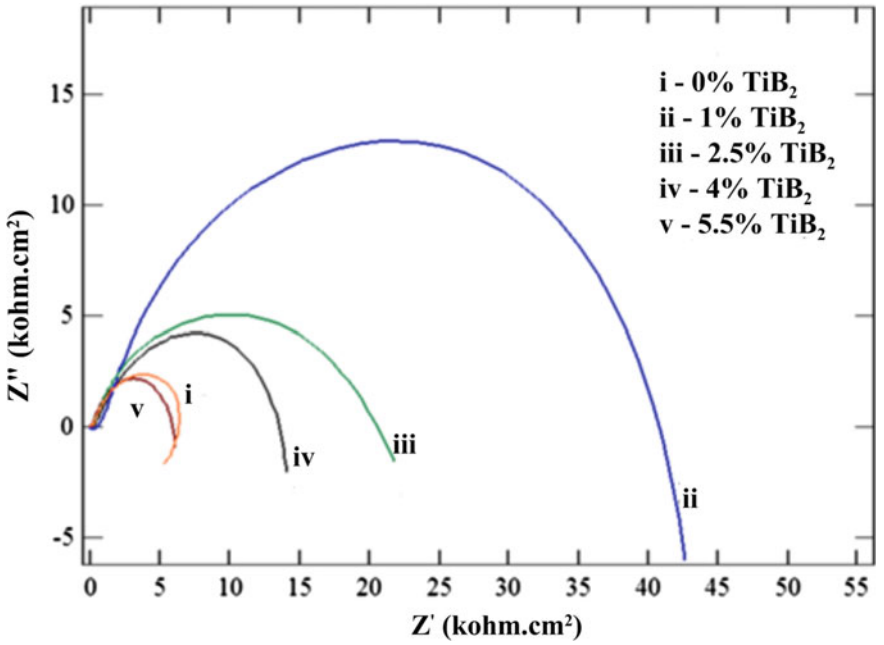

Fig. 8 Nyquist plot for different wt% composites

fabrication of Al-TiB_2 composites are better than in situ techniques. Tribological behavior of Al–TiB_2 composites is very much promising as per discussion. With increase in wt% of TiB_2, wear resistance of composites increases accordingly. It is also discussed how higher amount of TiB_2 phase can effect negatively on the tribological performance of composites. Unlike tribological behavior, corrosion resistance of Al–TiB_2 composites is not so well, though up to 1 wt% reinforcement (TiB_2) it behaves properly.

Future lies in the present. Invention and progression of composites are totally driven by the need of material in adverse and newer working conditions. Applications are modified on daily basis with development of knowledge domain. Researches on materials are also expanding day by day to catch up the newer domains. Al base matrix has been discussed in this study. Magnesium base matrix is now in focus for making new MMCs. Change in fabrication methods is also tried by several researchers. Very recently, Song et al. [67] have published a paper in nature on processing of bulk natural wood and claim that their processed wood is superior than many widely used structural materials as plastics, steels, alloys and composites. Rekha et al. [64] have reported high entropy alloy nano-particle decorated graphene as new age material in very recent time. So it is clearly seen that materials already have been shifted from composite materials. Functionally graded materials are the shifted version of composite materials. But they are also not sufficient to meet the requirements. Now

focus is on 'self-healing materials' [77]. Composites being multi-phase can play role in that domain. Research on self-healing composites has been started.

Currently, it is observed that transportation sectors are shifting towards electrical drive vehicles. Electric drive is the new age technology and it requires huge modification in technology involved with battery cells. But materials are not ready to be adopted for electric drive cars. From the materials of batteries to materials of engines, all are different in electric drive cars from existing one. This is a challenge from a material point of view. It is expected that future of materials research is awaiting a major shift.

References

1. Abdizadeh H, Ebrahimifard R, Baghchesara MA (2014) Investigation of microstructure and mechanical properties of nano MgO reinforced Al composites manufactured by stir casting and powder metallurgy methods: a comparative study. Compos B Eng 56:217–221
2. Acharya SK, Dikshit V, Mishra P (2008) Erosive wear behaviour of redmud filled metal matrix composite. J Reinf Plast Compos 27(2):145–152
3. Akbari MK, Baharvandi HR, Shirvanimoghaddam K (2015) Tensile and fracture behavior of nano/micro TiB_2 particle reinforced casting A356 aluminum alloy composites. Mater Des 1980–2015(66):150–161
4. Alizadeh M, Paydar MH, Jazi FS (2013) Structural evaluation and mechanical properties of nano-structured Al/B_4C composite fabricated by ARB process. Compos Part B Eng 44(1):339–343
5. Antoniou R, Subramanian C (1988) Wear mechanism map for aluminium alloys. Scripta Metallurgica 22(6):809–814
6. Balasubramanian I, Maheswaran R (2015) Effect of inclusion of SiC particulates on the mechanical resistance behaviour of stir-cast AA6063/SiC composites. Mater Design (1980–2015) 65:511–520
7. Balci O, Agaogulları D, Gokçe H, Duman I, Ovecoglu ML (2014) Influence of TiB_2 particle size on the microstructure and properties of Al matrix composites prepared via mechanical alloying and pressureless sintering. J Alloy Compd 586:S78–S84
8. Bannister M (2001) Challenges for composites into the next millennium—a reinforcement perspective. Compos A Appl Sci Manuf 32(7):901–910
9. Ceschini L, Dahle A, Gupta M, Jarfors AEW, Jayalakshmi S, Morri A, Singh RA et al (2017) Aluminum and magnesium metal matrix nanocomposite. Springer, Berlin
10. Chawla KK, Chawla N (2014) Encyclopedia of automotive engineering. Wiley, New York
11. Clyne TW, Withers PJ (1995) An Introduction to Metal Matrix Composites. Cambridge university press
12. Dai LH, Ling Z, Bai YL (2001) Size-dependent inelastic behavior of particle-reinforced metal–matrix composites. Compos Sci Technol 61(8):1057–1063
13. Daniel SAA, Sakthivel M, Gopal PM, Sudhagar S (2018) Study on tribological behaviour of Al/SiC/MoS_2 hybrid metal matrix composites in high temperature environmental condition. Silicon 1–11
14. Dhokey NB, Ghule S, Rane K, Ranade RS (2011) Effect of KBF_4 and K_2TiF_6 on precipitation kinetics of TiB_2 in aluminium matrix composite. J Adv Mater Lett 2:210–216
15. Evans A, San Marchi C, Mortensen A (2003) Metal matrix composites. In: Metal matrix composites in industry an introduction and a survey. Springer, Boston
16. Ferguson JB, Sheykh-Jaberi F, Kim CS, Rohatgi PK, Cho K (2012) On the strength and strain to failure in particle-reinforced magnesium metal-matrix nano-composites (Mg MMNCs). Mater Sci Eng A 558:193–204

17. Girifalco LA, Good RJ (1957) A theory for the estimation of surface and interfacial energies. I. Derivation and application to interfacial tension. J Phys Chem 61(7):904–909
18. Goh CS, Wei J, Lee LC, Gupta M (2007) Properties and deformation behaviour of Mg–Y_2O_3 nano-composites. Acta Materialia 55(15):5115–5121
19. Gopinath K, Balasubramaniam R, Murthy VSR (2001) Corrosion behavior of cast Al-Al_2O_3 particulate composites. J Mater Sci Lett 20(9):793–794
20. Habibnejad-Korayem, M., Mahmudi, R., & Poole, W. J. (2009). Enhanced properties of Mg-based nano-composites reinforced with Al_2O_3nano-particles. Mater Sci Eng A 519(1–2):198–203
21. Haghshenas M (2016) Metal–matrix composites. In: Reference module in materials science and materials engineering, 03950-3
22. Halpin JC, Tsai SW (1967) Air Force Materials Laboratory. AFML-TR-67-42
23. Hanumanth GS, Irons GA (1993) Particle incorporation by melt stirring for the production of metal-matrix composites. J Mater Sci 28(9):2459–2465
24. Hashim J, Looney L, Hashmi MSJ (2001) The wettability of SiC particles by molten aluminium alloy. J Mater Process Technol 119(1–3):324–328
25. Hihara LH (1997) Corrosion of aluminium-matrix composites. Corros Rev 15(3–4):361–386
26. Hosseini N, Karimzadeh F, Abbasi MH, Enayati MH (2010) Tribological properties of Al6061–Al_2O_3 nanocomposite prepared by milling and hot pressing. Mater Design 31(10):4777–4785
27. Iacob G, Ghica VG, Buzatu M, Buzatu T, Petrescu MI (2015) Studies on wear rate and microhardness of the Al/Al_2O_3/Gr hybrid composites produced via powder metallurgy. Compos B Eng 69:603–611
28. Kainer KU (ed) (2006) Metal matrix composites: custom-made materials for automotive and aerospace engineering. Wiley, New York
29. Kang YC, Chan SLI (2004) Tensile properties of nanometric Al_2O_3 particulate-reinforced aluminum matrix composites. Mater Chem Phys 85(2–3):438–443
30. Kennedy AR, Karantzalis AE, Wyatt SM (1999) The microstructure and mechanical properties of TiC and TiB_2-reinforced cast metal matrix composites. J Mater Sci 34(5):933–940
31. Kim CS, Sohn I, Nezafati M, Ferguson JB, Schultz BF, Bajestani-Gohari Z, Cho K, et al (2013) Prediction models for the yield strength of particle-reinforced unimodal pure magnesium (Mg) metal matrix nano-composites (MMNCs). J Mater Sci 4(12):4191–4204
32. Kumar N, Gautam G, Gautam RK, Mohan A, Mohan S (2016) Synthesis and characterization of TiB_2 reinforced aluminium matrix composites: a review. J Inst Eng (India): Series D 97(2):233–253
33. Kumar S, Sarma VS, Murty BS (2010) High temperature wear behavior of Al–4Cu–TiB_2 in situ composites. Wear 268(11–12):1266–1274
34. Lakshmi S, Lu L, Gupta M (1998) In situ preparation of TiB_2 reinforced Al based composites. J Mater Process Technol 73(1–3):160–166
35. Lee HS, Jeon KY, Kim HY, Hong SH (2000) Fabrication process and thermal properties of SiCp/Al metal matrix composites for electronic packaging applications. J Mater Sci 35(24):6231–6236
36. Lee HS, Yeo JS, Hong SH, Yoon DJ, Na KH (2001) The fabrication process and mechanical properties of SiCp/Al–Si metal matrix composites for automobile air-conditioner compressor pistons. J Mater Process Technol 113(1–3):202–208
37. Lim SC, Ashby MF (1987) Overview no. 55 wear-mechanism maps. Acta Metallurgica 35(1):1–24
38. Liu CY, Wang Q, Jia YZ, Zhang B, Jing R, Ma MZ, Liu RP et al (2013) Evaluation of mechanical properties of 1060-Al reinforced with WC particles via warm accumulative roll bonding process. Mater Design 43:367–372
39. Llorca J, Gonzalez C (1998) Microstructural factors controlling the strength and ductility of particle-reinforced metal-matrix composites. J Mech Phys Solids 46(1):1–28
40. Lorusso M, Aversa A, Manfredi D, Calignano F, Ambrosio EP, Ugues D, Pavese M (2016) Tribological behavior of aluminum alloy AlSi10Mg-TiB_2 composites produced by direct metal laser sintering (DMLS). J Mater Eng Perform 25(8):3152–3160

41. Lu L, Lai MO, Chen FL (1997) Al-4 wt% Cu composite reinforced with in-situ TiB_2 particles. Acta Mater 45(10):4297–4309
42. Ma ZY, Bi J, Lu YX, Shen HW, Gao YX (1993) Microstructure and interface of the in situ forming TiB_2-reinforced aluminum composite. Compos Interfaces 1(4):287–291
43. Mallikarjuna C, Shashidhara SM, Mallik US, Parashivamurthy KI (2011) Grain refinement and wear properties evaluation of aluminum alloy 2014 matrix-TiB_2 in-situ composites. Mater Design 32(6):3554–3559
44. Mandal A, Murty BS, Chakraborty M (2009) Sliding wear behaviour of T6 treated A356–TiB_2 in-situ composites. Wear 266(7–8):865–872
45. McNelley TR, Edwards GR, Francois D, McCarthy WH, Shyne JC, Sherby OD (1972) Unusual high temperature mechanical effects in zinc-based particulate composite materials. Metallur Trans 3(5), 1316–1318
46. Miller WS, Humphreys FJ (1991) Strengthening mechanisms in particulate metal matrix composites. Scripta Metallurgica et Materialia 25(1):33–38
47. Miracle DB (2005) Metal matrix composites–from science to technological significance. Compos Sci Technol 65(15–16):2526–2540
48. Mouritz AP (2012) Introduction to aerospace materials. Woodhead Publishing Ltd
49. Natarajan S, Narayanasamy R, Babu SK, Dinesh G, Kumar BA, Sivaprasad K (2009) Sliding wear behaviour of Al 6063/TiB_2 in situ composites at elevated temperatures. Mater Design 30(7):2521–2531
50. Niranjan K, Lakshminarayanan PR (2013) Dry sliding wear behaviour of in situ Al–TiB_2 composites. Mater Design 47:167–173
51. Nishida Y (2013) Introduction to metal matrix composites: fabrication and recycling. Springer Science & Business Media
52. Pandey AB, Mishra RS, Mahajan YR (1993) On the anomalous creep behavior of an XD Al-TiB_2 composite. Scripta Metallurgica et Materialia (United States) 29(9)
53. Pérez-Bustamante R, Bolaños-Morales D, Bonilla-Martínez J, Estrada-Guel I, Martínez-Sánchez R (2014) Microstructural and hardness behavior of graphene-nanoplatelets/aluminum composites synthesized by mechanical alloying. J Alloys Cmpd 615:S578–S582
54. Poria S, Sahoo P, Sutradhar G (2016) Tribological characterization of stir-cast aluminium-TiB_2 metal matrix composites. Silicon 8(4):591–599
55. Poria S, Sutradhar G, Sahoo P (2018) High temperature tribological behavior of stir-cast Al–TiB_2 metal matrix composites. Surface Rev Lett 5(08):1850122, 1–17
56. Poria S, Sutradhar G, Sahoo P (2019) Corrosion behavior of stir-cast Al–TiB_2 metal matrix composites. Int J Mater Res 110(2):148–154
57. Prasad SV, Asthana R (2004) Aluminum metal-matrix composites for automotive applications: tribological considerations. Tribol Lett 17(3):445–453
58. Ramesh CS, Ahamed A (2011) Friction and wear behaviour of cast Al 6063 based in situ metal matrix composites. Wear 271(9–10):1928–1939
59. Ramakrishnan N (1996) An analytical study on strengthening of particulate reinforced metal matrix composites. Acta Mater 44(1):69–77
60. Rao RN, Das S, Mondal DP, Dixit G, Devi ST (2013) Dry sliding wear maps for AA7010 (Al–Zn–Mg–Cu) aluminium matrix composite. Tribol Int 60:77–82
61. Rittner M (2000) Metal matrix composites in the 21st century: markets and opportunities. Report GB-108R, Business Communications Co., Inc., Norwalk, CT
62. Rodopoulos, C. A., & Wessel, J. K. (2004). *The Handbook of Advanced Materials: Enabling New Designs.* Wiley Publication.
63. Rosso, M. (2006).Ceramic and metal matrix composites: Routes and properties.*Journal of Materials Processing Technology*, *175*(1–3), 364–375.
64. Rekha MY, Mallik N, Srivastava C (2018) First report on high entropy alloy nanoparticle decorated graphene. Sci Rep 8(1):8737
65. Singh J, Chauhan A (2016) Overview of wear performance of aluminium matrix composites reinforced with ceramic materials under the influence of controllable variables. Ceram Int 42(1):56–81

66. Skibo MD, Schuster DM (1988) U.S. Patent No. 4,759,995. U.S. Patent and Trademark Office, Washington, DC
67. Song J, Chen C, Zhu S, Zhu M, Dai J, Ray U, Yao Y (2018) Processing bulk natural wood into a high-performance structural material. Nature 554(7691):224
68. Sulima I, Kowalik R, Hyjek P (2016) The corrosion and mechanical properties of spark plasma sintered composites reinforced with titanium diboride. J Alloy Compd 688:1195–1205
69. Sun H, Ma N, Chen D, Li X, Wang H (2008) Fabrication and analysis of anti-corrosion coatings on in-situ TiB_2p reinforced aluminum matrix composite. Surf Coat Technol 203(3–4):329–334
70. Surappa MK (2003) Aluminium matrix composites: Challenges and opportunities. Sadhana 28(1–2):319–334
71. Suresh S, Moorthi NSV, Vettivel SC, Selvakumar N (2014a) Mechanical behavior and wear prediction of stir cast Al–TiB_2 composites using response surface methodology. Mater Des 59:383–396
72. Suresh S, Moorthi NSV, Vettivel SC, Selvakumar N, Jinu GR (2014b) Effect of graphite addition on mechanical behavior of Al6061/TiB_2 hybrid composite using acoustic emission. Mater Sci Eng A 612:16–27
73. Tee K, Lu L, Lai MO (1999) In situ processing of Al–TiB_2 composite by the stir-casting technique. J Mater Process Technol 89:513–519
74. Tee KL, Lu L, Lai MO (2000) Wear performance of in-situ Al–TiB_2 composite. Wear 240(1–2):59–64
75. Tian HF, Qiao JW, Yang HJ, Wang YS, Liaw PK, Lan AD (2016) The corrosion behavior of in-situ Zr-based metallic glass matrix composites in different corrosive media. Appl Surf Sci 363:37–43
76. Tjong SC, Tam KF (2006) Mechanical and thermal expansion behavior of hipped aluminum–TiB_2 composites. Mater Chem Phys 97(1):91–97
77. Toohey KS, Sottos NR, Lewis JA, Moore JS, White SR (2007) Self-healing materials with microvascular networks. Nat Mater 6(8):581
78. Vivekananda AS, Prabu SB (2018) Wear behaviour of in situ Al/TiB_2 composite: influence of the microstructural instability. Tribolo Lett 66(1):41. 1–14
79. Wang T, Chen Z, Zheng Y, Zhao Y, Kang H, Gao L (2014) Development of TiB_2 reinforced aluminum foundry alloy based in situ composites—Part I: an improved halide salt route to fabricate Al–5 wt% TiB_2 master composite. Mater Sci Eng A 605:22–32
80. Wilson S, Alpas AT (1997) Wear mechanism maps for metal matrix composites. Wear 212(1):41–49
81. Wilson S, Alpas AT (1999) Thermal effects on mild wear transitions in dry sliding of an aluminum alloy. Wear 225:440–449
82. Wu Y, Kim GY, Russell AM (2012) Effects of mechanical alloying on an Al6061–CNT composite fabricated by semi-solid powder processing. Mater Sci Eng A 538:164–172
83. Yang Y, Lan J, Li X (2004) Study on bulk aluminum matrix nano-composite fabricated by ultrasonic dispersion of nano-sized SiC particles in molten aluminum alloy. Mater Sci Eng A 380(1–2):378–383
84. Zhang Z, Chen DL (2008) Contribution of Orowan strengthening effect in particulate-reinforced metal matrix nanocomposites. Mater Sci Eng A 483:148–152
85. Zwilsky KM, Grant NJ (1957) Copper-silica and copper-alumina alloys of high temperature interest. JOM J Miner Metals Mater Soc (TMS) 9(10):1197–1201

Chapter 8
Mg-WC Nanocomposites—Recent Advances and Perspectives

Sudip Banerjee, Suswagata Poria, Goutam Sutradhar, and Prasanta Sahoo

1 Introduction

Nowadays, automotive and aerospace industries are fascinated toward lightweight materials like aluminum, magnesium and their composites due to excellent castability, good machinability, good damping capacity and high strength to weight ratio [46]. Particularly magnesium and its composites are becoming favorable choice as magnesium has 50% faster machinability index and 25–50% greater castability compared to aluminum. Due to above reasons, several automotive industries are replacing ferrous components like engine block, instrumental panel, transmission case, gear control housing, etc., and even some aluminum components with magnesium and its composites [4]. However, several factors like inherent brittleness, low thermal stability, poor corrosion resistance, low toughness and poor tribological properties at room and elevated temperature are some limiting factors of magnesium and its alloys. Many of these properties are improved by alloying (by adding Fe, Ni, Cu, Y, Nd, Zr, Ca) [19, 83] and precipitation hardening. But that limit of improvement is not adequate for many applications. Hence, further improvement is needed. Researchers have considered development of Mg composite as the next step of improvement. Recently, plenty of researches had been carried out on Mg composites and effect of various factors like reinforcements, size of reinforcement, wt% of reinforcement, fabrication method, secondary treatments, etc., on microstructural characteristics, mechanical properties, tribological properties along with machining

S. Banerjee (✉) · P. Sahoo
Jadavpur University, Kolkata, India
e-mail: banerjee.sudip71@gmail.com

S. Poria
Heritage Institute of Technology, Kolkata, India

G. Sutradhar
National Institute of Technology, Manipur, India

S. Sahoo (ed.), *Recent Advances in Layered Materials and Structures*,
Materials Horizons: From Nature to Nanomaterials,
https://doi.org/10.1007/978-981-33-4550-8_8

characteristics have been disclosed. Furthermore, magnesium matrix composites are developed by reinforcing ceramics and carbon-based particles in next step toward property improvement. In this context, ceramics like SiC, TiC, B_4C, Al_2O_3, MgO, ZnO, Y_2O_3, TiB_2, BN, AlN, graphite as well as intermetallics like Mg_2Si in the order of 2–20 μm are reinforced in magnesium matrix [5, 30, 39, 56, 58, 59, 61, 68, 78].

In last decade, researchers have focused on nanoparticle reinforcement in magnesium matrix as they have seen nanocomposites as potential candidate for functional and structural applications. Literatures observed that nano-reinforcements refine grain size and affect the dislocation motion to improve mechanical as well as tribological properties [47]. Fortification of nano-sized reinforcements helps to improve different properties like ductility, compressive and tensile behavior, creep resistance, elevated temperature mechanical behavior, damping behavior, tribological properties, dynamic mechanical properties, machining characteristics, thermal coefficient, corrosion resistance, ignition resistance. It is also found in available literature that very light amount ($\leq$2% by weight) of nanoparticle reinforcement can provide improved mechanical, microstructural and tribological properties [53]. It is also significant for nanocomposites that particle damage mechanism is minimal which helps to provide better elongation, fracture toughness, etc. It is observed that ceramic-based nanoparticles and carbon-based nanoparticles are majorly reinforced in Mg matrix to achieve desired properties. In this context, scientific community has reinforced nano-sized particles like SiC, TiB_2, TiC, ZnO, CNT, Y_2O_3, BN, graphite, MgO, Al_2O_3, grapheme nano-sheets, etc., in magnesium matrix [2, 22, 43, 53, 55, 60, 73]. In this study, emphasis is given on WC as reinforcement in Mg matrix because WC shows exceptional properties like high elastic modulus (630 GPa), high melting point (2870 °C), better thermal conductivity (110 Wm K^{-1}), high hardness (1400 HV), tolerable oxidation resistance till 600 °C, coefficient of thermal expansion (5.5 μm), etc. [12, 64]. WC has been reinforced in Al and Mg matrix by the scientific community till last decade. Positive inputs of WC in microstructural, mechanical, tribological and corrosion behavior of MMCs have already investigated which is quite inspiring in foregoing study on WC reinforced MMNCs. Based on this, Lekatou et al. [50] have investigated the wear and corrosion behavior of Al-WC/TiC composites and observed useful effect. Pal et al. [64] have investigated the contribution of WC on microstructural and tribological behavior and concluded that Al-WC MMCs show beneficial effect than base material. Razavi and Mobasherpour [70] have fabricated Al-WC nanocomposites and reported excellent microstructural stability with better mechanical properties.

Property of metal matrix composites and nanocomposites can be improved by considering different factors like cautious selection of base metal along with reinforcement having proper length scale and selection of fabrication route. Fabrication route and processing parameters are of crucial importance to generate uniform distribution and proper matrix-reinforcement interface. For mass scale production, i.e., casting, wettability and dispersion-related factors are of main concern. These issues are mainly tackled by preheating particles, applying proper stirring speed and providing ultrasonic vibration [20]. In case of stir casting, different process parameters like stirrer shape, stirrer location in melt and stirring speed are most influential.

But stir casting faces distribution-related problem [53]. In recent times, ultrasonic treatment (UST)-based stir casting method is used to achieve proper distribution. This process uses millions of mechanical waves to generate immense localized temperature, shock waves, pressure and acoustic streaming. Such intense impact and high temperature help to break clusters of nanoparticles [14]. However, researchers have also tried disintegrated melt deposition, powder metallurgy, squeeze casting and spray atomization method. Mg-MMNCs are considered as potential material in different sectors like aviation, biomedical, automobile, electronics, defense, etc. To cope with such demand first of all technologies must be improved as well as new MMNCs must be developed. In view of the potential advantages and applications of magnesium alloys and their composites, the present study reviews existing literatures of this area and tries to present a comprehensive discussion on several aspects of magnesium-based metal matrix nanocomposite. Particular emphasis is given on Mg-WC metal matrix nanocomposites. Main parameters which are discussed here are

1. Fabrication of Mg-WC MMNCs.
2. Microstructural characteristics of Mg-WC MMNCs.
3. Mechanical properties (Microhardness, tensile behavior) of Mg-WC MMNCs.
4. Tribological behavior of Mg-WC nanocomposites.

Finally, a concluding discussion on the potential of Mg-WC MMNCs for different application areas is presented.

2 Fabrication Methods

Mg-MMNCs are developed through different production routes, while main distinction is the matrix state (solid, liquid and semi-solid). Among different procedures, liquid metallurgy process is widely accepted due to its simple function, industrial scalability and cost effectiveness. Mainly followed liquid metallurgy route is stir casting, ultrasonic vibration associated stir casting method, disintegrated melt deposition (DMD) and infiltration technique. Moreover, powder metallurgy, semi-solid casting and friction stir processing are other well-known fabrication processes.

2.1 Stir Casting

Stir casting method is widespread method of fabricating MMNCs due to its simplicity, economic viability and large-scale productivity. In this well-known process, reinforcing particles are added and mixed in liquid base metal using mechanical stirrer [71]. Schematic diagram and flow diagram of this method are shown in Fig. 1a, b, respectively. Al_2O_3, ZnO, SiC, MgO and CNT nanoparticles are reinforced in Al matrix using stir casting method [35, 51, 71, 75, 82], while SiC, WC, Al_2O_3 particles are incorporated in Mg matrix [34, 42, 41, 72, 80] using stir casting method.

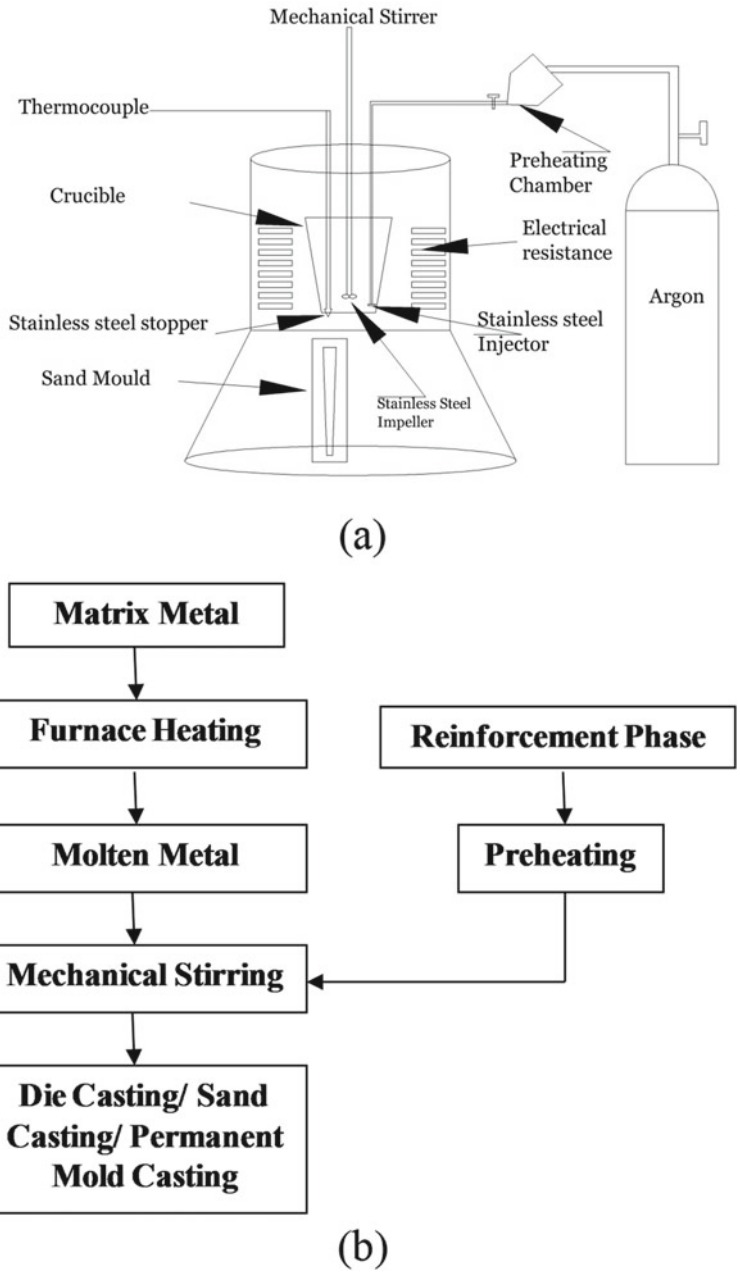

Fig. 1 Stir casting. **a** Schematic diagram, **b** process flowchart

Habibnejad-Korayem et al. [34] have mixed Al_2O_3 nanoparticles (100 nm) of weight percentage 0.5, 1 and 2% in C_p-Mg and AZ31 base alloy using stir casting. The mixture was stirred with stainless steel mechanical stirrer for 2 min. Habibnejad-Korayem et al. [34] reported uniform distribution of Al_2O_3 nanoparticles in C_p-Mg and AZ31 base matrix. Likewise, Karuppusamy et al. [42, 41] have developed AZ91-1.5WC MMNC through vacuum incorporated stir casting method and found good distribution of WC nanoparticles in base matrix. Praveenkumar et al. [69] have manufactured Mg-WC MMNCs by stir casting method. But Hamedan and Shahmiri [35], Sajjadi et al. [71] and Suresh et al. [75] yield that tendency of agglomeration, cluster formation, air entrapment leading high porosity, undesired chemical reaction are present in stir cast nanocomposites.

Uneven distribution can initiate microcracks, slip dislocations under applied stress, eventually causing premature failure of composites. On the other hand, agglomeration of particles formed weak bonds in material. As a result, mechanical properties of fabricated materials got reduced. Thus, segregation of particles in composites is of major concern during stir casting. Distribution of reinforcement mainly depends on material properties (i.e., wettability, relative density and mixing strength) and process parameters (i.e., stirring speed, stirrer geometry, stirrer depth in melt, melting temperature). Hence, particular attention should be given toward those parameters for further modification of stir casting process. Entrapment of gases and inclusions during stirring is also a major concern as magnesium is highly oxidation prone. Entrapped gas and unwanted inclusions increase viscosity of the melt. Thus, judiciously controlled stirring process is highly required. Hence, modified stirring system such as electromagnetic stirring, centrifugal force stirring and ultrasonic vibration assisted stirring are gradually adopted for fabricating composites Ye & Liu [83].

2.2 *Ultrasonic Cavitation*

Literatures report that stir casting process has faced distribution problem of nanoparticles as nanoparticles floats on liquid melt and forms cluster because of attractive nature of van der Waals force and deficiency of repulsive force [81]. That is why modification in stir casting method needs to be adopted for developing nanocomposites. In this regard, ultrasonic vibration is provided in the melt as ultrasonic waves provide nonlinear behavior in liquid in the form of acoustic streaming, high temperature and transient cavitations. Hence, ultrasonic treatment associated stir casting method is upgraded version of stir casting. In this process, sonotrode is straight away immersed in liquid melt, and high frequency ultrasonic waves (18–20 kHz) are applied. Elementary diagram and flowchart of ultrasonic treatment associated casting process are shown in Fig. 2a, b, respectively.

Ultrasonic waves generated tiny microscopic bubbles in large number. These bubbles collapse ($<10^{-06}$ s) after every successful cavitation cycle and produce hot spots of microscale which generates high temperature about 5000 °C, pressure

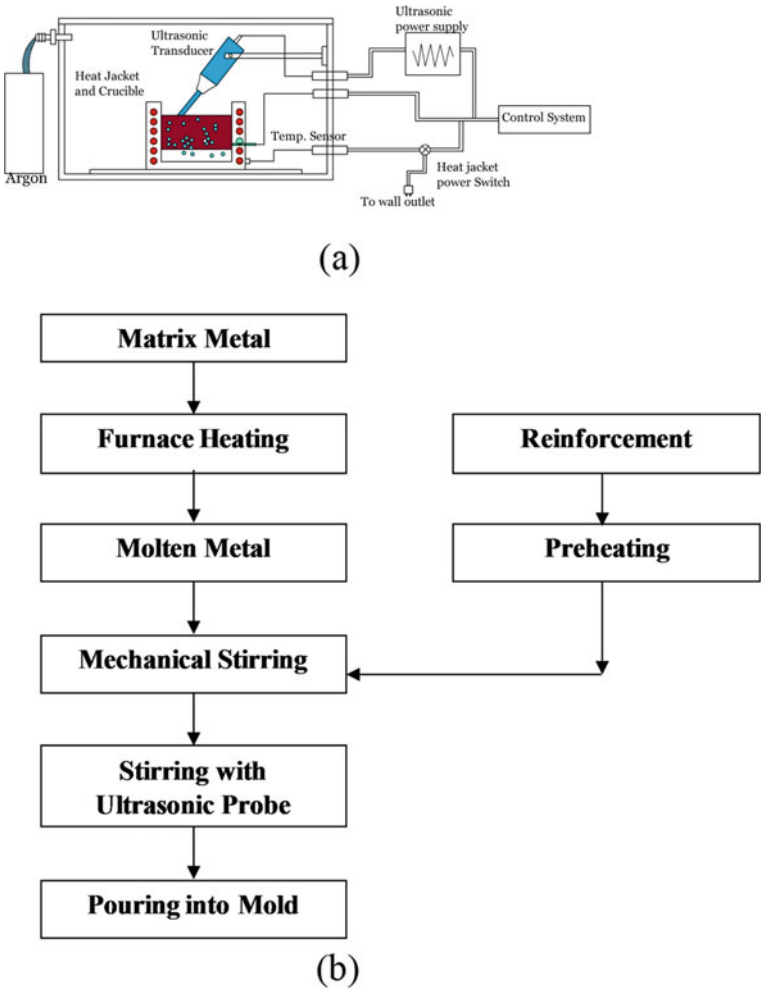

Fig. 2 Ultrasonic vibration. **a** Schematic diagram, **b** Process flowchart

(~1000 atm) and high heating or cooling rate (10^{10} K/s). All these after effects of bubble collapsing help in degassing of melt, dispersing of particles and microstructure refining [1, 76]. Mechanisms of de-agglomeration process of nanoparticles by ultrasonic vibration are shown in Fig. 3. Lan et al. [48] have successfully fabricated AZ91D-SiC nanocomposites using ultrasonic vibration. Melt is treated with ultrasonic power of 80 W to achieve fair distribution of SiC nanoparticles. Nie et al. [62] have ultrasonically casted AZ91-SiC nanocomposites using varying volume percentage (0.5, 1, 2%) of SiC nanoparticles (80 nm) under inert gas (CO_2/SF_6) environment. Ultrasonic vibration at 480 W and 20 kHz is provided in molten metal (700 °C) for 20 min, and high pressure (100 MPa) was employed at the time of

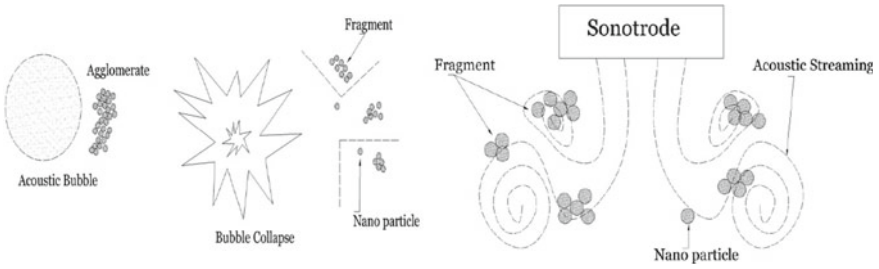

Fig. 3 Mechanisms of de-agglomeration process

solidification. Characterization results yield that 0.5 vol% SiC provides homogeneous distribution and enhanced mechanical properties while 2 vol% SiC provided sign of agglomeration and detrimental effect on UTS, ductility. Dieringa et al. [20] have employed ultrasonic treatment to develop Mg-AlN nanocomposite. Habibnejad-Korayem et al. [33] have used Al_2O_3 as reinforcement in Mg matrix to develop Mg-MMNCs. Accordingly, Banerjee et al. [9] have fabricated Mg-WC nanocomposites for differing weight percentages of tungsten carbide (0.5–2 wt%) with the support of ultrasonic treatment associated stir casting process. Khandelwal et al. [44] prepared AZ31/Al_2O_3 nanocomposites using ultrasound treatment assisted stir casting by adding varying weight percentage (0.5, 1.0, 2.0%) Al_2O_3 (30–70 nm). Melt was treated with ultrasonic vibration under two different states, i.e., during air cooling (outside furnace), iso-UST inside furnace. It was observed that reinforcing agents were well dispersed and improved mechanical properties. Similarly, Nie et al. [63], Cao et al. [13], Erman et al. [22] have used ultrasonic vibration to develop magnesium-based metal matrix nanocomposites using ceramic-based nanoparticles. Accordingly, ultrasonic treatment is also used to disperse carbon-based nanoparticles (CNT, graphene) in Mg matrix. Chen et al. [17] have used combination of ultrasonic vibration at liquid state and stirring at solid state to develop Mg-GNP nanocomposite. In this process, GNP were first mixed in Mg melt at 700 °C using ultrasonic vibration of amplitude 60 μm. Ultrasonic vibration was employed for 15 min, and plates of thickness 6 mm were casted. Then, friction stir processing (FSP) was exercised with pin (dia. 5 mm, velocity 25 mm/min and rotating speed 1800 rpm). It was reported that GNPs were more homogeneously distributed due to application of FSP. TEM study of developed Mg-GNP nanocomposites did not found any cavity, reaction product which suggested good bonding between matrix metal and reinforcement phase. Liu et al. [52] have fabricated Mg-1.5CNT nanocomposite combining mechanical stirring along with ultrasonic vibration. Primarily, CNT nanoparticles (20–40 nm) were incorporated in Mg melt during mechanical stirring which was continued for 2 min, then ultrasonic vibration (20 kHz) was employed for 15 min. This process helped to disseminate CNT uniformly in base matrix, and mechanical properties like UTS, ductility were improved by 22, 42%, respectively. Aung et al. [3] have fabricated Mg-CNT nanocomposites through ultrasonic vibration associated stir casting method.

2.3 Disintegrated Melt Deposition (DMD)

This process is also derived from stir casting process. It is combined of casting and spray process. Primarily composite slurry is produce through stir casting process. Then, that slurry is poured through pouring nozzle under inert gas environment at superheat condition and deposited in metallic substrate. Schematic diagram and flow diagram of DMD process are shown in Fig. 4a, b, respectively. Different nanoparticles like Al_2O_3, CNT, Y_2O_3, ZrO_2, B_4C have been mixed with Mg/Mg-alloys through this process to produce Mg-MMNCs [15, 27, 28, 31]. Srivastan et al. [74] have developed AZ31-1.5 Al_2O_3 nanocomposite using Al_2O_3 nanoparticles of size 50 nm through DMD process. Then as-cast bar was extruded at 350 °C. It is found that grain size of nanocomposite was much finer than base alloy. Hassan and Gupta [36] have used DMD process to develop Mg-1.1Al_2O_3 nanocomposite. Microstructural study yields grain refinement, uniform distribution of particles, negligible porosity and no shrinkage porosity. Goh et al. [36] have used 0.3, 1.3, 1.6 and 2 wt% of CNTs to fabricate Mg-MMNCs with the help of DMD process. TEM analysis of Mg and Mg-1.3 CNT disclosed that Mg had only basal dislocation whereas Mg-1.3 CNT had basal as well as prismatic slip planes. These occurrences influenced mechanical characteristics by improving ductility. Nguyen and Gupta [59] incorporated Al_2O_3 in AZ31 alloy to through DMD method and reported excellent interfacial bonding, near equiaxed grains in developed nanocomposites.

2.4 Infiltration Technique

Infiltration technique uses pressure to inject liquid metal to porous preform. The porous preform is developed by mixing metal melt, reinforcement and binder. The mixture is then subjected to filtration and dried as well as heat treated to achieve dimensional stability. Typically, pressure infiltration technique is executed either by gas infiltration or by squeeze infiltration. Schematic diagram and flowchart of infiltration technique are presented in Fig. 5a, b, respectively. Generally, inert gas or vacuum is employed for gas infiltration, while hydraulic pressure is employed for squeeze infiltration. This process is mainly followed to produce MMCs with micron-sized particles. Babu et al. [7] have developed Mg-MMCs by incorporating graphite and alumina particles in Mg melt. Nowadays, this process is also used to develop nanocomposites. CNT was reinforced in Mg matrix through infiltration process [8]. But larger infiltration time, segregation of phases, higher cost of preforms limited the application of this process for mass scale production.

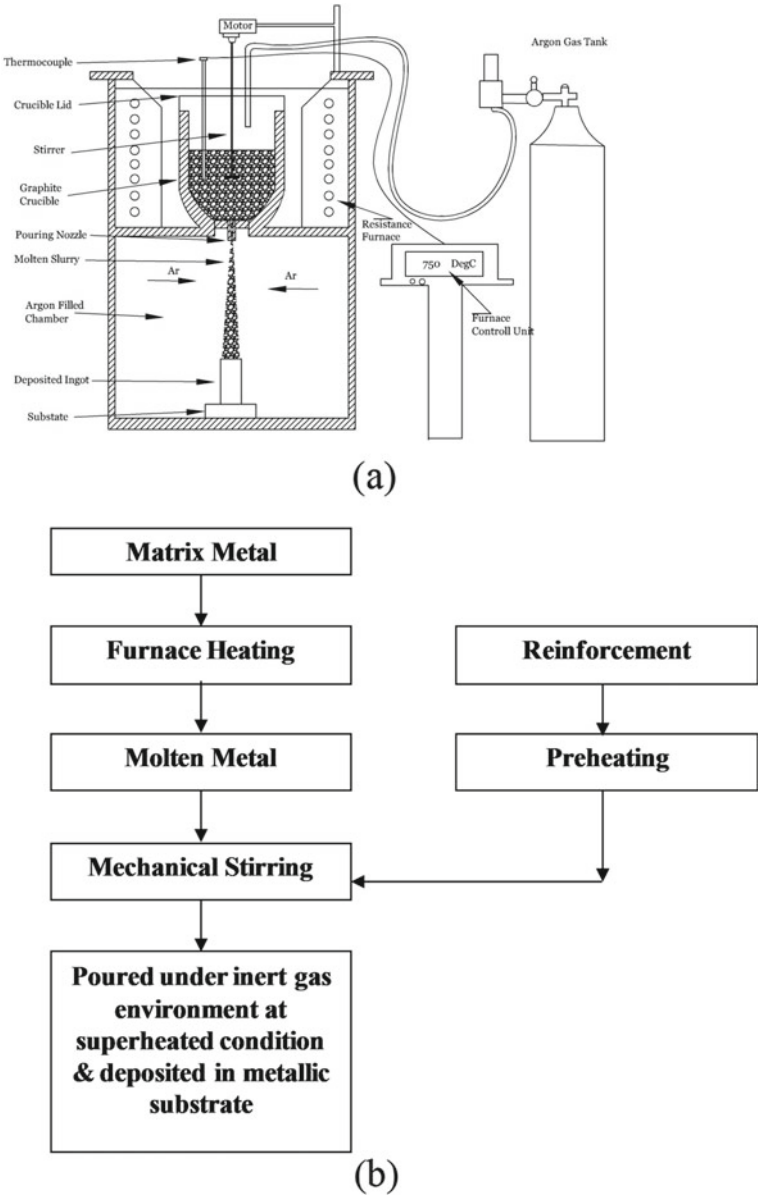

Fig. 4 DMD process. **a** Schematic diagram, **b** process flowchart

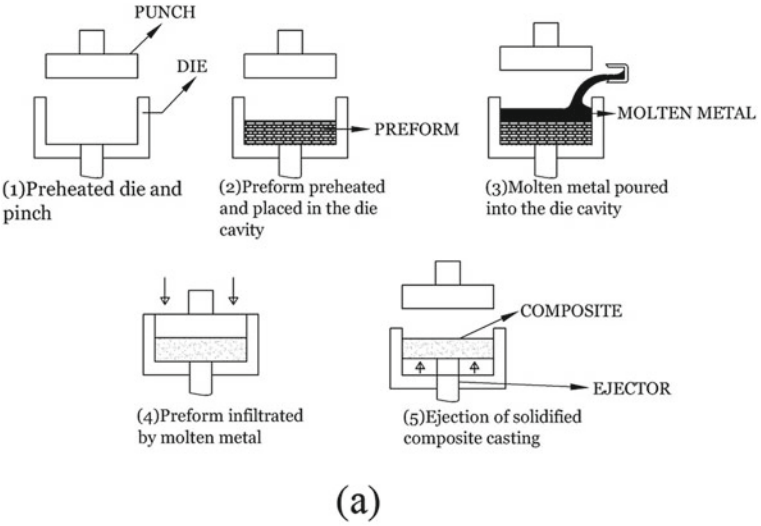

(a)

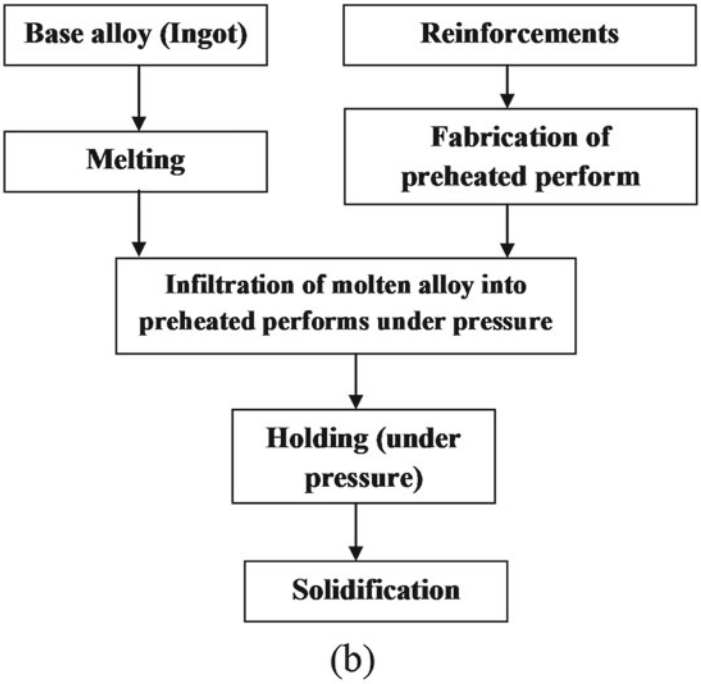

(b)

Fig. 5 Infiltration process. **a** Schematic diagram, **b** process flowchart

2.5 Semi-Solid Processing

In semi-solid processing, partially solid mixture is poured into cavity. This process possesses several advantages like non-turbulent filling, less energy demand, low shrinkage, less post molding activities, low porosity, etc. Semi-solid processing is mainly of two types, thixo-processing and rheo-processing. In thixo-processing, solid feedstock is partially melted by reheating, and liquid melt is partially solidified at rapid cooling and low superheated condition. Finally, the semi-solid mixture is infused in die. Schematic diagram and flow diagram of semi-solid process is displayed in Fig. 6a, b. Kleiner et al. [45] have used thixo-processing for magnesium and studied different microstructural conditions. In case of rheo-processing, no special feedstock is used but the melted slurry is cooled at the time of casting and semi-solid mixture is prepared. Chen et al. [18] have synthesized Mg–SiC nanocomposite through this process and reported equal distribution of SiC particles as well as very good mechanical properties.

2.6 Powder Metallurgy

Powder metallurgy is a well-known solid state process which uses blending, compacting and sintering to develop composites. Powder metallurgy helps to incorporate high amount of reinforcing particles, can develop large batches and can develop components with higher dimensional accuracy. Schematic diagram and flowchart of powder metallurgy are shown in Fig. 7a, b. Goh et al. [27] have synthesized Mg-CNT nanocomposites by powder metallurgy process and found increment in thermal stability, enhanced ductility, yield strength, fracture strength with increasing percentage of CNT. Tun and Gupta [78] have developed Mg-Y_2O_3 nanocomposites via microwave sintering and revealed well distribution of nano-yttria with minimal porosity. Incorporation of nano-yittra had decreased CTE and increased ductility, fracture strength and UTS.

2.7 Friction Stir Processing (FSP)

FSP is derived from friction stir welding, and it is widely used by recent researchers for producing surface as well as bulk nanocomposites. In FSP, at first groove is prepared in base metal. Afterwards, that groove is filled by reinforcements using rotating non-consumable tool. Finally, tool having pin is stirred to disperse reinforcement in matrix. Schematic diagram and flow diagram of FSP are shown in Fig. 8a, b. Morisada et al. [57] have developed Mg-MWCNT nanocomposites using FSP (stirring speed = 1500 rpm, traverse speed 25 mm/min) and yield excellent grain refinement. Lee et al. [49] have incorporated SiO_2 nanoparticles (20 nm) in

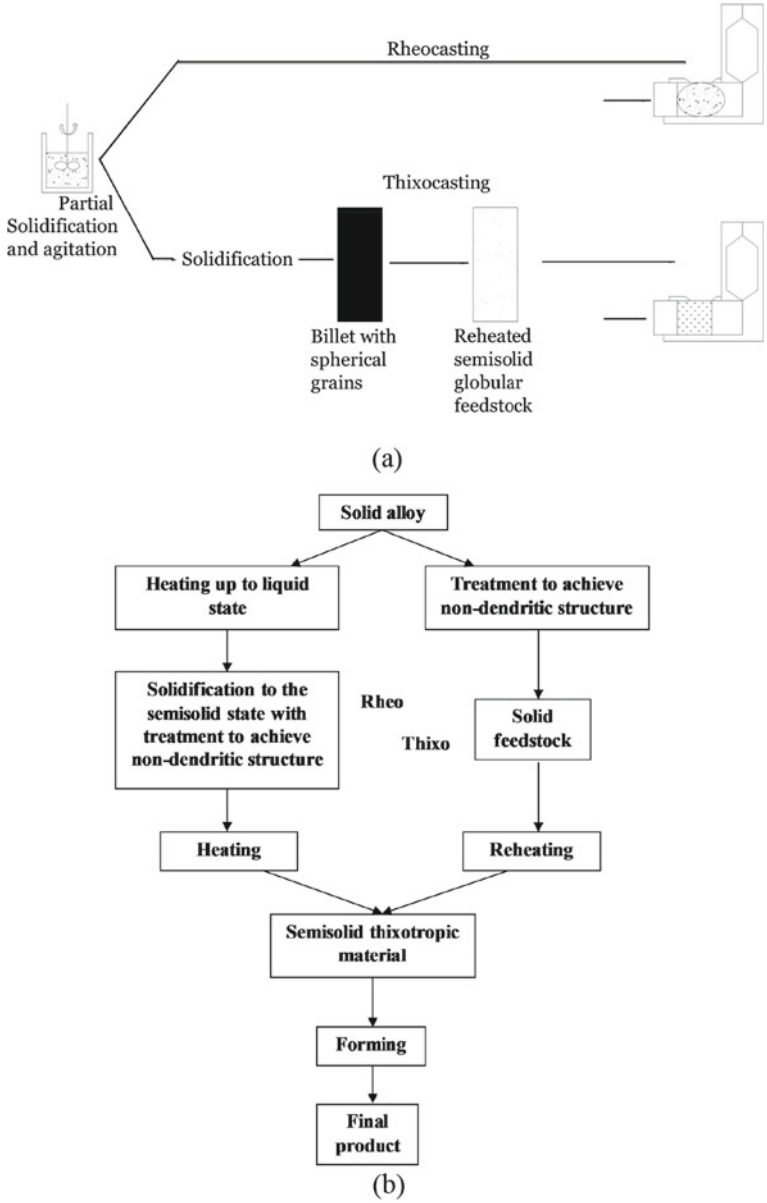

Fig. 6 Semi-solid process. **a** Schematic diagram, **b** process flowchart

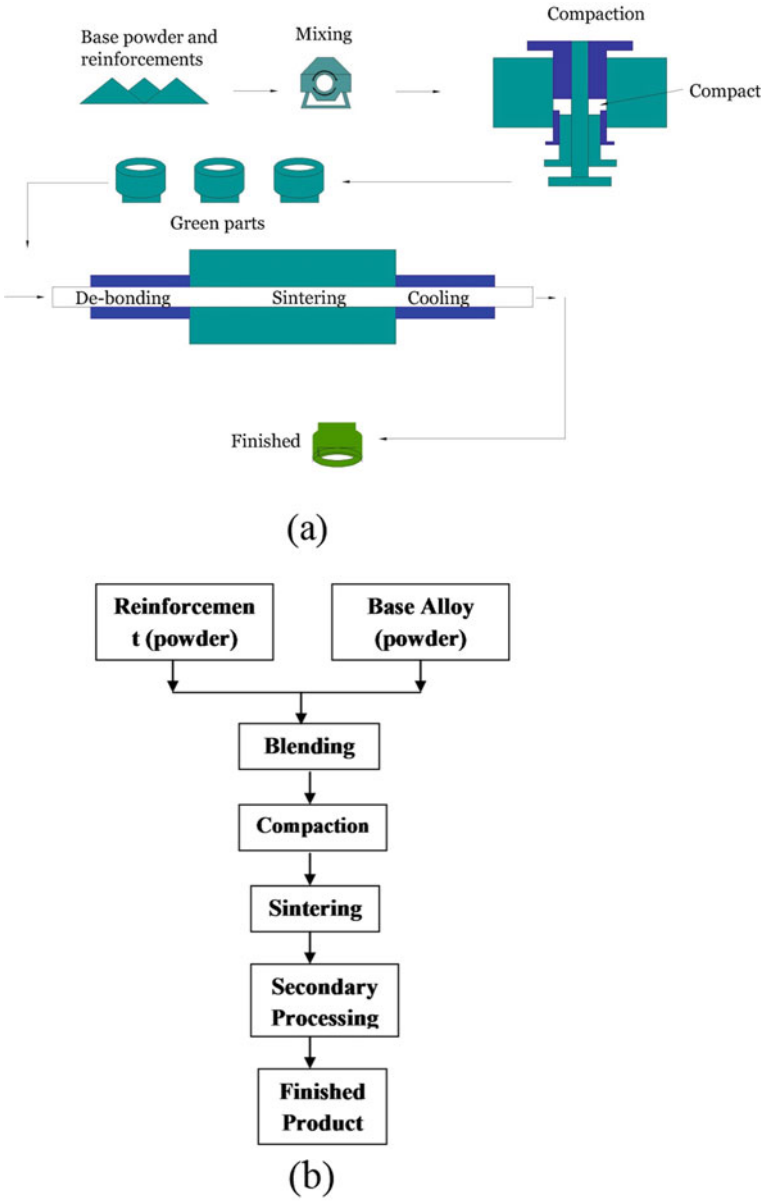

Fig. 7 Powder metallurgy process. **a** Schematic diagram, **b** process flowchart

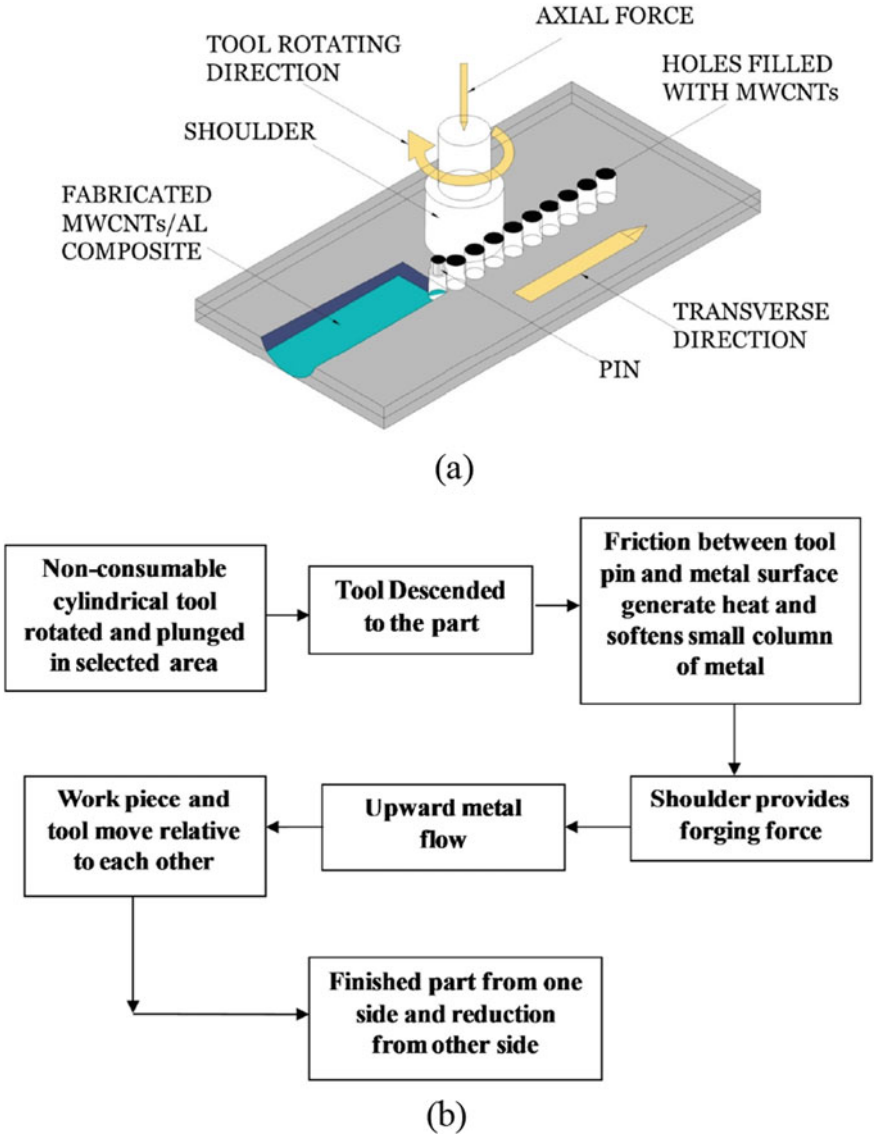

Fig. 8 Friction stir processing. **a** Schematic diagram, **b** process flowchart

AZ61 magnesium matrix using FSP with rotational speed 800 rpm and traverse speed 45 mm/min. Lee et al. [49] have reported excellent grain refinement and enhancement in mechanical properties. Azizieh et al. [6] have developed AZ31-Al_2O_3 nanocomposite by FSP and examined contribution of probe profile and speed on and microstructural characteristics and mechanical property like hardness. Grain size was improved to 1–5 μm, and macrohardness was also enhanced to 85–92 HV.

3 Selected Review of Nanocomposite Properties

3.1 Microstructural Properties

In the context of microstructural point of view, refined grain boundary, equiaxed and reduced grain size are major goals of incorporating nanoparticles in magnesium matrix. Literatures have shown that incorporation of nanoparticles like Al_2O_3, BN, TiC, SiC, CNT, graphite, Y_2O_3 has enhanced microstructural property of MMNCs compared to C_p Mg and base alloys. Effect of different particles on microstructure can be disclosed by studying grain size of that composite. It was found that Mg-1.1 Al_2O_3 (size 80 nm) produced by DMD method presented decrease in grain size from 49 to 6 μm [37]. Hassan and Gupta [38] again observed that addition of 1.11 vol% of Y_2O_3 have reduced the grain size from 60 to 13 μm. Hassan and Gupta [37] have shown that addition of 1.1 vol% ZrO_2 nanoparticles have reduced the grain size from 60 to 11 μm. In this study, emphasis is given on Mg-WC nanocomposites. It is observed in literatures that Banerjee et al. [9] have elaborately discussed about the effect of WC nanoparticle incorporation in AZ31 alloy. Praveenkumar et al. [69] synthesized AZ31B-WC composites and revealed well distribution of WC particles in Mg matrix by performing SEM study. Banerjee et al. [9] have mainly performed microstructural characterization considering optical microscopic images and scanning electron microscopic (SEM) images. Optical images and SEM images of Mg-WC nanocomposites with varying wt% of WC are shown in Figs. 9 and 10, respectively. Figure 9 showed that grain size of base alloy was refined due to addition of WC nanoparticles. It is described that equiaxed grains were present while good interfacial bonding was observed among matrix and reinforcement phase. It was also reported that presence of WC nanoparticles induced recrystallization by forming plate like β-$Mg_{17}Al_{12}$ at grain boundaries. Figure 10 revealed compact composite structures without significant clustering and almost uniform distribution of WC nanoparticles throughout the matrix. Karuppusamy et al. [41] performed a cryogenic treatment of fabricated AZ91-WC nanocomposite and observed microstructural changes by SEM. SEM micrographs revealed increase in β-$Mg_{17}Al_{12}$ at cryogenic treated AZ91-WC nanocomposites compared to other samples, and equal distribution of WC nanoparticles was also confirmed by SEM micrographs.

3.2 Mechanical Properties

Enhanced mechanical properties are basic objective of developed material. Mechanical properties like hardness, tensile response are of immense importance for any engineering material. Review of existing literatures revealed that incorporation of small amount (≤2 wt%) of nanoparticles like Al_2O_3, Y_2O_3, SiC, TiC, CNT, AlN, WC had significantly improved mechanical properties of magnesium and magnesium alloys [13, 36, 37, 65, 66]. Hassan and Gupta [37] have shown that base Mg

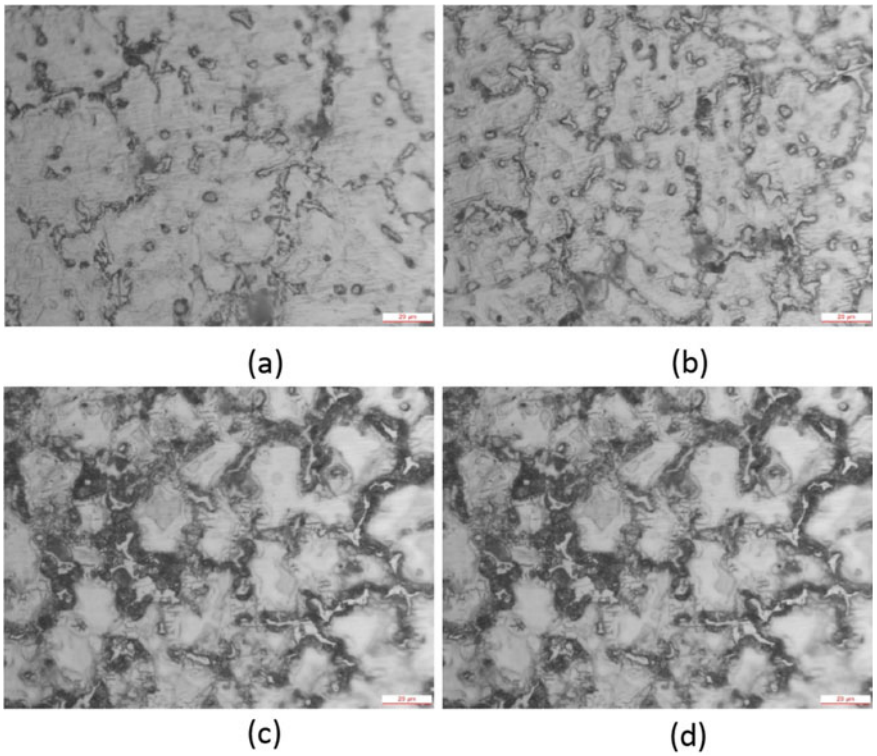

Fig. 9 Optical images of composites. **a** Mg-0.5WC, **b** Mg-1WC, **c** Mg-1.5WC, **d** Mg-2WC [9]

have yield strength, UTS and ductility as 132 Mpa, 193 MPa and 4.2%, respectively, while addition of 1.1 vol% Al_2O_3 have produced YS, UTS and ductility as 194 MPa, 250 Mpa and 6.9%. Addition of Y_2O_3 have shown YS, UTS and ductility as 153 MPa, 195 MPa and 9.1%, respectively, and addition of 1.1 vol% ZrO_2 shows 146 MPa, 199 MPa and 10.8%, respectively. Lan et al. [48] have yielded that fortification of 5 wt% of SiC nanoparticles has increased microhardness by 75% than base AZ91D alloy. Tekamulla et al. [77] have yielded that fortification of 1.53 wt% of ZnO nanoparticles has improved hardness, YS, UTS by 44%, 149% and 35%. Meenashisundaram and Gupta [54] have found significant improvement in YS and UTS by incorporating 0.58–1.98 wt% TiB_2 nanoparticle. Praveenkumar et al. [69] disclosed that microhardness, tensile strength, yield strength and flexural strength of AZ31B-WC composites have increased with increasing percentage of WC reinforcement. Banerjee et al. [9] reported around 43% improvement in microhardness with incorporation of 2wt% of WC nanoparticle compared to base AZ31 alloy. Variation of microhardness with varying wt% of WC is presented in Fig. 11. On the other hand, Karuppusamy et al. [42] reported 10.5% increment in Rockwell hardness and approximately 35% increment in ultimate tensile strength (UTS) for cryogenic treated AZ91-1.5WC nanocomposite than base alloy. Figure 12 presents detail

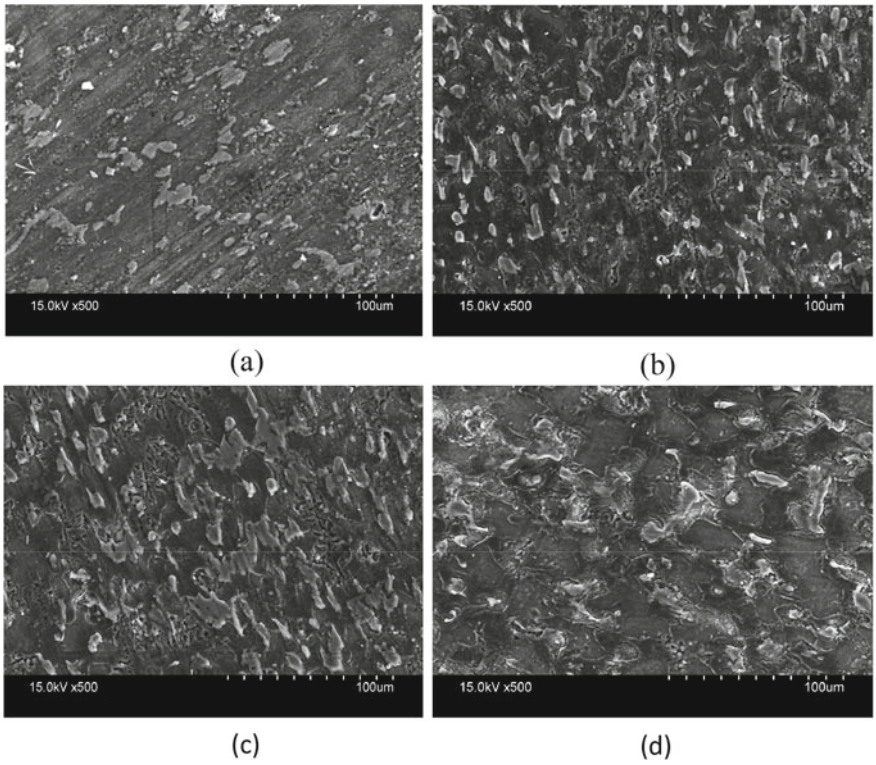

Fig. 10 SEM micrographs of composites. **a** Mg-0.5WC, **b** Mg-1WC, **c** Mg-1.5WC, **d** Mg-2WC [9]

variation of Rockwell hardness of AZ91 alloy, AZ91-1.5WC nanocomposite and cryogenic treated AZ91-1.5WC nanocomposite.

3.3 Tribological Properties

It is already discussed that Mg-WC nanocomposites possess excellent mechanical properties which makes them potential candidate as tribological material which should have weight reduction as typical factor. Tribological properties depend on process parameters, mechanical characteristics, microstructure, velocity, load and formation of protective layers. It is observed in literature that incorporation of different nanoparticles (Al_2O_3, BN, TiC, SiC, CNT, Y_2O_3) has improved tribological properties of magnesium. Zhang et al. [84] have yielded excellent wear resistance of Mg–SiC composites and concluded 23% increment in wear resistance than base alloy. Garces et al. [25] have examined wear characteristics of Mg–SiC composites

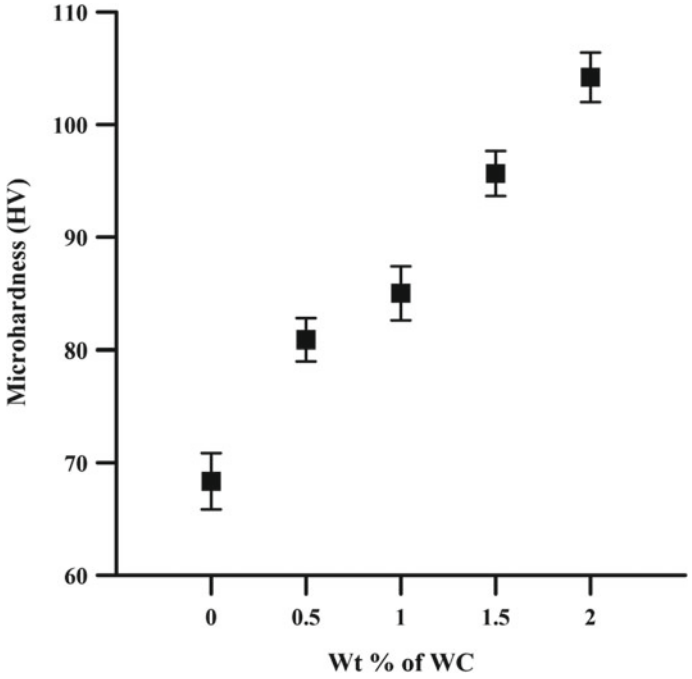

Fig. 11 Microhardness of Mg-WC nanocomposites [9]

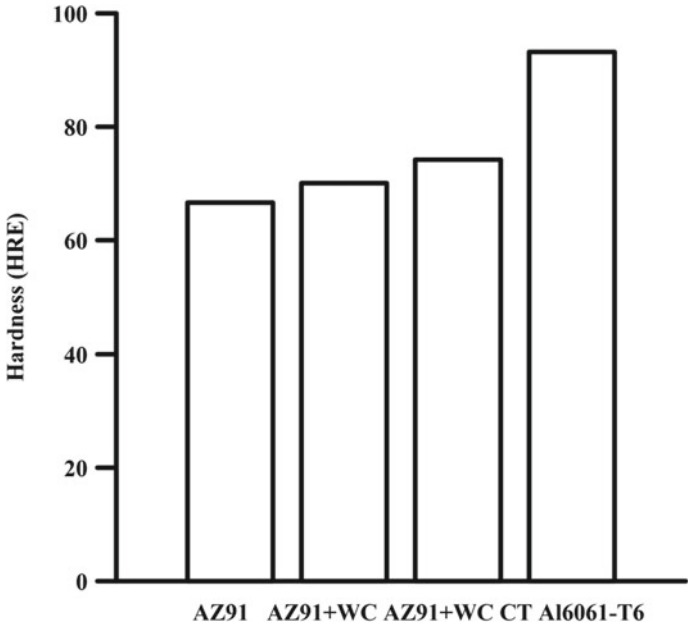

Fig. 12 Rockwell hardness AZ91, AZ91-WC, cryogenic treated AZ91-WC [42, 41]

and observed good wear resistance of composites. Labib et al. [47] have investigated wear characteristics of Mg–SiC composites at dry condition in room and high temperature and observed very good wear resistance of examined composites than base alloy at all conditions. Aydin et al. [5] have discussed tribological characteristics of Mg–B_4C composites and yielded significant improvement in wear resistance for composites. Nguyen et al. [60] have reported very good wear resistance by adding (0.66–1.50) wt% of Al_2O_3 in AZ31 alloy. Kaviti et al. [43] have disclosed excellent wear behavior of nanocomposites by incorporating (0.5–2.5) vol% of BN nanoparticles in Mg matrix. In this discussion, a comprehensive outlook on tribological investigations of Mg-WC composites is presented. Praveenkumar et al. [69] developed Mg composites with WC as reinforcement (0, 5, 10 and 15 wt%) using stir casting method. Tribological test results yield that AZ31B-15WC possess better wear resistant than AZ31B alloy. Karuppusamy et al. [42] have reported tribological behavior of AZ91 alloy and cryogenic treated AZ91-WC nanocomposite at different load and sliding speed. It was concluded that at 20 N load wear rate had decreasing trend while at 40 N load wear rate was maximum for all samples. With increase in sliding speed, wear rate primarily decreased, then it tended to increase. Worn surface morphology presented that abrasion was main wear mechanism, while oxidation, delamination and adhesion were present. Banerjee et al. [9] carried wear test of Mg-WC nanocomposites using pin-on-disc tribometer against EN 8 steel counterface disc for different loads (10–40 N) and speed (0.1–0.4 m/s). AZ31 base alloy had maximum wear rate, and it decreased with increase in WC percentage. Wear rate of base alloy increased with enhanced sliding speed, while wear rate of nanocomposites initially decreased then followed moderate increment. Plots of wear rate with respect to applied load and sliding speed are shown in Fig. 13. Coefficient of friction of all material had followed detrimental trend. All nanocomposites presented lower coefficient of friction (COF) than base matrix, but COF of nanocomposites had increased with rise in WC percentage. Detail trend of COF with respect to load and sliding speed are shown in Fig. 14. Banerjee et al. [9] further analyzed worn surfaces with SEM micrographs to reveal wear mechanisms. SEM micrographs of base alloy, Mg-1WC and Mg-2WC tested at 30 N load and 0.4 m/s sliding speed are shown in Fig. 15. SEM micrograph of base alloy had parallel abrasive grooves, oxidized debris and sign of plastic deformation. SEM micrographs of nanocomposites had comparatively smoother surface, sign of adhesion and some delamination. Hence, worn surface analysis disclosed abrasion as main mechanism for base alloy and nanocomposites with lower weight percentage (0.5–1%) WC, while combination of adhesion and delamination were presiding mechanism for other nanocomposites.

Banerjee et al. [10] had carried out elevated temperature wear and friction behavior of Mg-WC nanocomposites at different temperatures and loads. It was reported that base alloy continuous inflation in wear rate with respectto increment in temperature while wear rate of composites remained unchanged up to a typical temperature then wear rate increases drastically. Almost similar trend was observed for all loads, only that typical temperature varied. It was also noticed that wear resistance of nanocomposites upsurged with increase in WC percentage. Plot of wear rate with respect to temperature is presented in Fig. 16. COF of base alloy and nanocomposites

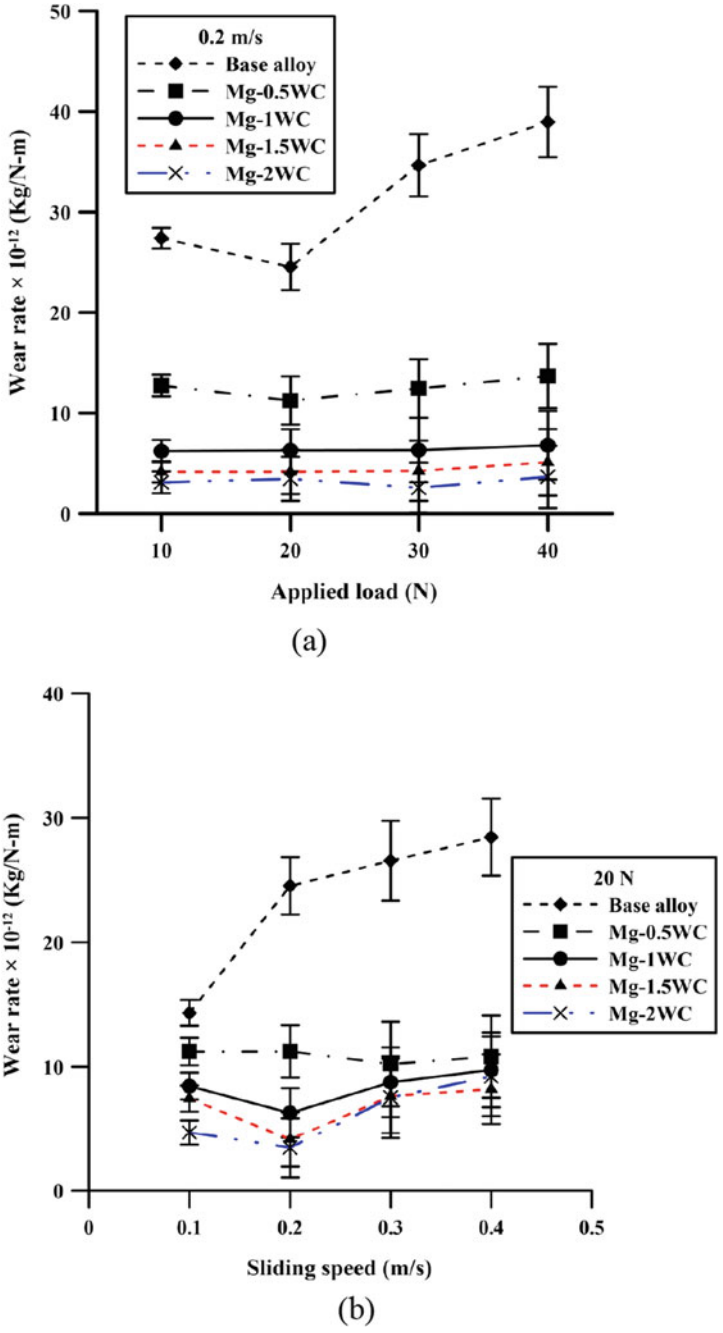

Fig. 13 Variation of wear rate with **a** load and **b** sliding speed for base alloy and composites [9]

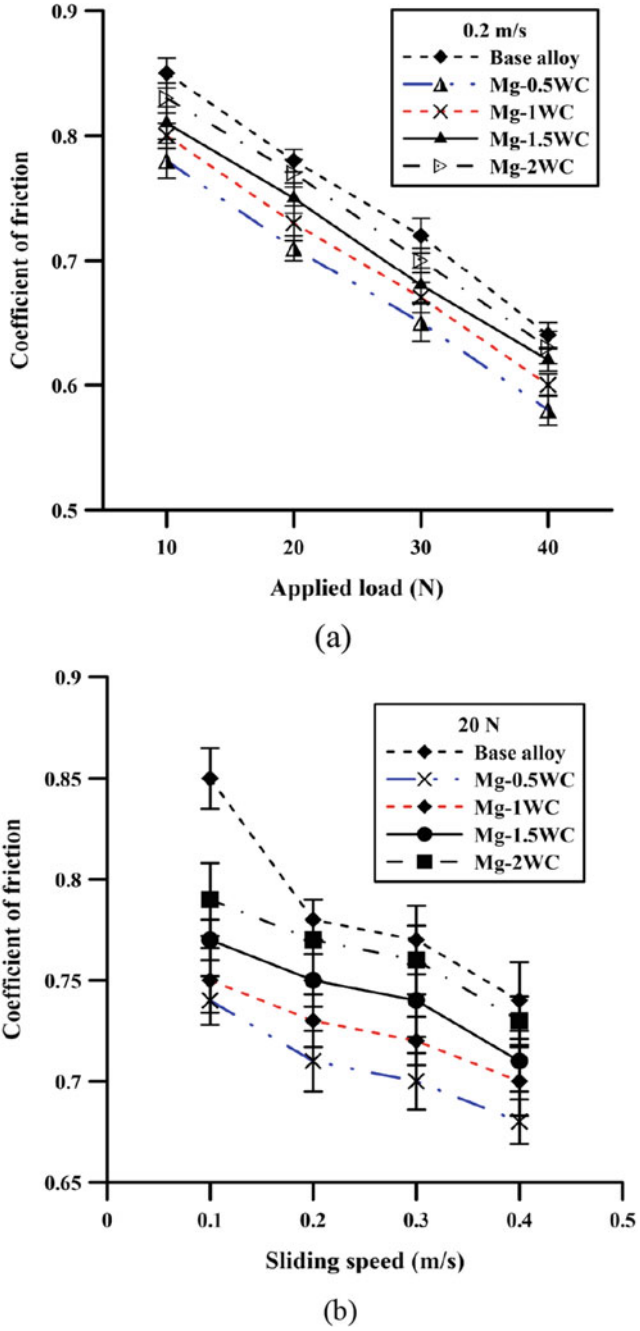

Fig. 14 Variation of COF with **a** load and **b** sliding speed for base alloy and composites [9]

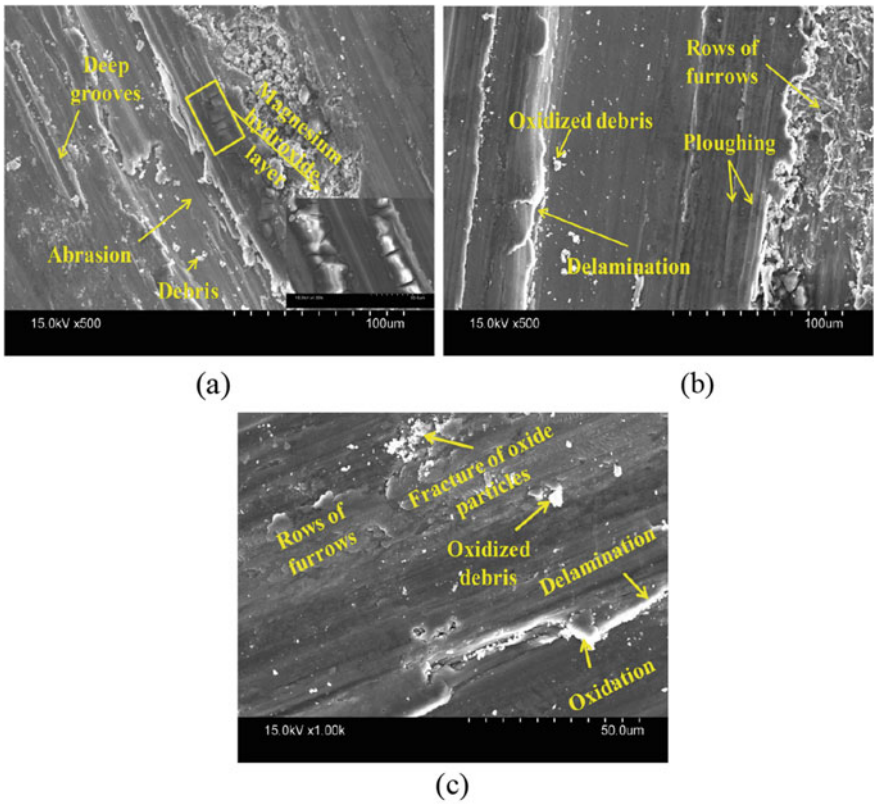

Fig. 15 SEM images of wear track at 30 N load and 0.4 m/s sliding speed: **a** AZ31, **b** Mg-1WC, **c** Mg-2WC [9]

were decreased slightly with respect to temperature. Plot of COF with respect to temperature is presented in Fig. 17. Worn surface analysis revealed that abrasion and delamination were dominant at 50 °C, delamination and adhesion were dominant at 100–150 °C, while adhesion and thermal softening were dominant mechanism for 200–250 °C. SEM micrographs Mg-1WC and Mg-2WC samples tested at 30 N and 200 °C are shown in Fig. 18.

Typically, design criterion of different components of transportation industry is bothered about density, corrosion resistance, mechanical stiffness and strength of selected material. Low density of material helps to provide high load carrying capacity and higher UTS provides requisite performances as well as safety criterion. In addition, increased corrosion resistance of selected material certifies high durability of the component. In this study, corrosion characteristics of Mg-MMCs are also discussed. Researchers have reported different nature of magnesium composites in context of corrosion behavior. Some researchers reported positive impact of reinforcement while some reported detrimental effect. Pardo et al. [67] have reported

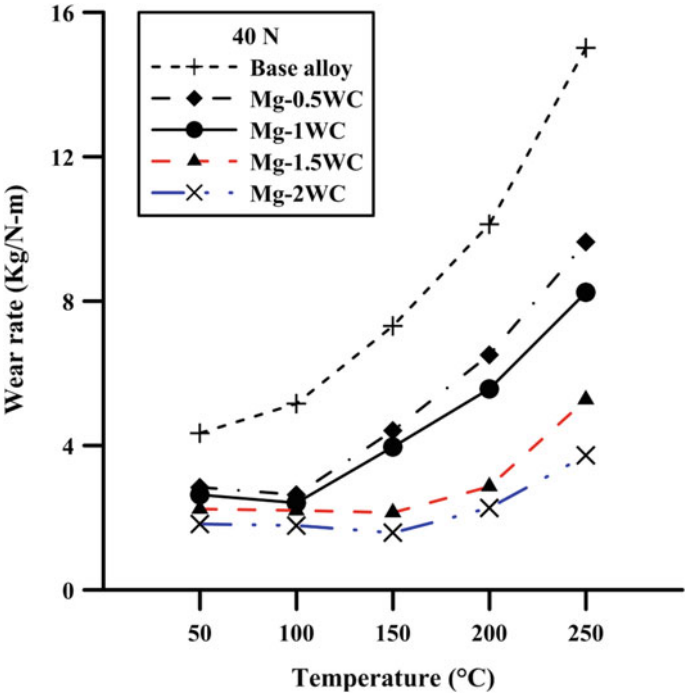

Fig. 16 Variation of wear rate with temperature for base alloy and composites for 20 N load [10]

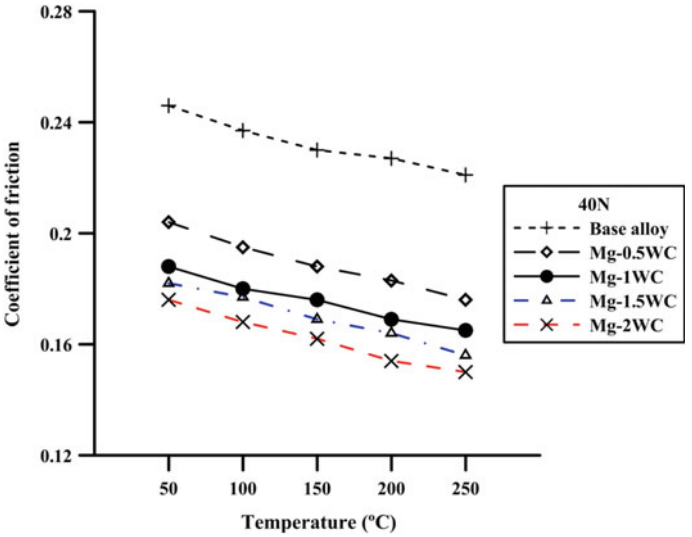

Fig. 17 Variation of COF with temperature for base alloy and composites at 40 N [10]

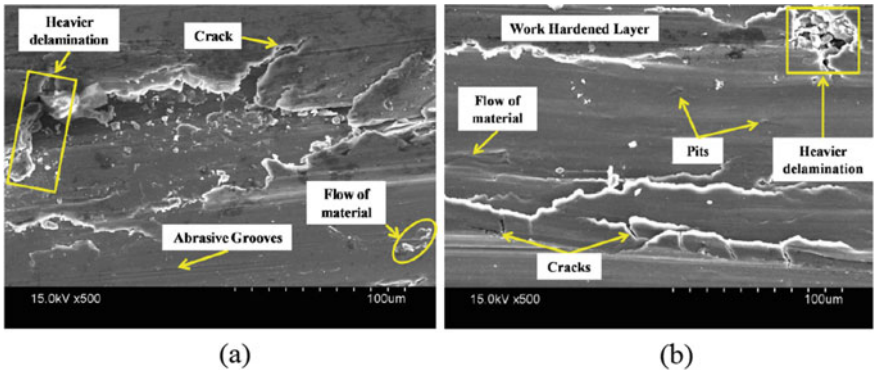

Fig. 18 SEM images of wear track at 30 N load and 200 °C temperature: **a** Mg-1WC, **b** Mg-2WC [10]

that incorporation of SiC possesses detrimental effect on corrosion behavior of Mg alloy. Chan et al. [16] have observed that Al_2O_3 particles in Mg matrix decrease corrosion resistance of Mg alloy when tested in 3.5% NaCl solution. Jia et al. [40] have disclosed that presence of TiC particle presents higher corrosion rate than Mg alloy in saline environment. Fukuda et al. [24] have reported higher corrosion rate for AZ31B-CNT composites than base alloy. On the other hand, Ghasali et al. [26] have observed that incorporation of Al_2O_3 nanoparticle in Mg matrix improves corrosion resistance of pure magnesium. Zhang et al. [85] have reported that Mg–SiC composites show better corrosion resistance, and corrosion resistance improves with improved volume percentage of SiC particles. Endo et al. [21] have found significant improvement in corrosion resistance with incorporation of MWCNT particles in Mg matrix. Falcon et al. [23] have reported increased corrosion resistance of Mg-TiC composites than base matrix. In this study, special emphasis is given on Mg-WC nanocomposites. Thus, corrosion behavior of Mg-WC nanocomposites is discussed in detail. Banerjee et al. [11] have examined the corrosion behavior of Mg-WC nanocomposites in 3.5% NaCl solution. Mg-WC nanocomposites with different wt% of WC (0, 0.5, 1, 1.5 and 2) are developed by ultrasonic treatment associated stir casting method. Nyquist plot (Fig. 19) of base alloy (AZ31) and nanocomposites composed of two capacitive loops (one high frequency and another low frequency) and one inductive loop (low frequency). High frequency capacitive loop represents film initiation, and low frequency capacitive curve represents mass transmission and inductive loop represent pit formation. Extra-polarization of Tafel plot (Fig. 20) gives corrosion potential values and current density values. Mg-0.5WC was reported as the most corrosion resistive material among all fabricated materials.

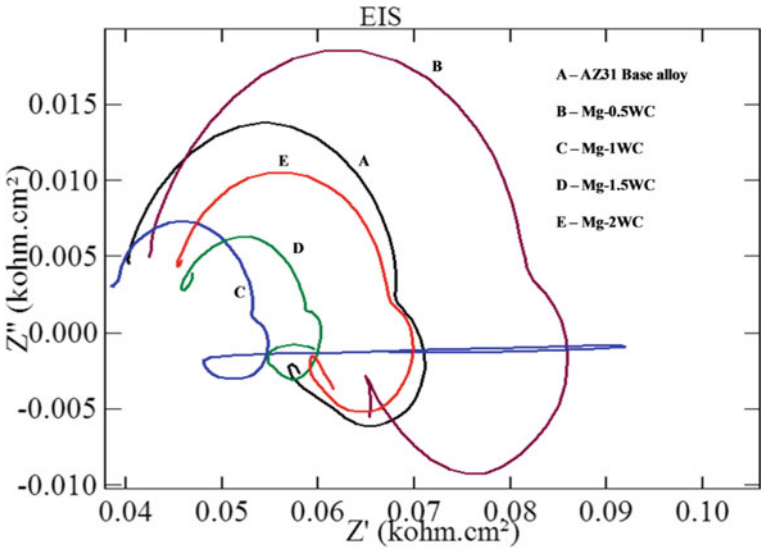

Fig. 19 Nyquist plot of base alloy and Mg-WC nanocomposites [11]

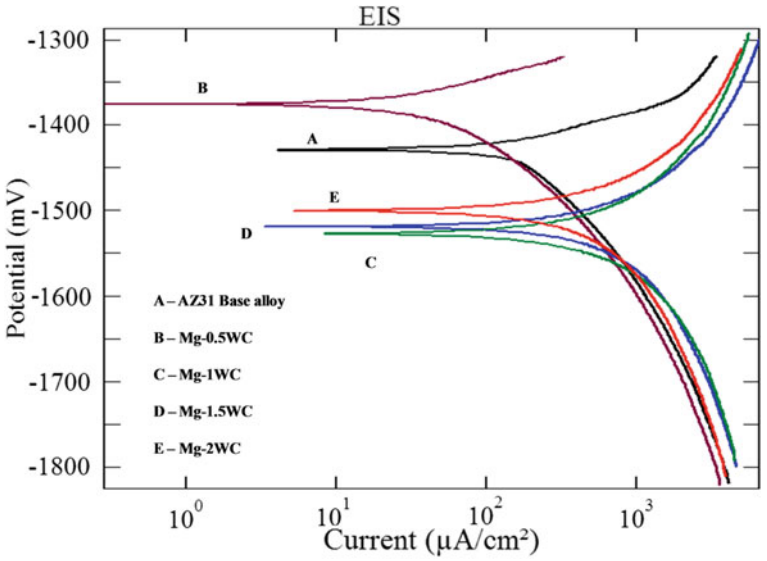

Fig. 20 Potentiodynamic polarization curve of base alloy and Mg-WC nanocomposites [11]

4 Conclusion and Future Remarks

In this study, various direction regarding fabrication, microstructure, mechanical property, wear behavior and friction behavior of Mg-WC nanocomposites have been discussed. It has been divulged that incorporation of WC particles notably intensifies above properties at different experimental conditions. At first, different fabrication processes have been discussed with their potential in the context of particle distribution and economical aspects. Fabrication-related literatures have been discussed to reveal prospect of different synthesis process. Literatures on fabrication of Mg-WC composites have also been discussed. Effect of WC particles and dispersal of WC in Mg matrix have been discussed in detail. Literatures yield that WC particles have been successfully fortified in Mg melt by vacuum assisted and ultrasonic treatment associated stir casting method. Ultrasonic vibration avoided agglomeration, better degassing of melt, decreased porosity and enhanced uniformity of particle distribution. Mechanical properties of nanocomposites have been increased significantly, and cryogenic treatment further helps to improve mechanical properties like microhardness, UTS, etc. Tribological properties like dry sliding wear behavior at room temperature and elevated temperature, friction behavior enhance notably with incorporation of WC particles. Corrosion behavior of Mg-WC nanocomposites along with different magnesium composites is also discussed. However, most of the work is currently practiced in lab-scale. Hence, full potential of MMNCs at industrial scale must be practiced. Product level transition of MMNCs must be considered. Different aspects, i.e., creep behavior, tensile property, corrosion properties, fatigue properties, recycling of Mg-WC nanocomposites are still partially revealed through literature. More studies needed to be performed considering energy efficiency, recyclability, reliability and economical aspect.

References

1. Abdullah A, Malaki M, Baghizadeh E (2012) On the impact of ultrasonic cavitation bubbles. Proc Inst Mech Eng Part C: J Mech Eng Sci 226(3):681–694
2. Alam ME, Han S, Nguyen QB, Hamouda AMS, Gupta M (2011) Development of new magnesium based alloys and their nanocomposites. J Alloy Compd 509(34):8522–8529
3. Aung NN, Zhou W, Goh CS, Nai SML, Wei J (2010) Effect of carbon nanotubes on corrosion of Mg–CNT composites. Corros Sci 52(5):1551–1553
4. Avedesian MM, Baker H (eds) (1999) ASM specialty handbook: magnesium and magnesium alloys. ASM international.
5. Aydin F, Sun Y, Ahlatci H, Turen Y (2018) Investigation of microstructure, mechanical and wear behaviour of B_4C particulate reinforced magnesium matrix composites by powder metallurgy. Trans Indian Inst Met 71(4):873–882
6. Azizieh M, Kokabi AH, Abachi P (2011) Effect of rotational speed and probe profile on microstructure and hardness of AZ31/Al_2O_3 nanocomposites fabricated by friction stir processing. Mater Design 32(4):2034–2041
7. Babu JSS, Nair KP, Unnikrishnan G, Kang CG, Kim HH (2010) Fabrication and properties of magnesium (AM50)-based hybrid composites with graphite nanofiber and alumina short fiber. J Compos Mater 44(8):971–987

8. Bakshi SR, Lahiri D, Agarwal A (2010) Carbon nanotube reinforced metal matrix composites-a review. Int Mater Rev 55(1):41–64
9. Banerjee S, Poria S, Sutradhar G, Sahoo P (2019) Dry sliding tribological behavior of AZ31-WC nano-composites. J Magn Alloys 7(2):315–327
10. Banerjee S, Poria S, Sutradhar G, Sahoo P (2019) Tribological behavior of Mg-WC nano-composites at elevated temperature. Mater Res Express 6(8):0865c6
11. Banerjee S, Poria S, Sutradhar G, Sahoo P (2019) Corrosion behavior of AZ31-WC nano-composites. J Magnes Alloy 7(4):681–695
12. Borodianskiy K, Zinigrad M (2016) Modification performance of WC nanoparticles in aluminum and an Al–Si casting alloy. Metall Mater Transa B 47(2):1302–1308
13. Cao G, Choi H, Konishi H, Kou S, Lakes R, Li X (2008) Mg–6Zn/1.5% Si Cnanocomposites fabricated by ultrasonic cavitation-based solidification processing. J Mater Sci 43(16):5521–5526
14. Casati R, Vedani M (2014) Metal matrix composites reinforced by nano-particles—a review. Metals 4(1):65–83
15. Ceschini L, Dahle A, Gupta M, Jarfors AEW, Jayalakshmi S, Morri A, Toschi S (2017) Aluminum and magnesium metal matrix nanocomposites. Springer, Singapore.
16. Chan WM, Cheng FT, Leung LK, Horylev RJ, Yue TM (1998) Corrosion behavior of magnesium alloy AZ91 and its MMC in NaCl solution. Corros Rev 16(1–2):43–52
17. Chen LY, Konishi H, Fehrenbacher A, Ma C, Xu JQ, Choi H, Li XC (2012) Novel nanoprocessing route for bulk graphene nanoplatelets reinforced metal matrix nanocomposites. Scr Mater 67(1):29–32
18. Chen LY, Peng JY, Xu JQ, Choi H, Li XC (2013) Achieving uniform distribution and dispersion of a high percentage of nanoparticles in metal matrix nanocomposites by solidification processing. Scr Mater 69(8):634–637
19. Dey A, Pandey KM (2015) Magnesium metal matrix composites—A review. Rev Adv Mater Sci 42(1)
20. Dieringa H (2018) Processing of magnesium-based metal matrix nanocomposites by ultrasound-assisted particle dispersion: a review. Metals 8(6):431
21. Endo M, Hayashi T, Itoh I, Kim YA, Shimamoto D, Muramatsu H, Koide S (2008) An anticorrosive magnesium/carbon nanotube composite. Appl Phys Lett 92(6):063105
22. Erman A, Groza J, Li X, Choi H, Cao G (2012) Nanoparticle effects in cast Mg-1 wt% SiC nano-composites. Mater Sci Eng: A 558:39–43
23. Falcon LA, Bedolla B, Lemus J, Leon C, Rosales I, Gonzalez-Rodriguez JG (2011) Corrosion behavior of Mg–Al/TiC composites in NaCl solution. Int J Corr
24. Fukuda H, Szpunar JA, Kondoh K, Chromik R (2010) The influence of carbon nanotubes on the corrosion behaviour of AZ31B magnesium alloy. Corros Sci 52(12):3917–3923
25. Garcés G, Rodríguez M, Pérez P, Adeva P (2010) Microstructural and mechanical characterisation of WE54–SiC composites. Mater Sci Eng, a 527(24–25):6511–6517
26. Ghasali E, Bordbar-Khiabani A, Alizadeh M, Mozafari M, Niazmand M, Kazemzadeh H, Ebadzadeh T (2019) Corrosion behavior and in-vitro bioactivity of porous Mg/Al_2O_3 and Mg/Si_3N_4 metal matrix composites fabricated using microwave sintering process. Mater Chem Phys 225:331–339
27. Goh CS, Wei J, Lee LC, Gupta M (2006) Simultaneous enhancement in strength and ductility by reinforcing magnesium with carbon nanotubes. Mater Sci Eng: A 423(1–2):153–156
28. Goh CS, Wei J, Lee LC, Gupta M (2007) Properties and deformation behaviour of $Mg–Y_2O_3$ nanocomposites. Acta Materialia 55(15):5115–5121
29. Goh CS, Wei J, Lee LC, Gupta M (2005) Development of novel carbon nanotube reinforced magnesium nanocomposites using the powder metallurgy technique. Nanotechnol 17(1):7
30. Gopal PM, Prakash KS, Nagaraja S, Aravinth NK (2017) Effect of weight fraction and particle size of CRT glass on the tribological behaviour of Mg-CRT-BN hybrid composites. Tribol Int 116:338–350
31. Gupta M, Wong WLE (2015) Magnesium-based nanocomposites: lightweight materials of the future. Mater Charact 105:30–46

32. Gupta M, Hassan SF, Eugene WWL (2006) Development of innovative magnesium based composite formulations using disintegrated melt deposition methodology. TMS Ann Meet 2006:217–226
33. Habibnejad-Korayem M, Mahmudi R, Ghasemi HM, Poole WJ (2010) Tribological behavior of pure Mg and AZ31 magnesium alloy strengthened by Al_2O_3 nano-particles. Wear 268(3–4):405–412
34. Habibnejad-Korayem M, Mahmudi R, Poole WJ (2009) Enhanced properties of Mg-based nano-composites reinforced with Al2O3 nano-particles. Mater Sci Eng: A 519(1–2):198–203
35. Hamedan AD, Shahmiri M (2012) Production of A356–1wt% SiC nanocomposite by the modified stir casting method. Mater Sci Eng: A 556:921–926
36. Hassan SF, Gupta M (2005) Enhancing physical and mechanical properties of Mg using nanosized Al_2O_3 particulates as reinforcement. Metall Mater Trans A 36(8):2253–2258
37. Hassan SF, Gupta M (2007) Development of nano-Y_2O_3 containing magnesium nanocomposites using solidification processing. J Alloy Compd 429(1–2):176–183
38. Hassan SF, Gupta M (2006) Effect of particulate size of Al_2O_3 reinforcement on microstructure and mechanical behavior of solidification processed elemental Mg. J Alloy compd 419(1–2):84–90
39. Imamura H, Sakasai N, Fujinaga T (1997) Characterization and hydriding properties of Mg-graphite composites prepared by mechanical grinding as new hydrogen storage materials. J Alloys Compounds 253:34–37
40. Jia S, Jia SS, Sun G, Yao J (2005) The corrosion behaviour of Mg alloy AZ91D/TiC_p metal matrix composite. In: Materials science forum, vol 488. Trans Tech Publications, pp 705–708
41. Karuppusamy P, Lingadurai K, Sivananth V (2019) To study the role of WC reinforcement and deep cryogenic treatment on AZ91 MMNC wear behavior using multilevel factorial design. J Tribol 141(4):041608
42. Karuppusamy P, Lingadurai K, Sivananth V (2019) Influence of cryogenic treatment on As-cast AZ91+ 1.5 wt% WC Mg-MMNC Wear Performance. In: Advances in materials and metallurgy. Springer, Singapore, pp 185–197
43. Kaviti RVP, Jeyasimman D, Parande G, Gupta M, Narayanasamy R (2018) Investigation on dry sliding wear behavior of Mg/BN nanocomposites. J Magnes Alloy 6(3):263–276
44. Khandelwal A, Mani K, Srivastava N, Gupta R, Chaudhari GP (2017) Mechanical behavior of AZ31/Al_2O_3 magnesium alloy nanocomposites prepared using ultrasound assisted stir casting. Compos B Eng 123:64–73
45. Kleiner S, Beffort O, Wahlen A, Uggowitzer PJ (2002) Microstructure and mechanical properties of squeeze cast and semi-solid cast Mg–Al alloys. J Light Met 2(4):277–280
46. Kulekci MK (2008) Magnesium and its alloys applications in automotive industry. Int J Adv Manuf Technol 39(9–10):851–865
47. Labib F, Ghasemi HM, Mahmudi R (2016) Dry tribological behavior of Mg/SiC_p composites at room and elevated temperatures. Wear 348:69–79
48. Lan J, Yang Y, Li X (2004) Microstructure and microhardness of SiC nanoparticles reinforced magnesium composites fabricated by ultrasonic method. Mater Sci Eng A 386(1–2):284–290
49. Lee CJ, Huang JC, Hsieh PJ (2006) Mg based nano-composites fabricated by friction stir processing. Scr Mater 54(7):1415–1420
50. Lekatou A, Karantzalis AE, Evangelou A, Gousia V, Kaptay G, Gácsi Z, Baumli P, Simon A (2015) Aluminium reinforced by WC and TiC nanoparticles (ex-situ) and aluminide particles (in-situ): Microstructure, wear and corrosion behaviour. Mater Des (1980–2015) 65:1121–1135
51. Li Q, Rottmair CA, Singer RF (2010) CNT reinforced light metal composites produced by melt stirring and by high pressure die casting. Compos Sci Technol 70(16):2242–2247
52. Liu SY, Gao FP, Zhang QY, Xue Z, Li WZ (2010) Fabrication of carbon nanotubes reinforced AZ91D composites by ultrasonic processing. Trans Nonferrous Met Soc China 20(7):1222–1227
53. Malaki M, Xu W, Kasar AK, Menezes PL, Dieringa H, Varma RS, Gupta M (2019) Adv Metal Matrix Nanocompos Metals 9(3):330

54. Meenashisundaram GK, Gupta M (2014) Low volume fraction nano-titanium particulates for improving the mechanical response of pure magnesium. J Alloy Compd 593:176–183
55. Meenashisundaram GK, Seetharaman S, Gupta M (2014) Enhancing overall tensile and compressive response of pure Mg using nano-TiB_2 particulates. Mater Charact 94:178–188
56. Mirshahi F, Meratian M (2012) High temperature tensile properties of modified Mg/Mg_2Si in situ composite. Mater Des 33:557–562
57. Morisada Y, Fujii H, Nagaoka T, Fukusumi M (2006) MWCNTs/AZ31 surface composites fabricated by friction stir processing. Mater Sci Eng A 419(1–2):344–348
58. Narayanasamy P, Selvakumar N, Balasundar P (2018) Effect of weight percentage of TiC on their tribological properties of magnesium composites. Mater Today: Proc Elsevier Publ 5(2):6570–6578
59. Nguyen QB, Gupta M (2008) Increasing significantly the failure strain and work of fracture of solidification processed AZ31B using nano-Al_2O_3 particulates. J Alloy Compd 459(1–2):244–250
60. Nguyen QB, Sim YHM, Gupta M, Lim CYH (2015) Tribology characteristics of magnesium alloy AZ31B and its composites. Tribol Int 82:464–471
61. Nie KB, Deng KK, Wang XJ, Wang T, Wu K (2017) Influence of SiC nanoparticles addition on the microstructural evolution and mechanical properties of AZ91 alloy during isothermal multidirectional forging. Mater Charact 124:14–24
62. Nie KB, Wang XJ, Hu XS, Xu L, Wu K, Zheng MY (2011) Microstructure and mechanical properties of SiC nanoparticles reinforced magnesium matrix composites fabricated by ultrasonic vibration. Mater Sci Eng: A 528(15):5278–5282
63. Nie KB, Wang XJ, Xu L, Wu K, Hu XS, Zheng MY (2012) Effect of hot extrusion on microstructures and mechanical properties of SiC nanoparticles reinforced magnesium matrix composite. J Alloy Compd 512(1):355–360
64. Pal A, Poria S, Sutradhar G, Sahoo P (2018) Tribologicalbehavior of Al-WC nano-composites fabricated by ultrasonic cavitation assisted stir-cast method. Mat Res Express 5(3):036521
65. Paramsothy M, Chan J, Kwok R, Gupta M (2011a) Adding TiC nanoparticles to magnesium alloy ZK60A for strength/ductility enhancement. J Nanomater 2011:50
66. Paramsothy M, Chan J, Kwok R, Gupta M (2011b) Addition of CNTs to enhance tensile/compressive response of magnesium alloy ZK60A. Compos Part A: Appl Sci Manuf 42(2):180–188
67. Pardo A, Merino S, Merino MC, Barroso I, Mohedano M, Arrabal R, Viejo F (2009) Corrosion behaviour of silicon–carbide-particle reinforced AZ92 magnesium alloy. Corros Sci 51(4):841–849
68. Ponappa K, Aravindan S, Rao PV (2013) Influence of Y_2O_3 particles on mechanical properties of magnesium and magnesium alloy (AZ91D). J Compos Mater 47(10):1231–1239
69. Praveenkumar R, Periyasamy P, Mohanavel V, Ravikumar MM (2019) Mechanical and tribological behavior of Mg-matrix composites manufactured by stir casting. Int J Veh Struct Syst (IJVSS) 11(1)
70. Razavi M, Mobasherpour I (2014) Production of aluminum nano-composite reinforced by tungsten carbide particles via mechanical milling and subsequent hot pressing. Int J Mater Res 105(11):1103–1110
71. Sajjadi SA, Ezatpour HR, Beygi H (2011) Microstructure and mechanical properties of Al–Al_2O_3 micro and nano composites fabricated by stir casting. Mater Sci Eng: A 528(29–30):8765–8771
72. Saravanan RA, Surappa MK (2000) Fabrication and characterisation of pure magnesium-30 vol.% SiCP particle composite. Mater Sci Eng: A 276(1–2):108–116
73. Selvam B, Marimuthu P, Narayanasamy R, Anandakrishnan V, Tun KS, Gupta M, Kamaraj M (2014) Dry sliding wear behaviour of zinc oxide reinforced magnesium matrix nanocomposites. Mater Des 58:475–481
74. Srivatsan TS, Godbole C, Quick T, Paramsothy M, Gupta M (2013) Mechanical behavior of a magnesium alloy nanocomposite under conditions of static tension and dynamic fatigue. J Mater Eng Perform 22(2):439–453

75. Suresh SM, Mishra D, Srinivasan A, Arunachalam RM, Sasikumar R (2011) Production and characterization of micro and nano Al_2O_3 particle-reinforced LM25 aluminium alloy composites. J Eng Appl Sci 6(6):94–97
76. Suslick KS, Didenko Y, Fang MM, Hyeon T, Kolbeck KJ, McNamara III WB, Wong M (1999) Acoustic cavitation and its chemical consequences. Philos Trans R Soc Lond Ser A: Math Phys Eng Sci 357(1751):335–353
77. Tekumalla S, Bibhanshu N, Shabadi R, Suwas S, Ha TMH, Gupta M (2018) Evolution of texture and asymmetry and its impact on the fatigue behaviour of an in-situ magnesium nanocomposite. Mater Sci Eng: A 727:61–69
78. Tun KS, Jayaramanavar P, Nguyen QB, Chan J, Kwok R, Gupta M (2012) Investigation into tensile and compressive responses of Mg–ZnO composites. Mater Sci Technol 28(5):582–588
79. Tun KS, Gupta M (2007) Improving mechanical properties of magnesium using nano-yttria reinforcement and microwave assisted powder metallurgy method. Compos Sci Technol 67(13):2657–2664
80. Wang XJ, Hu XS, Wu K, Zheng MY, Zheng L, Zhai QJ (2009) The interfacial characteristic of SiCp/AZ91 magnesium matrix composites fabricated by stir casting. J Mater Sci 44(11):2759–2764
81. Xu JQ, Chen LY, Choi H, Li XC (2012) Theoretical study and pathways for nanoparticle capture during solidification of metal melt. J Phys: Condens Matter 24(25):255304
82. Yar AA, Montazerian M, Abdizadeh H, Baharvandi HR (2009) Microstructure and mechanical properties of aluminum alloy matrix composite reinforced with nano-particle MgO. J Alloy Compd 484(1–2):400–404
83. Ye HZ, Liu XY (2004) Review of recent studies in magnesium matrix composites. J Mater Sci 39(20):6153–6171
84. Zhang L, Luo X, Liu J, Leng Y, An L (2018) Dry sliding wear behavior of Mg–SiC nanocomposites with high volume fractions of reinforcement. Mater Lett 228:112–115
85. Zhang C, Zhang T, Wang Y, Wei F, Shao Y, Meng G, Wu K (2015) Effect of SiC particulates on the corrosion behavior of extruded AZ91/SiC_p composites during the early stage of exposure. J Electrochem Soc 162(14):C754–C766

Chapter 9
Understanding Fabrication and Properties of Magnesium Matrix Nanocomposites

Sudip Banerjee, Suswagata Poria, Goutam Sutradhar, and Prasanta Sahoo

1 Introduction

Composites are well-known high-class materials which possess superiority than monolithic counterparts having unique capability of improving typical qualities of monolithic alloys [78, 79]. Enhancement of such properties of monolithic alloy can be restrained by perfectly selecting principle elements of composite design (size, type and amount). Primarily, research on metal matrix composites (MMCs) got momentum in 1970s. At that time, researchers mainly used powder metallurgy, stir casting and rheo-casting processes to develop MMCs by incorporating ceramic reinforcements and achieved impressive results [20, 45]. Improvements of typical properties, like elastic modulus, damping capability, creep behavior and wear resistance, were proclaimed [25, 39]. Researchers have incorporated micron scale continuous and discontinuous reinforcements in different metal matrix prior to twentieth century. But some limitations, like high cost, application in highly specialized area (space sector) and complex synthesis process, were observed for continuously reinforced MMCs. Conversely, MMCs with discontinuous reinforcement were successfully fabricated through different fabrication techniques [26, 68]. Around 2000, interest on nanoparticles was generated as reinforcement in metal matrix due to advancement in nano-science. In this regard, Al, Mg, Ni, Ti and Cu were mainly considered [26, 69]. In this study, concentration is given on magnesium as base metal because pure magnesium and magnesium alloys are extremely lightweight than other majorly used

S. Banerjee (✉) · P. Sahoo
Jadavpur University, Kolkata, India
e-mail: banerjee.sudip71@gmail.com

S. Poria
Heritage Institute of Technology, Kolkata, India

G. Sutradhar
National Institute of Technology, Manipur, India

S. Sahoo (ed.), *Recent Advances in Layered Materials and Structures*,
Materials Horizons: From Nature to Nanomaterials,
https://doi.org/10.1007/978-981-33-4550-8_9

metals, i.e., 77% lighter than steel, 33% lighter than aluminum and 61% lighter than titanium. Being the lightest metal, magnesium alloys also have good machinability (>50% Al), good damping capability and superb castability (>25–50% Al).

Nowadays, ceramic-based and carbon-based particles are procurable at much lower price than 1980–90s which promotes impressive increase in research and development of Mg-MMNCs. Moreover, incorporation of nanoscale reinforcement produces promising results by enhancing a number of typical properties. Normally, reinforcement particles are selected from carbide, nitride, oxide, boride and carbon families, especially Al_2O_3, SiC, B_4C, BN, TiB_2, AlN, CNT and graphite, to incorporate in metal matrix [73]. Through this incorporation, some typical properties, i.e., ductility, compressive and tensile property, creep, damping, elevated temperature mechanical properties, coefficient of thermal expansion (CTE), machining, wear resistance, friction behavior, corrosion resistance, ignition resistance, etc., were noticeably enhanced.

However, properties of MMNCs also depend on some other factors, i.e., primary and secondary fabrication process, process parameters, size of reinforcement, matrix metal, etc. In regard to fabrication of Mg metal matrix nanocomposites (Mg-MMNCs), agglomeration of nanoparticles, low wettability between nanoparticles and base matrix are of main concern. Fabrication methods of Mg-MMNCs are quite similar to Mg-MMCs. These processes are either solid processing or liquid metallurgy route. In liquid metallurgical method, stir casting, disintegrated melt deposition (DMD) and ultrasonic stirring technique (UST) are mostly used processing method. In stir casting, an impeller is employed in molten metal. Hence, stirring parameters, i.e., stirrer speed, stirrer location and stirrer design are significant parameters [1, 2]. In UST, high-frequency ultrasonic cavitation is applied to disperse nanoparticles which employ micro-hot spots, acoustic streaming and very high temperature to break agglomeration and disperse particles [53]. DMD is a spray-type processing method, in which molten composite is disintegrated prior to deposition [32]. Besides, some secondary processing like rolling, extrusion may be employed to further improve properties (refining grains, crushing secondary phase) or providing necessary shapes of composites.

In view of possible application of magnesium nanocomposites, the present study attempts to present a thorough review emerged on works and multi-dimensional sagacity of scientific community. Key points which are considered are as follows: (1) present status of fabrication method of Mg-MMNCs following liquid metallurgy, (2) strengthening mechanism of Mg-MMNCs, (3) mechanical properties of Mg-MMNCs, (4) tribological properties of Mg-MMNCs and (5) corrosion behavior of Mg-MMNCs.

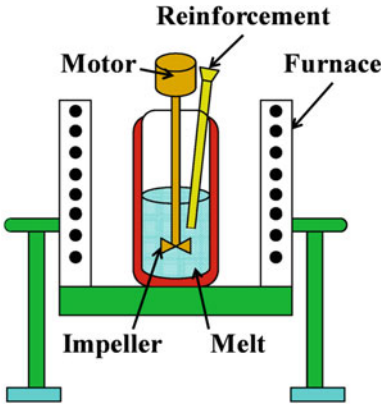

Fig. 1 Schematic diagram of stir casting

2 Preparation of Magnesium Matrix Composite Reinforced by Nanoparticles

2.1 Stir Casting

Stir casting is very naive and economical technique in which particles are incorporated in liquid metal using mechanical stirrer. Schematic diagram of stir casting process is presented in Fig. 1. Existing literature discloses that stir casting is extensively adopted to incorporate metal oxides, nitrides, carbide microparticles in magnesium matrix but limited numbers of literatures are available on incorporation of nanoparticles in magnesium matrix through this process. Main constraints of stir casting process are below par wettability of nanoparticles in molten metal, air entrapment due to rotation of stirrer and clusters of nanoparticles [3, 10, 11]. However, Habibnejad-Korayem et al. [35] have attempted to incorporate Al_2O_3 nanoparticles in Mg-matrix through stir casting method and reported homogeneous distribution of particles in magnesium matrix. Karuppusamy et al. [42] have incorporated WC nanoparticles in AZ91 melt using vacuum-assisted stir casting and achieved homogeneous distribution.

2.2 Ultrasonic Vibration

2.2.1 Principle of Ultrasonic Cavitation and Acoustic Streaming

Normally, high surface area of nanoparticles results in agglomeration in molten magnesium. Furthermore, wettability between Mg-melt and surfaces of nanoparticles is poor. In this regard, ultrasonic treatment (UST) is a widely used method to

effectively disburse nanoparticles in magnesium melt. Schematic diagram of ultrasonic vibration is shown in Fig. 2. Application of UST in Mg-melt generates different effects like cavitation and acoustic streaming. At the time of UST, application of high-frequency ultrasound through sonotrode generates alternating expansion and compression in definite area of melt near sonotrode. During expansion, small cavities in the form of cavitation bubble form for short duration [68]. These bubbles collapse and generate high pressure (1000 atm) as well as high temperature (several thousand degrees). On the other hand, agglomerated particles also include some entrapped gas. These gas bubbles also collapse and exert high intensity force which may exceed the Van der Waals force of agglomerated particles. At that instant, the agglomerated clusters are shattered which results in small clusters or individual particles. With repetition of this cavity formation and destruction, millions of shock waves generate in melt and disintegrate the agglomerated nanoparticles. Schematic diagram of de-agglomeration of nanoparticles due to acoustic streaming is shown in Fig. 3, and schematic diagram of effect of entrapped gas as well as sonotrode is shown in Fig. 4.

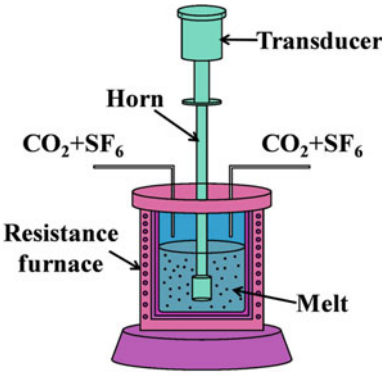

Fig. 2 Schematic diagram of ultrasonic vibration

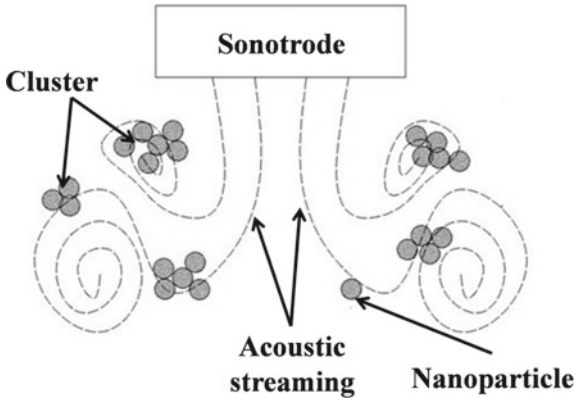

Fig. 3 Schematic diagram of de-agglomeration of nanoparticles due to acoustic streaming

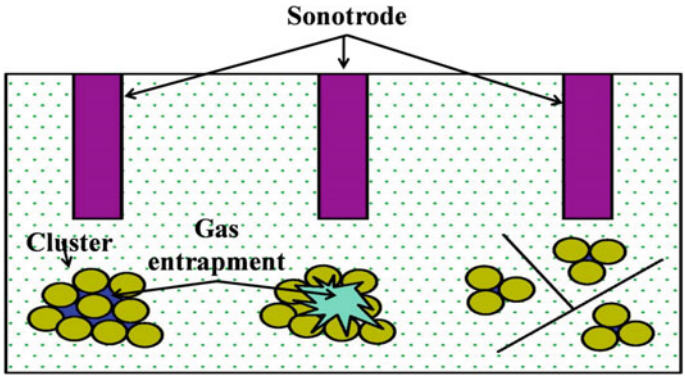

Fig. 4 Schematic diagram of effect of entrapped gas as well as sonotrode

Furthermore, UST causes acoustic streaming which depends on viscosity of melt, melt temperature and ultrasonic intensity. Eskin et al. [26] have described three types of acoustic streaming: (1) Schlichting flow which occurs at phase interfaces. These interfaces involve cavitation bubble. Heat and mass transfer is considered in this flow, (2) acoustic streaming of standing wave field and (3) acoustic streaming of bulk metal melt which develops by absorbing momentum of ultrasound flow. Hence, cavitation and acoustic streaming both help to disperse particles and contribute in grain refinement. In this context, Ishiwata et al. [40] have developed model on acoustic streaming separately for water and Al-melt. It is reported that acoustic streaming is mainly controlled by amplitude of ultrasonic vibration.

2.2.2 Effect of Ultrasound on Magnesium Alloy

Ramirez et al. [64] have discussed ultrasonic intensity (I) as follows:

$$I = \frac{\rho c (2\pi f A)^2}{2} \tag{1}$$

where ρ = density of molten metal, c = ultrasonic velocity, f = ultrasonic frequency and A = amplitude of horn. Eskin et al. [26] have reported that if intensity value exceeds 80 W cm^{-2} then generated cavitations are adequate for magnesium melt. Hence, ultrasonic intensity and corresponding wavelength can be regulated by following Eq. (1) to indulge specific requirement at the time of fabricating Mg-MMNC. Chen et al. [13] have shown the effect of ultrasonic vibration on capillary effect by improving penetration of melt in agglomerated nanoparticle. Critical osmotic pressure (p_s) is expressed by

$$p_s = \frac{6\lambda\sigma_{LG}\mathrm{Cos}\Theta(\emptyset - 1)}{d_{p\times}\emptyset} \tag{2}$$

where λ = geometric factor, d_p = average particle diameter, Θ = contact angle of particle and melt, σ_{LG} = surface tension and $\emptyset$ = volume fraction of particle porosity. Using Eq. (2), Nie et al. [58, 59] have found p_s to achieve required wettability of SiC nanoparticles in Mg-melt.

Accordingly, researchers have used UST to disperse nanoparticles in molten magnesium. Cao et al. [10] have incorporated AlN nanoparticles in AZ91 alloy using UST and achieved homogeneous distribution. Katsarou et al. [43] have incorporated AlN nanoparticles (1 wt%) in Elektron21 alloy using UST (0.3 kW and 20 kHz) and achieved refined grain along with enhanced mechanical properties. Khandelwal et al. [44] have employed UST to fortify nano-sized Al_2O_3 (0.5, 1 and 2 wt%) in AZ31 alloy in two conditions, i.e., during air cooling and isothermal in furnace. Lan et al. [48], Erman et al. [23] and Nie et al. [58, 59] have fortified SiC nanoparticles with different weight percentage in magnesium alloy with the help of high-frequency UST. Lan et al. [48] have incorporated 2 and 5 wt% SiC by applying 80 W ultrasonic power and reported fair distribution of SiC particles. Cao et al. [11] have reinforced 2 wt% SiC particles in molten Mg by inserting (25–31 mm) niobium probe into melt and applying 4.0 KW power and 17.5 kHz frequency. Erman et al. [23] have reinforced 2 wt% nano-SiC in Mg through UST and reported 60% reduction in average grain size. Cicco et al. [18] have ultrasonically dispersed nano-sized SiC particles in Mg–Zn alloys and concluded that nanoparticle induction has better effect than direct strengthening for metallic metals. Habibnejad et al. [35] have developed Mg-Al_2O_3 nanocomposite by incorporating different weight percentage of Al_2O_3 nanoparticles in magnesium matrix using UST. Chen et al. [14] have applied combination of evaporation and UST to dense uniform dispersion of nano-sized reinforcement (14 vol% SiC) in Mg-melt. Shiying et al. [67] have developed AZ91-SiC nanocomposites by incorporating different weight percentage (0.5, 1, 1.5 and 2%) of SiC particles (40 nm). Choi et al. [17] have fortified TiB_2 nanoparticles (25 nm) in AZ91D melt using niobium sonotrode which produce 20 kHz frequency and 60 μm amplitude. Bhingole and Chaudhari [9] have inoculated carbon black nanoparticles (42 nm) in different magnesium alloys using 20 kHz UST.

2.3 *Combination of Ultrasonic Vibration and Semisolid Stirring*

Further modification of UST is carried out in which both stirring of semisolid and application of UST in melt are combined. In this process, mechanical stirring normally helps in incorporating nanoparticles and UST helps to deal with agglomeration and wettability. Schematic diagram of combination of ultrasonic treatment and semisolid stirring is presented in Fig. 5. Following this process, Nie et al. [60] have used this technique to synthesize AZ91/SiC_p nanocomposite. Initially, preheated SiC nanoparticles (1 vol%, 60 nm) are initially brought in contact with semisolid matrix (550 °C) and mechanical stirring is conducted for 5–25 min. Then, UST is

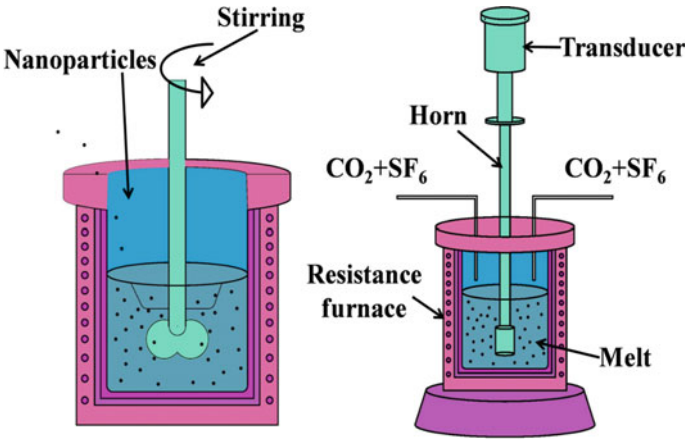

Fig. 5 Schematic diagram of combination of ultrasonic vibration and semisolid stirring

provided for 20 min at liquid state (700 °C) and solidified afterwards. Similarly, Shen et al. [66] have incorporated 3 vol% SiC nanoparticles in AZ31B matrix and observed no significant cluster of nano-SiC. Banerjee et al. [5–7] have incorporated WC nanoparticles (0.5, 1, 1.5 and 2 wt%) in AZ31 alloy using mechanical stirring as well as 20 kHz ultrasonic frequency and reported homogeneous distribution of nanoparticles in magnesium melt. Chen et al. [15] have used the same process (1400 rpm stirring, 20 kHz frequency and 60 μm amplitude) to incorporate high vol% SiC in Mg–Zn alloy. Liu et al. [52] have used the combination of mechanical stirring (300/500 rpm, 2 min) and ultrasonic vibration (20 kHz, 15 min) through titanium waveguide to incorporate CNT nanoparticles (20–40 nm). Zhou et al. [76] have produced Mg-hybrid composites by incorporating carbon nanotube and nano-SiC of different hybrid ratio through combination of mechanical stirring and ultrasonic vibration. Choi et al. [16] have employed the same process to develop Mg-1SiC nanocomposite using 3.5 kW power output and 17.5 kHz frequency for 15 min. In this process, a selective zone of melt pool is covered with 254 μm thin-walled truncated cone of niobium to confine SiC nanoparticles in that region.

2.4 Disintegrated Melt Deposition (DMD)

DMD technique possesses convenience of gravity die casting as well as spray forming, and in this process melting and pouring occur together. Schematic diagram of DMD process is presented in Fig. 6. In this process, atomized melt is rapidly solidified and low porosity, uniform grains as well as homogeneous distribution are found. But main limitation of this process is high viscosity of liquid melt with high volume percentage of reinforcement. Nguyen and Gupta [56] have tried DMD process to fortify Al_2O_3 in Mg-matrix and found equiaxed grain as well as good interfacial

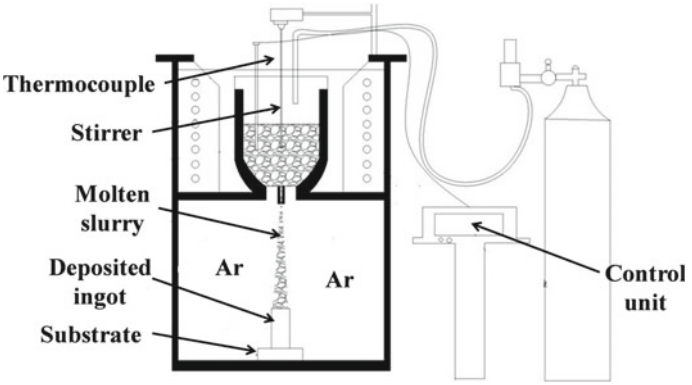

Fig. 6 Schematic diagram of DMD process

bonding. Hassan and Gupta [38] have attempted to use 1.1 vol% nano-Al_2O_3 (50 nm) following DMD process. Microstructural characterization revealed limited agglomeration and excellent distribution of particles throughout matrix. Goh et al. [32] have tried to incorporate CNT (0.3, 1.3, 1.6, 2 wt%) in magnesium through DMD process and observed microstructure as well as mechanical properties. Hassan and Gupta [36, 37] have incorporated nano-Y_2O_3/nano-ZrO_2 with varying weight percentages (0.22, 0.66 and 1.11 vol%) in Mg-matrix and reported good matrix-reinforcement interfacial integrity.

3 Secondary Processing Methods

Primary processed nanocomposites may have some defects or some microstructural irregularities which must be minimized or eliminated to improve typical properties. Hence, secondary processing techniques of nanocomposites are very essential. In secondary processing, either bulk material is deformed (extrusion, rolling, multidirectional forging) or severe plastic deformation is occurred (equal channel angular pressing, cyclic extrusion and compression).

3.1 Extrusion

In this secondary processing method, nanocomposite billets are pressurized in a die with high-pressure ram to minimize inappropriateness like voids, pores, cracks and cavity which are formed during primary processing. Schematic diagram of extrusion is shown in Fig. 7. This secondary processing method is typically applied at or above recrystallization temperature. In this process, main effective parameters are

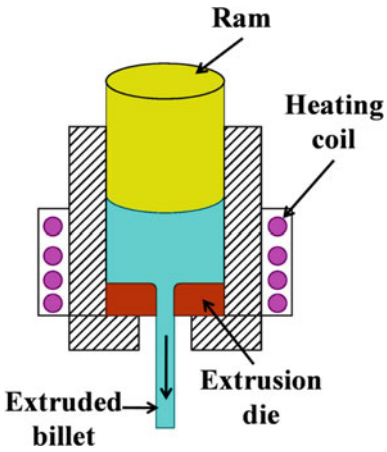

Fig. 7 Schematic diagram of extrusion

temperature, RAM speed and extrusion ratio, which should have optimum value to control oxidation and other noise factors. Nie et al. [60] have conducted hot extrusion on AZ91-SiC nanocomposites to further refine grain boundaries and reported that hot extrusion has further improved microstructural and mechanical properties than as-cast nanocomposites. Choi et al. [17] and Li et al. [49] have found similar results by applying hot extrusion. Occurrences of alignment of SiC particles toward direction of extrusion and grain refinement are documented.

3.2 Rolling

In rolling, high-pressure rolls are traveled over nanocomposites at plastic deformation stage to deform as-cast billets. High-pressure roll produces squeezing and compressive action which helps in further grain refinement. As a result, defects are eradicated and several typical properties are enhanced. In this process, key factors are number of passes and temperature. Wang et al. [72] have applied this process on AZ31/SiC nanocomposites and observed several beneficial effects on refined grains.

3.3 Multidirectional Forging (MDF)

In this process, the combination of plastic deformation and conventional mechanical process is applied to achieve exceptional refinement in grain structure. This process specially helps brittle and large workpieces. Nie et al. [58, 59] have studied microstructure of AZ91-SiC nanocomposites exposed to MDF. AZ91-SiC nanocomposites possess enhancement in dynamic recrystallization from the very

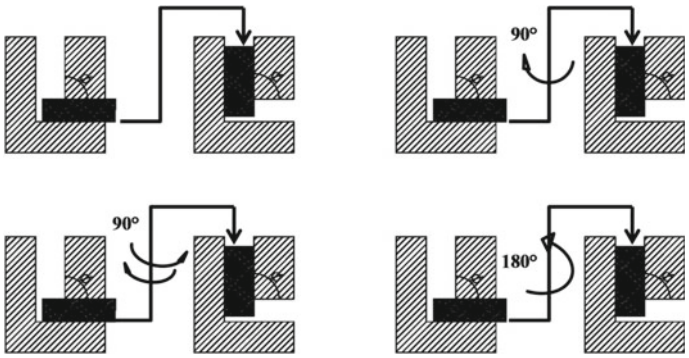

Fig. 8 Schematic diagram of equal channel angular pressing

first pass of MDF. With further increment in passes, conformity of microstructure and recrystallization increased.

3.4 Equal Channel Angular Pressing (ECAP)

ECAP is the process of modifying the microstructure with ultrafine grains (UFG). Schematic diagram of ECAP is shown in Fig. 8. Nanocomposite billet is passed through two identical intersecting channel die (channel intersection angle = Φ). In this process, geometrical cross section of the billet remains same but billet is subjected to extreme plastic deformation (shear), and this step is followed for several passes to generate UFG. Shear strain (γ) of each individual pass is calculated by Eq. 3.

$$\gamma = 2\cot\left(\frac{\Phi}{2}\right) \tag{3}$$

Zhu et al. [77] have suggested that the best result of grain refinement is achieved for $\Phi = 90°$.

3.5 Cyclic Extrusion and Compression (CEC)

CEC is also a severe plastic deformation process in which fine-grained microstructure can be achieved by passing nanocomposite billets in between annual die. Selections of number of passes and temperature are most important for achieving fine grain. Guo et al. [34] have used CEC to achieve fine grain for Mg–SiC nanocomposite. In this study, optimum number of passes and optimum temperature are considered as

up to 8 and 300–400 °C, respectively. Superior grain structure as well as enhanced hardness is obtained.

4 Strengthening Mechanism

Ceramic nanoparticles possess strong effect on yield strength depending on different strengthening mechanisms. Total strength can be determined by calculating the sum of yield strength due to grain refinement (Δ_{GR}), due to Orowan contribution (Δ_{OR}), due to difference in modulus of elasticity (Δ_{MOD}), due to coefficient of thermal expansion (Δ_{CTE}) and due to load-bearing factor (Δ_{LOAD}).

4.1 Orowan Strengthening

In Orowan strengthening, it is considered that particles are almost homogeneously distributed in matrix. These homogeneously distributed nanoparticles obstruct the movement of dislocations through matrix. When they try to interact with particles, the dislocations bend about the particles and connect with other dislocation. As a result, strength increases. Strength maintains inverse relationship with interparticle distance which yields that smaller particles impart higher strength for same volume or mass. Contributions of Orowan strengthening are described by Eq. (4), and interparticle distance (λ) is described by Eq. (5):

$$\Delta\sigma_{OR} = \frac{0.13BG_m}{\lambda} \ln \frac{d_p}{2b} \tag{4}$$

$$\lambda = d_p\left[\left(\frac{1}{2V_p}\right)^{(1/3)} - 1\right] \tag{5}$$

where b = burgers vector, d_p = average dia. of nano-particle, G_m = shear modulus and V_p = volume fraction.

Chen et al. [14] have reported the contribution of Orowan strengthening on yield strength of Mg-1SiC nanocomposite as 113 MPa. It is also yielded that this result is due to small interparticle distance. Cao et al. [10, 11] have performed the Orowan strengthening-related calculations of Mg-1AlN nanocomposite. It is shown that Orowan strengthening has improved yield strength by 44% which is around 35.8 MPa and grain refinement has contributed around 8.2 MPa on yield strength.

4.2 Hall–Petch

Due to the introduction of ceramic reinforcements, primary precipitation occurs at the time of solidification which leads to refinement of grains. Typically, reinforcing nanoparticles in magnesium alloys improve yield strength which results in refinement of grains. Increment of yield strength can be found by Hall–Petch equation (6), in which yield strength (σ_y) is

$$\sigma_y = \sigma_0 + k_y D^{(-1/2)} \tag{6}$$

where σ_0 = friction stress when no strengthening mechanism is present, k_y = stress concentration factor and D = grain size. Again, increment of yield strength for nanocomposites can be calculated by considering same fabrication process for alloy also. In this case, yield strength is found out by following Eq. (7) considering grain size of nanocomposite (D_{MMNC}) and base alloy (D_{O}):

$$\Delta_{\mathrm{GR}} = k_y \left(\frac{1}{\sqrt{D_{\mathrm{MMNC}}}} - \frac{1}{\sqrt{D_{\mathrm{O}}}} \right) \tag{7}$$

Dieringa et al. [21] have added AlN (1 wt%) nanoparticles in AM60 alloy melt and reported that incorporation of AlN nanoparticles has improved yield strength and tensile strength by 103% and 115%, respectively. Again, improvement of yield strength due to grain refinement is calculated as 42.7 MPa and same due to Orowan strengthening is 8.3 MPa.

4.3 Mismatch in the CTE

Usually matrix metal and reinforcement phase have different CTE which results in stresses at interface. Hence, increased difference in CTE generates higher stress which causes geometrical necessary dislocations (GND). GND normally helps to accommodate CTE difference. Typically, GNDs enhance the value of yield strength for nanocomposites like cold working. Yield strength due to CTE ($\Delta\sigma_{\mathrm{CTE}}$) can be computed by following Eq. (8) [71]:

$$\Delta\sigma_{\mathrm{CTE}} = \sqrt{3}\beta G_{\mathrm{m}} b \sqrt{\frac{12 V_{\mathrm{p}} \Delta\alpha \Delta T}{b d_{\mathrm{p}}}} \tag{8}$$

where β = coefficient of dislocation strengthening, $\Delta\alpha$ = CTE difference and ΔT = temperature difference.

4.4 Mismatch in Young's Modulus

Moreover, GNDs can also be created due to mismatch of Young's modulus between matrix and reinforcement phase. To make this happen, nanocomposite must be processed through secondary processing method (extrusion, rolling, etc.). Due to formation of GNDs, yield strength of nanocomposite enhances. Dai et al. [19] have proposed Eq. (9) to compute yield strength ($\Delta\sigma_{\text{Mod}}$) due to distinction of Young's modulus considering ε = bulk strain for composite and α = material coefficient.

$$\Delta\sigma_{\text{Mod}} = \sqrt{3}\alpha G_{\text{m}} b \sqrt{\frac{6V_{\text{p}}\varepsilon}{bd_{\text{p}}}} \tag{9}$$

4.5 Load-Bearing

Load-bearing mechanism is also considered as one strengthening mechanism which contributes in increasing yield strength. Moreover, it is also considered to have small influence as nanocomposites contain small amount of reinforcement. Yield strength due to load-bearing mechanism is calculated by following Eq. (10), where yield strength of base matrix is σ_{m}.

$$\Delta\sigma_{\text{Load}} = \frac{1}{2} V_p \sigma_{\text{m}} \tag{10}$$

5 Mechanical Properties

Basic objective of incorporating nanoparticles in magnesium matrix is to achieve enhanced mechanical properties like hardness, ultimate tensile strength (UTS), yield strength (YS), compressive strength, creep behavior, etc. For this purpose, researchers have incorporated different nanoparticles (Al_2O_3, SiC, Y_2O_3, AlN, TiB_2, WC, CNT) in magnesium base matrix.

5.1 Al_2O_3

Gnanavelbabu et al. [31] have studied the role of ultrasonic power (0, 1500, 2000 and 2500 W) at fixed time and frequency on mechanical properties of AZ91D-1Al_2O_3

nanocomposites. It is reported that microhardness is enhanced 18% for 2500 W UST-treated nanocomposite compared to untreated (0 W UST) nanocomposite. Again, YS, UTS and % elongation of 2500 W UST-treated nanocomposite have improved by 28%, 48% and 10%, respectively. Habibnejad-Korayem et al. [35] have shown that incorporation of nano-Al_2O_3 (2 wt%) in magnesium matrix has significantly improved microhardness and UTS than base alloy. Sameer Kumar et al. [46] have reported that incorporation of n-Al_2O_3 in AZ91E alloy through stir casting method has improved UTS and hardness than AZ91E alloy by 22.5% and 26.54%, respectively. Hassan and Gupta [38] have incorporated 1.1 wt% Al_2O_3 nanoparticle (50 nm) in Mg alloy and studied mechanical properties like microhardness, YS, UTS, elastic modulus and ductility. It was reported that all those mechanical properties have achieved significant enhancement due to presence of Al_2O_3 nanoparticles. Fractography study revealed that Al_2O_3 nanoparticles have activated non-basal slip which changed the fracture behavior from brittle to mixed system.

5.2 SiC

Lan et al. [48] have studied mechanical behavior of Mg-SiC nanocomposites fabricated by UST. It is reported that with incorporation of 5 wt% of n-SiC, microhardness has improved by 75% than base alloy. Nie et al. [61] have used extrusion (at 350 °C) on AZ91D-0.5SiC nanocomposite to enhance mechanical properties. It is concluded that YS and UTS of nanocomposites have increased with increase in extrusion temperature. Shen et al. [66] have synthesized Mg-SiC nanocomposites through semisolid stirring and UST followed by extrusion. Tensile test results indicated that incorporation of 1 vol% SiC has increased UTS and YS to 300 and 225 MPa while incorporation of 2 and 3 vol% of SiC has increased UTS to 335 MPa and 380 MPa, respectively. At same condition (2 and 3 vol% of SiC), YS was increased to 268 and 313 MPa. Bao et al. [8] have successfully incorporated SiC nanoparticles through UST followed by extrusion and achieved UTS as 299 MPa and YS as 220 MPa. Liu et al. [51] have incorporated nano-SiC particles in AZ91D alloy and attained 43.6% and 117% improvement of UTS and YS, respectively.

5.3 AlN

AZ91D was reinforced by AlN nanoparticles (1 wt%), and mechanical properties were studied. It was reported that only 1 wt% of AlN nanoparticle have enhanced YS at room temperature and elevated temperature (200 °C) by 44% and 21%, respectively. Sankaranarayanan et al. [65] have incorporated 0.2 and 0.8 wt% of AlN nanoparticles in pure magnesium. Mg-0.2AlN nanocomposite provided maximum improvement in ductility (85%) while Mg-0.8AlN nanocomposite has provided maximum improvement in tensile strength (30%). In compressive loading condition,

overall strength was improved by 30% without arousing effect on ductility. Katsarou et al. [43] have incorporated AlN nanoparticles in Elektron21 magnesium alloy and studied hardness, mechanical properties and creep resistance. It was reported that incorporation of 1 wt% of AlN has significantly enhanced creep resistance of developed nanocomposite.

5.4 CNT

Goh et al. [33] have developed Mg-1.3CNT nanocomposite and studied fatigue behavior and ductility of developed nanocomposite. It is observed that highly active basal slip has helped to enhance ductility significantly. Liu et al. [52] have incorporated 1.5 wt% CNT and observed improvement in YS, UTS and elongation by 21%, 22% and 42%, respectively, than AZ91D alloy.

5.5 WC

Banerjee et al. [5] have incorporated WC nanoparticles (0, 0.5, 1, 1.5 and 2 wt%) in AZ31 alloy and found that microhardness of Mg-2WC nanocomposite (104.20 $HV_{0.05}$) has enhanced significantly than AZ31 alloy (68.35 $HV_{0.05}$). Similarly, Karuppusamy et al. [42] have fortified 1.5 wt% WC nanoparticle in AZ91 magnesium alloy and compared the mechanical properties between cryogenic-treated (CT) and non-treated nanocomposites. It is reported that Rockwell hardness of CT-nanocomposite has enhanced by 10.5% than non-treated nanocomposite. Again, UTS of cryogenic-treated nanocomposite has improved by 35% than AZ91 alloy. Praveenkumar et al. [63] have developed AZ31-WC composite and studied mechanical properties like microhardness, YS, UTS and flexural strength. It is revealed that all those properties have improved significantly due to the presence of WC and rate of improvement of those properties are increased with increase in wt% of WC.

5.6 TiB_2

Meenashisundaram et al. [54] have incorporated 0.58–1.98 wt% of nano-TiB_2 in magnesium alloy and studied room temperature tensile properties. It is disclosed that Mg-1.98TiB_2 possesses best result and YS, UTS and fracture strain have improved by 54%, 15% and 79%, respectively. Study of compressive properties discloses that Mg-1.98TiB_2 yield strength has improved by 47% while ultimate compressive strength and fracture strain have improved by 10% and 11%, respectively. Choi et al. [17] have reinforced TiB_2 nanoparticles (1 and 2.7%) in AZ91D alloy using UST by applying 20 kHz frequency and generating 60 μm amplitude. Mechanical properties were

Table 1 Observation details [17]

Material	UTS (MPa)	YS (MPa)	E (%)
AZ91	162 ± 3	88 ± 3	2.88 ± 0.12
AZ91 + 1TiB_2	180 ± 1	104 ± 1	3.33 ± 0.05
AZ91 + 2.7TiB_2	188 ± 1	107 ± 1	4.27 ± 0.61

studied at room temperature and found improved strength and ductility. Observation details are tabulated in Table 1.

6 Tribological Properties

6.1 Al_2O_3

Gnanavelbabu et al. [31] have studied tribological properties of AZ91-n-Al_2O_3 composites treated with different UST power (0, 1500, 2000, 2500 W). Wear rate and coefficient of friction (COF) have been evaluated with respect to different sliding speed and load. It has been revealed that tribological properties have enhanced significantly due to enhancement in UST power. At 2500 W, wear rate and coefficient of friction have reduced than other samples in different experimental conditions. It has also been disclosed that adhesion, oxidation, abrasion and delamination are responsible wear mechanism. Lim et al. [50] have incorporated 0.22, 0.66 and 1.11 vol% Al_2O_3 nanoparticle in Mg-matrix and performed tribo-tests by varying sliding velocity at 10 N load. It has been revealed that wear rate has significantly reduced with incorporation of Al_2O_3 nanoparticles. It is also reported that Mg-1.11 Al_2O_3 possesses 1.8 times better wear resistance than base alloy for 10 m/s sliding velocity. Habibnejad-Korayem et al. [35] explored wear characteristics of magnesium, magnesium alloy and Mg-Al_2O_3 by varying sliding velocity and applied load. It is reported that nanocomposite possesses minimum wear rate among developed materials and wear rate follows inverse relation with sliding velocity while wear rate follows direct relation with load. Similarly, Nguyen et al. [57] have discussed wear behavior of AZ31B-Al_2O_3 nanocomposites by comparing load–speed condition. In this study, experiments were carried at 10 N load for different sliding speed (1, 3, 5, 7 and 10 m/s) and at 30 N load for different sliding speed (1, 3 and 5 m/s). It is indicated that wear resistance of nanocomposites has continuously curtailed throughout the speed range and loads. But, wear rate of nanocomposites is surpassing the wear rate of base alloy at low speeds and wear rate of nanocomposites reduced with increased value of sliding speed.

6.2 SiC

Zhang et al. [75] have investigated tribological characteristics of Mg-SiC nanocomposites (10 and 15 wt %) and compared with pure magnesium and AZ31B alloy. This study disclosed that COF of nanocomposites are much higher than AZ31B alloy. COF values of Mg-10SiC are almost similar to AZ31B and nearly 30% greater than commercially pure Mg (C_P-Mg). On the other hand, Mg-SiC nanocomposite displayed lowest wear rate compared to all other materials which is around 23 times lesser to C_P-Mg. Labib et al. [47] have explored wear and friction characteristics of Mg–SiC nanocomposites by varying loads (5–60 N) and temperatures (25–200 °C) at fixed sliding speed (0.4 m/s). At 25 °C, wear rates are almost similar for 5 and 20 N but at higher loads, composites possess far better wear resistance than base alloy. Again, composite maintains lesser wear rate than base alloy at elevated temperatures (100, 150 and 200 °C). Moreover, increase in applied load shifted the characteristics of wear from mild to severe at all temperatures.

6.3 WC

Banerjee et al. [5] have carried out dry sliding wear test of AZ31-WC nanocomposites for varying load and sliding speed systems where load range is 10–40 N and speed range is 0.1–0.4 m/s. It was revealed that wear rate is maximum for base alloy and decreased continuously with increasing percentage of WC. Again, continuous incremental trend of wear rate with respect to sliding speed and applied load was reported for base alloy while nanocomposites offered initial detrimental trend following moderate increment. Moreover, COF yielded continuous detrimental tendency for all experimental conditions. COF of nanocomposites have lower COF than base alloy. COF values for nanocomposites possess incremental trend with increase in weight percentage of WC. Banerjee et al. [6] have again reported the effect of elevated temperature and loads on tribological behavior of Mg-WC MMNCs. Wear rate increased continuously for base alloy but for MMNCs wear rate almost remains unchanged up to a transition limit, after that significant increase was noticed. COF provided slight increment with temperature for both alloy and nanocomposites. Karuppusamy et al. [42] have examined the effect of cryogenic treatment (−190 °C) on wear behavior of AZ91-WC nanocomposite at different experimental conditions. At lower load (20 N), wear rate followed detrimental slope for all samples but at higher load (40 N) wear rate of cryogenic-treated nanocomposite was significantly reduced.

7 Corrosion Behavior

Several researchers have studied corrosion behavior of Mg-MMNCs. But scientific community is splitted into two sides about corrosion characteristics of magnesium composites. Some researchers reported that corrosion resistance is decreased due to presence of reinforcement while others concluded that corrosion resistance is enhanced due to reinforcing agents.

7.1 Al_2O_3

Chan et al. [12] have incorporated alumina particles in AZ91 alloy and performed electrochemical impedance spectroscopy (EIS), potentio-dynamic polarization test and immersion tests in alkaline solution to study corrosion behavior. It was observed that composite possesses more corrosion than base alloy (three times) in 3.5% NaCl solution. Ghasali et al. [30] have incorporated Al_2O_3 and Si_3N_4 nanoparticles in magnesium matrix and reported that nanoparticles possess greater polarization resistance compared to C_p–Mg.

7.2 SiC

Pardo et al. [62] have incorporated SiC particles in magnesium matrix (AZ92) and studied corrosion resistance in neutral salt fog and 3.5 wt% NaCl solution. It was reported that Mg-SiC offered severe corrosion by forming different corrosion by-products in neutral fog solution while higher corrosion resistance is observed for high humidity condition. Zhang et al. [74] have reported corrosion behavior of extruded AZ91-SiC composites by evaluating electrochemical measurement and weight loss calculation. It was disclosed that corrosion resistance has decreased noticeably and accelerated hydrogen reduction with increasing volume percentage of SiC. Similarly, Tiwari et al. [70] have tested corrosion behavior of Mg-SiC composites (6 and 16 vol%) in 1 M NaCl. Composites possess higher corrosion than base alloy and SiC have not contributed that much in controlling corrosion rate.

7.3 Graphene and CNT

Aung et al. [4] have studied the examined corrosion behavior of Mg-CNT in 3.5% NaCl solution and discussed that presence of CNT deteriorates corrosion resistance. Fukuda et al. [28] have also studied galvanic corrosion behavior of Mg-CNT composite and revealed that galvanic corrosion has increased than AZ31 alloy due to

presence of CNT. Endo et al. [22] have incorporated MWCNT in magnesium alloy and examined corrosion behavior in salt water. It was disclosed that corrosion resistivity has significantly enhanced due to MWCNT particles. Funatsu et al. [29] have incorporated CNT in AZ61B magnesium alloy and investigated galvanic corrosion resistance which presented significant enhancement by forming gradient distribution.

7.4 WC

Banerjee et al. [7] have studied corrosion behavior of Mg-WC nanocomposites in 3.5% NaCl solution by varying wt% of WC. Presence of capacitive loop of high and low frequency as well as low-frequency inductive loop was observed in Nyquist plot. Loops signify film generation, mass transfer and pit formation. Tafel plot has provided current density and corrosion potential which revealed Mg-0.5WC provides best corrosion resistance. This study also investigated the role of surface roughness which iterated that surface roughness has direct impact on corrosion behavior. Corrosion resistance increased with decrease in roughness.

7.5 TiC

Jia et al. [41] have developed Mg-TiC composite and examined corrosion behavior in saline environment. It was observed that composites have higher galvanic corrosion and corrosion rate than base alloy. Falcon et al. [27] have developed AZ91E-TiC composites and reported that corrosion resistance and pitting resistance have enhanced due to the presence of TiC particles.

8 Conclusion

Typically, novel Mg-MMNCs are able to provide enhanced tensile property, compressive property, creep resistance, tribological properties and corrosion resistance than base alloy and MMCs. Large number of fabrication methods like primary casting and additional secondary deformations (extrusion, rolling, MDF) are available to develop Mg-MMNCs. In the present study, detail discussions about fabrication methods (primary and secondary), mechanical and tribological properties have been discussed. Indeed, present literatures highlighted that liquid metallurgy (ultrasonic vibration-assisted stir casting method, DMD) methods are more prominent and economical to homogeneously incorporate nanoparticles in magnesium matrix. However, role of some secondary methods is also extensive. That is why detailed discussion on liquid metallurgy-based fabrication methods is discussed here. Mechanisms of cavitation and acoustic streaming for UST are also been discussed in details. Presence of

particles also forms some strengthening mechanism in matrix. Details of those mechanisms are also presented in this study. Role of different nanoparticles like Al_2O_3, SiC, TiB_2, WC, CNT and TiC on mechanical and tribological behavior are discussed here by mentioning related literatures. Mechanical properties like microhardness, UTS, YS and creep behavior are mainly considered and related literatures yielded that presence of nanoparticles normally improves those properties. Literature on tribological behavior disclosed that nanoparticles help to improve wear and friction behavior of Mg-MMNCs at room as well as elevated temperatures. But researchers are split into two groups about corrosion characteristics of magnesium composites. Some researchers reported that corrosion resistance is decreased due to presence of reinforcement while others concluded that corrosion resistance is enhanced due to reinforcing particles. However, most studies are limited to laboratory scale which must be practiced in industrial scale also to reveal the exact potential of Mg-MMNCs. More studies on recyclability, energy efficiency and reliability of Mg-MMNCs are also needed to be performed in recent future.

References

1. Abdullah A, Malaki M, Baghizadeh E (2012) On the impact of ultrasonic cavitation bubbles. Proc. Inst. Mech. Eng Part C J Mech Eng Sci 226:681–694
2. Abdullah A, Pak A, Abdullah MM, Shahidi A, Malaki M (2014) Study of the behavior of ultrasonic piezo-ceramic actuators by simulations. Electron Mater Lett 10:37–42
3. Akbari MK, Mirzaee O, Baharvandi H (2013) Fabrication and study on mechanical properties and fracture behavior of nanometric Al_2O_3 particle-reinforced A356 composites focusing on the parameters of vortex method. Mater. Des. 46:199–205
4. Aung NN, Zhou W, Goh CS, Nai SML, Wei J (2010) Effect of carbon nanotubes on corrosion of Mg–CNT composites. Corros Sci 52(5):1551–1553
5. Banerjee S, Poria S, Sutradhar G, Sahoo P (2019a) Corrosion behavior of AZ31-WC nanocomposites. J Magnesium Alloys 7(4):681–695
6. Banerjee S, Poria S, Sutradhar G, Sahoo P (2019b) Tribological behavior of Mg-WC nanocomposites at elevated temperature. Mater Res Express 6(8):0865c6
7. Banerjee S, Poria S, Sutradhar G, Sahoo P (2019b) Dry sliding Tribological behavior of AZ31-WC nano-composites. J Magnesium Alloys 7:315–327
8. Bao S, Li L, Hong Y, Hu Z (2010) Study on the fabrication of SiCp/AZ31 nanocomposites by high energy ultrasonic vibration and its characteristics. J Plasticity Eng 1:139–143
9. Bhingole PP, Chaudhari GP (2012) Synergy of nano carbon black inoculation and high intensity ultrasonic processing in cast magnesium alloys. Mater Sci Eng A 556:954–961
10. Cao G, Choi H, Oportus J, Konishi H, Li X (2008) Study on tensile properties and microstructure of cast AZ91D/AlN nanocomposites. Mater Sci Eng A 494:127–131
11. Cao G, Kobliska J, Konishi H, Li X (2008) Tensile properties and microstructure of SiC nanoparticle-reinforced Mg-4Zn alloy fabricated by ultrasonic cavitation-based solidification processing. Metall Mater Trans A 39:880–886
12. Chan WM, Cheng FT, Leung LK, Horylev RJ, Yue TM (1998) Corrosion behavior of magnesium alloy AZ91 and its MMC in NaCl solution. Corros Rev 16(1–2):43–52
13. Chen K, Li ZQ, Zhou HZ, Wang WK (2007) Influence of high intensity ultrasonic vibration on microstructure of in-situ synthesized Mg_2Si/Mg composite. T Nonferr Metals Soc 17:s391–s395

14. Chen LY, Xu JQ, Choi H, Pozuelo M, Ma XL, Bhowmick S, Yang JM, Mathaudhu S, Li XC (2015) Processing and properties of magnesium containing a dense uniform dispersion of nanoparticles. Nature 528:539–543
15. Chen LY, Peng JY, Xu JQ et al (2013) Achieving uniform distribution and dispersion of a high percentage of nanoparticles in metal matrix nanocomposites by solidification processing. Scr Mater 69:634–637
16. Choi H, Alba-Baena N, Nimityongskul S et al (2011) Characterization of hot extruded Mg/SiC nanocomposites fabricated by casting. J Mater Sci 46:2991–2997
17. Choi H, Sun Y, Slater BP, Konishi H, Li X (2012) AZ91D/TiB_2 Nanocomposites fabricated by solidification nanoprocessing. Adv Eng Mater 14:291–295
18. Cicco M, Konishi H, Cao G et al (2009) Strong, ductile magnesium-zinc nanocomposites. Metall Mater Trans A 40A:3038–3045
19. Dai L, Ling Z, Bai Y (2001) Size-dependent inelastic behavior of particle-reinforced metal–matrix composites. Compos Sci Technol 61:1057–1063
20. Dieringa H, Huang Y, Wittke P, Klein M, Walther F, Dikovits M, Poletti C (2013) Compression creep response of magnesium alloy DieMag422 containing barium compared with the commercial creep-resistant alloys AE42 and MRI230D. Mater Sci Eng 585:430–438
21. Dieringa H, Katsarou L, Buzolin R, Szakács G, Horstmann M, Wolff M, Mendis C, Vorozhtsov S, StJohn D (2017) Ultrasound assisted casting of an AM60 based metal matrix nanocomposite, its properties, and recyclability. Metals 7:388
22. Endo M, Hayashi T, Itoh I, Kim YA, Shimamoto D, Muramatsu H, Shimizu Y, Morimoto S, Terrones M, Iinou S, Koide S (2008) An anticorrosive magnesium/carbon nanotube composite. Appl Phys Lett 92(6):063105
23. Erman A, Groza J, Li X, Choi H, Cao G (2012) Nanoparticle effects in cast Mg-1 wt% SiCnanocomposites. Mater Sci Eng A 558:39–43
24. Eskin DG, Eskin GI (2014) Ultrasonic treatment of light alloy melts, 2nd edn. CRC Press, Boca Raton, FL, USA
25. Eskin GI (1995) Cavitation mechanism of ultrasonic melt degassing. Ultrason Sonochem 2:S137–S141
26. Eskin GI (1998) Ultrasonic treatment of light alloy metallic melts. Gordon and Breach Science Publishers, Amsterdam, The Netherlands
27. Falcon LA, Bedolla B, Lemus J, Leon C, Rosales I, Gonzalez-Rodriguez JG (2011) Corrosion behavior of Mg–Al/TiC composites in NaCl solution. Int J Corros
28. Fukuda H, Szpunar JA, Kondoh K, Chromik R (2010) The influence of carbon nanotubes on the corrosion behaviour of AZ31B magnesium alloy. Corros Sci 52(12):3917–3923
29. Funatsu K, Fukuda H, Takei R, Umeda J, Kondoh K (2013) Quantitative evaluation of initial galvanic corrosion behavior of CNTs reinforced Mg–Al alloy. Adv Powder Technol 24(5):833–837
30. Ghasali E, Bordbar-Khiabani A, Alizadeh M, Mozafari M, Niazmand M, Kazemzadeh H, Ebadzadeh T (2019) Corrosion behavior and in-vitro bioactivity of porous Mg/Al_2O_3 and Mg/Si_3N_4 metal matrix composites fabricated using microwave sintering process. Mater Chem Phys 225:331–339
31. Gnanavelbabu A, Surendran KS, Kumar S (2020) Influence of ultrasonication power on grain refinement, mechanical properties and wear behaviour of AZ91D/nano-Al_2O_3 composites. Mater Res Express 7(1):016544
32. Goh CS, Wei J, Lee LC, Gupta M (2006) Simultaneous enhancement in strength and ductility by reinforcing magnesium with carbon nanotubes. Mater Sci Eng A 423(1–2):153–156
33. Goh CS, Wei J, Lee LC, Gupta M (2008) Ductility improvement and fatigue studies in Mg-CNT nanocomposites. Compos Sci Technol 68(6):1432–1439
34. Guo W, Wang Q, Ye B, Li X, Liu X, Zhou H (2012) Microstructural refinement and homogenization of Mg–SiC nanocomposites by cyclic extrusion compression. Mater Sci Eng A 556:267–270
35. Habibnejad-Korayem M, Mahmudi R, Poole WJ (2009) Enhanced properties of Mg-based nano-composites reinforced with Al_2O_3 nano-particles. Mater Sci Eng A 519(1–2):198–203

36. Hassan SF, Gupta M (2007a) Development of nano-Y_2O_3 containing magnesium nanocomposites using solidification processing. J Alloys Compd 429:176–183
37. Hassan SF, Gupta M (2007b) Effect of Nano-ZrO_2 particulates reinforcement on microstructureand mechanical behavior of solidification processed elemental Mg. J Compos Mater 41:2533–2543
38. Hassan SF, Gupta M (2005) Enhancing physical and mechanical properties of Mg using nanosized Al_2O_3 particulates as reinforcement. Metall Mater Trans A 36:2253–2258
39. Huang Y, Dieringa H, Kainer KU, Hort N (2014) Understanding effects of microstructural inhomogeneity on creep response—New approaches to improve the creep resistance in magnesium alloys. J Magnes Alloys 2:124–132
40. Ishiwata Y, Komarov S, Takeda Y (2012) Investigation of acoustic streaming in aluminum melts exposed to high-intensity ultrasonic irradiation. In: Proceedings of the 13th international conference on aluminum alloys (ICAA13), Pittsburgh, PA, USA, 3–7 June
41. Jia S, Jia SS, Sun G, Yao J (2005) The corrosion behaviour of Mg alloy AZ91D/TiCp metal matrix composite. In: Materials science forum, vol 488. Trans Tech Publications, pp 705–708
42. Karuppusamy P, Lingadurai K, Sivananth V (2019) Influence of Cryogenic Treatment On As-cast AZ91+ 1.5 wt% WC Mg-MMNC wear performance. In: Advances in materials and metallurgy. Springer, Singapore, pp 185–197
43. Katsarou L, Mounib M, Lefebvre W, Vorozhtsov S, Pavese M, Badini C, Dieringa H (2016) Microstructure, mechanical properties and creep of magnesium alloy Elektron21 reinforced with AlN nanoparticles by ultrasound-assisted stirring. Mater Sci Eng A 659:84–92
44. Khandelwal A, Mani K, Srivastava N, Gupta R, Chaudhari G (2017) Mechanical behavior of AZ31/Al_2O_3 magnesium alloy nanocomposites prepared using ultrasound assisted stir casting. Compos Part B Eng 123:64–73
45. Kubásek J, Vojtech D, Martínek M (2013) Structural characteristics and elevated temperature mechanical properties of AJ62 Mg alloy. Mater Charact 86:270–282
46. Kumar S, Suman KNS, Ravindra K, Poddar P, SB VS (2017) Microstructure, mechanical response and fractography of AZ91E/Al_2O_3 (p) nano composite fabricated by semi solid stir casting method. J Magnes Alloys 5(1):48–55
47. Labib F, Ghasemi HM, Mahmudi R (2016) Dry tribological behavior of Mg/SiCp composites at room and elevated temperatures. Wear 348:69–79
48. Lan J, Yang Y, Li X (2004) Microstructure and microhardness of SiC nanoparticles reinforced magnesium composites fabricated by ultrasonic method. Mater Sci Eng A 386:284–290
49. Li Q, Rottmair CA, Singer RF (2010) CNT reinforced light metal composites produced by melt stirring and by high pressure die casting. Compos Sci Technol 70(16):2242–2247
50. Lim CYH, Leo DK, Ang JJS, Gupta M (2005) Wear of magnesium composites reinforced with nano-sized alumina particulates. Wear 259(1–6):620–625
51. Liu S, Gao F, Zhang Q, Li W (2009) Mechanical properties and microstrutures of nano-sized sic particles reinforced AZ91D nanocomposites fabricated by high intensity ultrasonic assisted casting. Mater Sci Forum 618–619:449–452
52. Liu S-Y, Gao F-P, Zhang Q-Y, Xue Z, Li W-Z (2010) Fabrication of carbon nanotubes reinforced AZ91D composites by ultrasonic processing. Trans Nonferrous Met Soc China 20:1222–1227
53. Malaki M, Xu W, Kasar AK, Menezes PL, Dieringa H, Varma RS, Gupta M (2019) Advanced metal matrix nanocomposites. Metals 9(3):330
54. Meenashisundaram GK, Seetharaman S, Gupta M (2014) Enhancing overall tensile and compressive response of pure Mg using nano-TiB_2 particulates. Mater Charact 94:178–188
55. Murugan S, Nguyen QB, Gupta M (2019) Synthesis of magnesium based nano-composites. In: Magnesium—The wonder element for engineering/biomedical applications. IntechOpen
56. Nguyen QB, Gupta M (2008) Increasing significantly the failure strain and work of fracture of solidification processed AZ31B using nano-Al_2O_3 particulates. J Alloy Compd 459(1–2):244–250
57. Nguyen QB, Sim YHM, Gupta M, Lim CYH (2015) Tribology characteristics of magnesium alloy AZ31B and its composites. Tribol Int 82:464–471

58. Nie KB, Deng KK, Wang XJ, Wang T, Wu K (2017) Influence of SiC nanoparticles addition on the microstructural evolution and mechanical properties of AZ91 alloy during isothermal multidirectional forging. Mater Charact 124:14–24
59. Nie KB, Deng KK, Wang XJ, Wu K (2017) Characterization and strengthening mechanism of SiC nanoparticles reinforced magnesium matrix composite fabricated by ultrasonic vibration assisted squeeze casting. J Mater Res 32:2609–2620
60. Nie KB, Wang XJ, Wu K, Xu L, Zheng MY, Hu XS (2011) Processing, microstructure and mechanical properties of magnesium matrix nanocomposites fabricated by semisolid stirring assisted ultrasonic vibration. J Alloys Compd 509:8664–8669
61. Nie KB, Wang XJ, Xu L, Wu K, Hu XS, Zheng MY (2012) Influence of extrusion temperature and process parameter on microstructures and tensile properties of a particulate reinforced magnesium matrix nanocomposite. Mater Des 36:199–205
62. Pardo A, Merino S, Merino MC, Barroso I, Mohedano M, Arrabal R, Viejo F (2009) Corrosion behaviour of silicon–carbide-particle reinforced AZ92 magnesium alloy. Corros Sci 51(4):841–849
63. Praveenkumar R, Periyasamy P, Mohanavel V, Ravikumar MM (2019) Mechanical and tribological behavior of Mg-matrix composites manufactured by stir casting. Int J Veh Struct Syst (IJVSS) 11(1)
64. Ramirez A, Ma Q, Davis B, Wilks T, St John DH (2008) Potency of high-intensity ultrasonic treatment for grain refinement of magnesium alloys. Scripta Mater 59:19–22
65. Sankaranarayanan S, Habibi MK, Jayalakshmi S, Jia Ai K, Almajid A, Gupta M (2015) Nano-AlN particle reinforced Mg composites: microstructural and mechanical properties. Mater Sci Technol 31(9):1122–1131
66. Shen MJ, Ying WF, Wang XJ, Zhang MF, Wu K (2015) Development of high performance magnesium matrix nanocomposites using nano-SiC particulates as reinforcement. J Mater Eng Perform 24:3798–3807
67. Shiying L, Feipeng G, Qiongyuan Z, Wenzhen L (2009) Mechanical properties and microstructures of nano-sized SiC particle reinforced AZ91D nanocomposites fabricated by high intensity ultrasonic assisted casting. Mater Sci Forum 618–619:449–452
68. Suslick KS, Cline RE, Hammerton DA (1986) The sonochemical hot spot. J Am Chem Soc 108:5641–5642
69. Suslick KS, Matula TJ (1999) Ultrasonic physical mechanisms and chemical effects. In: Webster J (ed) Wiley encyclopedia of electrical and electronics engineering. Wiley, Hoboken, NJ, USA
70. Tiwari S, Balasubramaniam R, Gupta M (2007) Corrosion behavior of SiC reinforced magnesium composites. Corros Sci 49(2):711–725
71. Vogt R, Zhang Z, Li Y, Bonds M, Browning N, Lavernia E, Schoenung J (2009) The absence of thermal expansion mismatch strengthening in nanostructured metal–matrix composites. Scr Mater 61:1052–1055
72. Wang X, Liu W, Xiaoshi Hu, Kun Wu (2018) Microstructural modification and strength enhancement by SiC nanoparticles in AZ31 magnesium alloy during hot rolling. Mater Sci Eng A 715:49–61
73. Zarembo LK (1971) Part III: Acoustic streaming. In: Rozenberg LD (ed) High-intensity ultrasonic fields. Springer, New York, NY, USA
74. Zhang C, Zhang T, Wang Y, Wei F, Shao Y, Meng G, Wu K (2015) Effect of SiC particulates on the corrosion behavior of extruded AZ91/SiCp composites during the early stage of exposure. J Electrochem Soc 162(14):C754–C766
75. Zhang L, Luo X, Liu J, Leng Y, An L (2018) Dry sliding wear behavior of Mg-SiC nanocomposites with high volume fractions of reinforcement. Mater Lett 228:112–115
76. Zhou X, Su D, Wu C, Liu L (2012) Tensile mechanical properties and strengthening mechanism of hybrid carbon nanotube and silicon carbide nanoparticle-reinforced magnesium alloy composites. J Nanomater 1–7
77. Zhu YT, Lowe TC (2000) Observationsand issues on mechanisms of grain refinement during ECAP process. Mater Sci Eng A 291:46–53

78. Zhu SM, Easton MA, Gibson MA, Dargusch MS, Nie JF (2013) Analysis of the creep behaviour of die-cast Mg–3Al–1Si alloy. Mater Sci Eng A 578:377–382
79. Zhu SM, Gibson MA, Easton MA, Nie JF (2010) The relationship between microstructure and creep resistance in die-cast magnesium-rare earth alloys. Scr Mater 63:698–703

Chapter 10
Dynamics of Axially Functionally Graded Timoshenko Beams on Linear Elastic Foundation

Hareram Lohar, Anirban Mitra, and Sarmila Sahoo

1 Introduction

In the development of society throughout human history, materials have played a significant role. Advancement in the field of materials has seen development of new and improved materials and their utilization in engineering applications. Functionally graded materials (FGMs) are one such advanced category which combine materials, with continuous variation in composition from one surface to another along any orthogonal direction. As a result, material properties (e.g., elastic modulus, shear modulus, material density, and Poisson's ratio etc.) vary continuously and smoothly along the desired spatial directions. The advantage of FGMs over traditional composites is that, they retain most of the properties of their constituent materials. The continuous transition of materials also reduces residual and thermal stresses, stress concentration, and provides high strength-to-weight ratio. With these characteristics, FGMs naturally attract the attention of structural engineers and researchers and are gaining widespread applications in the various engineering industries including aerospace, mechanical, civil, and nuclear domains.

Most generalized kind of FGM involves properties gradation along multiple axis direction. In case of a beam, it entails functional variation of material properties along both thickness and axial direction [21, 30, 33, 42, 48]. However, analysis of such type of functionally graded (FG) beams naturally necessitates higher level of complexities in mathematical formulation. So, a large proportion of research papers available in the literature only deal with a single direction of variation. As a matter of fact, majority of such works consider the thickness direction gradation of FG

H. Lohar · A. Mitra (✉)
Jadavpur University, Kolkata, India
e-mail: anirban.mitra@jadavpuruniversity.in

S. Sahoo
Heritage Institute of Technology Kolkata, Kolkata, India

S. Sahoo (ed.), *Recent Advances in Layered Materials and Structures*,
Materials Horizons: From Nature to Nanomaterials,
https://doi.org/10.1007/978-981-33-4550-8_10

beam [2, 17–19, 31, 41]. Nevertheless, FG beams considering material gradation only along the axial direction are also important structural elements. Such structures are commonly referred to as axially functional graded (AFG) structures. They are advantageous in situations where revolving, overhanging, or cantilever structures are involved, such as helicopter rotor blades, spacecraft with flexible appendages, turbo-machine, turbine blades, etc.

In published literature, volume of research work dealing with AFG beams is significantly less, as compared to works involving transversely graded beams. While, thickness-wise graded elements have been studied for over 25 years, researchers have devoted considerable effort into analysing axially graded structures only in recent times (post 2010). Static structural, dynamic, and buckling characteristics of axially graded beams based on Euler–Bernoulli beam theory [1, 22, 38, 47, 10, 20, 35, 43, 39, 40] have been explored through various methods and techniques. However, Euler–Bernoulli beam model fails to accurately predict the response for sufficiently thick beam where shear deformation and rotary inertia are involved. Hence, in such cases, the Timoshenko beam theory must be employed for effective analysis. But only a few research works are available in the literature which evolves the study of axially graded thick beams following Timoshenko beam theory. In the following paragraph, some of the significant contributions to this field are summarized.

Rajasekaran [34] utilized differential quadrature elements and differential transformation methods to study free vibration behaviour of a geometrically non-uniform rotary AFG Timoshenko beams. Sarkar and Ganguli [36] presented closed form solution of a clamped and uniform cross-section AFG Timoshenko beam to study free vibrational characteristics. Shahba et al. [39] generated a new beam element and conducted a FE analysis to study the dynamics and buckling characteristics of AFG Timoshenko beam. Huang et al. [15, 16] introduced a unified approach to find out natural frequencies and critical buckling loads of AFG Timoshenko tapered beams. Shafiei et al. [37] performed a comparison analysis on free vibration of rotating AFG micro-beam on the basis Euler–Bernoulli and Timoshenko beam model utilizing generalized differential quadrature method. Calim [5, 6] employed complementary functions method and modified Durbin's algorithm to investigate transient behaviour of AFG Timoshenko non-uniform beams. Ghayesh [10, 11] conducted nonlinear forced vibration study on non-uniform cross-section AFG Timoshenko beams. Recently, Chen et al. [7] investigated free vibration characteristics of a nanoparticle carrying AFG nano-cantilevers considering the effect of mass and rotational inertia of the nanoparticle.

Several critical engineering systems are idealized and modelled, for analysis purpose, as beams on foundation and this brings to focus study of foundation supported FGM beam behaviour as an interesting domain of research. Issues related to such structures are taken up for investigation because they belong to a class of frequently used structural elements which generally serve as the key load-bearing components, like, rigid pavements, rail track, bridge decks, etc. So, it is natural to expect a lot of attention devoted towards analysing interactions between graded beams and elastic foundations. But, most of the attention has been concentrated on transversely functionally graded (TFG) beams and its various aspects are investigated

quite frequently and thoroughly Mohanty et al. [28], Yan et al. [45], Yas and Samadi [46], Esfahani et al. [9], Komijani et al. [19], Tossapanon and Wattanasakulpong [44], Deng et al. [8], Arefi and Zenkour [3, 4], Huang et al. [14]. On the other hand, considerably lesser number of research work is available relating to axially graded beams on foundation. The issue of AFG thin Euler–Bernoulli beams supported on elastic foundation is dealt with in a very small number of papers. Huang and Luo [12, 13] introduced a methodology to find out the buckling issues of AFG beam on elastic foundation. Free and forced vibration behaviour of AFG beam on elastic foundation were studied by Lohar et al. [23, 24]. AFG Timoshenko beam on elastic foundation is a more recent domain of research and till now, only a few articles are available in literature in this field. Calim [5] analysed free and forced vibrations of AFG Timoshenko beams on two-parameter viscoelastic foundation. Recently, Lohar et al. [25–27] employed a displacement based semi-analytical approach to study the nonlinear dynamic analysis of AFG Timoshenko beam resting on elastic foundation.

It is clear from the above discussion that the domain of AFG Timoshenko beam resting on foundation is comparatively unexplored domain. However, detailed investigation of such AFG components is warranted, considering their applications in critically important fields as structural element. Hence, the present study is focussed to investigate the dynamic behaviour, i.e., both free and forced vibration behaviour, of such system. As part of the free vibration study, a statically deflected configuration is used to determine loaded natural frequency and corresponding backbone curves for different system parameters. Nonlinear forced vibration analysis, which is undoubtedly a dynamic problem, is solved as an equivalent static problem on the basis of an assumption that considers all the forces acting on the system attains equilibrium at the peak amplitude. Steady-state response of undamped system is presented to study the effect of the various system parameter of the graded beam.

2 Mathematical Formulation

Figure 1 shows an AFG Timoshenko beam that is considered for the present analysis. As shown in the figure, this thick beam has a span of L, constant width b and tapering thickness $t(x)$ along the longitudinal direction of the beam. For thickness variation, two different taper patterns, parabolic and exponential, are considered (Fig. 1b) following the expressions,

Parabolic taper: $t(x) = t_0(1—\alpha x^2)$.

Exponential taper: $t(x) = t_0\ (—\alpha x^{1/2})$.

Here, t_0—Thickness at the left end of the beam (Fig. 1b).

α—Taper parameter.

Similarly, material properties are considered to be graded along the longitudinal direction. Elastic modulus ($E(x)$) and mass density ($\rho(x)$) (Fig. 1a) variations are as per the power-law expressions given below.

Elastic modulus: $E(x) = E_0 + (E_1 - E_0)\ (x/L)^n$.

Density: $\rho(x) = \rho_0 + (\rho_1 - \rho_0)\ (x/L)^n$.

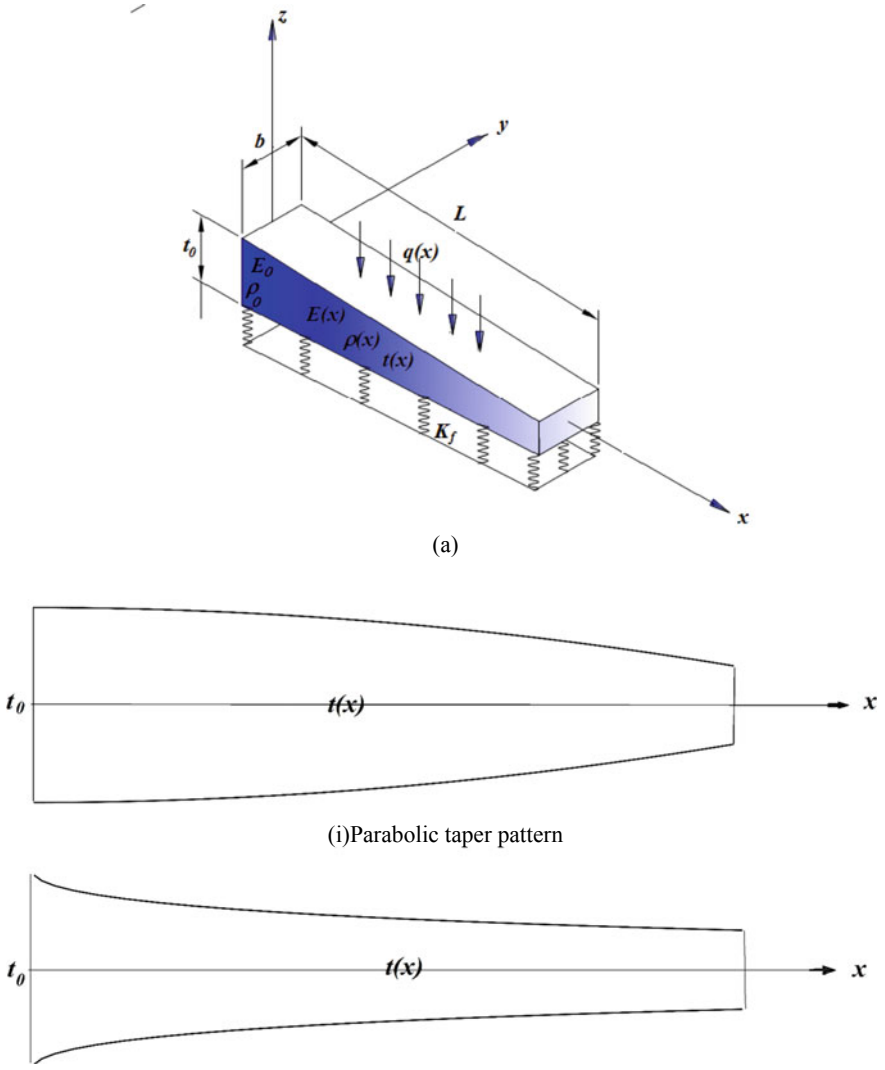

Fig. 1 **a** AFG non-uniform beam on elastic foundation **b** Parabolic and exponential taper profiles

Here, n describes the change of volume fraction of the two ingredients involved in the inhomogeneous mixture and it is called the gradient parameter.

In the present analysis, variation of Poisson ratio (μ) is not considered. Material gradation of the beam varies such that elastic modulus and density increase continuously from left to the right, providing a reverse pattern to thickness variation. Such a

variation is considered to obtain a proper weight distribution for the beam. Further, the beam is supported by an elastic foundation of linear nature as shown in Fig. 1a. The foundation stiffness is quantified by the stiffness coefficient of the linear spring and it is denoted by K_f.

Boundary conditions (both transverse and in-plane) of the system are important aspects that have significant influence on its response. In the present chapter, only variations in the transverse or flexural boundaries are considered, while the in-plane or membrane boundaries are taken as immovable, i.e., no displacement at the ends of the beam. In the present chapter, three types of flexural boundaries are included as part of the study. All these boundaries are made up of combinations of simply supported and clamped end conditions. Two of the boundary conditions taken into account are symmetric (Clamped–clamped, in short represented as CC and Simply supported-simply supported (SS)), while the other is asymmetric (clamped-simply supports (CS)). For free vibration, the beam is assumed to be under uniform pressure load, $q(x)$, to provide the requisite amount of static deflection, whereas in case of forced vibration study, uniformly distributed transverse harmonic excitation, $q(x, t)$, is assumed.

The mathematical formulation of the current chapter is based on energy methods. In order to incorporate the effects of rotary inertia and shear deformation, Timoshenko beam theory is utilized. Geometric nonlinearity is also accounted for through consideration of nonlinear strain–displacement relations. Free and forced vibration analyses are presented in two separate sections following some basic assumptions. Nonlinear free vibration analysis is performed on statically deflected configuration of the system. The assumption in the nonlinear forced vibration analysis is that all the forces acting on the system attains equilibrium at the peak amplitude.

2.1 Energy Expressions

The present study is a semi-analytical displacement-based approximate method, which indicates that in the expression of strain energies, the strains (axial as well as shear) are to be replaced by appropriate displacement relations. In order to express the strain energies in terms of displacement fields, following strain–displacement expressions are invoked for axial strain (ε_a) and shear strain (ε_s).

$$\varepsilon_a = \frac{1}{2}\left(\frac{dw}{dx}\right)^2 + \frac{du}{dx} - z\frac{d\psi}{dx} \tag{1}$$

$$\varepsilon_s = \frac{1}{2}\left(\frac{dw}{dx} - \psi\right) \tag{2}$$

It is important to note that on neglecting the third term of Eq. (1), it resembles von Karman nonlinear strain–displacement expression. The displacement fields associated with the above expressions are as follow: transverse displacement field

(w), in-plane displacement field (u) and rotational field (ψ) of beam section due to bending. All these displacement fields are dependent on the axial coordinate and they are defined at the mid-plane of the beam. Substituting the strain–displacement expressions, the strain energies, U_a, $U_s$and U_f, can be expressed as follows,

$$U_a = \frac{b}{2}\int_0^L \int_{-\frac{t}{2}}^{\frac{t}{2}} \left\{ \begin{array}{l} \frac{1}{4}\left(\frac{dw}{dx}\right)^4 + \left(\frac{du}{dx}\right)^2 + z^2\left(\frac{d\psi}{dx}\right)^2 \\ +\left(\frac{dw}{dx}\right)^2 \frac{du}{dx} - z\left(\frac{dw}{dx}\right)^2 \frac{d\psi}{dx} - 2z\frac{du}{dx}\frac{d\psi}{dx} \end{array} \right\} E(x)dxdz \tag{3}$$

$$U_s = \frac{bk_{sh}}{2}\int_0^L \int_{-\frac{t}{2}}^{\frac{t}{2}} \left\{ \left(\frac{dw}{dx}\right)^2 - 2\frac{dw}{dx}\psi + \psi^2 \right\} G(x)dxdz \tag{4}$$

$$U_f = \frac{1}{2}\int_0^L K_f w^2 dx \tag{5}$$

k_{sh} is termed as shear correction factor. It is well known that for rectangular cross-section, the numerical value of k_{sh} is taken as 5/6. Here, shear modulus is expressed by, $G(x) = E(x)/2(1 + \mu)$. In order to implement the minimum total potential energy principle, expression for potential for external work need to be obtained and it is provided corresponding to uniformly distributed load $q(x)$ (static) and harmonic excitation $q(x,t)$ (forced vibration) in Eq. (6). The external excitation has the following expression, $q = \bar{q}(x)e^{j\omega\tau}$, where, the excitation frequency is ω, with $\bar{q}$ representing the intensity of the harmonic excitation per unit length of the beam.

In formulating the present chapter, only uniformly distributed load/ harmonic excitation has been taken into account. However, this is not a limitation on the present methodology. Any other form of transverse loading or excitation can be accommodated in the analysis, as long as it can be expressed mathematically in terms of analytical or numerical functions.

$$V = \int_0^L q w dx \tag{6}$$

Kinetic energy of the present system of mass density $\rho(x)$ is expressed through the expression shown in Eq. (7).

$$T = \frac{b}{2}\int_0^L \int_{-\frac{t}{2}}^{\frac{t}{2}} \left\{ \left(\frac{dw}{dt}\right)^2 + \left(\frac{du}{dt}\right)^2 + z^2\left(\frac{d\psi}{dt}\right)^2 \right\} \rho(x)dxdz \tag{7}$$

2.2 Nonlinear Free Vibration Analysis

Presently, the strategy adopted to solve the free vibration problem has two distinct phases. In the first phase, the objective is to constitute a large deflection static analysis that provides the stiffness matrix in deflected configuration. In the second step, eigenvalues and eigenvectors are obtained by plugging in the matrix generated through static analyses directly into the dynamic system, represented by an eigenvalue problem. Finally, the natural frequencies and mode shapes of the system are determined. In this regard, it is clear that static analysis is an in-built part with the free vibration analysis.

2.2.1 Static Analysis

Minimum total potential energy principle is employed to derive the governing sets of equations in static analysis, which is mathematically expressed as,

$$\delta(U + V) = 0 \tag{8}$$

Here, δ represents variational operator. The mathematical expressions of U and V are provided in Eqs. (3), (4), (5) and (6). The static displacement fields (w, u and ψ) for the energy functional are assumed as linear combination of orthogonal admissible functions, φ_i, α_i and β_i and a set of unknown coefficients (d_i), expressed as,

$$w = \sum_{i=1}^{nw} d_i \phi_i(x) \tag{9a}$$

$$u = \sum_{i=1}^{nu} d_{nw+i} \alpha_i(x) \tag{9b}$$

$$\psi = \sum_{i=1}^{nsi} d_{nw+nu+i} \beta_i(x) \tag{9c}$$

Here, *nw*, *nu* and *nsi* represent the number of functions corresponding to w, u and ψ. The admissible functions are generated from the boundary conditions of the beam. The first one of these admissible functions, which is also known as start function (φ_1, α_1 and β_1), is selected from the flexural, in-plane and end rotation conditions, respectively. These functions are tabulated in the Table 1. For the aid of mathematical formulation, these functions require to be continuous and differentiable within the domain. Higher order functions (upto *nw*/*nu*/*nsi*) are generated from the previously selected start functions by implementing Gram–Schmidt orthogonalization scheme.

Substituting the assumed displacement fields (Eq. (9)) into energy functionals (Eqs. (3), (4), (5) and (6)), and hence generated energy functionals into energy

Table 1 Start functions for different boundary conditions

Displacement field	Boundary	Function
w	CC	$\phi_1 = (x/L)\{1\text{-}(x/L)\}$
	CS	
	SS	
u	CC	$\alpha_1 = (x/L)\{1\text{-}(x/L)\}$
	CS	
	SS	
ψ	CC	$\beta_1 = sin(\pi x/L)$
	CS	$\beta_1 = sin(\pi x/2L)$
	SS	$\beta_1 = cos(\pi x/L)$

principle (Eq. (8)), the governing set of equations are obtained in matrix form, as follows,

$$[K]\{d\} = \{f\} \tag{10}$$

Here, $[K]$ denotes the stiffness matrix and $\{f\}$ are the load vector. Each of them has the dimensions of $(nu + nw + nsi)$. The elements of these matrixes are provided in the Appendix. A brief look on the elements of $[K]$ reveals that the unknown coefficients (di) appear in certain terms. Hence, the problem is nonlinear in nature and cannot be solved directly. To obtain the solution in the present study an iterative scheme is employed which is known as direct substitution with relaxation method. Finally performing static analysis deformed configuration of transversely loaded beam system will be known and can be utilized for the following free vibration study.

2.2.2 Free Vibration Analysis

Hamilton's principle is utilized to formulate the free vibration problem, which is expressed as,

$$\delta\left(\int_{\tau_1}^{\tau_2}(T - U - V)d\tau\right) = 0 \tag{11}$$

Here, τ denotes the time. The expression of U and V are already provided, whereas the expression of V will reduce to zero as free vibration study is performed on the deformed beam whose static solution is already available. The assumed dynamic displacement fields associated with the above expression of energy functionals are completely separable by space and time and expressed as,

$$w(x,\tau) = \sum_{i=1}^{nw} d_i \phi_i(x) e^{j\omega\tau} \tag{12a}$$

$$u(x,\tau) = \sum_{i=1}^{nu} d_{nw+i} \alpha_i(x) e^{j\omega\tau} \tag{12a}$$

$$\psi(x,\tau) = \sum_{i=1}^{nsi} d_{nw+nu+i} \beta_i(x) e^{j\omega\tau} \tag{12c}$$

Here, ω denotes the natural frequency of the vibratory system and $j = \sqrt{-1}$. The spatial part of the above expression is same as that considered in the static analysis and d_i's are new set of unknown coefficients. However, φ_i, α_i and β_i are remain same as that of static problem. Substituting the expressions of strain energy (Eqs. (3), (4) and (5)) and kinetic energy (Eq. (7)), along with the assumed dynamic displacements (Eq. (12)) into Eq. (11), the governing equation is obtained as follows:

$$[K]\{d\} - \omega^2[M]\{d\} = 0 \tag{13}$$

Here, $[K]$ is the stiffness matrix is same as of static analysis and $[M]$ is mass matrix. The elements of $[M]$ are provided in Appendix.

2.3 Nonlinear Forced Vibration Analysis

Forced vibration problem is solved by assuming that at the time of maximum deflection of the system, i.e., when it is subjected to maximum excitation amplitude, the dynamic system satisfies force equilibrium condition. Hence, an equivalent static situation is derived from the dynamic one, where amplitude of the harmonic excitation and excitation frequency are the controlling parameters to system response. The present analysis is only concerned with steady–state behaviour of the system and it is assumed that frequency of external excitation equals response frequency of the system. As damping is assumed to be absent, phase lag of the system response is ignored.

The governing equations corresponding to nonlinear forced vibration of the system are derived from Hamilton's principle, whose mathematical form is provided in Eq. (11). Total strain energy (Eqs. (3), (4) and (5)), potential energy (Eq. (6)) and kinetic energy (Eq. (7)) are supplied to Eq. (11), along with the assumed dynamic displacements (Eq. (12)) to obtain governing equation.

$$[K]\{d\} - \omega^2[M]\{d\} = \{f\} \tag{14}$$

The elements of $[K]$, $[M]$ and $\{f\}$ are same as that of free vibration analysis which are provided in Appendix. A multidimensional quasi-Newton method, known

as Broyden's method [32], is employed to solve the system governing equations that are nonlinear. Following this method, initially, a Jacobian is evaluated on the basis of a starting guess and in the subsequent iterations, only updates are calculated, thereby reducing the computational load.

3 Result and Discussion

In the current chapter, nonlinear free and forced vibration analysis of a system, which comprises an axially graded Timoshenko beam supported on a linear elastic foundation, is performed to gain thorough insight into the dynamic behaviour of the system. In order to perform the free vibration analysis, a uniformly distributed load is applied first to obtain a statically deflected profile and a small amplitude linear eigenvalue analysis about the deflected profile determines loaded frequency frequencies of the system for different system parameters. However, as the transverse load produces a given static deflection, natural frequencies in the corresponding configuration are plotted against it to obtain the backbone curves in a normalized frequency-deflection plane. For the nonlinear forced vibration analysis, transverse harmonic excitation is applied on the system to find out its frequency response. The present analysis only deals with steady state response, where response frequency is assumed to be equal to forcing frequency.

For the non-uniform beam geometry, width (b) is considered as constant at 0.02 m, while, to consider the beam as thick beam, length-to-thickness ratio (L/t_0) value of 20 is taken with the length (L) as 0.2 m. Parabolic and exponential taper profiles, with their proportions controlled by variations of taper parameter (α), are considered. In order to keep the thickness at the end of the beam same for both taper patterns (so that a clear picture of taper parameter effects on generated results can be gained), four different α values are selected carefully. For parabolic pattern these values are 0, 0.2, 0.4, and 0.6 whereas for exponential taper these values are selected as 0, 0.223144, 0.510826, and 0.916291. It should be mentioned that $\alpha = 0$ represents a uniform beam. The variation of the normalized thickness for two different taper patterns along the normalized length is shown in Fig. 2. From Fig. 2, it is observed that $\alpha = 0$ indicates no variation in thickness for both taper pattern, whereas $\alpha = 0.6$ and $\alpha = 0.916291$ indicate maximum variation of thickness for parabolic and exponential taper pattern, respectively.

Continuous gradation along axial direction of the AFG beam is maintained in such way that pure Aluminium at root side ($x = 0$) will convert into pure Zirconia at other end ($x = L$). The material properties for Aluminium (Al) and Zirconia (ZrO_2) are considered as: Al: $E_0 = 70$ GPa, $\rho_0 = 2702$ kg/m^3; ZrO_2: $E_1 = 200$ GPa, $\rho_1 = 5700$ kg/m^3. Material property gradation for various gradient parameters (n) is shown in Fig. 3. Two different plots are obtained to indicate the gradation of elastic modulus and mass density. It is clear from figures, that $n = 1$ indicates the linear gradation of the material properties, in which 50% of each constituent material (Aluminium/Zirconia) is involved. Hence, for the best practice, these values should be selected in between

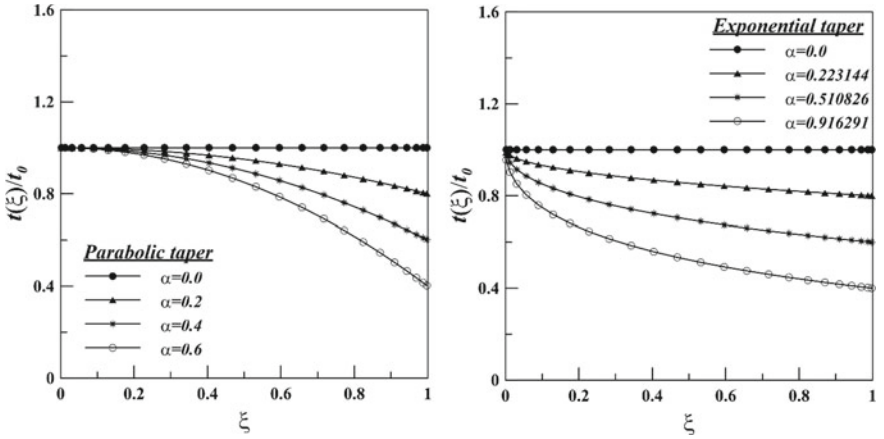

Fig. 2 Thickness variation of non-uniform along axial direction for parabolic and exponential taper profile

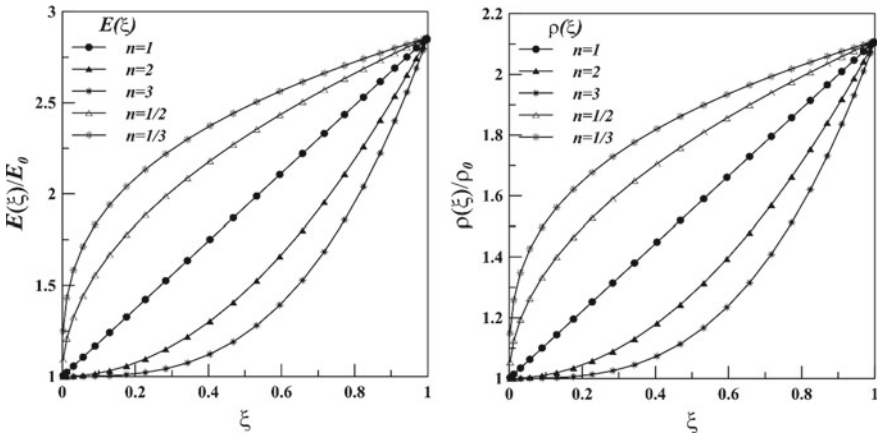

Fig. 3 Axial gradation of elastic modulus and density for different gradient parameter (n)

1/3 and 3 to maintain proper distribution of constituent materials [29]. Poisson ratio (μ) value throughout the entire analysis is taken as 0.3.

To represent the elastic foundation, four different values for dimensionless foundation stiffness [$K_f = k_f \{(L/t_0)^3/E_0 b\}$] are taken here, which are 0, 20, 40, and 60, respectively. It should also be pointed out that foundation stiffness '0' implies the case of beam without foundation support. Here, k_f is the dimensional (N/m) value of stiffness. In case of forced vibration analysis, four different dimensionless externally applied harmonic excitations [$\bar{q}^* = \bar{q}(L^4/E_0 I_0 t_0)$] are taken which are 20, 30, 40, and 50.

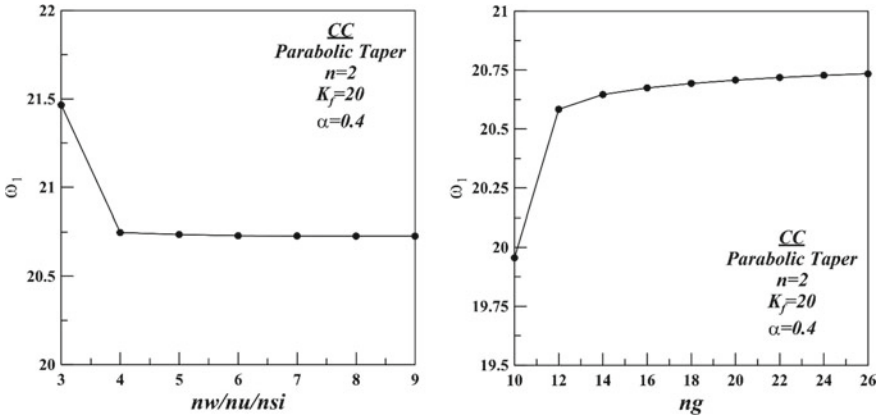

Fig. 4 Convergence study for selecting number of function (*nw/nu/nsi*) and number of gauss point (*ng*)

Numerical computations of the present study are performed on a normalized domain ($\xi = x/L$) that is discretized into certain number of Gauss points along the normalized length of the beam. Hence, a detailed convergence study is needed for selecting the number of gauss points. Another parameter that influences the outcome of the numerical study is the number of functions (*nw*,*nu* and *nsi*) and must, therefore, be chosen with great care. A similar convergence study is essential in fixing the appropriate values for the number of the functions. This study is conducted on a clamped AFG beam with parabolic taper ($\alpha = 0.4$), considering gradient parameter, $n = 2$ and elastic foundation parameter, $K_f = 20$. Results for comparison of dimensionless fundamental frequency are shown in Fig. 4 and from the figure, choice of number of gauss points (*ng*) as 24 and number of orthogonal functions ($nw = nu = nsi$) as 8 can be amply justified.

Validation of the present methodology and solution technique is established through comparison of the generated results with the published results of Huang et al. [14]. For that purpose, a non-uniform AFG Timoshenko beam (ZrO_2–Al) having clamped (CC) ends but without elastic foundation is considered. First four dimensionless linear natural frequencies $\left(\omega = \Omega L^2\sqrt{\rho_0 A_0 / E_0 I_0}\right)$ are compared for different gradation parameter (n) in Table 2 and it is evident that the current results are closely matching with the established results.

3.1 Natural Frequency

In case of free vibration analysis, dimensionless fundamental natural frequencies $\left(\Omega = \omega L^2\sqrt{\rho_0 A_0 / E_0 I_0}\right)$ for CC, CS, and SS boundary conditions of axially graded Timoshenko beams are provided in Tables 3, 4, 5, 6, 7 and 8 for different combination

Table 2 Comparisons of first four dimensionless $\left(\omega = \Omega L^2\sqrt{\rho_0 A_0 / E_0 I_0}\right)$ natural frequencies of AFG non-uniform Timoshenko CC beam for different n value

Literatures	ω	$n = 1$	$n = 2$	$n = 3$	$n = 4$
Huang et al. [14]	1	12.6816	12.4633	12.3753	12.3622
Present study		12.6487	12.4292	12.3405	12.3267
Huang et al. [14]	2	26.4910	26.3804	26.3188	26.3116
Present study		26.4306	26.3181	26.2551	26.2465
Huang et al. [14]	3	42.6420	42.9611	43.0839	43.135
Present study		42.5356	42.8552	42.9763	43.0256
Huang et al. [14]	4	58.6685	59.4023	59.6994	59.8150
Present study		58.5090	59.2332	59.5247	59.6382

Table 3 Values of dimensionless fundamental frequencies $\left(\Omega_1 = \omega_1 L^2\sqrt{\rho_0 A_0 / E_0 I_0}\right)$ for parabolic tapered CC AFG beam for different combinations of taper parameter, spring stiffness and gradation index

Taper pattern	Taper parameter (α)	Foundation stiffness (K_f)	Ω_1				
			$n = 1/3$	$n = 1/2$	$n = 1$	$n = 2$	$n = 3$
Parabolic taper	0.0	00	24.22	23.96	23.88	24.30	24.57
		20	24.75	24.52	24.53	25.06	25.40
		40	25.26	25.07	25.16	25.80	26.20
		60	25.77	26.61	25.77	26.52	26.98
	0.2	00	22.11	21.85	21.73	22.08	22.32
		20	22.72	22.50	22.47	22.95	23.28
		40	23.31	23.12	23.19	23.79	24.19
		60	23.88	23.73	23.89	24.60	25.07
	0.4	00	19.83	19.57	19.42	19.70	19.91
		20	20.55	20.34	20.29	20.73	21.03
		40	21.24	21.07	21.13	21.70	22.10
		60	21.91	21.78	21.94	22.64	23.11
	0.6	00	17.29	17.04	16.86	17.07	17.25
		20	18.18	17.98	17.94	18.33	18.63
		40	19.03	18.88	18.95	19.51	19.91
		60	19.84	19.74	19.92	20.62	21.11

of gradation index, taper patterns, taper parameters, and foundation stiffness values. For each boundary condition, two tables are furnished to accommodate parabolic and exponential taper pattern accordingly. The taper parameter (α) varies from 0.0 to 0.6 for parabolic taper pattern whereas for the case of exponential taper pattern the variation is considered from 0 to 0.916291. Under each taper pattern, four different

Table 4 Values of dimensionless fundamental frequencies $\left(\Omega_1 = \omega_1 L^2\sqrt{\rho_0 A_0 / E_0 I_0}\right)$ for exponential tapered CC AFG beam for different combinations of taper parameter, spring stiffness and gradation index

Taper pattern	Taper parameter (α)	Foundation stiffness (K_f)	Ω_1				
			$n = 1/3$	$n = 1/2$	$n = 1$	$n = 2$	$n = 3$
Exponential taper	0.223144	00	21.20	20.95	20.83	21.19	21.43
		20	21.89	21.69	21.69	22.19	22.53
		40	22.57	22.40	22.51	23.15	23.57
		60	23.22	23.10	23.30	24.07	24.57
	0.510826	00	17.87	17.63	17.48	17.76	17.98
		20	18.86	18.69	18.70	19.19	19.54
		40	19.81	19.70	19.85	20.52	20.98
		60	20.72	20.65	20.93	21.77	22.33
	0.916291	00	14.07	13.86	13.68	13.87	14.06
		20	15.73	15.61	15.68	16.20	16.60
		40	17.22	17.19	17.45	18.23	18.79
		60	18.60	18.64	19.06	20.06	20.76

Table 5 Values of dimensionless fundamental frequencies $\left(\Omega_1 = \omega_1 L^2\sqrt{\rho_0 A_0 / E_0 I_0}\right)$ for parabolic tapered CS AFG beam for different combinations of taper parameter, spring stiffness, and gradation index

Taper pattern	Taper parameter (α)	Foundation stiffness (K_f)	Ω_1				
			$n = 1/3$	$n = 1/2$	$n = 1$	$n = 2$	$n = 3$
Parabolic taper	0.0	00	16.44	16.10	15.68	15.53	15.48
		20	17.19	16.90	16.60	16.62	16.68
		40	17.90	17.66	17.48	17.65	17.81
		60	18.59	18.40	18.31	18.61	18.67
	0.2	00	15.66	15.35	14.97	14.86	14.83
		20	16.50	16.24	16.00	16.07	16.17
		40	17.30	17.09	16.97	17.20	17.40
		60	18.07	17.90	17.88	18.26	18.56
	0.4	00	14.75	14.46	14.13	14.07	14.06
		20	15.72	15.48	15.30	15.44	15.57
		40	16.62	16.45	16.39	16.70	16.95
		60	17.49	17.36	17.41	17.88	18.23
	0.6	00	13.62	13.35	13.07	13.07	13.10
		20	14.77	14.57	14.45	14.68	14.86
		40	15.84	15.70	15.71	16.13	16.45
		60	16.84	16.75	16.88	17.46	17.87

Table 6 Values of dimensionless fundamental frequencies $\left(\Omega_1 = \omega_1 L^2\sqrt{\rho_0 A_0 / E_0 I_0}\right)$ for exponential tapered CS AFG beam for different combinations of taper parameter, spring stiffness, and gradation index

Taper pattern	Taper parameter (α)	Foundation stiffness (K_f)	Ω_1				
			$n = 1/3$	$n = 1/2$	$n = 1$	$n = 2$	$n = 3$
Exponential taper	0.223144	00	14.67	14.36	13.98	13.86	13.83
		20	15.64	15.40	15.18	15.28	15.39
		40	16.57	16.38	16.29	16.57	16.80
		60	17.44	17.30	17.33	17.76	18.11
	0.510826	00	12.65	12.38	12.03	11.95	11.94
		20	14.03	13.84	13.71	13.91	14.10
		40	15.28	15.17	15.20	15.62	15.96
		60	16.44	16.39	16.56	17.17	17.63
	0.916291	00	10.25	10.02	09.72	09.65	09.67
		20	12.47	12.36	12.37	12.72	13.02
		40	14.35	14.33	14.54	15.17	15.66
		60	16.00	16.06	16.43	17.28	17.92

Table 7 Values of dimensionless fundamental frequencies $\left(\Omega_1 = \omega_1 L^2\sqrt{\rho_0 A_0 / E_0 I_0}\right)$ for parabolic tapered SS AFG beam for different combinations of taper parameter, spring stiffness, and gradation index

Taper pattern	Taper parameter (α)	Foundation stiffness (K_f)	Ω_1				
			$n = 1/3$	$n = 1/2$	$n = 1$	$n = 2$	$n = 3$
Parabolic taper	0.0	00	11.25	11.16	10.91	10.54	10.29
		20	12.34	12.31	12.24	12.15	12.09
		40	13.34	13.37	13.45	13.57	13.66
		60	14.27	14.34	14.55	14.86	15.06
	0.2	00	10.60	10.51	10.26	09.91	09.69
		20	11.82	11.80	11.76	11.71	11.69
		40	12.92	12.96	13.08	13.27	13.40
		60	13.94	14.03	14.28	14.67	14.91
	0.4	00	09.96	09.87	09.62	09.27	09.09
		20	11.33	11.32	11.30	11.31	11.33
		40	12.55	12.61	12.76	13.02	13.20
		60	13.66	13.77	14.07	14.53	14.84
	0.6	00	09.32	09.22	08.97	08.66	08.45
		20	10.87	10.87	10.88	10.95	11.02
		40	12.23	12.30	12.50	12.83	13.07
		60	13.45	13.58	13.93	14.48	14.84

Table 8 Values of dimensionless fundamental frequencies $\left(\Omega_1 = \omega_1 L^2\sqrt{\rho_0 A_0 / E_0 I_0}\right)$ for exponential tapered SS AFG beam for different combinations of taper parameter, spring stiffness, and gradation index

Taper pattern	Taper parameter (α)	Foundation stiffness (K_f)	Ω_1				
			$n = 1/3$	$n = 1/2$	$n = 1$	$n = 2$	$n = 3$
Exponential taper	0.223144	00	09.64	09.56	09.34	09.01	08.80
		20	11.09	11.10	11.11	11.14	11.16
		40	12.37	12.44	12.63	12.92	13.11
		60	13.53	13.66	13.99	14.48	14.79
	0.510826	00	07.92	07.85	07.66	07.38	07.21
		20	09.97	10.02	10.14	10.34	10.47
		40	11.67	11.80	12.13	12.62	12.94
		60	13.15	13.34	13.85	14.55	15.00
	0.916291	00	06.02	05.97	05.81	05.59	05.46
		20	09.22	09.33	09.62	10.04	10.32
		40	11.56	11.76	12.30	13.06	13.53
		60	13.50	13.78	14.49	15.50	16.11

foundation stiffness values are considered, as it is varied from 0 to 60 in the fixed interval of 20. Gradation parameter is also varied from 1/3 to 3. Corresponding to all three boundary conditions, the first table for parabolic taper (Tables 3, 5 and 7) includes results for $\alpha = 0$, (uniform beam). However, subsequently, the 2nd table for that boundary condition (Tables 4, 6 and 8) presenting the results for exponential taper omits the rows of results corresponding to $\alpha = 0$ to avoid duplication.

Tables 3, 4, 5, 6, 7, and 8 show that increase in foundation stiffness is reflected on system behaviour as an increase in the natural frequency, which is quite an expected outcome. A stiffer foundation makes for a system that is more rigid and hence there is an increase in the natural frequencies of the system. For a given stiffness value, natural frequency in CC beam is found to be the highest and in SS beam, it is the lowest. As is widely known, end conditions and in natural extension, boundary conditions have significant influence on free vibration behaviour. Another observation from the tables is that natural frequency decreases with rise in taper parameter. A softening effect, i.e., decrease in system stiffness, occurs due to decrease in taper parameter and it is accompanied with reduction in moment of inertia as well as cross-sectional area. So, the result is decrement in natural frequencies. It is observed that exponentially tapered beam shows greater decrease in frequencies in comparison with parabolic tapered beam. It is also observed that almost for all the cases gradation parameter at $n = 3$ the frequency has the highest value.

3.2 Backbone Curve

Amplitude dependency of natural frequencies is manifested through backbone curves of a dynamic system. Figures 5, 6, 7 and 8 exhibit the first mode of vibration backbone curves of the system in a dimensionless plane, where, dimensionless amplitude (w_{max}/t_0) and dimensionless frequency (ω_{nf}/ω_1) are the ordinate and abscissa, respectively. The fundamental natural frequencies (ω_1), which are already tabulated in Tables 3, 4, 5, 6, 7, and 8 are used to normalize nonlinear frequencies (ω_{nf}/ω_1). The natural frequency exhibits hardening type nonlinear behaviours as pre-loading on beam increases the stiffness of the system.

The influence of foundation stiffness is shown through the representation of 1st backbone curve, shown in Fig. 5. For this purpose, total six plots are obtained considering the above-mentioned boundary conditions (CC, CS and SS) and taper patterns (parabolic and exponential). Four backbone curves corresponding to the four spring stiffness, which varies from 0 to 60, are depicted in each of these plots. For parabolic pattern, taper parameter is constant at 0.4, whereas for exponential taper, it is taken as 0.510826. It is observed from figures, in all the cases, slope of the backbone curve increases as foundation stiffness increases. The effect is more noticeable in case of simply supported beam, whereas for clamped boundaries, backbone curves are relatively tightly grouped together.

Figure 6 shows the effect of taper parameters on backbone curve for AFG beam. Curves are depicted for two different taper patterns in which taper parameter varies from 0 to 0.6 parabolic taper whereas in case of exponential taper, variation of taper parameter is taken from 0 to 0.916291. Gradation parameter is selected as $n = 2$ for all the cases whereas foundation stiffness is fixed at 20. It is important to note that the case of uniform beam is represented by $\alpha = 0$ and provides a basis for comparison. From the figure, it is observed that backbone curves progressively tilt towards the right side with the increase of taper parameter values.

The effect of gradation parameter on backbone curve is presented in Fig. 7. For parabolic profile, taper parameter is considered as 0.4 whereas for exponential taper, this value is taken as 0.510826. In each of the cases, foundation stiffness has a fixed value of 20. Each plot in this figure has five backbone curves generated by varying the gradation parameter between 1/3 and 3. It is evident from the figures that in the normalized domain, these hardening-type backbone curves are quite close to one another.

Backbone curves for higher modes (modes 2–4) of the parabolic and exponential AFG beam corresponding to three boundary conditions are provided in Fig. 8. For all the cases, foundation stiffness and gradation parameter are considered as 20 and 2, respectively, whereas the taper parameter is considered as 0.4 for parabolic taper and 0.510826 for exponential taper.

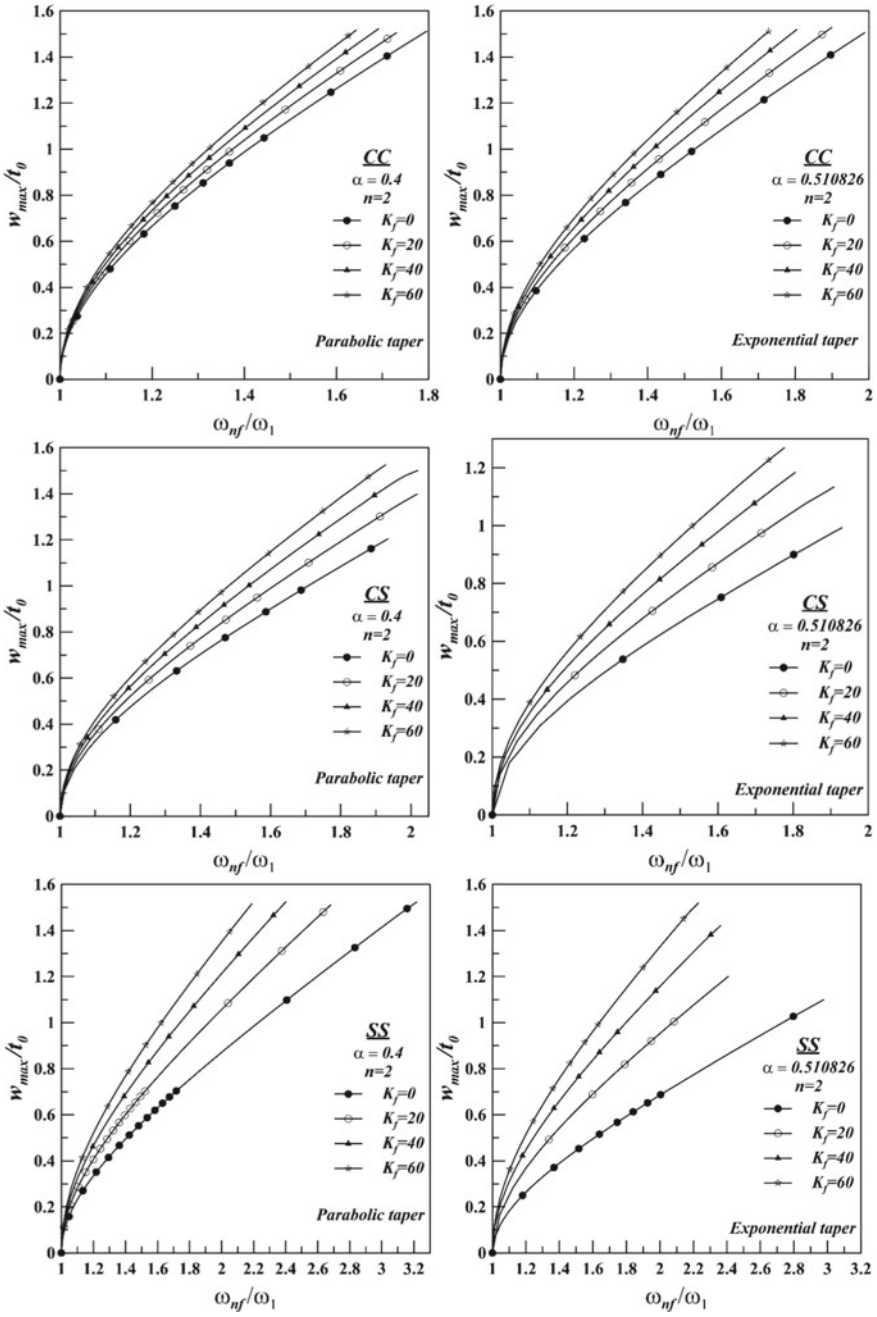

Fig. 5 Effect of foundation stiffness on backbone curve for different boundary conditions and taper pattern

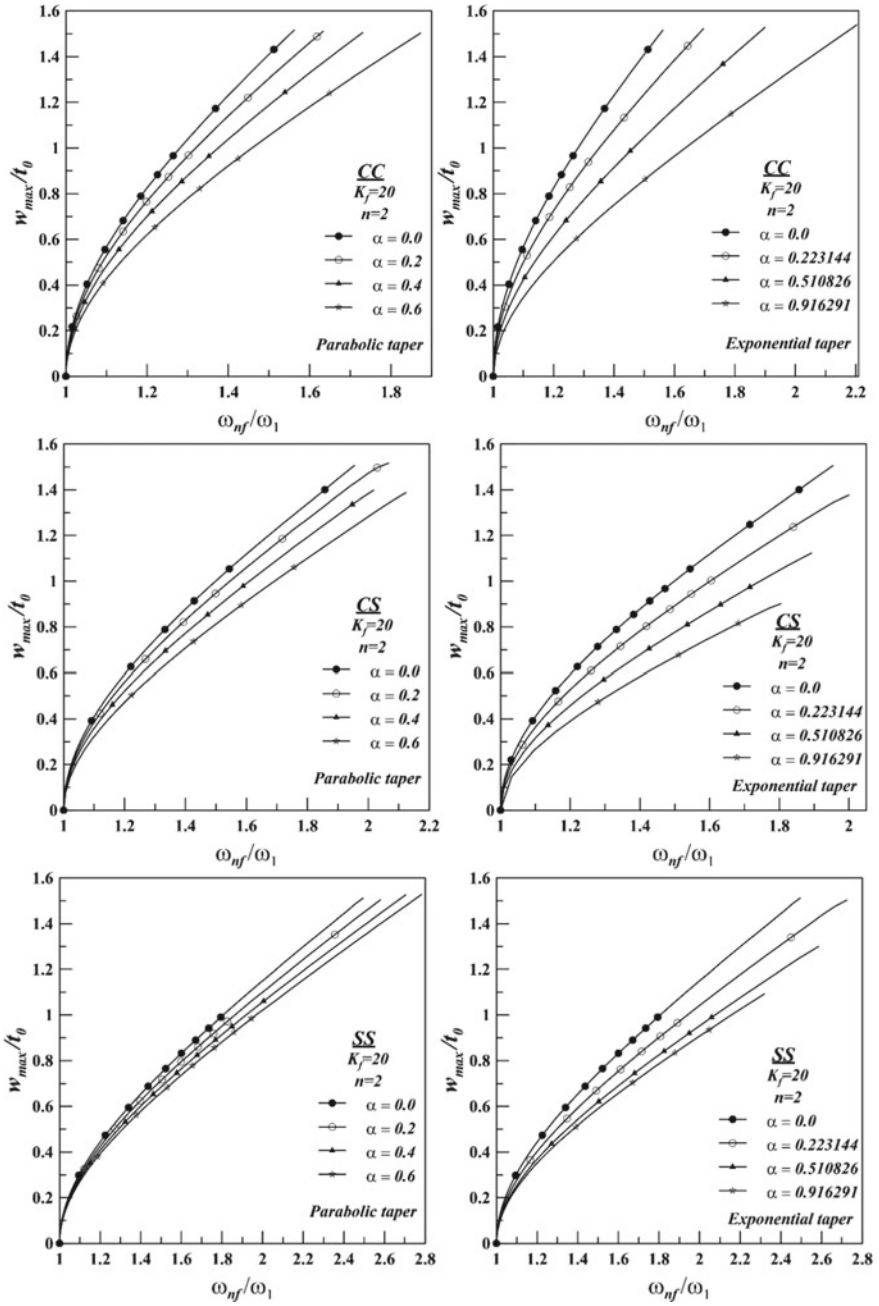

Fig. 6 Effect of taper parameter on backbone curve for different boundary conditions and taper pattern

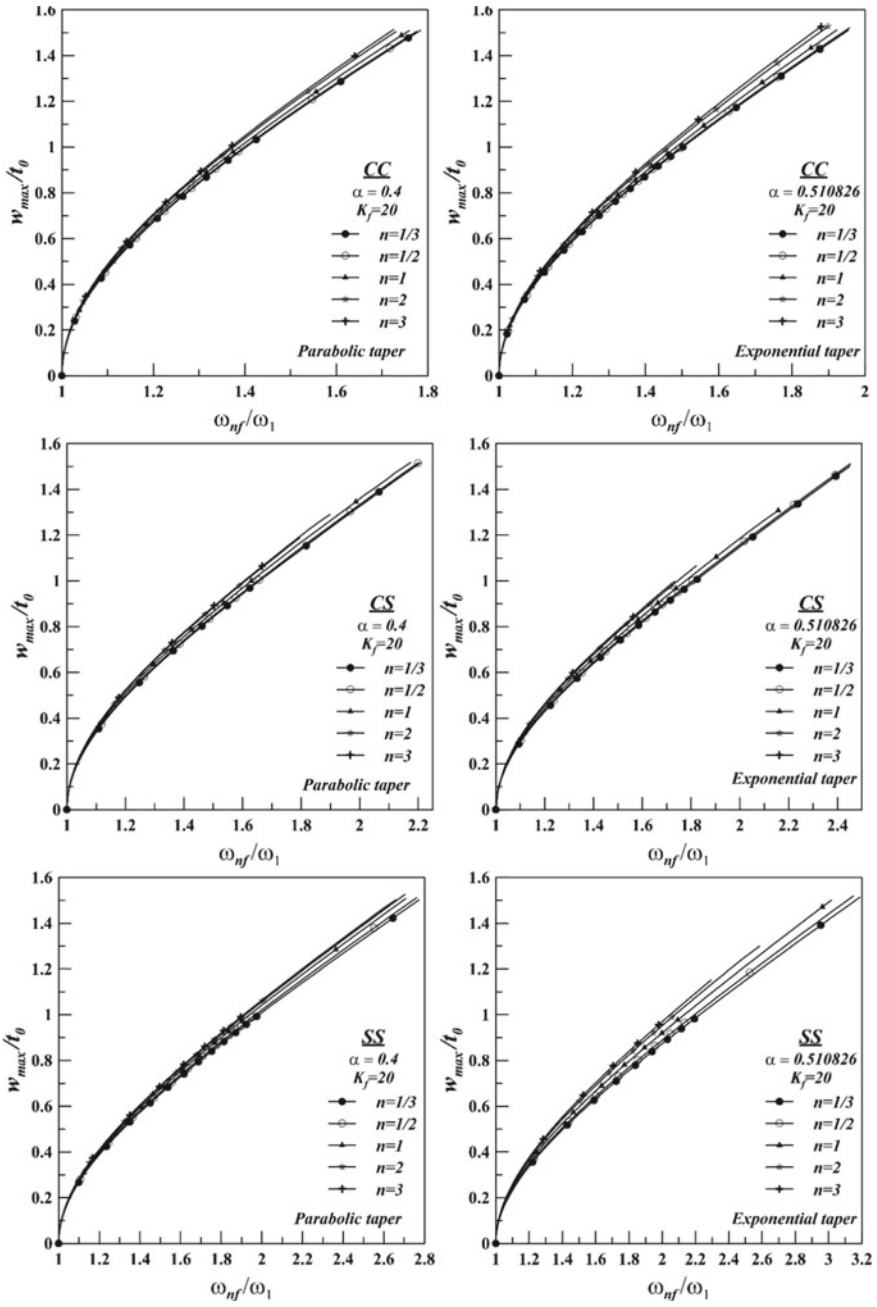

Fig. 7 Effect of gradation parameter on backbone curve for different boundary conditions and taper pattern

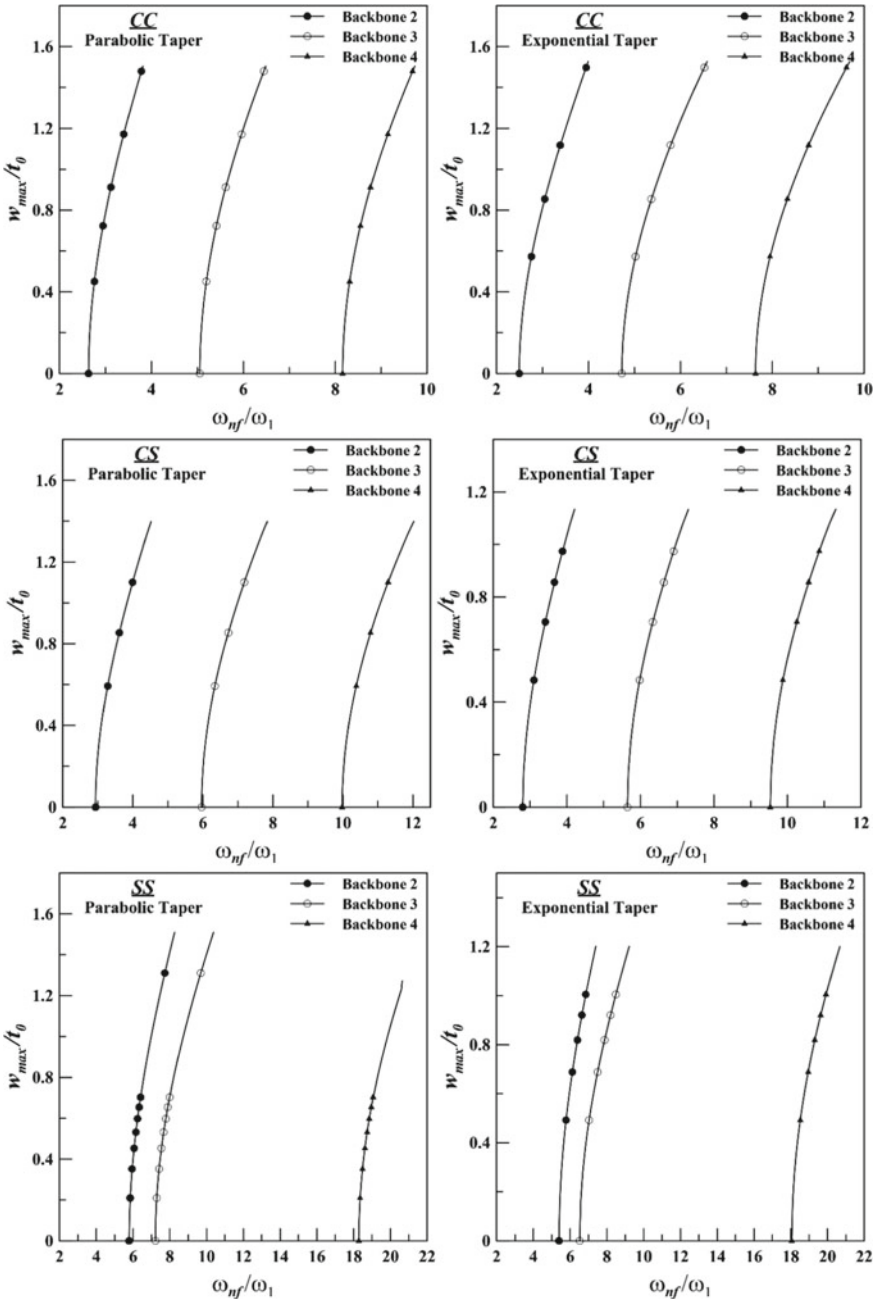

Fig. 8 Higher mode backbone curves for different boundary conditions and taper pattern

3.3 Mode Shape

Degree of nonlinearity in the dynamic system can be obtained by plotting mode shape diagram. First three mode shapes of the parabolic and exponential taper AFG beam corresponding to three different boundary conditions are presented in Fig. 9. Mode shapes of the vibrating system are influenced by the amplitude of vibration. To investigate this phenomenon for the present system, for each of the vibration modes linear ($w_{\max}/t_0 = 0$) and nonlinear ($w_{\max}/t_0 = 1.5$) shape plots are obtained. In the plots, maximum deflection is utilized to normalize the vibration amplitude in all the cases. Prominent difference between the linear and nonlinear mode shapes is observed as the boundary condition goes from CC to SS. This occurrence is perhaps indicative of decreasing rigidity for SS boundary. However, no noticeable change is identified in the mode shapes for the different taper pattern.

3.4 Frequency Response Plot

Frequency response plots for forced vibration analysis are generated considering the combined effects of excitation amplitudes, foundation stiffness, taper parameters, and gradation parameters in a non-dimensional frequency-amplitude plane. Dimensionless excitation frequency (ω_f/ω_1) and dimensionless response amplitude ($w_{\max}/t_0$) are considered as the independent and dependent axes of the plane. Fundamental natural frequencies (ω_1) which are tabulated previously are used to normalize the excitation frequency (ω_f), whereas for maximum deflection ($w_{\max}$), beam root thickness (t_0) is utilized to normalize it. To detect the effects with more accuracy, separate plots for the relevant boundary conditions (CC, CS and SS) and taper patterns (parabolic and exponential) are generated.

The frequency response plots are generated by performing two different frequency sweeps at a constant value of excitation frequency. First one is a forward sweep which is initiated at zero excitation frequency and gradually increased towards resonance. And another one is the backward sweep which is initiated at a finite high of excitation frequency and gradually decreasing towards the reverse direction. Hence, generated frequency response curves show two distinct zones. In the first zone, with increase in forcing frequency, the response amplitude increases, while, in the other one, it decreases. Multi-response zone, characterized by more than one response amplitudes at a fixed excitation frequency, is also observed. This multi-response zone is a typical nonlinear phenomenon. Another characteristic, where the nonlinearity of the system is exhibited, is the tilting of the response curves towards the right of the vertical and it is observed in all the cases. Such hardening-type behaviour is caused by the additional stiffening of the system due to stretching effect.

Figure 10 presents the influence of amplitude of excitation on frequency response. Total six plots are obtained considering CC, CS, and SS boundaries and parabolic ($\alpha = 0.4$) and exponential ($\alpha = 0.510826$) taper patterns for each of the boundaries.

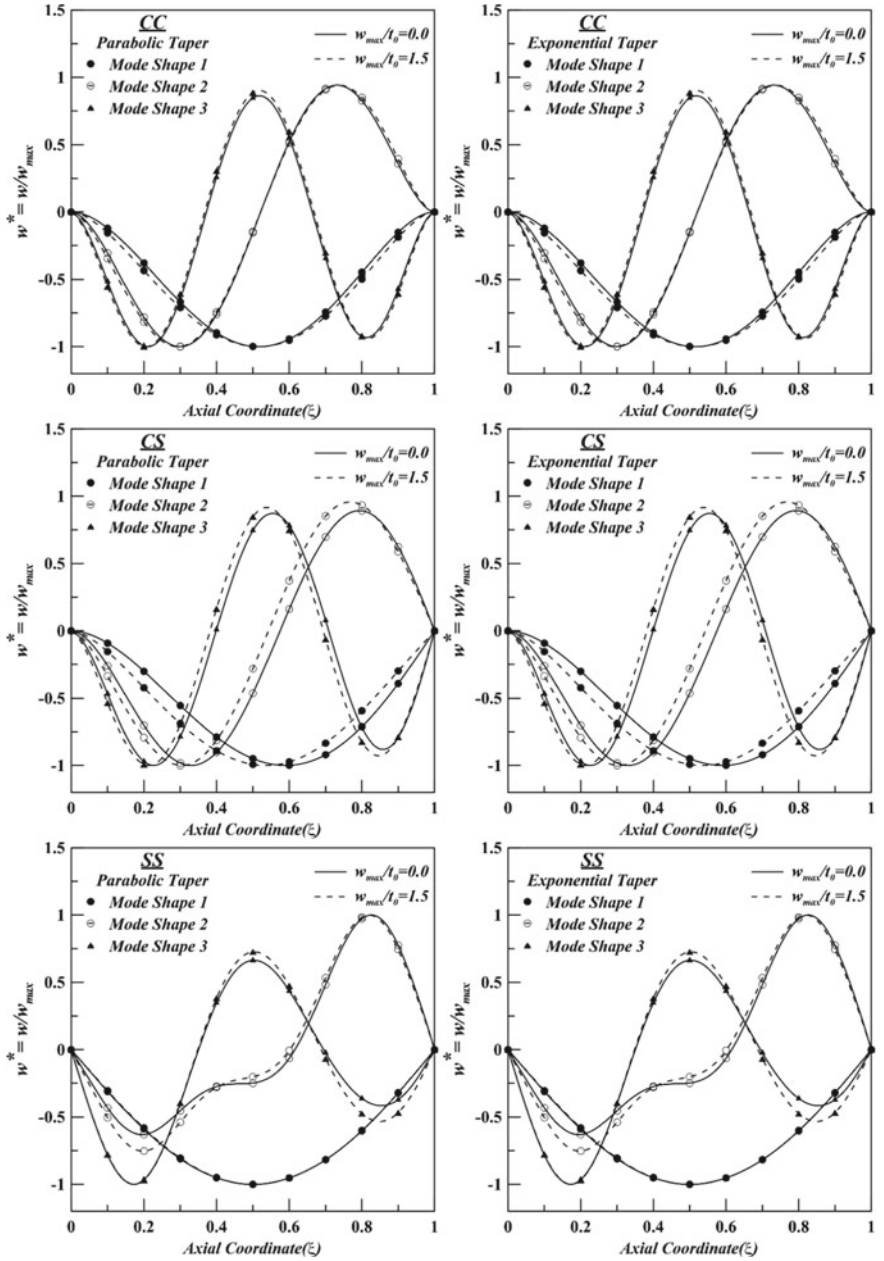

Fig. 9 First three linear and nonlinear mode shapes for different boundary conditions and taper pattern

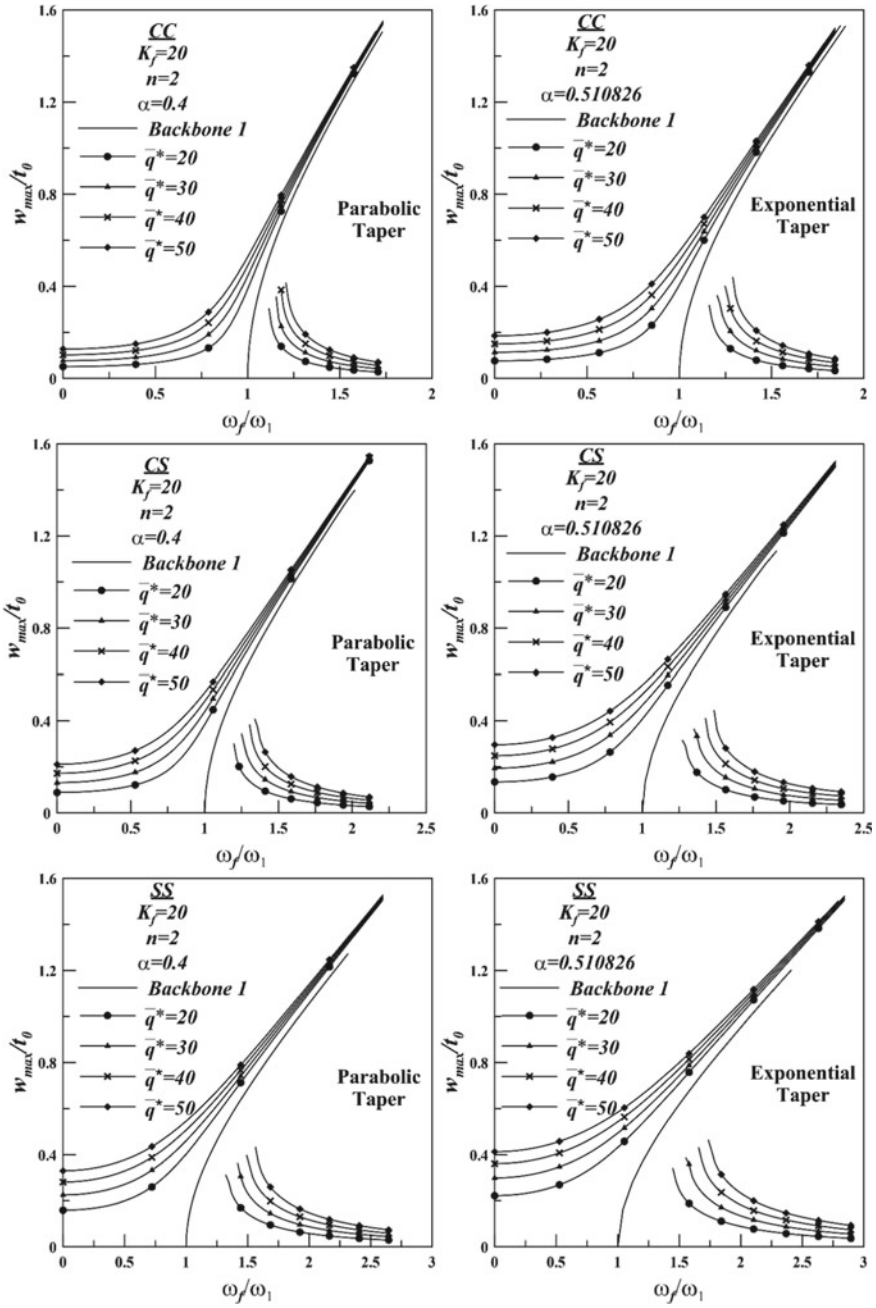

Fig. 10 Effect of excitation amplitude on frequency for different boundary conditions and taper pattern

Foundation stiffness is kept constant at 10, while, axial gradation is controlled by a parameter value of 2. Non-dimensional excitation amplitude is varied from 20 to 50 with equal intervals to generate four response curves. Backbone curves of the system are also included in the figures for completeness. From the figure, it is evident that response amplitude is lowest for CC beams, whereas it is highest for SS beams, at a given excitation frequency. The figures also confirm that response amplitude decreases with decrease of excitation amplitude. It leads to another observation that at zero value of excitation amplitude, the frequency response curve coincides with the backbone curve.

Figure 11 presents the plots depicting influence of foundation stiffness on response of the system. To generate these plots, excitation amplitude value is taken as 40 and gradient parameter is kept constant at 2. Same values of taper parameter as the previous scenario are retained for the parabolic (0.4) and exponential (0.510826) profiles.

In all the plots, frequency response curves corresponding to different spring stiffness (0 to 60 in steps of 20) are depicted. Foundation stiffness value '0' represents beam without foundation. The figures show that for all the cases, in the low forcing frequency range response amplitude decreases with rise in foundation stiffness. However, a reverse trend is seen in the higher frequency range. Around $\omega_f/\omega_1 = 1.00$ in each case, cross-over point in response curves appear. It is also observed that the response curves of CC beam are closely clustered as compared to other two boundaries.

Effect of taper parameter on system response is shown in Fig. 12 for different boundaries and different taper patterns. The gradient parameter, excitation amplitude, and foundation stiffness have been fixed at 2, 40, and 20, respectively. The taper parameter is varied from 0.0 to 0.916291 for exponential taper whereas for parabolic taper, it is varied from 0 to 0.6. Taper parameter 0 indicates uniform beam. It is clear from the figures that, with increase in taper parameter, response amplitude increases up to a certain frequency and after that the trend is reversed.

Figure 13 shows the influence of gradation parameter on system response. To generate these results, all other parameters are help at a constant value, while five different values of gradation parameters are considered between 1/3 and 3. The values of the other parameters are as follows: excitation amplitude—40, foundation stiffness—20, and taper parameter of 0.4 for parabolic profile and 0.510826 for exponential profile. Figures show that in all cases as the gradation parameter increases, there is increase in response amplitude.

4 Conclusion

A tapered AFG Timoshenko beam on elastic foundation under pre-loaded condition is analyzed. Three different boundary conditions (combinations of clamped and simply supported edges) are included in the present study. The elastic foundation, in the present study, is idealized as a set of parallel linear spring of constant stiffness and

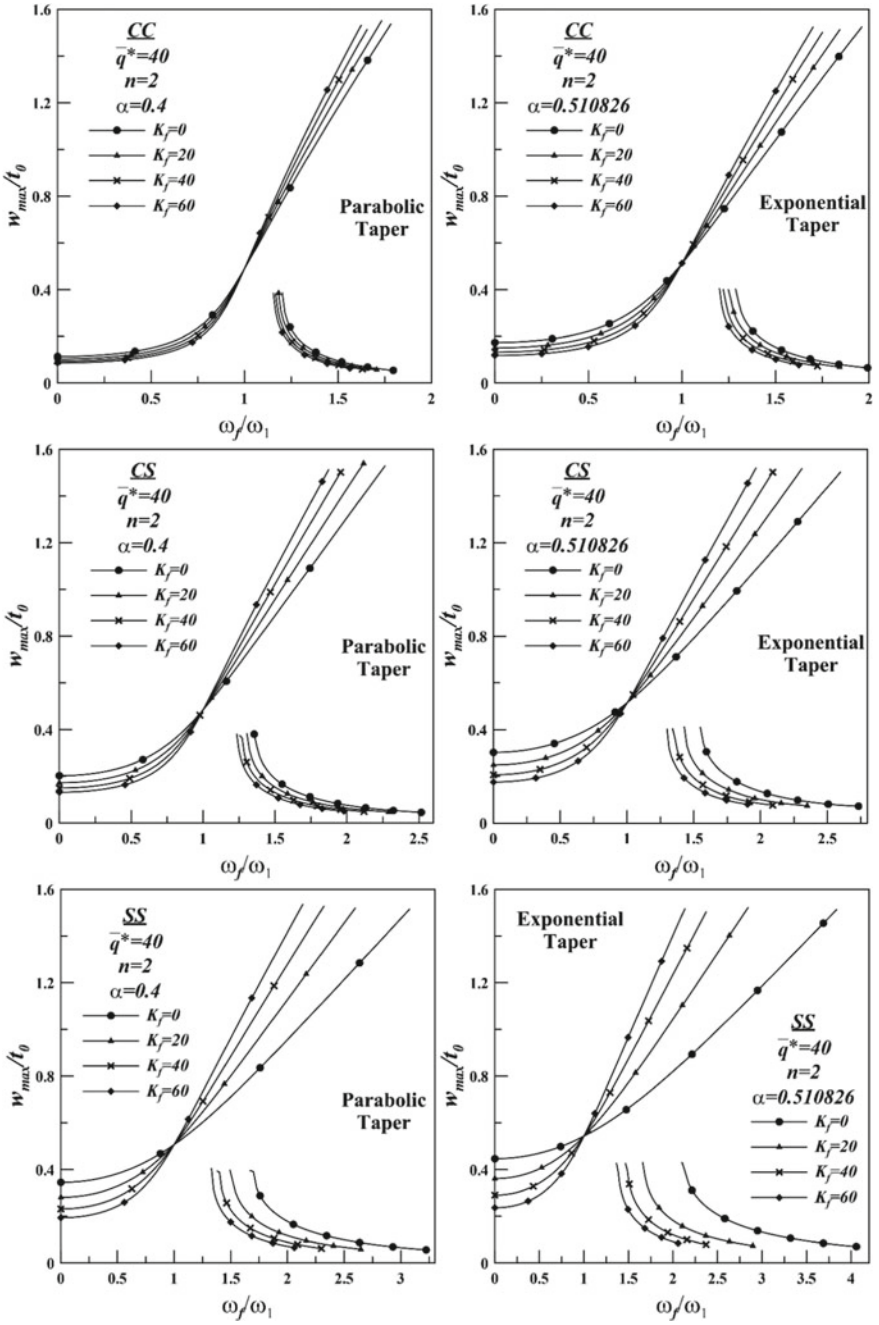

Fig. 11 Effect of foundation stiffness on frequency for different boundary conditions and taper pattern

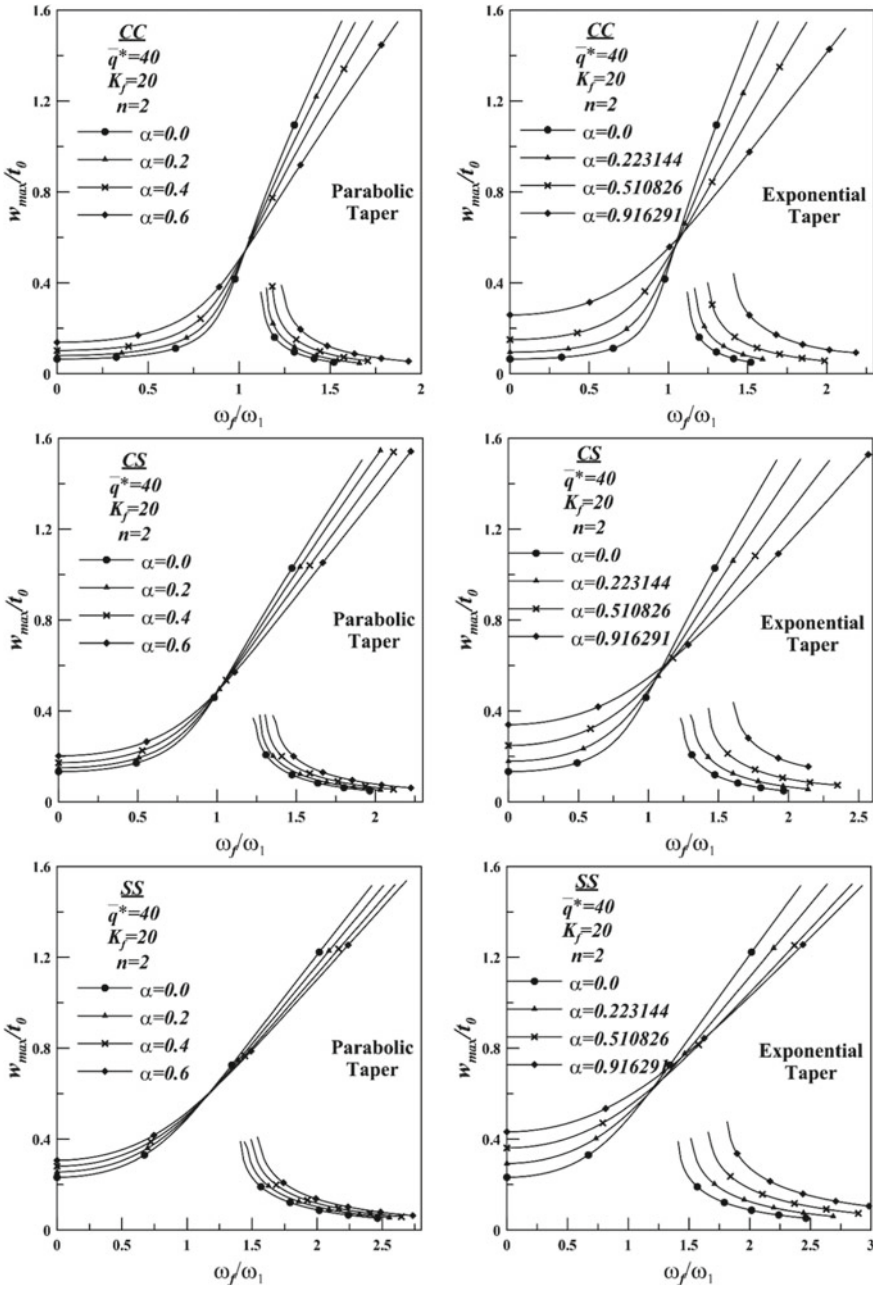

Fig. 12 Effect of taper parameter on frequency for different boundary conditions and taper pattern

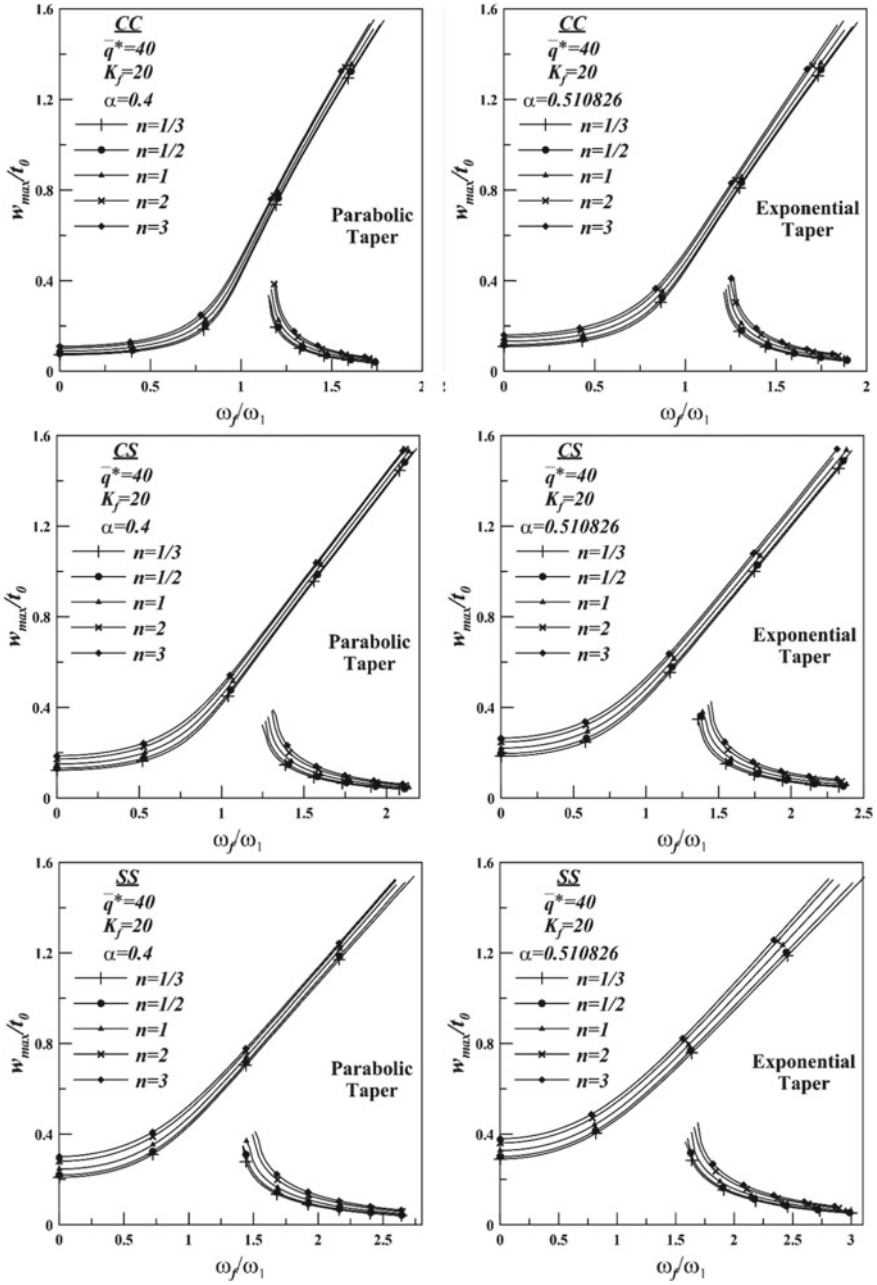

Fig. 13 Effect of gradation parameter on frequency for different boundary conditions and taper pattern

various values of the foundation stiffness are considered. The primary objective for free vibration study is to find out the effect of loading on the vibration frequencies of the system, whereas for forced vibration analysis, it is to represent the frequency response under harmonic excitation. The mathematical formulation for free vibration study is such that it sub-divides the problem into two distinct parts. At the initial stage, the geometrically nonlinear static problem is solved through a numerical scheme with relaxation. Next, the free vibration problem is formulated as an eigenvalue analysis with statically converged stiffness matrix as an input. Subsequently, forced vibration is taken into account by considering dynamic displacement field and solved using Broyden's method (quasi-Newton method). These problems are formulated using appropriate energy principles. The static analysis is based on total minimum potential energy principle, while the dynamic analyses are based on Hamilton's principle. The overall formulation and solution technique are general in nature and have enough flexibility to be adopted for other type of end conditions, gradation patterns, elastic foundations, taper patterns, and loading patterns. Results generated from the present method are compared with previously published results and a certain degree of accuracy is observed between the two sets of results. Overall, the present methodology and solution procedure are successfully validated, albeit for a system with reduced complexity (as the elastic foundation is not present in the validation problem). New results are furnished for an AFG Timoshenko beam in the normalized loaded natural frequency vs. normalized maximum deflection of the system for free vibration analysis and frequency response curve for forced vibration problem. These results are capable of serving as benchmark results.

Appendix

The elements of the stiffness matrix $[K_{ij}]$ are:

$$\left[K_{ij}\right]_{\substack{i=1,nw \\ j=1,nw}} = \frac{b}{2}\int_0^L \left(\sum_{k=1}^{nw} d_k \frac{d\phi_k}{dx}\right)^2 \frac{d\phi_i}{dx}\frac{d\phi_j}{dx} t(x)E(x)dx + b\int_0^L \left(\sum_{k=nw+1}^{nw+nu} d_k \frac{d\alpha_{k-nw}}{dx}\right)\frac{d\phi_i}{dx}\frac{d\phi_j}{dx} t(x)E(x)dx + k_{sh}b\int_0^L \frac{d\phi_i}{dx}\frac{d\phi_j}{dx} t(x)G(x)dx$$

$$\left[K_{ij}\right]_{\substack{i=1,nw \\ j=nw+1,nw+nu}} = 0$$

$$\left[K_{ij}\right]_{\substack{i=1,nw \\ j=nw+nu+1,nw+nu+nsi}} = -k_{sh}b\int_0^L \frac{d\phi_i}{dx}\beta_{j-nw-nu}t(x)G(x)dx$$

$$\left[K_{ij}\right]_{\substack{i=nw+1,nw+nu \\ j=1,nw}} = \frac{b}{2}\int_0^L \left(\sum_{k=1}^{nw} d_k \frac{d\phi_k}{dx}\right)\frac{d\alpha_{i-nw}}{dx}\frac{d\phi_j}{dx}t(x)E(x)dx$$

$$\left[K_{ij}\right]_{\substack{i=nw+1,nw+nu \\ j=nw+1,nw+nu}} = b\int_0^L \frac{d\alpha_{i-nw}}{dx}\frac{d\alpha_{j-nw}}{dx}t(x)E(x)dx$$

$$\left[K_{ij}\right]_{\substack{i=nw+1,nw+nu \\ j=nw+nu+1,nw+nu+nsi}} = 0$$

$$\left[K_{ij}\right]_{\substack{i=nw+nu+1,nw+nu+nsi \\ j=1,nw}} = -k_{sh}b\int_0^L \beta_{i-nw-nu}\frac{d\phi_j}{dx}t(x)G(x)dx$$

$$\left[K_{ij}\right]_{\substack{i=nw+nu+1,nw+nu+nsi \\ j=nw+1,nw+nu}} = 0$$

$$\left[K_{ij}\right]_{\substack{i=nw+nu+1,nw+nu+nsi \\ j=nw+nu+1,nw+nu+nsi}} = \frac{b}{12}\int_0^L \frac{d\beta_{i-nw-nu}}{dx}\frac{d\beta_{j-nw-nu}}{dx}t^3(x)E(x)dx + k_{sh}b\int_0^L \beta_{i-nw-nu}\beta_{j-nw-nu}t(x)G(x)dx$$

The elements of the mass matrix $[M_{ij}]$ are,

$$\left[M_{ij}\right]_{\substack{i=1,nw \\ j=1,nw}} = b\int_0^L \phi_i\phi_j t(x)\rho(x)dx$$

$$\left[M_{ij}\right]_{\substack{i=nw+1,nw+nu \\ j=nw+1,nw+nu}} = b\int_0^L \alpha_{i-nw}\alpha_{j-nw}t(x)\rho(x)dx$$

$$\left[M_{ij}\right]_{\substack{i=nw+nu+1,nw+nu+nsi \\ j=nw+nu+1,nw+nu+nsi}} = \frac{b}{12}\int_0^L \beta_{i-nw-nu}\beta_{j-nw-nu}t^3(x)\rho(x)dx$$

Rest all other elements of the mass matrix $[M_{ij}]$ are zero.
The elements of the load vector $\{f_i\}$ are,

$$\{f_i\}_{i=1,nw} = q \int_0^L \phi_i dx$$

$$\{f_i\}_{i=nw+1,nw+nu} = 0$$

$$\{f_i\}_{i=nw+nu+1,nw+nu+nsi} = 0$$

References

1. Akgöz B, Civalek Ö (2013) Free Vibration analysis of axially functionally graded tapered Bernoulli-Euler microbeams based on the modified couple stress theory. Compos Struct 98:314–322
2. Ansari R, Gholami R, Shojaei MF, Mohammadi V, Sahmani S (2013) Size-dependent bending, buckling and free vibration of functionally graded Timoshenko microbeams based on the most general strain gradient theory. Compos Struct 100:385–397
3. Arefi M, Zenkour AM (2017a) Wave propagation analysis of a functionally graded magneto-electro-elastic nanobeam rest on Visco-Pasternak foundation. Mech Res Commun 79:51–62
4. Arefi M, Zenkour AM (2017b) Analysis of wave propagation in a functionally graded nanobeam resting on visco-Pasternak's foundation. Theoretical & Applied Mechanics Letters 7:145–151
5. Calim FF (2016a) Free and forced vibration analysis of axially functionally graded Timoshenko beams on two-parameter viscoelastic foundation. Compos B 103:98–112
6. Calim FF (2016b) Transient analysis of axially functionally graded Timoshenko beams with variable cross-section. Compos B 98:472–483
7. Chen DQ, Sun DL, Li XF (2017) Surface effects on resonance frequencies of axially functionally graded Timoshenko nanocantilevers with attached nanoparticle. Compos Struct 173:116–126
8. Deng H, Chen KD, Cheng W, Zhao SG (2017) Vibration and buckling analysis of double-functionally graded Timoshenko beam system on Winkler-Pasternak elastic foundation. Compos Struct 160:152–168
9. Esfahani SE, Kiani Y, Eslami MR (2013) Non-linear thermal stability analysis of temperature dependent FGM beams supported on non-linear hardening elastic foundations. Int J Mech Sci 69:10–20
10. Ghayesh MH (2018) Nonlinear vibrations of axially functionally graded Timoshenko tapered beams. J Comput Nonlinear Dyn 13:1–10
11. Ghayesh MH, Farokhi H (2018) Bending and vibration analyses of coupled axially functionally graded tapered beams. Nonlinear Dyn 91:17–28
12. Huang Y, Luo QZ (2011) A simple method to determine the critical buckling loads for axially inhomogeneous beams with elastic restraint. Comput Math Appl 61:2510–2517
13. Huang Y, Wang T, Zhao Y, Wang P (2018) Effect of axially functionally graded material on whirling frequencies and critical speeds of a spinning Timoshenko beam. Compos Struct 192:355–367
14. Huang, Y., Yang, L. E., & Luo, Q. Z. (2013). Free vibration of axially functionally graded Timoshenko beams with non-uniform cross-section. *Composites: Part B*, 45, 1493–1498.
15. Huang Y, Zhang M, Rong H (2016) Buckling analysis of axially functionally graded and non-uniform beams based on Timoshenko Theory. Acta Mech Solida Sin 29(2):200–207
16. Ke LL, Wang YS, Yang J, Kitipornchai S (2012) Nonlinear free vibration of size-dependent functionally graded microbeams. Int J Eng Sci 50:256–267

17. Ke LL, Yang J, Kitipornchai S (2010) An analytical study on the nonlinear vibration of functionally graded beams. Meccanica 45:743–752
18. Khalili SMR, Jafari AA, Eftekhari SA (2010) A Mixed Ritz-DQ method for forced vibration of functionally graded beams carrying moving loads. Compos Struct 92:2497–2511
19. Komijani M, Esfahani SE, Reddy JN, Liu YP, Eslami MR (2014) Nonlinear thermal stability and vibration of pre/post-buckled temperature- and microstructure-dependent functionally graded beams resting on elastic foundation. Compos Struct 112:292–307
20. Kumar S, Mitra A, Roy H (2015) Geometrically nonlinear free vibration analysis of axially functionally graded taper beams. Engineering Science and Technology, an International Journal 18:579–593
21. Lezgy-Nazargah M (2015) Fully coupled thermo-mechanical analysis of bi-directional FGM beams using NURBS isogeometric finite element approach. Aerosp Sci Technol 45:154–164
22. Li XF, Kang YA, Wu JX (2013) Exact frequency equations of free vibration of exponentially functionally graded beams. Appl Acoust 74:413–420
23. Lohar H, Mitra A, Sahoo S (2016a) Geometric nonlinear free vibration of axially functionally graded non-uniform beams supported on elastic foundation. Curved and Layered Structures 3(1):223–239
24. Lohar H, Mitra A, Sahoo S (2016b) Natural frequency and mode shapes of exponential tapered AFG beams on elastic foundation. International Frontier Science Letters 9:9–25
25. Lohar H, Mitra A, Sahoo S (2018a) Free vibration of initially deflected axially functionally graded non-uniform Timoshenko beams on elastic foundation. Romanian Journal of Acoustics and Vibration 15(2):75–89
26. Lohar H, Mitra A, Sahoo S (2018b) Geometrically non-linear frequency response of axially functionally graded beams resting on elastic foundation under harmonic excitation. International Journal of Manufacturing, Materials, and Mechanical Engineering 8(3):23–43
27. Lohar H, Mitra A, Sahoo S (2019) Nonlinear response of axially functionally graded Timoshenko beams on elastic foundation under harmonic excitation. Curved and Layered Structures 6:90–104
28. Mohanty SC, Dash RR, Rout T (2011) Parametric instability of a functionally graded Timoshenko beam on Winkler's elastic foundation. Nucl Eng Des 241:2698–2715
29. Nakamura T, Wang T, Sampath S (2000) Determination of properties of graded materials by inverse analysis and instrumented indentation. Acta Mater 48:1444–1450
30. Nguyen DK, Nguyen QH, Tran TT, Bui VT (2017) Vibration of bi-dimensional functionally graded Timoshenko beams excited by a moving load. Acta Mech 228:141–155
31. Paul A, Das D (2016) Free vibration analysis of pre-stressed FGM Timoshenko beams under large transverse deflection by a variational method. Engineering Science and Technology, an International Journal 19:1003–1017
32. Press WH, Teukolsky SA, Vetterling WT, Flannery BP (2005) Numerical recipes in Fortran 77 (2nd ed.) Cambridge USA: Press Syndicate
33. Pydah A, Sabale A (2017) Static analysis of bi-directional functionally graded curved beams. Compos Struct 160:867–876
34. Rajasekaran S (2013) Free vibration of centrifugally stiffened axially functionally graded tapered Timoshenko beams using differential transformation and quadrature methods. Appl Math Model 37:4440–4463
35. Rajasekaran, S., & Khaniki, H. B. (2018). Finite element static and dynamic analysis of axially functionally graded nonuniform small-scale beams based on nonlocal strain gradient theory. *Mechanics of Advanced Materials and Structures*, 0, 1–15.
36. Sarkar, K., & Ganguli, R. (2014). Closed-form solutions for axially functionally graded Timoshenko beams having uniform cross-section and fixed–fixed boundary condition. *Composites: Part B*, 58, 361–370.
37. Shafiei N, Kazemi M, Ghadiri M (2016) Comparison of modelling of the rotating tapered axially functionally graded Timoshenko and Euler-Bernoulli microbeams. Physica E 83:74–87
38. Shahba A, Rajasekaran S (2012) Free vibration and stability of tapered Euler-Bernoulli beams made of axially functionally graded materials. Appl Math Model 36:3094–3111

39. Shahba A, Attarnejad R, Hajilar S (2011) Free vibration and stability of axially functionally graded tapered Euler-Bernoulli beams. Shock and Vibration 18:683–696
40. Shahba A, Attarnejad R, Marvi MT, Hajilar S (2011) Free vibration and stability analysis of axially functionally graded tapered Timoshenko beams with classical and non-classical boundary conditions. Composites: Part B 42:801–808
41. Simsek M (2010) Vibration analysis of a functionally graded beam under a moving mass by using different beam theories. Compos Struct 92:904–917
42. Simsek M (2016) Buckling of Timoshenko Beams composed of two-dimensional functionally graded material (2D-FGM) having different boundary conditions. Compos Struct 149:304–314
43. Sınıra S, Çevik M, Sınır BG (2018) Nonlinear free and forced vibration analyses of axially functionally graded Euler-Bernoulli beams with non-uniform cross-section. Compos B 148:123–131
44. Tossapanon P, Wattanasakulpong N (2016) Stability and free vibration of functionally graded sandwich beams resting on two-parameter elastic foundation. Compos Struct 142:215–225
45. Yan T, Kitipornchai S, Yang J, He XQ (2011) Dynamic behaviour of edge-cracked shear deformable functionally graded beams on an elastic foundation under a moving load. Compos Struct 93:2992–3001
46. Yas MH, Samadi N (2012) Free vibrations and buckling analysis of carbon nanotube-reinforced composite Timoshenko beams on elastic foundation. Int J Press Vessels Pip 98:119–128
47. Zeighampour H, Beni YT (2015) Free vibration analysis of axially functionally graded nanobeam with radius varies along the length based on strain gradient theory. Appl Math Model 39:5354–5369
48. Zhao L, Zhu J, Wen XD (2016) Exact analysis of bi-directional functionally graded beams with arbitrary boundary conditions via the symplectic approach. Structural Engineering and Mechanics 59(1):101–122

Chapter 11
Dynamic Sensitivity Analysis of Random Impact Behaviour of Hybrid Cylindrical Shells

Vaishali, Ravi Ranjan Kumar, and Sudip Dey

1 Introduction

Sandwich structures are advance structures mainly consisting of two facesheets (i.e. upper and lower facesheet) and middle core. The facesheets are generally made up of thin laminated composites having high strength. These facesheets are responsible for providing high strength and stiffness to structures, while the middle core is constructed of low-density material responsible for low weight of the structure. Because of these exclusive properties, they have wide range of applications like in aerospace, civil construction, marine and automobile industries. Apart from high structural strength and low weight, these structures are highly recommended for optimal design, which is nowadays most desirable feature. But these structures have some shortcomings like low temperature and corrosion resistance because of which delamination occurs. So for minimizing these shortcomings, the laminated composite facesheet can be replaced by the functionally graded facesheet (FGF). Functionally graded (FG) materials are inhomogeneous advance composite materials, generally metal and ceramic mixture. The construction is in such a way that one surface will be metal rich providing high strength and stiffness while the other surface will be ceramic rich providing high temperature and corrosion resistance [20] and throughout the thickness these metals and ceramics are distributed following various laws like power law, exponent law and sigmoid law. The final properties obtained in these FGMs are totally different from the parent materials [46]. By combining the sandwich structure with the FG structure, the outcome structure known as hybrid sandwich FG structure is obtained. These are new and improved structures having exclusive

Vaishali (✉) · S. Dey
National Institute of Technology Silchar, Silchar, India
e-mail: vaishali765@gmail.com

R. R. Kumar
Jawaharlal Nehru University, New Delhi, India

S. Sahoo (ed.), *Recent Advances in Layered Materials and Structures*,
Materials Horizons: From Nature to Nanomaterials,
https://doi.org/10.1007/978-981-33-4550-8_11

properties such as high temperature resistant, corrosion resistant, low weighted and at the same time not compromising with the strength and stiffness. In real life, various kinds of uncertainty such as manufacturing, geometric, material, operational and environmental exist. During manufacturing of these hybrid structures, some kinds of unavoidable uncertainties like (uncertainty in material property) are always present. So, designing and analysing these hybrid structures is quite difficult than that of conventional materials, because the variation of materials and geometrical properties of conventional materials from the nominal value is little or well known. But for safe and economical design of these hybrid FG-sandwich structures, it is very necessary to consider these uncertainties [10, 11, 16, 64–66]. Probabilistic approaches for predicting uncertainty-based dynamic responses in case of complex structures like composite plates and shells have gained extreme attention from the researchers [9, 17, 51, 52]. Uncertainty in the field of dynamic stability of composites was studied [15, 26–31]. Furthermore, study on composites considering various service conditions and analysing uncertainty effect was done [12, 54]; after that, the cut-out effect was studied [14]. Various works considering sandwich structure have gained immense popularity [13, 26, 28, 35, 37, 39–41, 48–50, 53]. However, the work in the field of hybrid is yet to be covered.

2 Background

The pioneering work on FGM [58] is conducted by Japanese scientist (1984) promoting it as thermal barrier coating. A large number of research work have been carried out on FGM [22–24, 43, 44] subsequently. Due to vast application range of FGM, it is very important to perform the static and dynamic analysis. A plenty of research has been conducted to determine the impact analysis of FGM, sandwich and composites. For attaining more superior properties, FGM core was introduced in sandwich structures which eliminated the chance of deformation. Because of the wide range of application of these structures, it is necessary to investigate the static and dynamic behaviour of these hybrid FG-sandwich structures for attaining a reliable structure. For achieving accuracy, a proper and accurate computational method should be adopted. For performing static and dynamic analysis of these hybrid FG-sandwich structures, various computational models have been developed by various researchers. The different plate theories are employed for static response of the FG-sandwich plate exposed to sinusoidal load [68]. Furthermore, for natural frequency analysis and for buckling load analysis on a simply supported hybrid FG-sandwich plate, sinusoidal shear deformation plate theory was used [69]. Application of thermo-mechanical load on sandwich structure whose core may or may not be made up of FG materials was studied [8]. Later unified shear deformation theory was developed which was used for analysing thermo-elastic bending in case of FG-sandwich plate [70]. A free vibration analysis using Ritz method for a simply supported hybrid FG-sandwich plate having rectangular geometry was studied [42]. A static analysis using three dimensional solutions for hybrid sandwich structure

having FG core was proposed [32]. The result shows that by using FG material for core, the discontinuity of the in-plane normal stress across the facesheet and core interface is minimized and also there is a reduction in the magnitude of stresses in the facesheets and deflection of the panel. Later on, use of advanced equivalent single layer and layer-wise models having expansion up to fourth order was done for static analysis of these hybrid structures [4]. According to the result, it is observed that advance computational methods are essentially required for analysing these hybrid FG-sandwich structures and it was also confirmed that these hybrid FG-sandwich structures are better than the conventional sandwich structures or conventional FGM structures. Under the influence of mechanical and thermal loads, the bending analysis on hybrid FG-sandwich plates was also studied [71, 72]. Later on, refined shear displacement models were used for carrying out the deflection and stress analysis in case of these hybrid FG-sandwich plate structures [47]. This shear displacement model showed consistent parabolic variation of shear stress in transverse direction without considering shear correction factor. The effect of thickness in functionally graded structures having various geometries like plates and shells using Carrera's unified formulation was studied [5]. After that, variable refined theories were used for analysing the thermo-elastic bending of hybrid FG-sandwich structures, taking into account parabolic variation of shear stress throughout the thickness [1]. Thereafter, a hyperbolic shear deformation theory was introduced for analysing buckling and natural frequency considering the effect of transverse shear deformation in case of these hybrid FG-sandwich plate structures [18]. Later on, a model of order-n was developed for carrying out natural frequency analysis for these hybrid FG-sandwich plates [67]. However, a suitable refined plate theory was used for carrying out vibration analysis of these FG-based sandwich plates [21]. A plenty of work related to static, buckling and natural frequency analysis of these hybrid FG-sandwich plates were performed using shear deformation theory of higher order [55–57]. An improved higher-order plate theory was introduced for free vibration of hybrid plates having FG facesheets so as to increase the endurance limit in case of facing varying thermal condition [33].

In recent years, various researches related to the analysis of impact on bare functionally graded structures and similarly on bare sandwich structures have been performed. A dynamic investigation of FG-based aluminium and foam core having varying density throughout the thickness, when subjected to impact loading, was found to have high energy absorption capacity [75]. Later on, a study was conducted for analysing the energy absorption capacity of FG-based polymer foams and it was observed that FG foams show superior properties related to uniform energy absorptions but this was limited to low impact load [7]. A study related to low-velocity impact, considering sandwich beam having multilayer, was conducted analytically, experimentally and numerically. It was observed that with the decrease in number of layers of facesheet and increase in the core strength, there is an increase in load carrying and energy absorption capacity of these sandwich structures [73, 74, 76]. A comparative study of low-velocity impact behaviour of simple sandwich structure and of FG-core-based sandwich was conducted, and it was observed that FG core causes maximum contact force and maximum strain compared to simple sandwich

structure [19]. Similarly, the low-velocity impact behaviour of sandwich structure with three-layer grading in core was conducted and it was observed that the grading in core increases the performance of structure [77]. In addition to it, some more studies were conducted for finding the efficient way for increasing the impact performance and for minimizing the damage caused by these impact loads [2]. From the earlier discussions, it can be concluded that a lot of works show that by adding FGM core to the sandwich structure, its performance becomes superior but some contradictory findings are also present in some of the literatures. For example, a study was conducted on FG core-based sandwich panel and it showed that these FG-based sandwiches had inferior performance as compared to those of ungraded cores [25].

It is observed that the impact behaviour of hybrid FG-sandwich structures has not been completely illustrated. Furthermore, instead of grading core, studies can also be conducted by replacing the facesheet material with FG materials. It is also observed that most of the work follows deterministic approach; very little study is conducted using uncertainty approach. These uncertainty approach should be taken into account while dealing with practical problems so as to minimizing the chances of structure failure making it reliable and safe.

3 Governing Equations

In the current chapter, the hybrid FG-sandwich cylindrical shell is subjected to low-velocity impact loads as shown in Fig. 1.

In this chapter, $\overrightarrow{V}_a$ is the volume fraction of an element of materials '*a*', whereas the function indicating material properties of hybrid FG-sandwich structure 'f_{impact}' can be represented as

$$f_{\text{impact}} = \sum_{a=1}^{z} f_a \overrightarrow{V}_a \tag{1}$$

where f_a represents the material property of an element of materials '*a*'. The temperature-dependent material properties of hybrid FG-sandwich structure were proposed [63] and can be expressed as

$$f = f_0 + f_{-1}T^{-1} + 1 + f_1T + f_2T^2 + f_3T^3 \tag{2}$$

where f_0, f_{-1}, f_1, f_2 and f_3 are coefficients of temperature and T represents the temperature in Kelvin.

In hybrid FG-sandwich structures, it is observed that there is a material property variation [45] throughout the depth which is smooth and continuous. These variations can be given by various laws. In this chapter, the effective material property is obtained by using power law as shown below

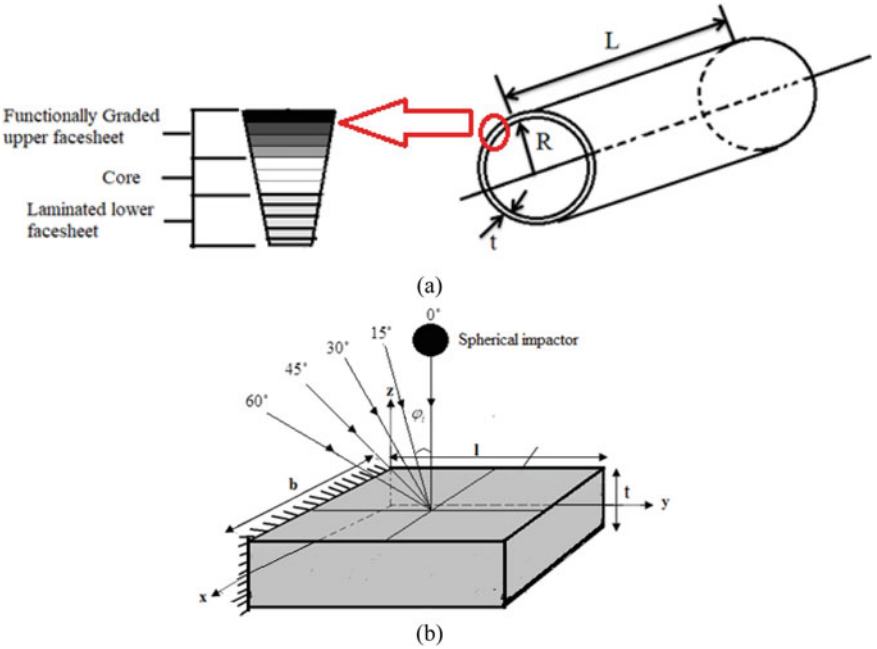

Fig. 1 **a** Hybrid FG-sandwich cylindrical shell structure and **b** impact loading (normal and oblique) on hybrid FG-sandwich plate

$$E(\psi) = E_M + (E_C - E_M)\left[{}^{x}/_{t} + 0.5\right]^n \tag{3}$$

$$\mu(\psi) = \mu_M + (\mu_C - \mu_M)\left[{}^{x}/_{t} + 0.5\right]^n \tag{4}$$

$$\rho(\psi) = \rho_M + (\rho_C - \rho_M)\left[{}^{x}/_{t} + 0.5\right]^n \tag{5}$$

where E represents the elastic modulus, μ represents Poisson's ratio and ρ represents the mass density, while 'C' shows top surface (ceramic rich) and 'M' shows the bottom surface (metal rich) of FG facesheet. 't' denotes the thickness and $x = (t/2)$, while 'n' indicates the power law index. The dynamic equilibrium equation is represented as

$$[M(\psi)]\left\{\ddot{\delta}\right\} + [K(\psi)]\{\delta\} = \left[F_{\text{impact}}\right] \tag{6}$$

where (ψ) represents degree of stochasticity and $\{\delta\}$ represents the displacement, whereas $[M(\psi)]$ represents the mass matrix and $[K(\psi)]$ represents the stiffness matrix.

In the present case, i.e. low-velocity impact condition, the external force $\left[F_{\text{impact}}\right]$ can be expressed as

$$\left[F_{impact}\right] = \left\{0\ 0\ 0\ \ldots\ F_{contact}\ \ldots\ 0\ 0\ 0\right\}^{T} \tag{7}$$

In the present case, as the impact is rigid then the equation can transformed as

$$\mathbf{m_{impact}R_{impact}} + \mathbf{F_{contact}} = \mathbf{0} \tag{8}$$

where m_{impact} represents the mass of the impactor while $\ddot{a}_{\text{impact}}$ represents the impact due to acceleration. In this chapter, the contact law given by Hertzian is used for determining the force exerted by impactor (here spherical geometry is considered). Thus, the contact force (F_{contact}) can be shown as [6]

$$F_{contact} = K\alpha^{1.5}0 < \alpha \leq \alpha_{max} \tag{9}$$

$$K = \frac{16}{3\pi}\frac{1}{K_M + K_{impact}}\sqrt{\frac{d}{\chi}}_{M} \tag{10}$$

where after modification, the contact stiffness is represented by K_M and the maximum indentation is represented by $\alpha_{\text{max.}}$ [60]. α is the local indentation and χ is a constant which is dependent on the structure of target and impactor. The constant d can be shown as

$$\frac{1}{d} = \frac{1}{r_{impactor}} + \frac{1}{r_{shell}} \tag{11}$$

where r_{impactor} and r_{shell} represent the radius of curvature of the impactor and the cylindrical shell. The local indentation ($\alpha(t)$) can be shown as

$$\alpha(t) = d_{impactor}(t)\cos\theta - \delta\left(x_c, y_c, t\right)\cos\varphi \tag{12}$$

where d_{impactor} represents the displacement because of impactor, δ represents the displacement where impact (x_c, y_c) takes place in the z-direction, while θ represents the impact angle and φ represents the twist angle. Globally, the force component can be expressed as

$$F_{impact,x} = 0,\ F_{impact,y} = F_{contact}\sin\varphi,\ F_{impact,z} = F_{contact}\cos\varphi \tag{13}$$

In the present chapter, Newmark's integration method is considered for calculating time-dependent equations [3]. The governing equation (Eq. 14) indicates that transient properties are exhibited by the structure under impact loading,

$$\left\{F_{\text{impact}}\right\}^{t+\Delta t} = \left\{F_{\text{impact}}\right\} + \left\{F_{\text{contact}}\right\}^{t+\Delta t} + \left[M\left(\overline{\Psi}\right)\right]\left(c_0\{\delta\}^t + c_1\{\dot{\delta}\}^t + c_2\{\ \ddot{\delta}\}^t\right) \tag{14}$$

$$w_i = \frac{F_{\text{impact}}^{t+\Delta t}}{M_{(i)}} \tag{15}$$

where $F_{\text{impact}}^{t+\Delta t} = M_{(i)}\left(c_0 w_i^t + c_1 \dot{w}_i^t + c_2 \ddot{w}_i^t\right) - F_{\text{contact}}^t$.

The above equation is an ordinary differential equation (ODE) with constant coefficients, with a time interval of Δt which is discrete in nature. At time interval $t + \Delta t$, we get

$$[\boldsymbol{K}]\{\boldsymbol{\delta}\}^{\boldsymbol{t+\Delta t}} = \left\{\boldsymbol{F}_{\boldsymbol{impact}}\right\}^{\boldsymbol{t+\Delta t}} \tag{16}$$

$$\left[\overline{\boldsymbol{K}}\right]\{\boldsymbol{a}_{\boldsymbol{i}}\}^{\boldsymbol{t+\Delta t}} = \{\boldsymbol{F}_{\boldsymbol{contact}}\}^{\boldsymbol{t+\Delta t}} \tag{17}$$

where $[K]$ and $[\bar{K}]$ are active stiffness matrices for impactor and cylindrical shell, respectively. It can be further expressed as Eqs. (18) and (19)

$$[K] = \left[K\left(\overline{\overline{\Psi}}\right)\right] + [K_\sigma] + c_0\left[M\left(\overline{\overline{\Psi}}\right)\right] \tag{18}$$

$$\left[\overline{\overline{K}}\right] = c_0 m_{(i)} \tag{19}$$

where $\left(\overline{\overline{\Psi}}\right)$ represents the stochasticity present in the function.

The velocity of the impactor and cylindrical shell can be expressed as

$$\left\{\ddot{\delta}\right\}^{t+\Delta t} = c_0\left(\{\delta\}^{t+\Delta t} - \{\delta\}^t\right) - c_1\left\{\dot{\delta}\right\}^t - c_2\left\{\ddot{\delta}\right\}^t \tag{20}$$

$$\left\{\dot{\delta}\right\}^{t+\Delta t} = \left\{\dot{\delta}\right\}^t + c_3\left\{\ddot{\delta}\right\}^t + c_4\left\{\ddot{\delta}\right\}^{t+\Delta t} \tag{21}$$

The acceleration of the impactor and cylindrical shell can be expressed as

$$\ddot{w}_i^{t+\Delta t} = c_0\left(w_i^{t+\Delta t} - w_i^t\right) - c_1\dot{w}_i^t - c_2\ddot{w}_i^t \tag{22}$$

$$\dot{w}_i^{t+\Delta t} = \dot{w}_i^{t\Delta t} + c_3\ddot{w}_i^t + c_4\ddot{w}_i^{t+\Delta t} \tag{23}$$

The initial boundary condition is expressed as

$$\{\delta\} = \left\{\dot{\delta}\right\} = \left\{\ddot{\delta}\right\} = 0 \tag{24}$$

$$w_i = \ddot{w}_i = 0 \text{ and } \dot{w}_i = V \tag{25}$$

The constants can be formulated as follows

$$c_0 = \frac{1}{A\Delta t^2}, c_1 = \frac{1}{A\Delta t}, c_2 = \frac{1}{2A} - 1, c_3 = (1 - B)\Delta t, c_4 = B\Delta t \tag{26}$$

The value of A is taken as 0.5 and B as 0.25. For the FE modelling, an isoparametric element which is quadratic in nature is considered with eight nodes. For every node, there are three translational and two rotational degrees of freedom. The shape function $\overline{S}_i$ for the same can be determined as

$$\overline{S}_i = \frac{1}{4}(1 + \varsigma\varsigma_i)(1 + \varphi\varphi_i)(\varsigma\varsigma_i + \varphi\varphi_i - 1) \quad (\text{for } i = 1, 2, 3, 4) \tag{27}$$

$$\overline{S}_i = \frac{1}{2}\left(1 - \varsigma^2\right)(1 + \varphi\varphi_i) \quad (\text{for } i = 5, 7) \tag{28}$$

$$\overline{S}_i = \frac{1}{2}\left(1 - \varphi^2\right)(1 + \varsigma\varsigma_i) \quad (\text{for } i = 6, 8) \tag{29}$$

where ς and φ signify the local natural coordinates of the element. Here, $\varsigma_i = +1$ for nodes 2, 3 and 6, $\varsigma_i = -1$ for nodes 1, 4 and 8, $\varphi_i = +1$ for nodes 3, 4 and 7 and $\varphi_i = -1$ for nodes 1, 2 and 5. The efficiency of the shape function is determined by Eq. (30)

$$\sum_{i=1}^{8} \overline{\boldsymbol{S}}_i = \mathbf{1}, \sum_{i=1}^{8} \frac{\partial \overline{\boldsymbol{S}}}{\partial \boldsymbol{\varphi}} = \mathbf{0}, \sum_{i=1}^{8} \frac{\partial \overline{\boldsymbol{S}}}{\partial \boldsymbol{\varsigma}} = \mathbf{0} \tag{30}$$

The coordinates (x, y) of any particular point for the eight-noded element are

$$\boldsymbol{x} = \sum_{i=1}^{8} \overline{\boldsymbol{S}}_i \boldsymbol{x}_i, \boldsymbol{y} = \sum_{i=1}^{8} \overline{\boldsymbol{S}}_i \boldsymbol{y}_i \tag{31}$$

The relation between the nodal degree of freedom and displacement with respect to the coordinates (ς, φ) can be derived as

$$\boldsymbol{u} = \sum_{i=1}^{8} \overline{\boldsymbol{S}}_i \boldsymbol{u}_i, = \sum_{i=1}^{8} \overline{\boldsymbol{S}}_i \boldsymbol{v}_i, \boldsymbol{w} = \sum_{i=1}^{8} \overline{\boldsymbol{S}}_i \boldsymbol{w}_i \tag{32}$$

$$\boldsymbol{\theta}_{\boldsymbol{x}} = \sum_{i=1}^{8} \overline{\boldsymbol{S}}_i \boldsymbol{\theta}_{xi}, \boldsymbol{\theta}_{\boldsymbol{y}} = \sum_{i=1}^{8} \overline{\boldsymbol{S}}_i \boldsymbol{\theta}_{yi} \tag{33}$$

The relation between the shape functions in terms of the Jacobian matrix ($[J]$) is given as

$$\begin{bmatrix} \overline{\boldsymbol{S}}_{i,x} \\ \overline{\boldsymbol{S}}_{i,y} \end{bmatrix} = [\boldsymbol{J}]^{-1} \begin{bmatrix} \overline{\boldsymbol{S}}_{i,\varsigma} \\ \overline{\boldsymbol{S}}_{i,\varphi} \end{bmatrix} \tag{34}$$

where

$$[J]^{-1} = \begin{bmatrix} x, \varsigma\ x, \varphi \\ y, \varsigma\ y, \varphi \end{bmatrix}$$

In this chapter, the framework for the stochastic low-velocity impact analysis is depicted in Fig. 2. Initially, the input parameters are identified like Young's modulus, shear modulus, Poisson's ratio, density, etc., to incorporate in the model to be designed. After that, a finite element method (FEM)-based approach is implemented to estimate the deterministic output. The next step is to evaluate the input and output data which are used to fit in the metamodel or surrogate model. In the present study, polynomial chaos expansion (PCE) is used as a metamodel and its predictability is verified by portraying percentage error and scatter plot with respect to Monte Carlo simulation (MCS).

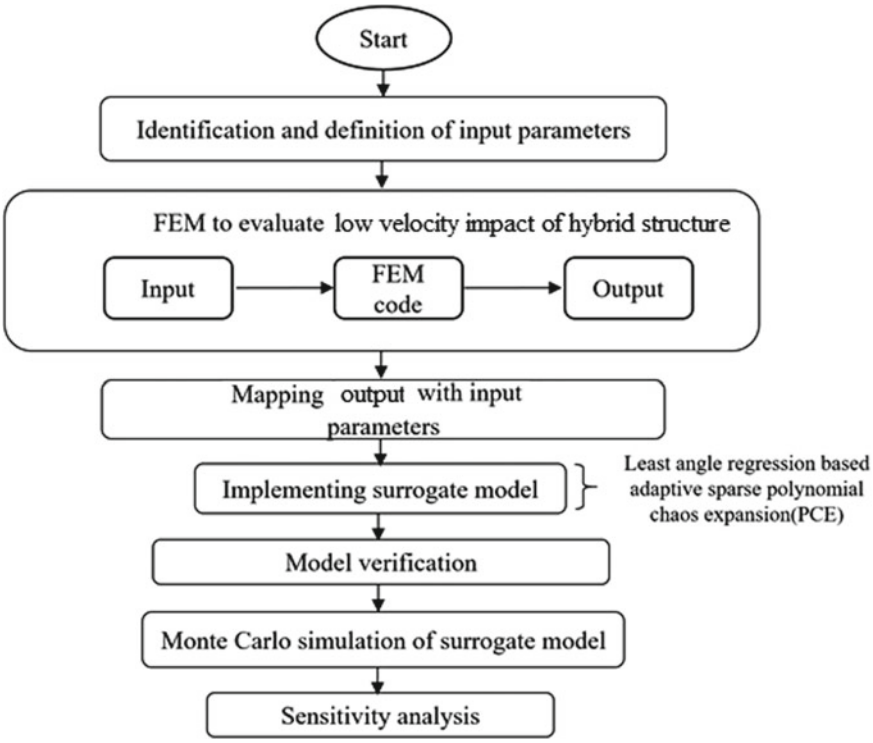

Fig. 2 Flow chart for probabilistic analysis of transient low-velocity impact response

4 Polynomial Chaos Expansion (PCE)

The uncertainty of each input parameter in the random variable approach is modelled by describing a probability density function (PDF) (refer to Fig. 3, $f_x(a)$). The aim of UQ is then to obtain the statistical moments of the random input response as presented in this section. In its least complex structure, the PCE of a stochastic response [62] $f\left(\vec{a}\left(\vec{\zeta}\right)\right)$ depends on the randomness of the input variables

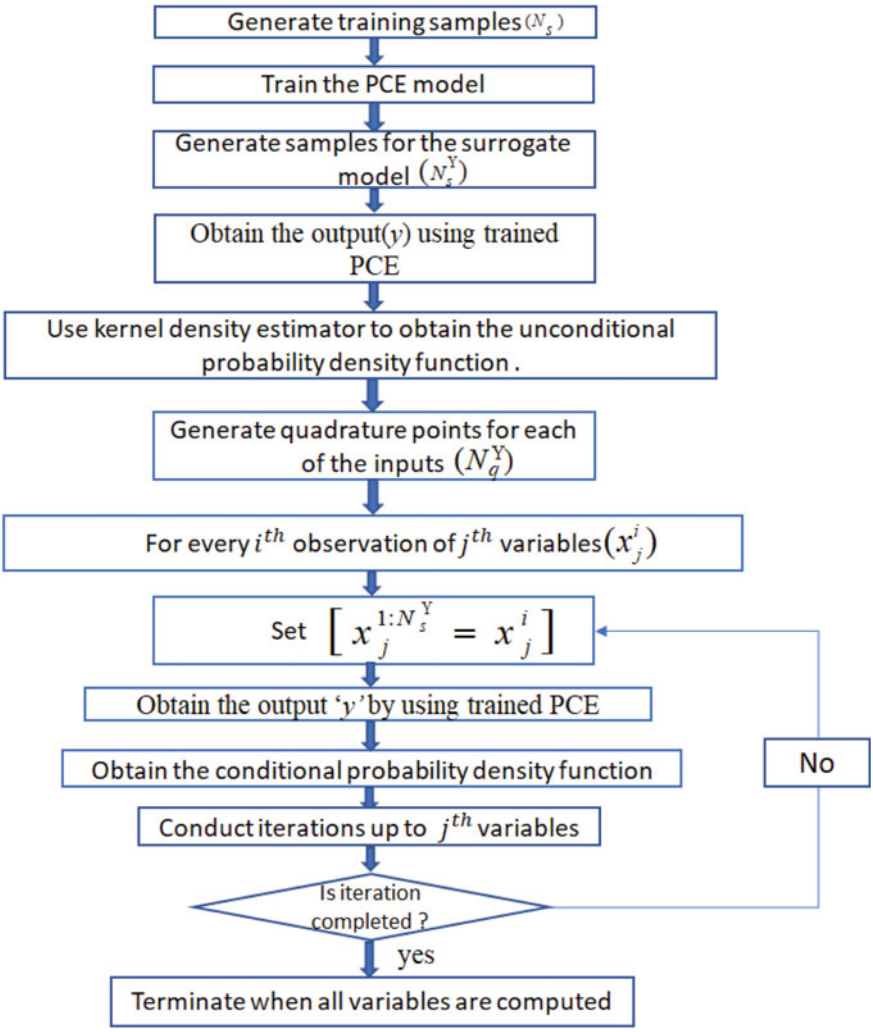

Fig. 3 Flow chart for moment-independent sensitivity analysis using PCE surrogate model

$$f\left(\vec{a}\left(\vec{\zeta}\right)\right) = \sum_{n=0}^{p} b_n \varphi_n\left(\vec{\zeta}\right) \tag{35}$$

where b_n is the PCE coefficients, φ_n is the multidimensional orthogonal polynomials which form the orthonormal basis in Hilbert space and $\vec{\zeta} = \{\zeta_1, \zeta_2, \ldots, \zeta_d\}$ shows the basic random variable vector. On the basis of PDF of random input variables, selection of multidimensional orthogonal polynomials in Eq. 35 is performed using the Askey scheme. After extending the random response, the next step is to determine the expansion coefficients, b_n. On obtaining the PCE coefficient, random response statistical moments can easily be obtained as shown below:

$$\kappa_y = b_0\ \sigma_y^2 = \sum_{n=1}^{p} b_n^2 \|\varphi_n\|^2 \tag{36}$$

The accompanying advances are engaged with getting PCE coefficients as per the following:

a. Random responses and random input parameters are expressed with the help of Eq. (35) by the selection of chaos order, m. For random input variables having a moment χ_{f1}. The PCE can be shown as:

$$\sum_{n=0}^{p} b_n \varphi_n\left(\vec{\zeta}\right) = f\left(\sum_{j=0}^{t} \chi_{f1}\varphi_1(\zeta_1), \ldots, \sum_{j=0}^{t} \chi_{fd}\varphi_1(\zeta_d)\right) \tag{37}$$

b. On differentiating both sides of Eq. (37) w.r.t. basis random variables, ζ_1 by using multi-indices $j^{(n)} = \left(j_1^{(n)}, j_2^{(n)}, \ldots, j_d^{(n)}\right)$ which depicts the differentiation order of the response w.r.t. basis random input variables. On summing up these multi-indices, all the potential estimation of chaos order greater than zero and less than its maximum order, n can be portrayed. On differentiating a linear system $Ax = b$ where matrix A represents analytical sensitivities, the unknown PC coefficients are stored in x and the sensitivities of the higher order of the responses are stored in b.
c. From step b, the linear system obtained can be evaluated both sides at $\zeta_1 = \zeta_1^*$, where ζ_1^* represents any random value taken from the standard domain.
d. Using the finite difference method, sensitivities of the higher order of the responses can be obtained.
e. To obtain PCE coefficients, put the sensitivities got in step d.

5 Results and Discussion

In the present chapter, hybrid functionally graded (FG)-sandwich is considered of cylindrical shell geometry having $R_x = R$ and $R_y = \infty$ where, R_x and R_y are radii of curvature in x- and y-direction, respectively (refer to Fig. 1a). The present hybrid structure consists of three layers. First layer is the FG-based upper facesheet, and this FG-based facesheet constitutes metal and ceramic mixture (here, considered materials are aluminium as metal and zirconia as ceramic) [61]. Then, the second layer is the core made up of low-density foam material and the last layer is the laminated facesheet [59] (refer to Table 1). The deterministic FE code is validated with respect to the available scientific literature [34] (refer to Fig. 4). For finding the relative effect of individual material properties like Young's modulus (E), shear modulus (G), Poisson's ratio (μ) and mass density (ρ), moment-independent sensitivity analysis is carried out in conjunction with polynomial chaos expansion (PCE) surrogate model. The probabilistic analysis for the impact analysis is obtained using PCE approach (the model is constructed using different sample sizes) and is compared with the results obtained from direct MCS. In the present study, the various sample sizes considered for carrying PCE are 64, 128 and 256 while for direct MCS, sample size considered is 10,000. Figure 5 shows the scatter plot, while Fig. 6 shows the percentage errors for the maximum contact force, maximum plate displacement and

Table 1 Material properties of the constituents of hybrid FG-sandwich cylindrical shell

	Material properties	E (GPa)	ν	ρ (kg/m^3)
FG Facesheet	Ceramic	151	0.3	3000
	Metal	70	0.25	2707
Core		0.85	0.42	1000
Lower facesheet		19.3	0.25	2600

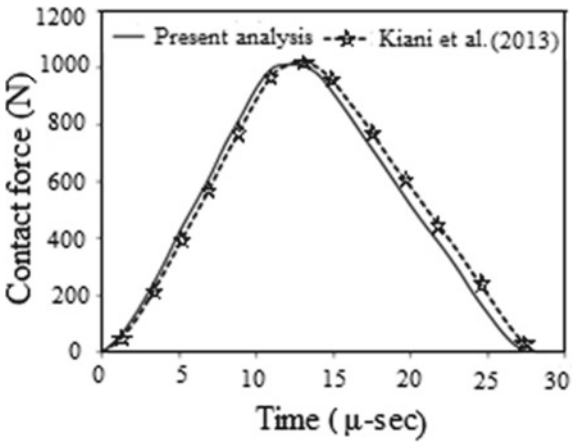

Fig. 4 Time versus contact force plot for functionally graded beam (made up of Si_3N_4 and SS) having both ends clamped [length (Lo) = 135 mm, thickness (t) = 10 mm, width (b) = 15 mm, time step (Δt_1) = 1.0 μ s, impactor mass (m_i) = 0.01 kg, impactor radius (r_i) = 12.7 mm, impactor velocity = 1.0 m/s]

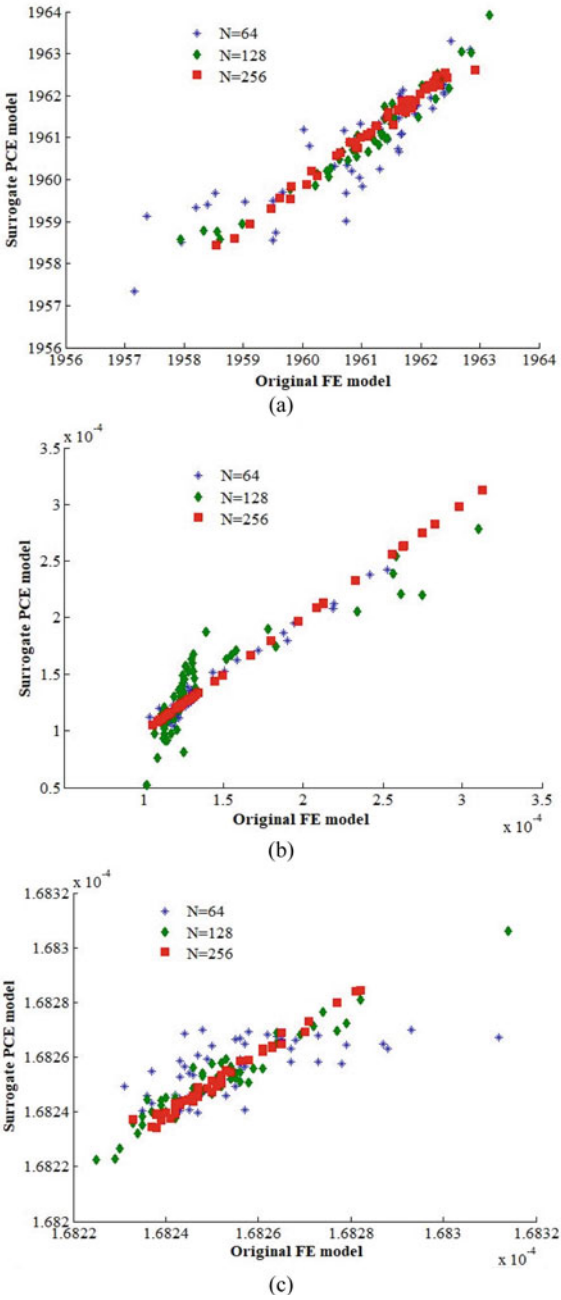

Fig. 5 Scatter plots for the original FE model and the metamodel having non-identical sample size for **a** maximum contact force, **b** maximum plate displacement and **c** maximum impactor displacement

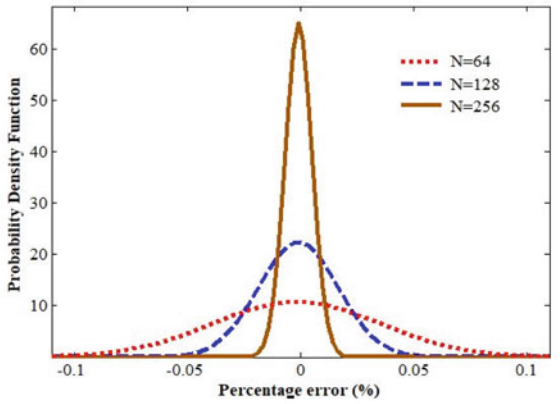

Fig. 6 PDF plots of the percentage error of metamodel having non-identical sample size for **a** maximum contact force, **b** maximum plate displacement and **c** maximum impactor displacement

maximum impactor displacement in case of low-velocity impact for cylindrical shell geometry obtained using PCE. From these two figures, it can be clearly observed that for sample size of 256, better results are obtained as the percentage error value is least in case of 256 sample size compared to sample size of 64 and 128. So, for carrying out further sensitivity analysis, sample size of 256 will be considered. Figure 7 shows the sensitivity plot of various random input material properties for hybrid functionally graded sandwich cylindrical shell. It is observed that mass density (ρ) is the most sensitive parameter followed by shear modulus (G_{23}) and the remaining parameters like Young's modulus (E_1, E_2), shear modulus (G_{12}), Poisson's ratio (ν) and ply orientation angle (θ) have insignificant influence on global response of the structure. Furthermore, it can be observed that these material properties are varying throughout the thickness of the shell and in most cases, the upper FG-based facesheet is the most sensitive compared to the middle core and bottom laminated facesheet.

6 Conclusion

In the present chapter, moment-independent sensitivity analysis is carried out for hybrid functionally graded (FG) sandwich structures having cylindrical shell geometry subjected to impact loading. For appropriate quality control, it is of prime importance to know the relative effect or importance of various input parameters on the overall dynamic response of the FGM shell and to fulfil the purpose moment-independent sensitivity analysis is carried out. Polynomial chaos expansion (PCE)-based surrogate model is used for carrying out the present sensitivity analysis. The surrogate model is applied to acquire computational proficiency without compromising the precision of the results. The present study is carried out on aiming the sensitivity analysis of material and geometrical properties of hybrid FG-sandwich shell for impact responses (mainly peak value of contact force, maximum displacement in the plate and maximum displacement due to impactor). The results illustrate the most significant parameters which affect the impact responses. The present approach is comprehensive which can be further extended for any structural design.

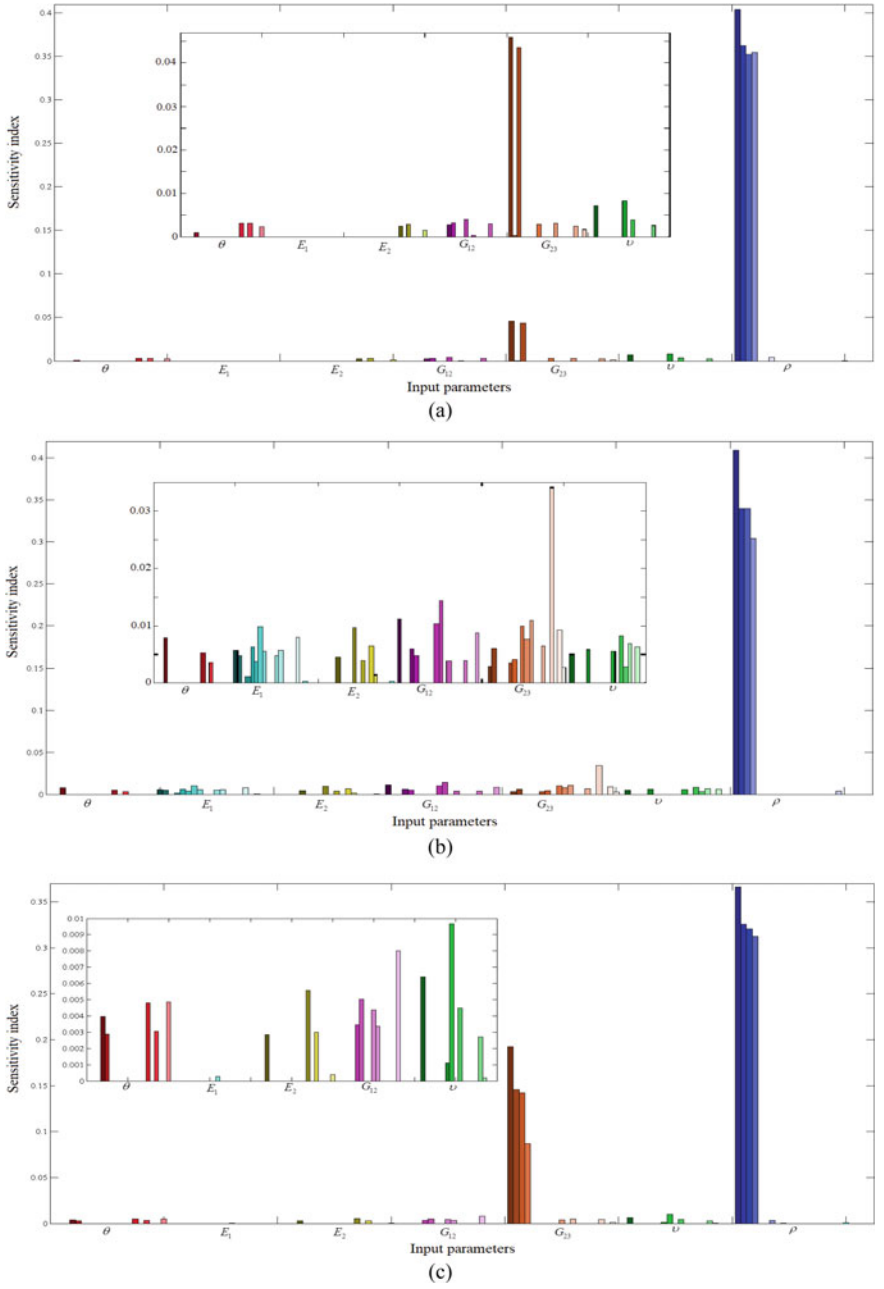

Fig. 7 SI of various material properties for **a** maximum contact force, **b** maximum plate displacement and **c** maximum impactor displacement

Acknowledgements The first author would like to acknowledge the financial support received from Ministry of Human Resource and Development (MHRD), Government of India, during this research work.

References

1. Ahmed Houari MS, Benyoucef S, Mechab I, Tounsi A, AddaBedia EA (2011) Two-variable refined plate theory for thermoelastic bending analysis of functionally graded sandwich plates. J Therm Stresses 34(4):315–334
2. Baba BO (2017) Curved sandwich composites with layer-wise graded cores under impact loads. Compos Struct 159:1–11
3. Bathe KJ (1990) Finite element procedures in engineering analysis. PHI, Google Scholar, New Delhi
4. Brischetto S (2009) Classical and mixed advanced models for sandwich plates embedding functionally graded cores. J Mech Mater Struct 4(1):13–33
5. Carrera E, Brischetto S, Cinefra M, Soave M (2011) Effects of thickness stretching in functionally graded plates and shells. Compos B Eng 42(2):123–133
6. Chen Y, Hou S, Fu K, Han X, Ye L (2017) Low-velocity impact response of composite sandwich structures: modelling and experiment. Compos Struct 168:322–334
7. Cui L, Kiernan S, Gilchrist MD (2009) Designing the energy absorption capacity of functionally graded foam materials. Mater Sci Eng, A 507(1–2):215–225
8. Das M, Barut A, Madenci E, Ambur DR (2006) A triangular plate element for thermoelastic analysis of sandwich panels with a functionally graded core. Int J Numer Methods Eng 68(9):940–966
9. Dey S, Mukhopadhyay T, Adhikari S (2017) Metamodel based high-fidelity stochastic analysis of composite laminates: a concise review with critical comparative assessment. Compos Struct 171:227–250
10. Dey S, Mukhopadhyay T, Khodaparast HH, Adhikari S (2015) Stochastic natural frequency of composite conical shells. Acta Mech 226(8):2537–2553
11. Dey S, Mukhopadhyay T, Khodaparast HH, Adhikari S (2016) A response surface modelling approach for resonance driven reliability based optimization of composite shells. Period Poly Civ Eng 60(1):103–111
12. Dey S, Mukhopadhyay T, Khodaparast HH, Kerfriden P, Adhikari S (2015) Rotational and ply-level uncertainty in response of composite shallow conical shells. Compos Struct 131:594–605
13. Dey S, Mukhopadhyay T, Naskar S, Dey TK, Chalak HD, Adhikari S (2019) Probabilistic characterisation for dynamics and stability of laminated soft core sandwich plates. J Sandwich Struct Mater 21(1):366–397
14. Dey S, Mukhopadhyay T, Sahu SK, Adhikari S (2016) Effect of cutout on stochastic natural frequency of composite curved panels. Compos B Eng 105:188–202
15. Dey S, Mukhopadhyay T, Sahu SK, Adhikari S (2018) Stochastic dynamic stability analysis of composite curved panels subjected to non-uniform partial edge loading. Eur J Mech A/Solids 67:108–122
16. Dey S, Mukhopadhyay T, Spickenheuer A, Adhikari S, Heinrich G (2016) Bottom up surrogate based approach for stochastic frequency response analysis of laminated composite plates. Compos Struct 140:712–727
17. Dey S, Mukhopadhyay T, Spickenheuer A, Gohs U, Adhikari S (2016) Uncertainty quantification in natural frequency of composite plates-an artificial neural network based approach. Adv Compos Lett 25(2):096369351602500203
18. El Meiche N, Tounsi A, Ziane N, Mechab I (2011) A new hyperbolic shear deformation theory for buckling and vibration of functionally graded sandwich plate. Int J Mech Sci 53(4):237–247

19. Etemadi E, Khatibi AA, Takaffoli M (2009) 3D finite element simulation of sandwich panels with a functionally graded core subjected to low velocity impact. Compos Struct 89(1):28–34
20. Gupta A, Talha M (2015) Recent development in modeling and analysis of functionally graded materials and structures. Prog Aerosp Sci 79:1–14
21. Hadji L, Atmane HA, Tounsi A, Mechab I, Bedia EA (2011) Free vibration of functionally graded sandwich plates using four-variable refined plate theory. Appl Math Mech 32(7):925–942
22. Han X, Liu GR (2002) Effects of SH waves in a functionally graded plate. Mech Res Commun 29(5):327–338
23. Han X, Liu GR, Lam KY, Ohyoshi T (2000) A quadratic layer element for analyzing stress waves in FGMs and its application in material characterization. J Sound Vib 236(2):307–321
24. Han X, Liu GR, Xi ZC, Lam KY (2001) Transient waves in a functionally graded cylinder. Int J Solids Struct 38(17):3021–3037
25. Jing L, Yang F, Zhao L (2017) Perforation resistance of sandwich panels with layered gradient metallic foam cores. Compos Struct 171:217–226
26. Karsh PK, Kumar RR, Dey S (2019) Stochastic impact responses analysis of functionally graded plates. J Brazil Soc Mech Sci Eng 41(11):501
27. Karsh PK, Mukhopadhyay T, Chakraborty S, Naskar S, Dey S (2019) A hybrid stochastic sensitivity analysis for low-frequency vibration and low-velocity impact of functionally graded plates. Compos B Eng 176:107221
28. Karsh PK, Mukhopadhyay T, Dey S (2019) Stochastic low-velocity impact on functionally graded plates: probabilistic and non-probabilistic uncertainty quantification. Compos B Eng 15(159):461–480
29. Karsh PK, Mukhopadhyay T, Dey S (2018) Spatial vulnerability analysis for the first ply failure strength of composite laminates including effect of delamination. Compos Struct 15(184):554–567
30. Karsh PK, Mukhopadhyay T, Dey S (2018) Stochastic dynamic analysis of twisted functionally graded plates. Compos B Eng 15(147):259–278
31. Karsh PK, Kumar RR, Dey S (2019) Radial basis function based stochastic natural frequencies anaysis of functionally graded plates. Int J Comput Methods
32. Kashtalyan M, Menshykova M (2009) Three-dimensional elasticity solution for sandwich panels with a functionally graded core. Compos Struct 87(1):36–43
33. Khalili SMR, Mohammadi Y (2012) Free vibration analysis of sandwich plates with functionally graded face sheets and temperature-dependent material properties: a new approach. Eur J Mech A/Solids 35:61–74
34. Kiani Y, Sadighi M, Salami SJ, Eslami MR (2013) Low velocity impact response of thick FGM beams with general boundary conditions in thermal field. Compos Struct 104:293–303
35. Kumar RR, Mukhopadhyay T, Naskar S, Pandey KM, Dey S (2019) Stochastic low-velocity impact analysis of sandwich plates including the effects of obliqueness and twist. Thin-Wall Struct 145:106411
36. Kumar RR, Mukhopadhyay T, Pandey KM, Dey S (2019) Stochastic buckling analysis of sandwich plates: the importance of higher order modes. Int J Mech Sci 152:630–643
37. Kumar RR, Pandey KM, Dey S (2020) Stochastic free vibration analysis of sandwich plates: a radial basis function approach, in reliability, safety and hazard assessment for risk-based technologies. Springer, Singapore, pp 449–458
38. Kumar RR, Vaishali, Pandey KM, Dey S (2020) Effect of skewness on random frequency responses of sandwich plates. In: Singh B., Roy A., Maiti D. (eds) Recent advances in theoretical, applied, computational and experimental mechanics. Lecture notes in mechanical engineering. Springer, Singapore. https://doi.org/10.1007/978-981-15-1189-9_2
39. Kumar RR, Karsh PK, Vaishali, Pandey KM, Dey S (2019) Stochastic natural frequency analysis of skewed sandwich plates. Eng Comput
40. Kumar RR, Mukhopadhya T, Pandey KM, Dey S, (2020a) Prediction capability of polynomial neural network for uncertain buckling behavior of sandwich plates, In: Handbook of probabilistic models. Butterworth-Heinemann, pp 131–140

41. Kumar RR, Pandey KM, Dey S (2020) Effect of skewness on random frequency responses of sandwich plates. In: Recent advances in theoretical, applied, computational and experimental mechanics. Springer, Singapore, pp 13–20
42. Li Q, Iu VP, Kou KP (2008) Three-dimensional vibration analysis of functionally graded material sandwich plates. J Sound Vib 311(1–2):498–515
43. Liu GR, Dai KY, Han X, Ohyoshi T (2003) Dispersion of waves and characteristic wave surfaces in functionally graded piezoelectric plates. J Sound Vib 268(1):131–147
44. Liu GR, Han X, Lam KY (1999) Stress waves in functionally gradient materials and its use for material characterization. Compos B Eng 30(4):383–394
45. Loy CT, Lam KY, Reddy JN (1999) Vibration of functionally graded cylindrical shells. Int J Mech Sci 41(3):309–324
46. Mahamood RM, Akinlabi ET (2015) Laser metal deposition of functionally graded Ti6Al4V/TiC. Mater Des 84:402–410
47. Merdaci S, Tounsi A, Houari MSA, Mechab I, Hebali H, Benyoucef S (2011) Two new refined shear displacement models for functionally graded sandwich plates. Arch Appl Mech 81(11):1507–1522
48. Mukhopadhyay T, Adhikari S (2016a) Equivalent in-plane elastic properties of irregular honeycombs: an analytical approach. Int J Solids Struct 91:169–184
49. Mukhopadhyay T, Adhikari S (2016b) Effective in-plane elastic properties of auxetic honeycombs with spatial irregularity. Mech Mater 95:204–222
50. Mukhopadhyay T, Adhikari S (2016c) Free-vibration analysis of sandwich panels with randomly irregular honeycomb core. J Eng Mech 142(11):06016008
51. Mukhopadhyay T, Chakraborty S, Dey S, Adhikari S, Chowdhury R (2017) A critical assessment of Kriging model variants for high-fidelity uncertainty quantification in dynamics of composite shells. Arch Comput Methods Eng 24(3):495–518
52. Mukhopadhyay T, Naskar S, Dey S, Adhikari S (2016) On quantifying the effect of noise in surrogate based stochastic free vibration analysis of laminated composite shallow shells. Compos Struct 140:798–805
53. Mukhopadhyay T, Adhikari S, Batou A (2017) Frequency domain homogenization for the viscoelastic properties of spatially correlated quasi-periodic lattices. Int J Mech Sci
54. Naskar S, Mukhopadhyay T, Sriramula S, Adhikari S (2017) Stochastic natural frequency analysis of damaged thin-walled laminated composite beams with uncertainty in micromechanical properties. Compos Struct 160:312–334
55. Neves AMA, Ferreira AJ, Carrera E, Cinefra M, Jorge RMN, Soares CMM (2012) Static analysis of functionally graded sandwich plates according to a hyperbolic theory considering Zig-Zag and warping effects. Adv Eng Softw 52:30–43
56. Neves AMA, Ferreira AJM, Carrera E, Roque CMC, Cinefra M, Jorge RMN, Soares CMM (2012) A quasi-3D sinusoidal shear deformation theory for the static and free vibration analysis of functionally graded plates. Compos B Eng 43(2):711–725
57. Neves AMA, Ferreira AJM, Carrera E,Cinefra M, Jorge RMN, Soares CMM (2012) Buckling analysis of sandwich plates with functionally graded skins using a new quasi3D hyperbolic sine shear deformation theory and collocation with radial basis functions. ZAMM J Appl Math Mech ZeitschriftfürAngewandteMathematik und Mechanik 92(9):749–766
58. Reddy JN, Wang CM, Kitipornchai S (1999) Axisymmetric bending of functionally graded circular and annular plates. Eur J Mech A/Solids 18(2):185–199
59. Rizov V, Shipsha A, Zenkert D (2005) Indentation study of foam core sandwich composite panels. Compos Struct 69(1):95–102
60. Shariyat M, Nasab FF (2014) Low-velocity impact analysis of the hierarchical viscoelastic FGM plates, using an explicit shear-bending decomposition theory and the new DQ method. Compos Struct 113:63–73
61. Singh H, Hazarika BC, Dey S (2017) Low velocity impact responses of functionally graded plates. Procedia Eng 173:264–270
62. Thapa M, Mulani SB, Walters RW (2019) Stochastic multi-scale modeling of carbon fiber reinforced composites with polynomial chaos. Compos Struct 213:82–97

63. Touloukian YS (ed) (1967) Thermophysical properties of high temperature solid materials, vol 1. Macmillan
64. Vaishali, Mukhopadhyay T, Karsh PK, Basu B, Dey S (2020) Machine learning based stochastic dynamic analysis of functionally graded shells. Compos Struct 237:111870
65. Vaishali, Dey S (2021) Support vector model based thermal uncertainty on stochastic natural frequency of functionally graded cylindrical shells. In: Saha S.K., Mukherjee M. (eds) Recent advances in computational mechanics and simulations. Lecture notes in civil engineering, vol 103. Springer, Singapore. https://doi.org/10.1007/978-981-15-8138-0_50
66. Vaishali, Mukhopadhyay T, Kumar RR, Dey S (2020) Probing the multi-physical probabilistic dynamics of a novel functional class of hybrid composite shells. Compos Struct 113294
67. Xiang S, Jin YX, Bi ZY, Jiang SX, Yang MS (2011) A n-order shear deformation theory for free vibration of functionally graded and composite sandwich plates. Compos Struct 93(11):2826–2832
68. Zenkour AM (2005a) A comprehensive analysis of functionally graded sandwich plates: Part 1—deflection and stresses. Int J Solids Struct 42(18–19):5224–5242
69. Zenkour AM (2005b) A comprehensive analysis of functionally graded sandwich plates: Part 2—Buckling and free vibration. Int J Solids Struct 42(18–19):5243–5258
70. Zenkour AM, Alghamdi NA (2008) Thermoelastic bending analysis of functionally graded sandwich plates. J Mater Sci 43(8):2574–2589
71. Zenkour AM, Alghamdi NA (2010a) Bending analysis of functionally graded sandwich plates under the effect of mechanical and thermal loads. Mech Adv Mater Struct 17(6):419–432
72. Zenkour AM, Alghamdi NA (2010b) Thermomechanical bending response of functionally graded nonsymmetric sandwich plates. J Sandwich Struct Mater 12(1):7–46
73. Zhang J, Qin Q, Xiang C, Wang TJ (2016) Dynamic response of slender multilayer sandwich beams with metal foam cores subjected to low-velocity impact. Compos Struct 153:614–623
74. Zhang J, Ye Y, Qin Q (2018) Large deflections of multilayer sandwich beams with metal foam cores under transverse loading. Acta Mech 229(9):3585–3599
75. Zhang X, Zhang H (2013) Optimal design of functionally graded foam material under impact loading. Int J Mech Sci 68:199–211
76. Zhang J, Qin Q, Chen S, Yang Y, Ye Y, Xiang C, Wang TJ (2018) Low-velocity impact of multilayer sandwich beams with metal foam cores: analytical, experimental, and numerical investigations. J Sandwich Struct Mater 1099636218759827
77. Zhou J, Guan ZW, Cantwell WJ (2013) The impact response of graded foam sandwich structures. Compos Struct 97:370–377

Chapter 12
Statistical Energy Analysis Parameters Investigation of Composite Specimens Employing Theoretical and Experimental Approach

Avinash Borgaonkar, Maruti Mandale, Shital Potdar, and Ch Sri Chaitanya

1 Introduction

Statistical energy analysis (SEA) is a modeling procedure to examine the dynamic characteristics in terms of vibro-acoustic response for complicated, resonating, built-up structures using energy flow co-relations. The SEA technique has been developed in the 1960s, heavily for handling structural-acoustic and vibration-field-related problems in conjunction with space-crafts. Since then, the method has been evolved and successfully employed in many other areas such as ships, buildings, aircraft, and cars. Even though the existing deterministic methods such as finite element method (FEM) and boundary element method (BEM) are helpful to estimate the vibrational response of structures computationally, but these methods have limitations such as higher time consumption and uneconomical. The SEA method demonstrates to be an effective tool for predicting vibro-acoustic response at high-frequency levels. In the resent, SEA method has been popularly used in a growing number of applications since it predicts the average vibrational amplitudes as well as sound pressures in aeroplanes, space vehicles, ships, heavy machines, buildings, etc.

A. Borgaonkar (✉) · S. Potdar · C. S. Chaitanya
National Institute of Technology, Warangal, India
e-mail: avi.borgaonkar@gmail.com

M. Mandale
Rajarambapu Institute of Technology Sakharale, Sangli, India

S. Sahoo (ed.), *Recent Advances in Layered Materials and Structures*,
Materials Horizons: From Nature to Nanomaterials,
https://doi.org/10.1007/978-981-33-4550-8_12

2 Overview of SEA

2.1 Approach of SEA

Lyon et al. [17] were the pioneers who contributed a lot in the area of Statistical Energy Analysis (SEA). The abbreviation 'SEA' exhibits its methodology. 'Statistical' corresponds to the systems considered for study, which are supposed to be taken from a statistical population with known distributions of their dynamical parameters. The 'Energy' depicts the behaviour of a system in terms of different forms of energies such as stored, dissipated, and exchanged in vibro-acoustics field. 'Analysis' represents the framework of the SEA method. In the SEA approach, big-complicated system is split into smaller subsystems. The subsystem is comprised of several physical elements which are having identical vibro-acoustic characteristics like damping, excitation, and coupling. The whole system modeled using SEA in such a way that the energy distribution over the subsystems is being balanced employing power balance equations. While employing the power balance equation, it is assumed that total incoming power is equal to total dissipated power. Beside it is hypothesized that the damping is directly related to the kinetic energy of a subsystem whereas the rate of flow of power between the subsystems is related to the energy level difference in subsystem. In practical cases, transmission coefficients assigned with the systems which need to be evaluated to understand the relation of power transferred in between the subsystems to their energy levels at equilibrium state. These coefficients can be estimated by different approaches in SEA such as the modal approach, the wave approach, and the mobility approach. In case of modal approach, the interactions between uncoupled modes in the subsystems have been controlled. The multimode power transfer coefficients can be expressed using decoupled boundary condition. This is an ideal approach for vibro-acoustic problems which involves acoustic interaction between enclosed volumes, but this not suits for coupling between solid structures. In such cases, the wave approach plays a significant role. In wave approach, the vibratory fields have been modeled as a superposition of travelling waves and transferred power within the subsystems acquired from the wave transmitting and reflecting interfaces. The mobility approach is based on the concept of dynamic mobility or impedance to demonstrate the interaction between the coupled subsystems.

2.2 Important Parameters in SEA

The main parameters of SEA are: modal density, damping loss factor (DLF), coupling loss factor (CLF), and the power (input, transmitted, and dissipated). The DLF deals with the power dissipated into a subsystem. The CLF relates to flow of energy between the subsystems. It is defined as the fractional energy which is transmitted from one subsystem to others. While dealing with structures, CLF is proportional to the transmission coefficient which depends upon the material properties, its thickness,

and structural orientation. In the acoustics field, the CLF is in proportion with the radiation efficiency. Modal density is another important parameter which deals with the number of modes per frequency bandwidth. The power flow from one subsystem to another can be estimated based on the evaluated loss factors which are dependent on the dimensions, material properties of the subsystems, and the energy transfer from one to another. The net power flow is estimated by evaluating individual power flows for all subsystems.

2.3 Some Limitations and Assumptions in SEA

At lower frequency range, the SEA technique cannot predict the response accurately generally below 200–400 Hz. At specific or narrowband frequencies, the SEA cannot predict the excitations. Because of the averaged frequency response at a particular frequency band, it is unable to predict modes or mode shapes of the system. Due to this, the information related to local distribution of vibration level and spatial distribution of the field variables within the interconnected subsystems is suppressed. Besides these limitations practically while employing SEA different assumptions made, these are listed as follows.

- The subsystems are coupled with linear and conservative coupling.
- It is assumed that the resonating modes in a specified frequency band possess same amount of energy.
- The DLF is assumed to be identical for all modes in any particular frequency band. In addition, the damping should not be too low or too high.
- The subsystems assumed to be homogeneous and the sound fields assumed to be reverberant and diffused.
- The power transmission takes place from one subsystem to another subsystem is assumed because of the present resonating modes in the specified frequency band. In addition, the flow of power within the subsystems varies in proportion with their energy level.

2.4 Deterministic and Statistical Approaches

The different numerical techniques employed for dynamic analysis of vibro-acoustic systems are categorized under deterministic or statistical approach as depicted in Fig. 1. The deterministic approach includes methods such as FEM and BEM which are restricted for the low-frequency range. The computational effort increases exponentially with frequency in case of deterministic techniques because of the increase in the spatial variation of the dynamic field variables. Also with an increase in frequency, the system response becomes highly sensitive to small perturbations because of its geometrical as well as material properties. This leads to a considerable scattering of the response of an identical system. Whereas the SEA approach has been employed

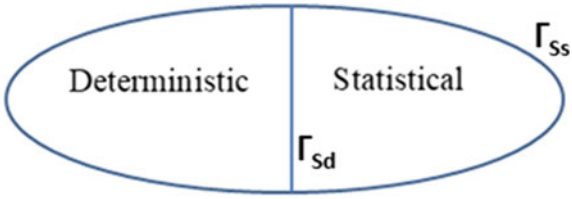

Fig. 1 Frequency-based approaches for vibro-acoustic problems

for estimating the mean and variance of the dynamic response of identical systems, by assuming a higher modal overlap and high modal density.

In comparison with the deterministic methods, the SEA approach does not have a problem with regard to field variable distribution throughout the domain. The SEA method involves the estimation of the frequency- and space-averaged energy quantities for a statistical ensemble. Mace [19] who contributed in this area which makes SEA as an important simulation technique for predicting the averaged response for big structures such as ships, aeroplanes, busses, etc. as well as smaller systems, for example, automotive vehicles. They proved that power flow is related with the modal energy difference in between coupled oscillators. They indicated that the power flow direction depends on the energy levels of two oscillators. They also applied the idea to two randomly excited multimodal systems.

To elaborate the working of SEA method, the system is split into a number of smaller subsystems as depicted in Fig. 2. Each subsystem has been assigned as an element of a SEA model corresponds to a substantial energy storage location. The selection is made on the basis of principle of similarity. In other words, the modes associated with a particular subsystem should possess the same energy and the same order of damping. Also it has been assumed that the modes associated with a subsystem are distributed equally in the particular frequency band as well as all these are equally energetic and the modal responses are incoherent.

The SEA global equations for a system can be obtained employing balance of energy approach for every subsystem and could be presented as

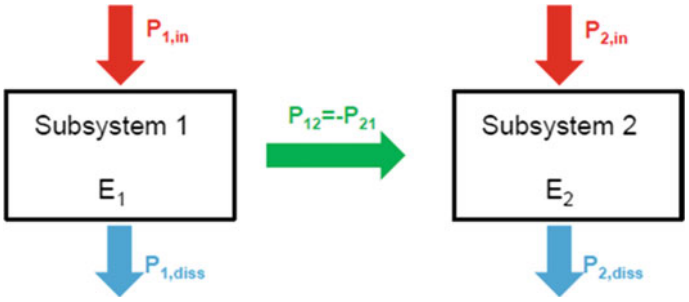

Fig. 2 Balance of energy for a two-subsystem problem

$$P_{i,\text{in}} = P_{i,\text{diss}} + \sum_{j \neq i}^{n} P_{ij} \tag{1}$$

where $P_{i,\text{in}}$ is power input from the surrounding, $P_{i,\text{diss}}$ is power dissipated, and $\text{P}_{\text{i,j}}$ is flow of power from subsystem i to j.

The averaged time energy flowing from subsystem i to j is assumed to be directly related to the modal energy difference.

$$P_{ij} = \omega \left(\eta_{ij} E_i - \eta_{ji} E_j \right) \tag{2}$$

where E_i is averaged time total energy associated with subsystem i and η_{ij} is the CLF. This has been estimated by measuring the transfer of energy from subsystem i to j because of coupling. The relation for the CLF for subsystem i and j (i.e. η_{ij} and η_{ji}) can be represented using reciprocity relation

$$n_i \eta_{ij} = n_j \eta_{ji} \tag{3}$$

with n_i the modal density associated with subsystem i. The CLF can also be evaluated on the grounds of the junction transmission coefficient. However, the transmission coefficient can be accurately predicted employing analytical method for semi-infinite systems or measurements of identical subsystems. The time-averaged dissipated power for subsystem i is:

$$P_{i,\text{diss}} = \omega \eta_i E_i = M_i \frac{E}{n_i} \tag{4}$$

with η_i and M_i the DLF and the modal overlap factor of subsystem i respectively.

There has been significant research in the field of estimating the SEA parameters of subsystems like plates, cylindrical shells, and panels by numerous researchers over the past decades. The SEA too has gained much attention in the past few decades due to its previously reported advantages compared to deterministic methods. The study of SEA has been broadened to facilitate its application in the various fields of engineering besides the aeronautical sector as initially intended. Here, the overviews of these researches related to the SEA application and computation of SEA parameters of different subsystems like (one dimensional, two dimensional, etc.) are briefly described. Sheng et al. [27] used SEA to analyse the random vibrations of structures. The authors aimed to better understand the energy balance mechanism for non-conservatively coupled systems. Authors addressed the difficulties faced for the energy balance mechanism. A method for evaluating CLF and effective internal loss factors associated with non-conservatively coupled systems has been introduced. Further to prove the accuracy of the method, Maxit and Guyader [22] demonstrated practical application of the same. They proposed SEA modal energy distribution

approach for analysis of structures. Equipartition of modal energies in selected systems was not assumed in this approach. Authors were obtained modal energy equations by using basic power flow equations between two oscillators. They concluded that the information related to modal energy of coupled subsystems can be obtained from the modal energy associated with the uncoupled subsystems.

Wilson and Hopkins [31] found out the errors involved with implementation of SEA and concentrated on the potentials of advanced SEA for investigating vibro-acoustic response in the low as well as mid-frequency ranges. Emphasis has been placed on the medium and low-frequency range because the idealized subsystems like plates only assists for local modes with a low number of modes. The SEA and advanced SEA forecasts were evaluated by comparison with finite element models. It is concluded that advanced SEA provides better accuracy than normal SEA. Hopkins [12] employed an experimental SEA approach to analyse plate subsystems with lower modal overlap and modal density. The test results reveal that the subsystem for considered conditions demonstrates large differences in SEA parameters due to relatively low uncertainty in physical properties. Cheng et al. [5] further extended the study employing isotropic as well as orthotropic material for plates. The non-resonating responses associated with isotropic and orthotropic plates because of acoustically induced vibrations were measured in a reverberation chamber. The obtained results of resonating and non-resonating responses for the reported plate materials were compared with experimental results. These results were close to the prediction of SEA model. Due to neglecting non-resonant part for an isotropic plate with a low dissipation loss factor, the expected response can cause large errors at close or above the critical frequencies. For the same condition, more error may occur in the expected response of orthotropic plate below the critical frequency. Authors emphasized that non-resonating response should be considered in case of both the isotropic and orthotropic plates.

Ma et al. [18] applied experimental SEA for the identification of noise sources, noise levels, and vibration levels encountered in the field of heating, ventilation, and air conditioning (HVAC). In the HVAC industry, a compressor is the most important component. It is required to identify the path of energy flow in the HVAC system. They have implemented mobility method to evaluate the modal density and half-power bandwidth method for DLF. In day-to-day life, lightweight structures are demanded because of its lightweight and high rigidity. The low inertia forces of lightweight structures results into higher vibration and noise levels. Tager et al. [28] simulated a vibro-acoustic analytical model that allows structural and sound radiation analysis which suits for multilayer composite plates comprised of anisotropic materials. The developed model permits physical-based and fast analysis of anisotropic composite plates as compared to the FEM or BEM. Eigen frequency and modal damping properties depend on the direction for anisotropic composite plates. It is concluded that a laminated composite exhibits damping-dominating acoustic radiation behaviour.

3 Theoretical Evaluation of SEA Parameters

3.1 Modal Density

The modal density of plane plates and cylinders has been estimated by [25]. They determined experimentally the modal density of a structure from the real part of its admittance. It is found that the experimental values of modal density correspond well to the theoretical ones. Finnveden [9] used the FEM-waveguide, to compute the propagation characteristics of waves in thin-walled structures. In particular, essential features such as group velocity, modal density, and waveform have been predicted. The formulation of a dispersion relation for a channel-shaped beam, presented from the output received by the finite element analysis. Wavenumber integration method was used to study the influence of different boundary conditions on mode number and modal density for 1D and 2D components by Xie et al. [32]. Beam and plate were used as one-dimensional and two-dimensional components, respectively. The average mode count lowered from 0 to 1 for single beam vibrating in bending mode for different types of boundary conditions. The results obtained from empirical relations of natural frequency and finite element analysis were used for comparison with the results obtained by wavenumber integration method for beam and plate employing different boundary conditions. Accuracy in the estimation of modal density for SEA increases due to the inclusion of boundary conditions for beam and plate. Ramachandran and Narayanan [24] developed an analytical method for evaluating the radiation efficiency and modal density of a longitudinally stiffened cylinder for use in SEA. The subsystem formulation employing SEA method based on combination of finite elemental analysis, periodic structure theory, and component mode synthesis has been described by Cotoni et al. [6]. The method efficiently calculates the SEA parameters for a common panel-like structure. Mathematical expressions were derived to estimate modal density, DLF, and unit engineering response of the panel-type structure. They employed Fourier transformation approach to estimate the resonating radiation efficiency, non-resonating transmission loss, and input acoustic power.

Bachoo and Bridge [1] developed an expression analytically for modal density of fibre-reinforced composite beams coupled in bending as well as torsion. The modal density variation with the implementation of different fibre orientations for a composite beam has been studied. From the test results, it has been found in different frequency bands, particular fibre orientation corresponds to a lower modal density. Borgaonkar et al. [2] investigated the modal density of glass fibre composite plates experimentally. They analysed the effect of different fibre orientations on the modal density values of composite plates. Han et al. [11] presented the modal density expressions for sandwiched panels made of orthotropic material. Hamilton principle was used to derive the governing equations for sandwiched panels by considering in-plane rigidity of core material. For carrying out the study, different materials and reference axes have been considered. Integration of wavenumber in space was used to obtain modal density. The study has been carried out to analyse the effects of the various boundary conditions. The empirical modal density expressions, finite

element models, and shear deformation theory were used to decide the accuracy of proposed models. The influence of transverse shear rigidity, ply angle of face sheets, boundary conditions, and in-plane rigidity of core material on modal density, parametric studies have been carried out. Elie et al. [7] demonstrated a novel method for evaluating young's modulus, density as well as modal loss factors for flat panel-type structures. For this, they considered the parameters such as mean mobility and modal density. The modal density has been evaluated from the obtained modal frequencies employing Estimation of Signal Parameters via Rotational Invariance Techniques (ESPRIT). This technique well suits in the low as well as the mid-frequency range. The close agreement between experimental and theoretical results for mean mobility and modal density and helps to predict young's modulus and density of flat panels. They concluded that the method proved to be very robust and it requires fewer measurement points to evaluate the material properties accurately.

3.1.1 Estimation of Modal Density of Two-Dimensional Systems (Rectangular Plates)

For a two-dimensional idealized subsystem such as rectangular plate, the expression for modal density can be obtained from the derivative of average mode count. The expression for modal density in connection with frequency is given by Lyon et al. [17].

$$\eta(\omega) = \frac{\partial N(\omega)}{\partial \omega} = \frac{S}{4\pi}\sqrt{\frac{m''}{B}} + \frac{1}{2}\left(\frac{m''}{B}\right)^{1/4} \left[\frac{(1-\delta x_{\text{left}} - \delta x_{\text{right}})b}{n} + \frac{(1-\delta y_{\text{top}} - \delta y_{\text{bottom}})a}{n}\right]\omega^{-1/2} \quad (5)$$

where $m'' = \rho h$.

From the above expression, it can be observed that the modal density of the plate is dependent on frequency. The first term mentioned in the expression is a constant term which is expressed as

$$\eta(\omega) = \frac{S}{4\pi}\sqrt{\frac{m''}{B}} \quad (6)$$

The first term depends only on the material properties and geometrical dimensions of the plate. The second term present in Eq. (5) is frequency dependent and geometric dimensions of the plate. As the frequency increases, the second term becomes smaller and less important. Hence, in higher frequency region, the modal density becomes constant.

The modal density of an idealized subsystem like rectangular plate considering the dispersion relation at free-free boundary condition is given by

$$\eta(\omega) = \frac{S}{4\pi}\sqrt{\frac{m''}{B}} + \frac{1}{2}\left(\frac{m''}{B}\right)^{1/4}\left(\frac{a+b}{\pi}\right)\omega^{-1/2} \tag{7}$$

3.2 Damping Loss Factor (DLF)

Generally, to evaluate the DLF accurately, experimental approach has been employed. The loss mechanism of connecting joints, damping treatments, and surface absorption is comparatively more than the internal dissipation of the subsystem material. The researchers estimated DLF for different materials are reviewed in this section.

Wang et al. [30] performed experimental analysis to predict damping loss factors of ship structure panels with constrained as well as unconstrained damping layers. They have considered different parameters such as material properties such as young's modulus, density, and its thickness, as well as the location of constrained damping layers. To reduce the vibration amplitude of a ship cabin, they performed optimization study considering constrained and unconstrained viscoelastic damping layers with different material properties, size, and thickness. Further [33] described the experimental method to predict DLF of ship structure panels with constrained or unconstrained damping layers. Various components of thickness, material properties as well as the partial location of constrained damping layers have been investigated. Liu and Ewing [16] determined the DLF employing both experimental and analytical approaches for sandwich panels considering different configurations with constrained layer damping treatments. They used the power injection method considering a broader frequency range. The obtained results have been compared with the experimental results received by implementing other methods. Based on the obtained data, they have proposed a novel analytical power input method for estimating the DLF of built-up structures. The predicted results obtained using this newly developed method co-related with results acquired from the modal strain energy method. They observed that the results obtained employing these three methods exhibits close agreement. Chandra et al. [4] performed an experimental study to evaluated DLF of glass fibre-reinforced composites. They employed a free decay method. They considered various shapes of the specimen such as beam, tubular, cuboidal, and tested at different loading conditions. They compared the obtained experimental results with theoretical predictions and are in close agreement with each other. Borgaonkar et al. [3] investigated the DLF of glass fibre composite plates experimentally. They studied the effect of various fibre orientations on the DLF of composite plates.

Iwaniek [13] ermined the DLF for plate elements. He has considered plates made of different materials like steel, brass, plexiglass, aluminium, etc. The comparison of DLF was made for different materials. Mandal et al. [21] measured DLF for orthotropic plates. The half-power bandwidth method was employed for estimating DLF of rectangular and trapezoidal plates. They have adopted a single degree of freedom system concept. Low-frequency range was selected for conducting the tests. Vatti [29] employed power input method and impulse response decay method for

estimating the DLF for plates. While performing the analysis different processing parameters have been taken into accounts such as frequency bandwidth, frequency resolution, number of measurement locations, and the signal-to-noise ratio. Moreover, for estimating the CLF, two algorithms were considered, one for individual plate and the other for plate-coupled plates. The CLF and modal density for the two sets of plates were evaluated experimentally and compared with the theoretical results. The comparison shows a close agreement between these results.

Theoretical estimation of damping capacity of a material is complex in nature since it depends on the number of factors, such as molecular structure, loading rate, strain distribution, and temperature. In order to understand the terminology of DLF, an empirical relation demonstrated by Lyon et al. [17] has been considered.

$$\eta = \frac{E_{\text{diss}}}{2\Pi E_{\text{tot}}} = \frac{D_i}{D_r} \tag{8}$$

where E_{tot} is the total dynamical energy, E_{diss} is the energy dissipated per cycle, and D_r is the real part while D_i is the imaginary part of the complex dynamic modulus.

3.3 Coupling Loss Factor (CLF)

In SEA modeling for permanently connected two subsystems, it is necessary to evaluate the CLF accurately. Yoo et al. [34] determined CLF using the power injection method for the single beam-plate system. In this study, frequency averaging approach has been employed considering octave bands. In addition to the beam-plate structure, beam-plate-beam structure was also analysed using SEA approach. The result shows that in case of indirect coupling (i.e. beam-plate-beam coupled structure) SEA predicts very well. Ji and Huang [14] recommended a simple SEA modeling approach by replacing continuously coupled interfaces with the sets of discrete points maintaining the appropriate distance between the points. On the basis of performed numerical study for two thin plates connected with line junction, they recommended a criterion for point spacing by adjusting the points on a line junction for the coupled plates. It has been observed that the spacing between the points depends on the wavelengths, as well as the wavelength ratio for the two coupled subsystems. Grushetsky and Smolnikov [10] presented the technique of determining CLF considering the uncertainty of subsystems. Two junction beams took into consideration as an example. The random variables were the length of the beams, which obeyed the law of normal distribution. The FEM was employed for estimating the CLF. Calculations were made using two techniques: the FEM and energy method. It has been shown that the calculation of the results according to two techniques agrees well for the average values and for the dispersion. Average modal spacing, input power, transmission coefficient, and CLF were evaluated for symmetrically coupled laminated composite plates by Secgin [26]. For this modal approach through discrete

singular convolution method was used for composite plates fabricated with 4 and 6 plies with different orientations. The CLF was estimated analytically for composite plates and compared with numerical results. Natural frequencies were used to find average modal spacing by analytical as well as an experimental method for uncoupled composite plates. Modal impedances were used for input power measurements. He concluded that the proposed methodology well suits in high frequency as well as in mid-frequency region for SEA of composite plates.

Fahy and Gardonio [8] presented the effect of geometrical and material properties of plates and beams on vibratory averaged power flow over frequency and CLF. Authors proved that two important parameters such as modal overlap factor and coupled modes of plates or beams affect the power flow as well as CLF. They reported that for a good estimation of CLF, at least five natural frequencies need to be considered in the selected frequency band. Mace [20] considered a system comprising of two plates coupled at edges. They predicted theoretically power flow and CLF employing the traditional asymptotic wave theory approach. The obtained results were compared with the values obtained using finite element analysis for the whole system. In their study, they considered various shapes plates and different damping levels. They concluded that if the damping is large enough, the response does not depend on the geometry of the plates but in case of low damping, the response remarkably depends on the geometry of each plate. Panuszka et al. [23] presented the effect of joints and plate thickness ratio on the estimation of CLF. Two types of connections were included: welded line junctions and point junctions. The test results reveal that welded line junctions tend to decrease CLF as the plate thickness ratio increases. However, the CLF increases in line with increase in density of the junction points.

The theoretical expression of CLF for two coupled plates with line junction represented by Le Bot (15) is as follow.

$$\eta_{12} = \frac{Lc_{g1}}{\Pi\omega S_1} \int_0^{\Pi/2} T(\theta) \cos\theta \, \mathrm{d}\theta \tag{9}$$

where S_1 is the area of plate 1. If c_{g1} the group speed, T is the ratio of transmitted intensity to the incident intensity, θ is the angle normal to the boundary. L is the total length of coupling junction.

4 Experimental Evaluation of SEA Parameters

4.1 Fabrication of Composite Specimens

Generally, vacuum bag moulding and hand layup techniques are used for the fabricating the composite plates. In the present work, the vacuum bag moulding technique is employed as depicted in Fig. 3. In order to fabricate the composite specimens, epoxy resin and hardener are thoroughly mixed unless the homogeneous mixture is to be obtained. Later, the prepared mixture is applied layer by layer and the specimens are prepared as per required dimensions and fibre orientation as depicted in Fig. 4.

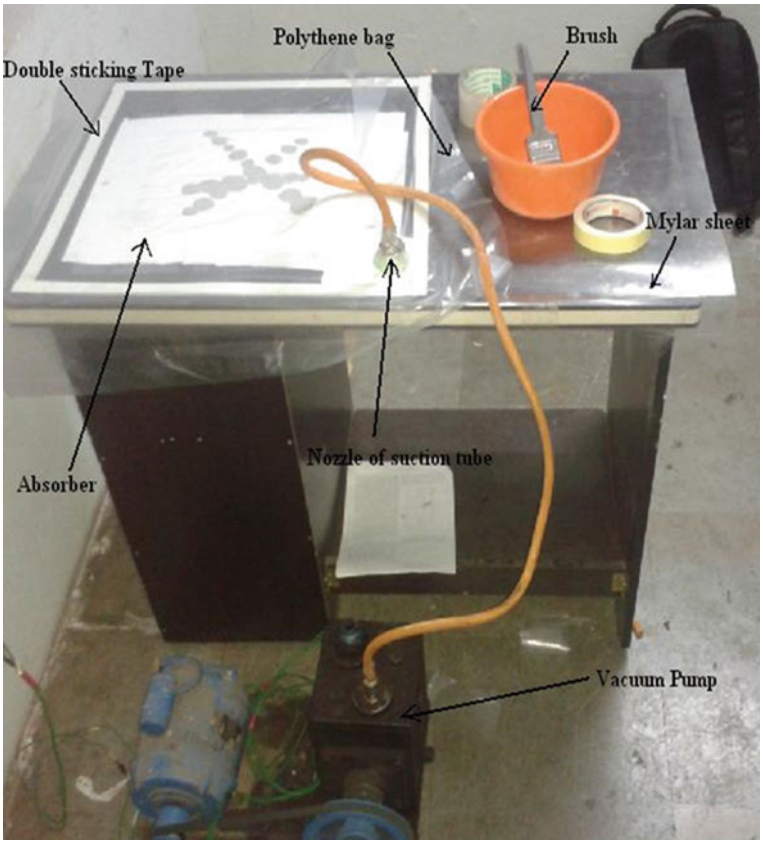

Fig. 3 Experimental set-up for preparation of composite specimen

Fig. 4 Fabricated composite specimens

4.2 Experimental Testing

Mostly for analysing the vibrational response of the system, free-free condition is considered. For evaluating the statistical energy parameters, the specimen was excited using an impact hammer. The accelerometer was placed on the surface of specimen which requires being excited. The output signals generating from an accelerometer were transmitted as an input to the data acquisition system (FFT analyzer). The data acquisition system connected with the personal computer is used to visualize different spectrums such as time domain and frequency domain. The frequency spectrum is used to estimate the SEA parameters. The schematic set-up used for the experimental study is as depicted in Fig. 5.

In the present work, in order to estimate the SEA parameters for undamped plates, plates comprised of different materials have been considered. The materials used in this study for fabricating the plates are listed in Table 1. In the case of composite specimens, to analyse the effect of different fibre orientations on the SEA parameters, the composite specimen is prepared to employ different fibre orientations and listed in Table 2. As per the described procedure, the vibrational response for the considered specimens examined experimentally and the output responses are recorded. The estimation of each SAE parameter is explained with the help of the sample spectrum.

4.2.1 Modal Density

The composite plates fabricated employing various fibre orientations in order to analyse the effect of fibre orientations onto the modal density. In multimodal systems, modal density generally evaluated in selected frequency bands such as full octave bands, 1/3rd octave bands or bands with equal spaced bandwidths. Majorly, the

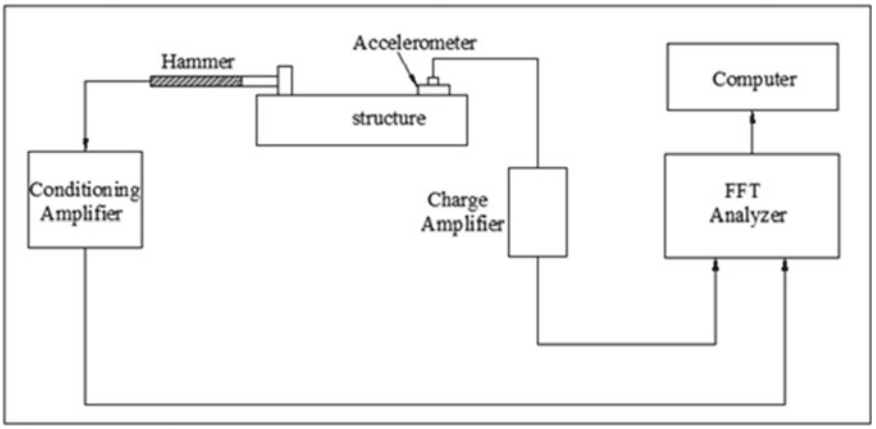

Fig. 5 Schematic set-up for evaluation of SEA parameters

Table 1 Material properties of the plates

Sr. no	Material	Breadth (*a*) (mm)	Width (*b*) (mm)	Thickness (*h*) (mm)	Density(ρ) (kg/m^3)	Poisson's ratio (ν)
1	Mild steel	400	305	2	7023.15	0.3
2	Aluminium	400	305	2	2601.04	0.33
3	Stainless steel	400	305	2	7982.72	0.3

Table 2 Details of material and fibre orientations used for preparations of composite specimens

Sr. no	Materials	Fibre orientations	Dimensions *a*, *b*, *h*) (mm)
1	E-Glass Epoxy (10% E-Glass fibres, LY556 Epoxy resin)	$[0]_{12}$ (unidirectional orientation)	305 × 400 × 2
2	E-Glass Epoxy (10% E-Glass fibres, LY556 Epoxy resin)	$[0_3, \pm 45, 90]_s$ (Quasi-isotropic orientation)	305 × 400 × 2
3	E-Glass Epoxy (10% E-Glass fibres, LY556 Epoxy resin)	$[(0,90)_2, 0, 90]_s$ (cross ply orientation)	305 × 400 × 2

energy transfer and energy loss take place at the natural frequencies. Hence, in order to keep the estimated modal density statistically relevant, the bandwidth required to be chosen in such a way that the frequency band should at least contain few modes in it. In this present study, the modal densities are evaluated considering full octave band.

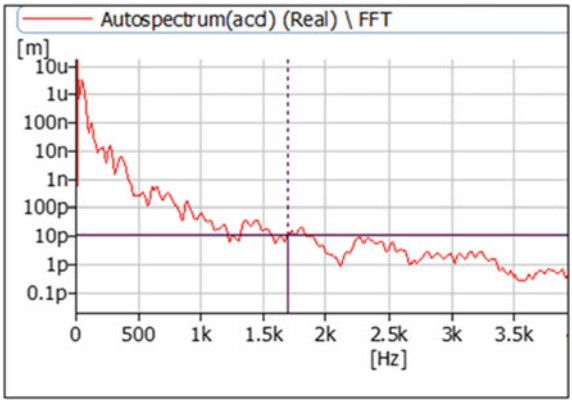

Fig. 6 Amplitude versus frequency sample spectrum for 10LY556 (0)

For sample, calculations amplitude versus frequency sample spectrum for E-Glass Epoxy (10% E-Glass fibres, LY556 Epoxy resin) designated by 10LY556 (0) is considered as shown in Fig. 6. For comparing the vibro-acoustic behaviour of the specimen made with composite and conventional materials, the identical size of the specimen (i.e. plate with equal length, breadth and width) has been considered.

In order to estimate the modal density, the numbers of resonating modes within the particular frequency band were measured. The modal density is obtained from the ratio of the number of resonating modes to the length of a particular frequency band. The modal density comparison obtained for composite as well as conventional materials such as mild steel, aluminium, and stainless steel is shown in Fig. 7.

In case of conventional materials, aluminium plate has higher values of modal density than stainless steel and mild steel plates for free-free boundary conditions. The modal density of composite specimen is lower compared to the conventional once since their material properties such as young's modulus, density, etc., are different. Further in case of composite plates to found the effect of different fibre orientations on modal density, composite specimens comprised of different fibre orientations have been considered as depicted in Fig. 8. The composite plates considered are E-Glass Epoxy (10% E-Glass fibres, LY556 Epoxy resin) $[0]_{12}$ (unidirectional orientation), $[0_3, \pm 45, 90]_s$ (Quasi-isotropic orientation), $[(0,90)_2, 0, 90]_s$ (cross-ply orientation).

Figure 8 clearly depicts the effect of different fibre orientations on the modal density of composite plates. It has been observed that modal density for cross-ply as well as quasi-isotropic orientation is lower than that of the unidirectional fibre orientation. This study demonstrates that in the case of composite specimens, the fibre orientations play a remarkable role to enhance the damping property of the material.

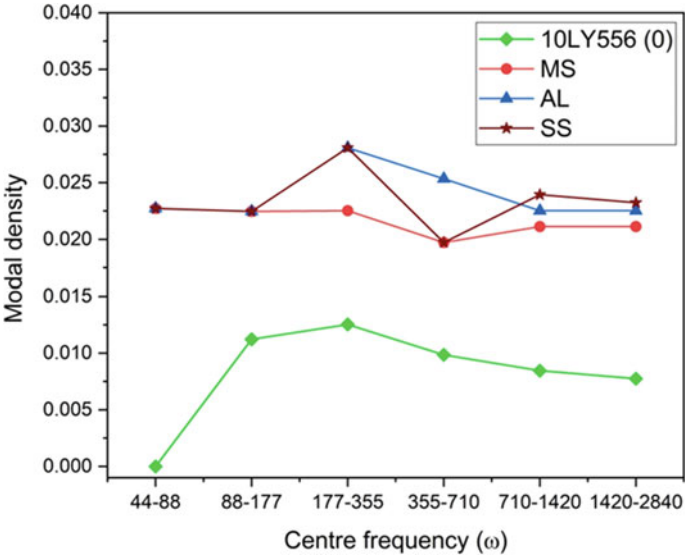

Fig. 7 Comparison of modal density of composite plate with conventional materials such as MS, AL, SS

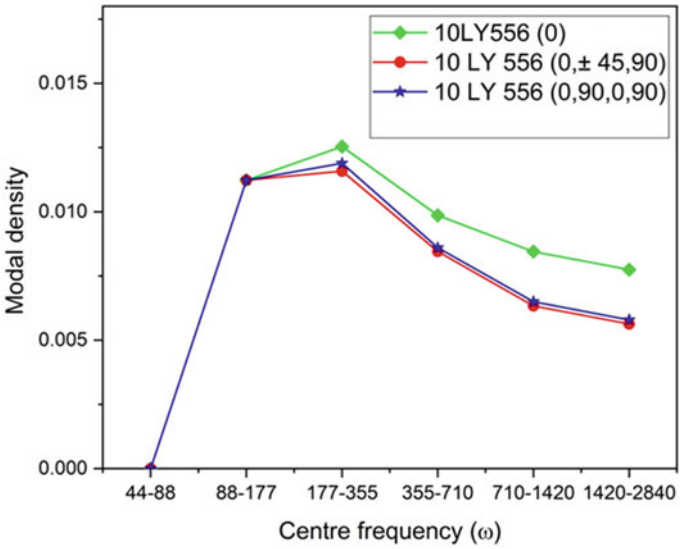

Fig. 8 Variation in modal density of composite plates with different fibre orientations

4.2.2 Damping Loss Factor (DLF)

The damping property of a system can be estimated employing a simplest method by Wang et al. [30] carrying out by measuring frequency bandwidth between the points resting on a characteristic curve. As depicted in Fig. 9, points A_1 and A_2 which are located at frequencies, having the amplitude value $1/\sqrt{2}$ times the maximum amplitude. Generally the bandwidth at these points is defined as 'half-power bandwidth'. In case of low damping, for half-power points locations (i.e. 3 dB) corresponds to the frequencies $\omega_1 = \omega_n(1 + \zeta)$ and $\omega_2 = \omega_n(1 - \zeta)$ where 'ζ' is the damping ratio. The interval between these two half-power points is $\Delta\omega = \omega_2 - \omega_1$. The DLF by this method can be estimated as follows,

The estimation of DLF is explained with the help of sample spectrum as depicted in Figs. 10 and 11. The similar process is adopted for all the remaining composite specimens.

Maximum amplitude $(A) = 3.367$ μm

$$\frac{A}{\sqrt{2}} = \frac{3.367}{\sqrt{2}} = 2.3808 \text{ μm}$$

$$\omega_1 = 44.51 \text{ Hz}$$

$$\omega_2 = 62.58 \text{ Hz}$$

$$\omega = 50 \text{ Hz}$$

$$\eta = \frac{\omega_2 - \omega_1}{\omega}$$

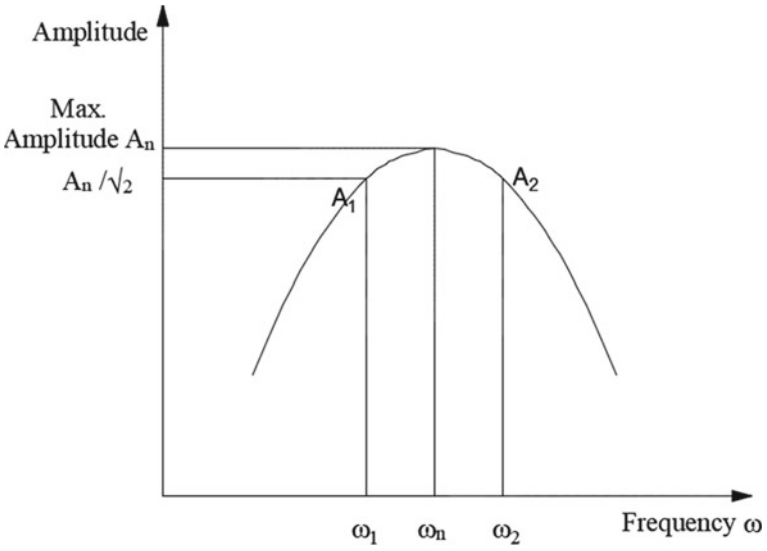

Fig. 9 Estimation of damping loss factor using half-power bandwidth method

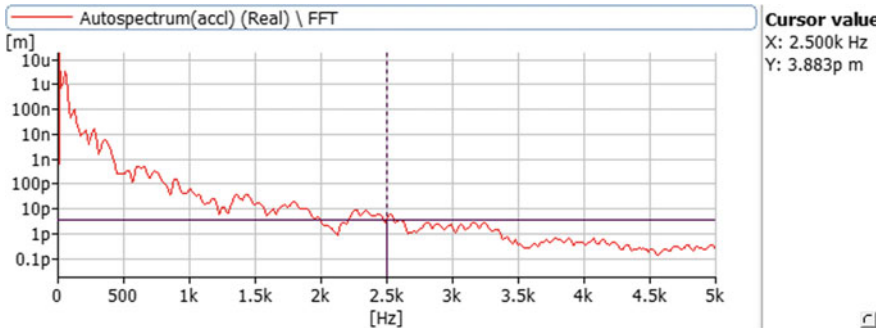

Fig. 10 Amplitude versus frequency sample spectrum for 10LY556 (0)

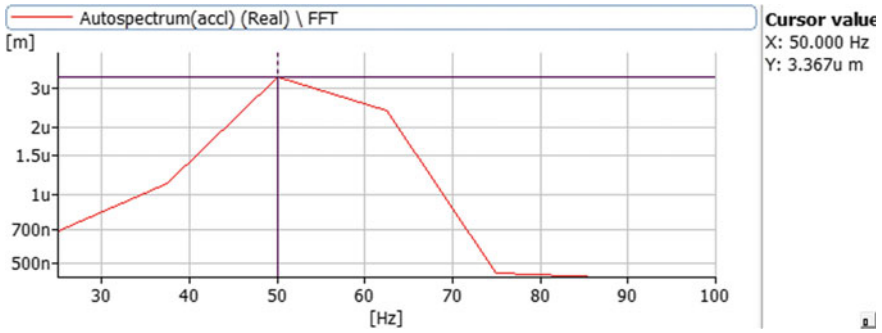

Fig. 11 Single peak considered for evaluation of damping loss factor

$$\eta = 0.3615$$

The DLF for previously reported materials have been evaluated considering free-free conditions. Aluminium plate exhibits higher values of DLF than stainless steel and mild steel plates. The comparison of DLF for the composite plate with conventional materials such as mild steel, aluminium, and stainless steel is shown in Fig. 12. The test results reveal that DLF for composite plate is higher than that for the conventional plate materials due to the difference in damping capacity of the material.

Further in case of composite plates to found the effect of various fibre orientations on DLF; plates with different fibre orientations have been considered as depicted in Fig. 13.

The test results show that the composite plate with unidirectional fibre orientation has higher DLF than cross-ply fibre orientation and quasi-isotropic fibre orientation plates. Unidirectional fibre orientation helps to improve the capacity to dissipative energy. The experimental study of DLF helps to design of structural component for specific applications.

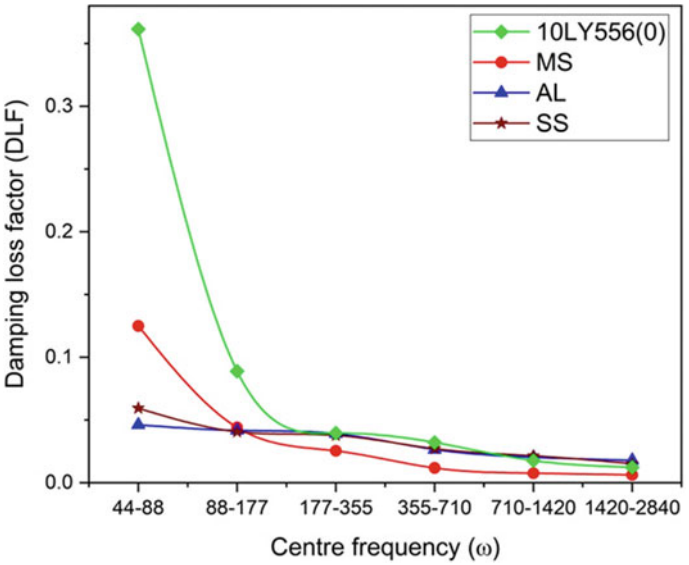

Fig. 12 Damping loss factor comparison of composite plate with conventional materials such as MS, Al, SS

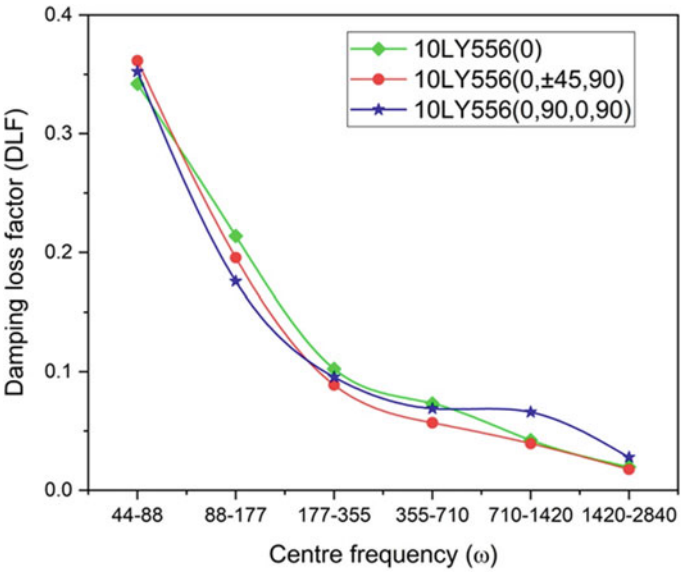

Fig. 13 Variation in damping loss factor of composite plates with different fibre orientations

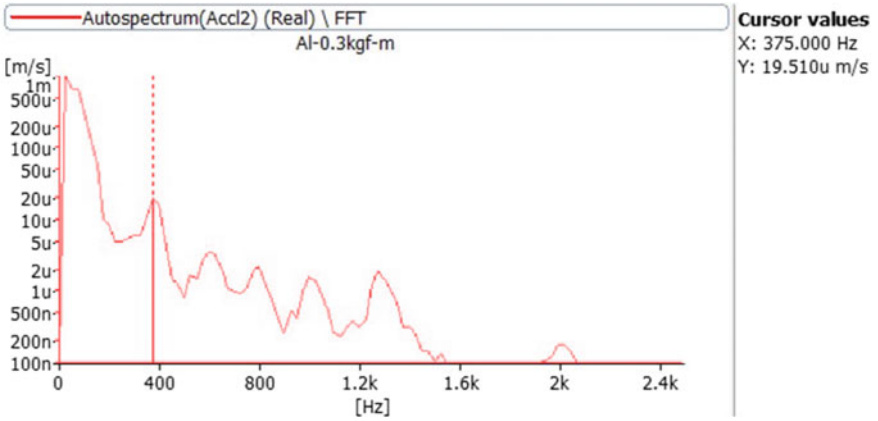

Fig. 14 Amplitude versus frequency sample spectrum for Aluminium plates with bolted junction

4.2.3 Coupling Loss Factor (CLF)

The CLF for the composite specimens which are in the same plane are evaluated by using energy level difference method. The vibrational energy (E) is estimated corresponds to 50 Hz frequency. The velocity values are obtained from an auto-spectrum of accelerometer 1 and 2 corresponds to 50 Hz frequency. The values of CLF for aluminium plates connected with bolted junctions have been evaluated. For sample calculation of the CLF, the sample spectrum is considered as depicted in Fig. 14.

The sample calculations for the value of CLF is given as,

$$
\begin{aligned}
E_2 &= M * V^2 \\
E_2 &= (0.648) * (1.22\mathrm{e}^{-4})^2 \\
E_2 &= 9.65\mathrm{e}^{-9}\mathrm{J} \\
E_1 &= 1.13\mathrm{e}^{-7}\mathrm{J} \\
\eta_{12} &= \eta_2 * \frac{E_2}{E_1} \\
\eta_{12} &= 0.57 * \left(\frac{9.65\mathrm{e}^{-9}}{1.13\mathrm{e}^{-7}}\right) \\
\eta_{12} &= 0.05
\end{aligned}
$$

The comparison of CLF for composite plates and plates with conventional material such as aluminium connected with a bolted junction is depicted in Fig. 15.

The test results reveal that the CLF of a composite specimen is higher than that of conventional Aluminium plates. The ratio of young's modulus to the density of plate material significantly affects the CLF. Further in case of composite plates, to

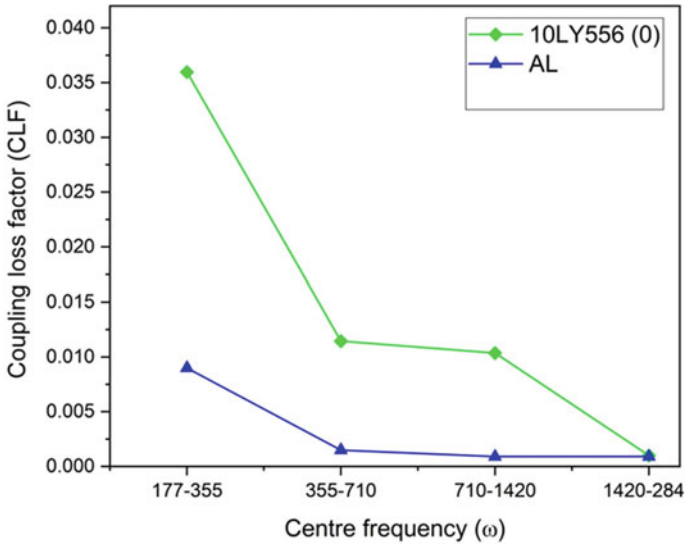

Fig. 15 Coupling loss factor comparisons for composite plates and plates with conventional material such as aluminium connected with bolted junction

investigate the effect of different fibre orientations on CLF, composite plates with different fibre orientations have been considered as depicted in Fig. 16. The composite plate with cross-ply fibre orientations exhibits higher CLF compared to unidirectional and quasi-isotropic fibre orientations. This indicates that due to the implementation of cross-ply and quasi-isotropic fibre orientation improves the damping capacity of the composite specimen which results in lower CLF values.

5 Conclusion and Future Scope

The SEA approach which is easy and economical can be employed to carry out a dynamic analysis of various structural elements. The SEA parameters like modal density, DLF, and CLF can be effectively predicted employing SEA approach. In this work, theoretical expressions for SEA concerning modal densities, DLF, and CLF have been presented.

To determine the effect of material properties such as young's modulus, density, and damping capacity on SEA parameters different conventional materials like mild steel, stainless steel, aluminium, and composites with different fibre orientations have been experimentally tested. Modal density is useful to give insight into the vibro-acoustic analysis of structures when subjected to random excitations without complete knowledge of frequencies and mode shapes. In case of conventional materials, aluminium plate has higher values of modal density than stainless steel and

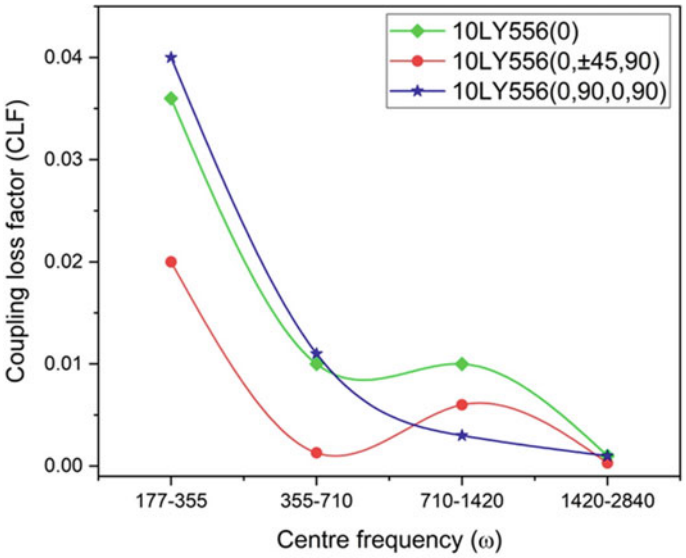

Fig. 16 Variation in coupling loss factor of composite plates employed with different fibre orientations and connected with bolted junction

mild steel plates for free-free boundary conditions. The young's modulus and density of material affect the values of modal density. In case of composite specimens with different fibre orientations, the unidirectional fibre orientation plate has higher values of modal density than quasi-isotropic and cross-ply fibre orientation plates for free-free boundary conditions. Knowledge of modal density with fibre orientations and boundary conditions aid the designer in the optimal design of the structure.

The damping loss factor of a material is related to the damping capacity which depends on different factors like the molecular structure, the loading rate, the strain distribution, and temperature. The damping loss factors for previously reported materials have been evaluated considering free-free conditions. Aluminium plate exhibits higher values of the damping loss factor than stainless steel and mild steel plates for free-free boundary conditions. The density of material affects the values of the damping loss factor. Unidirectional fibre orientation plate has higher damping loss factors than cross-ply fibre orientation and quasi-isotropic fibre orientation plates. Unidirectional fibre orientation helps to improve the capacity to dissipative energy. The experimental study of damping loss factor helps to design of structural component for specific applications.

The coupling loss factor of a system deals with the noise and vibration level. The prediction of coupling loss factor is very helpful at the design phase. The composite plates with bolted junction exhibit higher coupling loss factor than the aluminium plates. The ratio of young's modulus to the density of plate material affects the values of coupling loss factor. The magnitude of coupling loss factor changes with fibre orientation in case of composite specimens. The values of CLF are significant

at low as well as mid-frequency range. However, its values are negligible at higher frequency range. The experimental test shows that in case of composite plates, the CLF is higher for cross-ply fibre orientation as compared to unidirectional fibre orientation.

Further studies can be carried out to understand the influence of strength of connecting elements such as riveted, screwed, and welded in structural junctions on statistical energy analysis parameters. This study can be further extended for designing the composite structures with suitable nano-fillers to alter statistical energy analysis parameters as per the requirement.

References

1. Bachoo R, Bridge J (2013) The modal distribution and density of fibre reinforced composite beams. J Sound Vib 332(8):2000–2018
2. Borgaonkar AV, Mandale MB, Potdar SB (2018) Effect of changes in fiber orientations on modal density of fiberglass composite plates. Mater Today: Proc 5(2):5783–5791
3. Borgaonkar AV, Mandale MB, Salunkhe VG, Potdar SB (2019) Experimental investigations of different fiber orientations on damping loss factor of fiberglass composite specimens. Mater Today: Proc.
4. Chandra R, Singh SP, Gupta K (2003) Experimental evaluation of damping of fiber-reinforced composites. J Compos Tech Res 25(2):1–12
5. Cheng CY, Shyu RJ, Liou DY (2007) Statistical energy analysis of non-resonant response of isotropic and orthotropic plates. J Mech Sci Technol 21(12):2082
6. Cotoni V, Langley RS, Shorter PJ (2008) A statistical energy analysis subsystem formulation using finite element and periodic structure theory. J Sound Vib 318(4–5):1077–1108
7. Elie B, Gautier F, David B (2013) Estimation of mechanical properties of panels based on modal density and mean mobility measurements. Mech Syst Signal Process 40(2):628–644
8. Fahy FJ, Gardonio P (2007) Sound and structural vibration: radiation, transmission and response. Elsevier.
9. Finnveden S (2004) Evaluation of modal density and group velocity by a finite element method. J Sound Vib 273(1–2):51–75
10. Grushetsky I, Smolnikov A (2006) Computing of coupling loss factors using FEM, probabilistic approach. Electron J Tech Acoust 10
11. Han J, Yu K, Li X, Zhao R (2015) Modal density of sandwich panels based on an improved ordinary sandwich panel theory. Compos Struct 131:927–938
12. Hopkins C (2002) Statistical energy analysis of coupled plate systems with low modal density and low modal overlap. J Sound Vib 251(2):193–214
13. Iwaniec M (2003) Damping loss factor estimation in plates. Mol Quant Acoust 24:61–68
14. Ji L, Huang Z (2014) A simple statistical energy analysis technique on modeling continuous coupling interfaces. J Vib Acoust 136(1):014501
15. Le Bot A (2015) Foundation of statistical energy analysis in vibroacoustics. OUP Oxford.
16. Liu W, Ewing MS (2007) Experimental and analytical estimation of loss factors by the power input method. AIAA J 45(2):477–484
17. Lyon RH, DeJong RG, Heckl M (1995) Theory and application of statistical energy analysis.
18. Ma YC, Bolton JS, Jeong H, Ahn B, Shin C (2002) Experimental statistical energy analysis applied to a rolling piston-type rotary compressor.
19. Mace B (2003) Statistical energy analysis, energy distribution models and system modes. J Sound Vib 264(2):391–409
20. Mace BR (2005) Statistical energy analysis: coupling loss factors, indirect coupling and system modes. J Sound Vib 279(1–2):141–170

21. Mandal NK, Rahman RA, Leong MS (2004) Experimental study on loss factor for corrugated plates by bandwidth method. Ocean Eng 31(10):1313–1323
22. Maxit L, Guyader JL (2001) Estimation of SEA coupling loss factors using a dual formulation and FEM modal information, part I: theory. J Sound Vib 239(5):907–930
23. Panuszka R, Wiciak J, Iwaniec M (2005) Experimental assessment of coupling loss factors of thin rectangular plates. Arch Acoust 30(4):533–551
24. Ramachandran P, Narayanan S (2007) Evaluation of modal density, radiation efficiency and acoustic response of longitudinally stiffened cylindrical shell. J Sound Vib 304(1–2):154–174
25. Renji K (2000) Experimental modal densities of honeycomb sandwich panels at high frequencies. J Sound Vib 237(1):67–79
26. Secgin A (2013) Numerical determination of statistical energy analysis parameters of directly coupled composite plates using a modal-based approach. J Sound Vib 332(2):361–377
27. Sheng MP, Wang MQ, Sun JC, Qian B (2004) Statistical energy analysis for complicated coupled system and its application in engineering. J Sound Vib 274(3–5):877–891
28. Tager O, Dannemann M, Hufenbach WA (2015) Analytical study of the structural-dynamics and sound radiation of anisotropic multilayered fibre-reinforced composites. J Sound Vib 342:57–74
29. Vatti K (2011) Damping estimation of plates for statistical energy analysis. Doctoral dissertation, University of Kansas
30. Wang A, Yin X, Li X, Chen L (2013) Numerical and experimental study on modal damping loss factor of structural panels with damping treatments. In: 20th international congress on sound and vibration
31. Wilson D, Hopkins C (2015) Analysis of bending wave transmission using beam tracing with advanced statistical energy analysis for periodic box-like structures affected by spatial filtering. J Sound Vib 341:138–161
32. Xie G, Thompson DJ, Jones CJC (2004) Mode count and modal density of structural systems: relationships with boundary conditions. J Sound Vib 274(3–5):621–651
33. Xie Z, Shepard WS Jr (2009) An enhanced beam model for constrained layer damping and a parameter study of damping contribution. J Sound Vib 319(3–5):1271–1284
34. Yoo JW, Thompson DJ, Ferguson NS (2007) Investigation of beam-plate systems including indirect Coupling in terms of Statistical Energy Analysis. J Mech Sci Technol 21(5):723

Chapter 13
Surrogate Model Validation and Verification for Random Failure Analyses of Composites

Subrata Kushari, Arunasis Chakraborty, Tanmoy Mukhyopadhyay, Ravi Ranjan Kumar, Saiket Ranjan Maity, and Sudip Dey

1 Introduction

The laminated composite is one of the most prominent forms of fibre-reinforced composites where in the lay-up technique is utilized to sequentially arrange unidirectionally reinforced plies. Each ply is typically a thin sheet of fibres combined with an epoxy or other resin-based thermosetting or thermoplastic material. The orientation of each ply is made according to the desired properties and its application. A plenty of application of laminated composites can be observed, especially for aerospace, marine, ground transport, building and architectural purposes. Carbon fibre laminate has extensive applications in the satellite structure due to its high specific stiffness which ensures dimensional stability, along with high stiffness. It also possesses a negligible coefficient of thermal expansion which enables it to withstand huge fluctuation of temperature in space. In space-based application, the thermosetting material plays a vital role. The epoxy-based resin is not preferred in space application because of moisture formation at low atmospheric pressure than that of the earth. It can be resolved by replacing epoxy-based resins with isocyanates-based resin which has low hygroscopic property [3]. In the locomotive sectors, the laminated composites has

S. Kushari (✉) · S. Ranjan Maity · S. Dey
National Institute of Technology Silchar, Silchar, India
e-mail: subrata734@gmail.com

A. Chakraborty
Indian Institute of Technology Guwahati, Guwahati, India

T. Mukhyopadhyay
Indian Institute of Technology Kanpur, Kanpur, India

R. Ranjan Kumar
Jawaharlal Nehru University, Delhi, India

S. Sahoo (ed.), *Recent Advances in Layered Materials and Structures*,
Materials Horizons: From Nature to Nanomaterials,
https://doi.org/10.1007/978-981-33-4550-8_13

wide range of applications such as, in cars, lorries, aircraft, subway trains, boats, helicopters and trams. Composites are preferred in these industries because of its flexibility to produce complex and designable shapes at economic cost. The computational study of three-dimensional laminated composites is complex and time-consuming. In order to achieve computational efficiency, the classical theories are considered as the benchmark to verify the related theories which help in reducing the dimension for complex analysis. In past, various theories such as higher-order shear deformation plate theories (HSDT) [55], layer-wise theories and hierarchic plate theories [43] are developed for laminates [44] and shells to reduce the computational time. HSDT is one of the significant theories (Phan and Reddy 1985) which can evaluate free vibration, buckling and bending of a laminate composite. It is further validated with the classical laminate theory. This theory provided an improvement from first-order shear deformation theory (FSDT) [57].The shear correction factor is necessary in order to calculate shear deformation, coupling, material anisotropy, deflections, frequencies and buckling loads which depended on the detailed lamination scheme. On the other hand, HSDT provides no hassle of shear correction factor. This theory provides a pathway for future researchers to develop complex computational model for laminated composites with comparatively fewer complexities. The displacement components in hierarchic plate theories represent a hierarchic or zig-zag pattern along its thickness for a laminated plate [1, 2].

The failure analysis of laminated composites is an important aspect from design point of view. All the important parameters can be considered, and the exhaustive analysis is essential to characterize the root-cause behind the failure of the laminates. Some of the important parameters in analysing the failure of a laminates are elastic modulus, shear modulus, density and Poisson's ratio. A detailed study about the world-wide failure in composites can be observed in Hinton et al. [21]. In order to characterize the failure of laminated plates, various theories and models are developed, but most of them are confined in the deterministic regime. Some of the important research work and books in the current field are Onkar et al. [52], Hélénon et al. [20], Torabi et al. [65], Talreja et al. [62, 63]. A finite element model (FEM) for laminated plate is proposed by Tolson and Zabaras [64] where in seven degrees of freedom (DOF) are considered for determining the laminate stress and based on that first-ply failure as well as last-ply failure are deduced. The effect of progressive failure [58] considering the effects of scratch geometry under tensile stress, its effect on failure propagation response and crack propagation level is analysed. In a chemical composition analysis of glass fibre by Hossain [17], it is proposed that among boron-free E-glass, AR-glass, E-glass and C-glass, AR-glass is highly corrosion and temperature resistant in similar situations. Hochard and Thollon [22] devised a model to analyse the failure of a laminated plate considering stress concentrations due to static and fatigue loads. In another investigation by Zubillaga et al. [68], the factor of delamination is considered to propose a new failure criterion for prediction of matrix cracking under the effects of delamination. The effects of preload moment under the application of traction force are investigated by Kapti et al. [25] for failure mode in bolted and pin-jointed laminated plates made of carbon–epoxy. It is suggested

that the ultimate failure loads are directly influenced under the variation of interference fit, geometrical parameters and preload moments. It is also suggested that there is an increment in the rate of failure under preload moments in wet condition; on the other hand, there are no significant effects for non-preloaded specimen. Miguel et al. [7] evaluated the failure indices using Hashin's three-dimensional failure criterion for 1D and 3D elements. The out-of-plane stress components are considered to predict the failure load accurately. Another interesting damage analysis for carbon fibre laminates is investigated by Sun and Hallett [61] where the damage tolerance is analysed. The extreme ply strain after the delamination is observed to increase to a fatal point due to failure of the ply in laminated composite plates. Most of the studies concerning failure analysis of composites are carried out in the deterministic regime. In this chapter, we aim to focus on the computational aspects of a comprehensive stochastic analysis using surrogate approach.

2 Brief Literature Review on Stochastic Analyses of Composite Laminates

The uncertainty which influences the failure of material must be analysed with proper quantifiable approach; i.e., for the safe and economical design of the material it is important to consider the uncertainty in material and geometric properties [9]. Deterministic analysis of failure for laminates provides the mean value or exact value for every input value according to the mode of the operation, but in order to analyse the detailed output value for failure load, extensive investigation in probabilistic regime is necessary. It provides a much broader perspective. Some of the noteworthy research accomplished following probabilistic approach is mentioned hereon. The probability density function and power spectrum density is employed by Chen et al. [4] for stochastic analysis of carbon fibre-based composite under the effect of probabilistic fatigue load. The developed model predicts the failure probability with respect to time at better computational efficiency. A novel stochastic method is developed in order to analyse the ballistic projectile impact [53], and the MCS results are compared with Gaussian process response surface method. It is suggested that the current method is computationally efficient compared to the traditional MCS which requires a very high number of sample size. Chen and Qiu [5] proposed a novel stochastic approach using polynomial chaos expansion (PCE) method in order to investigate the effect of mixed uncertainties on account of interval variables and normal-random variables. The first-ply failure of laminates under the effect of spatial variation is analysed by Karsh et al. [26] wherein MCS is employed in order to analyse the failure strength of laminate and its effects are shown by using probability distribution function. The critical stress intensity factor for solo edge notched fibre-reinforced composite plates [41] having arbitrary material properties under uniaxial tensile loadings are investigated. Hashin's failure criterion is adopted to determine the tensile load for the laminated plate. Lal et al. [42] investigated the second-order statistics of critical

stress intensity factor by increasing the input parameters in order to achieve higher efficiency. Various effects like length of crack formation, ply orientation, thickness of the plate are evaluated, and the results are validated with MCS. Stochastic failure analysis is performed on composite pipes [54] under the effect of random excitation of white noise. The root mean square of on-axis stress and power spectral density function was applied to evaluate the failure of the pipe. The effects of resin pockets for failure development and transverse stiffness are studied by Ghayoor et al. [18]. Resin pockets are formed due to multiple layers of resins between the plies of a single-layer laminate. Samples are prepared with and without developed resin pockets. The results reveal that the samples induced with resin pockets exhibits significant reduction in the failure initiation strain in the matrix. Layer-wise uncertainty propagation scheme is considered for the analysis of vibration response due to variation in combined as well as individual stochastic input parameters [11]. Here, generalized high-dimensional model representation and diffeomorphic modulation under observable response preserving homotopy regression is considered as the surrogate model. It is observed that the computational time is reduced drastically. Rotational and ply-level uncertainty is quantified for random natural frequency in a composite laminate shell by incorporating central composite design as the surrogate model [13]. Sensitivity analyses is carried for the same, and it is found that ply orientation angle is highly sensitive for first and second outermost layer compared to the middle layers. Reliability-based optimization is analysed in order to optimize width and thickness of laminated composite spherical shell. Genetic algorithm and D-optimal design is incorporated for weight reduction and avoiding resonance by Dey et al. [10]. The effect of noise on metamodel-based random natural frequency analysis of laminated plates is studied by Mukhopadhyay et al. [48]. Stochastic investigation is carried out for curved laminated panels based on support vector regression model in conjunction with Latin hypercube sampling [14]. A critical comparison is accomplished for surrogate models due to uncertainty in natural frequencies of laminated plates, and results are validated with Monte Carlo simulation [8]. A detailed comparison for pre-twisted functionally graded plates is analysed by Karsh et al. [27] by incorporating polynomial neural network (PNN) and artificial neural network (ANN) in stochastic regime. It is found that ANN is more suitable to analyse the uncertainty in natural frequency. The effect of delamination is investigated by Mukhopadhyay et al. [46] by incorporating a hybrid high-dimensional model representation as a surrogate model along with probabilistic finite element model. A damage identification method is developed for web core fibre-reinforced polymer composite by incorporating MARS along with multi-objective goal-attainment optimization algorithm in order to identify the damages in composite structures [47]. Similarly, MARS is incorporated as a metamodel by Dey et al. [12] for dynamics and stability analysis of sandwich plates. Fuzzy-based multi-scale uncertainty propagation framework is developed for stability and dynamic analysis for composite laminate plates by incorporating radial basis function as a metamodel for spatially varying material properties [51]. The results reveal that the developed model portrays lower fuzzy bounds for global response as compared to conventional approach. MARS is incorporated as a surrogate model to quantify low-velocity impact responses due to twist in the plate

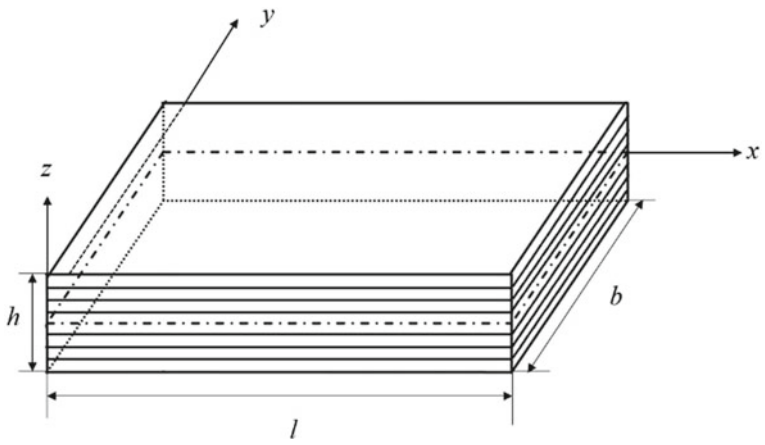

Fig. 1 Geometric view of a laminated plate

geometry and obliqueness in impact angle [34]. Genetic programming along with D-optimal design is incorporated to analyse multi-scale optimization problems of composites [24]. The results show that the incorporation of metamodel significantly reduced the computational costs. A detailed study of surrogate-based approach in quantifying uncertainty can be found in Dey et al. [15], Karsh et al. [28–32], Kumar et al. [35–40] and Naskar et al. [49–51]. It is important to analyse the uncertainty in the physical and geometrical parameters involved for the quantification of the failure in the ply of the laminate. A minute change in the input parameter might result in unreasonable effects in the failure of the component. These effects can be analysed in the probabilistic study for the failure initiation of the component unlike in deterministic analysis. Hence, it is of paramount importance to do stochastic analysis for the failure of the laminated plate so that the uncertainty in parameters can be quantified. In this chapter, the effects of uncertainty in the failure initiation of first ply of the laminate are presented using an efficient surrogate model. Figure 1 shows a geometric view of the laminated plate along with the direction of its axis.

3 Governing Equations

The classical laminate plate theory (CLPT) is employed to form the load intensity equation for a laminated plate. This theory provides the foundation for the minimum total potential energy theorem which is used for the structural analysis of laminated plate through finite element modelling approach. The summation of total strain energy and total work potential gives us the total potential energy of the plate on account of external forces. The total potential energy (T) is expressed as:

$$T = S + W \tag{1}$$

where the total strain energy (S) is the total volume integral

$$S = \frac{1}{2} \int_v \{\sigma\}\{s\}^{\mathrm{T}} \mathrm{d}v \tag{2}$$

where S implies the total strain energy, $\{s\}$ implies the strain vector, $\{\sigma\}$ symbolises the stress vector and 'v' is the volume integral for the overall laminate plate.

For externally applied load, the total amount of work done can be defined as an integral of the total area

$$W = \iint_A [u]^{\mathrm{T}}[q]\mathrm{d}A \tag{3}$$

where

$$q = \{0\ 0\ q_z\ 0\ 0\}^{\mathrm{T}} \tag{4}$$

q_z = load intensity of laminate.

The final equation for the laminate can be given by:

$$[F] = [\varepsilon][D] \tag{5}$$

where

F = final stress vector

ε = strain vector

D = elastic matrix of the laminate

For the present first-ply failure (FPF), macroscopic analysis of the laminate with the ply orientation of [45°, −45°, 45°, −45°]s is considered. The graphite fibre of the laminate is considered to be parallel and unidirectional. The loads in which the ply fails are considered linear in nature as it reduces the iteration process and minimizes the complexity of the mathematical formulation. The failure criteria for laminated plate are established on the basis of tensor polynomial criteria given by Tsai et al. [67].

$$F_i\sigma_i + F_{ij}\sigma_i\sigma_j + F_{ijk}\sigma_i\sigma_j\sigma_k + \cdots \geq 1 \tag{6}$$

According to the number of the axis of laminate, Eq. (6) can be expressed as follows:

$$\begin{aligned} &F_1\sigma_1 + F_2\sigma_2 + F_3\sigma_3 + 2F_{12}\sigma_1\sigma_2 + 2F_{13}\sigma_1\sigma_3 + 2F_{23}\sigma_2\sigma_3 \\ &\quad + F_{11}\sigma_1^2 + F_{11}\sigma_1^2 + F_{22}\sigma_2^2 + F_{33}\sigma_3^2 + F_{44}\sigma_4^2 + F_{55}\sigma_5^2 + F_{66}\sigma_6^2 \cdots \geq 1\pi \end{aligned} \tag{7}$$

where F_i and F_{ij} are the first-order and fourth-order strength tensors of the material. Here, σ_i denotes the difference between compressive and tensile induced stress. The term $\sigma_i \sigma_j$ defines an ellipsoid along with the stress space. On the basis of tensor polynomial criteria, the five failure criteria, i.e. maximum strain theory, Hoffman theory, Tsai–Hill theory, maximum stress theory, Tsai–Wu theory is modelled.

1. **Maximum stress theory**
   The maximum stress theory [66] states that a particular material reaches its yielding point when its principal stress in a tri-axial system reaches its yield value due to external application of tension. Here, normal stress components are represented by $\sigma_1, \sigma_2, \sigma_3$, whereas $\sigma_4, \sigma_5, \sigma_6$ implies shear stress components; X_t, Y_t, Z_t implies normal strengths of lamina along the 1, 2 and 3 directions for tensile strengths and X_c, Y_c, Z_c for compressive strengths. Shear strain strengths can be represented by T, R and S for planes 1–2, 2–3 and 1–3. In tensor polynomial form, it can be expressed as:

$$(\sigma_1 - X_t)(\sigma_1 + X_c)(\sigma_2 - Y_t)(\sigma_2 + Y_c)(\sigma_3 - Z_t)(\sigma_3 + Z_c) \\ (\sigma_4 - R)(\sigma_4 + R)(\sigma_5 - S)(\sigma_5 + S)(\sigma_6 - T)(\sigma_6 + T) = 0 \tag{8}$$

   The necessary force components can be calculated by comparing Eqs. (7) and (8) after neglecting the higher-order terms.
2. **Maximum strain theory**
   Maximum strain theory [59] states that a particular material will yield at a point when at least one of the strain components along its principal axis exceeds the equivalent strain component in that particular direction. In tensor polynomial criteria, it can be expressed as follows:

$$(s_1 - X_{st})(s_1 + X_{sc})(s_2 - Y_{st})(s_2 + Y_{sc})(s_3 - Z_{st})(s_3 + Z_{sc}) \\ (s_4 - R_s)(s_4 + R_s)(s_5 - S_s)(s_5 + S_s)(s_6 - T_s)(s_6 + T_s) = 0 \tag{9}$$

   where s_1,$s_2$ands_3 signifies the strain components in principal direction.X_{st}, Y_{st} and Z_{st} represents the components of normal strain along the direction 1, 2 and 3. Similarly, X_{sc}, Y_{sc} and Z_{sc} are compressive strengths. Similar to maximum stress criteria, the force components can be deduced by comparing Eqs. (7) and (9).
3. **Tsai–Hill theory**
   Tsai–Hill theory [45] considers the interaction amo–ng the three unidirectional lamina strength parameter and considers both compressive and tensile strength in its equation. The distortion energy theory is the base for present theory. It can be expressed as

$$\left(\frac{\sigma_1}{X}\right)^2 + \left(\frac{\sigma_2}{Y}\right)^2 + \left(\frac{\sigma_3}{Z}\right)^2 - \sigma_1\sigma_2\left(\frac{1}{X^2} + \frac{1}{Y^2} - \frac{1}{Z^2}\right) - \sigma_1\sigma_3\left(\frac{1}{X^2} - \frac{1}{Y^2} + \frac{1}{Z^2}\right)$$

$$-\sigma_2\sigma_3\left(-\frac{1}{X^2}+\frac{1}{Y^2}+\frac{1}{Z^2}\right)+\left(\frac{\sigma_4}{R}\right)^2+\left(\frac{\sigma_5}{S}\right)^2+\left(\frac{\sigma_6}{T}\right)^2\geq 1 \tag{10}$$

4. **Tsai–Wu (Interaction tensor polynomial) theory**
   The Tsai–Wu failure principle is a special case for general quadratic failure criteria developed by Gol'denblat and Kopnov [19]. In mathematical form, it is given as

$$F_i\sigma_i+F_{ij}\sigma_i\sigma_j\geq 1 \tag{11}$$

   where $F_1=\frac{1}{X_n}-\frac{1}{X_c}$, $F_2=\frac{1}{Y_n}-\frac{1}{Y_c}$, $F_3=\frac{1}{Z_n}-\frac{1}{Z_c}$, $F_{11}=\frac{1}{X_nX_c}$, $F_{22}=\frac{1}{Y_nY_c}$ $F_{55}=\frac{1}{S^2}$, $F_{66}=\frac{1}{T^2}$, $F_{12}=\frac{1}{\sqrt{X_nX_cY_nY_c}}$, $F_{13}=\frac{1}{\sqrt{X_nX_cZ_nZ_c}}$ and $F_{23}=\frac{1}{\sqrt{Y_nY_cZ_nZ_c}}$.
   where i and j iterates from one to six and X_n, Y_n and Z_n represents the normal lamina strengths in 1, 2 and 3 directions for the stress components σ_1, σ_2 and σ_3 while X_c, Y_c and Z_c represents the compressive lamina strengths, respectively.
5. **Tsai–Hill's Hoffman failure criteria**

Tsai–Hill Hoffman failure criteria [23] is the extension of the Tsai–Hill failure criteria where the strength for tension and compression are considered independently. It can be expressed as

$$\begin{aligned}&\frac{1}{2}\left(\frac{1}{Y_tY_c}+\frac{1}{Z_tZ_c}-\frac{1}{X_tX_c}\right)(\sigma_2-\sigma_3)^2+\frac{1}{2}\left(-\frac{1}{X_tX_c}+\frac{1}{Y_tY_c}+\frac{1}{Z_tZ_c}\right)(\sigma_3-\sigma_1)^2\\&+\frac{1}{2}\left(\frac{1}{X_tX_c}+\frac{1}{Y_tY_c}-\frac{1}{Z_tZ_c}\right)(\sigma_1-\sigma_2)^2+\left(\frac{1}{X_t}-\frac{1}{X_c}\right)\sigma_1+\left(\frac{1}{Y_t}-\frac{1}{Y_c}\right)\sigma_2\\&-\left(\frac{1}{Z_t}-\frac{1}{Z_c}\right)\sigma_3+\left(\frac{\sigma_4}{R}\right)^2+\left(\frac{\sigma_5}{S}\right)^2+\left(\frac{\sigma_6}{T}\right)^2\end{aligned} \tag{12}$$

4 Mathematical Modelling

In the present study, the finite element analysis is utilized to mathematically model the first-ply failure load of laminated composite plates. The laminated composite plate model is discretized wherein a single element consists of eight nodes and each node has five degrees of freedom (three translational and two rotational). In order to solve the equations, first-order shear deformation theory (FSDT) is employed. The generalized stress–strain relationship in the principal axis direction of the material (1, 2 and 3) is expressed as

$$\begin{Bmatrix} \sigma_1 \\ \sigma_2 \\ \tau_{12} \\ \tau_{23} \\ \tau_{13} \end{Bmatrix} = \begin{bmatrix} L_{11} & L_{12} & 0 & 0 & 0 \\ L_{21} & L_{22} & 0 & 0 & 0 \\ 0 & 0 & L_{33} & 0 & 0 \\ 0 & 0 & 0 & L_{44} & 0 \\ 0 & 0 & 0 & 0 & L_{55} \end{bmatrix} \begin{Bmatrix} \varepsilon_1 \\ \varepsilon_2 \\ \varepsilon_{12} \\ \varepsilon_{23} \\ \varepsilon_{13} \end{Bmatrix} \tag{13}$$

where

$$L_{11} = \frac{E_1}{1 - \nu_{12}\nu_{21}}, L_{12} = \frac{\nu_{12}E_2}{1 - \nu_{12}\nu_{21}}, L_{22} = \frac{E_2}{1 - \nu_{12}\nu_{21}},$$
$$L_{33} = G_{12}, L_{44} = G_{23}, L_{55} = G_{13}.$$

The generalized equation of the lamina for the three directions (1, 2 and 3) is formulated as

$$\begin{Bmatrix} \sigma_{xx} \\ \sigma_{yy} \\ \tau_{xy} \\ \tau_{yz} \\ \tau_{xz} \end{Bmatrix} = \begin{bmatrix} \overline{L}_{11} & \overline{L}_{12} & \overline{L}_{13} & 0 & 0 \\ \overline{L}_{21} & \overline{L}_{22} & \overline{L}_{23} & 0 & 0 \\ L_{31} & \overline{L}_{32} & \overline{L}_{33} & 0 & 0 \\ 0 & 0 & 0 & \overline{L}_{44} & \overline{L}_{45} \\ 0 & 0 & 0 & \overline{L}_{54} & \overline{L}_{55} \end{bmatrix} \begin{Bmatrix} \varepsilon_{xx} \\ \varepsilon_{yy} \\ \varepsilon_{xy} \\ \varepsilon_{yz} \\ \varepsilon_{xz} \end{Bmatrix}. \tag{14}$$

where

$$\overline{L}_{11} = L_{11}Cos^4\theta + 2(L_{12}+2L_{33})\mathrm{Sin}^2\theta\mathrm{Cos}^2\theta + L_{22}\mathrm{Sin}^4\theta$$
$$\overline{L}_{12} = (L_{11}Q_{22} - 4L_{33}) + \mathrm{Sin}^2\theta\{2(L_{12}+2L_{33})\mathrm{Cos}^2\theta + L_{22}\mathrm{Sin}^2\theta$$
$$\overline{L}_{13} = \mathrm{Sin}\theta\mathrm{Cos}\theta\big\{(L_{11} - L_{12} - 2L_{33})\mathrm{Cos}^2\theta + (L_{12} - L_{22} + 2L_{33})\mathrm{Sin}^2\theta\big\},$$
$$\overline{L}_{22} = \mathrm{Sin}^2\theta\{L_{11}\mathrm{Sin}^2\theta + 2(L_{12} + 2L_{66})\mathrm{Cos}^2\theta\} + L_{22}\mathrm{Cos}^4\theta,$$
$$\overline{L}_{23} = \mathrm{Sin}\theta\mathrm{Cos}\theta\big\{(L_{11} - L_{12} - 2L_{33})\mathrm{Sin}^2\theta + (L_{12} - L_{22} + 2L_{33})\mathrm{Cos}^2\theta\big\},$$
$$\overline{L}_{31} = \mathrm{Sin}^2\theta\mathrm{Cos}^2\theta\big\{(L_{11} + L_{22} - 2L_{12} - 2L_{33}) + L_{33}\big(\mathrm{Sin}^2\theta + \mathrm{Cos}^2\theta\big)\big\},$$
$$\overline{L}_{44} = L_{44}\mathrm{Cos}^2\theta + L_{55}\mathrm{Sin}^2\theta,$$
$$\overline{L}_{55} = L_{55}\mathrm{Cos}^2\theta + L_{44}\mathrm{Sin}^2\theta.$$

From the mid-plane, the displacement in the plane at point (u, v) at distance z can be expressed by

$$u(x, y, z) = u^0(x, y) - z\theta_x(x, y).$$
$$v(x, y, z) = v^0(x, y) - z\theta_y(x, y)$$
$$w(x, y, z) = w^0(x, y) = w(x, y) \tag{15}$$

In Eq. (15), u^0, v^0 and w^0 signifies the displacement of a particular point (x, y) in the z_0 (mid-plane). The resultants due to moment and force for a single lamina can

be expressed as

$$\{F\} = \{N_{xx}N_{yy}N_{xy}M_{xx}M_{yy}M_{xy}Q_{xx}Q_{yy}\}^{\mathrm{T}}$$
$$= \int_{-h/2}^{h/2} \{\sigma_x\sigma_y\tau_{xy}\sigma_x z\sigma_y z\tau_{xy}z\tau_{yz}\tau_{xz}\}^{\mathrm{T}}\mathrm{d}z \tag{16}$$

The stress resultants can be expressed as

$$(N_{xx}, N_{yy}, N_{xy}) = \int_{-\frac{h}{2}}^{\frac{h}{2}} (\sigma_x, \sigma_y, \sigma_{xy},)\mathrm{d}z$$
$$(M_{xx}, M_{yy}, M_{xy}) = \int_{-\frac{h}{2}}^{\frac{h}{2}} (\sigma_x, \sigma_y, \sigma_{xy},)z\mathrm{d}z$$
$$(Q_{xx}, Q_{yy}) = \int_{-\frac{h}{2}}^{\frac{h}{2}} (\sigma_{xz}, \sigma_{yz})\mathrm{d}z$$
$$(Q_{xx}, Q_{yy}) = \int_{-\frac{h}{2}}^{\frac{h}{2}} (\sigma_{xz}, \sigma_{yz})\mathrm{d}z \tag{17}$$

while FSDT together with finite element is utilized to obtain the wide-ranging displacement variables, which can be expressed as:

$$u_0(x, y, t; \xi) = \sum_{j=1}^{m} u_j(t; \xi)\psi_j^e(x, y)$$
$$v_0(x, y, t; \xi) = \sum_{j=1}^{m} v_j(t; \xi)\psi_j^e(x, y)$$
$$w_0(x, y, t; \xi) = \sum_{j=1}^{m} w_j(t; \xi)\psi_j^e(x, y)$$
$$\phi_x(x, y, t; \xi) = \sum_{j=1}^{m} S_j^1(t; \xi)\psi_j^e(x, y)$$
$$\phi_y(x, y, t; \xi) = \sum_{j=1}^{m} S_j^2(t; \xi)\psi_j^e(x, y) \tag{18}$$

where $u_j, v_j\ w_j, S_j^1$ and S_j^2 are values of the nodes for the corresponding displacements. ψ_j^e represents the shape functions or interpolation functions. ξ represents the randomness in the equation, and (ξ, η) shows the principal coordinate system of the principal domain. If the order of the shape functions (ψ_j^e) are same, then the

generalized equation for the whole domain can be formulated as

$$x(\xi, \eta) = \sum_{j=1}^{n} x_j^e \psi_j^e(\xi, \eta)$$
$$y(\xi, \eta) = \sum_{j=1}^{n} y_j^e \psi_j^e(\xi, \eta) \tag{19}$$

The terminologies in Eq. (19) signifies the displacement variables and can be further replaced to formulate a FSDT-based semi-distinct finite element model

$$[F^e] = [K_e][\Delta^e] + [M^e][\ddot{\Delta}^e]$$

while in the matrix form, transverse shear resultant $[Q]$, displacement resultant(in-plane) $[N]$ and resultant due to the moment $[M]$ are formulated as

$$[Q] = \left[A^*\right]\{y\}$$
$$[N] = [B]\{k\} + [A]\left\{\varepsilon^0\right\}$$
$$[M] = [D]\{k\} + [B]\left\{\varepsilon^0\right\} \tag{21}$$

5 Probabilistic First-Ply Failure Load Analysis

In this section, the framework for probabilistic failure analysis of the first-ply is depicted in a flowchart (refer to Fig. 2). Initially, the input parameters are identified like Young's modulus, ply angle, ply thickness, Poisson's ratio, density, etc., to incorporate in the model to be designed. A finite element-based approach is used to compute the output through the deterministic approach. The next process is to evaluate the input and output data which are used to fit in the surrogate model. In this study, multivariate adaptive regression splines (MARS) is used as the surrogate model. It is verified using Monte Carlo simulation (MCS) technique employed by Dey et al. [16]. Finally, the result obtained from the surrogate model and MCS model are compared and the best-fitted model is chosen to replace the computationally time-consuming MCS model.

The compound variation ($g\left(\bar{\varphi}\right)$) of all the stochastic parameters is provided as furnished in Eq. (22),

$$g\{\theta(\overline{\varphi}), E_1(\overline{\varphi}), E_2(\overline{\varphi}), G_{12}(\overline{\varphi}), G_{23}(\overline{\varphi}), \rho(\overline{\varphi}), \nu(\overline{\varphi})\}$$
$$= \left\{ \begin{array}{c} \alpha_1(\theta_1 \ldots \theta_l), \alpha_2(E_1 \ldots E_{1l}), \alpha_3(E_2 \ldots E_{2l}), \\ \alpha_4(G_{12} \ldots G_{12l}), \alpha_5(G_{23} \ldots G_{23l}), \alpha_6(\rho_1 \ldots \rho_l), \alpha_7(\nu_1 \ldots \nu_l) \end{array} \right\} \tag{22}$$

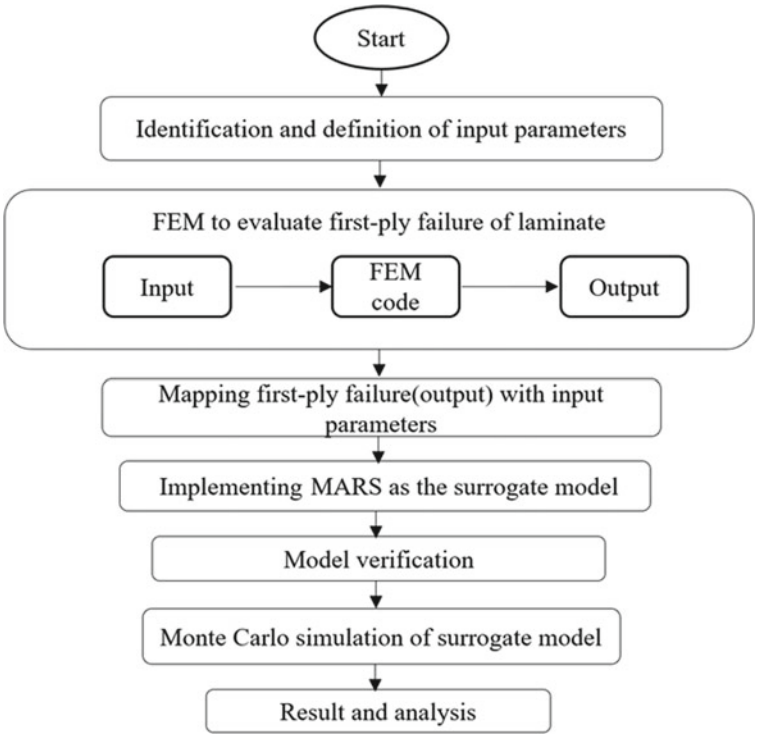

Fig. 2 Flowchart for stochastic first-ply failure analysis

where E_1, E_2, G_{12}, G_{23}, ρ, θandν are the elastic and shear modulus along the longitudinal and transverse direction, density, ply orientation angle and Poisson's ratio, respectively, and the number of layer in the laminate is denoted by 'l' which is eight in this case. '$\bar{\varphi}$' signifies the stochasticity in the characteristic input properties and 'α_x' denotes the stochastic output parameters. The components of the input vector 'P' can be either dependent or independent variables or maybe in functional data format or a set of data with particular relation.

6 Multivariate Adaptive Regression Splines (Mars) as Surrogate Model

MARS is a non-parametric regression technique which can be used to model linear systems that automatically models nonlinearities and the relation between the considered variables. The mathematical formulation for MARS as given by Sudjianto et al. [60]. The algorithm of MARS selects a base function according to the MCS model in order to provide an approximate response function over an onward and recessive

iterative approach. It is used to approximate the result similar to MCS with a much less time. The model can be expressed as summation of tensor product of truncated splines.

$$f(x) = \sum_{i=1}^{n} m_i A_i(x) \tag{23}$$

where m_i is the coefficient of expansion and $A_i(x)$ implies the basis function.

$$A_i(x) = \prod_{k=1}^{K_i} s_{k,i}(x_{j(k,i)} - t_{k,i})_{tr}^{q} \tag{24}$$

where $s_{k,i} = \pm 1$, K_i signifies the number of splines, x_j is the variation of jth element, tr signifies the location of a knot and the order of the splines is depicted by q.

For multivariate splines, $A_i(x)$ is the product of every single univariate function $s_{k,i}$. There are some conditions for the univariate functions which can be expressed as

$$\begin{aligned} &s_{k,i}(x_{j(k,i)} - t_{k,i})_{tr}^{q} = s_{k,i}\left(x_{j(k,i)} - t_{k,i}\right)^{q} \quad \text{when } \left[s_{k,i}\left(x_{j(k,i)} - t_{k,i}\right)\right] < 0 \\ &s_{k,i}(x_{j(k,i)} - t_{k,i})_{tr}^{q} = 0 \quad \text{otherwise} \end{aligned} \tag{25}$$

The model screens the variables automatically by using a modified form of criterion known as generalized cross-validation (GCV) [6]. MARS selects the exact value and location of the particular element for the required spline basis functions in a onward or backward manner. It over-fit the spline function according to the position of defined knot. After that, the model removes the unnecessary knots which contribute the least in the model according to the generalized cross-validation criterion. The knots which are not required can be evaluated by lack-of-fit (Z) criterion and is expressed as

$$Z = G_c(k) = \frac{\frac{1}{h}\sum_{i=1}^{h}[Y_i - Y_k(x_i)]^2}{[1 - \frac{\tilde{c}(\tilde{k})}{n}]^2}. \tag{26}$$

where $\tilde{c}\left(\tilde{k}\right) = c\left(\tilde{k}\right) + C.\left(\tilde{k}\right)$

'h' signifies the total number of samples, the number of linearly independent basis functions can be denoted as '$\widetilde{c}\ \left(\widetilde{k}\right)$', and the number of knots in forward process can be indicated by '$\widetilde{k}$', 'Y' is the approximated function and 'C' is the cost for basis function. The value of cost function estimates the smoothness of the function. As 'C' is inversely proportional to the number of knots, so when the value of '$\widetilde{k}$' is less, C is large and due to which the function is estimated in a smoother fashion.

7 Result and Discussion

The present investigation considers a laminated composite plate with an eight-layered angle ply [45, −45, 45, −45, −45, 45, −45, 45] laminate. The dimension of the plate is considered as length (l) = 1 m, breadth (b) = 1 m and thickness (t) = 0.005 m. T300/5208 graphite–epoxy laminate material with properties as furnished in Table 1 is considered for the present analysis.

The comparative outcomes of the material properties and ply orientation angle are considered for first-ply strength by considering five different failure criteria (maximum stress, maximum strain, Tsai–Hill, Tsai–Wu and Hoffman failure theories). The validation of the present FEM model is performed by comparing the deterministic results with the experimental results. The deterministic model is validated with previous literatures as furnished in Table 2.

The result from MARS model is obtained for the same sample size as that of MCS model. The traditional MCS approach uses 10,000 finite element (FE) iterations while the FE based MARS approach uses the five different sample sizes (64, 128, 256, 512 and 1024) for model formation and validation. The probability density function plot for result obtained from different sample-sized FE-based MARS approach and full-scale MCS approach is depicted in Fig. 3 for MARS surrogate model validation.

From the diagram of probability density function corresponding to the respective five failure criteria, it can be observed that for sample size n = 1024, the MARS model is almost similar to the MCS model. This is further validated by depicting scatter plot for sample size (n) = 1024 for the respective failure criteria as furnished in Fig. 4.

Table 1 Material properties of T300/5208 graphite–epoxy laminate [33]

E_1 (GPa)	E_2 (GPa)	G_{12} (GPa)	G_{13} (GPa)	G_{23} (GPa)	μ	ρ (kg/m^{3}m^3)
132.37	10.7	5.65	5.65	3.37	0.3	1600

Table 2 Validation of the present finite element model with experimental results [56] for five failure criteria considered for the composite laminate [45°/−45°/45°]

Failure theory	First-ply failure load					
	(2 × 2)		(4 × 4)		(8 × 8)	
	Reddy and Pandey [56]	Present FEM	Reddy and Pandey [56]	Present FEM	Reddy and Pandey [56]	Present FEM
Max. stress	2854.40	3408.70	2164.32	2486.50	1908.16	1962.50
Max. strain	2947.68	3273.20	2268.60	2421.70	1940.48	1994.75
Tsai–Hill	2788.80	3091.40	1803.84	1897.91	1530.40	1563.70
Tsai–Wu	2886.72	3337.70	2218.88	2432.73	1917.76	1957.32
Hoffman	2850.24	3224.50	2156.80	2269.53	1905.76	1962.10

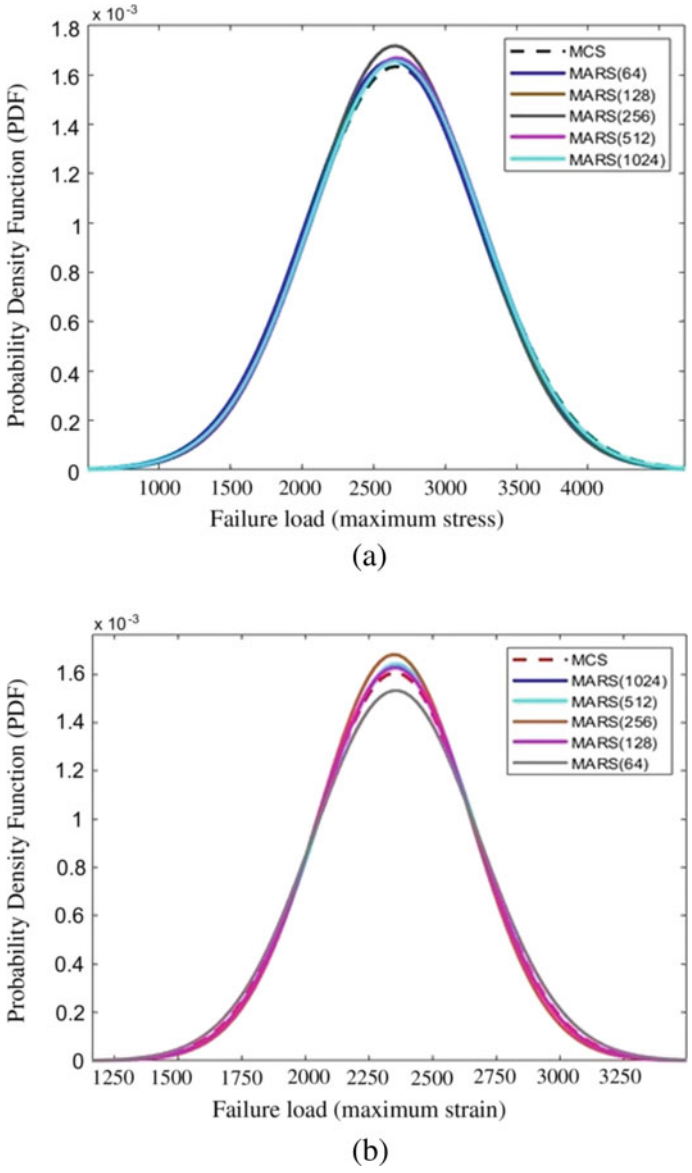

Fig. 3 Probability density functions of MCS and MARS model considering first-ply failure loads (in Newton) for **a** maximum stress **b** maximum strain **c** Tsai–Hill **d** Tsai–Wu and **e** Hoffman failure criteria

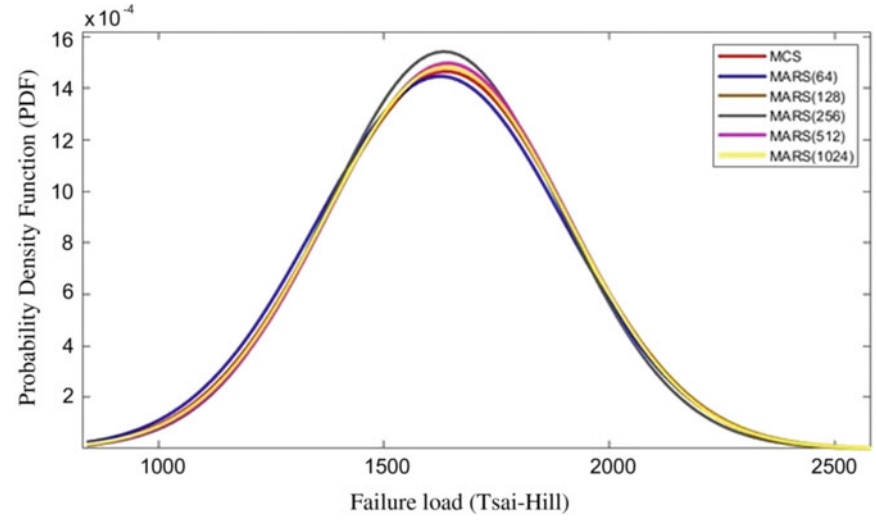

(c)

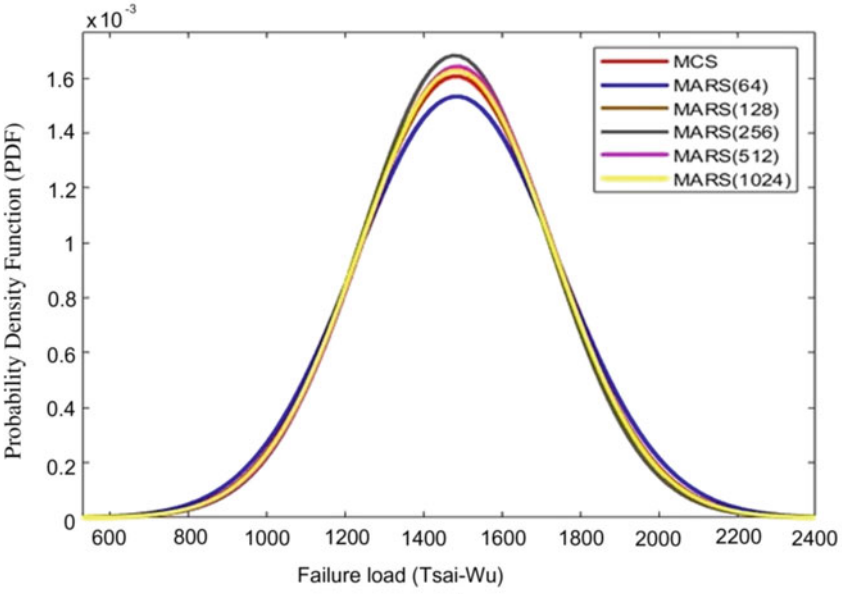

(d)

Fig. 3 (continued)

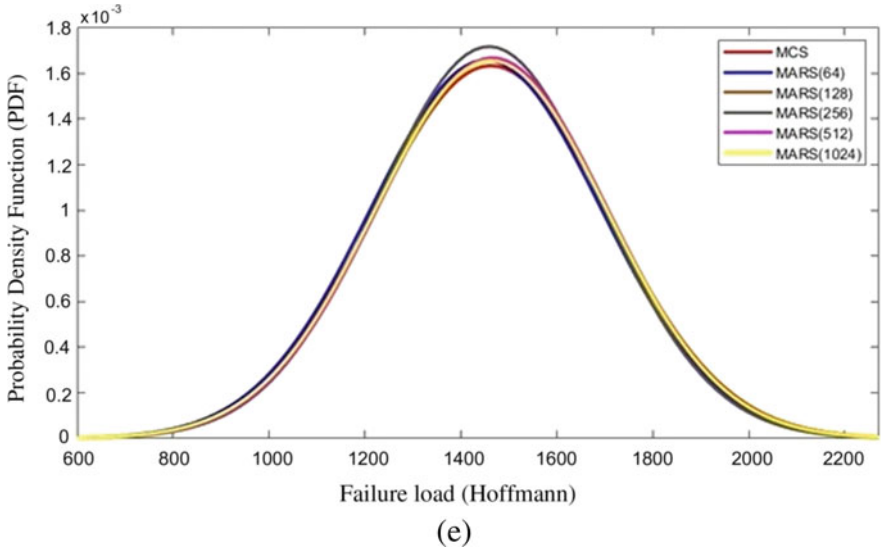

Fig. 3 (continued)

8 Conclusion

In present chapter, the MARS model is employed as a surrogate model. Here the random failure analysis of laminated composite plates is performed using a two-step analysis. Firstly, a deterministic finite element model is developed and validated with previous literature. Secondly, the MARS model is validated with direct MCS. During the direct MCS modelling, it is observed that the computational time required to complete the analysis is high due to the requirement of carrying out more than 10,000 finite element iterations. In order to reduce the computational intensiveness in MCS, MARS model is utilized here. The MARS model coupled with the finite element model provides adequate efficacy as compared with the MCS model by reduction in sample size. The probability density function and scatter plots are presented to show that a significant level of computational efficiency can be achieved without compromising the accuracy of results. The current MARS model can be utilized to analyse first-ply failure of complex laminates.

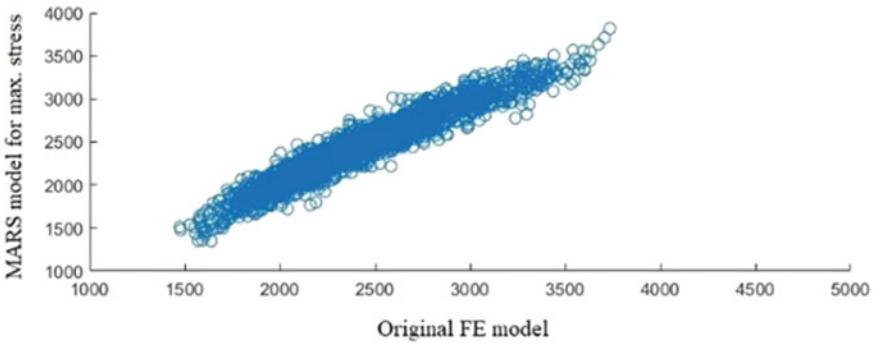

(a)

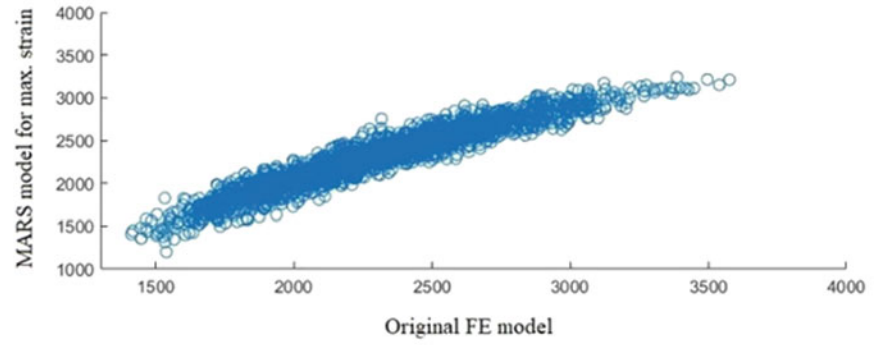

(b)

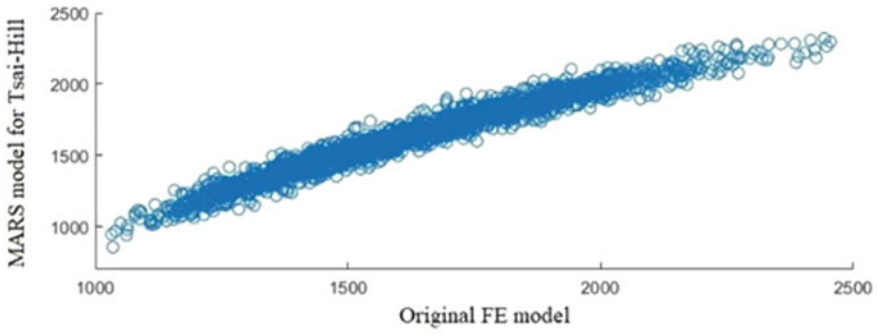

(c)

Fig. 4 Scatter plot of the 1024 samples-sized MARS model with respect to the original finite element (FE) model for **a** max. stress **b** max. strain **c** Tsai–Hill **d** Tsai–Wu and **e** Hoffman failure criteria

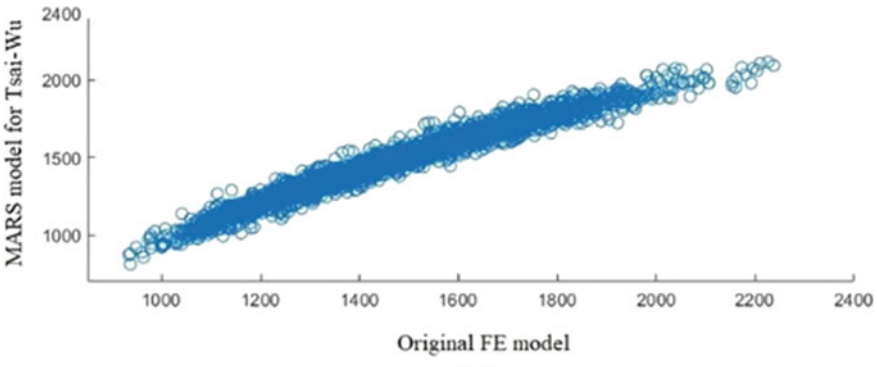

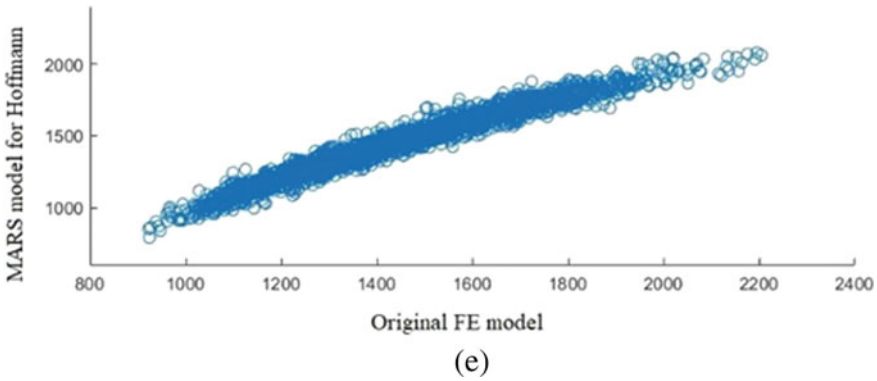

Fig. 4 (continued)

Acknowledgements The authors acknowledge the financial support received from Aeronautics Research and Development Board (AR&DB), Government of India (Project Sanction no.: ARDB/01/105885/M/I) dtd.26.06.2018.

References

1. Actis RL, Szabo BA, ' C (1999) Hierarchic models for laminated plates and shells. Comput Methods Appl Mech Eng 172(1–4):79–107
2. Babuška I, Szabo BA, Actis RL (1992) Hierarchic models for laminated composites. Int J Numer Meth Eng 33(3):503–535
3. Bunsell AR, Renard J (2005) Fundamentals of fibre reinforced composite materials. CRC Press
4. Chen X, Sun Y, Wu Z, Yao L, Zhang Y, Zhou S, Liu Y (2019) An investigation on residual strength and failure probability prediction for plain weave composite under random fatigue loading. Int J Fatigue 120:267–282
5. Chen X, Qiu Z (2018) A novel uncertainty analysis method for composite structures with mixed uncertainties including random and interval variables. Compos Struct 184:400–410

6. Craven P, Wahba G (1978) Smoothing noisy data with spline functions. Numerischemathematik 31(4):377–403
7. de Miguel AG, Kaleel I, Nagaraj MH, Pagani A, Petrolo M, Carrera E (2018) Accurate evaluation of failure indices of composite layered structures via various FE models. Compos Sci Technol 167:174–189
8. Dey S, Mukhopadhyay T, Adhikari S (2017) Metamodel based high-fidelity stochastic analysis of composite laminates: A concise review with critical comparative assessment. Compos Struct 171:227–250
9. Dey S, Mukhopadhyay T, Adhikari S (2018a) Uncertainty quantification in laminated composites: a meta-model based approach. CRC Press
10. Dey S, Mukhopadhyay T, Khodaparast HH, Adhikari S (2016) A response surface modelling approach for resonance driven reliability based optimization of composite shells. Period Polytech Civil Eng 60(1):103–111
11. Dey S, Mukhopadhyay T, Khodaparast HH, Kerfriden P, Adhikari S (2015) Rotational and ply-level uncertainty in response of composite shallow conical shells. Compos Struct 131:594–605
12. Dey S, Mukhopadhyay T, Naskar S, Dey TK, Chalak HD, Adhikari S (2019) Probabilistic characterisation for dynamics and stability of laminated soft core sandwich plates. J Sandwich Struct Mater 21(1):366–397
13. Dey S, Mukhopadhyay T, Sahu SK, Li G, Rabitz H, Adhikari S (2015) Thermal uncertainty quantification in frequency responses of laminated composite plates. Compos B Eng 80:186–197
14. Dey S, Mukhopadhyay T, Sahu SK, Adhikari S (2016) Effect of cutout on stochastic natural frequency of composite curved panels. Compos B Eng 105:188–202
15. Dey S, Mukhopadhyay T, Sahu SK, Adhikari S (2018) Stochastic dynamic stability analysis of composite curved panels subjected to non-uniform partial edge loading. Eur J Mech-A/Solids 67:108–122
16. Dey S, Mukhopadhyay T, Spickenheuer A, Adhikari S, Heinrich G (2016) Bottom up surrogatebased approach for stochastic frequency response analysis of laminated composite plates. Compos Struct 140:712–727
17. Enamul Hossain M (2011) The current and future trends of composite materials: an experimental study. J Compos Mater 45(20):2133–2144
18. Ghayoor H, Marsden CC, Hoa SV, Melro AR (2019) Numerical analysis of resin-rich areas and their effects on failure initiation of composites. Compos a Appl Sci Manuf 117:125–133
19. Gol'denblat II, Kopnov VA (1965) Strength of glass-reinforced plastics in the complex stress state. Polym Mech 1(2):54–59
20. Hélénon F, Wisnom MR, Hallett SR, Trask RS (2013) Investigation into failure of laminated composite T-piece specimens under bending loading. Compos a Appl Sci Manuf 54:182–189
21. Hinton MJKA, Kaddour AS, Soden PD (eds) (2004) Failure criteria in fibre reinforced polymer composites: the world-wide failure exercise. Elsevier
22. Hochard C, Thollon Y (2014) Fatigue of laminated composite structures with stress concentrations. Compos B Eng 65:11–16
23. Hoffman O (1967) The brittle strength of orthotropic materials. J Compos Mater 1(2):200–206
24. Kalita K, Mukhopadhyay T, Dey P, Haldar S (2019) Genetic programming-assisted multi-scale optimization for multi-objective dynamic performance of laminated composites: the advantage of more elementary-level analyses. Neural Comput Appl, 1–25
25. Kapti S, Sayman O, Ozen M, Benli S (2010) Experimental and numerical failure analysis of carbon/epoxy laminated composite joints under different conditions. Mater Des 31(10):4933–4942
26. Karsh PK, Mukhopadhyay T, Dey S (2018) Spatial vulnerability analysis for the first ply failure strength of composite laminates including effect of delamination. Compos Struct 184:554–567
27. Karsh PK, Mukhopadhyay T, Dey S (2018) Stochastic dynamic analysis of twisted functionally graded plates. Compos B Eng 147:259–278
28. Karsh PK, Mukhopadhyay T, Chakraborty S, Naskar S, Dey S (2019) A hybrid stochastic sensitivity analysis for low-frequency vibration and low-velocity impact of functionally graded plates. Compos B Eng 176:107221

29. Karsh PK, Mukhopadhyay T, Dey S (2019) Stochastic low-velocity impact on functionally graded plates: probabilistic and non-probabilistic uncertainty quantification. Compos B Eng 15(159):461–480
30. Karsh PK, Kumar RR, Dey S (2019) Stochastic impact responses analysis of functionally graded plates. J Br Soc Mech Sci Eng 41(11):501
31. Karsh PK, Kumar RR, Dey S (2019d) Radial basis function based stochastic natural frequencies analysis of functionally graded plates. Int J Comput Methods
32. Karsh PK, Raturi HP, Kumar RR, Dey S (2020) Parametric uncertainty quantification in natural frequency of sandwich plates using polynomial neural network. In: IOP conference series materials science engineering 798, 012036
33. Köhler L, Spatz HC (2002) Micromechanics of plant tissues beyond the linear-elastic range. Planta 215(1):33–40
34. Kumar RR, Mukhopadhyay T, Naskar S, Pandey KM, Dey S (2019) Stochastic low-velocity impact analysis of sandwich plates including the effects of obliqueness and twist. Thin-Walled Struct 145:106411
35. Kumar RR, Mukhopadhyay T, Pandey KM, Dey S (2019) Stochastic buckling analysis of sandwich plates: the importance of higher order modes. Int J Mech Sci 152:630–643
36. Kumar RR, Pandey KM, Dey S (2019) Probabilistic assessment on buckling behavior of sandwich panel: a radial basis function approach. Struct Eng Mech 71(2):197–210
37. Kumar RR, Karsh PK, Pandey KM, Dey S (2019d) Stochastic natural frequency analysis of skewed sandwich plates. Eng Comput
38. Kumar RR, Mukhopadhya T, Pandey KM, Dey S (2020a) Prediction capability of polynomial neural network for uncertain buckling behavior of sandwich plates. In: Handbook of probabilistic models. Butterworth-Heinemann, pp 131–140
39. Kumar RR, Pandey KM, Dey S (2020) Stochastic free vibration analysis of sandwich plates: a radial basis function approach, In: Reliability, safety and hazard assessment for risk-based technologies. Springer, Singapore, pp 449–458
40. Kumar RR, Pandey KM, Dey S (2020c) Effect of skewness on random frequency responses of sandwich plates. In: Recent advances in theoretical, applied, computational and experimental mechanics. Springer, Singapore, pp 13–20
41. Lal A, Kapania RK (2013) Stochastic critical stress intensity factor response of single edge notched laminated composite plate. In: 54th AIAA/ASME/ASCE/AHS/ASC structures, structural dynamics, and materials conference, p 1615
42. Lal A, Mulani SB, Kapania RK (2018) Stochastic critical stress intensity factor response of single edge notched laminated composite plate using displacement correlation method. Mech Adv Mater Struct, 1–15
43. Mantari JL, Oktem AS, Soares CG (2012) A new trigonometric shear deformation theory for isotropic, laminated composite and sandwich plates. Int J Solids Struct 49(1):43–53
44. Mindlin RD (1951) Influence of rotatory inertia and shear on flexural motions of isotropic, elastic plates. J Appl Mech 18:31–38
45. Mises RV (1913) 1913. Mathematisch-PhysikalischeKlasse, Mechanik der festenKörperimplastisch-deformablenZustand. Nachrichten von der Gesellschaft der WissenschaftenzuGöttingen, pp 582–592
46. Mukhopadhyay T (2018) A multivariate adaptive regression splines based damage identification methodology for web core composite bridges including the effect of noise. J Sandwich Struct Mater 20(7):885–903
47. Mukhopadhyay T, Naskar S, Karsh PK, Dey S, You Z (2018) Effect of delamination on the stochastic natural frequencies of composite laminates. Compos B Eng 154:242–256
48. Mukhopadhyay T, Naskar S, Dey S, Adhikari S (2016) On quantifying the effect of noise in surrogate based stochastic free vibration analysis of laminated composite shallow shells. Compos Struct 140:798–805
49. Naskar S, Mukhopadhyay T, Sriramula S, Adhikari S (2017) Stochastic natural frequency analysis of damaged thin-walled laminated composite beams with uncertainty in micromechanical properties. Compos Struct 160:312–334

50. Naskar S, Mukhopadhyay T, Sriramula S (2018) Probabilistic micromechanical spatial variability quantification in laminated composites. Compos B Eng 151:291–325
51. Naskar S, Mukhopadhyay T, Sriramula S (2019) Spatially varying fuzzy multi-scale uncertainty propagation in unidirectional fibre reinforced composites. Compos Struct 209:940–967
52. Onkar AK, Upadhyay CS, Yadav D (2007) Probabilistic failure of laminated composite plates using the stochastic finite element method. Compos Struct 77(1):79–91
53. Patel S, Ahmad S, Mahajan P (2018) Safety assessment of composite beam under ballistic impact. Thin-Walled Structures 126:162–170
54. Rafiee R, Sharifi P (2019) Stochastic failure analysis of composite pipes subjected to random excitation. Constr Build Mater 224:950–961
55. Reddy JN (1984) A simple higher-order theory for laminated composite plates. J Appl Mech 51(4):745–752
56. Reddy JN, Pandey AK (1987) A first-ply failure analysis of composite laminates. Comput Struct 25(3):371–393
57. Reissner E (1945) The effect of transverse shear deformation on the bending of elastic plates. J Appl Mech, A69-A77
58. Shams SS, El-Hajjar RF (2013) Effects of scratch damage on progressive failure of laminated carbon fiber/epoxy composites. Int J Mech Sci 67:70–77
59. Sokolnikoff IS, Specht RD (1956) Mathematical theory of elasticity, vol 83. McGraw-Hill, New York
60. Sudjianto A, Juneja L, Agrawal H, Vora M (1998) Computer aided reliability and robustness assessment. Int J Reliab Qual Saf Eng 5(02):181–193
61. Sun XC, Hallett SR (2018) Failure mechanisms and damage evolution of laminated composites under compression after impact (CAI): experimental and numerical study. Compos a Appl Sci Manuf 104:41–59
62. Talreja R, Singh CV (2012) Damage and failure of composite materials. Cambridge University Press
63. Talreja R, Varna J (eds) (2015) Modeling damage, fatigue and failure of composite materials. Elsevier
64. Tolson S, Zabaras N (1991) Finite element analysis of progressive failure in laminated composite plates. Comput Struct 38(3):361–376
65. Torabi AR, Pirhadi E (2019) Notch failure in laminated composites under opening mode: the virtual isotropic material concept. Compos B Eng 172:61–75
66. Tresca HE (1864) Sur l'ecoulement des corps solidessoumis a de fortes pressions. Imprimerie de Gauthier-Villars, successeur de Mallet-Bachelier, rue de Seine-Saint-Germain, 10, prèsl'Institut
67. Tsai SW (1984) A survey of macroscopic failure criteria for composite materials. J Reinf Plast Compos 3(1):40–62
68. Zubillaga L, Turon A, Maimí P, Costa J, Mahdi S, Linde P (2014) An energy based failure criterion for matrix crack induced delamination in laminated composite structures. Compos Struct 112:339–344

Chapter 14
Iosipescu Shear Test of Glass Fibre/epoxy Composite with Different Delamination Geometries: A Shear Behaviour Study

Tanmoy Bose, Subhankar Roy, and Nudurupati S. V. N. Hanuman

1 Introduction

In recent times, composite material has shown tremendous growth of application in the aerospace industry. Composite material is formed by combining more than one material in order to achieve better properties than any one or all of the individual materials. So, this type of material possesses superior properties like low weight, good fatigue properties, resistance to corrosion, high tensile strength, and low thermal expansion. Composites mainly consist of two different types of material, namely matrix and reinforcement materials. According to matrix material type, composites are categorized into three different classes, namely polymer matrix composite (PMC), ceramic matrix composites (CMC), and metal matrix composite (MMC). Among the three, polymer matrix composites (PMCs) have found wide application in aviation and automotive structures due to their adequate strength, lightweight, and cheaper compared to conventional metals. A new class of aviation material known as the fibre metal laminates (FML) has also been developed which is based on the hybrid composite concept. Different types of fibre metal laminate like aramid-reinforced aluminium laminate (ARALL) followed by glass laminate aluminium-reinforced epoxy (GLARE) are some of the recent advances in aerospace industry which are used for manufacturing upper part of aircraft fuselage. In this chapter, polymer matrix composite and its shear behaviour will be discussed primarily. PMCs can be categorized according to different reinforcing materials such as glass fibre-reinforced plastics (GFRP), carbon fibre-reinforced plastics (CFRP), and Kevlar fibre-reinforced plastics. Some hybrid composites can also be manufactured by introducing multiple reinforcement materials.

T. Bose · S. Roy (✉) · N. S. V. N. Hanuman
National Institute of Technology Meghalaya, Shillong, India
e-mail: subhankar.roy@nitm.ac.in

S. Sahoo (ed.), *Recent Advances in Layered Materials and Structures*,
Materials Horizons: From Nature to Nanomaterials,
https://doi.org/10.1007/978-981-33-4550-8_14

Glass fibre-reinforced plastics (GFRPs) are a form of fibre-reinforced plastics (FRP) and were first introduced in the 1940s for applications in Navy. The fishing industry was the foremost industry that used commercial FRP vessels in the late 1960s. This led to the widespread acceptance of FRP materials for building racing boats, yachts, fishing vessels, pleasure crafts, etc. In the present time, FRP structures are accounted for about 50% of fishing vessels. Composites are used extensively for fabricating sailboats, canoes, performance craft, and kayaks all over the world. As the primary concern of such structures is lightweight, composites have proven to be the most efficient material for building state-of-the-art vessels. Moreover, FRP materials are found to be economical as well as efficient when it comes to lifeboats and utility boats. This is mainly because of the longevity and low maintenance of these materials.

In this chapter, shear behaviour of delaminated as well as non-delaminated GFRP specimen is investigated both experimentally and numerically. Iosipescu shear test has been performed for understanding the role of delaminations and its geometry on shear behaviour of the GFRP specimen. Specimens with three delamination shapes such as circular, square, and rectangular are considered along with one non-delaminated specimen. The chapter is organized as follows: First, the background of delaminated composite testing and shear behaviour is provided. Then, the fabrication of GFRP specimens using hand layup process and Iosipescu shear test details is provided. The numerical modelling using ABAQUS is provided thereafter. Finally, the results for numerical and experimental parts are presented followed by a summary of the chapter.

2 Background

Glass fibres possess very good properties like higher strength, stiffness, resistant to chemical reactions and flexibility (as mentioned by Sathishkumar et al. [31]). GFRP composite provides advantages like resistance to corrosion and humid or acidic environment. It also shows better performance due to better resin bonding and lightweight and is easy to handle [18]. They are extensively used in automobile, sports, marine, construction, and electrical industries (according to Chavan and Gaikwad [6], Vinay et al. [37]). The combination of reinforcement material and single polymer matrix improves the performance of a composite which further helps in material development such as hybrid composites [16]. In aviation industries, fibre metal laminates (FML), especially glass-laminated aluminium-reinforced epoxy (GLARE), are widely used. GLARE is generally a stack of unidirectional glass fibres sandwiched between thin aluminium sheets (as discussed by Guocai and Yang [12]). It is described that the GLARE can be designed to have various applications by modifying the fibre/resin system, thickness and stacking sequence. Bhaskar and Srinivas [5] discussed the mechanical properties of GFRP composites with woven glass fibre mat as well as chopped strand mat under various loading parameters. The fabrication of glass fibre composites using hand layup process is

also discussed for performing flexural, compression and impact tests as per ASTM standards. The study showed that mechanical properties of composites based on chopped strand mat glass fibre are better than the woven mat glass fibre. The chopped strand mat glass fibre composite was also studied by varying the glass fibre content and performing the mechanical tests which illustrates the advantage of using higher proportion of glass fibre (by Mathapati and Mathapati [22]). A numerical approach for performing tensile, compressive, and flexural test has also been performed to compare with the experimental results. The results from experiment showing fracture toughness of delamination were studied for glass–epoxy composites developed by compression resin transfer moulding (CRTM) and conventional resin transfer moulding process [36]. It is concluded that the fracture toughness of the specimen completely depends on the fibre structure. The influence of delamination during drilling of a glass/epoxy composite was studied and a noble delamination factor was introduced by Nagarajan et al. [24]. Herakovich and Bergner [14] carried out FEA for determining the in-plane shear behaviour of composites using double V-notched coupon specimen. It was observed that the finite element method is able to predict uniform shear in the centre of all the specimens. However, the stress concentration depends on the laminate configuration. Walrath and Adams [38] discussed the Iosipescu shear test for composites along with the fixture and specimen design. The Iosipescu shear test is compared with asymmetrical four-point bending technique for obtaining both the in-plane and through the thickness shear strength of various composites like random and continuous sheet moulding compounds, unidirectional graphite epoxy, and double polymer materials. Sullivan et al. [32] used Iosipescu shear specimens for determining shear properties in case of a vinyl ester resin. The results show that anti-symmetric four-point bending fixture gives better shear stress at the gauge section and provides a reliable shear modulus. The tensile stress at the gauge section of Iosipescu specimen is found to be almost similar to the failure data acquired in tension. Swanson et al. [33] compared the Iosipescu in-plane shear test with torsion tube in case of carbon fibre composite. The results for both cases are found to be agreeing with each other. The deviation in average initial modulus, failure stress, and failure strain is obtained as 1%, 5%, and 31%, respectively. Adams and Walrath [1] used finite element analysis for predicting the shear stress in the specimen. The effect of notch depth, notch root radius, and notch angle on the shear strength of the composite was discussed. The existing Wyoming shear test fixture was redesigned for establishing better test procedures. Lee and Munro [20] established experimental methods for Iosipescu test on advanced composites. It is suggested that the notch for the specimen can be created by conventional machining tools; however, the base of notch must be inspected for any micro-damage. Tension and compression strain gauges are good tools to measure the shear strain field at the test section. Pindera et al. [28] performed analytical and experimental investigation on the stress deformation in case of graphite/epoxy and boron/aluminium Iosipescu specimen. The analytical and experimental results are found to be in good match in case of graphite/epoxy specimens. However, boron/aluminium specimen shows some discrepancies due to localized yielding at the notch tips due to a change in boundary condition. Morton et al. [23] further presented a modified Wyoming shear

test fixture based on finite element method for studying the shear stress field variation near the notch. Non-uniform stress field and its effect on the strain gauge measurement, while determining the shear modulus, was also discussed. Xing et al. [40] used Iosipescu specimen for performing a whole field strain analysis using moiré interferometry and FEM. A graphite/epoxy woven (0°/90°) laminate was used to determine the strain distribution outside as well as inside the section. It is observed that most of the experimental errors are caused due to bending moment, twist and loading points. Gipple and Hoyns [10] investigated out-of-plane shear for unidirectional and thick cross-ply laminates using Iosipescu shear test. Both theoretical and experimental approaches are used. Conventional strain gauges, moiré interferometry, full section strain gauges are used to determine the shear strain in the composite. Uniform strain distribution was observed in case of cross-ply laminates whereas the unidirectional laminates showed non-uniform distribution. Pierron and Vautrin [27] measured the in-plane shear stress for unidirectional composite by implementing the Iosipescu test. The test results are supported by finite element method results. The effect of boundary conditions on failure is studied both experimentally and numerically. It is concluded that the in-plane shear strength can be determined with a criteria related to quadratic failure. He et al. [13] performed the shear test with V-notch on unidirectional composites to measure shear strength and in-plane shear modulus. Glass fibre reinforced polymer and carbon fibre reinforced polymer composites are investigated by incorporating a finite element method (FEM) simulation technique. Both the numerical and experimental results show uniform stress–strain rate between the two V-notches which is very necessary for a desired shear test. Hence, it was concluded that double V-notch (Iosipescu) test is applicable to shear test of composite materials. Franco and Gonzalez [9] studied the properties of short fibre composites and the fibre/matrix interaction. The fibre/matrix interaction shear strength was obtained in order to decide the fibre length of the composite. It was observed that interface of fibre and matrix can have higher shear strength by varying the mechanical and chemical interactions among the matrix and fibre. Use of scanning electron microscope also shows a better fibre–matrix adhesion when silane coupling agent is used for treating the fibres. Yuan et al. [42] studied shear behaviour of inter-metallic composites using Iosipescu shear test. It was observed that off-axial two-path fractures occur when Iosipescu shear test is performed on inter-metallic composites. In order to study the failure mechanism, an extended finite element method-based simulation was carried out. Elanchezhian et al. [7] studied the behaviour of CFRP and GFRP specimens subject to different temperatures as well as strain rates. Fabrication of fibre-reinforced polymers using hand layup process is discussed. Subsequently, different tests were conducted like tensile (based on strain rate and temperature), flexural (based on strain rate), and impact. The tensile and flexural tests show better properties of CFRP composite as compared to GFRP. Further, scanning electron microscope (SEM) is used for observing the internal structure of both the composites for any voids, fractures as well as delamination between the fibre layers. Ramnath et al. [30] further studied on glass fibre-based SiC polymer composite which is fabricated using the hand layup process. A sandwich structure of two-layered GFRP in between SiC layers is considered. Fracture at different modes of the composite is

measured using an Arcan fixture with butterfly specimen. The stress variation is determined based on the type of resin. Moreover, the effect of glass fibre polymer in SiC composites is also investigated. It is observed that polyester resin shows much better shear strength in glass fibre polymer-based SiC polymer structure. Jimit et al. [17] investigated tensile and fatigue behaviour of GFRP fabricated with hand layup process. The influence of fibre orientation (0°, 90° and 45°) on the fatigue strength of the composite is investigated. It is observed that the glass fibre composite with 0°/90° fibre orientation shows much better mechanical and fatigue properties than that of the composite having 45° fibre orientations. This is mainly because the longitudinal fibre orientation in case of 0°/90° can sustain more number of fatigue cycles than 45° composites. Fajrin and Sari [8] investigated fibre-reinforced polymer composites based on Iosipescu shear test. Natural fibres of jute and hemp are used as reinforcement for preparation of the composites using vacuum bagging process. An MTS machine was used for conducting shear test with a 10 kN load cell attached to it. It was concluded that both the jute fibre composite and hemp fibre composite show cracking in diagonal direction, also called as the off-axial failure. Yang et al. [41] studied the bending, shear, and compression of stitched woven GFRP composite fabricated by resin transfer moulding. The shear test was done by grooved coupon as well as short beam test approaches for various stitching patterns. It is reported that increasing density of fibre stitching in z-direction makes composite lesser prone to delamination. Ramnath et al. [29] studied shear behaviour of golf shaft made of polymer composite material. The shear characteristics of golf shaft were investigated, and it was observed that the shear behaviour of the polymer composite is safe and can be used for sports application. Therefore, the polymer composite shaft may replace the steel golf shaft used conventionally due to its low weight and good shear strength. Swentek and Wood [34] introduced a lap shear test that can be incorporated for measuring the interfacial shear strength of a GFRP composite. The test was affected by curing condition of epoxy as well as the chemical treatment at interface. The location of fracture in the specimen was determined by using time of flight secondary ion mass spectrometry. The validated results from experiment signify that the method can be applied for obtaining shear properties of composite specimen. Naik et al. [25] investigated polymer composites under shear stress in case of high strain rate. The composites used in the study are in form of E-glass/epoxy and carbon/epoxy specimens. Experiments were conducted using the torsional split Hopkinson bar. The shear modulus and interlaminar strength of both specimens are obtained with respect to strain rate. It was noted that increase in shear strain rate leads to higher interlaminar shear strength, when considered within shear strain rate range. Totry et al. [35] conducted experiments as well as simulations for studying in-plane shear in case of cross-ply GFRP composite. It was seen that shear deformation fracture along fibre direction and at perpendicular to fibres is different to each other. Shear deformation along the fibre direction leads to local matrix shear parallel to fibres. For perpendicular shear deformation, plastic deformation is observed in matrix and fibre rotation. Further, increase in the applied strain leads to increase in response between both orientations. However, the response for the cross-ply laminate can be obtained by averaging both the individual responses. The effect on shear behaviour due to fibre

orientation was studied (by Almeida et al. [2]). Four different orientations of fibre mats along with four different types of test methods were considered in the study. The 0° fibre orientation shows better shear strength as compared to the 90° fibre orientation. The double-notched and V-notched test methods were found to be more useful for finding out the shear strength of a material. Godara et al. [11] investigated influence of carbon nanotube in GFRP composites by performing the single-fibre push-out test. The results showed better interfacial strength in the presence of carbon nanotubes in glass-reinforced epoxy composites. Amaro et al. [3] investigated the bending behaviour of CFRP composites both numerically and experimentally. It has been found that the maximum load carrying capacity decreases with an increase in delamination size but increases with a change in delamination position from middle towards periphery along thickness direction. The influence of low shear stress is found to be the major factor for the early failure of delaminated specimens. Aslan and Daricik [4] studied the compression and buckling behaviour of delaminated composite plate. Different delamination shapes like strip, circular, and peanut are tested. It was reported that compressive load carrying is least for strip delamination, and it is highest for peanut shape delamination. Also, it was found by the author that influence of multiple delaminations affects compressive more compared to tensile strength. Xie and Waas [39] used different delamination growth models for failure prediction numerically which is later verified by experimental results. The numerical modelling is done in ABAQUS with the use of user-subroutine. From the literature, it is evident that Iosipescu shear test has not been performed to GFRP composite with different geometries of delamination. Hence, this chapter discusses the shear behaviour of GFRP composite having different shapes of delamination between the V-notches of an Iosipescu specimen.

3 Main Focus of the Chapter

3.1 Experimental Details

3.1.1 Fabrication of Glass/Epoxy Composites

In order to fabricate the glass fibre-reinforced polymer (GFRP) composite, plain woven E-glass fibre was used as reinforcement. The strands of E-glass fibre are plain woven in orthogonal directions. The matrix material used for the composite fabrication is epoxy resin (Araldite AW106). The epoxy has creamy viscous colour which is mixed with a hardener (HV953) having golden brown colour. The ratio of proportion in which epoxy AW106 and hardener HV953 mixed was 1:1. The mixture of AW106/HV953 does not release any volatile constituents and gives good resistance to static and dynamic loads. The range of curing temperature for chosen resin was

around 20°–150° and that of minimum curing time is 15 h–5 min, respectively. The following steps have been carried out for fabricating the glass/epoxy composites:

Type A: Composite Specimen Without Delamination

A mould of cast iron having dimensions of 200 mm × 200 mm has been made for fabricating the composite. The surface of the mould has been kept smooth by machining process using surface grinding machine. This is mainly done for obtaining better surface finish on the specimen composite. The cast iron mould comprises two different parts, namely the lower mould and the top mould. Both the top and lower moulds have corner through holes for inserting bolts for tightening. Hence, the composite material can be sandwiched between the two mould plates during the curing process. This leads to uniform pressure on the composite layers, providing better quality as well as material property of the final product. This also helps in preventing formation of any air bubbles in the composite during curing process. The step-by-step procedure of fabricating glass fibre-reinforced polymer using hand layup process is explained briefly in the following section.

First of all, both the mould parts are checked for any surface roughness. If the surface has any corrosion or dust particles, it is cleaned by the use of emery paper followed by acetone. Subsequently, the size of the GFRP composite to be fabricated is decided, and plain woven glass fibre is cut according to desired dimensions. Multiple numbers of glass fibre mats are cut of same size according to number of layers required for the GFRP. In the present work, 16 layers of glass fibre are cut as per the required dimension. Moreover, two transparent sheets/mylar films are also cut of dimensions more than the mould size. These films are used so that the resin does not flow and damage the mould surface leading to rough surface of the mould after curing. One of the mylar films is attached to the lower mould and taped at the edges. Simultaneously, the epoxy Araldite AW106 along with hardener Araldite HV953 is mixed in weight ratio of 1:1. The mixing ratio is as per the standard recommended by the epoxy manufacturer. Proper care must be taken during the mixing of the epoxy and hardener, as the mixing ratio decides the quality of the resin that is being applied for fabricating the composite. The mixture must be stirred continuously for 5–10 min until it mixes uniformly showing a light golden creamy colour. The resin mixture is then applied to the lower surface of the mould and spread evenly with a brush. A cylindrical roller is used to apply uniform pressure and distribution of the epoxy without leaving any air bubbles or voids in the epoxy layer. One glass fibre mat cut previously is placed over the first later of resin followed by the rolling process for applying uniform pressure over the fibre mat. This helps in proper wetting of the glass fibre mat by the epoxy resin layer. Another layer of resin is applied over the glass fibre mat, and the roller is used in a similar way. The process of placing a glass fibre mat and application of resin layer is repeated as long as the desired layers are stacked. After final stacking of all fibre mats, a last layer of epoxy is applied and is distributed uniformly using a roller. Finally, the stacked composite layers are covered with the second mylar film. The upper mould is then placed over the composite pile and then screwed from all the corner using nuts and bolts. It is ensured that the bolts are tightened uniformly so that there is no deviation in the thickness direction of

GFRP plate. The mould is then kept at ambient temperature for 24 h to finish off the curing process. In order to reduce the curing time, pre-heating of the mould can be performed at a temperature as recommended by the resin manufacturer. The mould is opened after the curing period, and the two layers of mylar films are peeled off carefully from the glass/epoxy specimen. Finally, a 16-layered and 3.6-mm-thick GFRP composite is obtained with good surface finish.

Type B: Composite Specimens with Delamination
In addition to the steps mentioned for type A, for creating a delamination, Teflon tape can be used with required dimension to insert between the glass fibre layers at a desired location. In this case, a Teflon tape cut in the required shape and dimension was introduced at the middle layer, i.e. within the eighth and ninth layer of glass fibre. Three different geometries of delamination have been introduced with different dimensions. Firstly, a circular delamination is introduced with radius 5 mm. The second specimen is provided with a square delamination of dimension 5×5 mm^2, and the third specimen is having a rectangular delamination with 10×5 mm^2. The Teflon tape does not allow adhesion between the eighth and ninth layers of glass fibre and epoxy, thus creating a delamination in the final specimen. The fabrication of the four types of glass/epoxy composite specimen was followed by Iosipescu shear testing of the specimens and analysis of the results. The above steps are represented in the form of flowchart in Fig. 1. The cured glass/epoxy composite was taken out of the mould and is cut using a saw in the form of a double-edged notched specimen as recommended by Odegard and Kumosa [26] for performing the Iosipescu shear test. The double-edged notch is created on the specimen in order to ensure maximum shear stress in between the notches where the delamination is created. According to ASTM D 5379-93 standard, the dimensions of the specimen are: length = 78 mm, width = 20 mm, thickness = 3.6 mm, notch angle = 90°, and notch depth = 4.4 mm. All the four types of specimen before undergoing Iosipescu shear test are shown in Fig. 2.

3.1.2 Experimental Setup

The setup used for carrying out the Iosipescu shear test comprises universal testing machine (shown in Fig. 3) along with the in-house fabricated Wyoming Iosipescu shear test attachment (as shown in Fig. 4). Iosipescu shear test has been developed by Iosipescu [15]. A double V-notch is created on the specimen that is subjected to a pair of force couples acting in opposite directions. This is considered as a type of four-point load test for measuring the interlaminar shear strength of the specimen. By considering a notch angle of 90° and notch depth of 22% of the width, a constant shear stress can be obtained. In the case of fibre-reinforced composite, a stress concentration occurs near notch tip which is directly proportional with fibre volume fraction as well as fibre orientation. The Wyoming Iosipescu shear test attachment has been fabricated by using mild steel blocks by performing cutting, milling, and welding process. The attachment is placed below the movable cross-head of the universal

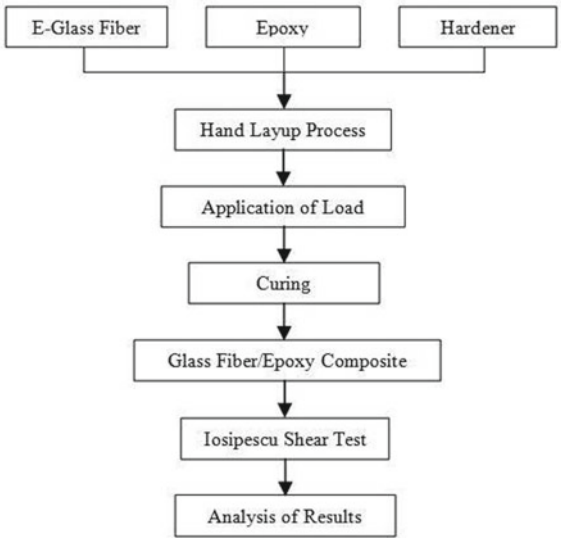

Fig. 1 Flowchart of the manufacturing process of GFRP composites

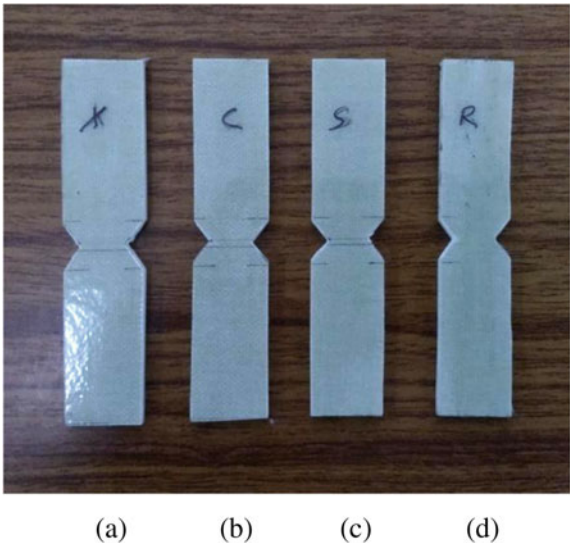

Fig. 2 Glass/epoxy composite specimen **a** without defect; and having **b** circular, **c** square, and **d** rectangular delamination

testing machine (UTM) such that one side of the attachment is fixed with the bottom of movable cross-head of the UTM. The other part of the Iosipescu attachment is placed at the UTM base as shown in Fig. 4. Both the parts are aligned properly such that the glass/epoxy specimen sits properly inside the fixture. Two wedge blocks are inserted in the fixture which is screwed from the sides in order to hold the specimen intact during the shear test. The wedge should be positioned carefully such that the specimen centre falls in the junction between two parts of the Iosipescu fixture.

Fig. 3 UTM setup

Fig. 4 Iosipescu shear test fixture

During the test, movable cross-head applies vertically downward force to the fixture fixed to it, leading to generation of shear stress near the centre (delamination location) of the specimen. The specimen deforms with increasing displacement until the load in the UTM monitor falls. Finally, the UTM is stopped, and the force is released from

Table 1 Properties used during numerical modelling

Material	ρ (kg/m^3)	E (GPa)	ν
Epoxy [24]	1540	70.0	0.33
E-glass [2]	2580	80.0	0.35
GFRP specimen (rule of mixture) [21]	2092	75.3	0.34

the fixture followed by removal of the specimen. The experimental data is captured, and the required results are plotted.

3.2 Numerical Modelling

3.2.1 Selection of Materials

The modelling of the glass/epoxy specimen for performing Iosipescu shear test is done using ABAQUS software. The reinforcement material in form of plain woven E-glass fibre mat and matrix material in form of epoxy (Araldite AW106) is used for assigning the properties of the numerical model. Rule of mixture for composite materials is incorporated for calculating the properties to be assigned for the GFRP composite during simulation (1998). This analytical method for calculating material properties of a composite is based on the individual properties of its constituents. Table 1 presents the properties used for modelling of the Iosipescu specimen. As the fibre type is considered as plain woven, the properties are considered same in orthogonal direction of fibre and hence considered isotropic. The property of the epoxy is calculated based on the mixture ratio (i.e. 1:1) of resin (AW106) and hardener (HV953). Therefore, the final GFRP specimen properties are considered as per the number of layers/ volume fractions of fibre and resin layers using rule of mixtures.

3.2.2 Numerical Modelling of GFRP Iosipescu Specimen Without Delamination

A double-edged V-notch specimen is modelled using part module of ABAQUS software. The total specimen thickness is considered as 3.6 mm. The primary dimensions of the specimen are taken as length: 78 mm, width: 20 mm, notch depth: 4.4 mm, and notch angle: 90°. The specimen modelling in part module was followed by assignment of material properties (mentioned in Table 1). In order to have uniform mesh geometry, arc-shaped partition was created near the V-notch. Ten-noded tetrahedral element (C3D10R) is used for meshing the model with around 6982 number of elements (as shown in Fig. 2a). The deformation scale in visualization module is kept a constant value of 7.76 in case of all the models. Moreover, half portion of the model was provided with clamped boundary condition, while a 0.5 and 1 mm

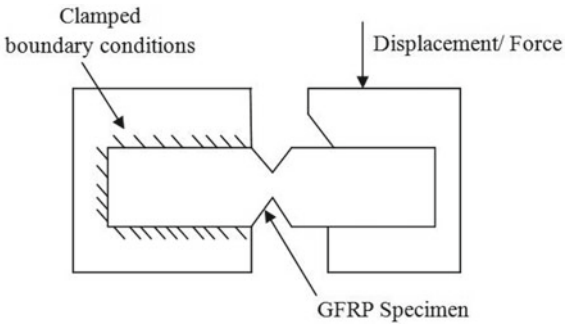

Fig. 5 Schematic diagram showing boundary and load conditions on the GFRP Iosipescu specimen

displacement was considered (one at a time) on other half, as shown in Fig. 5. The displacement is provided uniformly by selecting all the surface nodes at the right top portion of the Iosipescu specimen. This helps in generating maximum stress near the V-notch of the specimen due to smaller cross section at that point. The stress analysis was performed by using the static general step in ABAQUS. In the field output history of simulation tool, the whole model was selected to get an idea of how the stress is generated at the centre of the specimen. Parameters such as von Misses, S_X, S_Y, and S_{XY} stresses were considered for the study. The field output request in simulation helps in viewing animation of deformed state of the specimen with respect to undeformed one, in case of any of the selected parameters.

3.2.3 Numerical Modelling of GFRP Iosipescu Specimen with Delamination

Three different shapes of delaminations are considered such as circular, square, and rectangular that is modelled by providing sliding contact between the middle layers of GFRP. The delamination is modelled by creating partition sketch of required shape and dimension at the middle layer of the composite specimen in between the double notches. The first delaminated specimen is modelled using a circular partitioned surface of 5 mm diameter acting as a circular delamination at the central layer of the specimen. The square and rectangular delaminated specimens are also modelled in similar way with central partitioned surfaces having dimensions of 5 mm $\times$ 5 mm and 10 mm $\times$ 5 mm, respectively. Variable mesh element size of the specimen is used as per the mesh convergence test. Mesh elements near the notch and delamination are kept much smaller than the rest of the specimen. This is done to obtain better precision of stress values at the defect location. Tie constraint is applied between the fibre layers (except in the delaminated location) for preventing any sliding of the composite layers. For imitating the case of realistic delaminations, delaminated portion in the model is provided with sliding contact interaction properties. This helps in simulating the rubbing and sliding action of the delamination surfaces over each other when subjected to load, while the rest of the specimen remains intact. The meshed model for all Iosipecu specimens is shown in Fig. 6.

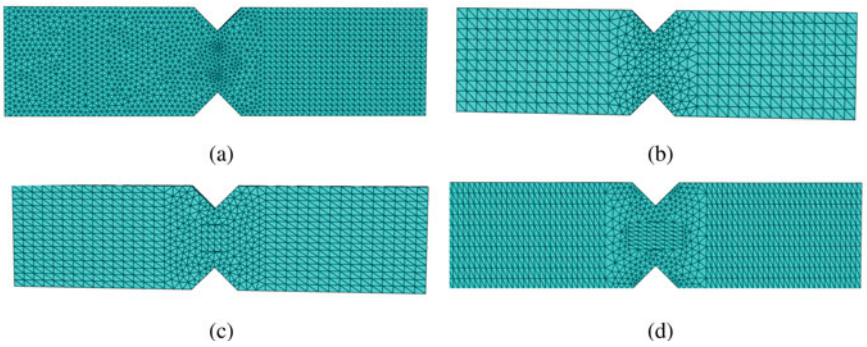

Fig. 6 Meshed model of the Iosipescu specimen **a** without defect and with **b** circular, **c** square, **d** rectangular delamination

4 Solutions and Recommendations

4.1 Experimental Results

The properties of glass/epoxy composites depend on its composition, orientation of the fibres, and the number of fibre layers used. In the present work, 16 layers of woven glass fibre mats were used to bond with the epoxy resin. The composite properties are also dependent on bonding between the fibre and resin. Thus, the shear properties of composites (with and without delamination) were evaluated using Iosipescu shear test fixture. Table 2 shows the maximum load and the maximum shear stress determined for two sets of specimens. The fractured specimens after performing the Iosipescu shear test are shown in Fig. 7.

The shear test on the glass/epoxy composite specimen with double-edge notch shows that a maximum load value of 14.75 kN is obtained while the displacement is around 12 mm for the specimen without delamination (Fig. 8a). The maximum

Table 2 Experimental results obtained from Iosipescu shear test

Specimen type	Maximum load (kN)			Maximum shear stress (MPa)		
	Specimen set 1	Specimen set 2	Average value	Specimen set 1	Specimen set 2	Average value
Without delamination	14.25	15.25	14.75	262.84	281.28	272.06
Circular delamination	13.95	13.00	13.48	257.30	239.78	248.54
Square delamination	13.25	14.50	13.88	244.39	267.45	255.92
Rectangular delamination	12.50	14.50	13.50	230.56	267.45	249.01

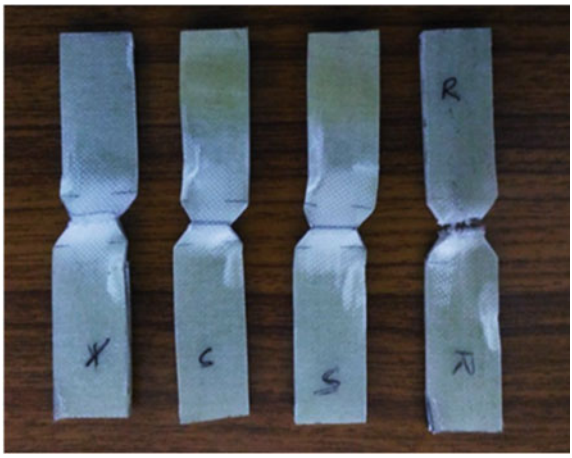

Fig. 7 Fractured specimens after performing Iosipescu shear test

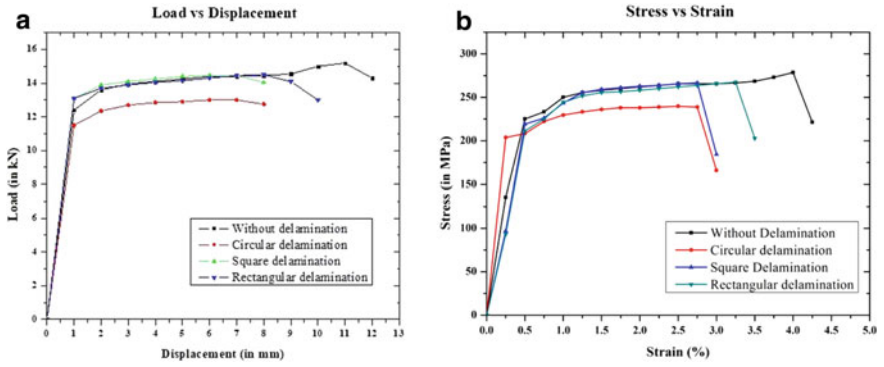

Fig. 8 **a** Load versus displacement curve and **b** stress versus strain curve

shear stress for the glass/epoxy specimen without delamination is around 272.06 MPa (Fig. 8b). The specimen breaks drastically after the maximum shear stress is reached. The results obtained for the glass/epoxy composite with different shapes of delamination namely circular, square, and rectangular are illustrated in Fig. 8. From the figure, it is clear that the maximum load (13.48 kN) that can be sustained is much lower in case of circular delamination followed by rectangular (13.50 kN) and square (13.88 kN) delamination, respectively. Similarly, the stress versus strain plot shows a same trend where the maximum shear stress for circular delamination (248.54 MPa) was found to be lower than that of the square (255.92 MPa) and rectangular delamination (249.01 MPa). Thus, it can be suggested that glass/epoxy composite with circular delamination is more prone to damage and crack growth as compared to square and rectangular delamination under shear loading. Among different shapes of delamination, the sequence of maximum shear strength in descending order was found to be: square, rectangular, and circular delamination.

4.2 Numerical Results

4.2.1 Mesh Convergence and Comparison with Experiment

Tetrahedral quadratic explicit elements (C3D10R) are used for meshing the Iosipescu specimens. In case of 0.5 mm displacement, 6982 number of tetrahedral elements is used, while, in case of 1 mm displacement, 36,853 elements are used. The reaction force values (in case of 0.5 mm displacement) obtained from the simulation are found to be 7.59 kN and 6.462 kN for element size of 2 mm and 1 mm, respectively. The error percentage calculated among two different element sizes is obtained as 14%. Lowering the element size gives negligible change of error percentage while the computation time increases. Hence, the mesh size is fixed at 1 mm in this case, and it is concluded that the mesh convergence is achieved. Similarly, there is negligible change in percentage error (found to be 16%) when the element size is lowered in case of 1 mm displacement. The mesh convergence details are provided in Table 3. The mesh convergence test was performed in order to select proper mesh element size such that the error % with respect to the computing time is less. The mesh element size was also varied near the V-notch and at delamination surface to obtain better results.

The results obtained from the load versus displacement curve for the model without defect is validated after comparison with experimental results. Validation of the numerical results compared to the Iosipescu test results is presented in Table 4. The load value obtained in numerical simulation is of 6.462 kN in case of 0.5 mm displacement, which matches with the experimental results, i.e. 6 kN. Similarly, 12.92 kN was noted in case of 1 mm displacement which agrees with that of the experimental result. Finally, the error percentage was calculated between the experimental and numerical study which shows 7% and 4% error for the two load values, respectively.

Table 3 Convergence test showing error percentage for variable mesh element size

Mesh size (in mm)	Displacement applied (in mm)	Load (in kN)	% error
2	0.5	7.590	14
1	0.5	6.462	
2	1.0	15.55	16
1	1.0	12.92	

Table 4 Comparison of experimental and numerical results

Displacement (mm)	Experimental load (kN)	Numerical Load (kN)	% error
0.5	6.00	6.462	7
1.0	12.4	12.92	4

4.2.2 Stress Contours of Different GFRP Specimens

The visualization module of the simulation tool is used for obtaining the contour plots corresponding to stresses values such as von Mises, S_X, S_Y, and S_{XY} for GFRP composite without delamination. Figure 9 shows the enlarged view of GFRP specimen where the stress concentration is high and at the central layer of the specimen. This helps in observing the contour and profile of the delamination surface when subjected to a shear stress. The numerical results for different stress values corresponding to all the four GFRP models are presented in Table 5. The specimen having no delamination has maximum shear strength when compared to specimens with circular, square, and rectangular delamination. Hence, specimen without delamination has less chances of failure under shear load when compared to delaminated specimens.

The deformation process of the delamination shape depicting the delamination growth is shown in Fig. 10 for a circular delamination. The force applied on the

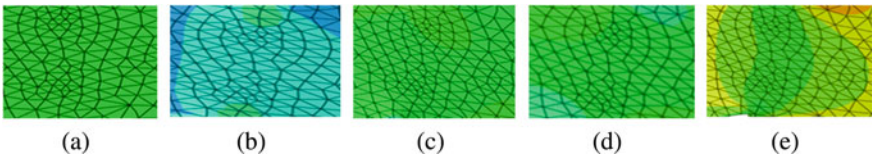

Fig. 9 **a** Undeformed, **b** von Mises, **c** S_X, **d** S_Y and **e** S_{XY} stress contours for GFRP Iosipescu specimen without delamination

Table 5 Comparison of stresses for non-delaminated and delaminated Iosipescu specimen under shear loading

Model	von Mises (GPa)	S_X (GPa)	S_Y (GPa)	S_{XY} (GPa)
Without delamination	9.877	10.31	6.084	0.089
Circular delamination	6.20	6.52	3.590	0.074
Square delamination	6.840	7.660	3.753	0.074
Rectangular delamination	7.127	7.422	4.687	0.439

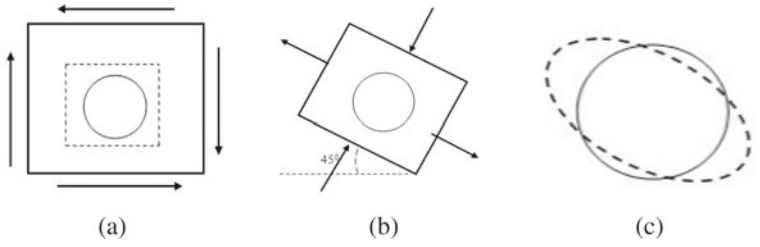

Fig. 10 Growth of delamination in case of circular delaminated Iosipescu specimen

specimen near the delamination zone is shown in Fig. 10a. The forces are acting orthogonal to each other intersecting at opposite corners of the specimen. Hence, two resultant forces are obtained which provides compressive loading in +45° directions and tensile loading in −45° directions, as shown in Fig. 10b. As the compression and tension are experienced from two directions that are orthogonal to each other, the delamination growth for circular shape forms an ellipse. Higher stress concentration occurs due to elliptical delamination shape which further leads to lowest shear strength in this case. This concept of delamination growth can be well accounted from the case of an infinite plate having elliptical hole using fundamental theory of fracture mechanics [19]. Therefore, composite specimens with circular delaminations tend to fail faster under shear loading as compared to other shapes. The stress contours related to all different stress values in circular delaminated specimen is shown in Fig. 11.

The delamination growth in square delaminated GFRP specimen is illustrated in Fig. 12. Similar to the previous case, a pair of tensile and a pair of compressive force are experienced at the delamination region which leads to the change of delamination shape into rhombical form, as shown in Fig. 12c. It is evident from the results that the shear stress for square delamination is more than that of the circular case. The reason for this is that the rhombic area has stress concentration at the notches under shear

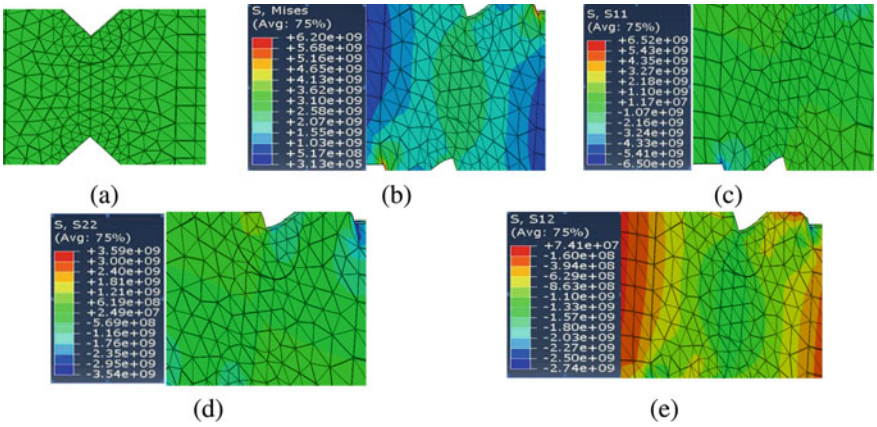

Fig. 11 **a** Undeformed, **b** von Mises, **c** S_X, **d** S_Y and **e** S_{XY} stress contours for GFRP Iosipescu specimen with circular delamination

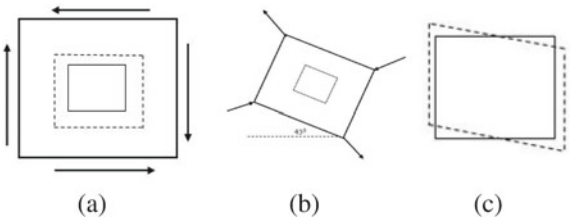

Fig. 12 Growth of delamination in case of square delamination

loading. Moreover, the area under shear in this case is almost analogous to that of the circular delamination, and hence, it experiences approximately same amount of shear stress. The square delaminated specimen with all stress contours is illustrated in Fig. 13.

Finally, the results corresponding to rectangular delamination are presented in similar manner, as shown in Fig. 14. In this case, the shear load leads to formation of quadrilateral shape of delamination, as shown in Fig. 14c. As observed from Table 5, rectangular delaminated specimen has the highest strength under shear loading among all the different delamination shapes. The primary reason for this is that the loading area has much lower side edges as compared to the edges normal to shear force. It helps in uniform load distribution on the delamination that is not found in rest of the cases. Hence, it can be concluded that composite specimens having rectangular delamination are less prone to failures as compared to other shapes when subjected to shear. Figure 15 shows the numerical stress contours for rectangular delaminated GFRP specimen.

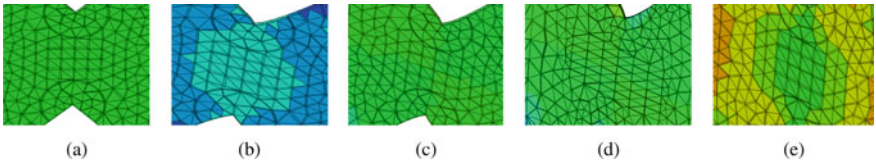

Fig. 13 **a** Undeformed, **b** von Mises, **c** S_X, **d** S_Y and **e** S_{XY} stress contours for GFRP Iosipescu specimen with square delamination

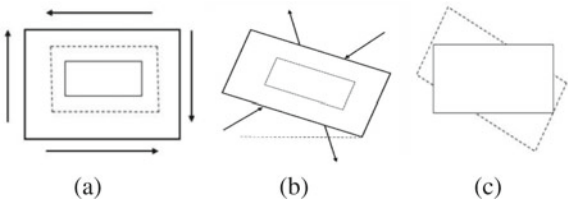

Fig. 14 Growth of delamination in case of rectangular delamination

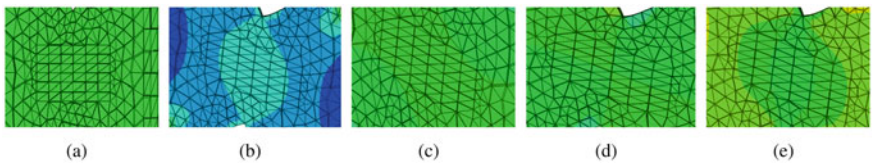

Fig. 15 **a** Undeformed, **b** von Mises, **c** S_X, **d** S_Y and **e** S_{XY} stress contours for GFRP Iosipescu specimen with rectangular delamination

5 Conclusions

In this chapter, the process of fabrication for glass/epoxy composite is explained in detail by using the hand layup process. Four different configurations of glass/epoxy composite have been fabricated, one without delamination and the rest three with different geometries of delaminations. The delaminated specimen is provided with circular, square, and rectangular delamination that was fabricated by introducing Teflon tape in between the glass fibre layers at the middle section. Subsequently, a Wyoming fixture for shear test is developed for performing the Iosipescu shear test. The Iosipescu shear tests are successfully carried out for all type of specimen, viz. with delamination and without delamination, in order to study their behaviour under shear loading. The load versus displacement and stress vs strain graph are plotted for each test specimen. Moreover, numerical simulation has been performed to compare with the experimental data. The simulated results for glass/epoxy specimen without delamination show good agreement with the experimental data and have very less deviation. The stress contours of all four glass/epoxy specimens generated due to shear load are presented by using von Mises, S_x, S_y, S_{xy} values. It is observed that glass/epoxy specimen without defect has the highest shear strength. The specimen with circular delamination shows the lowest shear strength when compared with square and rectangular delamination. This is mainly because the circular delamination grows in elliptical shape due to shear loading. Therefore, the circular delamination is more prone to delamination growth that may lead to failure of glass/epoxy composite under shear loading.

6 Future Research Directions

In future, the shear behaviour of different delamination geometries in glass/epoxy specimen can be carried out for other types of shapes at different positions as well as at different layers other than the middle. Subsequently, the strain developed in the glass/epoxy specimen during Iosipescu shear test can be measured by the help of strain gauges based on Wheatstone bridge circuit. Moreover, different types of composites like carbon fibre-reinforced polymer (CFRP) can also be studied with different delamination geometries. Realistic delamination created using low velocity impacts with different shapes of indenters can also be tested using Iosipescu shear test. This will help in investigating shear behaviour of composites having arbitrary shapes and sizes of real delaminations. However, numerical simulation of such realistic defects cannot be performed due to the complexity of the delamination geometry. Other types of shear tests such as V-notched rail shear test can also be investigated followed by a comparison study with Iosipescu shear test described in this chapter.

References

1. Adams DF, Walrath DE (1987) Further development of the Iosipescu shear test method. Exp Mech 27(2):113–119
2. Almeida JHS Jr, Angrizani CC, Botelho EC, Amico SC (2015) Effect of fiber orientation on the shear behavior of glass fiber/epoxy composites. Mater Des 65:789–795
3. Amaro AM, Reis PNB, de Moura MFSF (2011) Delamination effect on bending behaviour in carbon-epoxy composites. Strain 47:203–208
4. Aslan Z, Daricik F (2016) Effects of multiple delaminations on the compressive, tensile, flexural, and buckling behaviour of E-glass/epoxy composites. Compos B 100:186–196
5. Bhaskar V, Srinivas K (2017) Mechanical characterization of glass fiber (woven roving/chopped strand mat E-glass fiber) reinforced polyester composites. In: International conference on functional materials, characterization, solid state physics, power, thermal and combustion energy, vol 1859, p 020108:1–5
6. Chavan VB, Gaikwad MU (2016) Review on development of glass fiber/epoxy composite material and its characterizations. Int J Sci Eng Technol Res 5(6):2224–2228
7. Elanchezhian C, Ramnath BV, Hemalatha J (2014) Mechanical behaviour of glass and carbon fibre reinforced composites at varying strain rates and temperatures. Proc Mater Sci 6:1405–1418
8. Fajrin J, Sari NH (2018) Shear properties evaluation of natural fibre reinforced epoxy composites using V-notch shear test. MATEC web of conferences, p 195
9. Franco PJH, Gonzalez AV (2005) A study of the mechanical properties of short natural-fiber reinforced composites. Compos B Eng 36(8):597–608
10. Gipple KL, Hoyns D (1994) Measurement of the out-of-plane shear response of thick section composite materials using the V-notched beam specimen. J Compos Mater 28(6):543–572
11. Godara A, Gorbatikh L, Kalinka G, Warrier A, Rochez O, Mezzo L (2010) Interfacial shear strength of a glass fiber/epoxy bonding in composites modified with carbon nanotubes. Compos Sci Technol 70:1346–1352
12. Guocai W, Yang JM (2005) The mechanical behavior of GLARE laminates for aircraft structures. J Min Metal Mater Soc 57(1):72–79
13. He J, Chiang MYM, Hunston DL, Han CC (2002) Application of the V-notch shear test for unidirectional hybrid composites. J Compos Mater 36(23):2653–2666
14. Herakovich CT, Bergner HW Jr (1980) Finite element stress analysis of a notched coupon specimen for in-plane shear behaviour of composites. Composites 11(3):149–154
15. Iosipescu N (1967) New accurate procedure for single shear testing of metals. J Mater 2(3):537–566
16. Jagannatha TD, Harish G (2015) Mechanical properties of carbon/glass fiber reinforced epoxy hybrid polymer composites. Int J Mech Eng Robot Res 4(2):131–137
17. Jimit RH, Zakaria KA, Bapokutty O, Malingam SD (2018) Tensile and fatigue behaviour of glass fibre reinforced polyester composites. Int J Eng Technol 7(3.17):25–27
18. Kumar D, Ravish G (2015) Use of GFRP (glass fiber reinforced polymer) for strengthening of reinforced concrete beam. SSRG Int J Civ Eng 2:58–61
19. Kumar P (2009) Elements of fracture mechanics, 1st edn. Tata Mcgraw Hill Publishing Co. Ltd., New Delhi
20. Lee S, Munro M (1990) Evaluation of testing techniques for the iosipescu shear test for advanced composite materials. J Compos Mater 24(4):419–440
21. Liu GR (1998) A step-by-step method of rule-of-mixture of fiber- and particle-reinforced composite materials. Compos Struct 40(3):313–322
22. Mathapati SS, Mathapati SS (2015) Testing and analysis of mechanical properties of E-glass fiber reinforced epoxy polymer composites. Int J Res Innov Sci Technol 2(1):46–52
23. Morton J, Ho H, Tsai MY, Farley GL (1992) An evaluation of the iosipescu specimen for composite materials shear property measurement. J Compos Mater 26(5):708–750

24. Nagarajan VA, Sundaram S, Thyagarajan K, Rajadurai JS, Rajan TPD (2013) Measuring delamination severity of glass fiber-reinforced epoxy composites during drilling process. Exp Tech 37(2):66–73
25. Naik NK, Asmelash A, Kavala VR, Veerraju C (2007) Interlaminar shear properties of polymer matrix composites: strain rate effect. Mater Sci. https://doi.org/10.1016/j.mechmat.2007.05.003
26. Odegard G, Kumosa M (2000) Determination of shear strength of unidirectional composite materials with the Iosipescu and 10° off-axis shear tests. Compos Sci Technol 60:2917–2943
27. Pierron F, Vautrin A (1998) Measurement of the in-plane shear strengths of unidirectional composites with the Iosipescu test. Compos Sci Technol 57(12):1653–1660
28. Pindera MJ, Ifju P, Post D (1990) Iosipescu shear characterization of polymeric and metal matrix composites. Exp Mech 30(1):101–108
29. Ramnath BV, Jeykrishnan J, Elanchezhian C, Keshavan D, Deepak M (2017) Investigation of shear behaviour of polymer composite golf shaft. Mater Today Proc 4(8):9218–9223
30. Ramnath BV, Rajesh S, Elanchezhian C, Vignesh V, Rahul VV, Tamilselvan V, Narayanan SUS (2014) Investigation of mechanical behaviour of glass fibre based SiC polymer composites. Appl Mech Mater 591:142–145
31. Sathishkumar TP, Satheeshkumar S, Naveen J (2014) Glass fiber-reinforced polymer composites—a review. J Reinf Plast Compos 33(13):1258–1275
32. Sullivan JL, Kao BG, Oene HV (1984) Shear properties and a stress analysis obtained from vinyl-ester Iosipescu specimens. Exp Mech 24(3):223–232
33. Swanson SR, Messick M, Toombes GR (1985) Comparison of torsion tube and Iosipescu in-plane shear test results for a carbon fibre-reinforced epoxy composite. Composites 16(3):220–224
34. Swentek I, Wood JT (2013) Using the lap-shear test to measure polymer composite interfacial strength. In: The 19th international conference on composite materials, pp 4356–4363
35. Totry E, Gonzalez C, Lorca JL, Aldareguia JMM (2009) Mechanisms of shear deformation in fiber-reinforced polymers: experiments and simulations. Int J Fract 158(2):197–209
36. Treber D, Haspel B, Elsner P, Weidenmann KA (2017) Delamination fracture toughness of continuous glass-fiber/epoxy composites for structural applications. Int J Plast Technol 21(1):39–54
37. Vinay HB, Govindaraju HK, Banakar P (2015) Processing and characterization of glass fiber and carbon fiber reinforced vinyl ester based composites. Int J Res Eng Technol 4(5):401–406
38. Walrath DE, Adams DF (1983) The iosipescu shear test as applied to composite materials. Exp Mech 23(1):105–110
39. Xie J, Waas AM (2015) Predictions of delamination growth for quasi-static loading of composite laminates. J Appl Mech 82(8):081004
40. Xing YM, Poon CY, Ruiz C (1993) A whole-field strain analysis of the Iosipescu specimen and evaluation of experimental errors. Compos Sci Technol 47(3):251–259
41. Yang B, Kozey V, Adanur S, Kumar S (2000) Bending, compression, and shear behavior of woven glass fiber-epoxy composites. Compos B Eng 31:715–721
42. Yuan Y, Feng C, Xu Z, Li HP (2011) Investigation in shear behavior of intermetallic composites using V-notched beam test method. Exp Appl Mech 6:55–60

Chapter 15
Parametric Study of Dispersed Laminated Composite Plates

Celal Cakiroglu and Gebrail Bekdaş

1 Introduction

Fiber-reinforced composite materials are increasingly used in structural engineering because of their superior strength and stiffness properties compared to more conventional structural materials. Laminated composite plates are one type of structural members which is made of a number of layers with different fiber orientations. The sequence of fiber angles and ply thicknesses in laminated composite plates largely determines the performance of these structural members. There has been extensive research on the optimization of laminated composite plates in order to obtain maximum performance from these structural members while reducing their weight as much as possible.

The research in the area of laminated composite plate optimization can be categorized according to the optimization objective or according to the method of optimization used in the research. Some of the most frequently investigated research objectives in this field can be listed as the maximization of the fundamental frequency, maximization of the buckling load, minimization of the structural weight or cost and the minimization of the structural deformation.

On the other hand, the methods of optimization used in this area are much more diverse. Earlier literature in this field contains mostly gradient-based methods and nonlinear programming techniques, whereas more recent literature contains various genetic and metaheuristic algorithms. Among these algorithms, harmony search, ant colony, Tabu search and scatter search were most frequently used in the literature.

C. Cakiroglu (✉)
Turkish German University, Istanbul, Turkey
e-mail: cakiroglu@tau.edu.tr

G. Bekdaş
Istanbul University, Istanbul, Turkey

S. Sahoo (ed.), *Recent Advances in Layered Materials and Structures*,
Materials Horizons: From Nature to Nanomaterials,
https://doi.org/10.1007/978-981-33-4550-8_15

1.1 Hybrid Laminated Composite Plates

Most of the research in this area analyzes carbon fiber-reinforced composites (CFRP), whereas boron/epoxy and glass/epoxy composites received less attention from researchers. In addition to laminated plates made of a single type of composite material, also hybrid laminated composite plates are increasingly being investigated in the composites literature. In these structures, the more expensive composites with higher stiffness are used in the surface layers of the plate while the less expensive and lower stiffness composites are used in the middle layers. The hybridization approach makes use of the fact that the surface layers with higher stiffness carry the larger portion of the load. As a result of this structural behavior, it is possible to significantly reduce the structural cost without compromising on the structural performance by using hybrid laminates. The performance of hybrid laminates was extensively investigated in the literature. Reis et al. [11] performed static and fatigue tests using a single hemp fiber/polypropylene middle layer and two glass fiber/polypropylene surface layers. It was shown that the hybrid laminated composites have higher specific static stiffness and specific fatigue strength compared to the regular laminated composite plates made of glass fiber/polypropylene layers only. In one of the earliest studies dealing with the optimization of hybridized laminated plates [3], investigated fundamental frequency maximization and cost minimization of graphite–epoxy/glass–epoxy hybrid laminates. Similarly [1, 2], investigated hybrid laminates where the core laminae consist of glass/epoxy composite with less stiffness and the surface laminae consist of CFRP with high stiffness. In these multi-objective optimization studies, the fundamental frequency of the laminated plate was maximized and the cost of the structure was minimized using the ant colony optimization algorithm. Luersen and Lopez [10] present the application of a genetic algorithm in material cost minimization of hybrid laminated composite plates with glass–epoxy and carbon–epoxy layers. The angles of fiber orientation, number of laminae and the material used in each lamina were assigned as the design variables. As the optimization constraints, an upper bound for the weight, global buckling and failure of an individual ply were chosen. For the ply failure constraint, the maximum stress, Tsai–Wu and Puck failure criterions were applied separately, and the optimization outcome was compared for each one of these failure criteria. In another study dealing with the vibration behavior of hybrid laminated composites [6], investigated the natural frequencies and buckling loads of plates with glass fiber-reinforced polymer (GFRP) cores and aluminum surface layers. Furthermore, the variation of the buckling loads and natural frequencies of the hybrid plates with respect to the thickness to length ratio of the middle and surface laminae was presented. The sensitivity of laminated composite plates with respect to various geometric dimensions and mechanical parameters is an extensively investigated area of research. Thakur et al. [12] carried out a sensitivity analysis of displacement and natural frequency with changing fiber orientation angles, radius of curvature of the shell structure, material density and external loading. In order to identify the most important properties having an impact on the structural response, an

importance factor was assigned to each one of these material and geometric parameters based on the sensitivity analysis. The elasticity and shear moduli were found to be the most significant parameters affecting the structural response of laminated shells. Kurhe Nikhil et al. [9] carried out various parametric studies with respect to the fundamental frequency, mode shapes and deflections of laminated composite sandwich plates using the finite element software ANSYS. The results of these studies showed that fiber angle orientations and boundary conditions can significantly alter the structural response.

1.2 Thermal Buckling Analysis of Composite Laminates

In the literature concerned with the buckling analysis of laminated composite plates, a significant amount of research is about the thermal buckling of laminated plates. In one of the earlier works in this field [13], investigated the buckling of laminated plates for critical temperatures. Cross-ply (fiber angles alternating between 0° and 90°) and angle-ply (fiber angles alternating between arbitrary predetermined values $-\theta$ and $+\theta$) laminations with symmetric and antisymmetric stacking sequences were investigated. It was found that the critical temperature increases with the aspect ratio of the plate. Avcı et al. [5] investigated the buckling of glass–epoxy and boron–epoxy plates with a hole under thermal loading. Symmetric (−60°/60°/60°/−60°) and antisymmetric (60°/−60°/60°/−60°) fiber angle sequences were investigated. The buckling temperature was found to increase rapidly once the d/b ratio (the ratio of the hole diameter to the side length) exceeds 0.2.

In this parametric study, we are aiming at getting an optimal stacking sequence for laminated composite plates (Fig. 1) made of CFRP which was chosen because of being the most widely used composite material in structural components. Similar to most studies dealing with hybrid laminated composite plates, the plates in this parametric study consist of two surface layers and one core layer. Table 1 shows the mechanical properties of the CFRP composite used in this parametric study. In Table 1, E_1 and E_2 are the elasticity moduli of a lamina in directions parallel and transverse to the longitudinal fiber directions, respectively. G_{12} is the shear modulus, and ν_{12} is Poisson's ratio of a lamina.

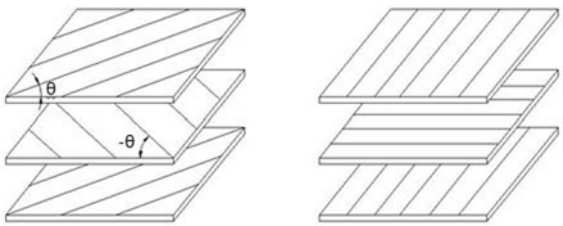

Fig. 1 Angle-ply(left) and cross-ply(right) laminations

Table 1 Material properties of the CFRP plates [8]

Mechanical properties	Carbon fiber (CFRP)
E_1 (N/mm^2)	157,000
E_2 (N/mm^2)	8500
G_{12} (N/mm^2)	4200
ν_{12}	0.35

In this research, a comprehensive parametric study is conducted in order to achieve the best possible stacking sequence for a rectangular laminated composite plate with a given ratio of side lengths. The performance of each stacking sequence is evaluated based on its buckling load which is computed using the eigenvalue buckling analysis procedure of the finite element software Abaqus. The fiber orientations and ply thicknesses are chosen to be the design variables, whereas the fiber orientations in the literature are mostly fixed at 0°, ±45°, 90°; our research is focused on dispersed laminated composite plates where the fiber orientation angles can take any value between −90° and 90°. However, due to the high computational overhead simulating all possible stacking sequences would entail, the buckling loads are only computed at certain predetermined fiber angle combinations. In this way, a large number of possible combinations of fiber orientations are simulated in this study. The second design variable which is the ply thickness is varied in 0.25 mm increments. The lowest ply thickness included in the parametric study was 0.25 mm, and the highest ply thickness value was 1 mm. An upper bound of 2.25 mm was set for the total plate thickness. In this parametric study, all possible combinations of the fiber orientation angles 0°, ±22°, ±44°, ±66, ±88° were simulated. Furthermore, for any given fiber angle sequence, all possible combinations of 0.25, 0.5, 0.75 and 1 mm ply thicknesses were simulated for a three-layered laminated CFRP plate. This led to a better understanding of the significance the individual ply thicknesses and their positions in the stack have. The visualizations of the results showed that for any given fiber angle sequence, the distribution of the ply thicknesses can lead to more than 50% fluctuations in the buckling load of a laminated plate.

2 Method

Rectangular laminated plates with the aspect ratio (ratio of the side lengths) of 3.2 are simulated. All stacking sequences with a total plate thickness less than 2.25 mm have been eliminated. This plate configuration is adopted from Führer [8]. The stacking sequences are chosen to consist of three layers (one mid-layer and two outer layers). The fiber angles are varied with increments of 22°. In this way, fiber angles outside of the conventional range of (0°, ±45°, ±90°) are analyzed. At the same time, the total number of analyzed stacking sequences is kept within the range of what is computationally viable. In this way, a total number of 7290 unique stacking sequences were produced. The sample space for the stacking sequences is limited to plates with

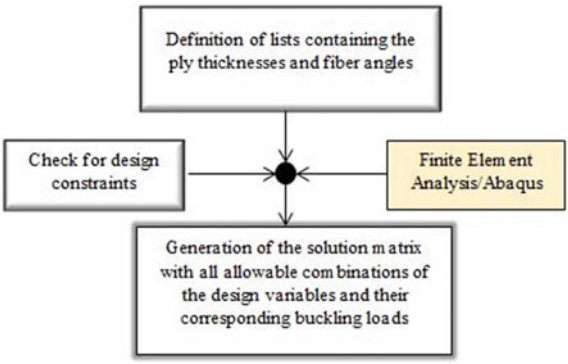

Fig. 2 Flowchart of the parametric study

exclusively 2.25 mm total thickness. The reason behind this limitation is that the plate thicknesses vary with 0.25 mm steps, and the highest buckling loads are unlikely to occur at smaller plate thicknesses. Furthermore, including a larger variation of ply numbers and thicknesses increases the total number of stacking sequences by several orders of magnitude so that the parametric study becomes intractable. Therefore, optimization problems with greater numbers of variables are often addressed using various metaheuristic or genetic algorithms. For each stacking sequence, the corresponding buckling loads are computed using the eigenvalue buckling analysis procedure of Abaqus. Following flowchart illustrates the entire process of this parametric study (Fig. 2).

2.1 Eigenvalue Buckling Analysis

For any given loading condition, the eigenvalue buckling analysis provides us with the magnitude of loading that would bring about an unstable equilibrium of the structure. This corresponds to a state of loading where the model tangent stiffness matrix ($\boldsymbol{K_t}$) becomes singular, i.e., the equation $\boldsymbol{K_t v} = 0$ has non-trivial solutions for $\boldsymbol{v}$. In order to determine the critical loading level at which $\boldsymbol{K_t}$ becomes singular, the applied load is increased in small increments. The initial loading pattern is determined through unit loads. Subsequently, these initial loads are multiplied by the load multiplier λ which controls the magnitude of load increase at each load increment.

The tangent stiffness matrix $\boldsymbol{K_t}$ is separated into a base state component $\boldsymbol{K}_0$ and a nonlinear component $\boldsymbol{K_{NL}}$ the mathematical derivation of which can be found in [7]. Following equation determines the values of λ that correspond to the load levels at which instability can occur as follows:

$$\det(\boldsymbol{K}_0 + \lambda \boldsymbol{K_{NL}}) = 0$$

The smallest value of λ obtained from the above equation is used as the critical loading level or the buckling load.

3 Results

Among the 7290 unique stacking sequences simulated in this parametric study, the best performing stacking sequence was (44°/−44°/44°/0.5 mm/1 mm/0.75 mm) with a buckling load of 3278.1 N. Obviously, the same performance can be obtained from a stacking sequence (−44°/44°/−44°/0.75 mm/1 mm/0.5 mm) as well. The critical buckling mode of this plate configuration is shown in Figs. 3 and 4.

The second highest buckling load in this study was 3185.3 kN for a stacking sequence of (44°/−66°/44°/0.5/1/0.75). The third highest buckling load of 3096.7 N was obtained from the stacking sequence (22°/−66°/22°/0.5/1/0.75), and the fourth highest load of 3049.8 N was obtained from (44°/−44°/44°/0.25/1/1). This ranking of stacking sequences shows that the best performing stacking sequences are the ones where the core layer has the greater thickness than the surface layers. A comparison of the best performing stacking sequence with the fourth best performing stacking sequence shows that they have identical fiber angle sequences. However, in the latter stacking sequence the ply thicknesses are not well balanced which leads to a 7.5% decrease in the buckling load. We can further analyze the effect of the ply thickness distribution on the buckling load by visualizing the variation of the buckling load for

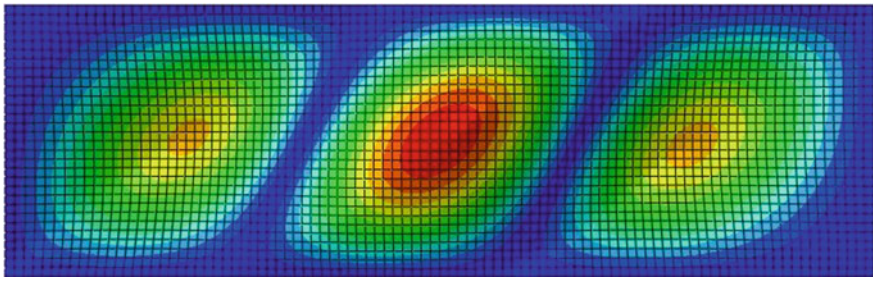

Fig. 3 Top view of the critical buckling mode of the plate configuration with the highest buckling load

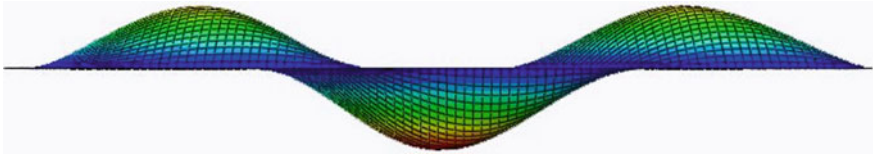

Fig. 4 Side view of the critical buckling mode of the plate configuration with the highest buckling load

Table 2 Variation of the buckling load with respect to ply thickness sequence for the fiber angle sequence (44°/−44°/44°)

Thickness sequence (mm)	P_{buck} (N)
(0.5/1/0.75)	3277.5
(0.25/1/1)	3049.8
(0.5/0.75/1)	2693.3
(0.75/0.75/0.75)	2664.5
(0.75/0.5/1)	2274.8
(1/0.25/1)	2086.8

a fixed fiber angle sequence. We start this visualization with the fiber angle sequence (44°/−44°/44°) which delivered the highest buckling load in our parametric study. A list of all different ply thickness combinations and their corresponding buckling loads for the fiber angle sequence of (44°/−44°/44°) can be found in Table 2. A visualization of the values in Table 2 is given in Fig. 5.

Table 2 and Fig. 5 show that the ply thickness distribution (0.75/0.75/0.75) where all plies have equal thickness is one of the least favorable distributions even though stacking sequences with identical ply thicknesses are commonly applied in the industry and composite laminates research [4, 8, 14]. It can be observed that there is a 57% difference between the best performing and worst performing ply thickness distributions in Table 2 and Fig. 5. This is a clear indication that optimization procedures have the potential to significantly increase the buckling load of a laminated composite plate. On the other hand, using the information contained in Table 2 and Fig. 5 one can conclude that there is a correlation between the thickness of the core layer and the buckling load of the plate. Clearly, as the core layer thickness increases from 0.25 to 1 mm, the buckling load also increases. Furthermore, there is not a single example of an increase in the core layer thickness which is accompanied by a decrease in the buckling load in Table 2.

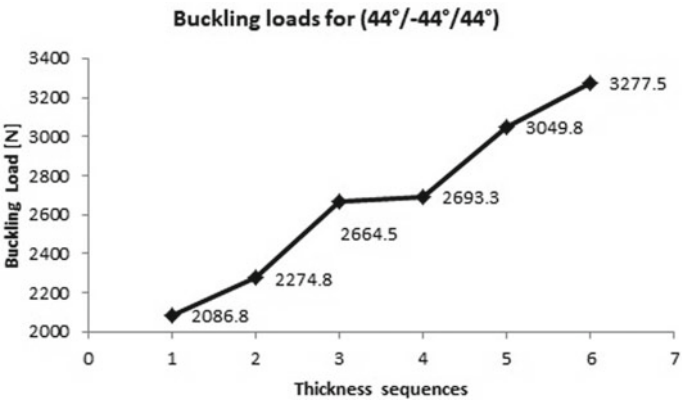

Fig. 5 Variation of the buckling load with respect to ply thickness sequence for the fiber angle sequence (44°/−44°/44°)

In order to better understand how the core layer thickness effects the buckling load, the visualization in Fig. 5 is repeated for the fiber angle sequences that delivered the highest buckling load values mentioned in the beginning of this section. A similar pattern is observed for the other two angle sequences. In case of the angle sequence (22°/−66°/22°), the thickness sequence with the identical ply thicknesses has a slightly greater buckling load compared to the other two angle sequences (Figs. 6 and 7; Tables 3, 4 and 5).

Figure 8 shows the distribution of the buckling loads for a constant core layer thickness of 1 mm and constant outer layer thicknesses of 0.5 mm and 0.75 mm which is the thickness sequence that resulted in the highest buckling load. The fiber orientation angle of the core layer is fixed at 44°. In this image, the buckling loads between 2000 and 3000 N are shown with gray color, and a small number of buckling loads

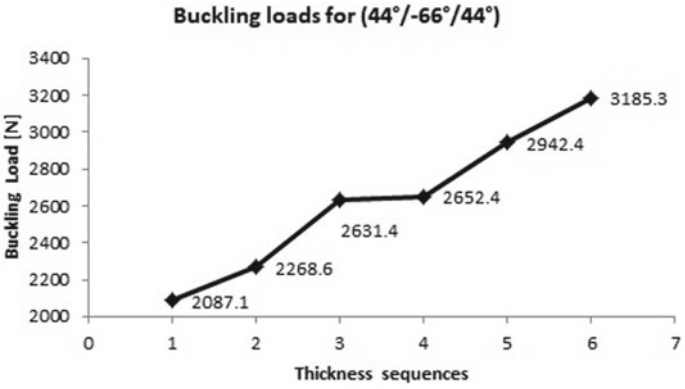

Fig. 6 Variation of the buckling load with respect to ply thickness sequence for the fiber angle sequence (44°/−66°/44°)

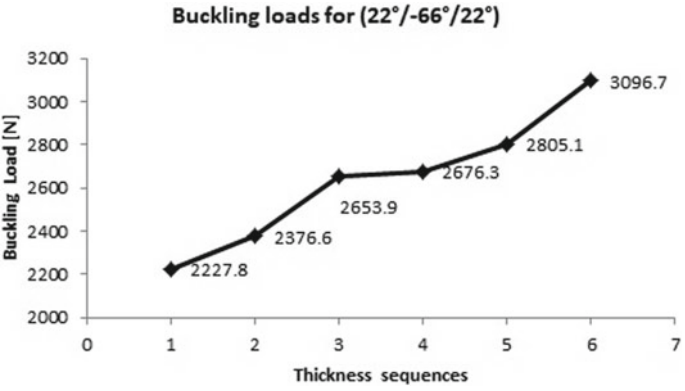

Fig. 7 Variation of the buckling load with respect to ply thickness sequence for the fiber angle sequence (22°/−66°/22°)

Table 3 Variation of the buckling load with respect to ply thickness sequence for the fiber angle sequence (44°/−66°/44°)

Thickness sequence (mm)	P_{buck} (N)
(1/0.25/1)	2087
(0.75/0.5/1)	2269
(0.75/0.75/0.75)	2631
(0.5/0.75/1)	2652
(0.25/1/1)	2942
(0.5/1/0.75)	3185

Table 4 Variation of the buckling load with respect to ply thickness sequence for the fiber angle sequence (22°/−66°/22°)

Thickness sequence (mm)	P_{buck} (N)
(1/0.25/1)	2227.8
(0.75/0.5/1)	2376.6
(0.5/0.75/1)	2653.9
(0.75/0.75/0.75)	2676.3
(0.25/1/1)	2805.1
(0.5/1/0.75)	3096.7

Table 5 Percentage difference between the best and worst performing ply thickness sequences for a given fiber angle sequence

Fiber angle sequence	Difference (%)
(44°/−44°/44°)	57
(44°/−66°/44°)	53
(22°/−66°/22°)	39

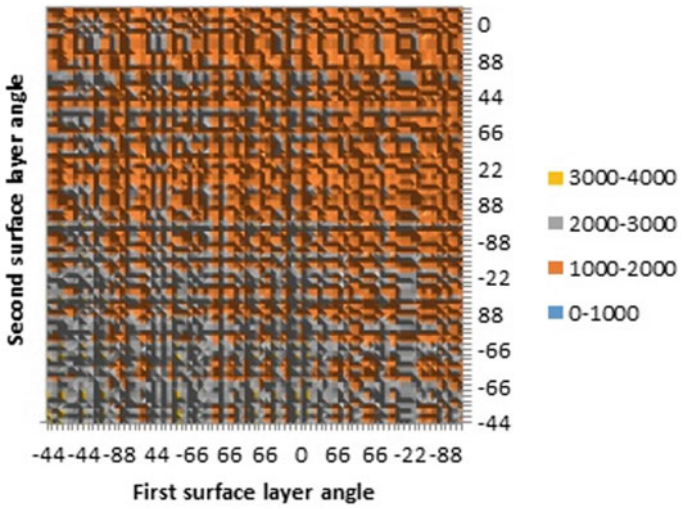

Fig. 8 Core layer thickness is 1 mm, core fiber angle is 44°, thicknesses of the surface layers are 0.5 and 0.75 mm

in the 3000–4000 N range are shown with yellow color. Clearly in Fig. 8 the higher buckling loads are concentrated at the lower left corner where also the (−44/44/−44) fiber angle sequence is located. The upper right portion of the image where the fiber angles of the surface layers are close to ±90° or 0° is largely populated by lower buckling loads. The upper side of Fig. 8 also contains the worst performing stacking sequence of the entire parametric study which is 0°/44°/88°/1 mm/0.5 mm/0.75 mm. Overall, the stacking sequences having ±88° degrees and 0° surface fiber angles performed worse than the other stacking sequences with an average buckling load of 1474.9 N.

4 Conclusions

The structural performance of laminated composite plates can be significantly affected by their stacking sequence. In this study, laminated CFRP plates consisting of three layers were analyzed with respect to the influence of their stacking sequences on their buckling loads. After a parametric study of the buckling load corresponding to 7290 different stacking sequences, it was found that the distribution of the ply thicknesses in a laminated composite plate can have a profound effect on the structural performance. The plates with the best performance were the ones where the core layer has greater thickness than the surface layers. Significant differences were observed between the buckling loads of the best and worst performing thickness sequences for any given fixed fiber angle sequence.

Furthermore, it was observed that the thickness sequence (0.75/0.75/0.75) is one of the less favorable thickness sequences despite the fact that stacking sequences with identical ply thicknesses are commonly used in the industry. The best result out of a parametric study was obtained from a plate with the stacking sequence of (44°/−44°/44°/0.5 mm/1 mm/0.75 mm) corresponding to a buckling load of 3278.1 N. The worst performing stacking sequence of this parametric study was (0/44/88/1 mm/0.5 mm/0.75 mm) with a buckling load of 1232.1 N. This corresponds to a 166% fluctuation in the buckling load due to changes in the stacking sequence. This outcome elucidates the importance of choosing the right stacking sequence and draws attention to the fact that the choice of a proper stacking sequence is a decisive factor that can have a significant impact on the structural cost and performance.

Further research in this field can be carried out using different material types for the core and surface layers. A limiting factor of this study was the computational impracticality of simulating stacking sequences with a larger number of layers. In the future, a similar study can be carried out using metaheuristic optimization algorithms to maximize the structural performance as a function of the stacking sequence and the material properties.

References

1. Abachizadeh M, Shariatpanahi M, Yousefi-Koma A, Dizaji AF (2010) Multi-objective optimal design of hybrid laminates using continuous ant colony method. In: Proceedings of the ASME 2010 10th biennial conference on engineering systems design and analysis ESDA 2010
2. Abachizadeh M, Tahani M (2008) An ant colony optimization approach to multi-objective optimal design of symmetric hybrid laminates for maximum fundamental frequency and minimum cost. Struct Multidiscip Opt 37(4):367–376
3. Adali S, Verijenko VE (2001) Optimum stacking sequence design of symmetric hybrid laminates undergoing free vibrations. Compos Struct 54:131–138
4. Almeida FS (2016) Stacking sequence optimization for maximum buckling load of composite plates using harmony search algorithm. Compos Struct 143:287–299. https://doi.org/10.1016/j.compstruct.2016.02.034
5. Avcı A, Kaya S, Dagdan B (2005) Thermal buckling of rectangular laminated plates with a hole. J Reinf Plast Compos 24(3). https://doi.org/10.1177/1731684405043554
6. Chen CS (2005) Investigation on the vibration and stability of hybrid composite plates. J Reinf Plast Compos 24:1747. https://doi.org/10.1177/0731684405052186
7. Crisfield MA (1997) Non-linear finite element analysis of solids and structures, 2nd edn. Wiley
8. Führer T (2017) Stiffness degradation of composite skin fields due to strength and buckling onset. Thin-Wall Struct 119(2017):522–530. https://doi.org/10.1016/j.tws.2017.07.012
9. Kurhe Nikhil M, Shedbale IB, Charapale UD, Manoharan R (2018) Modal analysis of hybrid laminated composite sandwich plate. Mater Today Proc 5:12453–12466
10. Luersen MA, Lopez RH (2013) A genetic algorithm for optimization of hybrid laminated composite plates. Opt Struct Compon, 49–71
11. Reis PNB, Ferreira JAM, Antunes FV, Costa JDM (2007) Flexural behaviour of hybrid laminated composites. Compos A Appl Sci Manuf 38:1612–1620. https://doi.org/10.1016/j.compositesa.2006.11.010
12. Thakur SN, Ray C, Chakraborty S (2018) Response sensitivity analysis of laminated composite shells based on higher-order shear deformation theory. Arch Appl Mech 88(8):1429–1459. https://doi.org/10.1007/s00419-018-1380-z
13. Thangaratnam K, Palaninathan R, Ramachandran J (1989) Thermal buckling of composite laminated plates. Comput Struct 32:1117–1124. https://doi.org/10.1016/0045-7949(89)90413-6
14. Zhang J (2012) The ply stacking optimization for composite laminated structure: application of tabu search algorithm. Adv Mater Res 366:514–517. https://doi.org/10.4028/www.scientific.net/AMR.366.514

Chapter 16
Modeling Fracture in Straight Fiber and Tow-Steered Fiber Laminated Composites—A Phase Field Approach

Hirshikesh, Ratna Kumar Annabattula, and Sundararajan Natarajan

1 Introduction

The word *composite* implies a material consisting of at least two distinct constituents (phases/materials) of entirely different physical/chemical properties. They are also referred to as engineered materials and some of them are inspired from natural composites, viz., wood, human teeth, bone, muscle, to name a few. The salient feature of such engineered materials is that the equivalent property of composite is better than its individual constituents. Within the composite, however, the constituent elements can be easily identified as they do not dissolve/blend into each other [1]completely. This is because, a composite material is manufactured by embedding the matrix (host) material, with reinforcements, such as filaments or stacking of laminae [2]. A careful choice of constituents can lead to a composite materials that is lighter, increased fatigue life, improved wear and corrosion resistance [3].

Of these, laminated composites are preferred as they have better mechanical characteristics and are more convenient to manufacture than the particle-reinforced composites; further, the volume fraction of the constituent components is easy to control [4, 5]. In addition, due to the presence of interface (matrix-fiber interface), the mechanical properties are improved. The interfaces act as barriers to crack propagation and deflect the cracks at the interface, thus enabling more fracture energy consumption [6, 7]. The laminated composite can be categorized as: (a) constant stiffness composite laminates (CSCL), and (b) tow-steered composite laminates (TSCL) based on the stiffness variation within the laminates. The CSCL is considered as a single domain with uniform staking sequence, fiber density, fiber orientation, and ply thickness. Whereas, TSCL is regarded as a domain consisting of multiple elements with different stacking sequence and modifies the load-carrying directions within the

Hirshikesh · R. K. Annabattula · S. Natarajan (✉)
Department of Mechanical Engineering,
Indian Institute of Technology Madras, Chennai 600036, India
e-mail: snatarajan@iitm.ac.in

S. Sahoo (ed.), *Recent Advances in Layered Materials and Structures*,
Materials Horizons: From Nature to Nanomaterials,
https://doi.org/10.1007/978-981-33-4550-8_16

laminate, such that the stress distributions are within design tolerances and uniform; further, it improves the global response of structures in terms of failure stress, critical buckling load, and stiffness [8]. The flexibility offered by the TSCL, i.e., it allows the fiber to be placed at any angle, also increases the computational complexity of adequately predicting their response. Several approaches are presented to predict their response accurately [9–11].

In spite of the improved material properties that the composites offer, the presence of different constituents introduces interface macroscopically. The presence of an interface can lead to stress raisers and potential region for crack initiation; further, this can lead to failure of the structure. Typical failure processes in composite laminates include cracking of fibers, crack formation in the matrix, and debonding of matrix-fiber interface and/or delamination of plies [12, 13]. The catastrophic collapse of the system is associated to the matrix cracking, while, loss of strength is associated to stiffness and strength degradation [14]. Experiments have shown that the free edges or the presence of discontinuities is the prominent region for the delamination to start [15]. Such diverse damage mechanisms cause the composite to lose strength gradually and eventually to catastrophic failures [16]. Brittle fracture is the prominent failure mode of unidirectional composites and the energy release mechanisms are by the deflection of the crack at the interface, shielding of crack by interfaces/other discontinuities, and branching of cracks [17, 18]. The crack orientation and propagation is highly influenced by the strength of the interface and the fracture toughness [19].

Complex fracture mechanisms in composites prohibit theoretical studies and often numerical approaches combined with experimental tests are employed. There are various numerical approaches that have been adopted in the literature to model the fracture characteristics in a composite laminate, some of them are: cohesive zone models [20], discrete element method [21], the eXtended finite element method [22, 23], and diffuse crack approach [24]. Aforementioned approaches requires a priori knowledge of the crack path, a criteria for changing crack morphology. This is circumvented by the introduction of phase field method for fracture by the seminal work of Francfort and Marigo [25], and Bourdin et al. [26]. The phase field method (PFM) was originally developed for interface problems and applied to the material solidification process [27–30]. Within the PFM framework, sharp interfaces are approximated by a scalar field variable that is continuous that distinguishes between multiple phases within the system through a smooth transition. In the last decade, the PFM is used by the physics and mechanics community to simulate fracture problems. In the context of fracture, order the parameter (termed as the phase field parameter) used to represent the fully broken and intact material phase with smooth transition (see Fig. 1c). The physics community models are generally based on the Landau-Ginzburg phase transition [31], and the mechanic's community uses a model based on Griffith's theory. Different models used by

- physics community: Aranson et al. model [32], Karma et al. model [33], Henry and Levine model [34],

- mechanics community[1]: Francfort and Marigo model [25], Bourdin model [26], Kuhn and Müller model [35, 36], Amor, Marigo and Maurini model [37], Miehe model [38, 39], Borden model [40], Hybrid model [41].

Due to its attractive features, the PFM is applied to wider range of engineering problems; some of them include: ductile fracture [42], thermal fracture [43], brittle fracture in functionally graded materials [44, 45], failure in composites [46, 47] and ceramics [48], crack growth in rocks [49], strength prediction in fiber-reinforced composite [12, 50, 51], and laminated composite [52], to name a few. Some researchers have used the UEL feature of the commercial software Abaqus [53, 54] to implement the phase field method, while Hirhikesh et al. [55] implemented the method in the open source finite element software, FEniCS.

The primary objective of this chapter is to discuss the implementation aspects of the PFM for an orthotropic material, and constant and tow-steered stiffness composite laminates in FEniCS. The effect of different parameters, such as, the inter-matrix spacing and the angle of the fiber on the load-carrying capacity is discussed with a few carefully chosen examples. This will enhance the understanding of fracture in composites.

2 Overview of Phase Field Method

A linear elastic body with a discontinuity (material and crack) occupying the domain $\Omega \subset \mathbb{R}^d$, where $d = 2,3$, represents the dimension of the problem (See Fig. 1). The domain is bounded by Γ with a unit outward normal $\mathbf{n}$, accommodates the following disjoint sets, viz., $\Gamma = \Gamma_D \cup \Gamma_t \cup \Gamma_c$ and $\Gamma_D \cap \Gamma_t = \emptyset$, where on Γ_D represents the region over which Dirichlet boundary conditions are specified and Neumann conditions are enforced on Γ_t. The discontinuous surface that denotes the crack is represented by Γ_c, which in this study is denoted by a phase field variable $\phi \in [0, 1]$ with $\phi = 1$ represents the completely damaged state (see Fig. 1b, c).

2.1 Governing Balance Equations

The evolution of the fracture topology within PFM is captured by minimizing the total potential energy [25]. The total potential energy is given by the sum of bulk and surface energy as:

$$\Psi = \Psi_b + \Psi_s = \underbrace{\int_\Omega \psi(\boldsymbol{\varepsilon}) \mathrm{d}\Omega}_{\text{bulk energy}} + \underbrace{\int_\Gamma \mathcal{G}_c \mathrm{d}\Gamma}_{\text{surface energy}}, \tag{2.1}$$

[1]The phase-field models used by the mechanics community and further improvements will be discussed in Sect. 2 in detail.

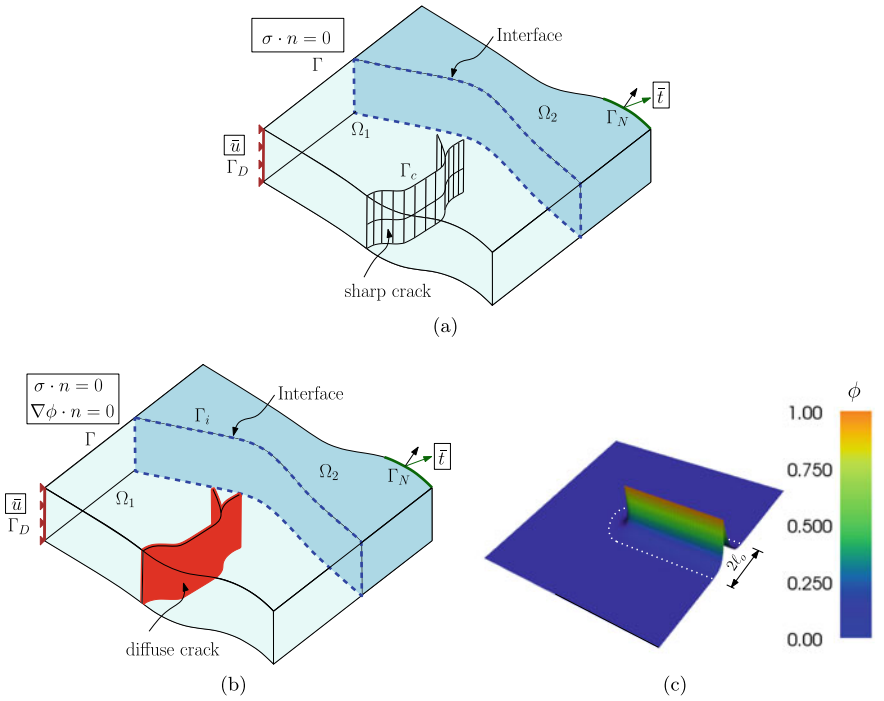

Fig. 1 **a** A discrete representation of the interface Γ and a sharp crack Γ_c in a domain Ω, **b** conforming representation of the interface, while a diffuse representation for the crack and **c** schematic of the scalar field variable ϕ, used to represent crack. Note that width of the crack is controlled by ℓ_o

where the small strain tensor is $\boldsymbol{\varepsilon} = \frac{1}{2}\left(\nabla^e \mathbf{u}^{\mathrm{T}} + \nabla^e \mathbf{u}\right)$, $\mathcal{G}_c$ is the critical energy release rate, $\psi(\boldsymbol{\varepsilon}) = \frac{1}{2}\lambda\,(\mathrm{tr}\ \ \boldsymbol{\varepsilon})^2 + \mu \mathrm{tr}(\boldsymbol{\varepsilon}^2)$ is the elastic energy density and Lamé constants are denoted by μ and λ. where ∇^{e^T} is a vector Laplacian which is defined as

$$\nabla^{e^T} = \begin{bmatrix} \frac{\partial}{\partial x} & 0 & \frac{\partial}{\partial y} \\ 0 & \frac{\partial}{\partial y} & \frac{\partial}{\partial x} \end{bmatrix}.$$

Upon introducing a damage variable to the strain energy, Ψ_b is modified as:

$$\Psi_b = \int_{\Omega} \left[(1-\phi)^2 + k\right] \psi(\boldsymbol{\varepsilon}) \mathrm{d}\Omega, \tag{2.2}$$

where $k < 0$ is introduced for numerical stability. Further, by constructing a crack density functional Γ_{ℓ_o} using a scalar field variable (ϕ), Ψ_s in Eq. (2.1) can be written as [56]:

$$\int_{\Gamma} \mathcal{G}_c \mathrm{d}\Gamma \approx \int_{\Omega} \mathcal{G}_c \left(\frac{1}{2\ell_o}\phi^2 + \frac{\ell_o}{2}|\nabla\phi|^2 \right) \mathrm{d}\Omega. \tag{2.3}$$

With these modifications to the surface and the bulk energy, Ψ is rewritten as:

$$\Psi = \int_{\Omega} \left[(1-\phi)^2 + k\right] \psi(\boldsymbol{\varepsilon}) + \mathcal{G}_c \left(\frac{1}{2\ell_o}\phi^2 + \frac{\ell_o}{2}|\nabla\phi|^2 \right) \mathrm{d}\Omega. \tag{2.4}$$

Governing differential equations are derived by employing the variational principle that includes the internal and the external work; $\delta\mathcal{W}_{\text{int}}$ and $\delta\mathcal{W}_{\text{ext}}$. The internal energy $\delta\mathcal{W}_{\text{int}}$ is computed by taking the variation of Ψ as

$$\delta\mathcal{W}_{\text{int}} = \int_{\Omega} \left[\boldsymbol{\sigma}\delta\boldsymbol{\varepsilon} - (2-2\phi)\delta\phi\ \psi(\boldsymbol{\varepsilon}) + \mathcal{G}_c \left(\frac{1}{\ell_o}\phi\delta\phi + \ell_o \nabla\phi \cdot \nabla\delta\phi \right) \right] \mathrm{d}\Omega. \tag{2.5}$$

The variation of the external work $\delta\mathcal{W}_{\text{ext}}$ is obtained as

$$\delta\mathcal{W}_{\text{ext}} = \int_{\Gamma} \bar{\mathbf{t}} \cdot \delta\mathbf{u}\ \mathrm{d}\Gamma, \tag{2.6}$$

where $\bar{\mathbf{t}}$ is the external traction imposed on Γ_{t}. In the above equation, it is assumed that there are no body forces and inertial forces. Imposing the constraint $\delta\mathcal{W}_{\text{int}} - \delta\mathcal{W}_{\text{ext}} = 0$, results, find $(\mathbf{u}, \phi) : \Omega \to \mathbb{R}^d$ such that:

$$\nabla \cdot \boldsymbol{\sigma} = \mathbf{0} \quad \text{in} \quad \Omega, \tag{2.7a}$$

$$-\mathcal{G}_c \ell_o \nabla^2\phi + \left[\frac{\mathcal{G}_c}{\ell_o} + 2H \right] \phi = 2H \quad \text{in} \quad \Omega, \tag{2.7b}$$

$$\boldsymbol{\sigma} \cdot \boldsymbol{n} = \bar{\mathbf{t}} \quad \text{on} \quad \Gamma_{\text{t}}, \tag{2.7c}$$

$$\mathbf{u} = \bar{\mathbf{u}} \quad \text{on} \quad \Gamma_{\text{D}}, \tag{2.7d}$$

$$\nabla\phi \cdot \boldsymbol{n} = 0 \quad \text{on} \quad \Gamma, \tag{2.7e}$$

where H is the history variable that depends on the strain energy, $\psi(\boldsymbol{\varepsilon})$ and is given by:

$$H = \begin{cases} \psi(\boldsymbol{\varepsilon}), & \text{if } \psi(\boldsymbol{\varepsilon}) > H_n, \\ H_n, & \text{otherwise}, \end{cases} \tag{2.8}$$

where n denotes the load step and $\boldsymbol{\sigma} = \left[(1-\phi)^2 + k\right] \frac{\partial\psi(\boldsymbol{\varepsilon})}{\partial\boldsymbol{\varepsilon}}$ is the modified Cauchy stress tensor. This model is known as an isotropic model in the literature [41]. The shortcoming of this model is that if fails to distinguish between the crack propagation in the tensile and compressive regions. Table 1 presents the various approaches that been postulated in the literature to alleviate some of the difficulties associated with the

Table 1 Difficulties associated with the phase field method and proposed advances

Area of concern	Solution scheme
Convergence of solutions (non-convex problem)	Staggered scheme [39]
	Arc-length control method [58]
	Line search assisted with monolithic approach [59]
Unphysical crack propagation in compressive region [41, 60]	Decomposition of strain tensor into deviatoric and volumetric part [37]
	Spectral decomposition of the strain tensor [39]
	The hybrid approach [41]
	Improved volumetric and deviatoric decomposition of the strain tensor [61]
	Decomposition of stress tensor [62]
Irreversible constraints	Introduction of history-field variable H^+ [39]
Unphysical crack propagation at the boundary	Fourth order phase-field model [63, 64]
Γ-convergence	The scaled fracture energy [60]
Computationally expensive	Adaptive PFM [63, 65–67]
Length scale sensitivity	Scale insensitive phase-field damage model [62]
Crack widening on the boundary [57]	Still open to solve
Mixed mode fracture in rock	Modify crack driving force [68, 69]

conventional PFM, such as: (a) prevent crack propagation in the compressive region, (b) non-physical crack propagation at the boundary and (c) length scale sensitivity. Readers are referred to [41, 57] that gives a comprehensive overview of different phase field approaches.

In this chapter, we employ the hybrid formulation that has the advantages of an isotropic model (i.e., the elastic equilibrium equation remains linear) and anisotropic model, that ensures that the crack propagates only by the tensile elastic energy, ψ^+.

$$-\mathcal{G}_c \ell_o \nabla^2 \phi + \left[\frac{\mathcal{G}_c}{\ell_o} + 2H^+\right]\phi = 2H^+ \quad \text{in} \quad \Omega, \tag{2.9}$$

$$\forall \boldsymbol{x} : \Psi^+ < \Psi^- \Rightarrow \phi := 0 \tag{2.10}$$

H^+ in Eq. (2.10) is give by: $H^+ := \max_{\tau\in[0,t]}\Psi^+(\boldsymbol{\varepsilon}(\mathbf{x}, \tau))$ and second constrain in Eq. (2.10) ensures that the crack faces do not inter penetrate. and

$$\Psi^{\pm}(\boldsymbol{\varepsilon}) = \frac{1}{2}\lambda\langle \mathrm{tr}(\boldsymbol{\varepsilon})\rangle_{\pm}^2 + \mu \mathrm{tr}(\boldsymbol{\varepsilon}_{\pm}^2), \tag{2.11}$$

with $\langle\cdot\rangle_{\pm} := \frac{1}{2}(\cdot \pm |\cdot|)$, $\boldsymbol{\varepsilon}_{\pm} := \sum_{I=1}^{3}\langle\varepsilon_I\rangle_{\pm}\boldsymbol{n}_I \otimes \boldsymbol{n}_I$ and $\varepsilon = \sum_{I=1}^{3}\langle\varepsilon_I\rangle \boldsymbol{n}_I \otimes \boldsymbol{n}_I$, where ε_I and $\boldsymbol{n}_I$ are the principal strains and the principal strain directions, respectively.

2.2 Numerical Implementation

A Bubnov-Galerkin procedure is adopted to develop the weak form for the coupled Eq. (2.7). The domain is decomposed into non-overlapping regions called elements and a polynomial representation is adopted for the unknown field and the geometry. In this chapter, the unknown fields ($\mathbf{u}$, ϕ) is represented by Lagrange basis functions as:

$$\mathbf{u} = \{u, v\} = \sum_{I}^{n} N_I \{u_I, v_I\} \tag{2.12a}$$

$$\phi = \sum_{I}^{n} N_I \phi_I \tag{2.12b}$$

where N_I are the hat functions, n is the total number of nodes in the domain and $\mathbf{u}_I$, ϕ_I denotes nodal variables. The corresponding weak form is given by: Find ($\mathbf{u}$, ϕ) such that:

$$\int_{\Omega} \boldsymbol{\sigma}(\mathbf{u}) : \boldsymbol{\varepsilon}(\mathbf{v}) \, \mathrm{d}\Omega = \int_{\Gamma_t} \hat{\mathbf{t}} \cdot \mathbf{v} \, \mathrm{d}\Gamma, \tag{2.13a}$$

$$\int_{\Omega} \left\{ \nabla\theta \, G_c \ell_o \nabla\phi + \theta \left[\frac{G_c}{\ell_o} + 2H^+ \right] \phi \right\} \mathrm{d}\Omega = \int_{\Omega} 2H^+ \theta \, \mathrm{d}\Omega + \int_{\Gamma} \nabla\phi \cdot \mathbf{n} \, \theta \, \mathrm{d}\Gamma \tag{2.13b}$$

The unknown field variables ($\mathbf{u}$, ϕ) are computed by solving the coupled equations (Eq. 2.13). Typical choices are Newton-Raphson and staggered approach. Due to the different nature of the equations, the Newton-Raphson approach has been known to yield converged results, and hence, the staggered approach is employed. Algorithm 1 shows the pseudo code for the staggered approach, where the unknown variables are solved sequentially within each time step until the convergence. For convergence, a user defined tolerance is specified and the convergence for the displacement and the phase field variable between successive staggered iteration steps is checked using $\max\left\{ \frac{||\{\mathbf{u}_{i+1}^h - \mathbf{u}_i^h\}||}{||\{\mathbf{u}_{i+1}^h\}||}, \frac{||\{\phi_{i+1} - \phi_i\}||}{||\{\phi_{i+1}\}||} \right\} \leq$ tolerance. Once the convergence is achieved, ϕ, H and $\mathbf{u}$ is updated and then the next load increment is applied. In this work, we use FEniCS, an open source finite element package is used to solve.

2.3 Implementation Aspects in FEniCS

The nice feature of FEniCS is that it is independent of the dimension of the problem and takes weak form directly as an input (see Listings 16.1 and 16.2). By using the unified form language embedded in Python, the weak from and the required finite element discretization is specified. Upon invoking V = FunctionSpace(mesh,'P',m),

Algorithm 1: Algorithm for the PFM

Initialize at step (i): $\{\mathbf{u}_i^h\}$, $\{\phi_i^h\}$ and $\{H_i^+\}$, $\tilde{u} = \Delta u$
for $\tilde{u}$=Δu, $2\Delta u$, ..., $n_{\text{total}}\Delta u$ **do**
  while max $\left(||\{\mathbf{u}_{i+1}^h - \mathbf{u}_i^h\}||/||\{\mathbf{u}_{i+1}^h\}|| \;\&\; ||\{\phi_{i+1}^h - \phi_i^h||\}/||\{\phi_{i+1}^h\}||\right) \geq$ tolerance **do**
    compute phase-field variable $\{\phi_{i+1}^h\}$ from Eq. (16.2.13b)
    compute displacement field $\{\mathbf{u}_{i+1}^h\}$ from Eq. (16.2.13a)
    compute $\{\psi^+\}$ and $\{\psi^-\}$, and $\{H^+\}$ from Eq. (16.2.11)
  update $\mathbf{u}^h$ and ϕ^h and history variable $\{H^+\}$

the domain is discretized with 3-noded triangular or 4-noded tetrahedra elements in two and three dimensions, respectively, 'P' defines the family of Lagrange elements and 'm' the order of polynomial that needs to employed to represent the unknown field variables. Listings 16.1 to 16.3 depicts the Python code for the staggered scheme adopted in FEniCS.

Listing 16.1 FEniCS implementation for modified elasticity, Eq. (16.2.13a)

```
def epsilon(v):
    return sym(grad(v))
def sigma(u):
    return 2.0*mu*epsilon(u) + lmbda*tr(epsilon(u))*Identity(ndim)
# The weak form
W_du = (pow((1.0 - phi_old),2) + k)*inner(grad(v),sigma(u))*dx
u = Function(W)
# bc_disp = boundary conditions for the elasticity
problem_disp = LinearVariationalProblem(lhs(W_du),rhs(W_du),u,bc_disp)
solver_disp = LinearVariationalSolver(problem_disp)
solver_disp.solve()
```

Listing 16.2 FEniCS implementation for phase-field, Eq. (16.2.13b)

```
# without energy decomposition
def hist(u):
    str_ele = 0.5*(grad(u) + grad(u).T)
    IC = tr(str_ele)
    ICC = tr(str_ele * str_ele)
    return (0.5*lmbda*IC**2) + mu*ICC
# The weak form
E_phi = ( Gc*lo*inner(grad(p),grad(q))+\
            ((Gc/lo) + 2.*hist(unew))*inner(p,q)-\
            2.*hist(unew)*q)*dx
p = Function(V)
# bc_phi = boundary conditions for the phase-field (if any)
problem_phi = LinearVariationalProblem(lhs(E_phi),rhs(E_phi),p,bc_phi)
solver_phi = LinearVariationalSolver(problem_phi)
solver_phi.solve()
```

Listing 16.3 FEniCS implementation for updating history variable

```
def History(uold,u_conv, Histold):
    history = conditional(lt(hist(u_old),hist(u_conv)), hist(u_conv),
    Histold)
    return history
```

A three-dimensional domain with three holes subjected to far field tension (see Fig. 2a is solved first to show the capability of FEniCS to handle three dimensional problems and can also do parallel processing. The crack trajectory computed through the phase field framework is compared against the solution available in the literature [70]. The material properties used for the analysis: Young's modulus $E = 210 \times 10^3$ N/mm^2, Poisson's ratio $\nu = 0.3$ and strain energy release rate $\mathcal{G}_c = 1.0$ N/m. Four noded tetrahedra elements are used to discretized the domain, this is done using Gmsh. The mesh is then converted to FEniCS readable format by using the following command: *dolfin-convert inputmesh.msh outputmesh.xml*. The simulation is performed on an Intel Core i5-4590 CPU@3.30GHz × 4 using 3 cores. Figure 2c shows the corresponding splitting of the domain in the three parallel cores.

Figure 3 shows the crack trajectory. The crack trajectory is compared with the work of [70] and the results show very good agreement. The crack is initially attracted toward the first hole and then resumes to propagate between the holes. Hence, larger size problems can be solved using the parallel computation in FEniCS with the same accuracy. In the following, the implementation is verified for the orthotropic materials. For an orthotropic material, the Cauchy stress tensor in Eq. (2.13a) is defined as: $\boldsymbol{\sigma} = \left[(1-\phi)^2 + k\right] \mathbb{D}\boldsymbol{\varepsilon}$, where

$$\mathbb{D} = \begin{bmatrix} \cos\theta & -\sin\theta & 0 \\ \sin\theta & \cos\theta & 0 \\ 0 & 0 & 1 \end{bmatrix} \begin{bmatrix} \dfrac{E_1}{1-\nu_{12}\nu_{21}} & \dfrac{\nu_{12}E_2}{1-\nu_{12}\nu_{21}} & 0 \\ \dfrac{\nu_{12}E_2}{1-\nu_{12}\nu_{21}} & \dfrac{E_2}{1-\nu_{12}\nu_{21}} & 0 \\ 0 & 0 & G_{12} \end{bmatrix} \begin{bmatrix} \cos\theta & \sin\theta & 0 \\ -\sin\theta & \cos\theta & 0 \\ 0 & 0 & 1 \end{bmatrix}, \tag{2.14}$$

where $\nu_{21} = \dfrac{E_2}{E_1}\nu_{12}$, the Young's modulus along the transverse and longitudinal direction is represented by E_2 and E_1, Shear modulus is represented by G_{12}, ν_{21} and ν_{12} are the minor and the major Poisson's ratio, respectively. To account for the material orientation, we introduce $\mathbb{A} = \mathbf{I} + \beta\,[\mathbf{I} - \mathbf{n} \otimes \mathbf{n}]$ with $\mathbf{n} = \{\cos\theta, \sin\theta\}^{\mathrm{T}}$ into Eq. (2.10) to give:

$$-\mathcal{G}_c \ell_o \nabla\phi \mathbb{A} \nabla\phi + \left[\frac{\mathcal{G}_c}{\ell_o} + 2H^+\right]\phi = 2H^+ \text{ in } \Omega, \tag{2.15}$$

The parameter β ensures that the crack propagates perpendicular to the cleavage plane orientation. For the current study, $\beta = 20$ is used for anisotropic case and for isotropic case, Eq. (2.10) is employed. The domain and the boundary conditions for a plate with circular hole subjected to tension is considered (see, Fig. 4a). Unidirectional fibers are embedded in the plate with an angle θ with the vertical axis (see Fig. 4). The material properties are chosen as, $(E_1, E_2, G_{12}, \nu_{12}) = (114.8,\ 11.7,\ 9.66,\ 0.21\ \text{GPa})$. Figures 4b–d show the crack propagation trajectory for different material orientations. The crack path depends on the material orientations which agrees well with results presented in [71, 72].

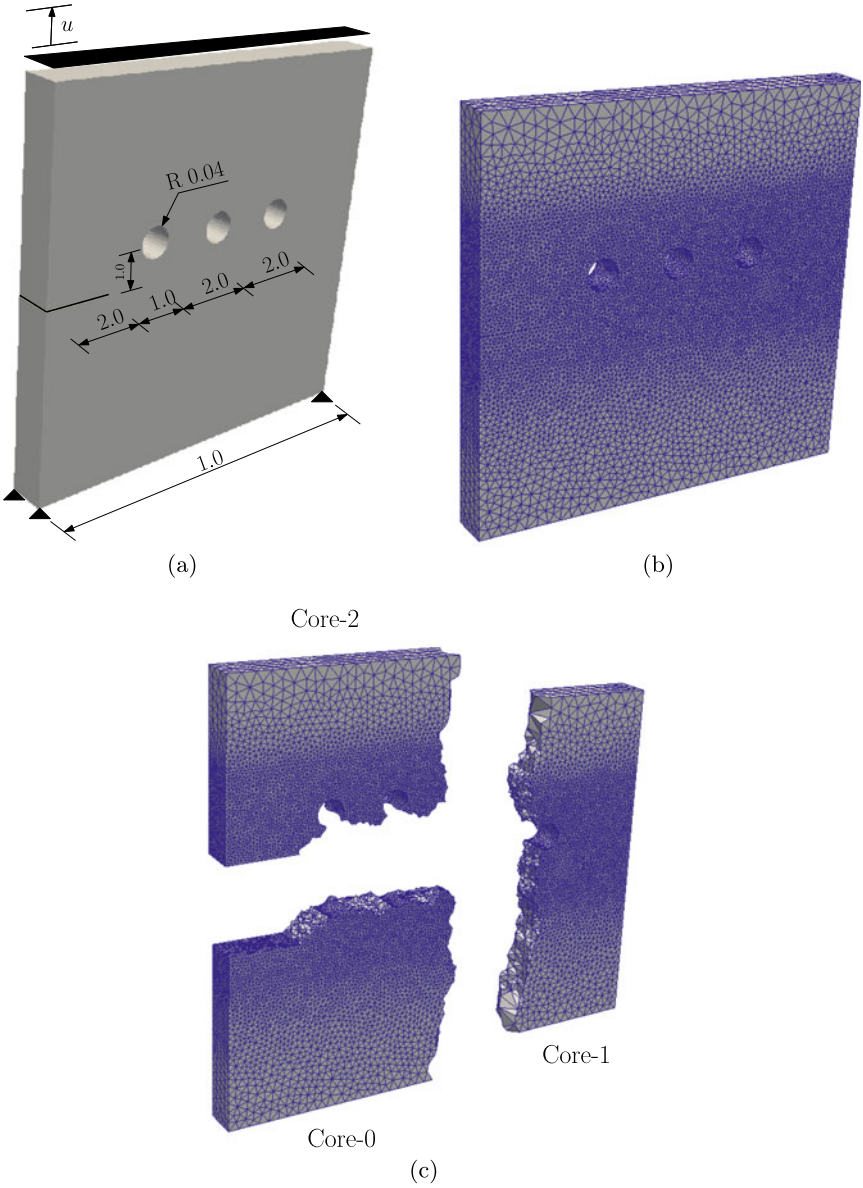

Fig. 2 Three-dimensional edge crack specimen with holes: **a** domain description with boundary conditions, **b** domain discretization, and **c** domain discretization using parallel core

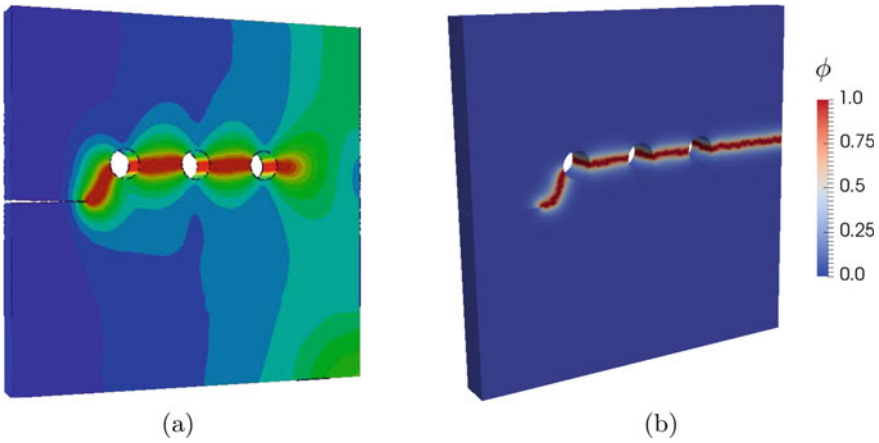

Fig. 3 Crack propagation trajectory from **a** final crack trajectory as reported in Msekh [70], **b** FEniCS implementation

3 Laminated Composite Fracture

In this section, we study the fracture processes in a two-dimensional CSCL/TSCL using the presented framework (see Fig. 5). The influence of the matrix thickness, t_m and fiber orientations on the crack propagation path and the maximum load for fracture is systematically studied. In all the examples, the domain is subjected to a far field tension, with $a = 0.25\,\text{mm}$ as the initial crack length, $\ell_o = 2h$ (where h denotes the diameter of the smallest element in the domain) is employed, unless mentioned otherwise. The displacement increment is set to $\Delta u = 1\times10^{-5}$ until complete fracture. Further, a no-slip condition is assumed between the fiber-matrix interface and the fibers inclined at an angle $\vartheta(\boldsymbol{x})$. In case of TSCL, the fiber angle is dictated by the angle at the center of the plate, θ_O and angle at the free edge, θ_1. The variation of the fiber angle within the laminae is then given by [73–75]:

$$\vartheta(\boldsymbol{x}) = \frac{2(\theta_1 - \theta_0)}{2W}\text{abs}(\boldsymbol{x}) + \theta_0, \tag{3.1}$$

where W is half-width of the plate. For the present study, we assume $2W = 3\,\text{mm}$ and $2L = 6\,\text{mm}$.

The TSCL with different fiber orientations is represented as $\langle\theta_1, \theta_0\rangle$, and the CSCL fiber orientation is represented for a particular choice of the TSCL with $\theta_1 \equiv \theta_0$ (see Fig. 5a). The material properties for the individual layered constituents are given in Table 2. In the model considered, alternate layers of fiber and matrix are arranged and assumes absence of the interface cracking and the micro-cracking mechanisms.

Remark 1 The mode mixity at the crack tip is discussed through the fringe pattern, which is the given: $\sigma_1 - \sigma_2 = n\frac{f_\sigma}{t}$, where h is the plate thickness, f_σ is the fringe

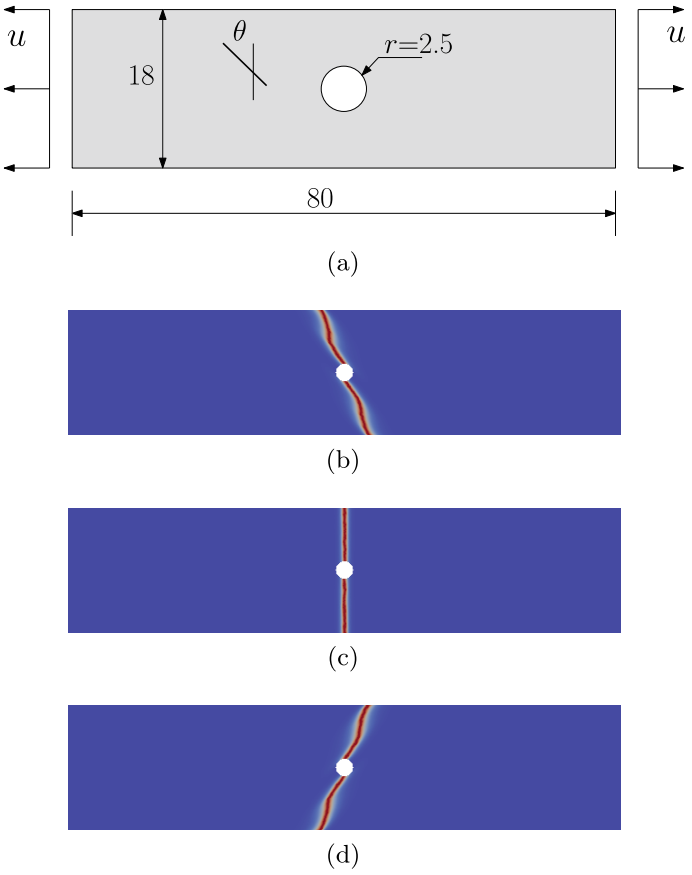

Fig. 4 Plate with circular hole in tension: **a** problem description and boundary conditions, crack trajectory for **b** 45°, **c** 0°, and **d** −45° fiber orientation

constant and the maximum and the minimum principal stresses are given by σ_1 and σ_2, respectively. The orientation of the fringes ahead of the crack tip is an indicator of the crack propagation direction and the fringes can be used to identify the fracture modes [76].

The fracture characteristics of CSCL is discussed first. After the application of the load, when $\mathcal{G} = \mathcal{G}_c$ of the domain, the crack starts to propagate. For a pure far field tension, in case of an isotropic material, the direction of the crack is perpendicular to the loading direction. However, in case of laminates, due the presence of the matrix and the fiber with different material properties, the crack path deviates. This depends on the relative fracture toughness of the matrix and the fiber. In this present study, as the fracture toughness of the fiber is less than that of the matrix, the crack easily propagates in the fiber than the matrix. Figure 6 shows the crack path for CSCL with different fiber orientations, 30°, 45° and 60°. In all the different cases, the crack

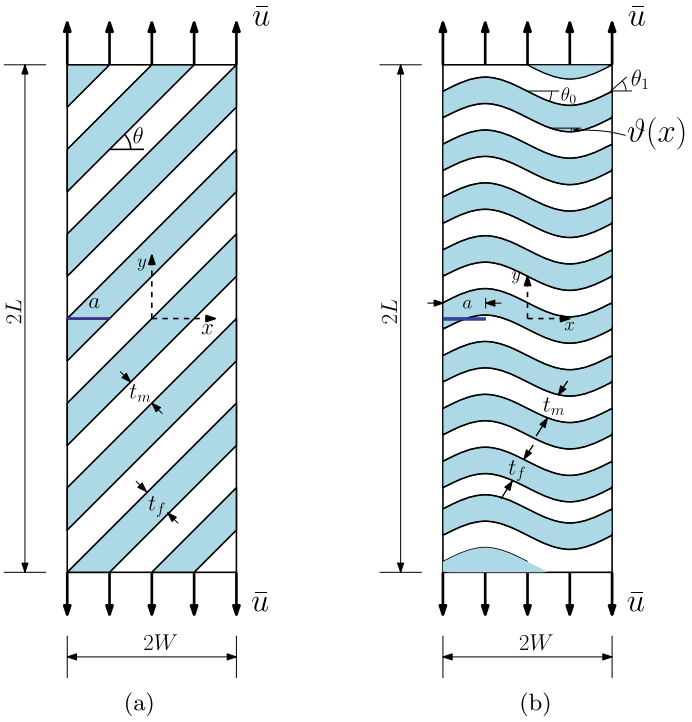

Fig. 5 Schematic representation boundary value problem for: **a** CSCL, **b** TSCL

Table 2 Material parameters for the fiber and the matrix [12]

Material	Young's modulus (N/mm^2)	ν	Fracture toughness (N/mm)
Matrix	$E_{\mathrm{m}} = 70 \times 10^3$	$\nu_{\mathrm{m}} = 0.34$	$\mathcal{G}_{\mathrm{m}} = 0.025$
Fiber	$E_{\mathrm{f}} = 300 \times 10^3$	$\nu_{\mathrm{f}} = 0.14$	$\mathcal{G}_{\mathrm{f}} = 0.005$

growth is along the interface. It is seen that for fiber orientations 45° and 60°, as the initial crack tip is inside the matrix, the crack propagates in the matrix, until it reaches the interface and upon further increase in the load, the propagation is along the interface. Figures 8 and 9 shows the fringe pattern for fiber orientations 45° and 60°. A symmetric pattern is an indicator of mode I fracture whilst an anti-symmetric indicates mixed mode. This is seen in Fig. 8a. It is seen that the crack growth in the matrix is because the influence of the mode-mixity is greater than the fracture toughness of the matrix (see Fig. 6b). Similar behavior has been observed in Fig. 6c, e, f.

Figures 7a, b shows the load-carrying capacity of CSCL for different fiber orientations, viz., 30°, 45° and 60° and for different matrix thickness, $t_m = 0.25$, 0.5 and 0.75. The stress state experienced by the crack tip is strongly influenced by the fiber

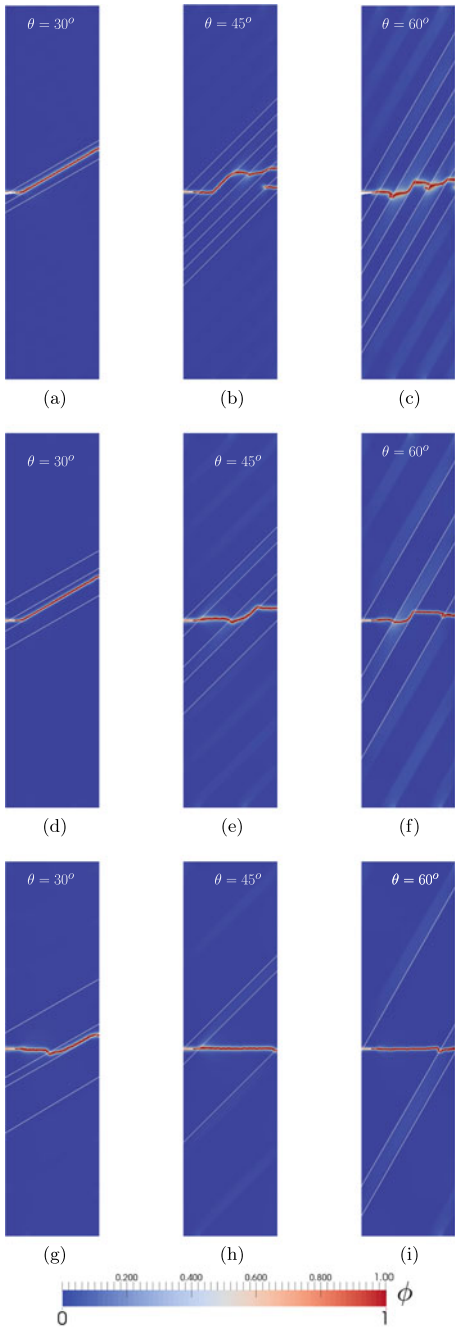

Fig. 6 Phase field variable evolution for CSCL with different fiber orientation and for **a**–**c** $t_{\mathrm{m}} = 0.25$, **d**–**f** $t_{\mathrm{m}} = 0.5$, **g**–**i** $t_{\mathrm{m}} = 0.75$, the interface between the matrix and the fiber is represented by white line

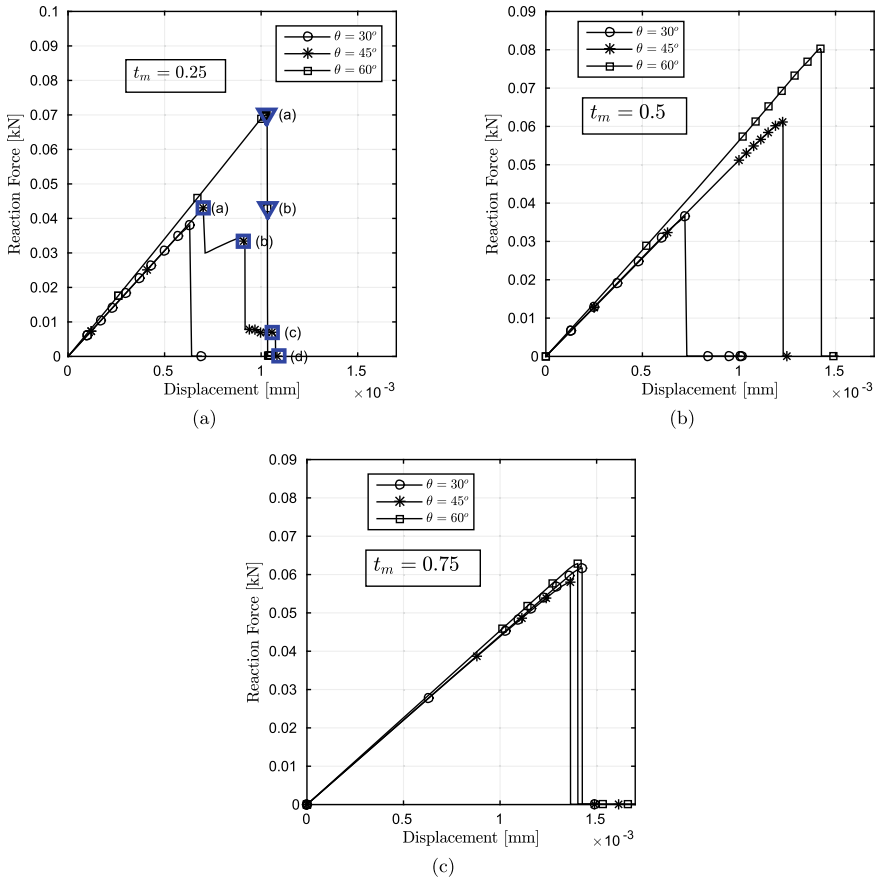

Fig. 7 CSCL subjected to tension: load-displacement for the various fiber orientations for different matrix thickness: **a** $t_{\mathrm{m}} = 0.25$ ([the symbols (**a**–**d**) are the instances at which $\sigma_{\max} - \sigma_{\min}$ are plotted in Figs. 8 and 9), **b** $t_{\mathrm{m}} = 0.5$, **c** $t_{\mathrm{m}} = 0.75$

orientation. Fiber angle with $\theta = 60^\circ$ experiences higher mode-mixity than other orientations. Thus, a laminate with fiber orientation 60° offers higher resistance to crack propagation for a constant matrix thickness. However, the peak load at which the propagation starts is almost independent of the matrix thickness. This is because, as the matrix thickness increases, the inter-matrix spacing increases and the crack grows without the influence of the interface. The evolution of the damage variable, an indicator of the crack propagation, is shown in Fig. 6 for different fiber orientations and for different matrix thicknesses. The while line in Fig. 6 represents the fiber-matrix interface. As seen from Fig. 6 that as the matrix thickness increases, the crack tip is mostly in the matrix, an isotropic material. Hence, the crack grows perpendicular to the direction of the load and independent of the fiber orientation. The presence of the fiber offers less resistance to the crack path.

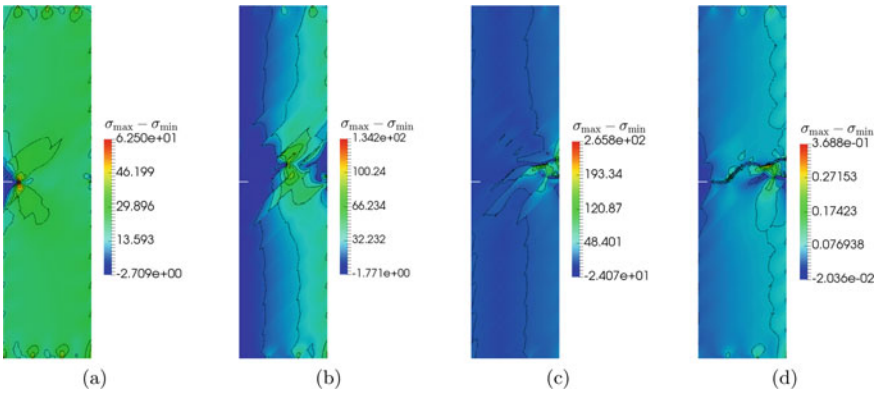

Fig. 8 Fringe pattern for CSCL with fibers at 45° at selected points on the load-displacement curve (c.f. Fig. 7a) for the matrix thickness, $t_{\mathrm{m}} = 0.25$

As seen earlier, for particular fiber orientations and matrix thickness, the growth of the crack is along the matrix-fiber interface. The influence of the fiber orientation on this is depicted in Fig. 10. From the numerical study, it is observed that the greater the matrix thickness and fiber orientation, the longer the crack length along the interface. The mode mixity experienced by the crack tip in case of fiber oriented at 60° is less when compared to the fiber oriented at 45° (see Figs. 8b and 9b). It is also seen that for a particular matrix thickness and fiber orientation 30°, the crack first propagates along the matrix-fiber interface before propagating further in the fiber and this is because, $\mathcal{G}_c^{\mathrm{fiber}} < \mathcal{G}_c^{\mathrm{matrix}}$.

3.1 Tow-Steered Composite Laminates (TSCL)

Next, the crack propagation in the TSCL is analyzed. The domain, the initial crack location, and the essential conditions are shown in Fig. 11. For the analysis, two cases are considered: the initial crack is in the matrix (see, Fig. 11a) and the initial crack is in the fiber (see, Fig. 11b). These are referred to as case I and case II whilst discussing the results. The aim of this is to study the influence of the initial location on the crack trajectory and the load-carrying capacity.

For both cases, the crack growth is in the direction that minimizes mode-II stress intensity factor, until it reaches the fiber-matrix interface (see Fig. 12. However, in case of Case I, the crack kinks into the soft compliant material (fiber) (see, Fig. 12a). This is because the fracture toughness of the fiber is less when compared to the matrix and so it offers less resistance, while it propagates along the interface for case II (see Fig. 12b). This can be attributed to the relatively higher fracture toughness of the matrix. It is further opined that the angle of the fiber does not have a strong influence on the crack propagation path for both cases as seen in Fig. 12.

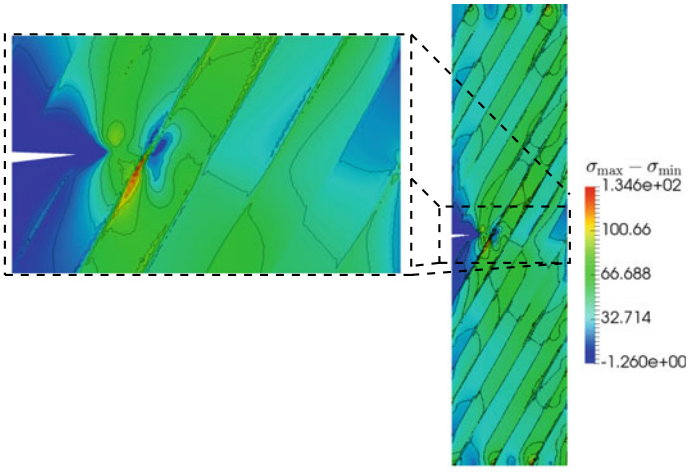

(a)

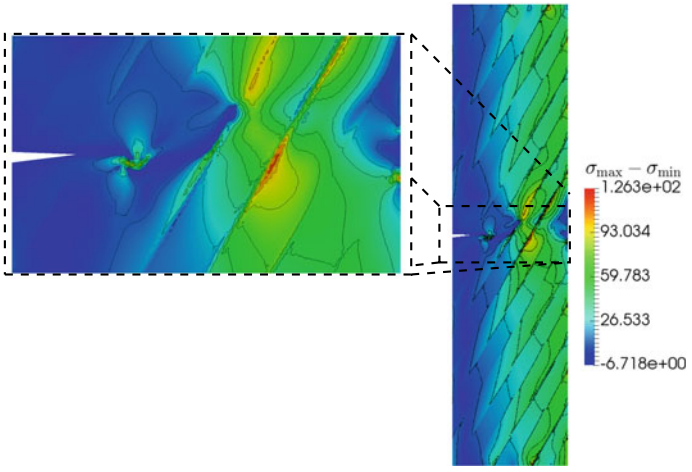

(b)

Fig. 9 Fringe pattern for CSCL with fibers at 60° at selected points on the load-displacement curve (c.f.Fig. 7a) for the matrix thickness, $t_m = 0.25$

The influence of the applied displacement on the reaction force for TSCL (both cases) with fiber orientations $\langle -30°, 0° \rangle$ and $\langle -45°, 0° \rangle$ are shown in Fig. 13. The results for CSCL with fiber orientations 30° and 45° is also shown for comparison. In both cases, the peak load-carrying capacity is higher and this is due to the stiffer matrix material that resists crack propagation. It is inferred that the peak load for TSCL is independent of the cases considered here and significantly higher than the

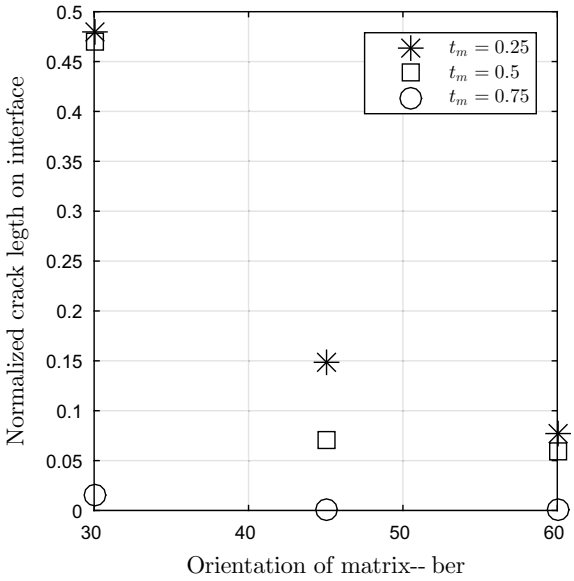

Fig. 10 Dependence of the fiber orientation on the crack length (on the interface) for different matrix thickness, t_{m}

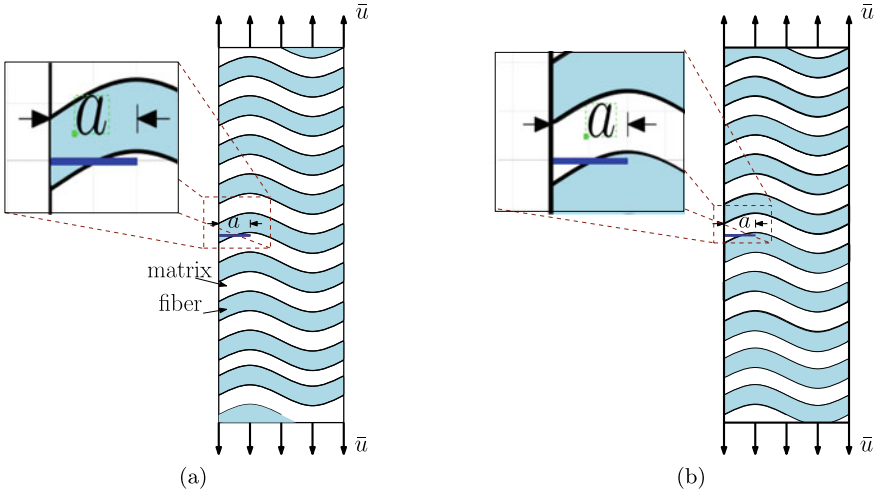

Fig. 11 Representation of an initial crack in TSCL, **a** initial crack in matrix and **b** initial crack tip in the fiber

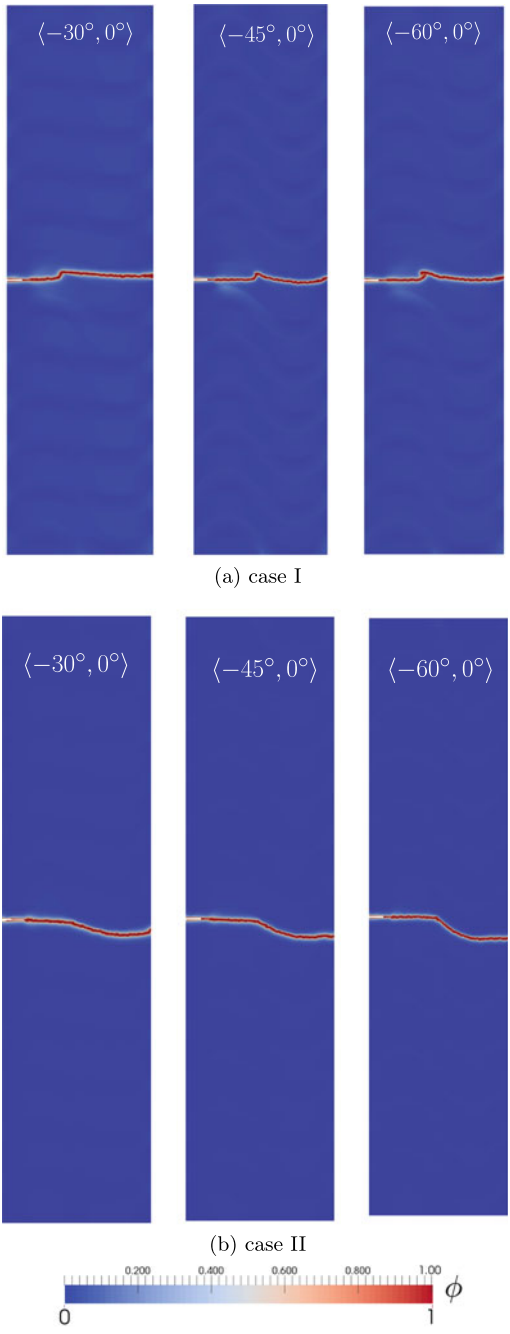

Fig. 12 Crack propagation in TSCL with different fiber orientations ($\langle -30°, 0° \rangle$, $\langle -45°, 0° \rangle$, $\langle -60°, 0° \rangle$)

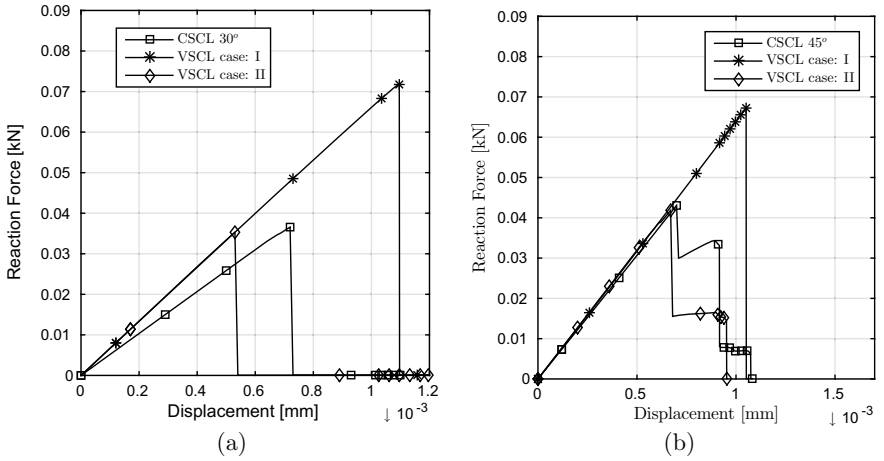

Fig. 13 Load-displacement for CSCL and the TSCL: **a** $\langle -30°,\ 0° \rangle$ and **b** $\langle -45°, 0° \rangle$. In case of TSCL, both the cases are considered

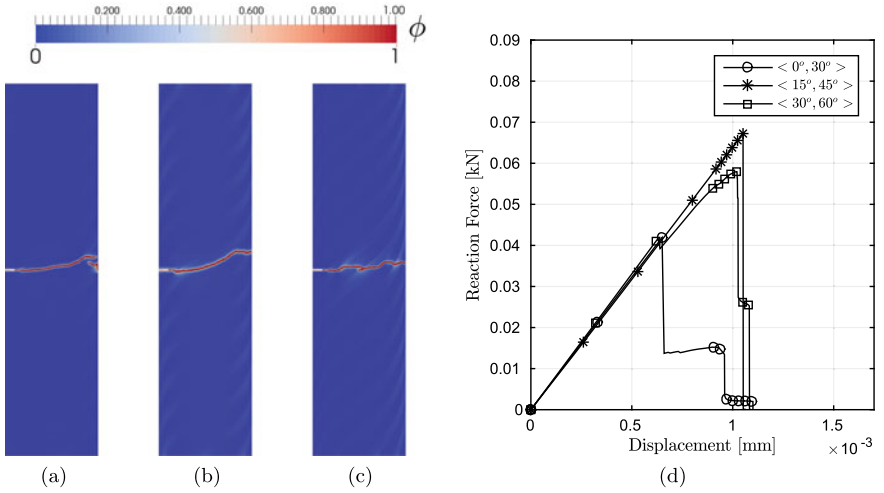

Fig. 14 **a**–**c** evolution of damage for different fiber orientations: $\langle 0°, 30° \rangle$, $\langle 15°, 45° \rangle$ $\langle 30°, 60° \rangle$, respectively, and **d** load-displacement curve for TSCL

CSCL. Figure 14 shows the effect of the combination of center angle θ_0 and θ_1 on the damage evolution and shows that the fiber orientation strongly influences the crack path. The corresponding load-displacement is shown in Fig. 14d.

4 Concluding Remarks

In this chapter, using the phase field method, the fracture characteristics of laminated composites (both straight fibers and tow-steered) are studied. The open source finite element software, FEniCS was used to solve the coupled phase field-elasticity equations. Fracture processes in the homogeneous and orthotropic material are compared against the available results in the literature. The influence of the fiber orientation, tow angle, inter-matrix spacing on the peak load at which the crack starts to propagate and the crack morphology are systematically studied. It can be inferred that for the cases considered, mode-mixity and the matrix material properties significantly influence the crack propagation. The maximum load at which the fracture happens for the CSCL is strongly influenced by the fiber angle for small fiber thickness and is relatively less sensitive for higher inter-fiber spacing. Further, the inter-matrix spacing and the fiber angle directly influences the crack length along the matrix-fiber interface.

References

1. Jones RM (1999) Mechanics of composite materials. Materials science & engineering series, 2nd edn. Taylor & Francis
2. Lugovy M, Orlovskaya N, Berroth K, Kuebler J (1999) Macrostructural engineering of ceramic-matrix layered composites. Compos Sci Technol 59(9):1429–1437
3. Armstrong KB, Bevan LG, Cole WF (2005) Care and repair of advanced composites. Premiere Series Bks, SAE International
4. Clegg WJ, Kendall K, Button TW, McN Alford N, Birchall JD, (1990) A simple way to make tough ceramics. Nature 347(6292):455–457
5. Zhang Y, Tang C, Zhang Y, Liang Z (2007) Fractural process and toughening mechanism of laminated ceramic composites. Acta Mechan Solida Sinica 20(2):141–148
6. de Portu G, Micele L, Pezzotti G (2006) Laminated ceramic structures from oxide systems. Compos Part B Eng 37(6):556–567
7. Tarlazzi A, Roncari E, Pinasco P, Guicciardi S, Melandri C, de Portu G (2000) Tribological behaviour of Al2O3/ZrO2-ZrO2 laminated composites. Wear 244(1):29–40
8. Lopes CS, Gürdal Z, Camanho PP (2008) Variable-stiffness composite panels: Buckling and first-ply failure improvements over straight-fibre laminates. Comput Struct 86(9):897–907
9. Hyer M, Charette R (1989) Use of curvilinear fiber format in composite structure design. In: AIAA/ASME/ASCE/AHS/ASC 30th structures, structural dynamics and materials conference, mobile, AL, pages 2137–2145
10. Hyer M, Lee H (1991) The use of curvilinear fiber format to improve buckling resistance of composite plates with central circular holes. Compos Struct 18:239–261
11. Nagendra S, Kodiyalam S, Parthasarathy V (1995) Optimization of tow fiber paths for composite design. AIAA/ASME/ASCE/AHS/ASC 36th structures, structural dynamics and materials conference, New Orleans, pp 1031–1041
12. Carollo V, Reinoso J, Paggi M (2018) Modeling complex crack paths in ceramic laminates: a novel variational framework combining the phase field method of fracture and the cohesive zone model. J Eur Ceram Soc 38(8):2994–3003
13. Margarita A, Eelco J, Hallett Stephen R, Paul W, Raimund R (2018) Analysis of skin-stringer debonding in composite panels through a two-way global-local method. Compos Struct 202:1280–1294

14. Wang BL, Sun YG, Zhang HY (2008) Multiple cracking of fiber/matrix composites-analysis of normal extension. Int J Solids Struct 45(14):4032–4048
15. Greco F, Leonetti L, Lonetti P, Nevone Blasi P (2015) Crack propagation analysis in composite materials by using moving mesh and multiscale techniques. Comput Struct 153:201–216
16. Maimì P, Camanho PP, Mayugo JA, Turon A (2011) Matrix cracking and delamination in laminated composites. Part I: ply constitutive law, first ply failure and onset of delamination. Mech Mater 43(4):169–185
17. Junya I, Shoichi N, Yoshitake I, Toshihiko K (2008) Fracture elongation of brittle/ductile multilayered steel composites with a strong interface. Scripta Mater 59(10):1055–1058
18. Lacondemine T, Roux-Langlois C, Rouxel T (2017) Role of Poisson's ratio mismatch on the crack path in glass matrix particulate composites. Int J Fract 207(1):73–85
19. Rebillat F, Lamon J, Guette A (2000) The concept of a strong interface applied to SiC/SiC composites with a BN interphase. Acta Mater 48(18):4609–4618
20. Qingda Y, Brian C (2005) Cohesive models for damage evolution in laminated composites. Int J Fract 133:107–137
21. Mohammadi S, Owen DRJ, Peric D (1998) A combined finite/discrete element algorithm for delamination analysis of composites. Finite Elements Anal Des 28:321–336
22. XFEM simulation of delamination in composite laminates (2016) Compos Part Appl Sci Manuf 80:61–71
23. Cahill LMA, Natarajan S, Bordas SPA, O'Higgins RM, McCarthy CT (2013) An Experimental/Numerical investigation in to the main driving force for crack propagation in uni-directional fibre-reinforced composite laminae. Compos Struct 107:119–130
24. Adaptive discrete-smeared crack (A-DiSC) model for multi-scale progressive damage in composites. Compos Part Appl Sci Manuf 125:105513
25. Francfort GA, Marigo JJ (1998) Revisiting brittle fracture as an energy minimization problem. J Mechan Phys Solids 46(8):1319–1342
26. Bourdin B, Francfort GA, Marigo JJ (2000) Numerical experiments in revisited brittle fracture. J Mechan Phys Solids 48(4):797–826
27. Cahn JW, Hilliard JE (1958) Free energy of a nonuniform system. I. interfacial free energy. J Chem Phys 28(2):258–267
28. Chen LQ, Khachaturyan AG (1991) Computer simulation of structural transformations during precipitation of an ordered intermetallic phase. Acta Metall et Mater 39(11):2533–2551
29. Galenko PK, Herlach DM, Funke O, Phanikumar G (2005) Phase-field modeling of dendritic solidification: verification for the model predictions with latest experimental data, chapter 7. Wiley, pp 52–60
30. Nele M, Bart B, Patrick W (2008) An introduction to phase-field modeling of microstructure evolution. Calphad 32(2):268–294
31. Hohenberg PC, Krekhov AP (2015) An introduction to the Ginzburg-Landau theory of phase transitions and nonequilibrium patterns. Phys Rep 572:1–42
32. Aronson I, Kalatsky VA, Vinokur VM (2000) Continuum field description of crack propagation. Phys Rev Lett 85(1):118–121, 7
33. Karma A, Kessler DA, Levine H (2001) Phase-field model of mode III dynamic fracture. Phys Rev Lett 87(4):045501–1–045501–4
34. Hervé H, Herbert L (2004) Dynamic instabilities of fracture under biaxial strain using a phase field model. Phys Rev Lett 93:105504
35. Kuhn C, Müller R (2008) A phase field model for fracture. Proc Appl Math Mech 8(1):10223–10224
36. Kuhn C, Müller R (2010) A continuum phase field model for fracture. Eng Fract Mech 77:3625–3634
37. Amor H, Jacques Marigo J, Maurini C (2009) Regularized formulation of the variational brittle fracture with unilateral contact: numerical experiments. J Mech Phys Solids 57(8):1209–1229
38. Miehe C, Welschinger F, Hofacker M (2010) Thermodynamically consistent phase-field models of fracture: Variational principles and multi-field FE implementations. Int J Numer Methods Eng 83:1273–1311

39. Miehe C, Hofacker M, Welschinger F (2010) A phase field model for rate-independent crack propagation: Robust algorithmic implementation based on operator splits. Comput Methods Appl Mech Eng 199(45–48):2765–2778
40. Borden MJ, Verhoosel CV, Scott MA, Hughes TJR, Landis CM (2012) A phase-field description of dynamic brittle fracture. Comput Methods Appl Mech Eng 217:77–95
41. Marreddy A, Tymofiy G, Le Laura D (2015) A review on phase-field models of brittle fracture and a new fast hybrid formulation. Comput Mech 55(2):383–405
42. Ambati M, Gerasimov T, De Lorenzis L (2015) Phase-field modeling of ductile fracture. Comput Mech 55(5):1017–1040
43. Schlüter A, Kuhn C, Müller R, Tomut M, Trautmann C, Weick H, Plate C (2017) Phase field modelling of dynamic thermal fracture in the context of irradiation damage. Continuum Mech Thermodyn 29(4):977–988
44. Hirshikesh, Natarajan S, Annabattula RK, Martínez-Pañeda E (2019) Phase field modelling of crack propagation in functionally graded materials. Compos Part Eng 169:239–248
45. Doan DH, Bui TQ, Duc ND, Fushinobu K (2016) Hybrid phase field simulation of dynamic crack propagation in functionally graded glass-filled epoxy. Compos Part Eng 99:266–276
46. Zhang P, Yao W, Hu X, Bui TQ (2020) 3D micromechanical progressive failure simulation for fiber-reinforced composites. Compos Struct, page 112534
47. Hirshikesh, Natarajan S, Annabattula RK (2019) Modeling crack propagation in variable stiffness composite laminates using the phase field method. Compos Struct 209:424–433
48. Wilson ZA, Borden MJ, Landis CM (2013) A phase-field model for fracture in piezoelectric ceramics. Int J Fract 183(2):135–153
49. Alex S, Ralf D, Erika T, Ola D (2020) Phase-field fracture modelling of crack nucleation and propagation in porous rock. Int J Fract 224(1):31–46
50. Yin BB, Zhang LW (2019) Phase field method for simulating the brittle fracture of fiber reinforced composites. Eng Fract Mech 211:321–340
51. Espadas-Escalante JJ, van Dijk NP, Isaksson P (2019) A phase-field model for strength and fracture analyses of fiber-reinforced composites. Compos Sci Technol 174:58–67
52. Alessi R, Freddi F (2017) Phase-field modelling of failure in hybrid laminates. Compos Struct 181:9–25
53. Martínez-Pañeda E, Gallego R (2015) Numerical analysis of quasi-static fracture in functionally graded materials. Int J Mech Mater Des 11(4):405–424
54. Kristensen Philip K, Martínez-Pañeda E (2020) Phase field fracture modelling using quasi-newton methods and a new adaptive step scheme. Theoret Appl Fract Mech 107:102446
55. Hirshikesh, Natarajan S, Annabattula RK (2019) A FEniCS implementation of the phase field method for quasi-static brittle fracture. Front Struct Civil Eng 13(2):380–396
56. Bourdin B, Francfort GA, Marigo J-J (2000) Numerical experiments in revisited brittle fracture. J Mech Phys Solids 48(4):797–826
57. Wu J-Y, Nguyen V-P, Nguyen CT, Sutula D, Sinaie S, Bordas S (2019) Phase-field modeling of fracture. Advances in applied mechanics. Elsevier
58. May S, Vignollet J, de Borst R (2015) A new arc-length control method based on the rates of the internal and the dissipated energy. Eng Comput 33(1):100–115
59. Gerasimov T, De Lorenzis L (2016) A line search assisted monolithic approach for phase-field computing of brittle fracture. Comput Methods Appl Mech Eng 312:276–303
60. Blaise B, Francfort GA, Marigo JJ (2008) The variational approach to fracture. Springer, Netherlands
61. Fei Z, Weizhang H, Xianping L, Shicheng Z (2018) Moving mesh finite element simulation for phase-field modeling of brittle fracture and convergence of newton's iteration. J Comput Phys 356(1):127–149
62. Wu J-Y, Nguyen VP (2018) A length scale insensitive phase-field damage model for brittle fracture. J Mech Phys Solids 119:20–42
63. Borden MJ, Hughes TJR, Landis CM, Verhoosel CV (2014) A higher-order phase-field model for brittle fracture: formulation and analysis within the isogeometric analysis framework. Comput Methods Appl Mech Eng 273:100–118

64. Amiri F, Millán D, Arroyo M, Silani M, Rabczuk T (2016) Fourth order phase-field model for local max-ent approximants applied to crack propagation. Comput Methods Appl Mech Eng 312:254–275
65. Markus K, Daniele R, Marc K, McMeeking Robert M (2015) An assessment of the phase field formulation for crack growth. Comput Methods Appl Mech Eng 294:313–330
66. Artina M, Fornasier M, Micheletti S, Perotto S (2015) Anisotropic mesh adaptation for crack detection in brittle materials. SIAM J Sci Comput 37(4):B633–B659
67. Hirshikesh, Jansari C, Kannan K, Annabattula RK, Natarajan S (2019) Adaptive phase field method for quasi-static brittle fracture using a recovery based error indicator and quadtree decomposition. Eng Fract Mech 220:106599
68. Xue Z, Sloan Scott W, Chet V, Daichao S (2017) A modification of the phase-field model for mixed mode crack propagation in rock-like materials. Comput Methods Appl Mech Eng 322:123–136
69. Shuwei Z, Xiaoying Z, Timon R (2019) Phase field modeling of brittle compressive-shear fractures in rock-like materials: a new driving force and a hybrid formulation. Comput Methods Appl Mech Eng 355:729–752
70. Abdulrazzak Msekh M (2017) Phase field modeling for fracture with applications to homogeneous and heterogeneous materials. Phd thesis, Bauhaus-Universität Weimar
71. Felger J, Stein N, Becker W (2017) Mixed-mode fracture in open-hole composite plates of finite-width: an asymptotic coupled stress and energy approach. Int J Solids Struct 122–123:14–24
72. Zhang P, Hu X, Bui TQ, Yao W (2019) Phase field modeling of fracture in fiber reinforced composite laminate. Int J Mech Sci 161–162:105008
73. Yazdani S, Rust W, Wriggers P (2016) Delamination growth in composite laminates of variable stiffness. Int J Numer Methods Eng 108:1406–1424
74. Wu Z, Weaver PM, Raju G, Kim BC (2012) Buckling analysis and optimisation of variable angle tow composite plates. Thin-Walled Struct 60:163–172
75. Wu Z, Raju G, Weaver Paul M (2013) Post-buckling analysis of variable angle tow composite plates. Int J Solids Struct 50(10):1770–1780
76. Ramesh K, Gupta S, Kelkar AA (1997) Evaluation of stress field parameters in fracture mechanics by photoelasticity–Revisited. Eng Fract Mech 56(1):25–45

Chapter 17
An Iso-Geometric Analysis of Tow-Steered Composite Laminates: Free Vibration, Mechanical Buckling and Linear Flutter Analysis

S. Natarajan, S. M. Dsouza, A. L. N. Pramod, Hirshikesh, D. Adak, and K. Kamdi

1 Introduction

Layered materials belong to a new class of engineered materials that typically constitutes of two or more different phases separated by an interface. Due to different chemical and physical properties of the constituent materials, the material properties can be custom tailored to meet demanding low weight-to-strength ratio, improved corrosion and wear resistance [1–4]. Of the available composite materials, fiber reinforced composites are widely studied. This is because, in fiber laminated composites, the fiber volume fraction can be controlled when compared to other composites, such as particle or filament refined composites. Until recently, fiber laminated composites are made up of straight fibers that are homogeneously distributed within a lamina. The macroscopic properties are improved by the constituents mechanical properties, the stacking sequence and thickness of each ply and fiber angle within a lamina. As the fiber angle is constant within a ply, these are also referred to as constant stiffness laminated composites. This has led the researchers to focus on improving the effective property. Thanks to the recent advances in manufacturing, stiffness can now be varied within a lamina [5, 6]. There are many approaches to achieve stiffness variation within a lamina. A few among them are by: (a) changing the fiber angle within a lamina (i.e., use curvilinear fiber) [7–9]; (b) changing the volume fraction of fibers [10, 11]; (c) addition or dropping of plies to the laminates [12, 13] and (d) attaching discrete stiffeners to the laminates. Amongst them, lamina with spatially changing fiber angle is advantageous because, continuous change in fiber orientation avoids sudden change in the thickness which could be a cause for stress concentrations [14]. As the angle of the fiber in the lamina depends on the spatial coordinate and the tow-placement machines control the fiber placement, they are called as tow-steered composite laminates (TSCL).

S. Natarajan (✉) · S. M. Dsouza · A. L. N. Pramod · Hirshikesh · D. Adak · K. Kamdi
Department of Mechanical Engineering, Indian Institute of Technology Madras, Chennai, India
e-mail: snatarajan@iitm.ac.in

S. Sahoo (ed.), *Recent Advances in Layered Materials and Structures*,
Materials Horizons: From Nature to Nanomaterials,
https://doi.org/10.1007/978-981-33-4550-8_17

Composite materials with varying stiffness has received considerable interest amongst researchers and practising engineers, as they may lead to lean design [15–18]. As early as 1990, Hyer and Lee [15] introduced a novel technique to improve the structural response of panels with cutouts by changing the stiffness of the panel in the lamina. Although, the concept of tailored composite was developed two decades back, only recently there is a surge in interest in understanding the response of two-steered composites [19–24]. This can be possible, thanks to the recent advances in manufacturing capability that has made tow-steered composite laminates a reality [25–27]. For TSCL plates, the stiffness coefficients are functions of spatial coordinates as the angle of the fiber is continuously changing. Apart from this, they also exhibit variable bending and coupling stiffness. This can be advantages as a varying fiber angle within a lamina can lead to altered loading paths with improved load carrying capacity. Different plate theories, such as classical plate theory and other shear deformation plate theories to study the response of tow-steered laminated composites. Honda and Narita [28] studied the natural frequencies of laminates with curvilinear paths using classical plate theory. Coburn et al. [29] used the first order shear deformation theory numerically studied the influence of varying fiber angle on the critical buckling load of TSCL panel by generalized Rayleigh-Ritz procedure. The third order shear deformation theory was adopted in the work of Akhavan and coworkers [20, 23, 24] to study both the dynamic and the static response of moderately thick and thin tow-steered composite plates. Their study concluded that the influence of tow-steered fibers are more pronounced in thin plates than thick plates. Aforementioned studies employed either Lagrange based finite elements and/or meshfree approaches and studied the global response of tow-steered composite plates.

In this chapter, vibration, mechanical buckling and linear flutter analysis of tow-steered composite laminates is studied using an iso-geometric analysis framework. Reissner-Mindlin plate theory is used for describing the displacement field and basis splines for spatial discretization. The chapter is organized as follows: an overview of plate theory is presented in Sect. 2, followed by a brief discussion on isogeometric analysis framework in Sect. 3. The section also discussed a numerical procedure to alleviate shear locking syndrome. Section 4 presents numerical results for tow-steered composite laminates, followed by conclusions.

2 Theoretical Formulation

Reissner and Mindlin theory (RMT), an improvement of the CLT to model moderately thick and relatively thin plate. The salient feature of this theory when compared to CLPT is that the through thickness distribution is assumed to be linear. In this section, we present an overview of the RMT and develop the corresponding weak form based on a Galerkin procedure. Figure 1 shows a representation of a three layered plate with a, b as in-plane dimensions and h representing the total plate thickness. The plate aspect ratio is $\frac{a}{b}$ and $\frac{a}{h}$ defines the thickness ratio. Here, only

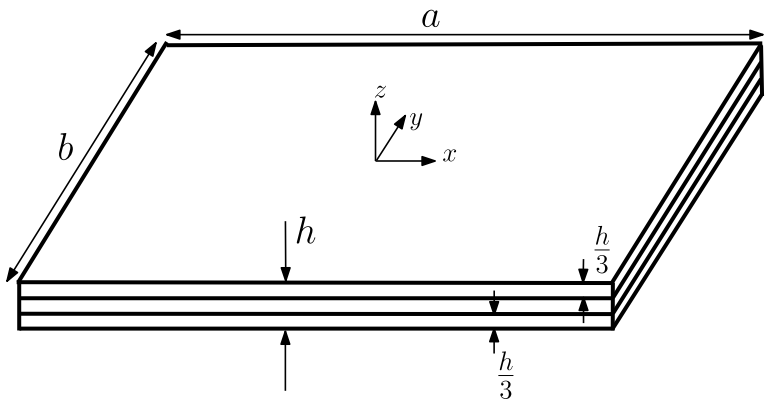

Fig. 1 Composite Laminate plate, a, b and h represents the in-plane dimensions and the total thickness of the plate, respectively

the midplane of the plate occupying an open domain $\Omega \subset \mathbb{R}^2$, with boundary Γ and unit outward normal, $\mathbf{n}$ is considered. The boundary of plate is assumed to accommodate the decompositions over which Dirichlet and Neumann boundary conditions are specified. Any point, P on the plate is represented by a triplet (x, y, z).

Let u_o, v_o, w_o represent the midplane displacements of the plate and β_x and β_y the rotations along x and y axis. The global displacements u, v, w are written in terms of the midplane displacements and rotations as:

$$\begin{pmatrix} u(\mathbf{x},t) \\ v(\mathbf{x},t) \\ w(\mathbf{x},t) \end{pmatrix} = \begin{pmatrix} u_o(x,y,t) \\ v_o(x,y,t) \\ w_o(x,y,t) \end{pmatrix} + z \begin{pmatrix} \beta_x(x,y,t) \\ \beta_y(x,y,t) \\ 0 \end{pmatrix} \tag{1}$$

where $\mathbf{x} = (x, y, z)$. The small strain tensor in vector form is expressed in terms of the displacements by:

$$\boldsymbol{\varepsilon} = \begin{Bmatrix} \varepsilon_{xx} \\ \varepsilon_{yy} \\ 2\varepsilon_{xy} \\ 2\varepsilon_{xz} \\ 2\varepsilon_{yz} \end{Bmatrix} = \begin{Bmatrix} \dfrac{\partial u_o}{\partial x} \\ \dfrac{\partial v_o}{\partial y} \\ \dfrac{\partial u_o}{\partial y} + \dfrac{\partial v_o}{\partial x} \\ \dfrac{\partial w_o}{\partial x} + \beta_x \\ \dfrac{\partial w_o}{\partial y} + \beta_y \end{Bmatrix} + z \begin{Bmatrix} \dfrac{\partial \beta_x}{\partial x} \\ \dfrac{\partial \beta_y}{\partial y} \\ \dfrac{\partial \beta_x}{\partial y} + \dfrac{\partial \beta_y}{\partial x} \\ 0 \\ 0 \end{Bmatrix} \tag{2}$$

The above strain-displacement relation in terms of the mid-plane strain $\boldsymbol{\varepsilon}_p$, bending strain $\boldsymbol{\varepsilon}_b$ and shear strain $\boldsymbol{\varepsilon}_s$ as:

$$\boldsymbol{\varepsilon} = \begin{Bmatrix} \boldsymbol{\varepsilon}_p \\ \mathbf{0} \end{Bmatrix} + \begin{Bmatrix} z\boldsymbol{\varepsilon}_b \\ \boldsymbol{\varepsilon}_s \end{Bmatrix} \tag{3}$$

where

$$\boldsymbol{\varepsilon}_p = \begin{Bmatrix} \dfrac{\partial u_o}{\partial x} \\ \dfrac{\partial v_o}{\partial y} \\ \dfrac{\partial u_o}{\partial y} + \dfrac{\partial v_o}{\partial x} \end{Bmatrix}, \quad \boldsymbol{\varepsilon}_b = \begin{Bmatrix} \dfrac{\partial \beta}{\partial x} \\ \dfrac{\partial \beta}{\partial y} \\ \dfrac{\partial \beta}{\partial y} + \dfrac{\partial \beta}{\partial x} \end{Bmatrix}, \quad \boldsymbol{\varepsilon}_s = \begin{Bmatrix} \beta_x + \dfrac{\partial w}{\partial x} \\ \beta_y + \dfrac{\partial w}{\partial y} \end{Bmatrix} \tag{4}$$

The membrane stress resultants $\mathbf{N}$ and the bending stress resultants $\mathbf{M}$ can be related to the membrane strain $\boldsymbol{\varepsilon}_p$ and bending strain $\boldsymbol{\varepsilon}_b$ through the following relation [30]:

$$\begin{aligned} \mathbf{N} &= \begin{Bmatrix} N_{xx} \\ N_{yy} \\ N_{xy} \end{Bmatrix} = \mathbf{A}\boldsymbol{\varepsilon}_p + \mathbf{B}\boldsymbol{\varepsilon}_b \\ \mathbf{M} &= \begin{Bmatrix} M_{xx} \\ M_{yy} \\ M_{xy} \end{Bmatrix} = \mathbf{B}\boldsymbol{\varepsilon}_p + \mathbf{D}_b\boldsymbol{\varepsilon}_b \end{aligned} \tag{5}$$

where the extensional coefficients $\mathbf{A} = A_{ij}$, bending-extensional coefficients $\mathbf{B} = B_{ij}$ and bending coefficient $\mathbf{D}_b = D_{ij}$ $(i, j = 1, 2, 6)$ are given by:

$$\{A_{ij}, B_{ij}, D_{ij}\} = \int_{-h/2}^{h/2} \overline{Q}_{ij}\{1, z, z^2\}\mathrm{d}z \tag{6}$$

The transverse shear force, $\{Q_{xz}, Q_{yz}\}$ and the transverse shear strain, $\boldsymbol{\varepsilon}$ are related by:

$$\begin{aligned} Q_{xz} &= K_s \int_{-h/2}^{h/2} \sigma_{xz}\mathrm{d}z = K_s\overline{Q}_{55}(\beta_x + w_{0,x}) \\ Q_{yz} &= K_s \int_{-h/2}^{h/2} \sigma_{yz}\mathrm{d}z = K_s\overline{Q}_{44}(\beta_y + w_{0,y}) \end{aligned} \tag{7}$$

with K_s the shear correction factor, $\overline{Q}_{ij}$ in the above equations are called as the global stiffness coefficients that depend on the local stiffness coefficients, which in turn depends on the fiber orientation within the ply. The first element of $\overline{Q}$, i.e., $\overline{Q}_{11}$ is given by:

$$\overline{Q}_{11} = Q_{11}\cos(T(x))^4 + Q_{12}\sin(T(x))^4 + 2(Q_{12} + 2Q_{33})\left[\cos(T(x))^2\sin(T(x))\right]^2 \tag{8}$$

$T(x)$ is the fiber angle in a lamina. In present study, angle within the fiber is a continuous function of the position and is given by:

$$T(x) = T0 - \frac{(T1 - T0)}{a/2}\text{abs}(x), \quad x = \pm a/2 \tag{9}$$

where $T0$ is the angle of the fiber at the center of the plate and $T1$ at the edge. The orientation of the fiber for the k^{th} layer is then represented as $< T0^k|T1^k >$ (see Fig. 2). Theoretically, the fiber can take any value between $-90°$ and $90°$, however, manufacturing difficulties dictate that certain orientations lead to larger curvature that can cause fiber breakage during tow placement [31]. To ensure that the local curvature does not exceed a critical value and that is feasible from a manufacturing guidelines, the following relation is employed:

$$\kappa(x) = -\frac{(T0 - T1)}{a/2}\cos\left(T0 - (T0 - T1)\frac{x}{a/2}\right) < \frac{82}{25} \tag{10}$$

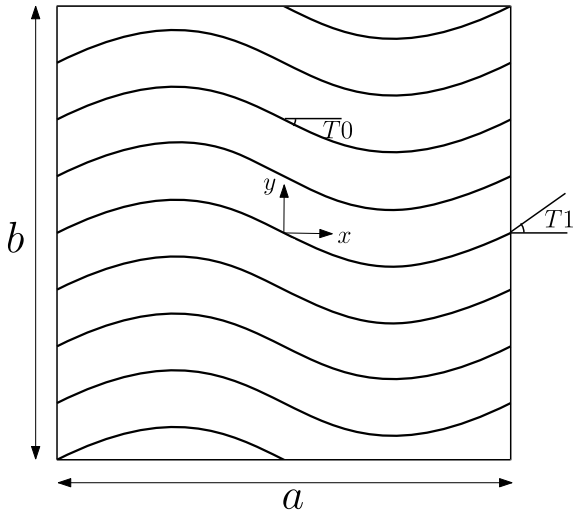

Fig. 2 Geometry of the plate and a representation of tow-steered fibers. The angle is measured in the anti-clockwise direction from the positive x-axis

The local stiffness coefficients, Q_{ij} are given by:

$$\begin{bmatrix} Q_{11} & Q_{12} & Q_{16} \\ Q_{12} & Q_{22} & Q_{26} \\ Q_{16} & Q_{26} & Q_{66} \end{bmatrix} = \begin{bmatrix} \dfrac{E_1}{1-\nu_{12}\nu_{21}} & \dfrac{\nu_{12}E_2}{1-\nu_{12}\nu_{21}} & 0 \\ \dfrac{\nu_{12}E_2}{1-\nu_{12}\nu_{21}} & \dfrac{E_2}{1-\nu_{12}\nu_{21}} & 0 \\ 0 & 0 & G_{12} \end{bmatrix} \tag{11}$$

and $Q_{44} = G_{23}$ and $Q_{55} = G_{13}$. The local fiber direction and the direction perpendicular to it is denoted by subscripts '1' and '2', respectively. This is measured within the plane of the lamina. The local stiffness coefficients, defined at the ply (or lamina) level are transformed to global coordinates by a simple coordinate transformation. In the present study, due to the curvilinear fibers, the coefficient matrices are functions of spatial direction, x. With the above definitions, the strain energy U, the kinetic energy T, externally applied forces V of the composite plate can be written as:
Strain energy:

$$\begin{aligned} U(\boldsymbol{\delta}) &= \frac{1}{2}\int_{\Omega} \{\boldsymbol{\varepsilon}_p^{\mathrm{T}}\mathbf{N} + \boldsymbol{\varepsilon}_b^{\mathrm{T}}\mathbf{M} + \boldsymbol{\varepsilon}_s^{\mathrm{T}}\mathbf{Q}\}\,\mathrm{d}\Omega \\ &= \frac{1}{2}\int_{\Omega} \{\boldsymbol{\varepsilon}_p^{\mathrm{T}}\mathbf{A}\boldsymbol{\varepsilon}_p + \boldsymbol{\varepsilon}_p^{\mathrm{T}}\mathbf{B}\boldsymbol{\varepsilon}_b + \boldsymbol{\varepsilon}_b^{\mathrm{T}}\mathbf{B}\boldsymbol{\varepsilon}_p + \boldsymbol{\varepsilon}_b^{\mathrm{T}}\mathbf{D}\boldsymbol{\varepsilon}_b + \boldsymbol{\varepsilon}_s^{\mathrm{T}}\mathbf{E}\boldsymbol{\varepsilon}_s\}\mathrm{d}\Omega \end{aligned} \tag{12}$$

Kinetic energy:

$$T(\boldsymbol{\delta}) = \frac{1}{2}\int_{\Omega} \{I_0(\dot{u}_0^2 + \dot{v}_0^2 + \dot{w}_0^2) + I_1(\dot{\theta}_x^2 + \dot{\theta}_y^2)\}\mathrm{d}\Omega \tag{13}$$

Work done due to externally applied forces

$$V(\boldsymbol{\delta}) = \int_{\Omega} N_x\left(\frac{\partial u_z}{\partial x}\right)^2 + N_y\left(\frac{\partial u_z}{\partial y}\right)^2 + 2N_{xy}\left(\frac{\partial u_z}{\partial x}\right)\left(\frac{\partial u_z}{\partial y}\right)\mathrm{d}\Omega \tag{14}$$

where $\boldsymbol{\delta} = \{u_o, v_o, w_o, \beta_x, \beta_y\}$ is the nodal degrees of freedom associated to the displacement field in finite element discretization, $I_0 = \int_{-h/2}^{h/2} \rho \mathrm{d}z$ and $I_1 = \int_{-h/2}^{h/2} z^2 \rho \mathrm{d}z$, ρ is the mass density. In addition, in the case of plate immersed in a supersonic flow, the work done by the fluid (non-conservative) should be accounted for, which is given by:

$$W(\boldsymbol{\delta}) = \int_{\Omega} \Delta p\, w\, \mathrm{d}\Omega \tag{15}$$

where Δp is the aerodynamic pressure, which in this study is based on first-order piston theory:

$$\Delta p = \frac{\rho_a U_a^2}{\sqrt{M_\infty^2 - 1}} \left[\frac{\partial w}{\partial x} \cos \Psi + \frac{\partial w}{\partial y} \sin \Psi \right] \tag{16}$$

where ρ_a, U_a, M_∞ and Ψ are the free stream air density, velocity of air, Mach number and flow angle, respectively. The governing equations of motion for: (a) free vibration and (b) mechanical buckling are obtained by writing the Lagrange equations of motion given by:

$$\left[\frac{\partial(-V - U + T)}{\partial \dot{\delta}_i} \right]_{,t} - \left[\frac{\partial(-V - U + T)}{\partial \delta_i} \right] = 0, \quad i = 1, 2, \cdots, n \tag{17}$$

Free vibration To get the finite element equation, we substitute Eqs. (12) and (13) in Eq. (17) and follow standard Galerkin procedure to get:

$$\mathbf{K}\boldsymbol{\delta} + \mathbf{M}\ddot{\boldsymbol{\delta}} = \mathbf{0} \tag{18}$$

where $\mathbf{M}$ is the consistent mass matrix and the following algebraic equation is obtained upon replacing $\ddot{\boldsymbol{\delta}} = \omega^2 \boldsymbol{\delta}$

$$(-\omega^2 \mathbf{M} + \mathbf{K})\boldsymbol{\delta} = 0 \tag{19}$$

where ω is the eigenvalue of the system, also known as the frequency.

Buckling In case of buckling, the discretized equations are obtained upon substituting Eqs. (12) and (14) into Eq. (17):

$$\left[\mathbf{K} - N^{\text{cr}} \mathbf{K}_G\right] \boldsymbol{\delta} = \mathbf{0} \tag{20}$$

where N^{cr} is the buckling load and $\mathbf{K}_G$ is the geometric stiffness matrix that depends on the residual stress. The residual stress state in turn depends on the ply lay-up. To estimate the stress state, for an assumed mechanical load, a pre-buckling displacement field is obtained by solving a static bending problem. Then the geometric stiffness matrix is computed using this stress state. The critical buckling load, N^{cr} is then obtained by solving Eq. (20) using standard eigen routines.

Linear flutter For linear flutter analysis, the Lagrange equations of motion is rewritten after introducing the contribution due to the non-conservative load as:

$$\left[\frac{\partial(-U + W + T)}{\partial \dot{\delta}_i} \right]_{,t} - \left[\frac{\partial(-U + W + T)}{\partial \delta_i} \right] = 0, \quad i \in (1, n) \tag{21}$$

Similar to free vibration and buckling, the finite element equations are obtained by following the Galerkin procedure and is given by:

$$(\mathbf{K} + \lambda \mathbf{K}_{\text{aero}})\, \boldsymbol{\delta} + \mathbf{M}\ddot{\boldsymbol{\delta}} = \mathbf{0} \tag{22}$$

The characteristic of the time function, $\ddot{\boldsymbol{\delta}} = -\omega^2\boldsymbol{\delta}$ is substituted to yield the following equation:

$$\left[-\omega^2\mathbf{M} + \left(\mathbf{K} + \frac{\rho_a U_a^2}{\sqrt{M_\infty^2 - 1}}\mathbf{K}_{\text{aero}}\right)\right]\boldsymbol{\delta} = \mathbf{0} \tag{23}$$

where $\mathbf{K}_{\text{aero}}$ represents the contribution due to the aerodynamic force, When $\frac{\rho_a U_a^2}{\sqrt{M_\infty^2 - 1}} = \lambda = 0$, the system is positive definite and hence $\omega \in \mathbb{R}$. The addition of the aerodynamic matrix to the stiffness matrix, makes the resulting matrix unsymmetric and leads to complex eigenvalue problem when $\lambda > 0$. This is because $\mathbf{K}_{\text{areo}}$ is unsymmetric. As λ is increased monotonically, for a particular pressure, two eigenmodes coalesce and the corresponding eigenvalue becomes complex conjugates. The critical value of the pressure at which the eigenvalue becomes complex conjugates is called the critical aerodynamic pressure, λ_{cr} and upon further increase, the system is unstable.

3 Overview of Iso-Geometric Analysis

This study employs the non-uniform rational basis spline (NURBS) as trial and test functions to represents the geometry and to approximate the unknown field variables within a finite element framework. This is in contrast to the conventional Lagrange type finite elements, where Lagrange polynomials represent the unknown fields and the domain. Introduced and coined as Iso-geometric analysis (IGA) by Hughes and co-workers [32, 33], the IGA has been applied to wider problems. Some of the salient features include: (a) higher continuity of the basis functions (b) exact representation of the geometry within the FE model and (c) seamless link between the CAD and the FEA.

The following information is required to define a B-spline basis functions:

- control points, P_i;
- knot vector, Ξ, a set of parametric values arranged in ascending sequence, $\xi_i \leq \xi_{i+1}, i = 0, 1, \ldots, m-1$;
- the degree of the curve p.

With this information, the B-spline basis function, $N_{i,p}$ of degree p is given by a recurrence relation:

$$\begin{aligned} N_{i,0}(\xi) &= \begin{cases} 1 \text{ if } \xi_i \leq \xi \leq \xi_{i+1} \\ 0 \quad \text{otherwise} \end{cases} \\ N_{i,p}(\xi) &= \frac{\xi - \xi_i}{\xi_{i+p} - \xi_i} N_{i,p-1}(\xi) + \frac{\xi_{i+p+1} - \xi}{\xi_{i+p+1} - \xi_{i+1}} N_{i+1,p-1}(\xi) \end{aligned} \tag{24}$$

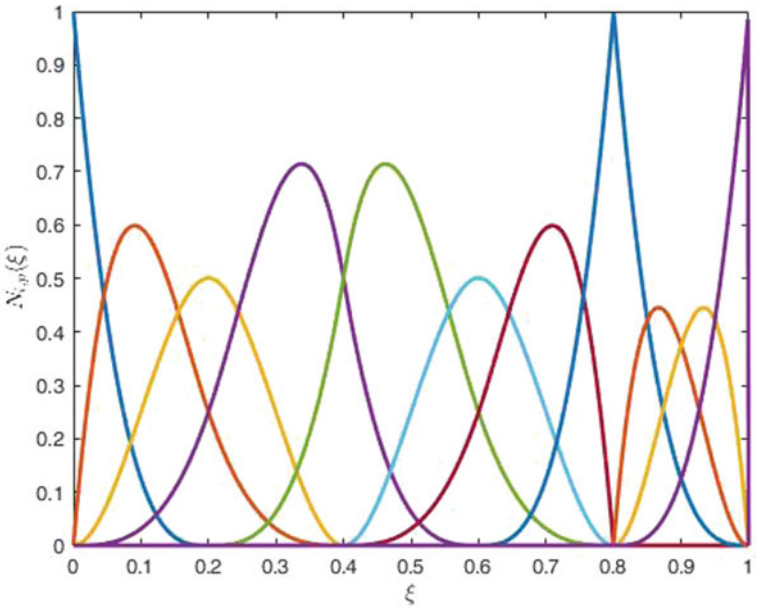

Fig. 3 B-splines for order of the curve, $p = 3$

If each of the control point has an associated weight defined, then the B-splines are termed as non-uniform rational B-splines. A pth degree NURBS curve is written as:

$$\mathbf{C}(\xi) = \frac{\sum_{i=0}^{m} N_{i,p}(\xi) w_i \mathbf{P}_i}{\sum_{i=0}^{m} N_{i,p}(\xi) w_i} \tag{25}$$

Figure 3 shows the fourth order B-splines with a knot vector,

$$\Xi = \{0, 0, 0, 0, 0.2, 0.4, 0.4, 0.6, 0.8, 0.8, 0.8, 1, 1, 1, 1\}$$

.

The important characteristics of NURBS basis functions is that it has all the necessary properties that a Galerkin framework requires, i.e., (i) the basis functions are positive everywhere within the span, (ii) sum of the basis functions is unity; (iii) interpolatory at the end points. Further the key advantage is that the geometry is exactly represented, as the same function is used to describe the geometry. One of the attractive features of these functions is that the continuity can be adapted to the specific needs of the problem. Typically, these are one-dimensional functions and a surface is presented by a tensor product of such one-dimensional functions with

separate knot vectors in each of the parametric dimensions (similar to the case of Lagrange type finite elements) given by:

$$\mathbf{C}(\xi, \eta) = \sum_{i=1}^{n} \sum_{j=1}^{m} N_{i,p}(\xi) M_{j,q}(\eta) \mathbf{P}_{i,j} \tag{26}$$

where $\mathbf{P}_{i,j}$ represents the coordinates of the control net and $N_{i,p}$ and $M_{j,q}$ are the unidirectional B-spline basis functions defined on the knot vectors. With this definition, a NURBS surface can be written as:

$$\mathbf{C}(\xi, \eta) = \frac{\sum_{i=1}^{n} \sum_{j=1}^{m} N_{i,p}(\xi) M_{j,q}(\eta) \mathbf{P}_{i,j} w_i w_j}{w(\xi, \eta)} \tag{27}$$

where $w(\xi, \eta)$ represents the weighting function. The vector of nodal unknowns $\boldsymbol{\delta}$ within the control mesh is approximated by:

$$\boldsymbol{\delta} = \sum_{J} \mathbf{C} \boldsymbol{\delta} \tag{28}$$

Figure 4 shows a representative geometry of the plate and a control net. As seen earlier, the Mindlin theory includes transverse shear deformations and the following condition must be satisfied if Mindlin plate theory is employed to study thin plates:

$$\nabla w + \theta = 0 \tag{29}$$

which states that the shear strain vanishes as the plate becomes thinner. However, when applied to thin plates the NURBS basis functions suffer from shear locking. In this chapter, we employ an artificial shear correction factor introduced by Kikuchi and Ishii [34] originally for 4-noded bilinear element to alleviate the shear locking syndrome, given by:

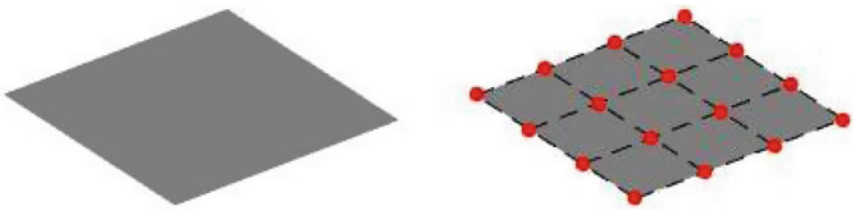

Fig. 4 **a** Plate represented using the NURBS basis functions $p = 3$, with the knot vector, $\Xi = \{0, 0, 0, 0, 1, 1, 1, 1\}$ in both the spatial directions. **b** Red dots indicate the control points and the black dashed lines represent the control mesh

$$K_s^e = K_s \frac{\left(\frac{h}{\beta l_e}\right)^2}{\left(1 + \left(\frac{h}{\beta l_e}\right)^{2n}\right)^{1/n}}, \quad n, \beta \in \mathbb{Z}^+ \tag{30}$$

where l_e is the diameter of the element.

4 Results

In this section, using the IGA framework, we numerically study the free vibration, mechanical buckling and flutter analysis of tow-steered laminated composites. The effect of the following parameters are considered on the output characteristics whilst discussing the results: plate thickness, number of plies and angle of the fiber within the lamina. For all the examples, it is assumed that all layers are of equal thickness and the angle of the fiber is measure with respect to $x-$ axis. In all the cases, cubic NURBS are employed, unless mentioned otherwise. The following Dirichlet conditions are considered for the present study:
Clamped edges:

$$u_o = v_o = w_o = \beta_x = \beta_y = 0 \quad \text{on} \quad x = 0, a \quad \& \quad y = 0, b$$

Simply supported edges:

$$u_o = w_o = \beta_y = 0 \quad \text{on} \quad x = 0, a; \quad v_o = w_o = \beta_x = 0 \quad \text{on} \quad y = 0, b$$

4.1 Free Vibration

Before presenting the results from the present framework, the results from the developed formulation is compared against results in the literature. For this study, 4-layered cross-ply laminated composites with $h = 0.2$ and straight fibers, i.e., $T1 \equiv T0$ are considered. The material properties are: $E_1/E_2 = 10, 40$, $G_{12} = G_{13} = 0.6E_2$, $G_{23} = 0.5E_2$, $\nu_{12} = 0.25$, $\rho = 1$ and $E_2 = E_3$. Table 1 compares the normalized frequency, $\overline{\omega} = \omega \frac{a^2}{h}\sqrt{\frac{\rho}{E_2}}$ from the present framework with that of results in [35, 36]. It is inferred that with mesh refinement the solution converges and yield comparable results. For subsequent discussions, a control mesh of 20×20 with cubic NURBS is employed.

Table 1 First non-dimensionalized frequency $\overline{\omega}$ for a 4-layered cross-ply laminates with $h = 0.2$

Method	Mesh size	$\frac{E_1}{E_2}$	
		10	40
IGA	3× 3	8.1286	10.4800
	5 × 5	8.2355	10.7140
	10 ×10	8.2823	10.8184
	20 ×20	8.2942	10.8450
Ref. [36]		8.2924	10.8490
Ref. [35]		8.2982	10.8540

Table 2 First five fundamental frequency, ω (rad/s) for TSCL. The edges are simply supported

Ref. [14]	IGA			
	10 × 10	20 × 20	30 × 30	$\%\Delta_{30\times30}$
309.1	315.0	309.9	309.1	0.0136
503.3	530.5	509.3	505.9	0.5245
852.1	954.0	867.4	854.3	0.2627
1143.5	1203.4	1144.0	1134.3	0.8053
1297.3	1416.1	1324.8	1296.2	0.0805

Next, the results from the present framework are compared for tow-steered composite laminates. In this case, the laminated plate is consists of three layers with ply configuration:

$$\langle 30^\circ, 0^\circ\rangle, \langle 45^\circ, 90^\circ\rangle, \langle 30^\circ, 0^\circ\rangle$$

The plate thickness, $h = 0.01$ and the material properties are: (E_1, E_2, G_{12}, G_{13}, G_{23}, ν_{12}, ν_{13}, ν_{23}) = (173 GPa, 7.2 GPa, 7.2 GPa, 3.76 GPa, 3.76 GPa, 3.76 GPa, 0.29, 0.29, 0.29) and $\rho = 1540\,\mathrm{kg/m^3}$ are used for the study. The numerical convergence of the first five fundamental frequencies are presented in Table 2.

First, the free vibration characteristics of TSCL is studied. Two-layered anti-symmetric ($\langle T0, T1\rangle$, $\langle -T0, -T1\rangle$) and three-layered symmetric ($\langle T0, T1\rangle$, $\langle -T0, -T1\rangle$, $\langle T0, T1\rangle$) TSCL is considered. In both cases, $T0 \in [0, 90]^\circ$ and $T1 \in [-90, 90]^\circ$. It is noted that, some of these angles may not be feasible due to manufacturing constraints discussed earlier. However, they are presented here for qualitative discussions. The non-dimensionalized first fundamental frequency for two and three layered composites is depicted in Fig. 5. Following observations can be made for the two layered anti-symmetric laminate (see Fig. 5a):

→ the plate has maximum fundamental frequency when the fiber angle is in the range $T1 = -60^\circ$ and -45°;
→ the plate has minimum frequency when $T1 > 0$, irrespective of the angle at the center $T0$;

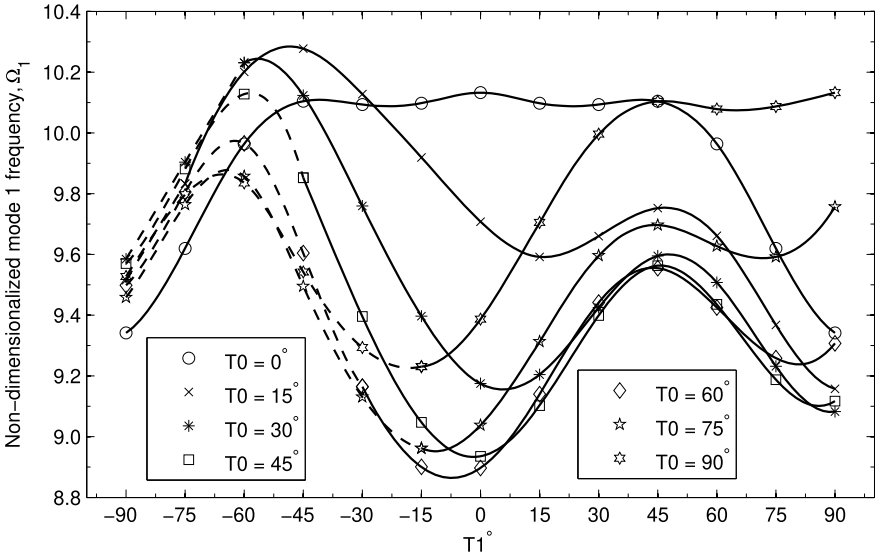

(a)

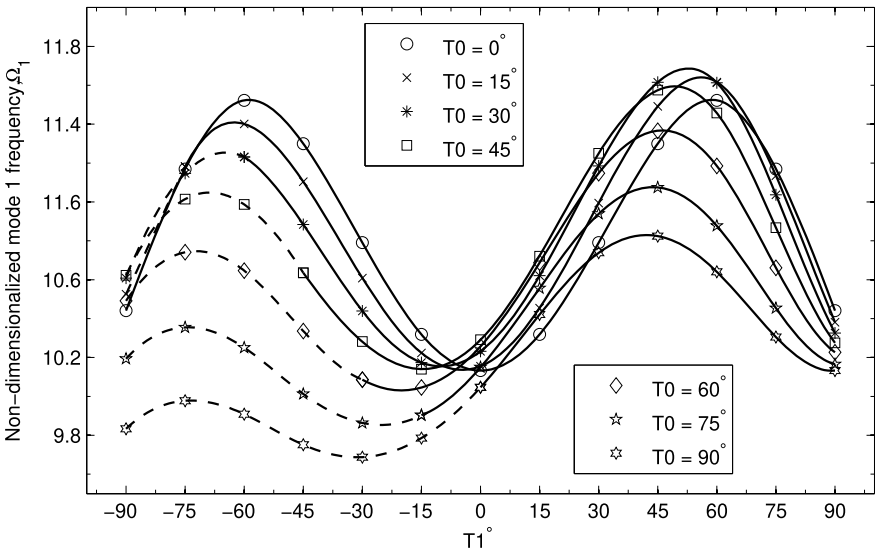

(b)

Fig. 5 Non-dimensional fundamental frequency as a function of tow-angles: **a** 2-layered anti-symmetric and **b** 3-layered symmetric tow-steered composite laminate

→ with increasing $T0$ from zero, the variation of fundamental frequency losses its symmetric with respect to $T1 = 0$;
→ the dotted lines represent the range of angles for which the constraint condition is violated.

Variation of non-dimensionalized first fundamental frequency with $T1$ for constant $T0$ for a three-layered symmetric laminate is shown in Fig. 5b. It is seen that for a particular choice of $T0$, the response of three-layered and two-layered are qualitatively similar. In this case, the maximum frequency occurs when $T1$ is $-45°$ and $60°$ for all choices of $T0$. Of all the combinations, the plate has the highest first mode frequency $\langle T0, T1\rangle = \langle 30°, 45°\rangle$. Similar to the two-layered composites, the dotted lines represent the combination of center and edge angle for which the manufacturing constraint on the curvature of the fiber is violated. It is noted that the value of the edge angle $T1$ at which the extremum frequency occurs is reversed between two and three layered composite laminates considered here.

4.2 Buckling

Next, for the two- and three- layered tow-steered composite laminate, the mechanical buckling characteristics is studied. In case of two-layered system, the layer configuration is represented by: $(\langle T0, T1\rangle, \langle -T0, -T1\rangle)$ and for three-layered symmetric the ply arrangement is as follows: $(\langle T0, T1\rangle, \langle -T0, -T1\rangle, \langle T0, T1\rangle)$. In this case, $T1$ is assumed to be between $-90°$ and $90°$ and $T0$ is varied between $0°$ and $90°$. Figure 6a shows the N_{xx}^{cr} due to mechanical forces. It is inferred that N_{xx}^{cr} is symmetric with respect to fiber edge angle ($T2 = 0$), when $T1 = 0°$, however, the symmetry is lost for other values of $T1$. The critical buckling load is maximum when center angle is $15°$ and end angle is $-60°$ and the minimum when $T1 > 0°$. Similarly,the influence of the spatial variation of the fiber angle ($T0/T1$) on the N_{xx}^{cr} for a 3-layered composite is studied. Critical buckling load numerically computed is depicted in Fig. 6b. From Fig. 6b, it is inferred that for a particular $T0$, the variation of buckling load is similar to two-layered composite. For 3-layered, the $\max(N_{xx}^{\text{cr}})$ occurs when $T1 = \pm 60°$ and $T0 = 0°$. The angles for which the manufacturing constraint is violated in shown with dashed lines in Fig. 6. For the three-layered composite laminate, the range of negatively tow-steered fiber angle $T1$, without violating the manufacturing constraint is limited, similar to the two-layered case. It is concluded that the $T1$ strongly influences the critical buckling load of the composite, irrespective of the number of layers.

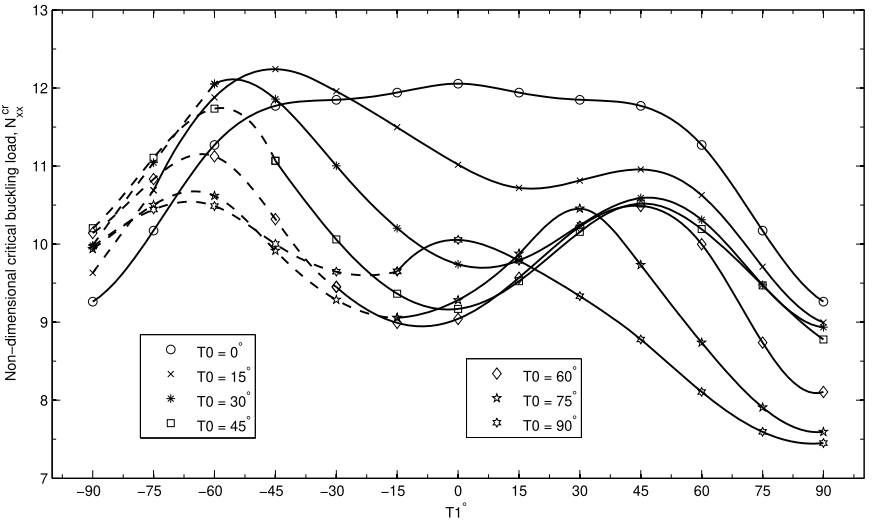

(a)

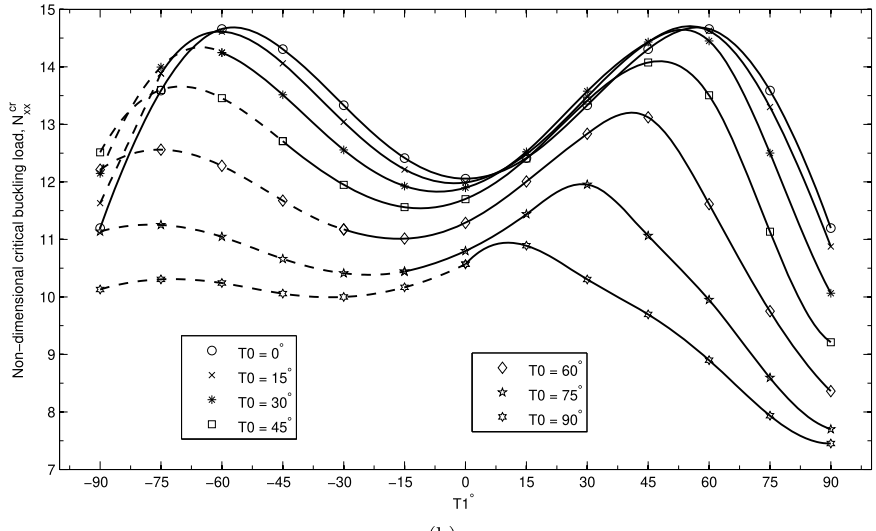

(b)

Fig. 6 Critical buckling load as a function of $T1$ for: **a** 2-layered and **b** 3-layered tow-steered composite laminates. Note that $T0 \in [0, 90]°$

4.3 Linear Flutter

Next, the aerodynamic response of tow-steered composite laminate is studied using the iso-geometric analysis framework. The plate is immersed in a supersonic flow. Although, the developed framework is general, the results are presented only for a square plate. The plate is assumed to consist of three layers with following three different ply configurations:

$$\langle 30°, 0°\rangle; \langle 45°, 90°\rangle; \langle 30°, 0°\rangle$$

$$\langle 45°, -45°\rangle, \langle -45°, -60°\rangle, \langle 0°, 45°\rangle$$

$$\langle 90°, 45°\rangle, \langle 60°, 30°\rangle, \langle 90°, 45°\rangle$$

The influence of h and the edge conditions on the critical aerodynamic pressure is also studied. Table 3 presents the effect of orientation of the fiber, plate thickness and the boundary condition on the critical aerodynamic pressure at which the plate experiences flutter and the corresponding frequency. It can be inferred that decreasing the plate thickness, the critical aerodynamic pressure increases and it is greater in case of clamped when compared to all edges simply supported, as expected. The

Table 3 Frequency—critical aerodynamic pressure for a tow-steered composite laminated for different boundary conditions and plate aspect ratios

Fiber orientation	$\frac{h}{a}$	SSSS		CCCC	
		λ_{cr}	ω_{cr} ($\times 10^4$)	λ_{cr}	ω_{cr} ($\times 10^4$)
$\langle 30°, 0°\rangle$, $\langle 45°, 90°\rangle$, $\langle 30°, 0°\rangle$	0.01	2937.69	0.6960	4145.51	1.8503
	0.02	2890.04	0.6931	3993.95	1.7842
	0.10	1931.45	0.5855	2200.98	0.9994
$\langle 45°, -45°\rangle$, $\langle -45°, -60°\rangle$, $\langle 0°, 45°\rangle$	0.01	3097.85	0.8779	4865.04	1.7863
	0.02	3045.51	0.8699	4655.66	1.7331
	0.10	2078.32	0.6986	2191.60	0.9599
$\langle 90°, 45°\rangle$, $\langle 60°, 30°\rangle$, $\langle 90°, 45°\rangle$	0.01	961.91	0.5692	1454.88	1.7307
	0.02	947.07	0.5601	1386.91	1.6345
	0.10	683.01	0.3941	515.82	1.5001

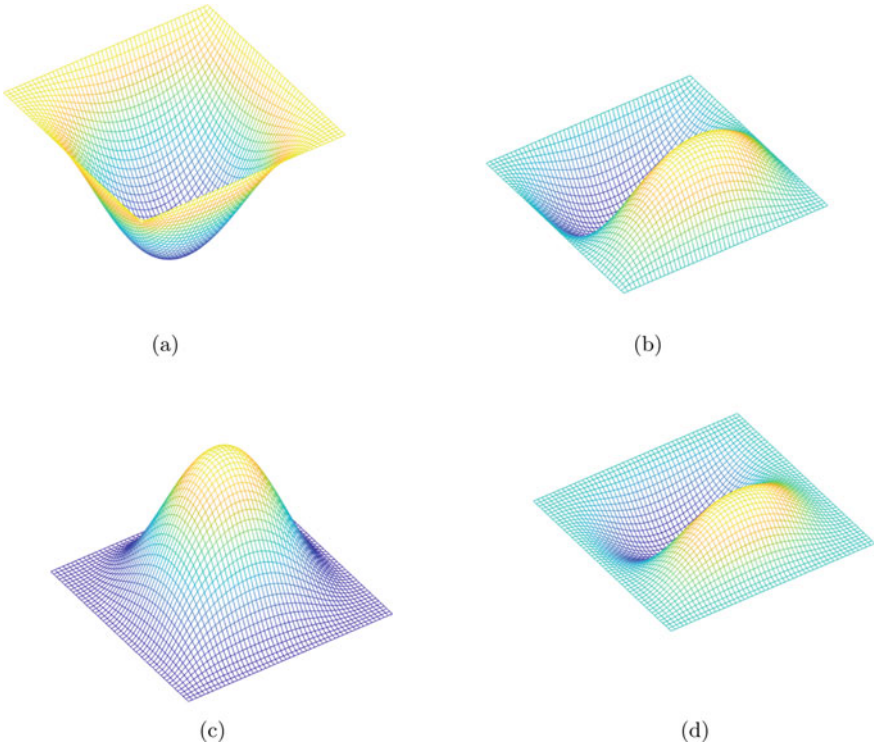

Fig. 7 First two mode shapes for: **a**–**b** simply supported and **c**–**d** fully clamped square plate with fiber orientation: $\langle 45°, -45° \rangle$, $\langle -45°, -60° \rangle$, $\langle 0°, 45° \rangle$ with $\frac{a}{h} = 100$

above observation is valid for the three different ply configurations considered. The free vibration and the flutter mode shapes for the first two fundamental frequency is shown in Figs. 7 and 8 for $h = 0.01$ and for clamped and simply supported edge conditions. The flutter mode shape is supported with the variation of frequency and critical aerodynamic pressure, depicted in Fig. 9. From Fig. 9 it is seen that with increasing pressure, the frequency increases and for a particular pressure, which is referred to as the critical aerodynamic pressure, the mode shape coalesce and the frequencies becomes complex conjugate.

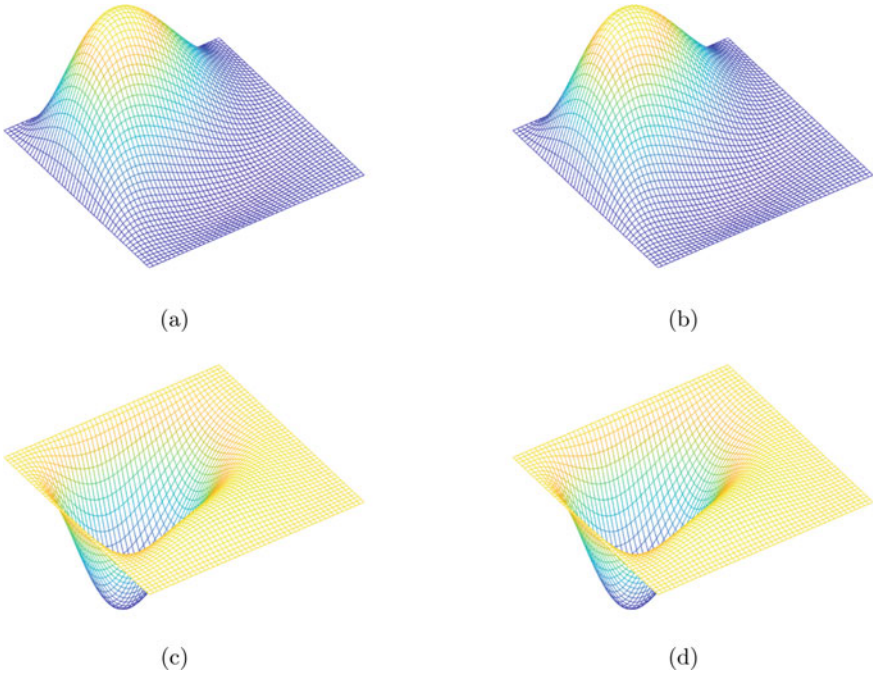

Fig. 8 Square plate immersed in a supersonic flow—mode shape for **a**–**b** all edges simply supported and **c**–**d** fully clamped plate. Plate thickness $h = 0.01$ and has three layers with fiber orientation: $\langle 45°, -45° \rangle$, $\langle -45°, -60° \rangle$, $\langle 0°, 45° \rangle$ with $\frac{a}{h} = 100$

5 Concluding Remarks

In this chapter, the free vibration, mechanical buckling and linear flutter characteristics of tow-steered composite laminate is numerically studied using an iso-geometric analysis. It is opined that the systematic parametric study done will be useful for practising designers who are interested in the design and the optimization of tow-steered laminates. Some observations are: the first fundamental frequency, buckling and flutter characteristics are strongly influenced by the spatial variation of the orientation of the fiber. The influence of increasing aspect/thickness ratio increases the fundamental frequency whilst it reduces the critical buckling load. Similar observations can be derived for the case when the plate is immersed in a supersonic flow. Due to manufacturing constraint, the practically feasible range of orientation of the fiber depends on angle at the center.

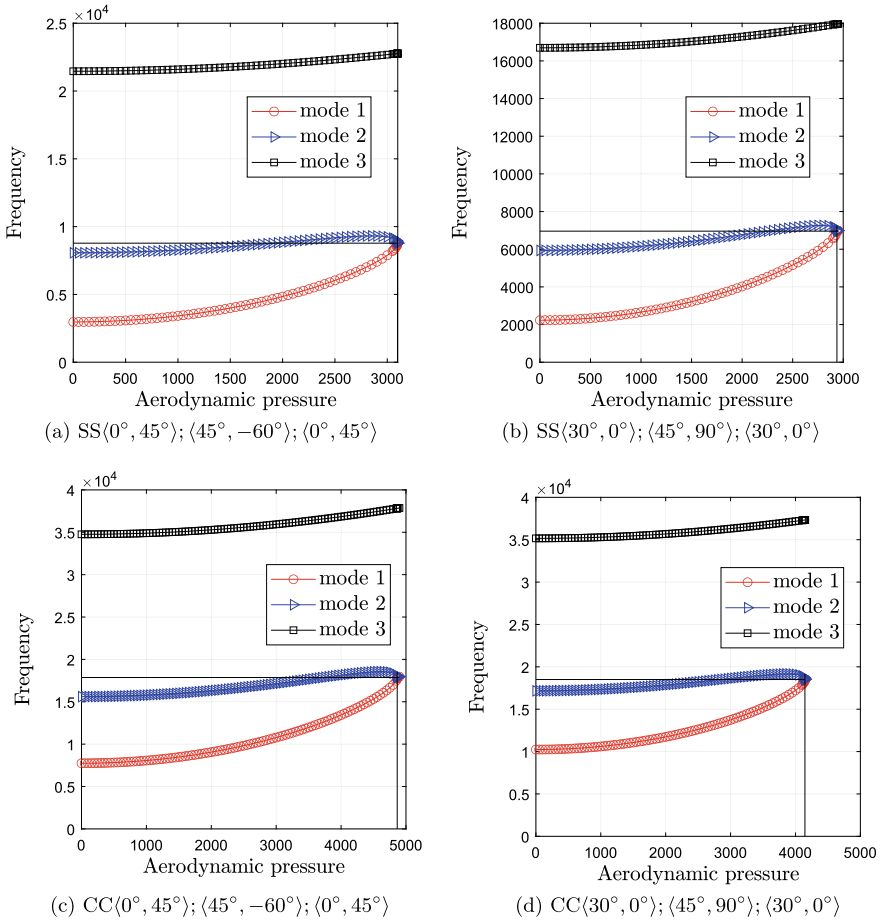

(a) SS$\langle 0°, 45°\rangle$; $\langle 45°, -60°\rangle$; $\langle 0°, 45°\rangle$

(b) SS$\langle 30°, 0°\rangle$; $\langle 45°, 90°\rangle$; $\langle 30°, 0°\rangle$

(c) CC$\langle 0°, 45°\rangle$; $\langle 45°, -60°\rangle$; $\langle 0°, 45°\rangle$

(d) CC$\langle 30°, 0°\rangle$; $\langle 45°, 90°\rangle$; $\langle 30°, 0°\rangle$

Fig. 9 Frequency-aerodynamic pressure plot for **a**–**b** full simply supported and **c**–**d** clamped square plate immersed in a supersonic flow

References

1. Altenbach H (2011) Mechanics of advanced materials for lightweight structures. Proc Inst Mech Eng Part C J Mech Eng Sci 225(11):2481–2496
2. Reddy JN (2004) Mechanics of laminated composite plates and shells: theory and analysis. CRC Press
3. Ullah H, Harland AR, Silberschmidt VV (2015) Mater Des 88:149–156
4. Wang Y, Liu X, Zhu C, Parsons A, Liu J, Huang S, Ahmed I, Rudd C, Sharmin N (2019) Production and characterisation of novel phosphate glass fibre yarns, textiles, and textile composites for biomedical applications. J Mech Behav Biomed Mater 99:47–55
5. Gurdal Z, Olmedo R (1993) In-plane response of laminates with spatially varying fiber orientations-variable stiffness concept. AIAA J 31(4):751–758
6. Hyer MW, Lee HH (1991) The use of curvilinear fiber format to improve buckling resistance of composite plates with central circular holes. Compos Struct 18(3):239–261

7. Tatting BF (1998) Analysis and design of variable stiffness composite cylinders. Ph.D. thesis. Virginia Tech
8. Wu KC, Gurdal Z (2006) Variable stiffness panel structural analyses with material nonlinearity and correlation with tests. In: 47th AIAA/ASME/ASCE/AHS/ASC structures, structural dynamics, and materials conference 14th AIAA/ASME/AHS adaptive structures conference 7th, p 2165
9. Lopes CS, Gürdal Z, Camanho PP (2008) Variable-stiffness composite panels: buckling and first-ply failure improvements over straight-fibre laminates. Comput Struct 86(9):897–907
10. Setoodeh S, Gürdal Z, Watson LT (2006) Design of variable-stiffness composite layers using cellular automata. Comput Methods Appl Mech Eng 195(9–12):836–851
11. Senocak E, Tanriover H (2007) Analysis of composite plates with variable stiffness using galerkin method. Aeronaut J 111(1118):247–255
12. Cairns DS, Mandell JF, Scott ME, Maccagnano JZ (1999) Design and manufacturing considerations for ply drops in composite structures. Compos Part B Eng 30(5):523–534
13. Her S-C (2002) Stress analysis of ply drop-off in composite structures. Compos Struct 57(1–4):235–244
14. Ribeiro P, Akhavan H, Teter A, Warmiński J (2014) A review on the mechanical behaviour of curvilinear fibre composite laminated panels. J Compos Mater 48(22):2761–2777
15. Hyer MW, Lee HH (1991) The use of curvilinear fiber format to improve buckling resistance of composite plates with central circular holes. Compos Struct 18:239–261
16. Setoodeh S, Abdalla MM, Ijsselmuiden ST, Gürdal Z (2008) Design of variable stiffness composite panels for maximum buckling load. Compos Struct 87:109–117
17. Lopes CS, Gürdal Z, Camanho PP (2010) Tailoring for strength of composite steered fibre panels with cutouts. Compos Part A Appl Sci Manufact 41:1760–1767
18. Khani A, IJsselmuiden MM, Abdalla Z, Gürdal ST (2011) Design of variable stiffness panels for maximum strength using lamination parameters. Compos Part B Eng 42:546–552
19. Abdalla MM, Gürdal Z, Abdelal GF (2009) Thermomechanical response of variable stiffness composite panels. J Therm Stress 32:187–208
20. Akhavan H, Ribeiro P (2011) Natural modes of vibration of variable stiffness composite laminates with curvilinear fibers. Compos Struct 93:3040–3047
21. Raju G, Wu Z, Kim BC, Weaver PM (2012) Prebuckling and buckling analysis of variable angle tow plates with general boundary conditions. Compos Struct 94:2961–2970
22. Raju G, Wu Z, Weaver PM (2013) Postbuckling analysis of variable angle tow plates using differential quadrature method. Compos Structs 106:74–84
23. Akhavan H, Ribeiro P, de Moura MFSF (2013) Large deflection and stresses in variable stiffness composite laminates with curvilinear fibers. Int J Mech Sci 73:14–26
24. Akhavan H, Ribeiro P, de Moura MFSF (2013) Composites laminates with linear varying fiber angles under static and dynamic loads. In: 54th AIAA/ASME/ASCE/AHS/ASC Structures, structural dynamics and materials Conference April 8–11, 2013 Boston, Massachusetts
25. Kim BC, Potter K, Weaver PM (2012) Continuous tow shearing for manufacturing variable angle tow composites. Compos Part A Appl Sci Manufact 43:1347–1356
26. Kim BC, Weaver PM, Potter K (2014) Manufacturing characteristics of the continuous tow shearing method for manufacturing of variable angle tow composites. Compos Part A Appl Sci Manufact 61:141–151
27. Falcó O, Mayugo JA, Lopes CS, Gascons N, Turon A, Costa J (2014) Variable stiffness composite panels: as-manufactured modeling and its influence on the failure behavior. Compos Part B Eng 56:660–669
28. Honda S, Narita Y (2012) Natural frequencies and vibration modes of laminated composite plates reinforced with arbitrary curvilinear fiber shape paths. J Sound Vib 331:180–191
29. Coburn BH, Wu Z, Weaver PM (2014) Buckling analysis of stiffened variable angle tow panels. Compos Struct 111:259–270
30. Natarajan S, Baiz PM, Bordas S, Rabczuk T, Kerfriden P (2011) Natural frequencies of cracked functionally graded material plates by the extended finite element method. Compos Struct 93(11):3082–3092

31. Akhavan H, Ribeiro P (2011) Natural modes of vibration of variable stiffness composite laminates with curvilinear fibers. Compos Struct 93(11):3040–3047
32. Cottrell JA, Hughes TJR, Bazilevs Y (2009) Isogeometric analysis: toward integration of CAD and FEA. Wiley
33. Nguyen VP, Simpson RN, Bordas SPA, Rabczuk T (2012) An introduction to isogeometric analysis with matlab implementation: Fem and xfem formulations, p 6. arXiv preprint arXiv:1205.2129
34. Kikuchi F, Ishii K (1999) An improved 4-node quadrilateral plate bending element of the Reissner-Mindlin type. Comput Mech 23:240–249
35. Khdeir AA, Librescu L (1988) Analysis of symmetric cross-ply elastic plates using a higher-order theory: part II: buckling and free vibration. Eur J Mech A Solids 31:259–277
36. Liew KM, Huang YQ, Reddy JN (2003) Vibration analysis of symmetrically laminated plates based on FSDT using the moving least squares differential quadrature method. Comput Methods Appl Mech Eng 192:2203–2222